*materials*

Special Issue Reprint

# Behavior of Metallic and Composite Structures (Third Volume)

Edited by
Tomasz Sadowski and Holm Altenbach

mdpi.com/journal/materials

MDPI

# Behavior of Metallic and Composite Structures (Third Volume)

# Behavior of Metallic and Composite Structures (Third Volume)

Guest Editors

**Tomasz Sadowski**
**Holm Altenbach**

MDPI

Basel • Beijing • Wuhan • Barcelona • Belgrade • Novi Sad • Cluj • Manchester

| *Guest Editors* | |
|---|---|
| Tomasz Sadowski<br>Department of Solid Mechanics<br>Lublin University of Technology<br>Lublin<br>Poland | Holm Altenbach<br>Institute of Materials, Technologies and Mechanics<br>Otto-von-Guericke-Universität Magdeburg<br>Magdeburg<br>Germany |

*Editorial Office*
MDPI AG
Grosspeteranlage 5
4052 Basel, Switzerland

This is a reprint of the Special Issue, published open access by the journal *Materials* (ISSN 1996-1944), freely accessible at: https://www.mdpi.com/journal/materials/special_issues/behavior_third.

For citation purposes, cite each article independently as indicated on the article page online and as indicated below:

Lastname, A.A.; Lastname, B.B. Article Title. *Journal Name* **Year**, *Volume Number*, Page Range.

**ISBN 978-3-7258-5133-1 (Hbk)**
**ISBN 978-3-7258-5134-8 (PDF)**
**https://doi.org/10.3390/books978-3-7258-5134-8**

# Contents

# About the Editors

**Tomasz Sadowski**

Tomasz Sadowski received his Ph.D. from the Institute of Fundamental Technological Research (Polish Academy of Sciences) in 1985. He is permanently employed at Lublin University of Technology (Poland), now in a full professor position. He worked as a visiting professor at the University of Illinois in Chicago (USA), the Technical University of Munich (Germany), the Technical University of Darmstadt (Germany), Martin Luther University Halle-Saale (Germany), the University of Wales Swansea (UK), Polytechnic Marche Ancona (Italy), and others. In 2005, within the 5th Framework Programme of the European Union, he received an Individual Marie Curie Fellowship for Transfer of Knowledge to University of Wales. He has published 185 papers (Scopus) and has been organiser or co-organiser of many international conferences and five scientific courses at the Centre for Mechanical Sciences in Udine (Italy). In 2016, he received a Doctor Honoris Causa from Ovidius University of Constanta, Romania. He coordinated four European Union projects within 5FP, 6FP and 7FP. T.S adowski' current research interests include continuum damage mechanics of materials and structures; modelling of ceramic polycrystalline materials; modelling of composites, such as ceramic and polymer matrices, polymer foams, wood and plywood; fracture mechanics of materials under mechanical loading and thermal shock; plates with damage and sandwich structures; and experimental testing of materials and structures under static, cyclic, thermal, and impact loading.

**Holm Altenbach**

The main research directions of Prof. Holm Altenbach include the modelling and simulation of structural elements under creep and damage conditions, the modelling of metallic and polymeric foams on different scales, the structural analysis of elements made from functionally graded materials, thin-walled structures made of composites, generalized continua, etc.

Prof. Holm Altenbach is involved in international scientific and educational projects with Poland, Ukraine, Latvia, China, Vietnam, and other countries. The results of his fundamental research are published in international reviewed journals, monographs, textbooks, and edited books. Prof. Holm Altenbach is involved in the organisation of national and international conferences as an invited or keynote speaker, as a section organiser, and as a member of the scientific committees. He has organised nine courses in the International Centre of Mechanics in Udine (Italy) (among them are courses devoted to creep mechanics, to composite mechanics, and to foam structures). He has been a member of four PhD Graduate Schools.

The achievements of prof. Holm Altenbach were recognised within the University and outside. He was awarded the Gold Medal of the Faculty of Mechanical Engineering of the Politechnika Lubelska, the Semko-Medal, and the Dr.h.c. of the National Technical University in Kharkov (Ukraine), of the Ovidius University of Constanța (Romania) and Ivane Javakhishvili Tbilisi State University (Georgia). He is a foreign member of the National Academy of Sciences, Ukraine. He is a Member of several Editorial boards (e.g., *Mechanics of Composite Materials*/Latvia, *Journal of Strain Analysis*/UK, *Technische Mechanik*/Germany). Since 2005, he has been the Editor-in-Chief of the oldest German journal in the field of Mechanics, *ZAMM*.

# Preface

Various types of metallic and composite structures are used in modern engineering practice. For aerospace, car industry, or civil engineering applications, the most important are thin-walled structures made of different types of metallic alloys, fibrous composites, laminates, and multifunctional materials with a more complicated internal microstructures of reinforcement, including nanoparticles or nanofibers. The current applications in modern engineering require the analysis of structures of various properties, shapes, and sizes (e.g. aircraft wings), including structural hybrid joints, subjected to different types of loadings: quasi-static, dynamic, cyclic, thermal, impact, penetration, etc.

The advanced metallic and composite structures should satisfy multiple structural functions during operating conditions. Structural functions include mechanical properties like strength, stiffness, damage resistance, fracture toughness, damping, etc. Non-structural functions include electrical and thermal conductivities, sensing, actuation, energy harvesting, self-healing capability, electromagnetic shielding, etc.

The aim of this SI is to understand the basic principles of damage growth and fracture processes in advanced metallic and composite structures that also include structural joints. Currently, it is widely recognized that important macroscopic properties, like macroscopic stiffness and strength, are governed by processes that occur at one to several scales below the level of observation. A thorough understanding of how these processes influence the reduction of stiffness and strength forms the key to the analysis and design of existing and improved innovative structural elements.

The study of how these various length scales, nano-, micro-, and meso-, can be bridged or taken into account simultaneously in multiscale models is particularly attractive for composite materials and structural elements, since they have a well-defined structure at the above-specified levels.

**Tomasz Sadowski and Holm Altenbach**
*Guest Editors*

materials

*Article*

# Some Inconsistencies in the Nonlinear Buckling Plate Theories—FSDT, S-FSDT, HSDT

**Zbigniew Kolakowski * and Jacek Jankowski**

Department of Strength of Materials, Faculty of Mechanical Engineering, Lodz University of Technology,
Stefanowskiego 1/15, PL-90-924 Lodz, Poland; jacek.jankowski@p.lodz.pl
* Correspondence: zbigniew.kolakowski@p.lodz.pl

**Abstract:** Bending and membrane components of transverse forces in a fixed square isotropic plate under simultaneous compression and transverse loading were established within the first-order shear deformation theory (FSDT), the simple first-order shear deformation theory (S-FSDT), and the classical plate theory (CPT). Special attention was drawn to the fact that bending components were accompanied by transverse deformations, whereas membrane components were not, i.e., the plate was transversely perfectly rigid. In the FSDT and the S-FSDT, double assumptions concerning transverse deformations in the plate hold. A new formulation of the differential equation of equilibrium with respect to the transverse direction of the plate, using a variational approach, was proposed. For nonlinear problems in the mechanics of thin-walled plates, a range where membrane components should be considered in total transverse forces was determined. It is of particular significance as far as modern composite structures are concerned.

**Keywords:** nonlinear theories of plate structures; CPT; FSDT; S-FSDT; shear forces; bending and membrane components of transverse forces; transversally inextensible plate; square plate

## 1. Introduction

Reissner [1,2] proposed to extend the Timoshenko linear beam theory accounting for a transverse shear effect on the plate theory based on the stress approach 75 years ago. A few years later, Mindlin [3] developed a displacement-based theory, in which it was assumed that transverse shear stresses were constant through the plate thickness. In the case of plates transversely perfectly rigid and at the Mindlin shear correction coefficient $k^2 = 5/6$, the same stresses were obtained from the Reissner and Mindlin plate theories [4]. Therefore, they are referred to under the common name of the Reissner–Mindlin plate theory. Theoretical considerations and a comparison of both the theories are to be found, for instance, in [5–7]. Shear theories of higher orders were discussed in [8–13]. In [13], for the functionally graded materials (FGM) plates, a general third-order shear plate theory, in which geometrical nonlinearities were analyzed, was presented. Simplifications of the general theory with 11 general displacements up to 5 displacements for the Reddy third-order theory through the first-order plate theory and to 3 displacements in the classical plate theory (CPT) were proposed.

In [14–16], particular attention was focused on the Reissner boundary effect by an introduction of the rotary potential being a fast-variable solution to the boundary layer. Expressions for the mixed finite element based on the mechanism of a shear locking phenomenon were introduced in [17]. The shear locking phenomenon for the boundary layer in membrane elements was discussed in [6,17–19] and was devoted to the finite element method. In the finite element method (FEM), the shear locking phenomenon occurs because a fast-variable solution to the boundary layer cannot be approximated with shape functions [14,20].

Within plate theories covering shearing the first-order shear deformation theory (FSDT), other approaches were developed as well, namely: a two-variable refined plate theory discussed in, for example, [21–27] and a single-variable refined theory [28].

Endo and Kimura [21] proposed the simple first-order shear deformation theory (S-FSDT). According to this theory, not the angle of rotation in bending but deflection is the primary variable. It imposed simultaneous restrictions on neglecting Reissner boundary effects [2,15]. A number of equations was reduced, and the boundary conditions were altered. In [25–27], two independent variables $\varphi$ and $w_s$ were considered, which yielded two differential equations together with boundary conditions. These differential equations are uncoupled in the static analysis, and thus the boundary conditions should be uncoupled as well, however it is impossible. It follows from the fact that a variation in operation of transverse forces is expressed through a difference in virtual displacements. Hence, the fundamental principle of independence of variations is not fulfilled, similarly as it takes place in the FSDT.

A more comprehensive literature survey was presented in [29]. Special attention was paid to membrane components of transverse forces which accompany an appearance of membrane forces in the plate, as predicted by the nonlinear theories: the CPT, the S-FSDT, and the FSDT. It is necessary to apply nonlinear theories to analyze post-buckling equilibrium paths, and in the cases when the plate is subject to loading (e.g., with a transverse load) leading to finite deflections of the plate.

Bending components of transverse forces depend on derivatives of moments, which are accompanied by transverse deformations. These components of forces are linearly dependent on deflection. Membrane components are related to projections of membrane forces on the transverse direction and are nonlinearly dependent on deflection, or more precisely, on deflection raised to the third power. Membrane components of transverse forces do not affect transverse deformations; that is to say, the plate is perfectly rigid with respect to the $z$ axis for these components. Thus, in the nonlinear theories—the FSDT and the S-FSDT—double assumptions hold in regard to transverse deformations. For the CPT, an assumption of the plate being perfectly rigid transversely, in which linear bending components, referred to as equivalent Kirchhoff forces and nonlinear membrane components occur, holds. In [29], resultants of these forces were called total equivalent Kirchhoff forces. According to a particular case of Stokes' theorem, i.e., Green's theorem, in which the surface integral for the equilibrium equations changes into a plate circumference-oriented integral (i.e., for the boundary conditions), a concept of total equivalent Kirchhoff transverse forces has to be introduced [30].

A transverse shear effect exerts an important influence on the behavior of composite materials characterized by low values of properties referring to transverse shearing [31, 32].

The achievements of the last decade in the shear deformation theory of thin-walled structures have been discussed in review articles [33–42], among others.

In the present study, the authors continue their considerations included in [29] in regard to components of transverse forces within the FSDT, the S-FSDT, and the CPT. A detailed analysis is devoted to a square steel plate fixed along all edges and subject to simultaneous compression and transverse loading. Such an example was assumed due to an easy interpretation of the results. In [29], the equations of equilibrium and the boundary conditions following from a variation of the system total energy were derived in detail. The Reissner boundary effect was neglected in the FSDT and the S-FSDT. In the variational approach to the CPT, total equivalent Kirchhoff forces 'emerge themselves' in the equations [29]. In the present study, only fundamental equations and their solution for the plate under consideration within the Reissner's FSDT and the Mindlin's approach to the S-FSDT (i.e., for two independent functions of displacements along the $z$ axis—the total lateral displacement $w$ and the bending deflection $\varphi$) and the CPT are discussed.

The three theories presented here, as well as the example, have been known for a long time. Special attention is paid to two components of total transverse forces, i.e., bending components, which are accompanied by transverse deformations, and membrane components, which are not accompanied by transverse shear deformations. Thus, various assumptions in regard to transverse deformations for components of transverse forces are discussed. The above remarks contribute to a disputable nature of this paper.

## 2. Formulation of the Problem

A nonlinear problem of the distribution of transverse forces in thin-walled plates under simultaneous compression along one direction and the transverse load $q$ was investigated. The problem was solved for a square isotropic plate fixed along the whole circumference. The material the plate was made of was assumed to be ruled by Hooke's law.

Attention was drawn to the theoretical background related to components of transverse forces and a detailed analysis of the distribution of transverse shear forces was carried out. In the analysis, three thin-walled plate theories were considered: the classical plate theory (CPT) (i.e., the Kirchhoff plate theory), the simple first-order shear deformation theory (S-FSDT) in a version of the two-variable refined plate theory, and the Reissner plate theory (FSDT).

The equations of equilibrium and the boundary conditions for the above-mentioned three theories were derived in detail within a variational approach in [29]. In the Appendix A to this study, only the equations necessary to make the paper more articulate are included. A solution for the square isotropic plate, with special attention focused on membrane and bending components of transverse forces, is presented as well.

Total transverse shear forces (cf. FSDT (A13), S-FSDT (A21), CPT (A28) in the Appendix A, respectively) have two components. Bending components are expressed with the formulas (A11)-FSDT, (A19)-S-FSDT, (A26)-CPT, correspondingly, and they depend on the derivatives of inner moments in the plate. On the other hand, membrane components are expressed with (A12)-FSDT, (A20)-S-FSDT, (A27)-CPT and are related to projections of membrane forces on the direction perpendicular to the central plate plane.

The problem under discussion was solved with two nonlinear equations within the nonlinear theories. One of the them is an equation of inseparability of deformations dependent on the function of forces $F$ and the deflection $w$. The second equation is an equation of equilibrium of transverse projections of inner forces on the transverse direction, where we account for the transverse loading $q$, which is written in a simplified version for the three theories under consideration according to (A14), (A22), and (A29) (see the Appendix A) as

$$\int_0^{\ell}\int_0^{b}\left[\left(\hat{Q}^{\theta}_{x,x}+\hat{Q}^{\theta}_{y,y}\right)+\left(\overline{Q}^{\theta}_{x,x}+\overline{Q}^{\theta}_{y,y}\right)+q\right]\delta w dx dy=0 \tag{1}$$

where the upper index $\theta = F, S, C$ refers to the FSDT, the S-FSDT, and the CPT, correspondingly.

Hence, further on, the following indexes are introduced: C for the CPT; S for the S-FSD, and F for the FSDT, respectively.

In the first round bracket in (1), linear bending components of transverse forces occur, whereas nonlinear membrane components are to be found in the second bracket. According to (A11) for the FSDT, bending components are expressed as a sum of partial derivatives of the bending moment and the torque. In regard to the S-FSDT, it is a similar sum, with such a difference that there is a factor 2 at the torque derivative (cf. (A19) to (A11)). Thus, bending components in the S-FSDT are higher than in the FSDT. For the CPT, formula (A26) is identical as for the S-FSDT. It should be remembered that the expressions for the component moments are, however, different. According to (A61), the respective membrane components of transverse forces $\overline{Q}^{\theta}_{x}, \overline{Q}^{\theta}_{y}$ in (1) for the three theories under consideration are identical, because they depend solely on the variables $F, w$, which do not affect transverse deformations.

Equation (1) has been expressed in an unusual way in order to draw attention to total transverse forces. When relationships (A13), (A21), and (A28) concerning total transverse forces are considered, Equation (1) can be formulated ultimately as

$$\int_0^\ell \int_0^b [\widetilde{Q}^\theta_{x,x} + \widetilde{Q}^\theta_{y,y} + q]\delta w dxdy = 0 \tag{2}$$

In the above-mentioned two equations, a variation with respect to the defection $w$ is included. For the equations derived in [29] in regard to the FSDT and the S-FSDT, components of transverse forces on possible displacements are, respectively

- FSDT

$$\int_0^\ell \int_0^b [Q_x\delta(w_{,x} - \psi_x) + Q_y\delta(w_{,y} - \psi_y)]dxdy \tag{3}$$

- S-FSDT

$$\int_0^\ell \int_0^b [Q_x\delta(w_{,x} - \varphi_{,x}) + Q_y\delta(w_{,y} - \varphi_{,y})]dxdy \tag{4}$$

when a variation in the plate total potential energy is used.

According to variational principles, Equations (3) and (4) have to be formulated with mutually independent variations of displacements, which is not satisfied in this case. From the authors' viewpoint, it causes the differential equations to be uncoupled with respect to variations, although the boundary conditions are coupled [29].

Equation (1) for the CPT, when (A24) and two first equations (A10) are accounted for according to (A8) and (A25), leads to one of the commonly known von Karman equations and the second equation is an equation of inseparability of deformations (A9).

$$\int_0^\ell \int_0^b [w_{,xxxx} + 2w_{,xxyy} + w_{,yyyy} + F_{,yy}w_{,xx} - 2F_{,xy}w_{,xy} + F_{,xx}w_{,yy}]\delta w dxdy = 0 \tag{5}$$

## 3. Results of the Calculations

A square steel plate (Figure 1) characterized by the geometrical dimensions and material constants equal to: $a$ = 100 mm, $h$ = 1 mm, E = 200 GPa, $\nu$ = 0.3 was analyzed in detail.

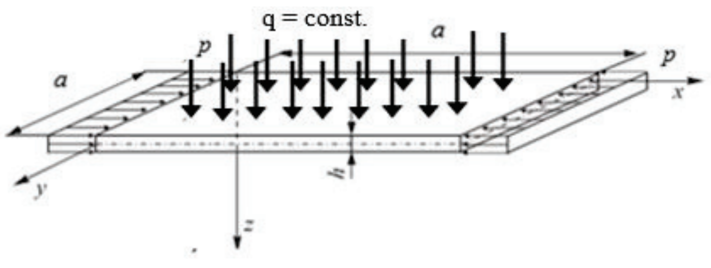

**Figure 1.** Square plate fixed along all edges and subject to simultaneous compression and uniform transverse load.

The perfect plate was fixed along each edge and uniformly compressed with the stresses $p$ along the $x$ axis direction and subject to the transverse load $q$. The boundary conditions for the three theories under analysis are to be found in the Appendix A.

In the theoretical solution to the nonlinear problem, a simultaneous interaction of the compression $p$ and the transverse load $q$ was considered so that membrane inner forces could occur, and, consequently, membrane components of transverse forces. In the numerical calculations, two particular cases were analyzed, namely:

- Case A—$p^C \neq 0$ and $q^C = 0$;
- Case B—$p^C = 0$ and $q^C \neq 0$.

It results from the fact that for the compressive load $p^C$ in the membrane component (A42) $\overline{Q}_x^C$ along the compression direction for the CPT, the last term is linearly dependent on the deflection $W$, similarly as the bending components. The remaining components of membrane forces are nonlinear with respect to $W$.

In Table 1, results of calculations for both the cases of loads for the assumed values of the dimensionless deflection *W/h* equal to 0.5, 1.0, 1.5, 2.0, respectively, are presented. For the compressive load (Case A), a critical value of load was given and a value of compressive stress, maximal absolute values of bending and membrane components, and total transverse forces were defined for the CPT for the fixed deflection. In regard to the transverse load (Case B), values of the load $q$, maximal absolute values of bending and membrane components, and total transverse forces were determined at the given deflection as in the former case. Concerning the S-FSDT and the FSDT, values of the reduction factor (A45) $\alpha = 1/(1+\eta)$ and values of total transverse forces only for both the cases were given additionally.

**Table 1.** Values of loads of the square plate and values of absolute maximal components and total transverse forces.

| **Symbole** | | | **Load** | | | | | | | |
|---|---|---|---|---|---|---|---|---|---|---|
| Theory | Symbol | Unit | Case A | | | | Case B | | | |
| | | | W/h | | | | | | | |
| | | | 0.5 | 1.0 | 1.5 | 2.0 | 0.5 | 1.0 | 1.5 | 2.0 |
| CPT | $p_{cr}^C$ | MPa | 192.8 | | | | 0.0 | | | |
| | $p^C$ | - | 203 | 236 | 291 | 368 | 0.0 | | | |
| | $q^C$ | MPa | 0.0 | | | | 0.075 | 0.17 | 0.32 | 0.54 |
| | $\left\lvert \hat{Q}_x^C \right\rvert_{\max}$ | $N/\text{mm}$ | 2.10 | 4.20 | 6.30 | 8.40 | 2.10 | 4.20 | 6.30 | 8.40 |
| | $\left\lvert \hat{Q}_y^C \right\rvert_{\max}$ | $N/\text{mm}$ | 2.10 | 4.20 | 6.30 | 8.40 | 2.10 | 4.20 | 6.30 | 8.40 |
| | $\left\lvert \overline{Q}_x^C \right\rvert_{\max}$ | $N/\text{mm}$ | 0.08 | 0.72 | 2.94 | 7.40 | 0.13 | 1.06 | 3.56 | 8.44 |
| | $\left\lvert \overline{Q}_y^C \right\rvert_{\max}$ | $N/\text{mm}$ | 0.13 | 1.06 | 3.56 | 8.44 | 0.13 | 1.06 | 3.56 | 8.44 |
| | $\left\lvert \widetilde{Q}_x^C \right\rvert_{\max}$ | $N/\text{mm}$ | 2.06 | 4.79 | 8.95 | 15.3 | 2.22 | 5.16 | 9.63 | 16.4 |
| | $\left\lvert \widetilde{Q}_y^C \right\rvert_{\max}$ | $N/\text{mm}$ | 2.22 | 5.16 | 9.63 | 16.4 | 2.22 | 5.16 | 9.63 | 16.4 |
| S-FSDT | $p_{cr}^S$ | MPa | 192.6 | | | | 0.0 | | | |
| | $\alpha$ | - | 0.9989 | | | | | | | |
| | $\left\lvert \widetilde{Q}_x^S \right\rvert_{\max}$ | $N/\text{mm}$ | 2.05 | 4.79 | 8.95 | 15.3 | 2.22 | 5.16 | 9.62 | 16.4 |
| | $\left\lvert \widetilde{Q}_y^S \right\rvert_{\max}$ | $N/\text{mm}$ | 2.21 | 5.16 | 9.62 | 16.4 | 2.22 | 5.16 | 9.62 | 16.4 |
| | $\left\lvert \overline{Q}_x^S \right\rvert_{\max} / \left\lvert \widetilde{Q}_x^S \right\rvert_{\max}$ | - | 0.04 | 0.15 | 0.33 | 0.48 | 0.06 | 0.20 | 0.37 | 0.51 |
| | $\left\lvert \overline{Q}_y^S \right\rvert_{\max} / \left\lvert \widetilde{Q}_y^S \right\rvert_{\max}$ | - | 0.06 | 0.20 | 0.37 | 0.51 | 0.06 | 0.20 | 0.37 | 0.51 |

**Table 1.** *Cont.*

| | Symbole | | Load | | | | | | | |
|---|---|---|---|---|---|---|---|---|---|---|
| FSDT | $p_{cr}^F$ | MPa | 192.6 | | | | 0.0 | | | |
| | $\alpha$ | - | 0.9989 | | | | | | | |
| | $\left\|\widetilde{Q}_x^F\right\|_{\max}$ | $N/\mathrm{mm}$ | 1.67 | 4.00 | 7.78 | 13.7 | 1.82 | 4.37 | 8.45 | 14.9 |
| | $\left\|\widetilde{Q}_y^F\right\|_{\max}$ | $N/\mathrm{mm}$ | 1.81 | 4.37 | 8.45 | 14.9 | 1.82 | 4.37 | 8.45 | 14.9 |
| | $\left\|\overline{Q}_x^F\right\|_{\max} / \left\|\widetilde{Q}_x^F\right\|_{\max}$ | - | 0.05 | 0.18 | 0.38 | 0.51 | 0.07 | 0.24 | 0.42 | 0.57 |
| | $\left\|\overline{Q}_y^F\right\|_{\max} / \left\|\widetilde{Q}_y^F\right\|_{\max}$ | - | 0.07 | 0.24 | 0.42 | 0.57 | 0.07 | 0.24 | 0.42 | 0.57 |

Values of bifurcational loads for the FSDT (A58) and the S-FSDT (A44) were the same and inconsiderably lower (by a factor $\alpha$) than for the CPT (A39). According to (A45), the reduction factor was $\alpha = 0.9989$ for the assumed data.

For the case of compression (Case A), values of the maximal absolute bending components of transverse forces $\left|\hat{Q}_x^C\right|_{\max}$ and $\left|\hat{Q}_y^C\right|_{\max}$ for the CPT, i.e., equivalent Kirchhoff forces, were identical due to two axes of symmetry of the system. Values of the maximal absolute membrane components $\left|\overline{Q}_x^C\right|_{\max}$ and $\left|\overline{Q}_y^C\right|_{\max}$ differed as a linear relationship between load and deflection occurred in the last term of the first equation of Equations (A42) (for a detailed analysis, see the Appendix A). It caused the total transverse forces (i.e., total equivalent Kirchhoff forces) $\left|\widetilde{Q}_x^C\right|_{\max}$ and $\left|\widetilde{Q}_y^C\right|_{\max}$ to be different as well. Maxima of the bending and membrane force components were various for the coordinates $x$ and $y$, which resulted in the fact that values of maximal total transverse forces did not sum algebraically. For the values of the dimensionless deflection $W/h \leq 1.5$, values of bending components were significantly higher than membrane components. For $W/h$ = 2.0, membrane and bending components were almost equal. That rapid increase in membrane components followed from a cubic dependence on the deflection $W$. For the case when only transverse load appeared (Case B), components of transverse forces were equal for the given load due to two axes of symmetry of the system. The remaining results were identical. For $W/h$ = 2.0, the value of the transverse load was $q$ = 0.54 MPa, which corresponded to uniform loading on the plate surface equal to 5.4 kN. As can be concluded from the above-mentioned considerations, membrane components began to play a significant role starting from deflections equal to the plate thickness.

For the S-FSDT, conclusions are the same in practice as for the CPT due to a reduction factor close to 1. Differences are to be found in the third or fourth significant figure. Therefore, only maximal values of the absolute forces $\left|\widetilde{Q}_x^S\right|_{\max}$ and $\left|\widetilde{Q}_y^S\right|_{\max}$ are listed in Table 1. For the FSDT, the value of critical load was identical to the one for the S-FSDT, as the reduction factors $\alpha$ were the same for both the theories. The bending components $\left|\hat{Q}_x^F\right|_{\max}$ and $\left|\hat{Q}_y^F\right|_{\max}$ in (A60) were lower than the bending components (A51) for the S-FSDT, because in the second term in the bracket (A60), the factor was equal to 2, whereas in (A51) for the assumed constants, when (A41) was considered, the factor was $(3 - \nu) = 2.7$. It should be remembered that the membrane components (A61) for the three theories were the same.

Table 1 presents also values of the ratios $\left|\overline{Q}_x^\theta\right|_{\max} / \left|\widetilde{Q}_x^\theta\right|_{\max}$ and $\left|\overline{Q}_y^\theta\right|_{\max} / \left|\widetilde{Q}_y^\theta\right|_{\max}$ (where $\theta = S, F$) to evaluate how membrane components affected total transverse forces. As can be easily noticed, for $W/h \geq 0.5$ that effect was at least 15%, and for $W/h$ = 2.0, it was as high as 50%. It can be said on this basis that for the linear theories S-FSDT and FSDT, membrane components of transverse forces can be neglected for $W/h$ < 0.5 (the error was up to approx. 15%). For higher deflections of $W/h$, a nonlinear analysis should be conducted, which enforces the consideration of membrane components of transverse forces.

In Figures 2–7, contour-plane charts of the transverse forces $\hat{Q}_x^C, \hat{Q}_y^C, \overline{Q}_x^C, \overline{Q}_y^C, \widetilde{Q}_x^C, \widetilde{Q}_y^C$ for Case A and the deflection *W*/*h* = 2.0 are presented for the CPT. It should be remembered that transverse forces are the anti-symmetry forces on the axes of symmetry. It causes the transverse forces $\hat{Q}_x^C, \overline{Q}_x^C, \widetilde{Q}_x^C$ to be anti-symmetrical with respect to the axis y = a/2 = 50 mm (see Figure 2, Figure 4, and Figure 6, respectively), and the forces $\hat{Q}_y^C, \overline{Q}_y^C, \widetilde{Q}_y^C$ with respect to the axis x = a/2 = 50 mm (see Figure 3, Figure 5, and Figure 7, respectively). In Figures 8 and 9, contour-plane charts for Case B and the deflection *W*/*h* = 2.0 are depicted also for the CPT. All transverse forces are practically identical for the CPT and the S-FSDT; moreover, they are higher for the S-FSDT than for the FSDT.

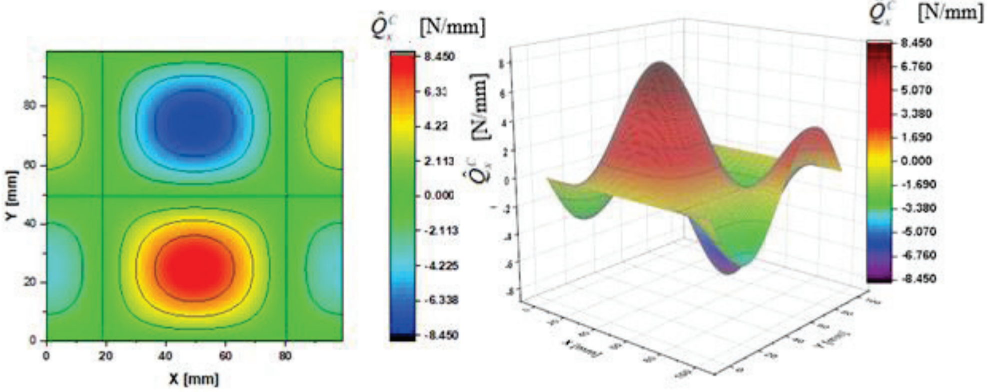

**Figure 2.** Contour-plane chart of $\hat{Q}_x^C$ for Case A.

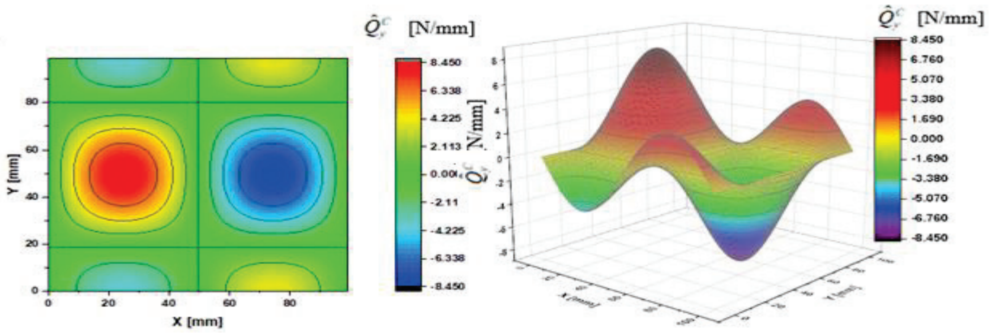

**Figure 3.** Contour-plane chart of $\hat{Q}_y^C$ for Case A.

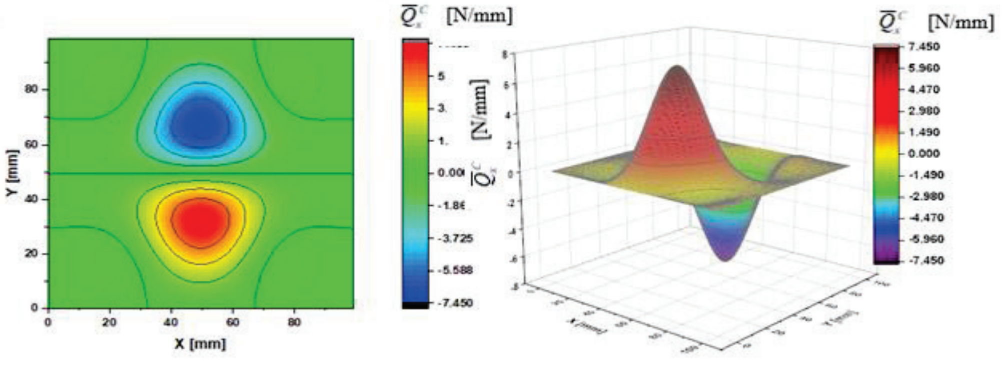

**Figure 4.** Contour-plane chart of $\overline{Q}_x^C$ for Case A.

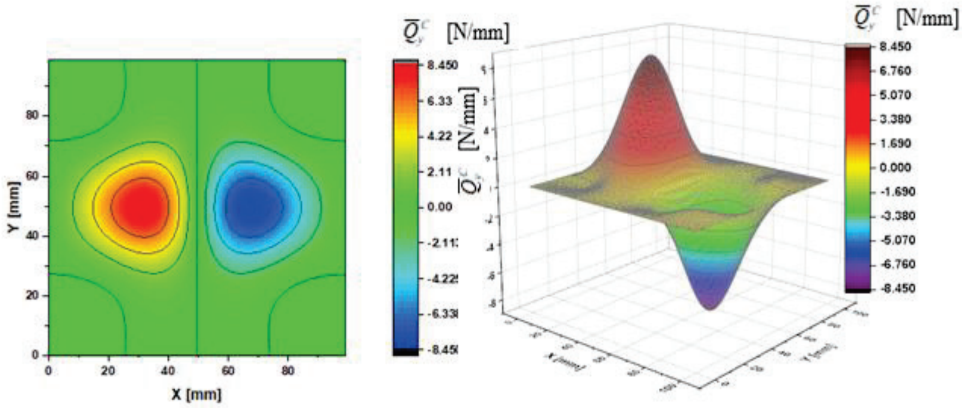

**Figure 5.** Contour-plane chart of $\overline{Q}_y^C$ for Case A.

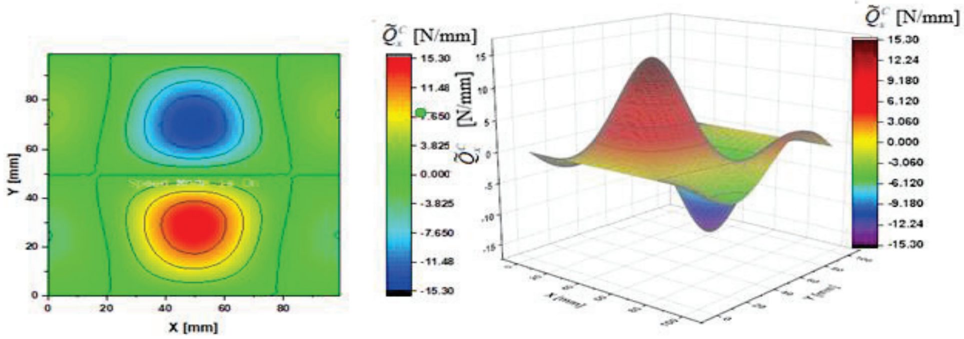

**Figure 6.** Contour-plane chart of $\widetilde{Q}_x^C$ for Case A.

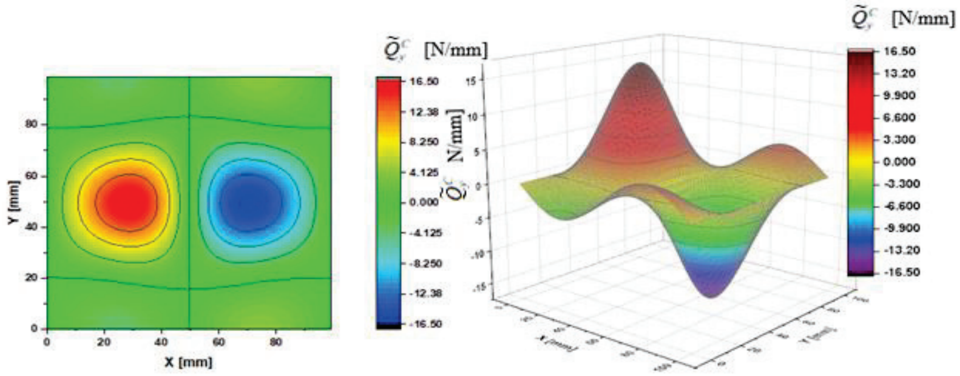

**Figure 7.** Contour-plane chart of $\widetilde{Q}_y^C$ for Case A.

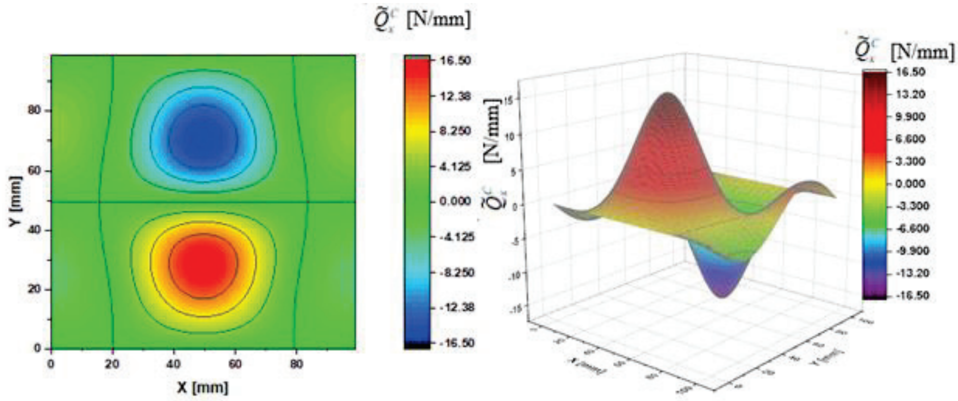

**Figure 8.** Contour-plane chart of $\widetilde{Q}_x^C$ for Case B.

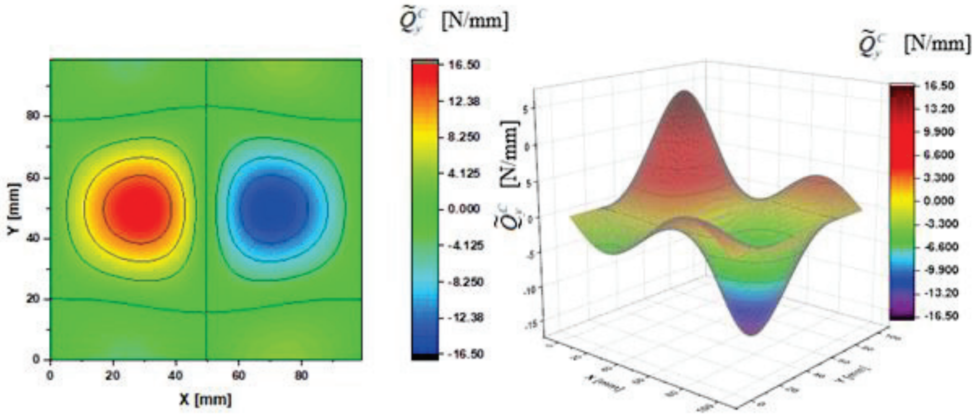

**Figure 9.** Contour-plane chart of $\widetilde{Q}_y^C$ for Case B.

The contour-plane charts for the bending components $\hat{Q}_x^C, \hat{Q}_y^C$ (Figures 2 and 3) are identical, which can be easily noticed when we turn in mind one of them by an angle of 90 deg. The charts have two global extrema and four distinct local extrema each. The charts of the membrane components $\overline{Q}_x^C, \overline{Q}_y^C$ (Figures 4 and 5) have only two distinct extrema each, however their absolute magnitudes are different. The extreme values $\overline{Q}_x^C$ are lower due to the linear term dependent on deflection and compressive load in contrast to $\overline{Q}_y^C$. The total transverse forces $\widetilde{Q}_x^C, \widetilde{Q}_y^C$ (Figures 6 and 7) arose from a superposition of the charts of components, respectively. Hence, there are two global extrema and four local ones on them like for the bending components. Of course, the relationship $\widetilde{Q}_x^C < \widetilde{Q}_y^C$ holds for the extrema. For the assumed value of the deflection *W*/*h* = 2.0, extreme values of the membrane and bending components are almost the same. Thus, the total components are twice as high in practice as the bending components.

In the formula for the membrane component of the force $\overline{Q}_x^C$ (A42), we have a term dependent on the compressive load, which vanishes for the uniform transverse load (Case B). Thus, the charts with the corresponding pairs of the components of transverse forces are of course equal when rotated by an angle of 90 deg (i.e., $\hat{Q}_x^C = \hat{Q}_y^C, \overline{Q}_x^C = \overline{Q}_y^C$, $\widetilde{Q}_x^C = \widetilde{Q}_y^C$). Due to the above-mentioned reasons, only charts for the total transvers forces $\widetilde{Q}_x^C, \widetilde{Q}_y^C$ are shown for Case B (Figures 8 and 9). The extreme values are the same for both forces of course. In the cases of global extrema in Figures 2–9, high gradients of transverse forces can be observed.

From the authors' viewpoint, the total transverse forces $\widetilde{Q}_x^C, \widetilde{Q}_y^C$ are crucial and they should be used in failure criteria, particularly while referring to composite structures.

In [15], Vasiliev proposed to call the version of S-FSDT accounting for the Reissner effect (i.e., the boundary layer) a modern form of the classical plate theory. In the light of the doubts in regard to the FSDT and the S-FSDT presented here, the authors lean to this suggestion, which is reflected in the title of the present study.

## 4. Conclusions

An influence exerted by bending and membrane components of transverse forces on total transverse forces was analyzed within the following three theories: the CPT, the S-FSDT, and the FSDT. For the S-FSDT and the FSDT, it was shown that bending components were accompanied by transverse deformations, whereas in regard to the membrane components, the plate was perfectly rigid transversely. For both the theories, various assumptions referring to transverse deformations of plates held. Bending transverse components were linearly dependent on the plate deflection, whereas membrane components—nonlinearly. Membrane components played a more and more important role with an increase in deflections above half the thickness of the plate and were higher than membrane components for the deflection corresponding to the doubled thickness of the plate.

Attention was also paid to a wrong formulation of the variation in operation of transverse forces that consisted in mutually dependent variations of displacements for the first-order shear deformation theory (Reissner–Mindlin plate theory). A modified formulation of the differential equilibrium equation on the transverse direction was proposed.

In composite materials, transverse shear effects exert a significant influence on structure delamination, which affects considerably integrity and failure of the structure. An effect of membrane components of transverse forces is neglected in composite failure criteria. From the authors' point of view, transverse components are predominant in the nonlinear problems of delamination. Thus, they should be included in composite failure criteria, e.g., the Hashin failure criterion for 3D, LaRC04(3D), and matrix failure under the additional condition of $\sigma_{33} = 0$.

**Author Contributions:** Conceptualization, Z.K.; Formal analysis, Z.K.; Methodology, Z.K. and J.J. Software, Z.K. and J.J.; Validation, Z.K. and J.J.; Visualization, J.J.; Writing—original draft, Z.K.; Writing—review & editing, J.J. Both authors have read and agreed to the published version of the manuscript.

**Funding:** This research received no external funding.

**Institutional Review Board Statement:** Not applicable.

**Informed Consent Statement:** Not applicable.

**Data Availability Statement:** Data sharing is not applicable to this article.

**Conflicts of Interest:** The authors declare no conflict of interest.

## Notation

| | |
|---|---|
| $a, h$ | geometrical dimensions of the plate |
| $D$ | plate bending stiffness |
| $E, G$ | Young's and Kirchhoff's modulus |
| $F$ | function of Airy forces |
| $N_x, N_y, N_{xy}$ | inner in-plane sectional forces |
| $M_x^\theta, M_y^\theta, M_{xy}^\theta$ | inner bending moment-sectional forces |
| $p_{cr}^\theta, \overline{p}_{cr}^\theta$ | critical stress, dimensionless critical stress |
| $q^\theta, \overline{q}^\theta$ | transverse loading, dimensionless transverse loading |
| $\overline{Q}_x^\theta, \overline{Q}_y^\theta$ | membrane components of transverse forces |
| $\hat{Q}_x^\theta, \hat{Q}_y^\theta$ | bending components of transverse forces |
| $\widetilde{Q}_x^\theta, \widetilde{Q}_y^\theta$ | total components of transverse forces |
| $u, v, w$ | components of the plate displacement along the axis $x, y, z$ |
| $w_s$ | shear deflection |
| $\alpha$ | reduction factor |
| $\beta_x,\ \beta_y$ | angles of transverse shear |
| $\varepsilon_x, \varepsilon_y, \gamma_{xy}$ | membrane strains |
| $\zeta$ | dimensionless amplitude deflection |
| $\eta$ | dimensionless coefficient |
| $\theta = F, S, C$ | upper index referring to the FSDT, the S-FSDT, the CPT |
| $\kappa_x,\ \kappa_y,\ \kappa_{xy}$ | bending strains |
| $\nu$ | Poisson's ratio |
| $\varphi$ | function of potential |
| $\psi_x, \psi_y$ | angles of rotation of the transverse normal due to bending |

## Appendix A

### *Appendix A.1. FSDT, S-FSDT, and CPT-Fundamental Equations*

The equations for the three theories: the first order shear deformation plate theory (FSDT), the simple first-order shear deformation theory (S-FSDT), and the classical plate theory (CPT), were derived in [29]. The equations of equilibrium and the boundary conditions were obtained within a variational approach. In this Appendix, only fundamental equations of these theories, supplemented with an additional inclusion of the transverse load $q$ in comparison to [29], are presented.

The geometrical relationships for the FSDT were assumed as

$$\begin{aligned} \varepsilon_x &= u_{,x} + \tfrac{1}{2} w_{,x}^2 \\ \varepsilon_y &= v_{,y} + \tfrac{1}{2} w_{,y}^2 \\ 2\varepsilon_{xy} &= \gamma_{xy} = u_{,y} + v_{,x} + w_{,x} w_{,y} \end{aligned} \tag{A1}$$

and

$$\kappa_x = -\psi_{x,x};\, \kappa_y = -\psi_{y,y};\, \kappa_{xy} = -(\psi_{x,y} + \psi_{y,x}) \tag{A2}$$

where: $u$, $v$, $w$—components of the vector of the plate displacement along the axis $x$, $y$, $z$ direction, respectively; $\psi_x$, $\psi_y$—angles of rotation of the transverse normal due to bending about the axis $x$, $y$, correspondingly; $x - y$—central plane prior to buckling; moreover, the notations, e.g., $u_{,x} = \partial u / \partial x$, are introduced.

In the transverse shear plate theory (FSDT), it was assumed that full angles of rotation of the normal to the central surface in two planes were as follows [29]:

$$w_{,x} = \psi_x + \beta_x \quad w_{,y} = \psi_y + \beta_y \tag{A3}$$

where $\beta_x$, $\beta_y$—angles of transverse shear.

The inner sectional forces were written as

$$\begin{aligned} N_x &= \tfrac{Eh}{1-\nu^2}(\varepsilon_x + \nu\varepsilon_y) \\ N_y &= \tfrac{Eh}{1-\nu^2}(\varepsilon_y + \nu\varepsilon_x) \\ N_{xy} &= \tfrac{Eh}{1-\nu^2}\tfrac{1-\nu}{2}\gamma_{xy} \end{aligned} \tag{A4}$$

$$\begin{aligned} M_x^F &= -D(\psi_{x,x} + \nu\psi_{y,y}) \\ M_y^F &= -D(\psi_{y,y} + \nu\psi_{x,x}) \\ M_{xy}^F &= -D\tfrac{1-\nu}{2}(\psi_{x,y} + \psi_{y,x}) \end{aligned} \tag{A5}$$

$$\begin{aligned} \hat{Q}_x^F &= k^2 Gh(w_{,x} - \psi_x) \\ \hat{Q}_y^F &= k^2 Gh(w_{,y} - \psi_y) \end{aligned} \tag{A6}$$

where the upper index $^F$ refers to the FSDT.

System of Equation (A1) can be brought to the form

$$\varepsilon_{x,yy} + \varepsilon_{y,xx} - \gamma_{xy,xy} = w_{,xy}^2 - w_{,xx} w_{,xy} \tag{A7}$$

When relationships (A4) are accounted for and the function of Airy forces $F$ defined as

$$\begin{aligned} N_x &= \sigma_x h = F_{,yy} \\ N_y &= \sigma_y h = F_{,xx} \\ N_{xy} &= \tau_{xy} h = -F_{,xy} \end{aligned} \tag{A8}$$

is introduced, then finally the equation of inseparability/continuity of deformations is obtained [29]:

$$\nabla\nabla F \equiv F_{,xxxx} + 2F_{,xxyy} + F_{,yyyy} = E(w_{,xy}^2 - w_{,xx} w_{,xy}) \tag{A9}$$

The above-mentioned equation is linear with respect to $F$ and nonlinear with respect to $w$.

### Appendix A.1.1. FSDT

For the FSDT, the equations of equilibrium within the variational approach are as follows [29]:

$$\begin{aligned}
&\int_0^l\int_0^b [N_{x,x}+N_{xy,y}]\delta u dxdy=0\\
&\int_0^l\int_0^b [N_{xy,x}+N_{y,y}]\delta v dxdy=0\\
&\int_0^\ell\int_0^b [\hat{Q}^F_{x,x}+\hat{Q}^F_{y,y}+(N_x w_{,x}+N_{xy}w_{,y})_{,x}+(N_{xy}w_{,x}+N_y w_{,y})_{,y}+q]\delta w dxdy=0\\
&\int_0^\ell\int_0^b [M^F_{x,x}+M^F_{xy,y}-\hat{Q}^F_x]\delta\psi_x dxdy=0\\
&\int_0^\ell\int_0^b [M^F_{xy,x}+M^F_{y,y}-\hat{Q}^F_y]\delta\psi_y dxdy=0
\end{aligned} \tag{A10}$$

The first two equations are satisfied identically by the function of forces $F$ (A8).

The following relationships result from the last two relationships (A10):

$$\begin{aligned}
\hat{Q}^F_x &= M^F_{x,x}+M^F_{xy,y}\\
\hat{Q}^F_y &= M^F_{y,y}+M^F_{xy,x}
\end{aligned} \tag{A11}$$

These bending components of transverse forces depend on derivatives of inner moments (A5). The angles of transverse shear $\beta_x,\ \beta_y$ in (A3) correspond to bending components only.

In [29], the following membrane components of transverse forces were introduced:

$$\begin{aligned}
\overline{Q}^F_x &= N_x w_{,x}+N_{xy}w_{,y}\\
\overline{Q}^F_y &= N_y w_{,y}+N_{xy}w_{,x}
\end{aligned} \tag{A12}$$

The above-mentioned forces are dependent on projections of membrane forces on the transverse direction and do not affect membrane deformations, i.e., membrane components are not accompanied by deformations in contrast to bending components in the FSDT. Thus, we deal with two different assumptions for bending and membrane components.

According to (A11) and (A12), a concept of components of total transverse forces $\widetilde{Q}^F_x$ and $\widetilde{Q}^F_y$ was introduced. They are expressed as

$$\begin{aligned}
\widetilde{Q}^F_x &= \hat{Q}^F_x+\overline{Q}^F_x=(M^F_{x,x}+M^F_{xy,y})+(N_x w_{,x}+N_{xy}w_{,y})\\
\widetilde{Q}^F_y &= \hat{Q}^F_y+\overline{Q}^F_y=(M^F_{y,y}+M^F_{xy,x})+(N_y w_{,y}+N_{xy}w_{,x})
\end{aligned} \tag{A13}$$

When (A12) is taken into consideration in the third relation (A10), an equation of equilibrium is obtained:

$$\int_0^\ell\int_0^b [(\hat{Q}^F_{x,x}+\hat{Q}^F_{y,y})+(\overline{Q}^F_{x,x}+\overline{Q}^F_{y,y})+q]\delta w dxdy=0 \tag{A14}$$

As can be easily noticed, membrane and bending components of transverse forces, as well as the load $q$, occur in the above equation.

On the basis of the analysis of relations (A5) and (A6), it can be stated that the bending components of transverse forces $\hat{Q}_x^F$ and $\hat{Q}_y^F$ are linearly dependent on the variables $\psi_x, \psi_y, w$. In turn, the analysis of Formulas (A8) and (A9) referring to the membrane components $\overline{Q}_x^F$ and $\overline{Q}_y^F$ points out to nonlinear dependencies on the variables $F, w$. Hence, Equation (A14) depends on $w$ raised to the third power.

### Appendix A.1.2. S-FSDT

If the angles of rotation $\psi_x,\ \psi_y$ (A2) are expressed with a new function of potential $\varphi(x, y)$ [29], such that $\varphi_{,x} = \psi_x,\ \varphi_{,y} = \psi_y$ and, moreover, if for (A3) the following relationships $\beta_x = w_{s,x},\ \beta_y = w_{s,y}$ hold, then

$$w_{,x} = \varphi_{,x} + \beta_x = \varphi_{,x} + w_{s,x} \quad w_{,y} = \varphi_{,y} + \beta_y = \varphi_{,y} + w_{s,y} \tag{A15}$$

An introduction of the function of deflection in bending $\varphi$ causes the Reissner boundary effects to be neglected [15,29], and the shear deflection is equal to $w_s = w - \varphi$. Moreover, the number of variables equal to five (i.e., $u$, $v$, $w$, $\psi_x$, $\psi_y$) for the FSDT is reduced to four variables $u$, $v$, $w$, $\varphi$ in the case of the S-FSDT [29]; however, the number of boundary conditions for each boundary does not alter. Thus, boundary conditions are coupled for the S-FSDT formulated in such a way.

To attain uncoupled boundary conditions, the Reissner boundary effect should be accounted for. Then, the equations of equilibrium ought to be supplemented with the second-order equation for the rotary potential (the so-called Helmholtz equation) being a fast-variable solution to the boundary layer. This equation increases the system order up to the sixth. Hence, the boundary conditions are uncoupled.

The Reissner boundary effect occurs under special boundary conditions only. In the FEM analysis, there is a mechanism of the shear locking phenomenon, because a fast-variable solution to the boundary layer cannot be approximated with shape functions.

When (A15) is accounted for, inner forces (A5) and (A6) for the S-FSDT are written as

$$\begin{aligned} M_x^S &= -D(\varphi_{,xx} + \nu\varphi_{,yy}) \\ M_y^S &= -D(\varphi_{,yy} + \nu\varphi_{,xx}) \\ M_{xy}^S &= -D(1-\nu)\varphi_{,xy} \end{aligned} \tag{A16}$$

$$\begin{aligned} \hat{Q}_x^S &= k^2 Gh(w_{,x} - \varphi_{,x}) \\ \hat{Q}_y^S &= k^2 Gh(w_{,y} - \varphi_{,y}) \end{aligned} \tag{A17}$$

and the equations of equilibrium [29], when the load $q$ is taken into consideration, are

$$\begin{gathered} \int_0^{\ell}\int_0^{b} [\hat{Q}_{x,x}^S + \hat{Q}_{y,y}^S + (N_x w_{,x} + N_{xy} w_{,y})_{,x} + (N_{xy} w_{,x} + N_y w_{,y})_{,y} + q]\delta w dxdy = 0 \\ \int_0^{l}\int_0^{b} [M_{x,xx}^S + 2M_{xy,xy}^S + M_{y,yy}^S - \hat{Q}_{x,x}^S - \hat{Q}_{y,y}^S]\delta\varphi dxdy = 0 \end{gathered} \tag{A18}$$

where the upper index $^S$ denotes the S-FSDT.

System of Equations (A18) should be supplemented by Equation (A9).

The bending components of transverse forces dependent on the variable $\varphi$ are expressed with the relationships

$$\begin{aligned} \hat{Q}_x^S &= M_{x,x}^S + 2M_{xy,y}^S \\ \hat{Q}_y^S &= M_{y,y}^S + 2M_{xy,x}^S \end{aligned} \tag{A19}$$

whereas the membrane components of transverse forces dependent on the variables $F, w$ take the form

$$\begin{aligned}\overline{Q}_x^S &= N_x w_{,x} + N_{xy} w_{,y} \\ \overline{Q}_y^S &= N_y w_{,y} + N_{xy} w_{,x}\end{aligned} \tag{A20}$$

By analogy to (A13), the components of total transverse forces $\widetilde{Q}_x^S$ and $\widetilde{Q}_y^S$ for the S-FSDT are expressed as

$$\begin{aligned}\widetilde{Q}_x^S &= \hat{Q}_x^S + \overline{Q}_x^S = (M_{x,x}^S + 2M_{xy,xy}^S) + (N_x w_{,x} + N_{xy} w_{,y}) \\ \widetilde{Q}_y^S &= \hat{Q}_y^S + \overline{Q}_y^S = (M_{y,y}^S + 2M_{xy,y}^S) + (N_y w_{,y} + N_{xy} w_{,x})\end{aligned} \tag{A21}$$

Comparing the formulas for the bending components of transverse forces (A11) and (A19), one can easily see that we have a factor 2 at the derivative of torque $M_{xy}$ for the S-FSDT, which is 1 in the FSDT. Formulas (A12) and (A20) are identical for the membrane components of transverse forces.

When (A20) is taken into account, the first Equation (A18) takes the form

$$\int_0^{\ell} \int_0^{b} [(\hat{Q}_{x,x}^S + \hat{Q}_{y,y}^S) + (\overline{Q}_{x,x}^S + \overline{Q}_{y,y}^S) + q] \delta w dx dy = 0 \tag{A22}$$

The above equation has the same structure as (A14). It should be remembered that bending components are expressed with various formulas (cf. (A11) and (A19)).

Analogously to the FSDT, the bending components of transverse forces $\hat{Q}_x^S$ and $\hat{Q}_y^S$ are linearly dependent on the variable $\varphi$, and thus $w$ as well, whereas the membrane components $\overline{Q}_x^S$ and $\overline{Q}_y^S$ are nonlinearly dependent on the variables $F, w$.

### Appendix A.1.3. CPT

Transverse forces are disregarded in the classical plate theory (CPT) (A6) and it should be additionally assumed that $\beta_x = \beta_y = 0$ in (A3), which leads to the equality

$$\begin{aligned}w_{,x} &= \psi_x \\ w_{,y} &= \psi_y\end{aligned} \tag{A23}$$

When (A23) is considered in (A5), then for the CPT,

$$\begin{aligned}M_x^C &= -D(w_{,xx} + \nu w_{,yy}) \\ M_y^C &= -D(w_{,yy} + \nu w_{,xx}) \\ M_{xy}^C &= -D(1-\nu) w_{,xy}\end{aligned} \tag{A24}$$

where the upper index $^C$ refers to the CPT.

When the above relations are included, the equation of equilibrium takes the form [29]

$$\int_0^{\ell} \int_0^{b} [M_{x,xx}^C + 2M_{xy,xy}^C + M_{y,yy}^C + (N_x w_{,x} + N_{xy} w_{,y})_{,x} + (N_{xy} w_{,x} + N_y w_{,y})_{,y} + q] \delta w dx dy = 0 \tag{A25}$$

The second equation is an inseparability Equation (A9).

In the history of the CPT, equivalent Kirchhoff transverse forces were defined as

$$\begin{aligned}\hat{Q}_x^C &= M_{x,x}^C + 2M_{xy,y}^C \\ \hat{Q}_y^C &= M_{y,y}^C + 2M_{xy,x}^C\end{aligned} \tag{A26}$$

These are bending components of transverse forces and their structure is analogous to (A19). Like for the FSDT and S-FSDT, the membrane components of transverse forces are assumed as

$$\begin{aligned} \overline{Q}_x^C &= N_x w_{,x} + N_{xy} w_{,y} \\ \overline{Q}_y^C &= N_y w_{,y} + N_{xy} w_{,x} \end{aligned} \tag{A27}$$

Thus, the above-mentioned components of transverse forces are the membrane components of Kirchhoff forces and they have an identical structure as for the FSDT and the S-FSDT.

Considering (A26) and (A27), the total equivalent Kirchhoff transverse forces $\widetilde{Q}_x^C$ and $\widetilde{Q}_y^C$ for the CPT are expressed in the following form:

$$\begin{aligned} \widetilde{Q}_x^C &= \hat{Q}_x^C + \overline{Q}_x^C = (M_{x,x}^C + 2M_{xy,y}^C) + (N_x w_{,x} + N_{xy} w_{,y}) \\ \widetilde{Q}_y^C &= \hat{Q}_y^C + \overline{Q}_y^C = (M_{y,y}^C + 2M_{xy,x}^C) + (N_y w_{,y} + N_{xy} w_{,x}) \end{aligned} \tag{A28}$$

When (A28) is accounted for in (A25), the equation of equilibrium is written as

$$\int_0^{\ell} \int_0^{b} [(\hat{Q}_{x,x}^C + \hat{Q}_{y,y}^C) + (\overline{Q}_{x,x}^C + \overline{Q}_{y,y}^C) + q]\delta w dx dy = 0 \tag{A29}$$

Formulas (A22) and (A29) are built analogously, but these equations have two variables $w, \varphi$ for the S-FDST and only one variable $w$ for the CPT. As in the FSDT and the S-FSDT, the bending components of transverse forces $\hat{Q}_x^C$ and $\hat{Q}_y^C$ are linearly dependent on the variable $w$, whereas the membrane components $\overline{Q}_x^C$ and $\overline{Q}_y^C$ are nonlinearly dependent on the variables $F, w$.

### *Appendix A.2. Nonlinear Problem of Distributions of Transverse Shear Forces in the Square Plate Subject Simultaneously to Compression and Transverse Loading*

A square isotropic plate fixed along all edges and simultaneously subject to the compression $p$ along the $x$ axis direction and the constant transverse load $q$ (Figure 1) was analyzed. The plate characterized by the length $a$, the thickness $h$, and the material constants Young's modulus $E$ and Poisson's ratio $\nu$ was investigated in an elastic range only. The problem was solved within the first-order nonlinear approximation.

#### Appendix A.2.1. Equation of Inseparability of Deformations

The equation of inseparability of deformations (A9) is identical for the three theories under investigation.

The deflection of the plate fixed along all edges within the first-order approximation was approximated with the following function [43]:

$$w = W \sin^2 \frac{\pi x}{a} \sin^2 \frac{\pi y}{a} \tag{A30}$$

which fulfilled the following boundary conditions:

$$\begin{aligned} w(x=0) = w(x=a) = w(y=0) = w(y=a) = 0 \\ w_{,x}(x=0) = w_{,x}(x=a) = w_{,y}(y=0) = w_{,y}(y=a) = 0 \end{aligned} \tag{A31}$$

After submission of (A30) into (A9), a function of Airy forces $F$ was defined:

$$\begin{aligned} F = -\tfrac{py^2}{2} + EW^2\big(\tfrac{1}{32}\cos\tfrac{2\pi x}{a} + \tfrac{1}{32}\cos\tfrac{2\pi y}{a} - \tfrac{1}{512}\cos\tfrac{4\pi x}{a} - \tfrac{1}{512}\cos\tfrac{4\pi y}{a} \\ + \tfrac{1}{800}\cos\tfrac{4\pi x}{a}\cos\tfrac{2\pi y}{a} + \tfrac{1}{800}\cos\tfrac{2\pi x}{a}\cos\tfrac{4\pi y}{a} - \tfrac{1}{64}\cos\tfrac{2\pi x}{a}\cos\tfrac{2\pi y}{a}\big) \end{aligned} \tag{A32}$$

from the above and from (A8) it follows

$$\begin{aligned}
&N_x = F_{,yy} = -p + EW^2\left(\tfrac{\pi}{a}\right)^2\left[-\tfrac{1}{8}\cos\tfrac{2\pi y}{a} + \tfrac{1}{32}\cos\tfrac{4\pi y}{a} - \tfrac{1}{200}\cos\tfrac{4\pi x}{a}\cos\tfrac{2\pi y}{a}\right.\\
&\left.-\tfrac{1}{50}\cos\tfrac{2\pi x}{a}\cos\tfrac{4\pi y}{a} + \tfrac{1}{16}\cos\tfrac{2\pi x}{a}\cos\tfrac{2\pi y}{a}\right]\\
&N_y = F_{,xx} = EW^2\left(\tfrac{\pi}{a}\right)^2\left[-\tfrac{1}{8}\cos\tfrac{2\pi x}{a} + \tfrac{1}{32}\cos\tfrac{4\pi x}{a} - \tfrac{1}{50}\cos\tfrac{4\pi x}{a}\cos\tfrac{2\pi y}{a}\right.\\
&\left.-\tfrac{1}{200}\cos\tfrac{2\pi x}{a}\cos\tfrac{4\pi y}{a} + \tfrac{1}{16}\cos\tfrac{2\pi x}{a}\cos\tfrac{2\pi y}{a}\right]\\
&N_{xy} = -F_{,xy} = -EW^2\left(\tfrac{\pi}{a}\right)^2\left[\tfrac{1}{100}\sin\tfrac{4\pi x}{a}\sin\tfrac{2\pi y}{a} + \tfrac{1}{100}\sin\tfrac{2\pi x}{a}\sin\tfrac{4\pi y}{a} - \tfrac{1}{16}\sin\tfrac{2\pi x}{a}\sin\tfrac{2\pi y}{a}\right]
\end{aligned} \tag{A33}$$

Functions of forces (A33) fulfill the boundary conditions [30,33]:

$$\begin{array}{ll} u(x=0) = u(x=a) = const & N_{xy}(x=0) = N_{xy}(x=a) = 0 \\ v(y=0) = v(y=a) = const & N_{xy}(y=0) = N_{xy}(y=a) = 0 \end{array} \tag{A34}$$

### A.2.2. CPT-Solution to the Nonlinear Problem of Stability

In regard to the CPT, the Galerkin–Bubnov method was used to solve the nonlinear problem of stability (A25) or (A29) with respect to *w*. When the function of forces (A32) and the function of deflection *w* (A30) were introduced, a nonlinear equation of equilibrium of the square plate subject to simultaneous compression and the uniform transverse loading *q* was attained for the CPT within the first approximation [43]:

$$\frac{533\pi^4}{3200}\zeta^3 - \frac{3\pi^2}{4}\overline{p}^C\zeta + \frac{2\pi^4}{3(1-\nu^2)}\zeta = \overline{q}^C \tag{A35}$$

where:

$$\overline{p}^C = \frac{p^C a^2}{Eh^2},\ \overline{q}^C = \frac{q^C a^4}{Eh^4} \text{ and } \zeta = W/h \tag{A36}$$

For Equation (A35), two particular cases can be considered, namely:

- $\overline{p}^C \neq 0$ and $\overline{q}^C = 0$ (the plate subject to uniform compression, transverse loading neglected)

In this case, we have a nonlinear stability problem of the plate in compression and Equation (A35) is simplified to

$$\frac{533\pi^4}{800}\zeta^3 + \left(\overline{p}^C_{cr} - \overline{p}^C\right)\zeta = 0 \tag{A37}$$

where:

$$\overline{p}^C_{cr} = \frac{p^C_{cr}a^2}{Eh^2} = \frac{8\pi^2}{9(1-\nu^2)} \text{—dimensionless critical stress.} \tag{A38}$$

The critical stress, according to (A38), can be expressed as

$$p^C_{cr} = \frac{32D\pi^2}{3a^2h} = 10.67\frac{D\pi^2}{a^2h} \tag{A39}$$

The value of the critical stress for the first approximation was deviated by 1.6% with respect to the accurate value of 10.5 [43].

- $\overline{p}^C = 0$ and $\overline{q}^C \neq 0$ (the plate subject to uniform transverse loading, compression neglected)

In this case, we have a nonlinear problem of deflection of the thin plate, accompanied by an appearance of membrane forces (A33):

$$\frac{533\pi^4}{3200}\zeta^3 + \frac{2\pi^4}{3(1-\nu^2)}\zeta = \overline{q}^C \tag{A40}$$

The determined dimensionless deflections $\zeta$ for the assumed value of transverse load from Equation (A40), within the first-order approximation, were lower by 3.5% with respect to the accurate solution [43].

The equivalent Kirchhoff transverse forces (A26), i.e., the bending components of transverse forces, when (A30) is considered, are expressed with the following relationships:

$$\begin{aligned}\hat{Q}_x^C &= M_{x,x}^C + 2M_{xy,y}^C = 2DW\left(\tfrac{\pi}{a}\right)^3\left(\sin\tfrac{2\pi x}{a} - (3-\nu)\sin\tfrac{2\pi x}{a}\cos\tfrac{2\pi y}{a}\right)\\ \hat{Q}_y^C &= M_{y,y}^C + 2M_{xy,x}^C = 2DW\left(\tfrac{\pi}{a}\right)^3\left(\sin\tfrac{2\pi y}{a} - (3-\nu)\cos\tfrac{2\pi x}{a}\sin\tfrac{2\pi y}{a}\right)\end{aligned} \tag{A41}$$

As one can easily notice in (A41), the bending components are linearly dependent on the deflection $W$.

When we take (A30) and (A33) into account, the membrane components (A27) are as follows:

$$\begin{aligned}&\overline{Q}_x^C = N_x w_{,x} + N_{xy} w_{,y} = -EW^3h\left(\tfrac{\pi}{a}\right)^3\left[\left(\tfrac{1}{8}\cos\tfrac{2\pi y}{a} - \tfrac{1}{32}\cos\tfrac{4\pi y}{a} + \tfrac{1}{200}\cos\tfrac{4\pi x}{a}\cos\tfrac{2\pi y}{a} + \right.\right.\\ &\tfrac{1}{50}\cos\tfrac{2\pi x}{a}\cos\tfrac{4\pi y}{a} - \tfrac{1}{16}\cos\tfrac{2\pi x}{a}\cos\tfrac{2\pi y}{a}\big)\sin\tfrac{2\pi x}{a}\left(\tfrac{1}{2} - \tfrac{1}{2}\cos\tfrac{2\pi y}{a}\right) + \\ &\left(\tfrac{1}{100}\sin\tfrac{4\pi x}{a}\sin\tfrac{2\pi y}{a} + \tfrac{1}{100}\sin\tfrac{2\pi x}{a}\sin\tfrac{4\pi y}{a} - \tfrac{1}{16}\sin\tfrac{2\pi x}{a}\sin\tfrac{2\pi y}{a}\right)\left(\tfrac{1}{2} - \tfrac{1}{2}\cos\tfrac{2\pi x}{a}\right)\sin\tfrac{2\pi y}{a}\Big] - \\ &p^C Wh\left(\tfrac{\pi}{a}\right)\sin\tfrac{2\pi x}{a}\left(\tfrac{1}{2} - \tfrac{1}{2}\cos\tfrac{2\pi y}{a}\right)\\ &\overline{Q}_y^C = N_y w_{,y} + N_{xy} w_{,x} = -EW^3h\left(\tfrac{\pi}{a}\right)^3\left[\left(\tfrac{1}{8}\cos\tfrac{2\pi x}{a} - \tfrac{1}{32}\cos\tfrac{4\pi x}{a} + \tfrac{1}{50}\cos\tfrac{4\pi x}{a}\cos\tfrac{2\pi y}{a} + \right.\right.\\ &\tfrac{1}{200}\cos\tfrac{2\pi x}{a}\cos\tfrac{4\pi y}{a} - \tfrac{1}{16}\cos\tfrac{2\pi x}{a}\cos\tfrac{2\pi y}{a}\big)\left(\tfrac{1}{2} - \tfrac{1}{2}\cos\tfrac{2\pi x}{a}\right)\sin\tfrac{2\pi y}{a} + \\ &\left(\tfrac{1}{100}\sin\tfrac{4\pi x}{a}\sin\tfrac{2\pi y}{a} + \tfrac{1}{100}\sin\tfrac{2\pi x}{a}\sin\tfrac{4\pi y}{a} - \tfrac{1}{16}\sin\tfrac{2\pi x}{a}\sin\tfrac{2\pi y}{a}\right)\sin\tfrac{2\pi x}{a}\left(\tfrac{1}{2} - \tfrac{1}{2}\cos\tfrac{2\pi y}{a}\right)\Big]\end{aligned} \tag{A42}$$

The membrane components (A42) are nonlinearly dependent on the deflection $W$, or strictly speaking, on $W$ raised to the third power. The last term in the first equation is linearly dependent on $W$ for the case of compression, whereas when we have the transverse load $q$ only, this term becomes zero.

The total components of transverse forces, i.e., total equivalent Kirchhoff forces, are expressed with Formula (A28).

### A.2.3. S-FSDT-Solution to the Nonlinear Problem of Stability

A solution to system of Equation (A18) for the S-FSDT is predicted as (A30) with respect to the variable $w$ and for the variable $\varphi$ in the form

$$\varphi = \Phi^S \sin^2\frac{\pi x}{a}\sin^2\frac{\pi y}{a} \tag{A43}$$

When variables (A30) and (A43) are substituted into (A16)–(A19) into the second equation, the following relationship is obtained:

$$\Phi^S = \frac{W}{1+\eta} = \alpha W \tag{A44}$$

where: $\eta = \frac{2\pi^2}{3(1-\nu)k^2}\left(\frac{h}{a}\right)^2$, and, moreover, the reduction factor

$$\alpha = 1/(1+\eta) \tag{A45}$$

When (A44) is taken into account, the first nonlinear Equation (A18) is solved with the Galerkin–Bubnov method to obtain

$$\frac{533\pi^4}{3200}\zeta^3 - \frac{3\pi^2}{4}\overline{p}^S\zeta + \frac{2\pi^4}{3(1-\nu^2)}\alpha\zeta = \overline{q}^S \tag{A46}$$

where:

$$\overline{p}^S = \frac{p^S a^2}{Eh^2} \overline{q}^S = \frac{q^S a^4}{Eh^4} \tag{A47}$$

Like for the CPT, two particular cases were considered for (A46), namely:

- $\overline{p}^S \neq 0$ *and* $\overline{q}^S = 0$ *(the plate subject to uniform compression, transverse loading neglected)*

  In this case, (A46) is simplified to

$$\frac{533\pi^4}{800}\zeta^3 + (\overline{p}^S_{cr} - \overline{p}^S)\zeta = 0 \tag{A48}$$

where the dimensionless critical load, when (A39) is accounted for, can be written as

$$\overline{p}^S_{cr} = \frac{p^S_{cr} a^2}{Eh^2} = \frac{8\pi^2}{9(1-\nu^2)}\alpha = \overline{p}^C_{cr}\alpha \tag{A49}$$

- $\overline{p}^S = 0$ *and* $\overline{q}^S \neq 0$ *(the plate subject to uniform transverse loading, compression neglected)*

  In this case, we have a nonlinear problem of deflection of the plate, accompanied by an appearance of membrane forces:

$$\frac{533\pi^4}{3200}\zeta^3 + \frac{2\pi^4}{3(1-\nu^2)}\alpha\zeta = \overline{q}^S \tag{A50}$$

The bending components of transverse forces for the S-FSDT, when (A41) and (A44) were accounted for, are expressed with the formula

$$\hat{Q}^S_x = \hat{Q}^C_x \alpha \quad \hat{Q}^S_y = \hat{Q}^C_y \alpha \tag{A51}$$

Similarly as for the CPT, the bending components are linearly dependent on the deflection $W$.

The membrane components of transverse forces for the S-FSDT, according to (A20) and (A27) and when (A42) was considered, have the form

$$\overline{Q}^S_x = \overline{Q}^C_x \quad \overline{Q}^S_y = \overline{Q}^C_y \tag{A52}$$

whereas the components of total transverse forces–(A21), correspondingly.

### Appendix A.2.4. FSDT-Solution to the Nonlinear Problem of Stability

For the FSDT, a solution to the system of the last three Equations (A10) was predicted like (A30) with respect to the variable $w$ and for the variables $\psi_x$, $\psi_y$ in the form

$$\begin{aligned} \psi_x &= \Psi^F_x \sin\tfrac{2\pi x}{a}\sin^2\tfrac{\pi y}{a} \\ \psi_y &= \Psi^F_y \sin^2\tfrac{\pi x}{a}\sin\tfrac{2\pi y}{a} \end{aligned} \tag{A53}$$

When variables (A30), (A53), and (A45) were substituted, the following relationships were obtained:

$$\Psi^F_x = \Psi^F_y = W\alpha\left(\frac{\pi}{a}\right)^2 \tag{A54}$$

$$\frac{533\pi^4}{3200}\zeta^3 - \frac{3\pi^2}{4}\overline{p}^F\zeta + \frac{2\pi^4}{3(1-\nu^2)}\alpha\zeta = \overline{q}^F \tag{A55}$$

where:

$$\overline{p}^F = \frac{p^F a^2}{Eh^2},\ \overline{q}^F = \frac{q^F a^4}{Eh^4} \tag{A56}$$

Like for the CPT and S-FSDT, two particular cases were considered for (A55), namely:

- $\overline{p}^F \neq 0$ *and* $\overline{q}^F = 0$ *(the plate subject to uniform compression, transverse loading neglected)*

In this case, (A55) simplifies to

$$\frac{533\pi^4}{800}\zeta^3 + (\overline{p}^F_{cr} - \overline{p}^F)\zeta = 0 \tag{A57}$$

where the dimensionless critical stress, when (A49) and (A39) were considered, takes the form

$$\overline{p}^F_{cr} = \frac{p^F_{cr}a^2}{Eh^2} = \frac{8\pi^2}{9(1-\nu^2)}\alpha = \overline{p}^S_{cr} = \overline{p}^C_{cr}\alpha \tag{A58}$$

- $\overline{p}^F = 0$ *and* $\overline{q}^F \neq 0$ *(the plate subject to uniform transverse loading, compression neglected)*

The nonlinear problem of deflection of the thin plate, accompanied by an appearance of membrane components, was expressed as

$$\frac{533\pi^4}{3200}\zeta^3 + \frac{2\pi^4}{3(1-\nu^2)}\alpha\zeta = \overline{q}^F \tag{A59}$$

When (A59) and (A50) are compared, one can see that $\overline{q}^S = \overline{q}^F$.

The bending components of transverse forces according to (A11) are equal to

$$\begin{aligned} \hat{Q}^F_x &= M^F_{x,x} + M^F_{xy,y} = 2DW\left(\tfrac{\pi}{a}\right)^3\left(\sin\tfrac{2\pi x}{a} - 2\sin\tfrac{2\pi x}{a}\cos\tfrac{2\pi y}{a}\right)\alpha \\ \hat{Q}^F_y &= M^F_{y,y} + M^F_{xy,x} = 2DW\left(\tfrac{\pi}{a}\right)^3\left(\sin\tfrac{2\pi y}{a} - 2\cos\tfrac{2\pi x}{a}\sin\tfrac{2\pi y}{a}\right)\alpha \end{aligned} \tag{A60}$$

Like for the CPT and S-FSDT, the bending components are linearly dependent on the deflection $W$. Comparing (A60) and (A51), we can see that there is a factor equal to 2 at the second term in the bracket for the FSDT, whereas for the S-FSDT, the factor is (3-ν).

The membrane components of transverse forces (A12) for the FSDT are identical as in the case of the S-FSDT and the CPT (A52):

$$\overline{Q}^F_x = \overline{Q}^S_x = \overline{Q}^C_x \qquad \overline{Q}^F_y = \overline{Q}^S_y = \overline{Q}^C_y \tag{A61}$$

whereas the components of total transverse forces are the same and are given in (A13), (A21), and (A28), respectively.

## References

1. Reissner, E. On the theory of bending of elastic plates. *J. Math. Phys.* **1944**, *23*, 184–191. [CrossRef]
2. Reissner, E. The effect of transverse shear deformation on the bending of elastic plates. *ASME J. Appl. Mech.* **1945**, *12*, A69–A77. [CrossRef]
3. Mindlin, R.D. Influence of rotary inertia and shear on flexural motions of isotropic, elastic plates. *ASME J. Appl. Mech.* **1951**, *18*, 31–38. [CrossRef]
4. Baptista, M. An elementary derivation of basic equations of the Reissner and Mindlin plate theories. *Eng. Struct.* **2010**, *32*, 906–909. [CrossRef]
5. Baptista, M. Comparison of Reissner, Mindlin and Reddy plate models with exact three dimensional solution for simply supported isotropic and transverse inextensible rectangular plate. *Meccanica* **2012**, *47*, 257–268. [CrossRef]
6. Chróścielewski, J.; Makowski, J.; Pietraszkiewicz, W. *Statyka i Dynamika Powłok Wielopłatowych*; IPPT PAN: Warsaw, Poland, 2004. (In Polish)
7. Wu, S.R. Reissner-Mindlin plate theory for elastodynamics. *J. Appl. Math.* **2004**, *3*, 179–189. [CrossRef]
8. Lo, K.H.; Christensen, R.M.; Wu, E.M. A high-order theory of plate deformation. Part 1: Homogeneous plates. *ASME J. Appl. Mech.* **1977**, *44*, 663–668. [CrossRef]
9. Lo, K.H.; Christensen, R.M.; Wu, E.M. A high-order theory of plate deformation. Part 2: Laminated plates. *ASME J. Appl. Mech.* **1977**, *44*, 669–676. [CrossRef]
10. Reddy, J.N. A general non-linear third-order theory of plates with moderate thickness. *Int. J. Non-Linear Mech.* **1990**, *25*, 677–686. [CrossRef]
11. Reddy, J.N.; Phan, N.D. Stability and vibration of isotropic, orthotropic and laminated plates according to a higher-order shear deformation theory. *J. Sound Vib.* **1985**, *98*, 157–170. [CrossRef]
12. Reddy, J.N. *Mechanics of Laminated Composite Plates and Shells: Theory and Analysis*, 2nd ed.; CRC Press: Boca Raton, FL, USA, 2004.

13. Reddy, J.N. A general nonlinear third-order theory of functionally graded plates. *Int. J. Aerosp. Lightweight Struct.* **2011**, *1*, 1–21. [CrossRef]
14. Taylor, M.W.; Vasiliev, V.V.; Dillard, D.A. On the problem of shear-locking in finite elements based on shear deformable plate theory. *Int. J. Solids Struct.* **1997**, *34*, 859–875. [CrossRef]
15. Vasiliev, V.V. Modern conceptions of plate theory. *Compos. Struct.* **2000**, *48*, 39–48. [CrossRef]
16. Vasiliev, V.V.; Lure, S.A. On refined theories of beams, plates, and shells. *J. Comput. Math.* **1992**, *26*, 546–557. [CrossRef]
17. Cai, L.; Rong, T.; Chen, D. Generalized mixed variational methods for Reissner plate and its applications. *Comput. Mech.* **2002**, *30*, 29–37. [CrossRef]
18. Cen, S.; Shang, Y. Developments of Mindlin-Reissner plate elements. *Math. Probl. Eng.* **2015**, *12*, 456740. [CrossRef]
19. Zienkiewicz, O.C.; Taylor, R.L. *The Finite Element Method*, 4th ed.; McGraw-Hill Book Co.: London, UK, 1991; Volume 2.
20. Bathe, K.J. *Finite Element Procedures*; Prentice-Hall International, Inc.: Watertown, MA, USA, 1996.
21. Endo, M.; Kimura, N. An alternative formulation of the boundary value problem for the Timoshenko beam and Mindlin plate. *J. Sound Vib.* **2007**, *301*, 355–373. [CrossRef]
22. Kim, S.E.; Thai, H.-T.; Lee, J. A two variable refined plate theory for laminated composite plates. *Compos. Struct.* **2009**, *89*, 197–205. [CrossRef]
23. Kim, S.-E.; Thai, H.-T.; Lee, J. Buckling analysis of plates using the two variable refined plate theory. *Thin-Walled Struct.* **2009**, *47*, 455–462. [CrossRef]
24. Park, M.; Choi, D.-H. A two-variable first-order shear deformation theory considering in-plane rotation for bending, buckling and free vibration analyses of isotropic plates. *Appl. Math. Model.* **2018**, *61*, 49–71. [CrossRef]
25. Shimpi, R.P.; Patel, H.G. A two variable refined plate theory for orthotropic plate analysis. *Int. J. Solids Struct.* **2006**, *43*, 6783–6799. [CrossRef]
26. Shimpi, R.P.; Patel, H.G. Free vibrations of plate using two variable refined plate theory. *J. Sound Vib.* **2006**, *296*, 979–999. [CrossRef]
27. Shimpi, R.P. Refined plate theory and its variants. *AIAA J.* **2002**, *40*, 137–146. [CrossRef]
28. Shimpi, R.P.; Shetty, R.A.; Guha, A. A single variable refined theory for free vibrations of a plate using inertia related terms in displacements. *Eur. J. Mech. A/Solids* **2017**, *65*, 136–148. [CrossRef]
29. Kolakowski, Z.; Jankowski, J. Effect of membrane components of transverse forces on magnitudes of total transverse forces in the nonlinear stability of plate structures. *Materials* **2020**, *13*, 5262. [CrossRef]
30. Kolakowski, Z.; Krolak, M. Modal coupled instabilities of thin-walled composite plate and shell structures. *Compos. Struct.* **2006**, *76*, 303–313. [CrossRef]
31. Ghugal, Y.M.; Shimpi, R.P. A review of refined shear deformation theories of isotropic and anisotropic laminated plates. *J. Reinf. Plast. Compos.* **2002**, *21*, 775–813. [CrossRef]
32. Jones, R.M. *Mechanics of Composite Materials*, 2nd ed.; Taylor and Francis, Inc.: Philadelphia, PA, USA, 1999.
33. Adim, B.; Daouadji, T.H.; Rabahi, A. A simple higher order shear deformation theory for mechanical behavior of laminated composite plates. *Int. J. Adv. Struct. Eng.* **2016**, *8*, 103–117. [CrossRef]
34. Daouadji, T.H.; Tounsi, A.; Adda Bedia, E.A. A new higher order shear deformation model for static behavior of functionally graded plates. *Adv. Appl. Math. Mech.* **2013**, *5*, 351–364. [CrossRef]
35. Navale, K.U.; Pise, C.P. A review on high order shear deformation theory for orthotropic composite laminates. *Int. J. Eng. Res. Technol.* **2021**, *10*, 477–481.
36. Neves, A.M.A.; Ferreira, A.J.M.; Carrera, E.; Cinefra, M.; Roque, C.M.C.; Jorge, R.M.N.; Soares, C.M.M. Buckling behaviour of cross-ply laminated plates by a higher-order shear deformation theory. *Sci. Eng. Compos. Mater.* **2012**, *19*, 119–125. [CrossRef]
37. Reddy, J.N. *Introduction to the Finite Element Method*; McGraw-Hill Education: New York, NY, USA, 2019.
38. Shi, P.; Dong, C.; Sun, F.; Liu, W.; Hu, Q. A new higher order shear deformation theory for static, vibration and buckling responses of laminated plates with the isogeometric analysis. *Compos. Struct.* **2018**, *204*, 342–358. [CrossRef]
39. Srividhya, S.; Kumar, B.; Gupta, R.K.; Rajagopal, A. Nonlinear analysis of FGM plates using generalised higher order shear deformation theory. *Int. J. Mater. Struct. Integr.* **2019**, *13*, 3–15. [CrossRef]
40. Swain, P.R.; Adhikari, B.; Dash, P. A higher-order polynomial shear deformation theory for geometrically nonlinear free vibration response of laminated composite plate. *Mech. Adv. Mater. Struct.* **2019**, *26*, 129–138. [CrossRef]
41. Thai, H.-T.; Choi, D.-H. A simple first-order shear deformation theory for laminated composite plates. *Compos. Struct.* **2013**, *106*, 754–763. [CrossRef]
42. Yi, S.-C.; Yao, L.-Q.; Tang, B.-J. A novel higher-order shear and normal deformable plate theory for the static, free vibration and buckling analysis of functionally graded plates. *Math. Probl. Eng.* **2017**, 6879508. [CrossRef]
43. Volmir, A.S. *Flexible Plates and Shells*; State Publishing House of Technical-Theoretical Literature: Moscow, Russia, 1956. (In Russian)

materials

Article

# Determining the Shear Capacity of Steel Beams with Corrugated Webs by Using Optimised Regression Learner Techniques

**Ahmed S. Elamary [1,*] and Ibrahim B. M. Taha [2]**

[1] Civil Engineering Department, College of Engineering, Taif University, P.O. Box 11099, Taif 21944, Saudi Arabia
[2] Electrical Engineering Department, College of Engineering, Taif University, P.O. Box 11099, Taif 21944, Saudi Arabia; i.taha@tu.edu.sa
* Correspondence: a.elamary@tu.edu.sa; Tel.: +966-581338825

**Abstract:** The use of corrugated webs increases web shear stability and eliminates the need for transverse stiffeners in steel beams. Optimised regression learner techniques (ORLTs) are rarely used for calculating shear capacity in steel beam research. This study proposes a new approach for calculating the maximum shear capacity of steel beams with trapezoidal corrugated webs (SBCWs) by using ORLTs. A new shear model is proposed using ORLTs in accordance with plate buckling theory and previously developed formulas for predicting the shear strength of SBCWs. The proposed ORLT models are implemented using the regression learner toolbox of MATLAB software (2020b). The available data of more than 125 test results from different specimens prepared by previous researchers are used to create the model. In this study, web geometry and relevant web steel grades determine the shear capacity of SBCWs. Four regression methods are adopted. Results are compared with those of an artificial neural network model. The model output factor represents the ratio of the web vertical shear stress to the normalised shear stress. Shear capacity can be estimated on the basis of the resulting factor from the model. The proposed model is verified using two methods. In the first method, a series of tests are performed by the authors. In the second method, the results of the model are compared with the shear values obtained experimentally by other researchers. On the basis of the test results of previous studies and the current work, the proposed model provides an acceptable degree of accuracy for predicting the shear capacity of SBCWs. The results obtained using Gaussian process regression are the most appropriate because its recoded mean square error is 0.07%. The proposed model can predict the shear capacity of SBCWs with an acceptable percentage of error. The recoded percentage of error is less than 5% for 93% of the total specimens. By contrast, the maximum differential obtained is ±10%, which is recorded for 3 out of 125 specimens.

**Keywords:** shear strength; corrugated web; regression learner techniques; steel beams

## 1. Introduction

Extensive studies have been conducted regarding the shear strength (SS) of steel beams with trapezoidal corrugated webs (SBCWs). This section presents some of these studies. An experimental study was conducted by Lindner and Aschinger [1] to calculate the SS of SBCWs. They suggested using 70% of shear buckling stress as the nominal SS for designing SBCWs. Worthy experimental and analytical research conducted by Elgaaly et al. [2], using loaded predominantly in shear. Large-scale SBCW investigations were conducted by Sause et al. [3], Abbas [4] and Driver et al. [5] to estimate the SS of SBCWs. They provided an equation for estimating the lower bound of the SS of SBCWs. In addition, they recommended precluding global buckling because this phenomenon requires a significant loss of strength and a low degree of post-buckling strength. Yi et al. [6] presented a formula for the nominal SS of SBCWs. This formula was validated by comparing the obtained values of 15 test results and finite element analysis results. Moon et al. [7] reported the results of three tests and described the SS formula presented by Yi et al. [6]. Moon et al. [7] compared the results of their proposed formula with the results of several formulas developed by other researchers from 17 tests. Sause and Braxtan [8] theoretically investigated the SS of SBCWs. They collected a database of 102 tests from 8 previous studies and developed an analytical model for estimating the normalised SS. Their formula was consistent with only one subset (i.e., 22 test results) of the 120 available published test results. These researchers attributed the inconsistency to the test conditions. Consequently, their proposed model was valid only for SBCWs that fulfil the geometric criteria they set. From the previous research, numerous buckling formulas have been proposed to calculate global shear buckling and interaction buckling (IB). The proposed formulas for calculating IB were given by [6,8–13] from 1984 to 2008. Regarding the hybrid steel beams with corrugated web, Elamary et al. [14] presented an experimental study concerned with the failure mechanism of SBCW's non-welded inclined fold. The case of non-welded inclined folds, owing to decrease the effect of the fatigue cracks initiated along the inclined folds. Additionally, they studied the influence of using a limited number of flange stiffeners at certain places to postpone the earlier flange buckling that may occur in these places.

Extensive research was conducted and focus on the computational methods and their uses for validating experiments; some of it is presented herein, which carried out by [15–20]. Manoj et al. [15] studied the flexural behaviour of steel beams by using ANSYS software. They reported that the load-carrying capacity of the CW beam increased by increasing the web thickness as well as the optimum corrugated angle is recommended to be 45°. Krejsa et al. [16] and Čajka et al. [17,18] discussed an application of the original and probabilistic method—"Direct Optimized Probabilistic Calculation"—as a faster completion method of computations. They used this approach for modelling and experimental validation of reliability in the pre-stressed masonry construction.

Research on the shear capacity of SBCW calculation by using optimised regression learner techniques (ORLTs) is limited. The only previous study that used regression techniques in SBCWs was that by Barakat et al. [21] in 2015. They proposed a model for predicting the shear buckling strength of SBCWs. The model calculation was based on the calculated interaction shear buckling of the specimen. They collected 93 experimental data from previous studies. These researchers concluded that the accurate prediction of the shear buckling strength of SBCWs was within a 95% confidence interval when minimal processing of data was performed.

The problem is that using some input parameters representing web dimensions and properties can contribute to a qualitatively higher level of the reliability assessment in computing the shear capacity of SBCWs. For this reason, the current study presents an alternative method for calculating the maximum shear capacity of SBCWs by using ORLTs through the known dimensions and steel grade of specimen webs. The model considers only web material properties and dimensions as major factors in the calculation without determining local, global and interaction shear buckling. The advantage of this model is that it requires extremely limited input data (i.e., web dimension and steel grade). In addition, the result obtained from the model parameters considers the interaction amongst various shear failure modes (i.e., local, global and interaction).

The objective of this research is to propose such a model that can predict the shear capacity of SBCWs computationally by using the steel grade and dimensions of a web determined from the preliminary design. The input data required for the model are web dimensions (thickness, height, shear span and corrugation geometric profile) and web yield stress. The resulting factor from the model represents the ratio of the web vertical shear stress to the normalised shear stress. The maximum shear capacity of the beam can be regarded as the model's resulting factor multiplied by the normalised shear strength multiplied by the yielding vertical shear force. The research procedure can be summarised in seven steps. (1) Data relevant to more than 125 experimentally tested specimens are collected from the published studies of other researchers. (2) Test data and results from previous studies are organised in accordance with the corresponding parameters of the test specimens. (3) A summary of previously proposed formulas for predicting the SS of SBCWs with their corresponding theories is presented to identify the most dominant parameter that influences the SS of SBCWs. (4) The regression learner toolbox of MATLAB software is used for the regression process, which adopts four major optimised regression methods: decision tree (DT), support vector machines (SVM), Gaussian process regression (GPR) and ensemble trees (EN). Each regression method has different parameters obtained from the optimisation process. (5) The four ORLTs are tested by comparing the mean square error (MSE) and root-mean-square error (RMSE) calculated for each method. (6) In addition, another comparison is conducted between the results obtained from each of the four methods with that obtained from an artificial neural network (ANN) model. (7) Validation of the new modelling technique is achieved in two ways. Firstly, an experimental programme is conducted to test three specimens with different web geometries, steel grades and load setups. Secondly, the model results are compared with the test results obtained from two previous studies.

## 2. Theoretical Background

The local shear buckling stress of a corrugated web can be predicted in accordance with plate buckling theory [22]. Equation (1) expresses the corresponding local elastic shear buckling stress, $\tau_{L,el}$, on a single fold (longitudinal or inclined, Figure 1). In this case, each fold is assumed to be supported by the adjacent folds along its vertical edges and by the flanges along its horizontal edges.

$$\tau_{el,\,L} = k_L \frac{\pi^2\,E}{12(1-v^2)(\omega/t_W)^2} \tag{1}$$

where, $k_L$ is the local shear buckling coefficient that depends on the fold aspect ratio and the boundary conditions; $E$ and $\nu$ are Young's modulus and Poisson's ratio, respectively; $w$ is the fold width; $t_w$ is the web thickness. To determine the smallest value of $\tau_{L,el}$, $w$ is set to be larger than c and b, as illustrated in Figure 1. Equation (1) has been used in many studies [1,2,4–6,23] to predict the local elastic shear buckling stress of corrugated webs.

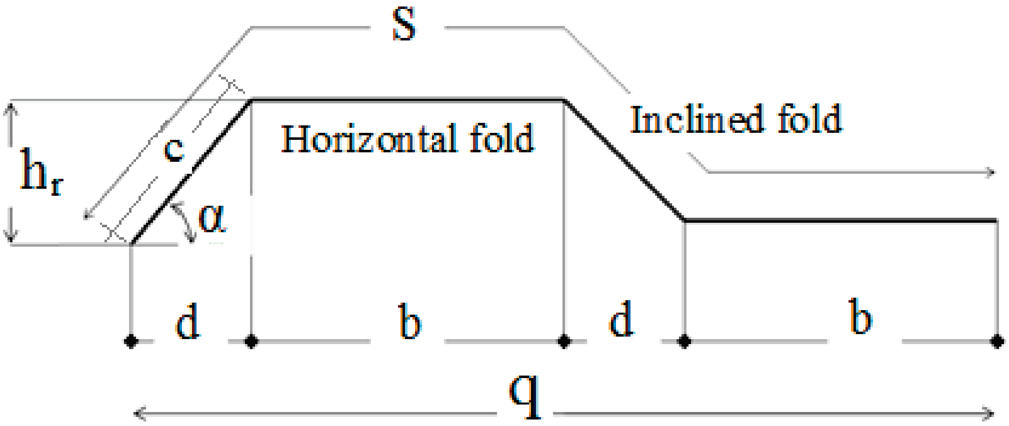

**Figure 1.** Corrugated web: profile configuration.

On the basis of the expression for the global elastic shear buckling stress $\tau_{G,\ el}$ of corrugated plates proposed by Easley [24], Abbas [25] developed an equation to express the global shear buckling stress from geometric properties, i.e., Equation (2).

$$\tau_{G,\ el} = k_G F(\alpha,\ \beta) \frac{E\ {t_W}^{1/2}\ b^{3/2}}{12\ h_w^2} \tag{2}$$

where $F(\alpha,\ \beta)$ is a relation between coefficient $(\beta)$ and corrugation profile slope $(\alpha)$; $(\beta)$ is a coefficient based on the relation between the ratio of b to c and the corrugation profile slope $(\alpha)$. This relation is proposed in Equation (3).

$$F(\alpha,\ \beta) = \sqrt{\frac{(1+\beta)\ \sin^3\alpha}{\beta + cos\ \alpha}} \left\{ \frac{3\beta + 1}{\beta^2(\beta+1)} \right\} \tag{3}$$

where, $h_w$ and $t_w$ are the web height and thickness, respectively.

To minimise $k_L$, a small aspect ratio, $w/hw$, must be considered. In this case, $k_L$ lies between 5.34 and 8.98, assuming simply supported and fixed edges, respectively. In addition, a minimised $k_G$ can be obtained by assuming that the web is infinitely long [8]. By assuming that the web is long relative to *hw,* Elgaaly et al. [2] suggested in 1996 that $k_G$ should be set as 31.6 or 59 (assuming that the web is simply supported by flanges or flanges provide the web with fixed support, respectively). However, Easely [24] suggested in 1975 that $k_G$ varies between 36 and 68.4.

The general IB shear stress formula originally proposed by Lindner and Aschinger [1] is given in Equation (4).

$$\frac{1}{(\tau_{I,\ \mathrm{el}})^n} = \frac{1}{(\tau_{L,\ \mathrm{el}})^n} + \frac{1}{(\tau_{G,\ \mathrm{el}})^n} \tag{4}$$

where, $\tau_{I,el}$, $\tau_{L,el}$ and $\tau_{G,el}$ are interaction, local and global elastic shear buckling stresses.

Corresponding to Equation (4), Lindner and Aschinger [1] proposed two interaction formulas with $n = 1$ and $n = 2$. Yi et al. [6] used a formula that corresponds to Equation (4) with $n = 1$. Equation (4) is solved for $\tau_{I,el}$, as shown in Equation (5).

$$\tau_{I,n,\ \mathrm{el}} = \frac{\tau_{L,\ \mathrm{el}}\ \tau_{G,\ \mathrm{el}}}{\left[(\tau_{L,\ \mathrm{el}})^n + (\tau_{G,\ \mathrm{el}})^n\right]^{1/n}} \tag{5}$$

On the basis of local, global and interaction buckling shear stresses, local, global and interaction buckling slenderness ratios can be, respectively, expressed as follows:

$$\lambda_L = \sqrt{\frac{\tau_y}{\tau_{\mathrm{el},L}}} = \frac{\omega}{t_w}\sqrt{\frac{12\ (1-v^2)\ \tau_y}{k_L \pi^2\ E}}, \tag{6}$$

$$\lambda_G = \sqrt{\frac{\tau_y}{\tau_{\mathrm{el},G}}} = \sqrt{\frac{12\ \tau_y\ h_w^2}{k_G\ F(\alpha,\ \beta)\ E\ {t_w}^{1/2}\ b^{3/2}}}, \tag{7}$$

$$\lambda_{I,\ n} = \sqrt{\frac{\tau_y}{\tau_{I,\ n,el}}} = \lambda_L \lambda_G \left[(1/\lambda_L)^{2n} + (1/\lambda_G)^{2n}\right]^{1/2n}. \tag{8}$$

where $\lambda_L$, $\lambda_G$ and $\lambda_{I,n}$ are local, global and interaction buckling slenderness ratios; whereas, the $\tau_y$ is shear yield stress, and $\tau_I$ is the interaction shear buckling. Numerous studies have used these slenderness ratios to calculate the normalised local, global and interaction elastic shear buckling strength. The following formula was proposed by Yi et al. [6] for calculating normalised shear strength $(\rho_{n,Y})$:

$$\rho_{n,\ Y} = \frac{\tau_{n,\ Y}}{\tau_Y} = 1 - 0.614\ (\lambda_{I,1} - 0.6) \le 1.0\ if\ \lambda_{I,1} \le \sqrt{2}\,,$$

$$\rho_{n,\,Y} = \frac{\tau_{n,\,Y}}{\tau_Y} = \frac{1}{(\lambda_{l,1})^2}\; if\; \lambda_{l,1} > \sqrt{2}, \tag{9}$$

where $\rho_{n,Y}$ is the normalised shear strength proposed by YI et al. [6]; $\lambda_{l,1}$ is derived from Equation (8) with $n$ = 1; $\tau_Y$ is the shear yield stress, which is equal to $\frac{F_Y}{\sqrt{3}}$.

## 3. Assessment of SBCW Shear Capacity Formulas

In accordance with previous studies and theories, maximum shear capacity can be largely determined from the contribution of the web. Therefore, the proposed formula is based on the calculated local, global and IB shear stresses for each specimen from Equations (6)–(8). Assume that web shear stress is constant over web height and equal to the average calculated shear stress. Hence, the web vertical shear stress can be calculated using Equation (10) as reported by [8].

$$\tau = \frac{v_n}{h_w\, t_w}, \tag{10}$$

where $V_n$ is the nominal vertical shear force in the steel beam.

Assume that ($\zeta$) represents the ratio of the web vertical shear stress ($\tau$) to the normalised shear stress ($\tau_{n,Y}$) as indicated in Equation (11) as reported by [8].

$$\zeta = \frac{\tau}{\tau_{n,\,Y}} \tag{11}$$

Accordingly, from Equations (9)–(11), the following formula is proposed by the author to calculate the normalised shear force ($V_n$) (i.e., maximum shear capacity of a test specimen), and it is equal.

$$V_n = \zeta\, \rho_{n,\,Y} \frac{F_Y}{\sqrt{3}}\, h_w\, t_w \tag{12}$$

where ($\rho_{n,\,Y}$) is the normalised shear strength, and ($\zeta$) is the ratio factor previously defined in Equation (11).

## 4. Test Data

The current study presents the database of 122 SS tests collected from 13 published studies [1,2,7,26–31]. This database is divided into two groups. The first group contains 115 published sources used in creating ORLT models. The second group consists of five shear tests collected from [32,33]. The group with three shear tests conducted by the authors is used to validate the model.

### *4.1. Test Data Published by Other Researchers*

The published test data are listed in Tables A1–A9 (Appendix A). The dimensions of the test specimens are provided in Tables A1–A9. These tests were conducted by the following authors. In 1996, Elgaaly et al. [2] reported the results of 42 tests (Table A1). The results of 25 tests from Sweden, Germany and Finland were reported by Lindner and Aschinger [1] in 1998 (Table A2). Johnson and Cafolla [26] summarised the results of three specimens in 1997 (Table A3). The results of 20 specimens were tested under shear forces by Peil [27] in 1998 (Table A4). Driver et al. [5] presented the shear test results of two steel girders with corrugated webs in 2002 (Table A5). Lee et al. [28] reported the results of nine shear tests in 2003 (Table A6). Moon et al. [7] summarised the results of three shear tests in 2008 (Table A7). Moussa et al. [29] provided the results of nine tests in 2018 (Table A8). Wang et al. [30], Sause and Clarke [23] and Hannebauer et al. [31] reported the results of one test each in 2019 (Table A9). In these tables, the definitions of symbols $h_w$, $b_p$, $t_w$, $b$, $d$, $h_r$ and $F_y$ are the same as those given earlier; whereas $h_w/t_w$ is the web slenderness. From a previous study [6], a conclusion is drawn that the normalised SS exhibits an indirect relation with the slenderness interaction shear buckling strength. Therefore, for all the test specimens listed in Tables A1–A9, Figure 2 shows the normalised experimental SS $\rho_e = \tau_e/\tau_y$ versus the interaction slenderness ratio at n = 1 ($\lambda_{I,1}$). The comparison between the normalised SS proposed by Yi et al. [6] ($\rho_{n,Y}$) and the normalised experimental SS is illustrated in Figure 2. The horizontal axis in this figure represents the slenderness interaction shear buckling strength with the exponent n = 1. As shown in this figure, the major factors that affect shear capacity are web height, web panel, web thickness, corrugation geometry and web yield stress.

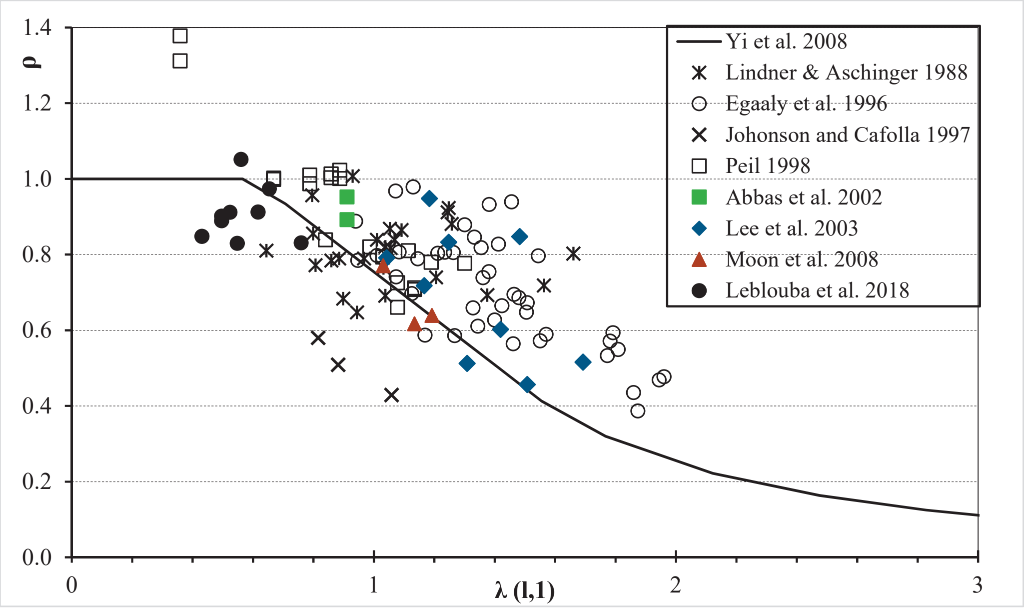

**Figure 2.** Relation between slenderness interaction shear buckling strength and normalised experimental shear strength.

### *4.2. Test Data from the Authors*

To validate the model, a series of three tests were conducted on SBCWs with different properties, dimensions and load cases (Figure 3). The load cases and dimensions of the test beams, which are denoted as 3PCW350, 4PCW275 and 3PCW200, and the material yield strength are provided in Table 1. In this table, 'P' and 'CW' represent 'point load' and 'corrugated web,' respectively; the number before 'P' represents the number of line loads applied. Meanwhile, the number following 'CW' indicates horizontal fold (HF) length (in mm). All the specimens were simply supported and loaded on a hydraulic testing machine by applying displacement control techniques at the civil engineering laboratories of Taif University. Specimens 3PCW350 and 3PCW200 have an HF of 350 mm and 200 mm, respectively. The two specimens have the same web yield stress and tested under a three-point load, as shown in Figure 3a,c. Specimen 4PCW275 has an HF of 275 mm and different yield stresses. It was tested under a four-point load as shown in Figure 3b. The three specimens analogised one another in the inclined fold dimensions and corrugation angle.

**Table 1.** Test data from the authors.

| Specimen ID | $h_w$ (mm) | a (mm) | $t_w$ (mm) | Corrugation Dimensions (mm) | | | $F_{yw}$ MPa | Web Slenderness | Variables |
|---|---|---|---|---|---|---|---|---|---|
| | | | | $b$ | $h_r$ | $d$ | | | |
| 3PCW350 | 384 | 900 | 2.80 | 350 | 100 | 100 | 325 | 137.14 | $b$, Load |
| 4PCW275 | 384 | 750 | 3.00 | 275 | 100 | 100 | 357 | 128.00 | $a, t_w, F_{yw}$ |
| 3PCW200 | 384 | 900 | 2.80 | 200 | 100 | 100 | 325 | 137.14 | $b$, Load |

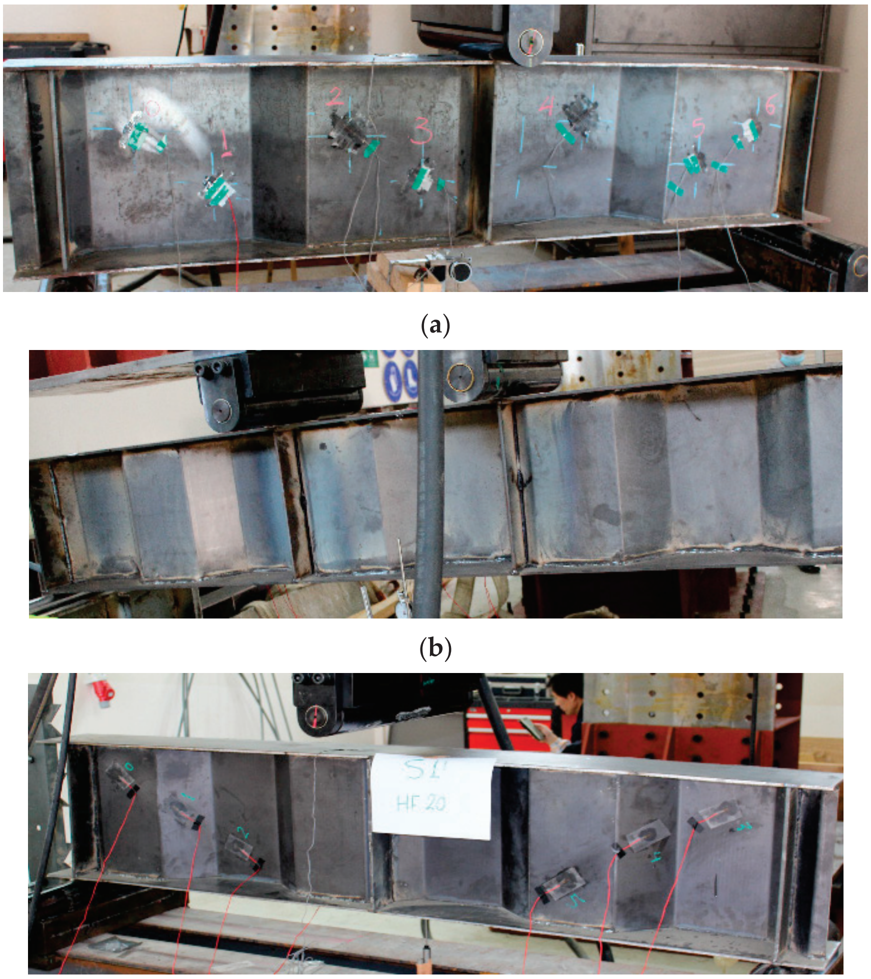

(**a**)

(**b**)

(**c**)

**Figure 3.** Sample of SBCW specimens: (**a**) Specimen 3PCW350, (**b**) Specimen 4PCW275 and (**c**) Specimen 3PCW200.

### *4.3. Test Setup*

The specimens were tested at Taif University in Saudi Arabia by using a 2000 kN capacity test frame, as shown in Figure 4. The specimens were tested under different loading conditions (three- and four-line loads). The unbraced length of the compressive flange was 1800 mm and 2250 mm for the three- and four-line loads, respectively, in accordance with the locations of the supports. The total length of a specimen was longer than the unbraced length of the compression flange by 100 mm (50 mm from each side). The shear span for the three-line loads was 900 mm, and for the four-line loads was 750 mm. The primary objective for fabricating and testing the specimens was to validate the proposed model under variable parameters and not to compare it with each other. The parameters were different for each specimen, such as HF length, loading type, shear span, web thickness and web yield stress. The specimens were loaded using displacement control techniques with an increment of 0.005 mm/s. To measure the vertical deflections of the specimens, a linear variable differential transformer (LVDT) was installed under the mid-span of each specimen, as illustrated in Figure 4.

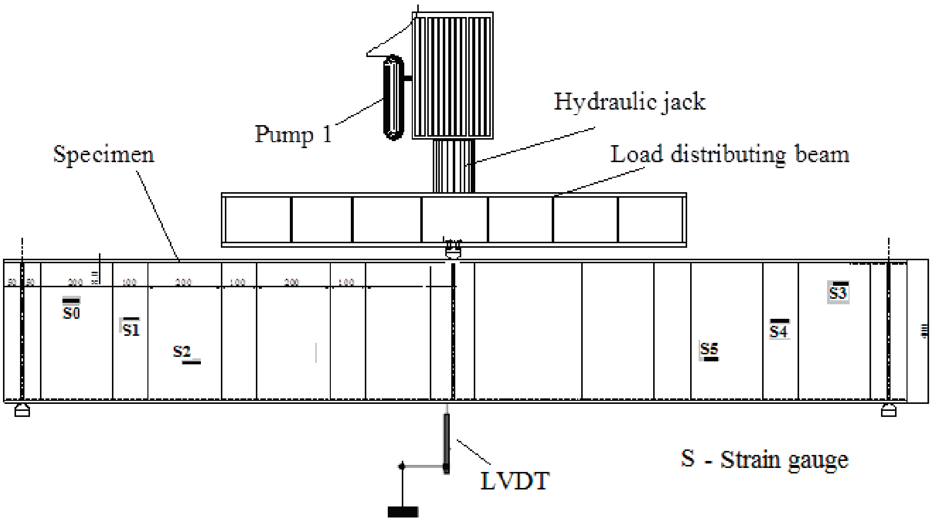

**Figure 4.** Test scheme.

The fabricated specimens had the same flange material properties and dimensions, whilst the webs had different material and geometric (HF length and thickness) properties. For all the specimens, the web slenderness ratio belongs to Class 4 in accordance with the Eurocodes. From the test results, the plot of the vertical load versus the mid-span vertical deflection of each tested specimen is shown in Figure 5. The maximum deflections achieved by the three-line load specimens (3PCW200 and 3PCW350) were 3.8 mm and 5 mm, respectively, before failure. Meanwhile, the maximum deflection recorded for specimen 4PCW275 was nearly 6 mm. Specimen 4PCW275 exhibited lower initial stiffness than the two specimens subjected to three-line loads. Conversely, the maximum shear force sustained by Specimen 4PCW275 (147.50 kN) was higher than those of the three-line load specimens, i.e., 3PCW200 (117.5 kN) and 3PCW350 (105 kN). Such difference is attributed to the four-line load specimen having higher web thickness and web yield stress than the three-line load specimens. This result is reasonable because web thickness and web yield stress are the most dominant parameters that influence the shear capacity of SBCWs.

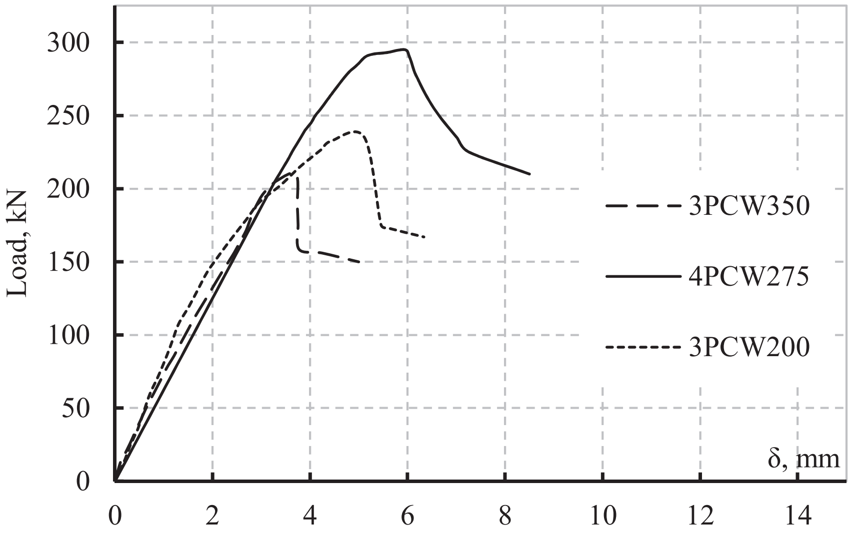

**Figure 5.** Load deflection curves of the specimens.

## 5. ORLTs

The regression learner toolbox of MATLAB software is one of the most frequently used techniques for regression. It has four major optimised regression methods [34]:

DT, SVM, GPR and EN. Each regression has different parameters obtained from the optimisation process. For example, the SVM hyperparameter search range is selected as follows: box constraints varied from 0.001 to 1000; the kernel scale varied from 0.001 to 1000; epsilon varied from 0.00030022 to 30.0222; the kernel functions were Gaussian, linear, quadratic, and cubic; the standardised data were true and false [34]. The optimal parameters of each ORLT were determined and evaluated based on the Bayesian optimisation (BO) technique [35–37]. The acquisition function used in the optimisation process was an expected improvement per second plus, and the total number of iterations was 30. The BO technique is the most effective approach used to determine the hyperparameters of the ORLTs during the training stage [35]. The BO technique determines the optimal parameters of each regression technique during each training step based on the prior and the probability space value of each parameter and choosing the highest probability values used to enhance the predicting accuracy of the ORLT model [36]. The details determining the best parameters of each regression technique using the BO technique were presented in [36] and [37].

The input features of the dataset samples were firstly normalised before the training process, as follows:

$$x_i = \frac{x_i - MIN_i}{MAX_i - MIN_i},\ i = 1,\ 2,,\ ....,\ 8, \tag{13}$$

where $x_i$ is the $i$th input feature; $MIN_i$ and $MAX_i$ are the minimum and maximum values of the $i$th input feature, respectively.

Figure 6 introduces the training procedure of ORLTs by using MATLAB's regression learner toolbox in 2020b MATLAB/Software.

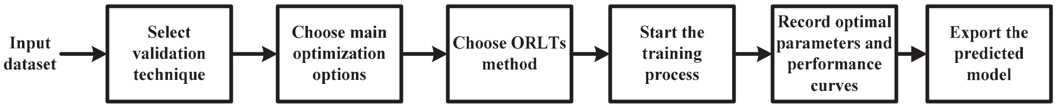

**Figure 6.** Training procedure of ORLTs.

The training procedure of the ORLTs can be summarised as follows:

1. The validation technique was selected, the cross-validation technique with 10 folds was chosen before the training process.
2. The primary optimisation options were selected, and the option used was the BO technique, with an expected improvement per second plus and 30 iterations.
3. One of the ORLTs was selected (DT, SVM, GPR or EN).
4. The training process is started to determine the optimal parameters and predicted model of this method.
5. The optimal parameters and performance model of the selected method were recorded.
6. Finally, the ORLT model of the selected method was exported to be used in the prediction of the original and new datasets.

Figure 7a presents the minimum MSE versus the training iteration numbers of DT, SVM, GPR and EN during training. The MSE values of the four regression methods illustrated that GPR achieved the lowest MSE amongst the four methods. Meanwhile, DT exhibited poor training performance. Figure 7b illustrates the relation between the predicted responses versus the true responses of the four regression methods. GPR exhibited the best response amongst the four methods.

Table 2 provides the optimal parameters of the four ORLT models. For example, the optimal parameters of the EN model are as follows: the selected ensemble method is the bag; the number of learners is 57; the minimum leaf size is 2; the number of predictors to samples is 8. The optimal parameters of the DT, SVM and GPR models are listed in Table 2.

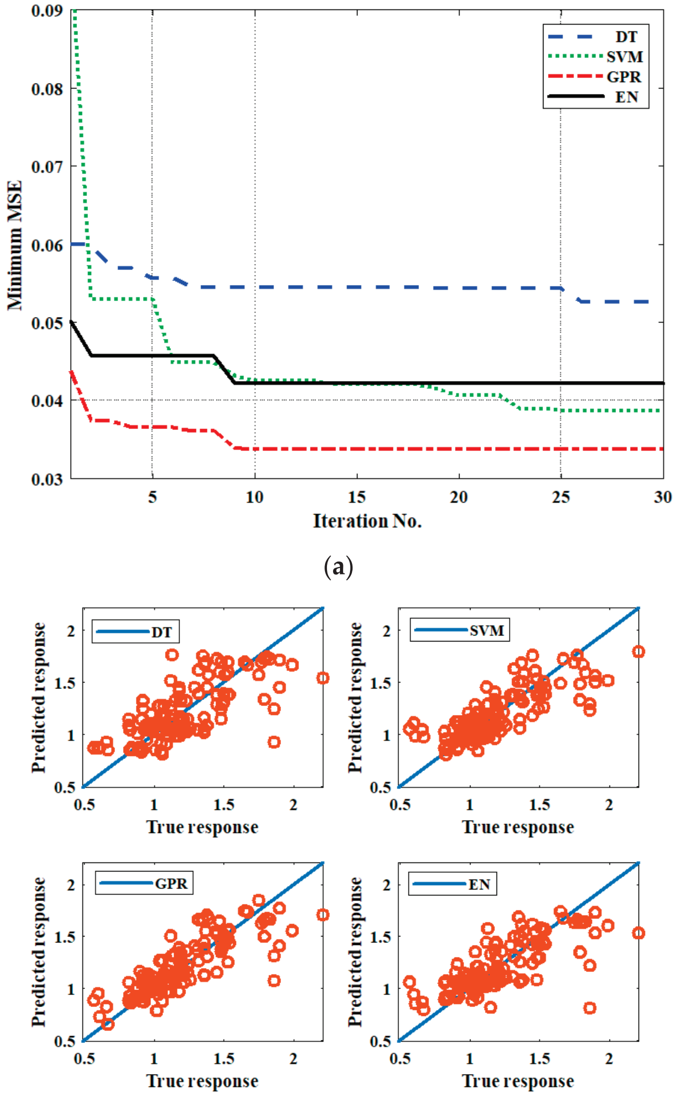

(**a**)

(**b**)

**Figure 7.** (**a**) Minimum MSE vs. iteration number; (**b**) predicted response vs. true response during training.

**Table 2.** Optimal parameters of each ORLT.

| ORLTs | Optimal Parameters |
|---|---|
| DT | Minimum leaf size: 12 |
| SVM | Box constraints: 992.584<br>Epsilon: 0.00031804<br>Kernel function: Linear<br>Standardised data: False |
| GPR | Sigma: 0.16623<br>Basis function: Zero<br>Kernel function: Isotropic exponential<br>Kernel scale: 0.66404<br>Standardised data: True |
| EN | Ensemble method: Bag<br>Number of learners: 57<br>Minimum leaf size: 2<br>Number of predictors to samples: 8 |

## 6. Model Validation and Comparison

The four ORLTs were tested and validated by comparing the calculated ratio for each specimen (ratio of web vertical shear stress to normalised shear stress) with that obtained from an ANN. MATLAB's ANN toolbox was used to train and test the ANN model. The normalised dataset (120 samples) was used as input for the ANN, and the corresponding ratio of web vertical shear stress ($\tau$) to normalised shear stress ($\tau_{n,Y}$) (Equation (11)) was used as the output for the training stage of the ANN. The ANN model consisted of three layers: the input, hidden and output layers. The number of neurons in the input layer was equal to the number of input features (eight input layers). The number of neurons in the hidden layer was selected to enhance the performance of the ANN model (24 neurons were used here). The number of output layers is equal to the number of output variables (one layer is used here). The normalised 120 dataset samples were divided during the training stage of the ANN model into three sets: for training (84 samples, 70%), validation (18 samples, 15%) and testing (18 samples, 15%). The MSE performance of the ANN model and the predicted responses for the training, validation and testing sets are presented in Figure 8.

Table 3 provides the MSE and RMSE of the differences between the values of $\zeta$ estimated using the model and calculated theoretically from the test database using Equation (11). From the results in Table 3, the authors concluded that GPR is the most suitable and accurate method for estimating the ratio $\zeta$ with an acceptable degree of accuracy.

**Table 3.** Comparison of the ORLT models with the ANN model.

| Evaluation Techniques | DT | SVM | GPR | EN | ANN |
|---|---|---|---|---|---|
| MSE | 0.04212 | 0.03962 | 0.00074 | 0.00391 | 0.01088 |
| RMSE | 0.20522 | 0.19906 | 0.02723 | 0.06253 | 0.10432 |

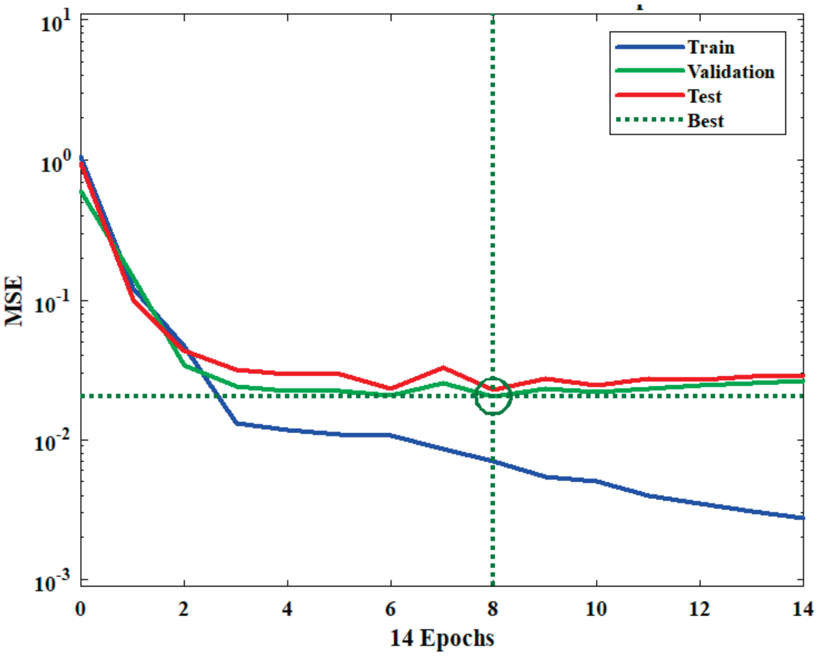

(a)

**Figure 8.** *Cont.*

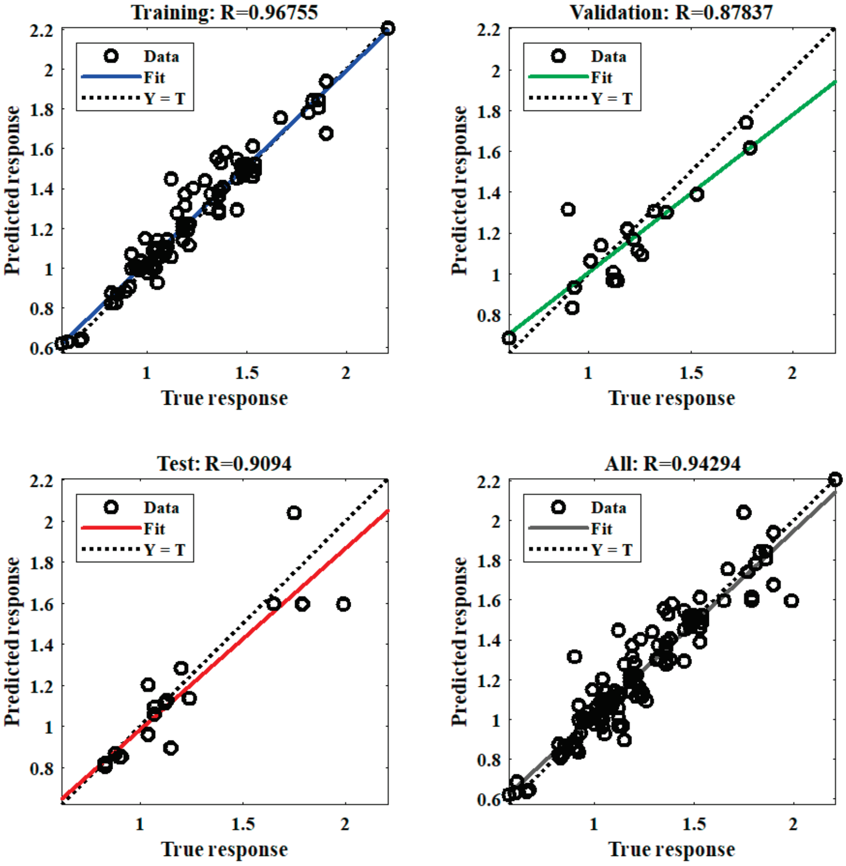

(**b**)

**Figure 8.** Validation and testing sets: (**a**) MSE vs. iteration epochs and (**b**) predicted response vs. true response.

## 7. Initial Comparison with Published Experimental Data

The analysis of the test results of the test specimens is presented in Appendix A (Tables A10–A18). A specimen identifier is given in the first column, and the local slenderness ratio is provided in the second column. The third column presents the global slenderness ratio, and the fourth column shows the interaction slenderness ratio $\lambda_{I,1}$ [Equation (8), with n = 1]. The fifth column provides the normalised SS from Equation (9), $\rho_{n,Y}$. The sixth column lists the values of $\zeta$ calculated using GPR. The seventh column gives the anticipated maximum shear force ($V_n$) by using Equation (12), whilst the eighth column provides the shear test results ($V_T$). The last column indicates the ratio of $V_n$ to $V_T$.

Table 4 provides a summary of the results divided into three groups. The first group represents the results of 76 specimens. The number of specimens in this group is equivalent to 65% of the total number, and the results of shear forces from the proposed model are between ±1% of the test shear results. The second group represents the results of 38 specimens, which is equivalent to 32% of the total number of collected specimens. The maximum shear force calculated in Group 2 by using the proposed model is ±5% of the corresponding specimen's test shear results. The last group included three specimens, which is equivalent to nearly 3% of the total. The maximum shear forces anticipated by the model exhibit −8% to 10% of the corresponding specimen's test shear results.

To validate the proposed model, the database of six tests from two previous studies and three tests conducted by the authors were presented in this paper. Table 5 provides the dimensions of the test specimens from the following studies: Moussa et al. [32] reported the results of four tests, and Nie et al. [33] summarised the results of two specimens. The database of the three tests conducted by the authors is presented in Table 1.

**Table 4.** Mean, standard deviation (Std. dev.), coefficient of variation (Co. Var.), maximum (Max.) and minimum (Min).

| Number of Test Data | Mean | Std. Dev. | Co. Var. | Max. | Min. |
|---|---|---|---|---|---|
| 116 | 1.0018 | 0.021 | 0.021 | 1.10 | 0.926 |
| 76 out of 116 (65%) | 0.987 | 0.015 | 0.015 | 1.015 | 0.986 |
| 38 out of 116 (32%) | 1.0033 | 0.029 | 0.028 | 1.055 | 0.955 |
| 3 out of 116 (3%) | 1.0185 | 0.071 | 0.07 | 1.10 | 0.926 |

**Table 5.** Data of specimens tested in previous studies.

| Specimen ID | $h_w$ | a | $t_w$ | Corrugation Dimensions | | | $F_{yw}$ | Web Slenderness |
|---|---|---|---|---|---|---|---|---|
| | | | | $b$ | $h_r$ | $d$ | | |
| Moussa et al. [32] | | | | | | | | |
| A12-305-30 | 305 | 557.0 | 1.20 | 40 | 20.00 | 34.64 | 230 | 254.17 |
| A12-410-30 | 410 | 557.0 | 1.20 | 40 | 20.00 | 34.64 | 230 | 341.67 |
| A12-505-30 | 505 | 557.0 | 1.20 | 40 | 20.00 | 34.64 | 230 | 420.83 |
| A12-505-45 | 505 | 526.5 | 1.20 | 40 | 28.28 | 28.28 | 230 | 420.83 |
| Nie et al. [33] | | | | | | | | |
| S2-1 | 260 | 1200 | 0.90 | 80 | 48 | 64 | 385.50 | 288.89 |
| S2-2 | 360 | 1200 | 0.90 | 80 | 48 | 64 | 385.50 | 400.00 |

By using the preceding data as a database for the proposed model, the maximum capacity of the shear force that can be resisted by each specimen is provided in Table 6. The ratio of the model results to the experimental results is ±9%.

**Table 6.** Analysis results of test specimens reported in previous studies.

| Specimen ID | $\lambda_L$ | $\lambda_G$ | $\lambda_{I,1}$ | $\rho_e$ | $\zeta$ | $V_n$ (kN) | $V_T$ (kN) | $V_n/V_T$ |
|---|---|---|---|---|---|---|---|---|
| Moussa et al. [32] | | | | | | | | |
| A12-305-30 | 0.391 | 0.34 | 0.52 | 1.00 | 0.94 | 45.60 | 49.8 | 0.92 |
| A12-410-30 | 0.391 | 0.46 | 0.60 | 1.00 | 0.98 | 64.21 | 66.3 | 0.97 |
| A12-505-30 | 0.391 | 0.56 | 0.69 | 0.95 | 1.03 | 78.46 | 72 | 1.09 |
| A12-505-45 | 0.391 | 0.43 | 0.58 | 1.00 | 1.03 | 82.99 | 89.1 | 0.93 |
| Nie et al. [33] | | | | | | | | |
| S2-1 | 1.349 | 0.21 | 1.37 | 0.53 | 0.90 | 24.88 | 25.24 | 0.99 |
| S2-2 | 1.349 | 0.29 | 1.38 | 0.52 | 0.97 | 36.58 | 39.31 | 0.93 |
| Authors | | | | | | | | |
| 3PCW350 | 1.74 | 0.16 | 1.75 | 0.327 | 1.56 | 102.94 | 105.00 | 0.98 |
| 4PCW275 | 1.339 | 0.15 | 1.35 | 0.54 | 1.16 | 149.36 | 147.50 | 1.01 |
| 3PCW200 | 0.995 | 0.13 | 1.00 | 0.752 | 0.80 | 121.45 | 117.50 | 1.03 |

## 8. Conclusions

This study presented a new approach for calculating the maximum shear capacity of SBCWs. The approach was implemented using ORLTs. Four regression methods were used to select the most appropriate one, which could achieve the least MSE. The model was created on the basis of 125 test results of different specimen parameters obtained by previous researchers. The input parameters were the web dimensions (thickness, height, shear span and corrugation geometric profile) and web yield stress. The model output was the ratio of the web vertical shear stress to the normalised shear stress. Validation of the model results was determined using both an experimental programme conducted by the authors and an experimental database from previous studies. The following conclusions can be drawn from the obtained results: (i) The model procedures to calculate the maximum shear capacity of steel beams with corrugated web are well-suited for the design of beam elements in load-carrying with the required level of reliability. (ii) The shear capacity of SBCWs can be predicted to an acceptable degree of accuracy by using the resulting factor from the proposed model. (iii) The proposed model exhibited a percentage error on the shear capacity of less than ±5% for 97% of the total number of specimens. (iv) ORLTs methods can be used in calculating the design shear of SBCWs. (v) The most appropriate method for calculating the shear force of SBCWs is the GPR method. (vi) The mean square error (MSE), as the difference between the resulting output factors and those calculated for each specimen, was less than 0.1%.

**Author Contributions:** Conceptualisation, A.S.E. and I.B.M.T.; methodology, A.S.E. and I.B.M.T.; software, I.B.M.T.; validation, A.S.E. and I.B.M.T.; formal analysis, A.S.E. and I.B.M.T.; investigation, A.S.E. and I.B.M.T.; resources, A.S.E. and I.B.M.T.; data curation, A.S.E.; writing—original draft preparation, A.S.E. and I.B.M.T.; writing—review and editing, A.S.E. and I.B.M.T.; visualisation, A.S.E. and I.B.M.T.; supervision, A.S.E.; project administration, A.S.E.; funding acquisition, I.B.M.T. All authors have read and agreed to the published version of the manuscript.

**Funding:** This research received no external funding.

**Institutional Review Board Statement:** Not applicable.

**Informed Consent Statement:** Not applicable.

**Data Availability Statement:** The data presented in this study are available on request from the corresponding author.

**Acknowledgments:** The authors would like to acknowledge the financial support received from Taif University Researchers Supporting Project Number (TURSP-2020/61), Taif University, Taif, Saudi Arabia.

**Conflicts of Interest:** The authors declare that no conflict of interest.

## Appendix A. Experimental Data

**Table A1.** Data of specimens tested by Lindner and Aschinger [1].

| Specimen ID | $h_w$ | $a$ | $t_w$ | Corrugation Dimensions | | | $F_{yw}$ | Web Slenderness |
|---|---|---|---|---|---|---|---|---|
| | | | | $b$ | $h_r$ | $d$ | | |
| L1A | 994 | 974 | 2 | 140 | 50.03 | 50 | 292 | 512.37 |
| L1B | 994 | 984 | 3 | 140 | 50.03 | 50 | 335 | 383.78 |
| L2A | 1445 | 1503 | 2 | 140 | 50.03 | 50 | 282 | 744.85 |
| L2B | 1445 | 1503 | 3 | 140 | 50.03 | 50 | 317 | 568.90 |
| L3A | 2005 | 2005 | 2 | 140 | 50.03 | 50 | 280 | 997.51 |
| L3B | 2005 | 2005 | 3 | 140 | 50.03 | 50 | 300 | 792.49 |
| B1 | 600 | 798 | 2 | 140 | 50.03 | 50 | 341 | 285.71 |
| B4 | 600 | 798 | 2 | 140 | 50.03 | 50 | 363 | 284.36 |
| B4b | 600 | 798 | 2 | 140 | 50.03 | 50 | 363 | 284.36 |
| B3 | 600 | 798 | 3 | 140 | 50.03 | 50 | 317 | 229.01 |
| B2 | 600 | 702 | 3 | 140 | 50.03 | 50 | 315 | 229.01 |
| M101 | 600 | 600 | 1 | 70 | 15.01 | 15 | 189 | 606.06 |
| M102 | 800 | 800 | 1 | 70 | 15.01 | 15 | 190 | 808.08 |
| M103 | 1000 | 1000 | 1 | 70 | 15.01 | 15 | 213 | 1052.63 |
| M104 | 1200 | 1200 | 1 | 70 | 15.01 | 15 | 189 | 1212.12 |
| L1 | 1000 | 1500 | 2 | 106 | 50.02 | 87 | 410 | 476.19 |
| L1 | 1000 | 1490 | 3 | 106 | 50.02 | 87 | 450 | 333.33 |
| L2 | 1498 | 2157 | 2 | 106 | 50.02 | 87 | 376 | 749.00 |
| L2 | 1498 | 2142 | 3 | 106 | 50.02 | 87 | 402 | 499.33 |
| No. 1 | 850 | 1131 | 2 | 102 | 55.55 | 86 | 355 | 425.00 |
| No. 2 | 850 | 1131 | 2 | 91 | 56.30 | 72 | 349 | 425.00 |
| V1/1 | 298 | 2819 | 2 | 144 | 102.06 | 102 | 298 | 145.37 |
| V1/2 | 298 | 2000 | 2 | 144 | 102.06 | 102 | 283 | 141.90 |
| V1/3 | 298 | 1001 | 2 | 144 | 102.06 | 102 | 298 | 149.00 |
| V2/3 | 600 | 1650 | 3 | 144 | 102.06 | 102 | 279 | 200.00 |

**Table A2.** Data of specimens tested by Elgaaly et al. [2].

| Specimen ID | $h_w$ | $a$ | $t_w$ | Corrugation Dimensions | | | $F_{yw}$ | Web Slenderness |
|---|---|---|---|---|---|---|---|---|
| | | | | $b$ | $h_r$ | $d$ | | |
| V-PILOTA | 305 | 305 | 0.78 | 38.10 | 25.42 | 25.40 | 621 | 390.03 |
| V-PILOTB | 305 | 305 | 0.79 | 38.10 | 25.42 | 25.40 | 638 | 388.54 |
| V121216A | 305 | 305 | 0.64 | 38.10 | 25.42 | 25.40 | 676 | 478.06 |
| V121216B | 305 | 305 | 0.77 | 38.10 | 25.42 | 25.40 | 665 | 398.69 |
| V181216B | 457 | 305 | 0.61 | 38.10 | 25.42 | 25.40 | 618 | 749.18 |
| V181216C | 457 | 305 | 0.76 | 38.10 | 25.42 | 25.40 | 679 | 602.11 |
| V181816A | 457 | 457 | 0.64 | 38.10 | 25.42 | 25.40 | 591 | 719.69 |
| V181816B | 457 | 457 | 0.74 | 38.10 | 25.42 | 25.40 | 614 | 620.08 |
| V241216A | 610 | 305 | 0.64 | 38.10 | 25.42 | 25.40 | 591 | 960.63 |
| V241216B | 610 | 305 | 0.79 | 38.10 | 25.42 | 25.40 | 588 | 775.10 |
| V121221A | 305 | 305 | 0.63 | 41.90 | 33.45 | 23.40 | 665 | 484.13 |
| V121221B | 305 | 305.00 | 0.79 | 41.90 | 33.45 | 23.40 | 665 | 388.54 |
| V122421A | 305 | 609.60 | 0.68 | 41.90 | 33.45 | 23.40 | 621 | 451.18 |
| V122421B | 305 | 609.60 | 0.78 | 41.90 | 33.45 | 23.40 | 638 | 390.03 |
| V181221A | 457 | 305 | 0.61 | 41.90 | 33.45 | 23.40 | 578 | 749.18 |
| V181221B | 457 | 305 | 0.76 | 41.90 | 33.45 | 23.40 | 606 | 599.74 |
| V181821A | 457 | 457 | 0.64 | 41.90 | 33.45 | 23.40 | 552 | 719.69 |
| V181821B | 457 | 457 | 0.74 | 41.90 | 33.45 | 23.40 | 596 | 620.08 |
| V241221A | 610 | 305 | 0.61 | 41.90 | 33.45 | 23.40 | 610 | 1000.00 |
| V241221B | 610 | 305 | 0.76 | 41.90 | 33.45 | 23.40 | 639 | 800.52 |
| V121232A | 305 | 305 | 0.64 | 49.80 | 50.77 | 26.40 | 665 | 476.56 |
| V121232B | 305 | 305 | 0.78 | 49.80 | 50.77 | 26.40 | 641 | 391.03 |
| V121832A | 305 | 457 | 0.64 | 49.80 | 50.77 | 26.40 | 703 | 476.56 |
| V121832B | 305 | 457 | 0.92 | 49.80 | 50.77 | 26.40 | 562 | 331.88 |
| V122432A | 305 | 609.60 | 0.64 | 49.80 | 50.77 | 26.40 | 714 | 476.56 |
| V122432B | 305 | 609.60 | 0.78 | 49.80 | 50.77 | 26.40 | 634 | 392.54 |
| V181232A | 457 | 305 | 0.60 | 49.80 | 50.77 | 26.40 | 552 | 765.49 |
| V181232B | 457 | 305 | 0.75 | 49.80 | 50.77 | 26.40 | 602 | 610.15 |
| V181832A | 457 | 457 | 0.61 | 49.80 | 50.77 | 26.40 | 689 | 749.18 |
| V181832B | 457 | 457 | 0.75 | 49.80 | 50.77 | 26.40 | 580 | 610.15 |
| V241232A | 610 | 305.00 | 0.62 | 49.80 | 50.77 | 26.40 | 673 | 980.71 |
| V241232B | 610 | 305.00 | 0.76 | 49.80 | 50.77 | 26.40 | 584 | 800.52 |
| V121809A | 305 | 457.00 | 0.71 | 19.80 | 14.19 | 11.90 | 572 | 432.01 |
| V121809C | 305 | 457.00 | 0.63 | 19.80 | 14.19 | 11.90 | 669 | 482.59 |
| V122409A | 305 | 609.60 | 0.71 | 19.80 | 14.19 | 11.90 | 586 | 427.17 |
| V122409C | 305 | 609.60 | 0.66 | 19.80 | 14.19 | 11.90 | 621 | 460.03 |
| V181209A | 457 | 305.00 | 0.56 | 19.80 | 14.19 | 11.90 | 689 | 817.53 |
| V181209C | 457 | 305.00 | 0.61 | 19.80 | 14.19 | 11.90 | 592 | 749.18 |
| V181809A | 457 | 457.00 | 0.61 | 19.80 | 14.19 | 11.90 | 618 | 749.18 |
| V181809C | 457 | 457.00 | 0.62 | 19.80 | 14.19 | 11.90 | 559 | 734.73 |
| V241209A | 610 | 305.00 | 0.62 | 19.80 | 14.19 | 11.90 | 606 | 980.71 |
| V241209C | 610 | 305.00 | 0.64 | 19.80 | 14.19 | 11.90 | 621 | 960.63 |

**Table A3.** Data of specimens tested by Johnson and Cafolla [26].

| Specimen ID | $h_w$ | $a$ | $t_w$ | Corrugation Dimensions | | | $F_{yw}$ | Web Slenderness |
|---|---|---|---|---|---|---|---|---|
| | | | | $b$ | $h_r$ | $d$ | | |
| CW1 | 440.36 | 730.92 | 3.06 | 180 | 45.01 | 44.99 | 320 | 143.91 |
| CW2 | 437.92 | 730.92 | 3.29 | 180 | 45.01 | 44.99 | 312 | 133.11 |
| CW3 | 437.18 | 940.92 | 3.26 | 250 | 45.01 | 44.99 | 284 | 134.10 |

**Table A4.** Data of specimens tested by Peil [27].

| Specimen ID | $h_w$ | $a$ | $t_w$ | Corrugation Dimensions | | | $F_{yw}$ | Web Slenderness |
|---|---|---|---|---|---|---|---|---|
| | | | | $b$ | $h_r$ | $d$ | | |
| SP1 | 800 | 1750 | 2 | 146 | 104.07 | 104 | 307 | 400 |
| SP2 | 800 | 1750 | 2 | 170 | 80.05 | 80 | 299 | 400 |
| SP3 | 800 | 1750 | 2 | 185 | 65.04 | 65 | 292 | 400 |
| SP4 | 800 | 1800 | 2 | 117 | 83.05 | 83 | 298 | 400 |
| SP5 | 800 | 1800 | 2 | 136 | 64.04 | 64 | 291 | 400 |
| SP6 | 800 | 1800 | 2 | 148 | 52.03 | 52 | 294 | 400 |
| SP2-2-400 1 | 400 | 1000 | 2 | 170 | 80.05 | 80 | 263 | 200 |
| SP2-2-400 2 | 400 | 1000 | 2 | 170 | 80.05 | 80 | 263 | 200 |
| SP2-2-800 1 | 800 | 1000 | 2 | 170 | 80.05 | 80 | 272 | 400 |
| SP2-2-800 2 | 800 | 1000 | 2 | 170 | 80.05 | 80 | 272 | 400 |
| SP2-3-600 1 | 600 | 1000 | 3 | 170 | 80.05 | 80 | 294 | 200 |
| SP2-3-600 2 | 600 | 1000 | 3 | 170 | 80.05 | 80 | 294 | 200 |
| SP2-3-1200 1 | 1200 | 1000 | 3 | 170 | 80.05 | 80 | 294 | 400 |
| SP2-3-1200 2 | 1200 | 1000 | 3 | 170 | 80.05 | 80 | 294 | 400 |
| SP2-4-800 1 | 800 | 1000 | 4 | 170 | 80.05 | 80 | 326 | 200 |
| SP2-4-800 2 | 800 | 1000 | 4 | 170 | 80.05 | 80 | 326 | 200 |
| SP2-4-1600 1 | 1600 | 1000 | 4 | 170 | 80.05 | 80 | 328 | 400 |
| SP2-4-1600 2 | 1600 | 1000 | 4 | 170 | 80.05 | 80 | 328 | 400 |
| SP2-8-800 1 | 800 | 1000 | 8 | 170 | 80.05 | 80 | 270 | 100 |
| SP2-8-800 2 | 800 | 1000 | 8 | 170 | 80.05 | 80 | 270 | 100 |

**Table A5.** Data of specimens tested by Driver et al. [5].

| Specimen ID | $h_w$ | $a$ | $t_w$ | Corrugation Dimensions | | | $F_{yw}$ | Web Slenderness |
|---|---|---|---|---|---|---|---|---|
| | | | | $b$ | $h_r$ | $d$ | | |
| G7A | 1500 | 4500 | 6 | 300 | 150 | 200 | 465 | 250 |
| G8A | 1500 | 4500 | 6 | 300 | 150 | 200 | 465 | 250 |

**Table A6.** Data of specimens tested by Lee et al. [28].

| Specimen ID | $h_w$ | $a$ | $t_w$ | Corrugation Dimensions | | | $F_{yw}$ | Web Slenderness |
|---|---|---|---|---|---|---|---|---|
| | | | | $b$ | $h_r$ | $d$ | | |
| L1 | 1500 | 3000 | 4.80 | 450 | 200.00 | 300 | 250 | 312.50 |
| L2 | 1500 | 3400 | 4.80 | 550 | 188.80 | 300 | 250 | 312.50 |
| L3 | 1500 | 3000 | 4.80 | 450 | 49.60 | 300 | 250 | 312.50 |
| L4 | 1500 | 3400 | 4.80 | 550 | 55.60 | 300 | 250 | 312.50 |
| I1 | 2000 | 3600 | 4.80 | 320 | 44.60 | 100 | 250 | 416.67 |
| I2 | 2000 | 3600 | 3.80 | 350 | 28.60 | 100 | 250 | 526.32 |
| G1 | 2000 | 3000 | 4.80 | 200 | 45.40 | 180 | 250 | 416.67 |
| G2 | 2000 | 3000 | 3.80 | 160 | 33.00 | 50 | 250 | 526.32 |
| G3 | 2000 | 3000 | 3.80 | 160 | 26.90 | 100 | 250 | 526.32 |

**Table A7.** Data of specimens tested by Moon et al. [7].

| Specimen ID | $h_w$ | $a$ | $t_w$ | Corrugation Dimensions | | | $F_{yw}$ | Web Slenderness |
|---|---|---|---|---|---|---|---|---|
| | | | | $b$ | $h_r$ | $d$ | | |
| PG2 | 2000 | 2600 | 4 | 250 | 60 | 220 | 296 | 500 |
| PG1 | 2000 | 2800 | 4 | 220 | 60 | 180 | 296 | 500 |
| PG3 | 2000 | 2800 | 4 | 220 | 75 | 180 | 296 | 500 |

**Table A8.** Data of specimens tested by Moussa et al. [29].

| Specimen ID | $h_w$ | $a$ | $t_w$ | Corrugation Dimensions | | | $F_{yw}$ | Web Slenderness |
|---|---|---|---|---|---|---|---|---|
| | | | | $b$ | $h_r$ | $d$ | | |
| TP20-300-30 | 3050 | 664.90 | 2 | 60 | 20.01 | 34.64 | 290 | 152.50 |
| A20-410-30-N | 410 | 578.10 | 2 | 40 | 20.01 | 34.64 | 290 | 205.00 |
| A20-410-45-N | 410 | 524.80 | 2 | 40 | 28.29 | 28.28 | 290 | 205.00 |
| A20-505-30-N | 505 | 575.70 | 2 | 40 | 20.01 | 34.64 | 290 | 252.50 |
| A20-505-45-N | 505 | 525.20 | 2 | 40 | 28.29 | 28.28 | 290 | 252.50 |
| B20-305-30 | 305 | 427.00 | 2 | 40 | 20.01 | 34.64 | 680 | 152.50 |
| B20-305-45 | 305 | 390.40 | 2 | 40 | 28.29 | 28.28 | 680 | 152.50 |
| B20-505-45 | 505 | 388.85 | 2 | 40 | 28.29 | 28.28 | 680 | 252.50 |
| B20-505-45-N | 505 | 388.85 | 2 | 40 | 28.29 | 28.28 | 290 | 252.50 |

**Table A9.** Test data reported by Wang et al. [30], Sause [8] and Hannebauer [31].

| Specimen ID | $h_w$ | $a$ | $t_w$ | Corrugation Dimensions | | | $F_{yw}$ | Web Slenderness |
|---|---|---|---|---|---|---|---|---|
| | | | | $b$ | $h_r$ | $d$ | | |
| W1 | 1200 | 2000 | 3 | 110 | 55 | 90 | 400 | 400 |
| SC1 | 1500 | 4500 | 6.27 | 300 | 150 | 200 | 465 | 239.23 |
| V1b | 500 | 1000 | 2.50 | 30 | 40 | 47 | 270 | 200 |

**Table A10.** Analysis results of test specimens reported by Lindner and Aschinger [1].

| Specimen ID | $\lambda_L$ | $\lambda_G$ | $\lambda_{I,1}$ | $\rho_e$ | $\zeta$ | $V$ (kN) | $V_T$ (kN) | $V/V_T$ |
|---|---|---|---|---|---|---|---|---|
| L1A | 0.953 | 0.53 | 1.09 | 0.70 | 1.255 | 281.72 | 280.93 | 1.01 |
| L1B | 0.765 | 0.53 | 0.93 | 0.80 | 1.238 | 495.08 | 501.34 | 0.98 |
| L2A | 0.937 | 0.76 | 1.21 | 0.63 | 1.222 | 347.69 | 337.50 | 1.04 |
| L2B | 0.759 | 0.75 | 1.07 | 0.71 | 1.182 | 571.69 | 563.51 | 1.00 |
| L3A | 0.901 | 1.04 | 1.38 | 0.52 | 1.384 | 465.59 | 451.22 | 1.05 |
| L3B | 0.741 | 1.02 | 1.26 | 0.60 | 1.460 | 776.65 | 773.57 | 0.99 |
| B1 | 0.952 | 0.34 | 1.01 | 0.75 | 1.056 | 202.53 | 208.04 | 0.94 |
| B4 | 0.977 | 0.35 | 1.04 | 0.73 | 1.062 | 203.28 | 183.46 | 1.12 |
| B4b | 0.977 | 0.35 | 1.04 | 0.73 | 1.062 | 203.28 | 217.66 | 0.95 |
| B3 | 0.735 | 0.31 | 0.80 | 0.88 | 1.008 | 255.36 | 246.01 | 1.04 |
| B2 | 0.733 | 0.31 | 0.80 | 0.88 | 1.061 | 263.45 | 273.42 | 0.98 |
| M101 | 0.751 | 0.74 | 1.05 | 0.72 | 1.153 | 53.46 | 52.96 | 1.02 |
| M102 | 0.753 | 0.99 | 1.24 | 0.60 | 1.507 | 79.10 | 79.19 | 1.00 |
| M103 | 0.831 | 1.32 | 1.56 | 0.41 | 1.751 | 83.79 | 83.95 | 1.00 |
| M104 | 0.751 | 1.48 | 1.66 | 0.36 | 2.168 | 102.33 | 103.98 | 0.98 |
| L1 | 0.790 | 0.66 | 1.03 | 0.74 | 1.045 | 383.35 | 380.08 | 1.01 |
| L1 | 0.579 | 0.63 | 0.86 | 0.84 | 0.945 | 617.09 | 610.72 | 1.01 |
| L2 | 0.794 | 0.96 | 1.25 | 0.60 | 1.506 | 592.39 | 600.20 | 0.98 |
| L2 | 0.548 | 0.90 | 1.05 | 0.72 | 1.202 | 899.87 | 905.32 | 1.00 |
| No. 1 | 0.743 | 0.48 | 0.88 | 0.83 | 0.948 | 272.59 | 275.01 | 0.99 |
| No. 2 | 0.657 | 0.47 | 0.81 | 0.87 | 0.918 | 272.46 | 264.27 | 1.04 |
| V1/1 | 0.939 | 0.10 | 0.94 | 0.79 | 0.820 | 67.96 | 67.98 | 1.00 |
| V1/2 | 0.894 | 0.09 | 0.90 | 0.82 | 0.837 | 69.87 | 69.84 | 1.00 |
| V1/3 | 0.963 | 0.10 | 0.97 | 0.77 | 0.992 | 79.08 | 80.93 | 0.97 |
| V2/3 | 0.621 | 0.17 | 0.64 | 0.97 | 0.844 | 236.78 | 234.89 | 1.01 |

**Table A11.** Analysis result of test specimens reported by Elgaaly et al. [2].

| Specimen ID | $\lambda_L$ | $\lambda_G$ | $\lambda_{I,1}$ | $\rho_e$ | $\zeta$ | $V$ (kN) | $V_T$ (kN) | $V/V_T$ |
|---|---|---|---|---|---|---|---|---|
| V-PILOTA | 0.939 | 0.52 | 1.07 | 0.71 | 1.284 | 76.65 | 82.73 | 0.94 |
| V-PILOTB | 0.948 | 0.52 | 1.08 | 0.70 | 1.290 | 78.78 | 71.17 | 1.12 |
| V121216A | 1.200 | 0.57 | 1.33 | 0.55 | 1.249 | 50.51 | 50.05 | 1.05 |
| V121216B | 0.993 | 0.54 | 1.13 | 0.67 | 1.300 | 80.36 | 87.63 | 0.90 |
| V181216B | 1.200 | 0.82 | 1.46 | 0.47 | 1.870 | 89.05 | 93.41 | 0.94 |
| V181216C | 1.011 | 0.82 | 1.30 | 0.57 | 1.537 | 117.97 | 119.47 | 1.00 |
| V181816A | 1.128 | 0.80 | 1.38 | 0.52 | 1.492 | 75.66 | 74.73 | 1.03 |
| V181816B | 0.990 | 0.78 | 1.26 | 0.59 | 1.370 | 96.48 | 96.17 | 1.01 |
| V241216A | 1.128 | 1.06 | 1.55 | 0.42 | 1.423 | 77.15 | 75.57 | 1.04 |
| V241216B | 0.908 | 1.01 | 1.35 | 0.54 | 1.494 | 133.19 | 133.35 | 0.98 |
| V121221A | 1.326 | 0.45 | 1.40 | 0.51 | 1.238 | 47.01 | 46.26 | 1.01 |
| V121221B | 1.064 | 0.42 | 1.15 | 0.67 | 1.188 | 75.75 | 72.50 | 1.00 |
| V122421A | 1.194 | 0.42 | 1.27 | 0.59 | 1.034 | 44.47 | 43.28 | 1.04 |
| V122421B | 1.046 | 0.41 | 1.13 | 0.68 | 1.017 | 61.61 | 61.20 | 0.99 |
| V181221A | 1.277 | 0.63 | 1.42 | 0.49 | 1.380 | 64.04 | 61.83 | 1.02 |
| V181221B | 1.046 | 0.61 | 1.21 | 0.62 | 1.301 | 99.89 | 97.86 | 1.01 |
| V181821A | 1.198 | 0.61 | 1.34 | 0.54 | 1.208 | 58.44 | 56.49 | 1.07 |
| V181821B | 1.073 | 0.61 | 1.23 | 0.61 | 1.269 | 92.84 | 93.41 | 0.96 |
| V241221A | 1.312 | 0.86 | 1.57 | 0.41 | 1.481 | 78.46 | 77.26 | 1.02 |
| V241221B | 1.075 | 0.84 | 1.36 | 0.53 | 1.403 | 130.66 | 126.72 | 1.01 |
| V121232A | 1.782 | 0.30 | 1.81 | 0.31 | 1.702 | 39.58 | 41.14 | 0.95 |
| V121232B | 1.436 | 0.28 | 1.46 | 0.47 | 1.460 | 59.92 | 61.16 | 0.98 |
| V121832A | 1.833 | 0.31 | 1.86 | 0.29 | 1.493 | 34.40 | 34.47 | 0.99 |
| V121832B | 1.141 | 0.25 | 1.17 | 0.65 | 0.994 | 54.68 | 53.38 | 1.10 |
| V122432A | 1.847 | 0.31 | 1.87 | 0.28 | 1.360 | 31.35 | 31.14 | 1.00 |
| V122432B | 1.434 | 0.28 | 1.46 | 0.47 | 1.175 | 49.14 | 48.93 | 0.98 |
| V181232A | 1.741 | 0.42 | 1.79 | 0.31 | 1.848 | 49.76 | 51.60 | 0.97 |
| V181232B | 1.449 | 0.41 | 1.51 | 0.44 | 1.536 | 79.59 | 80.06 | 1.00 |
| V181832A | 1.904 | 0.47 | 1.96 | 0.26 | 1.810 | 52.07 | 52.93 | 0.99 |
| V181832B | 0.939 | 0.52 | 1.07 | 0.71 | 1.284 | 76.65 | 82.73 | 0.94 |
| V241232A | 1.422 | 0.41 | 1.48 | 0.46 | 1.505 | 78.12 | 78.64 | 1.00 |
| V241232B | 1.845 | 0.61 | 1.94 | 0.26 | 1.765 | 69.16 | 69.08 | 1.00 |
| V121809A | 1.403 | 0.54 | 1.50 | 0.44 | 1.485 | 103.31 | 101.46 | 1.01 |
| V121809C | 0.519 | 0.78 | 0.94 | 0.79 | 1.070 | 62.39 | 63.16 | 0.95 |
| V122409A | 0.626 | 0.87 | 1.07 | 0.71 | 1.101 | 56.55 | 55.16 | 1.05 |
| V122409C | 0.519 | 0.79 | 0.95 | 0.79 | 1.026 | 59.74 | 57.82 | 1.03 |
| V181209A | 0.575 | 0.83 | 1.01 | 0.75 | 1.061 | 57.65 | 57.82 | 1.00 |
| V181209C | 0.719 | 1.37 | 1.54 | 0.42 | 1.880 | 79.95 | 80.95 | 0.99 |
| V181809A | 0.611 | 1.24 | 1.38 | 0.52 | 1.766 | 87.08 | 88.78 | 0.99 |
| V181809C | 0.624 | 1.27 | 1.41 | 0.50 | 1.626 | 83.94 | 82.29 | 0.99 |
| V241209A | 0.582 | 1.20 | 1.33 | 0.55 | 1.584 | 77.56 | 77.62 | 1.03 |
| V241209C | 0.606 | 1.67 | 1.77 | 0.32 | 1.737 | 71.90 | 70.77 | 1.04 |

**Table A12.** Analysis results of test specimens reported by Johnson and Cafolla [26].

| Specimen ID | $\lambda_L$ | $\lambda_G$ | $\lambda_{I,1}$ | $\rho_e$ | $\zeta$ | $V$ (kN) | $V_T$ (kN) | $V/V_T$ |
|---|---|---|---|---|---|---|---|---|
| CW1 | 0.813 | 0.34 | 0.88 | 0.83 | 0.660 | 133.74 | 126.59 | 1.07 |
| CW2 | 0.747 | 0.33 | 0.82 | 0.87 | 0.669 | 152.26 | 150.56 | 1.00 |
| CW3 | 0.999 | 0.35 | 1.06 | 0.72 | 0.667 | 110.05 | 100.22 | 1.12 |

**Table A13.** Analysis results of test specimens reported by Peil [27].

| Specimen ID | $\lambda_L$ | $\lambda_G$ | $\lambda_{I,1}$ | $\rho_e$ | $\zeta$ | $V$ (kN) | $V_T$ (kN) | $V/V_T$ |
|---|---|---|---|---|---|---|---|---|
| SP1 | 0.996 | 0.26 | 1.03 | 0.74 | 1.077 | 224.99 | 225.00 | 1.00 |
| SP2 | 1.136 | 0.35 | 1.19 | 0.64 | 1.202 | 213.74 | 215.30 | 0.98 |
| SP3 | 1.222 | 0.44 | 1.30 | 0.57 | 1.324 | 205.69 | 209.50 | 0.97 |
| SP4 | 0.783 | 0.30 | 0.84 | 0.85 | 0.999 | 232.31 | 230.80 | 1.02 |
| SP5 | 0.897 | 0.41 | 0.99 | 0.76 | 1.095 | 222.07 | 220.50 | 1.02 |
| SP6 | 0.981 | 0.53 | 1.11 | 0.68 | 1.177 | 218.68 | 220.00 | 0.99 |
| SP2-2-400 1 | 1.066 | 0.16 | 1.08 | 0.71 | 0.981 | 84.29 | 80.25 | 1.05 |
| SP2-2-400 2 | 1.066 | 0.16 | 1.08 | 0.71 | 0.981 | 84.29 | 88.13 | 0.95 |
| SP2-2-800 1 | 1.084 | 0.33 | 1.13 | 0.67 | 1.060 | 178.87 | 178.88 | 1.00 |
| SP2-2-800 2 | 1.084 | 0.33 | 1.13 | 0.67 | 1.060 | 178.87 | 177.75 | 1.01 |
| SP2-3-600 1 | 0.751 | 0.24 | 0.79 | 0.89 | 1.121 | 302.98 | 301.50 | 1.00 |
| SP2-3-600 2 | 0.751 | 0.24 | 0.79 | 0.89 | 1.121 | 302.98 | 308.63 | 0.98 |
| SP2-3-1200 1 | 0.751 | 0.47 | 0.89 | 0.82 | 1.221 | 614.51 | 611.25 | 1.01 |
| SP2-3-1200 2 | 0.751 | 0.47 | 0.89 | 0.82 | 1.221 | 614.51 | 625.13 | 0.98 |
| SP2-4-800 1 | 0.593 | 0.31 | 0.67 | 0.96 | 1.056 | 603.28 | 601.50 | 1.01 |
| SP2-4-800 2 | 0.593 | 0.31 | 0.67 | 0.96 | 1.056 | 603.28 | 603.38 | 1.01 |
| SP2-4-1600 1 | 0.595 | 0.62 | 0.86 | 0.84 | 1.197 | 1218.89 | 1215.38 | 1.00 |
| SP2-4-1600 2 | 0.595 | 0.62 | 0.86 | 0.84 | 1.197 | 1218.89 | 1227.00 | 0.99 |
| SP2-8-800 1 | 0.270 | 0.24 | 0.36 | 1.00 | 1.330 | 1332.58 | 1308.38 | 1.01 |
| SP2-8-800 2 | 0.270 | 0.24 | 0.36 | 1.00 | 1.330 | 1332.58 | 1374.75 | 0.97 |

**Table A14.** Analysis results of test specimens reported by Driver et al. [5].

| Specimen ID | $\lambda_L$ | $\lambda_G$ | $\lambda_{I,1}$ | $\rho_e$ | $\zeta$ | $V$ (kN) | $V_T$ (kN) | $V/V_T$ |
|---|---|---|---|---|---|---|---|---|
| G7A | 0.834 | 0.37 | 0.91 | 0.81 | 1.084 | 2190.70 | 2299.82 | 0.92 |
| G8A | 0.834 | 0.37 | 0.91 | 0.81 | 1.084 | 2190.70 | 2155.05 | 0.98 |

**Table A15.** Analysis results of test specimens reported by Lee et al. [28].

| Specimen ID | $\lambda_L$ | $\lambda_G$ | $\lambda_{I,1}$ | $\rho_e$ | $\zeta$ | $V$ (kN) | $V_T$ (kN) | $V/V_T$ |
|---|---|---|---|---|---|---|---|---|
| L1 | 1.146 | 0.22 | 1.17 | 0.65 | 1.097 | 743.50 | 745.62 | 1.00 |
| L2 | 1.401 | 0.23 | 1.42 | 0.50 | 1.209 | 624.38 | 625.56 | 1.00 |
| L3 | 1.146 | 0.63 | 1.31 | 0.57 | 0.921 | 540.06 | 532.02 | 1.02 |
| L4 | 1.401 | 0.56 | 1.51 | 0.44 | 1.052 | 480.55 | 474.73 | 1.01 |
| I1 | 0.815 | 0.86 | 1.18 | 0.64 | 1.463 | 1302.50 | 1313.50 | 0.99 |
| I2 | 1.126 | 1.26 | 1.69 | 0.35 | 1.475 | 565.15 | 565.66 | 1.00 |
| G1 | 0.509 | 0.91 | 1.04 | 0.73 | 1.077 | 1087.70 | 1095.96 | 0.99 |
| G2 | 0.515 | 1.14 | 1.25 | 0.60 | 1.392 | 916.69 | 912.94 | 1.01 |
| G3 | 0.515 | 1.39 | 1.48 | 0.46 | 1.759 | 888.05 | 929.62 | 0.94 |

**Table A16.** Analysis results of test specimens reported by Moon et al. [7].

| Specimen ID | $\lambda_L$ | $\lambda_G$ | $\lambda_{I,1}$ | $\rho_e$ | $\zeta$ | $V$ (kN) | $V_T$ (kN) | $V/V_T$ |
|---|---|---|---|---|---|---|---|---|
| PG2 | 0.831 | 0.85 | 1.19 | 0.64 | 0.998 | 869.56 | 873.60 | 0.99 |
| PG1 | 0.732 | 0.87 | 1.13 | 0.67 | 0.946 | 864.75 | 843.20 | 1.03 |
| PG3 | 0.732 | 0.73 | 1.03 | 0.74 | 1.053 | 1052.21 | 1052.80 | 1.01 |

**Table A17.** Analysis results of test specimens reported by Moussa [29].

| Specimen ID | $\lambda_L$ | $\lambda_G$ | $\lambda_{I,1}$ | $\rho_e$ | $\zeta$ | $V$ (kN) | $V_T$ (kN) | $V/V_T$ |
|---|---|---|---|---|---|---|---|---|
| TP20-300-30 | 0.395 | 0.38 | 0.55 | 1.00 | 0.833 | 84.89 | 84.72 | 1.00 |
| A20-410-30-N | 0.263 | 0.45 | 0.52 | 1.00 | 0.899 | 122.74 | 125.09 | 0.99 |
| A20-410-45-N | 0.263 | 0.34 | 0.43 | 1.00 | 0.857 | 118.28 | 116.46 | 1.01 |
| A20-505-30-N | 0.263 | 0.56 | 0.62 | 0.99 | 0.915 | 153.69 | 154.23 | 0.99 |
| A20-505-45-N | 0.263 | 0.42 | 0.50 | 1.00 | 0.895 | 152.72 | 152.49 | 0.99 |
| B20-305-30 | 0.403 | 0.51 | 0.65 | 0.97 | 1.006 | 233.51 | 233.20 | 1.00 |
| B20-305-45 | 0.403 | 0.39 | 0.56 | 1.00 | 1.044 | 248.99 | 251.72 | 0.99 |
| B20-505-45 | 0.403 | 0.64 | 0.76 | 0.90 | 0.976 | 335.82 | 329.34 | 1.06 |
| B20-505-45-N | 0.263 | 0.42 | 0.50 | 1.00 | 0.852 | 150.59 | 150.43 | 0.96 |

**Table A18.** Analysis results of test specimens reported by Wang et al. [30], Sause [8] and Hannebauer [31].

| Scheme 1. | $\lambda_L$ | $\lambda_G$ | $\lambda_{I,1}$ | $\rho_e$ | $\zeta$ | $V$ (kN) | $V_T$ (kN) | $V/V_T$ |
|---|---|---|---|---|---|---|---|---|
| W1 | 0.567 | 0.66 | 0.87 | 0.83 | 0.858 | 587.62 | 567.00 | 1.05 |
| SC1 | 0.798 | 0.36 | 0.88 | 0.83 | 1.088 | 2127.47 | 2007.53 | 1.14 |
| V1b | 0.314 | 0.24 | 0.39 | 1.00 | 1.028 | 200.94 | 206.50 | 0.97 |

## References

1. Lindner, J.; Aschinger, R. *Grenzschubtragfähigkeit von I-trägern mit trapezför- mig profilierten Stegen*; Stahlbau: Aurich, Germany, 1988; Volume 57, pp. 377–380.
2. Elgaaly, M.; Hamilton, R.; Seshadri, A. Shear strength of beams with corrugated webs. *J. Struct. Eng.* **1996**, *122*, 390–398. [CrossRef]
3. Sause, R.; Abbas, H.; Wassef, W.; Driver, R.; Elgaaly, M. *Corrugated Web Girder Shape and Strength Criteria: Work area 1. Pennsylvania Innovative High Performance Steel Bridge Demonstration Project, ATLSS Report No. 03–18*; Lehigh University ATLSS Center: Bethlehem, PA, USA, 2003.
4. Abbas, H. Analysis and Design of Corrugated Web I—Girders for Bridges Using High Performance Steel. Ph.D. Thesis, Department of Civil and Environmental Engineering, Lehigh University, Bethlehem, PA, USA, 2003.
5. Driver, G.; Abbas, H.; Sause, R. Shear behavior of corrugated web bridge girders. *J. Struct. Eng.* **2006**, *132*, 195–203. [CrossRef]
6. Yi, J.; Gil, H.; Youm, K.; Lee, H. Interactive shear buckling behavior of trapezoidally corrugated steel webs. *Eng. Struct.* **2008**, *30*, 1659–1666. [CrossRef]
7. Moon, J.; Yi, J.; Choi, H.; Lee, H.-E. Shear strength and design of trapezoidally corrugated steel webs. *J. Constr. Steel Res.* **2008**, *65*, 1198–1205. [CrossRef]
8. Sause, R.; Braxtan, T. Shear strength of trapezoidal corrugated steel webs. *J. Constr. Steel Res.* **2011**, *67*, 223–236. [CrossRef]
9. Bergfelt, A.; Leiva, L. *Shear Buckling of Trapezoidally Corrugated Girders Webs, Report Part 2, Pibl.SS4:2*; Sweden Chalmers University of Technology: Gothenburg, Sweden, 1984.
10. El-Metwally, A. Prestressed Composite Girders with Corrugated Steel Webs. Master's Thesis, Department of Civil Engineering, University of Calgary, Calgary, AB, Canada, 1998.
11. Abbas, H.; Sause, R.; Driver, R. Shear strength and stability of high performance steel corrugated web girders. *Proc. Struct. Stab. Res. Counc.* **2002**, 361–387.
12. Hiroshi, S.; Hiroyuki, I.; Yohiaki, I.; Koichi, K. Flexural shear behavior of composite bridge girder with corrugated steel webs around middle support. *Doboku Gakkai Ronbunshu* **2003**, *724*, 49–67.
13. Ahmed, S. Plate girders with corrugated steel webs. *AISC Eng. J. First Quart* **2005**, *42*, 1–13.
14. Elamary, A.; Alharthi, Y.; Abdalla, O.; Alqurashi, M.; Sharaky, I. Failure mechanism of hybrid steel beams with trapezoidal corrugated-web non-welded inclined folds. *Materials* **2021**, *14*, 1424. [CrossRef] [PubMed]
15. Kumar, M.; Pradeep, D.; Patel, R.; Pandian, M.; Karthikeyan, K. A study on flexural capacity of steel beams with corrugated web. *Int. J. Civ. Eng. Technol.* **2018**, *9*, 679–689.
16. Krejsa, M.; Janas, P.; Čajka, R. Using DOProC method in structural reliability assessment. In *Applied Mechanics and Materials*; Trans Tech Publications Ltd.: Stafa-Zurich, Switzerland, 2013; pp. 300–301. [CrossRef]
17. Čajka, R.; Krejsa, M. Measured data processing in civil structure using the DOProC method. In *Advanced Materials Research*; Trans Tech Publications Ltd.: Stafa-Zurich, Switzerland, 2013; Volume 859, pp. 114–121. [CrossRef]
18. Čajka, R.; Krejsa, M. Validating a computational model of a rooflight steel structure by means of a load test. In *Applied Mechanics and Materials*; Trans Tech Publications Ltd.: Stafa-Zurich, Switzerland, 2014; pp. 592–598. [CrossRef]
19. Flodr, J.; Krejsa, M.; Mikolášek, D.; Sucharda, O.; Žídek, I. Mathematical modelling of thin-walled cold-rolled cross-section. In *Applied Mechanics and Materials*; Trans Tech Publications Ltd.: Stafa-Zurich, Switzerland, 2014; pp. 171–174. [CrossRef]

20. Zhu, L.; Guo, L.; Zhou, P. Numerical and experimental studies of corrugated-web-connected buckling-restrained braces. *Eng. Struct.* **2017**, *134*, 107–124. [CrossRef]
21. Barakat, S.; Mansouri, A.; Altoubat, S. Shear strength of steel beams with trapezoidal corrugated webs using regression analysis. *Steel Compos. Struct.* **2015**, *18*, 757–773. [CrossRef]
22. Timoshenko, S.; Gere, J. *Theory of Elastic Stability*, 2nd ed.; McGraw-Hill: New York, NY, USA, 1961.
23. Sause, R.; Clarke, T. *Bearing Stiffeners and Field Splices For Corrugated Web Girders, Work Area 4, Pennsylvania Innovative High Performance Steel Bridge Demonstration Project ATLSS Report No. 03–21*; Lehigh University: Bethlehem, PA, USA, 2003.
24. Easley, J. Buckling formulas for corrugated metal shear diaphragms. *J. Struct. Div.* **1975**, *101*, 1403–1413. [CrossRef]
25. Abbas, H.H.; Sause, R.; Driver, R.G. Behavior of corrugated web I-girders under in-plane loads. *J. Eng. Mech. ASCE* **2006**, *132*, 806–814. [CrossRef]
26. Johnson, R.; Cafolla, J. Local flange buckling in plate girders with corrugated steel webs. *Proc. Inst. Civ. Eng. Struct. Build.* **1997**, *122*, 148–156. [CrossRef]
27. Peil, U. *Statische versuche an trapezstegträgern untersuchung der querkraftbeanspruchbarkeit*; Institut für Stahlbau, Technischen University of Braunschweig: Braunschweig, Germany, 1998.
28. Gil, H.; Lee, S.; Lee, J.; Lee, H. Shear buckling strength of trapezoidally corrugated steel webs for bridges. *J. Transp. Res. Board* **2005**, 473–480. [CrossRef]
29. Moussa, L.; Barakat, S.; Al-Saadon, Z. Shear behavior of corrugated web panels and sensitivity analysis. *J. Constr. Steel Res.* **2018**, *151*, 94–107.
30. Wang, S.; He, J.; Liu, Y. Shear behavior of steel I-girder with stiffened corrugated web, Part I: Experimental study. *Thin Walled Struct.* **2019**, *1*, 248–262. [CrossRef]
31. Hannebauer, D. *Zur Querschnitts-und Stabtragfähigkeit von Trägern mit profilierten Stegen*; Brandenburgischen Technischen Universität: Cottbus, Germany, 2008.
32. Leblouba, M.; Barakat, S.; Altoubat, S.; Junaid, T.; Maalej, M. Normalized shear strength of trapezoidal corrugated steel webs. *J. Constr. Steel Res.* **2017**, *1*, 75–90. [CrossRef]
33. Nie, J.; Zhu, I.; Tao, M.; Tang, L. Shear strength of trapezoidal corrugated steel webs. *J. Constr. Steel Res.* **2013**, *85*, 105–115. [CrossRef]
34. Available online: https://ch.mathworks.com/help/stats/regression-learner-app.html (accessed on 5 June 2020).
35. Putatunda, S.; Rama, K. A Modified Bayesian Optimization based Hyper-Parameter Tuning Approach for Extreme Gradient Boosting. In Proceedings of the Fifteenth International Conference on Information Processing (ICINPRO), Bengaluru, India, 20–22 December 2019.
36. William, W.; Burank, B.; Efstratios, P. Hyperparameter optimization of machine learning models through parametric programming. *Comput. Chem. Eng.* **2020**, *139*, 1–12.
37. Jia, W.; Xiu, C.; Hao, Z.; Li-Diong, X.; Si-Hao, D. Hyperparameter optimization for machine learning models based on bayesian optimization. *J. Electron. Sci. Technol.* **2019**, *17*, 36–40.

materials

Article

# Test and Numerical Model of Curved Steel–Concrete Composite Box Beams under Positive Moments

**Zhi-Min Liu [1], Xue-Jin Huo [2,*], Guang-Ming Wang [1] and Wen-Yu Ji [1]**

[1] School of Civil Engineering, Beijing Jiaotong University, Beijing 100044, China; zhmliu@bjtu.edu.cn (Z.-M.L.); 14115279@bjtu.edu.cn (G.-M.W.); wyji@bjtu.edu.cn (W.-Y.J.)
[2] China Railway Major Bridge Reconnaissance & Design Institute Co., Ltd., Wuhan 430056, China
* Correspondence: huoxuejin@126.com

**Abstract:** Compared with straight steel–concrete composite beams, curved composite beams exhibit more complicated mechanical behaviors under combined bending and torsion coupling. There are much fewer experimental studies on curved composite beams than those of straight composite beams. This study aimed to investigate the combined bending and torsion behavior of curved composite beams. This paper presents static loading tests of the full elastoplastic process of three curved composite box beams with various central angles and shear connection degrees. The test results showed that the specimens exhibited notable bending and torsion coupling force characteristics under static loading. The curvature and interface shear connection degree significantly affected the force behavior of the curved composite box beams. The specimens with weak shear connection degrees showed obvious interfacial longitudinal slip and transverse slip. Constraint distortion and torsion behavior caused the strain of the inner side of the structure to be higher than the strain of the outer side. The strain of the steel beam webs was approximately linear. In addition, fine finite element models of three curved composite box beams were established. The correctness and applicability of the finite element models were verified by comparing the test results and numerical calculation results for the load–displacement curve, load–rotational angle curve, load–interface slip curve, and cross-sectional strain distribution. Finite element modeling can be used as a reliable numerical tool for the large-scale parameter analysis of the elastic–plastic mechanical behavior of curved composite box beams.

**Keywords:** curved steel–concrete composite box beams; coupled bending and torsion; experimental research; elaborate finite element model; elastoplastic behavior

## 1. Introduction

Steel–concrete composite beams have been widely used in the construction of engineering structures due to their light weight, strong spanning ability, high bearing capacity, and association with quick construction. However, unlike that of straight composite beams, the mass center of curved composite beams is not at the connections of the supporting points on both ends, so typical bending–torsion coupling stress characteristics can be found in curved composite beams. The deflection, torsion angle, and even interface slip between the steel beam and the concrete slab of a curved composite beam, owing to bending–torsion coupling, are more obvious than those of a straight composite beam. In addition, the kinds of torsion include free torsion and constrained torsion, and the latter more commonly occurs in structures with complex boundary conditions. Constrained torsion leads to a more complex and irregular strain distribution in the structure. Overstressing may occur when design schemes suitable for linear composite beams are applied to curved composite beams.

Generally, model tests are the most direct, effective, and accurate method for studying structural force behavior. There have been a large number of test studies on straight composite beams and relatively few studies on curved composite beams. Colville [1] conducted a static test study on four curved composite beams and proposed a simplified design method for interfacial shear connectors. Brennan and Mandel [2] conducted a static test study on a large-scale two-span continuous curved composite I-beam and studied the displacement and stress distribution under normal usage load. The Federal Highway Administration (FHWA) of the United States Department of Transportation [3] has carried out a series of experimental studies on the force behavior of curved beams, including a static test of a full-scale curved composite box I-beam that focuses on monitoring the displacement and internal force change of the structure under dead load, live load, and ultimate load. Thevendran et al. [4] conducted a static test study on five curved composite I-beams with different curvatures under concentrated load in the middle of the span, and the test results showed that the ultimate bearing capacity decreased with the ratio of the span to the radius. Krzmarzick and Hajjar (2006) [5] studied the trends of the displacement and stress distribution of a curved composite I-beam bridge through an actual bridge load test. Tan and Uy (2009) [6] carried out a static test study on eight curved composite I-beams. The test parameters included the ratio of the span to the radius and shear connection degree. The test results showed that curved composite beams enduring the bending moment could increase the torsional bearing capacity, but the flexural bearing capacity of the structure under torque was not affected. Zhang et al. (2012) [7] conducted static tests on six curved composite box beams under the combined action of bending and torsional loads. The test parameters were the ratio of the torque to the moment and the number of diaphragms. The test results showed that the failure modes of the specimens included bending failure and bending–torsion coupled failure; this failure mode increased the flexural bearing capacity of the structure to a certain extent when the structure was under torque, and significant longitudinal and transverse slip existed at the interface between the steel beam and the concrete slab. Through the static tests of two composite beams, Zhang concentrated on studying the effect of a large curvature, such as a width-to-radius ratio greater than 1/10, on the force behavior of the structure. Zhu [8] conducted a static loading test on a large-curvature-curve composite box beam with a positive bending moment under normal usage load. In 2020, Zhu [9] carried out a static loading test on a large-curvature-curve composite box beam with a negative bending moment under ultimate load, and the test results showed that, due to the large curvature, the stress on the inner side of the structural slabs was significantly greater than that on the outer side.

Compared to actual model tests, numerical models are not restricted by the production cost, geometric size, or boundary conditions. Under the premise that the accuracy of the numerical model has been verified, the structural parameters and boundary conditions can be changed through the numerical model to systematically analyze the force behavior of the structure. Numerical models of curved composite beams include frame models and fine models. A frame model is highly efficient, and a fine model is highly accurate. With the development of numerical computing capabilities, the efficiency of fine models in modeling and calculation has been greatly improved. Therefore, fine models can be used to analyze the parameters of curved composite beams at present. Ei-Tawil et al. [10] established a frame model and numerical model of a curved composite box beam. With the aid of parameter analysis, the influence of the curvature, cross-sectional geometric parameters, and the number of beam spans on the structural force behavior was studied. The results showed that the warping stress contributes to the stress level to a certain degree. Sennah et al. and Samman et al. [11–14] adopted fine models and conducted many studies on the force behavior of curved composite box beams under normal usage and the lateral load distribution coefficient among multibox beams, and they proposed a simplified calculation method for the lateral load distribution. Daniel et al. [15] studied the dynamic behavior of a curved composite I-beam under seismic loading through a fine model. The numerical model test parameters included the curvature, I-beam distance, and the structural form of the diaphragm. The research results showed that the curvature had a significant impact on the seismic responses of curved composite I-beams. Additionally, the curvature, I-beam distance, and diaphragm structure had a more significant influence on the inner side of the beam than on the outer side. Nie and Zhu [16] systematically studied the modeling strategies of fine models and frame models of curved composite box beams. A fine model and a frame model of an actual curved composite box beam bridge were established, and the accuracy and applicability of the established models were verified. Lin and Yoda [17] established a fine model based on a static load test of a straight composite beam with a negative bending moment; they extended it to the analysis of the elastoplastic mechanical behavior of a curved composite beam with a negative bending moment, studied the bearing capacities of structures and the strain distribution trends with changing curvature, and proposed a calculation formula suitable for the bearing capacity considering the coupling effect of bending and torsion. Fatemi et al. [18] established a fine model of curved composite box beams, studied the influence of the curvature, span, and number of lanes and box beams on the force behavior of the structure, and determined the structural form and reasonable space of the lateral support of structures. Zhu et al. [19] and Wang et al. [20] established a fine model of a curved composite box beam; this model was used as a benchmark for the frame model of a curved composite box beam considering constrained torsion, distortion, and bidirectional interface slip. Sucharda et al. [21] and Valikhani et al. [22] presented the possibilities of material models of concrete, approaches to the choice of parameters, or taking into account the uncertainties in the calculation or stochastic character of concrete. These strategies can be introduced to the FE simulation of curved composite beams.

In contrast to the experimental and numerical studies of straight composite beams, there are relatively few studies on curved composite beams. Additionally, there are relatively few experimental and numerical studies on curved composite box beams compared to studies on curved composite I-beams. In China, in overpasses and expressway ramp bridges, the number of curved composite box beams is greater than that of curved composite I-beams. To further enrich the test and numerical research results of curved composite box beams, this study included static loading tests on three curved steel–concrete composite box beam specimens to investigate their combined bending and torsion behaviors. The parameters of the specimens refer to the central angle and the degree of interfacial shear connection. The load–displacement curves, load–rotational angle curves, load–interface slip curves, and cross-sectional strain distributions of the specimens were reported. After that, the fine finite element models of the three specimens were established, and the test results were compared with the finite element calculation results to establish the accuracy and applicability of the finite element model. As a result, the model can be used as a numerical tool for subsequent parameter analysis.

## 2. Materials and Method

### *2.1. Specimen Design*

As per the Chinese code (CMC 2010 [23], 2017 [24]), three curved steel–concrete composite box beams were designed with different central angles and interface shear connection degrees, and the parameters of the three curved composite box beam specimens are shown in Table 1. Each specimen was composed of steel girders and concrete slabs and connected by shear studs. The steel beam consisted of a top flange, bottom flange, steel web, longitudinal and transverse stiffeners, and diaphragms. The span length (arc length between supports) was 6200 mm. The concrete slab was 750 mm in spacing and 50 mm in thickness. The tub steel box girder was 350 mm in width (the distance between the two webs) and 300 mm in height. The bottom flange was 410 mm in width and 12 mm in thickness. The top flange was 100 mm in width and 8 mm in thickness. The steel web was 280 mm in height and 12 mm in thickness. Seven diaphragms were applied at equal intervals along the beam span, and the thickness of the diaphragm was 8 mm. A total of 8 longitudinal steel rebars were arranged in the concrete slab with a spacing of 95 mm, and a total of 82 transverse steel rebars were arranged, each 12 mm in diameter. Samples CCB-1, CCB-2, and CCB-3 had central angles of 45°, 25°, and 45°, respectively. The shear studs were uniformly arranged in 83, 83, and 23 rows, respectively, along the longitudinal direction and connected the steel top flange and the concrete slab. Five shear studs were applied at the top of the end diaphragms of all specimens, and two studs were arranged on the five diaphragms in the middle to connect the diaphragms and the concrete slabs. The shear studs were 13 mm in diameter and 40 mm in height. The basic structure of the test beam is shown in Figure 1. The geometric dimensions and details of the test beam are shown in Figure 2.

**Table 1.** Parameters of the test specimens.

| Specimen | Central Angle | Shear Connection Degree |
|---|---|---|
| CCB-1 | 45° | Strong |
| CCB-2 | 25° | Strong |
| CCB-3 | 45° | Weak |

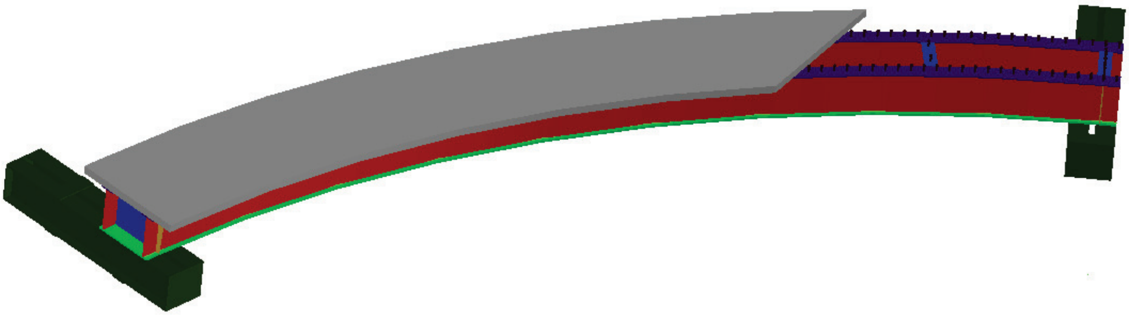

**(a) CCB-1.**

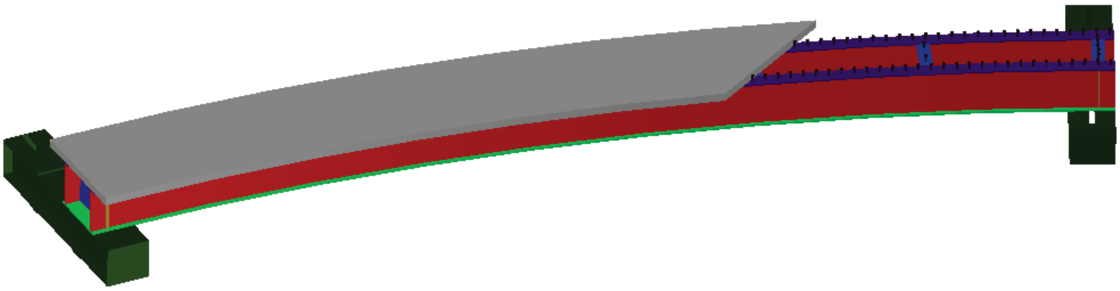

**(b) CCB-2.**

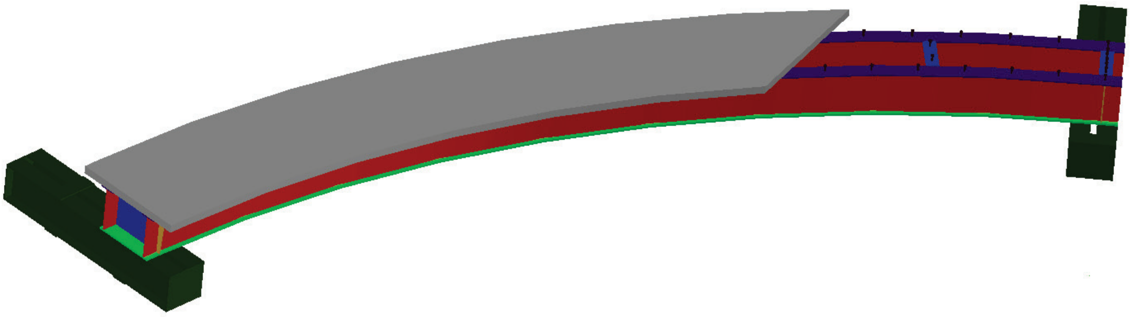

**(c) CCB-3.**

**Figure 1.** Schematic plots of the test specimens.

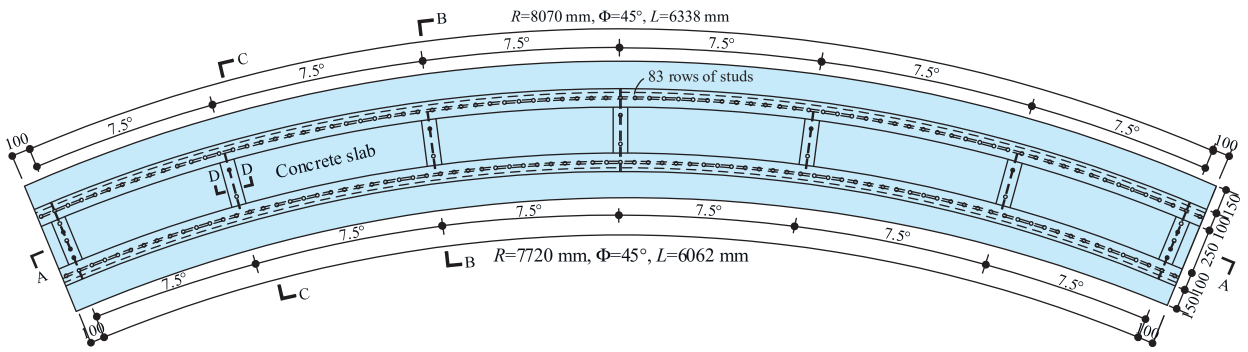

(a) Plan view of CCB-1.

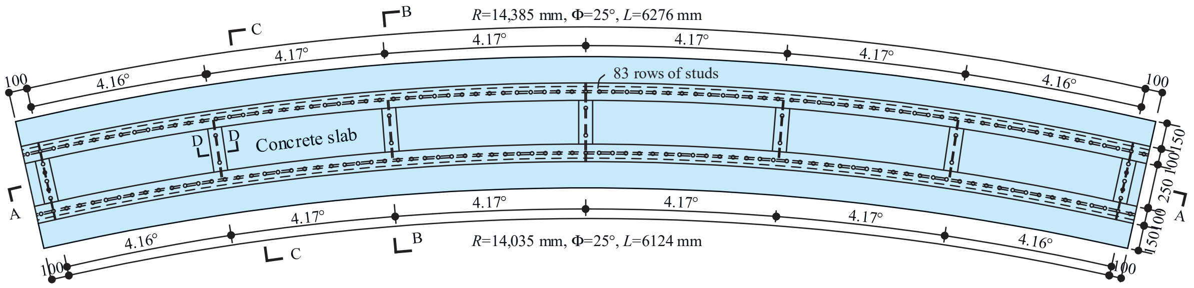

(b) Plan view of CCB-2.

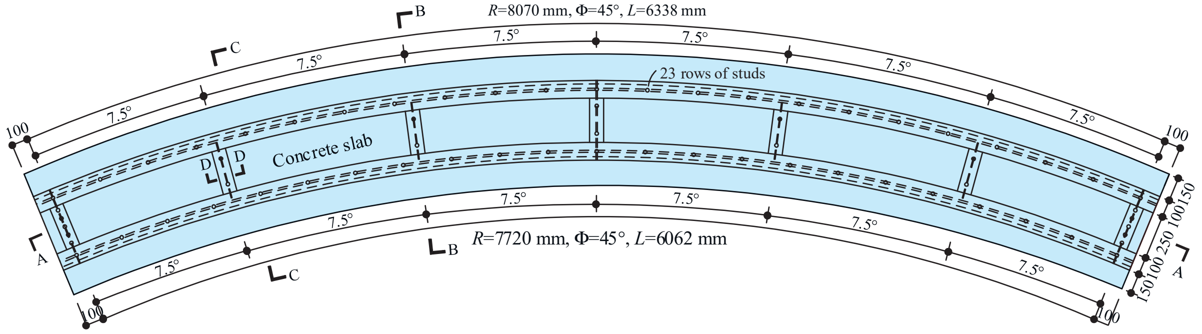

(c) Plan view of CCB-3.

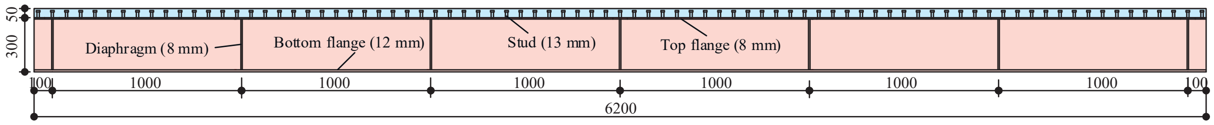

(d) Section A-A of CCB-1 and CCB-2.

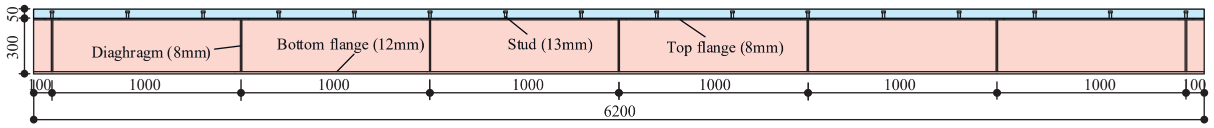

(e) Section A-A of CCB-3.

**Figure 2.** *Cont.*

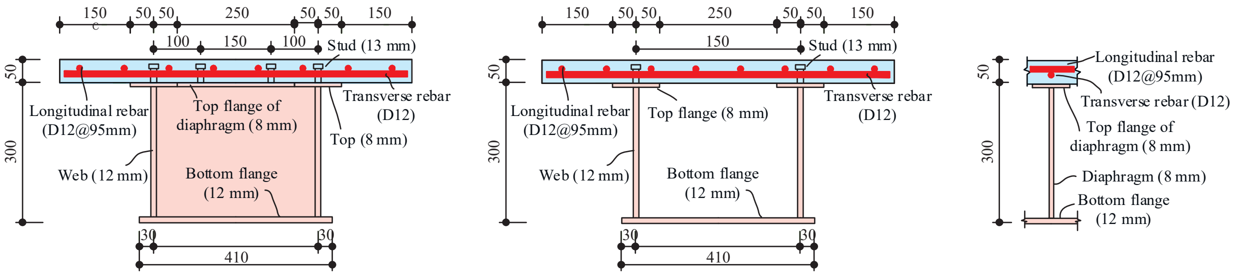

**(f) Section B-B of CCB-1–CCB-3** **(g) Section C-C of CCB-1–CCB-3** **(h) Section D-D of CCB-1–CCB-3.**

**Figure 2.** Details of the test specimens (in units of mm).

The construction process of the test specimens is shown in Figure 3. The steel beams, formwork, reinforcement, and shear studs were manufactured and welded in the factory, and the concrete slab was poured in the factory.

**(a) Fabricated steel girders.**

**(b) Curing concrete.**

**Figure 3.** *Cont.*

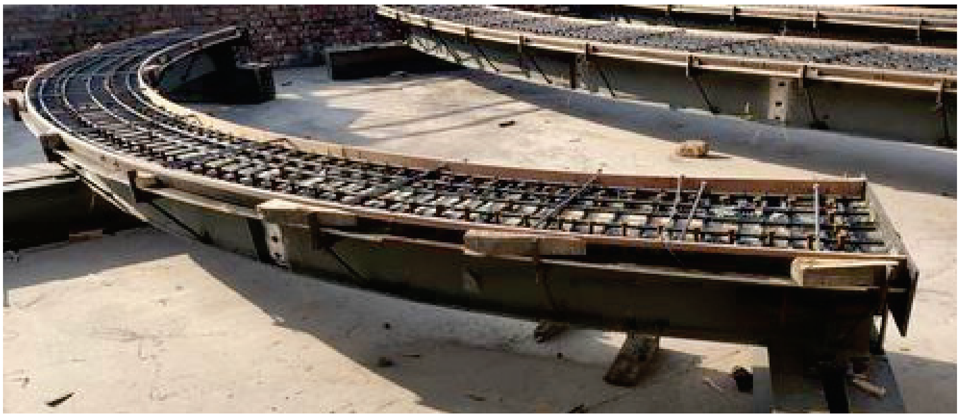

**(c) Assembling reinforcement.**

**(d) Completed specimens.**

**Figure 3.** The manufacturing process of the test specimens.

## 2.2. Material Properties

The steel plate had a strength grade of Q345c, and the specimens included two steel plate thicknesses: 8 and 12 mm. The longitudinal and transverse reinforcement had a strength grade of HRB335, and the rebar was 12 mm in diameter. As per the Chinese code (CMC 2010 [23], 2017 [24]), four coupon tests were conducted for steel plates of each thickness and reinforcement, and the average strength and elongation ratio are shown in Table 2.

**Table 2.** Material properties of the steel plates and rebar coupons.

| **Coupons** | | **Q345c Steel (Thickness 8 mm)** | **Q345c (Thickness 12 mm)** | **HRB335 (Diameter 12 mm)** |
|---|---|---|---|---|
| Yield strength (MPa) | Mean | 350.1 | 352.5 | 337.4 |
| | Standard deviation | 4.3 | 3.4 | 4.8 |
| Ultimate strength (Mpa) | Mean | 570.7 | 560.5 | 496.0 |
| | Standard deviation | 6.7 | 7.1 | 5.8 |
| Elongation ratio | Mean | 0.304 | 0.316 | 0.324 |
| | Standard deviation | 0.0031 | 0.0027 | 0.0040 |

The strength grade of the concrete was C50. When the concrete slab of each beam was poured, three 150 mm standard cube concrete test specimens of the same material were prepared as per the Chinese code (CMC 2009 [25]). Table 3 gives the mix proportion of C50 concrete coupons. The cube concrete test specimens were poured and cured under the same conditions as the concrete slabs of the specimens, and the material properties of the cube concrete test specimens were tested on the same day of loading. The 150 mm cube compressive strengths of the three cube concrete test specimens are shown in Table 4.

**Table 3.** Mix proportion of C50 concrete coupons (in units of kg/m$^3$).

| Component | Water | Cement | Sand | Aggregate |
|---|---|---|---|---|
| Proportion | 205 | 490 | 560 | 1197 |

**Table 4.** Material properties of the C50 concrete coupons (in units of MPa).

| Specimen | | CCB-1 | CCB-2 | CCB-3 |
|---|---|---|---|---|
| 150 mm cubic compressive strength (MPa) | Mean | 49.7 | 60.4 | 52.1 |
| | Standard deviation | 2.1 | 3.0 | 2.7 |

### 2.3. Test Setup

A static failure loading test was conducted for the curved composite box beam specimens at the midspan section through a vertical actuator. The loading device is shown in Figure 4, where Figure 4a,b show the CCB-1 positive bending moment failure, and the loading devices of CCB-2 and CCB-3 were the same as that of CCB-1. In addition, the inner side of the end of each specimen was connected to the steel beam and the ground beam by anchor bolts to prevent the curved composite beam specimen from overturning during the loading process. The loading beam, sensors, and vertical actuator were arranged. The hierarchical loading was used. Before the calculated yield load was reached, force control was applied. After the yield load was reached, the loading was switched to displacement control.

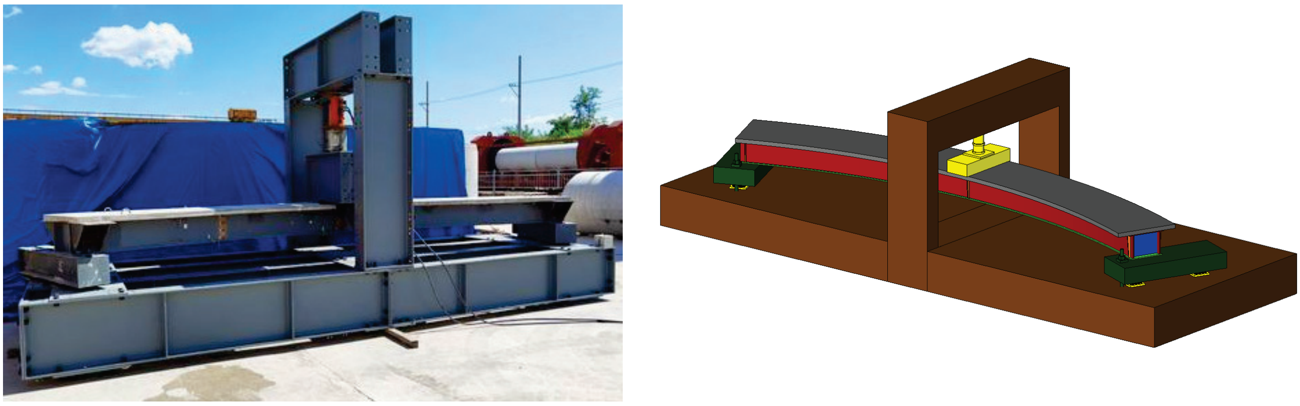

**(a) Photos of the test setup.** **(b) Schematic plot of the test setup**

**Figure 4.** Photos and schematic plot of CCB-1.

### 2.4. Instrumentation

In this test, the load and strain of the specimens were recorded by a computer data processing system, a displacement meter was used to record the vertical displacement and interface slip of the specimens, and a microscope for crack measurement was used to measure the crack width of the concrete slab. The measuring point arrangement scheme of the CCB-1 specimen is shown in Figure 5, and the measuring arrangement schemes of CCB-2 and CCB-3 were the same as that of the CCB-1 specimen. The midspan section and the 1/4-span section were selected as the control sections, and 16 strain gauges were arranged at each control section to measure the normal strain of the curved beam. The strain gauges were arranged on the top surface of the concrete slab, the longitudinal reinforcement in the concrete slab, and the bottom flange and web side of the steel girder, as shown in Figure 5. Two vertical displacement transducers were arranged in each of the midspan sections and the 1/4-span section to measure the vertical displacement and rotational angle of the curved beam. The two displacement transducers were located directly below the inner and outer webs, as shown in Figure 5c–e. A displacement transducer placed along the longitudinal direction was arranged at the end fulcrum section to measure the longitudinal interface slip of the specimens, as shown in Figure 5a,c. Two displacement transducers placed along the transverse direction were arranged on the midspan section to measure the transverse interface slip of the specimens, as shown in Figure 5a,b.

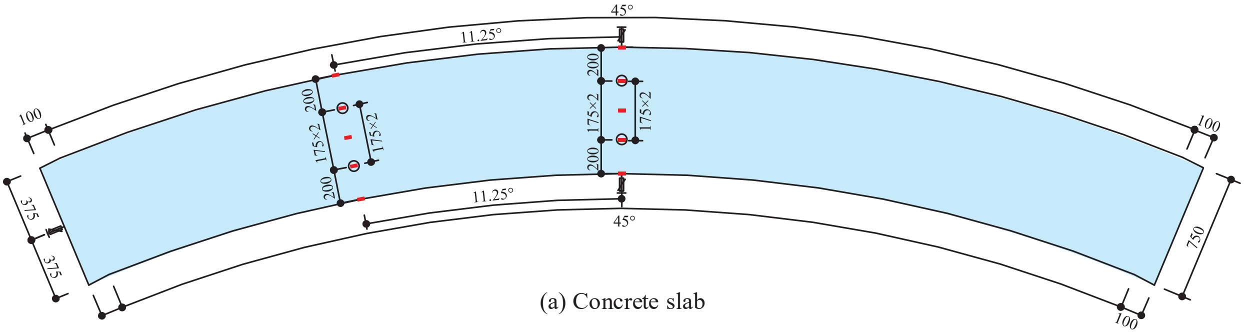

(a) Concrete slab

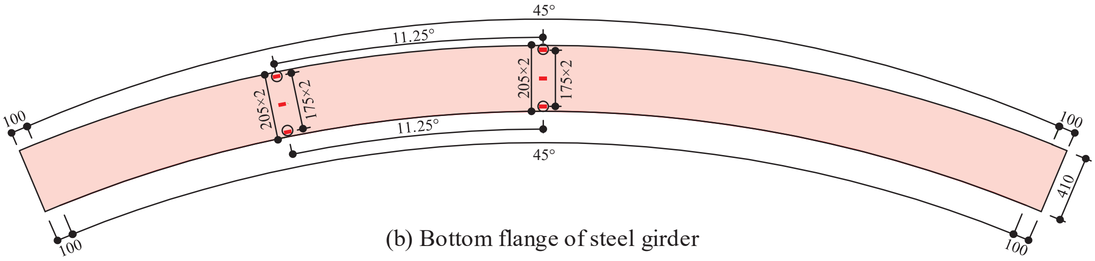

(b) Bottom flange of steel girder

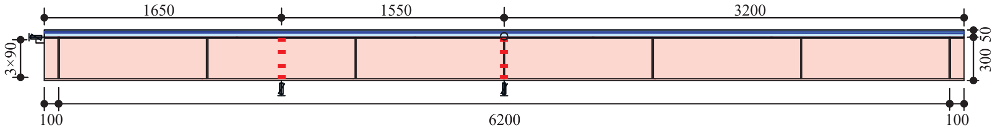

(c) Section of specimen along the longitudinal direction

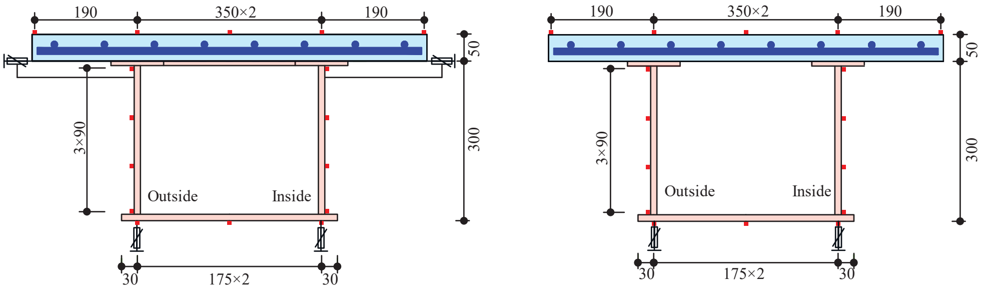

(d) Section of specimen along the transverse mid-span direction

(e) Section of specimen along the transverse 1/4-span direction

🟥 Strain gauge

○ Vertical displacement transducer

○ Interface slip transducer

**Figure 5.** Measurement of CCB-1 (in units of mm).

## 3. Results and discussion

### *3.1. Test Observations*

Figure 6a shows the vertical displacement and torsion of CCB-2. The figure indicates that the curved composite box beam showed typical bending–torsion coupling stress characteristics under the vertical load, and the vertical displacement and torsion of the other three specimens were similar. Figure 6b shows the longitudinal slip that occurs at the end of CCB-3. Due to the sparse arrangement of the studs and weak shear connections, CCB-3 presented significant longitudinal slip at the end of the beam, while those of the other specimens were not obvious. The crack distribution of CCB-3 is shown in Figure 7. The crack distributions of CCB-1 and CCB-2 were similar to that of CCB-3. Figure 7a shows that the concrete slab of CCB-3 was compressed during the loading process, and some cracks developed in the transverse direction due to tension in the midspan, whereas more shear diagonal cracks due to torsion occurred on both ends and extended from the end to the middle.

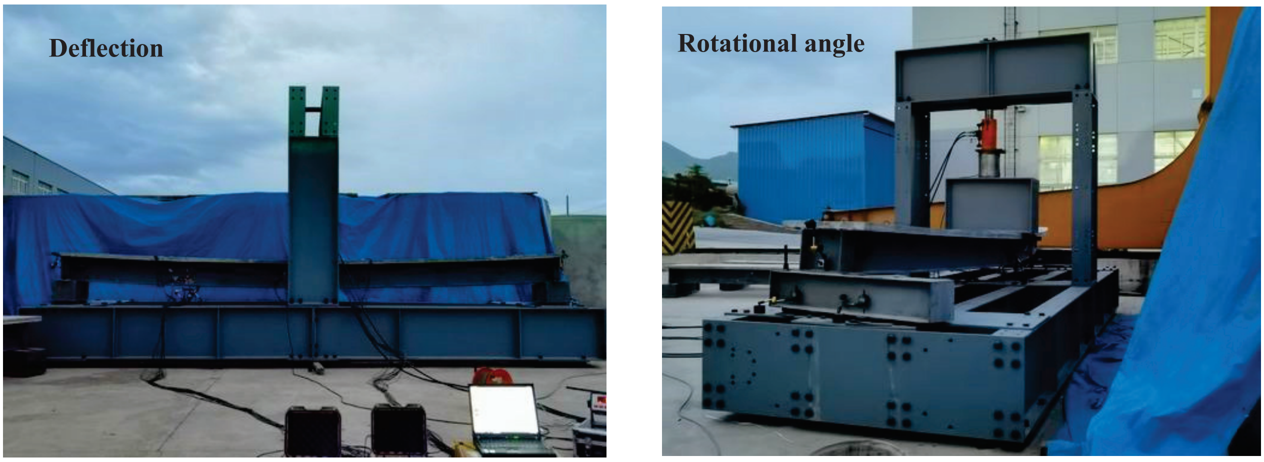

**(a) Deflection and torsion of CCB-2.**

**(b) Interface slip of CCB-3.**

**Figure 6.** Test observations.

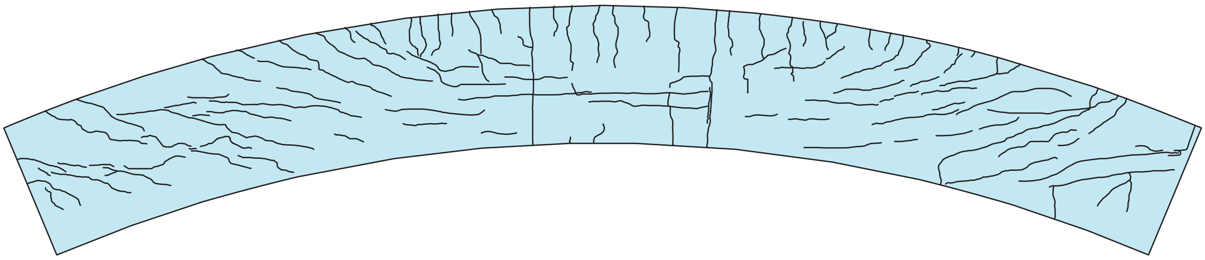

**Figure 7.** Crack profile of CCB-3.

### *3.2. Load–Displacement Curve and Capacity*

Figure 8 gives the load–displacement curves of CCB-1–CCB-3. Figure 8a presents the load–displacement curves of the midspan sections of CCB-1–CCB-3, and Figure 8b presents the load–displacement curves of the 1/4-span sections of CCB-1–CCB-3. The vertical displacement of the specimen is equal to the average of the values measured by the displacement sensor directly under the inner and outer webs. With the loading process, the vertical displacement of the specimen increased significantly, and the growth rate slowed with increasing load.

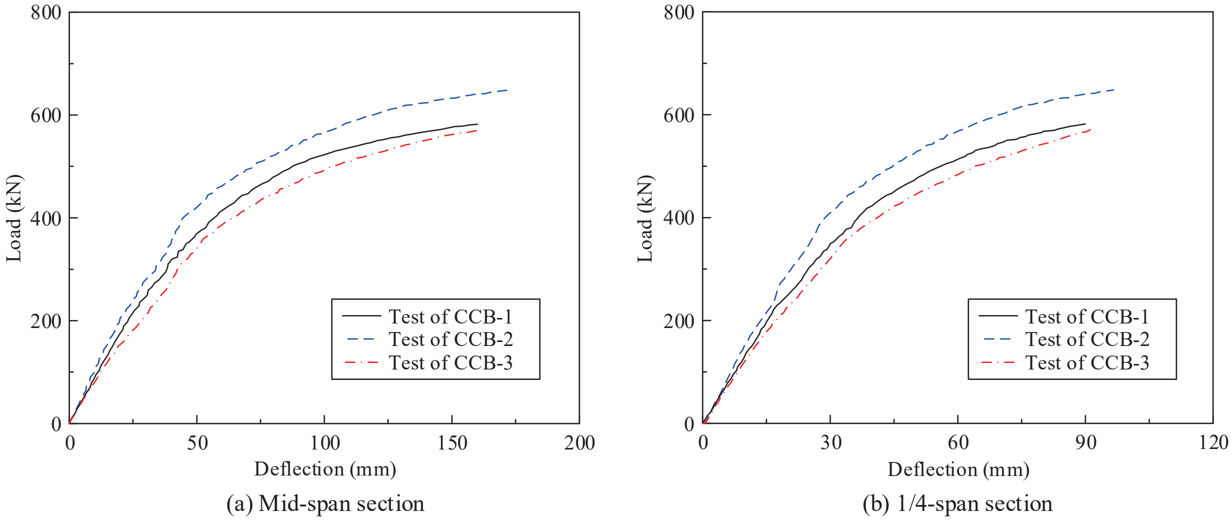

(a) Mid-span section

(b) 1/4-span section

**Figure 8.** Load–deflection curves of the test specimens.

Figure 8 shows that the ultimate bearing capacity of CCB-2 was 11.4% higher than that of CCB-1. The main reason is that the cubic compressive strength of the concrete slab of CCB-2 was higher than that of CCB-1; the secondary reason is that the central angle of CCB-1 was larger, and the bearing torque that weakens the flexural bearing capacity was stronger. The ultimate displacement of CCB-2 was 7.4% larger than that of CCB-1; the ultimate bearing capacity of CCB-1 was 1.9% higher than that of CCB-3, and its ultimate displacement was 1.2% less than that of CCB-3. The shear connection degree had no obvious effects on the ultimate bearing capacity and ultimate displacement of the specimen. The same phenomena were found for the study conducted by Nie and Cai [26]. The initial stiffness of CCB-1 was weaker than that of CCB-2 due to the more significant bending and torsion coupling behavior in CCB-1 and greater vertical displacement; the initial stiffness of CCB-3 was weaker than that of CCB-1, and the interface slips as a weak shear connection reduced the structural rigidity.

Figure 9 gives the load–rotational angle curves of CCB-1–CCB-3. Figure 9a presents the load–rotational angle curves of the midspan sections of CCB-1–CCB-3, and Figure 9b presents the load–rotational angle curves of the 1/4-span sections of CCB-1–CCB-3. The torsion angle of the specimen is equal to the ratio of the difference in the value measured by the displacement sensor directly under the inner and outer webs to the distance between the inner and outer webs. With the loading process, the rotational angle of the specimen increased significantly, and the growth rate slowed with increasing load. The developing trends of and the differences between the load–rotational angle curves of the three specimens were similar to the characteristics of their load–displacement curves.

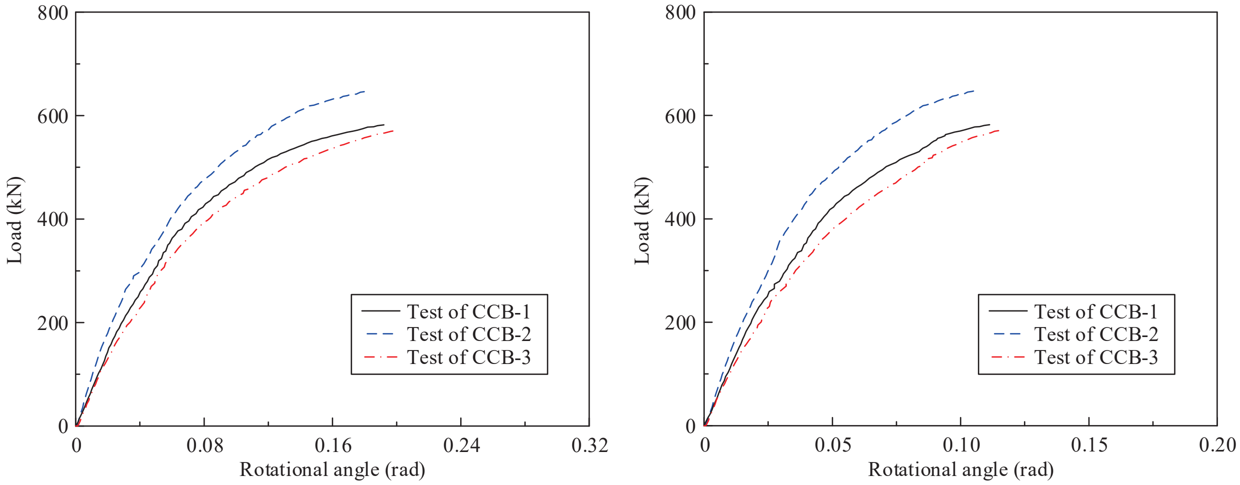

(a) Mid-span section (b) 1/4-span section

**Figure 9.** Load–rotational angle curves of the test specimens.

Figure 10 gives the load–interface slip curves of CCB-1–CCB-3. Figure 10a presents the load–interface slip curves of the 1/4-span section of CCB-1–CCB-3, and Figure 10b represents the load–interface slip curves of the sections on both ends of CCB-1–CCB-3. The transverse slip and vertical slip of the specimen were equal to the values measured by the displacement sensor at the midspan section and support sections on both ends, respectively. With the loading process, the interface slip of the specimen increased significantly, and the growth rate slowed with increasing load. Note that because the shear connection degree directly affects the interface slip, the initial stiffness of CCB-3 was weakest, and the ultimate slip was much larger than those of the other specimens.

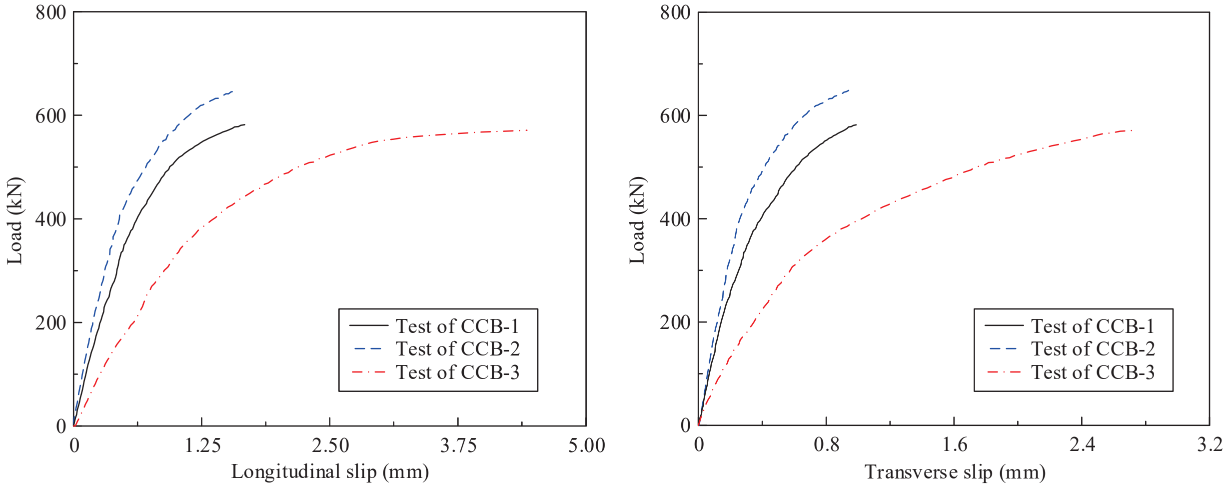

(a) Support section (b) Mid-span section

**Figure 10.** Load–interface slip curves of the test specimens.

The yield load, yield displacement, ultimate bearing capacity, and ultimate displacement of CCB-1–CCB-3 are shown in Table 5. The yield load of a specimen is obtained by the illustrated method, and the corresponding displacement is the yield displacement. As the steel beams or rebars of the three specimens do not break or fail during the loading process, the energy inside the structure is not released, and the load that the structure endures is constantly increasing. Ultimately, the test is stopped due to the loading capacity of the jack. As a result, the peak load of the specimens is their own ultimate bearing capacity, and the corresponding displacement is the ultimate displacement. Table 5 shows that the yield load was directly related to the initial stiffness of the load–displacement curve. The lower the initial stiffness of the specimen, the lower the yield load.

**Table 5.** Yield load and capacity of test specimens.

| Specimen | Yield Load (kN) | Yield Displacement (mm) | Ultimate Capacity $P_u$ (kN) | Ultimate Displacement (mm) |
|---|---|---|---|---|
| CCB-1 | 491.8868 | 84.4649 | 581.9083 | 160.0512 |
| CCB-2 | 526.3409 | 81.7638 | 648.2645 | 171.8867 |
| CCB-3 | 459.3324 | 83.6047 | 571.2004 | 161.9660 |

## *3.3. Strain Distribution*

Figure 11a,b show the normal strain distribution of the concrete slab of CCB-1 at the midspan section and the 1/4-span section, respectively; Figure 11c,d show the normal strain distribution values of the concrete slab of CCB-2 at the midspan section and the 1/4-span section, respectively; Figure 11e,f show the normal strain distribution values of the concrete slab of CCB-3 at the midspan section and the 1/4-span section, respectively.

As shown in Figure 11, the normal strain of the top slab of CCB-1 was larger than that of the top slab of CCB-2, which indicates that an increase in the central angle improved the overall level of structural strain. Additionally, the normal strain of the top slab of CCB-3 was slightly larger than the normal strain of the top slab of CCB-1, which indicates that the shear connection degree had no significant effect on the strain. The normal strain of the concrete slab at the midspan section and the 1/4-span section of each specimen was distributed unevenly in the transverse direction, and that of the inner side was larger than that of the outer side. This is due to the combined influence of restrained torsion and distortion effects. In particular, CCB-3 showed a very small tensile strain on the outer side of the concrete slab.

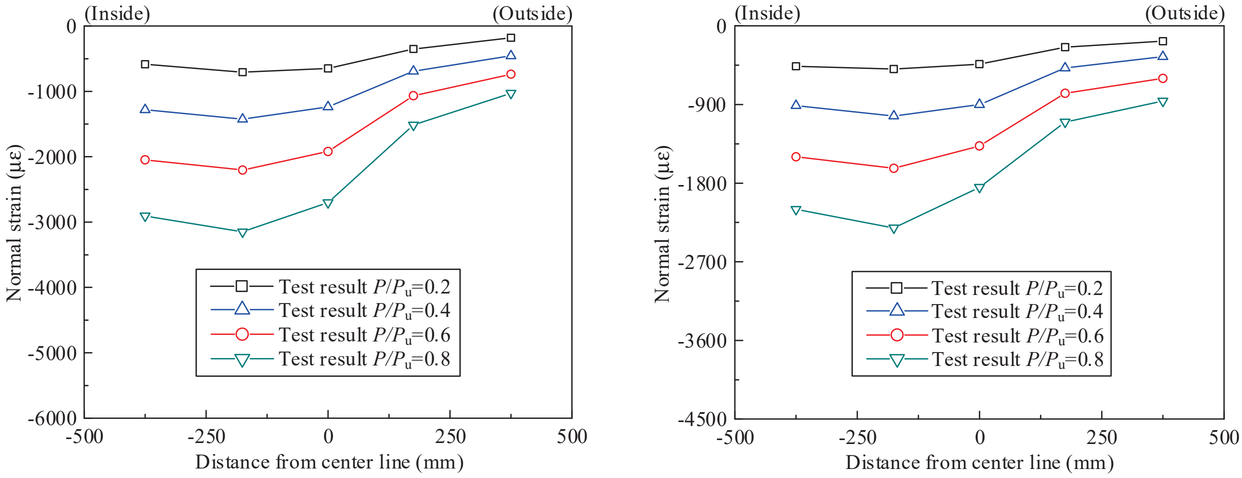

(a) Mid-span section of CCB-1

(b) 1/4-span section of CCB-1

**Figure 11.** *Cont.*

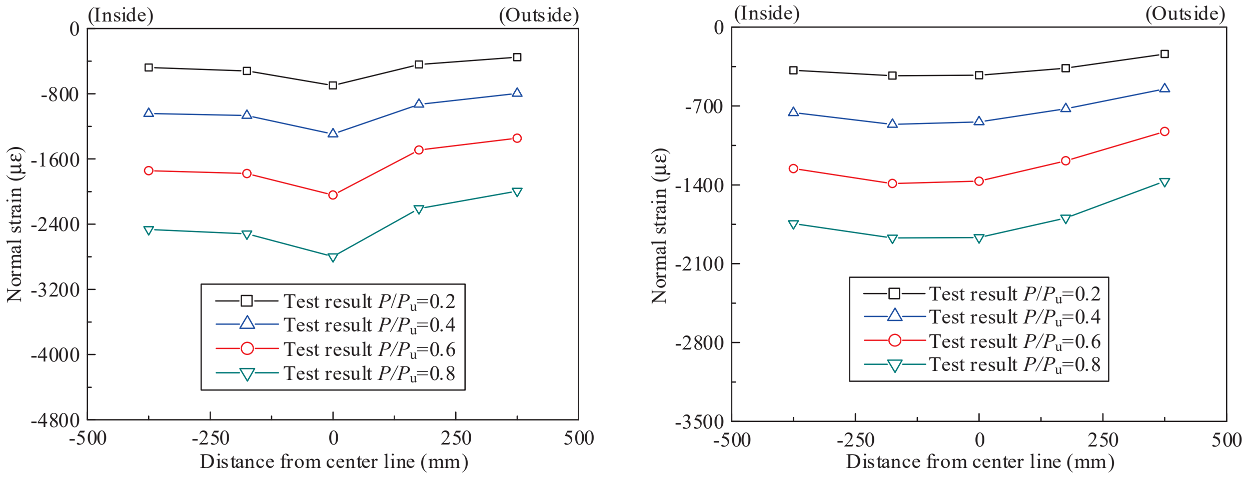

(c) Mid-span section of CCB-2

(d) 1/4-span section of CCB-2

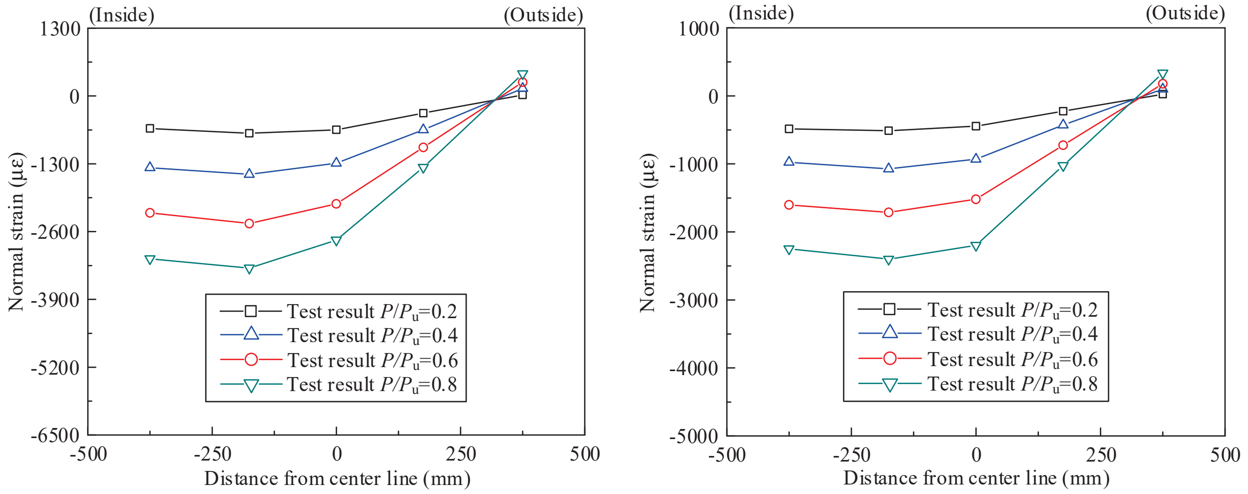

(e) Mid-span section of CCB-3

(f) 1/4-span section of CCB-3

**Figure 11.** Normal strain distribution of the concrete slab or rebar of the test specimens.

Figure 12 shows the normal strain distribution of the steel bottom flange of CCB-1 at the midspan section and the 1/4-span section. The key areas of the midspan sections of CCB-1–CCB-3 reached yield strains at $0.6P_u$, $0.8P_u$, and $0.6P_u$, respectively. The key areas of the 1/4-span sections of CCB-1 and CCB-3 reached yield strains at $0.8P_u$ and $0.8P_u$, respectively, and the 1/4-span section of CCB-2 was in the elastic stage. The trends of and differences in the strain distributions of the steel bottom flanges of each specimen were basically consistent with those of the concrete slab.

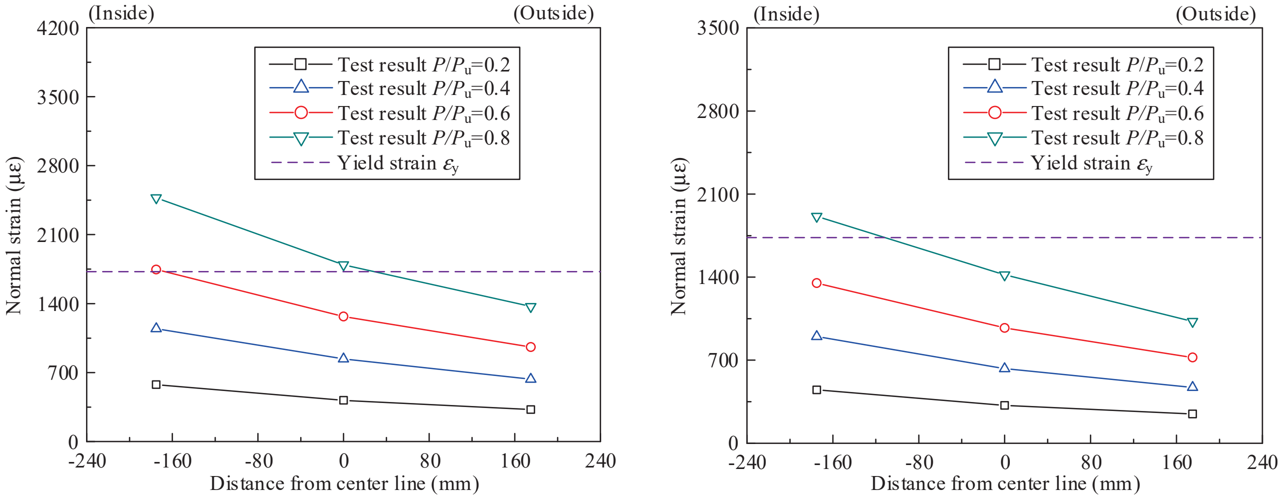

(a) Mid-span section of CCB-1 (b) 1/4-span section of CCB-1

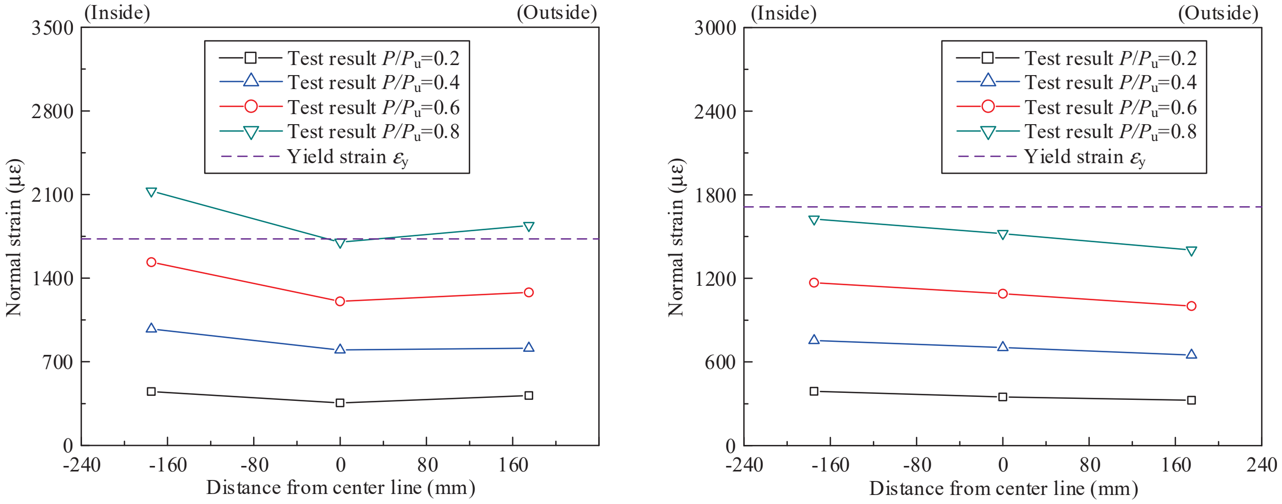

(c) Mid-span section of CCB-2 (d) 1/4-span section of CCB-2

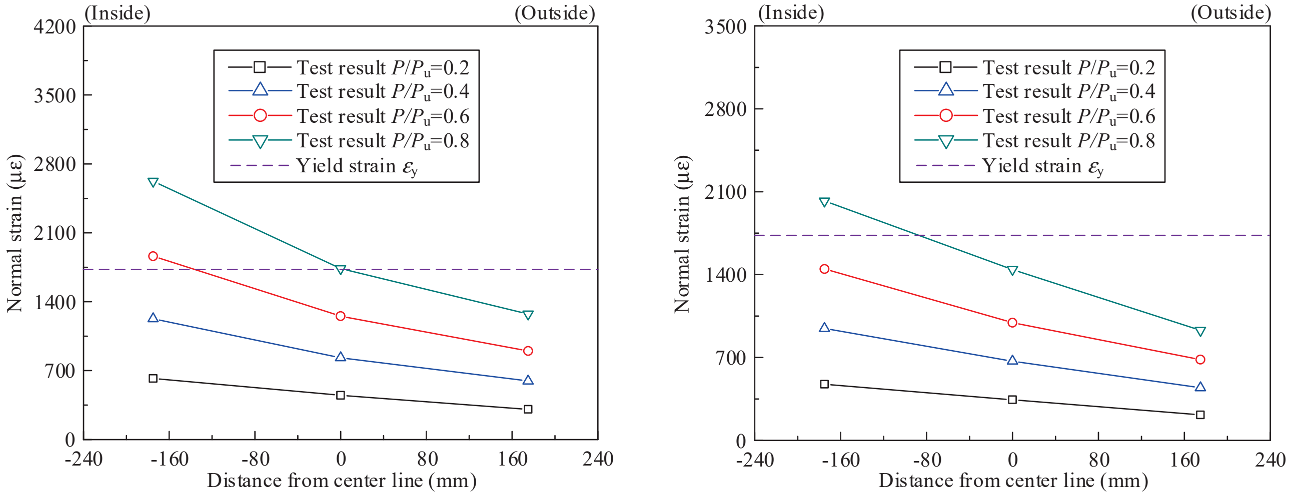

(e) Mid-span section of CCB-3 (f) 1/4-span section of CCB-3

**Figure 12.** Normal strain distributions of the steel bottom flanges of the test specimens.

Figure 13 gives the normal strain distributions of the steel webs of CCB-1–CCB-3 at the midspan sections and the 1/4-span sections. The vertical coordinate 0 in the figure represents the position of the interface of the composite beam, and the vertical coordinate 290 mm represents the lower flange slab of the steel beam. The figure shows that the strain distribution of the section was close to a straight line along the direction of the beam height.

Figure 13 shows that the key positions of the inner webs in the midspan sections of CCB-1–CCB-3 reached yield strains of $0.6P_u$, $0.8P_u$, and $0.6P_u$, respectively; the midspan section of the outer web of CCB-2 reached a yield strain of $0.8P_u$; and the midspan sections of the outer webs of CCB-1 and CCB-3 were both in the elastic stage. The key positions of the inner webs in the 1/4 sections of CCB-1–CCB-3 reached yield strains of $0.8P_u$, $0.8P_u$, and $0.8P_u$, respectively; the 1/4 section of the outer webs of CCB-1–CCB-3 were all in the elastic stage.

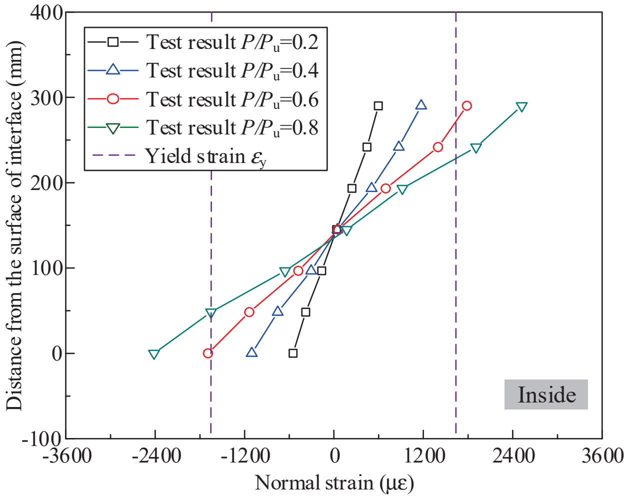

**(a) Midspan section of CCB-1.**

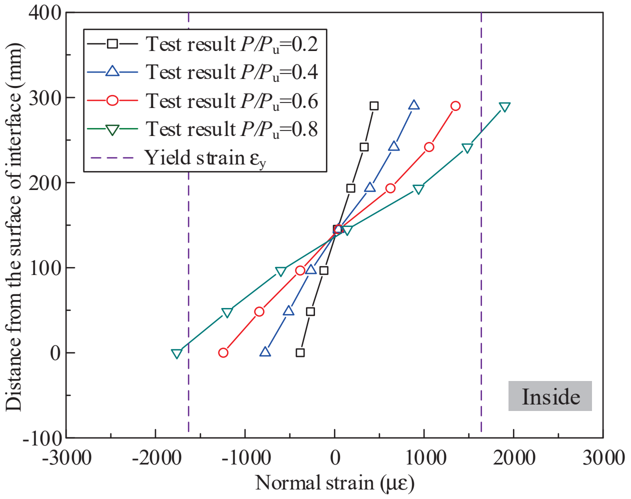

**(b) 1/4-span section of CCB-1.**

**Figure 13.** *Cont.*

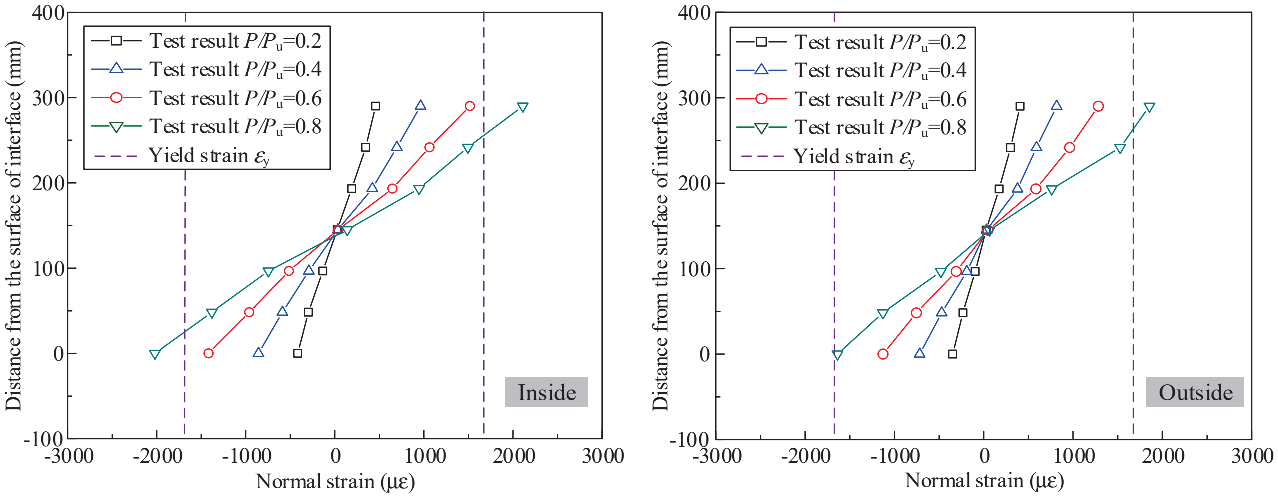

**(c) Midspan section of CCB-2.**

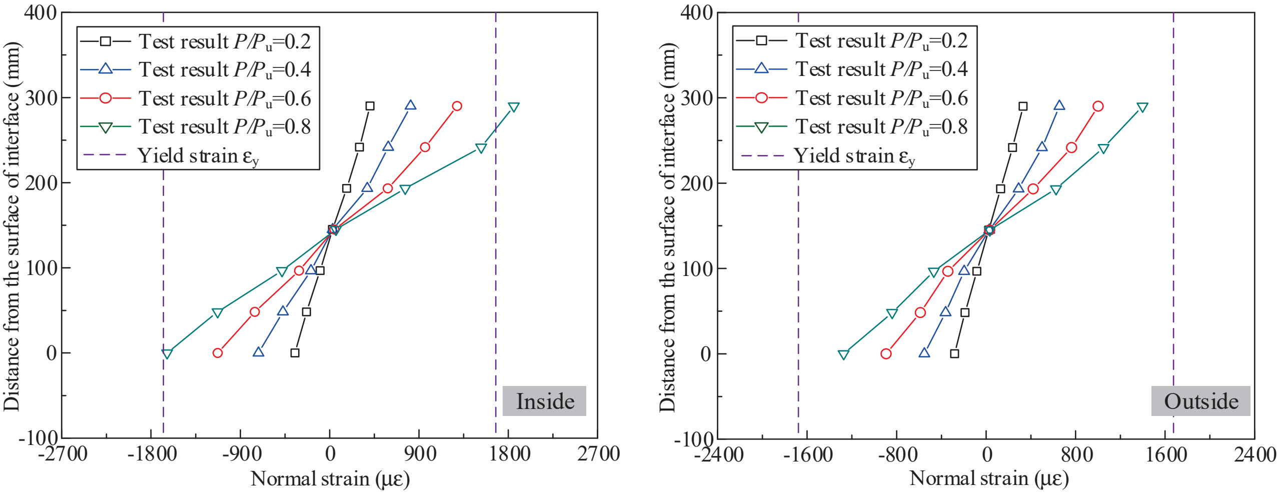

**(d) 1/4-span section of CCB-2.**

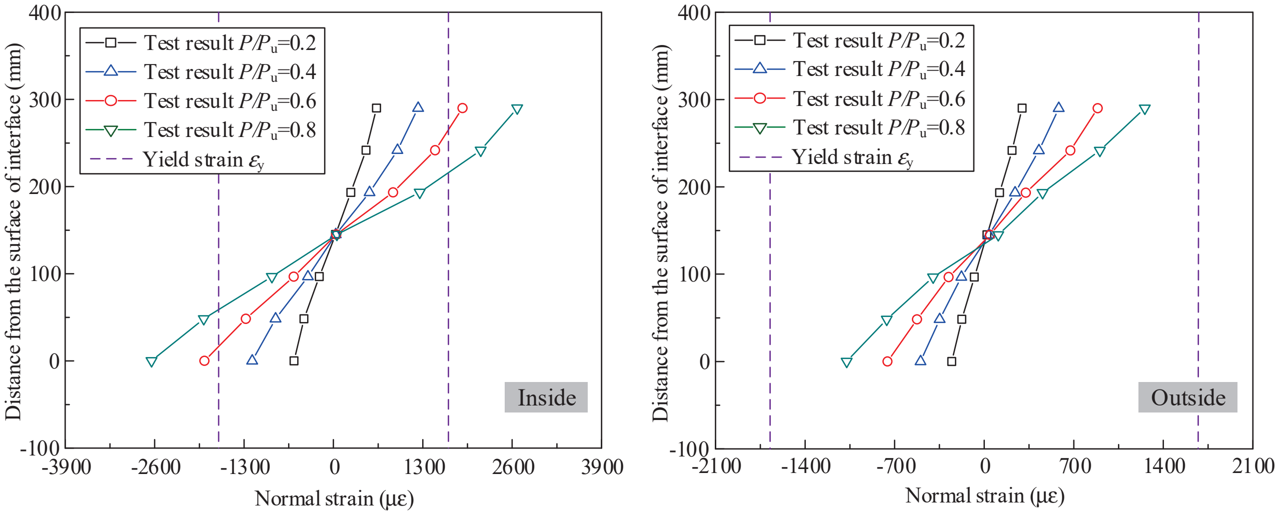

**(e) Midspan section of CCB-3.**

**Figure 13.** *Cont.*

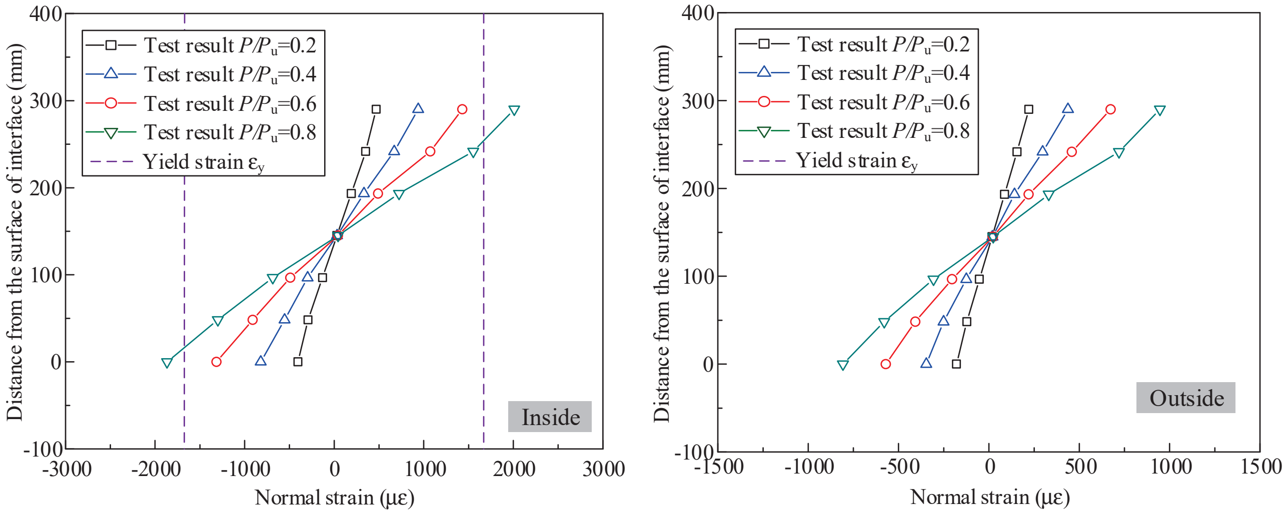

**(f) 1/4-span section of CCB-3.**

**Figure 13.** Normal strain distributions of the steel webs of the test specimens.

## 4. Finite Element Analysis

### 4.1. Elaborate Finite Element Model

In this paper, the force behaviors of CCB-1–CCB-3 during the whole loading process were simulated in ABAQUS [27]. Figure 14 shows the fine finite element model of CCB-2, and the fine finite element models of the other two specimens were similar. In terms of element selection, SOLID elements were used to simulate the concrete slabs, SHELL elements were used to simulate the steel beams, TRUSS elements were used to simulate the vertical and transverse rebars, CONNECTOR elements were used to simulate the studs, and SOLID elements were used to simulate the loading beams. In terms of the interaction condition settings between the elements, the TRUSS elements of the rebars were imported into the SOLID elements of the concrete slabs by the EMBED command, ignoring the bond–slip effects between the rebar and the concrete. When the CONNECTOR used elements to simulate the studs, vertical displacement between the concrete slab and the steel beam did not occur, which indicates that the vertical stiffness of the CONNECTOR element was infinitely large. Additionally, the vertical load was set on the midspan of the beam, and the model boundary conditions were simply supported. For meshing, the unit size was 25 mm, and the accuracy of the mesh convergence was verified by a mesh test.

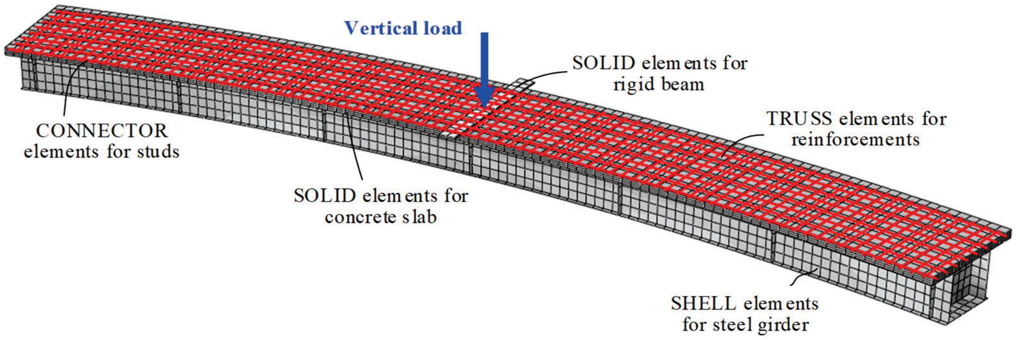

**Figure 14.** Finite element modeling scheme of CCB-2.

The constitutive relations of the materials in the test were as follows:

(1) Concrete

For compressed concrete, the yield rule is the von Mises yield surface, the hardening rule is isotropic strengthening, and the flow rule is associated flow. The concrete damage plastic (CDP) model is used. According to the Wang et al. study [28], some critical parameters, including the parameter controlling the projection of the yield surface onto the bias place $K_c$ = 0.67, the expansive angle related to the flow rule $\varphi$ = 37–42°, and the eccentricity of the plastic potential function $\lambda$ = 0.1, are determined. The uniaxial compression stress–strain relationship recommended by Hognestad et al. [29] is adopted, as shown in Figure 15a. The compressive strength of the concrete cylinder is calculated according to the suggestion of Chen et al. [30]. Equations (1) and (2) give the calculation formula of the curve in Figure 15a.

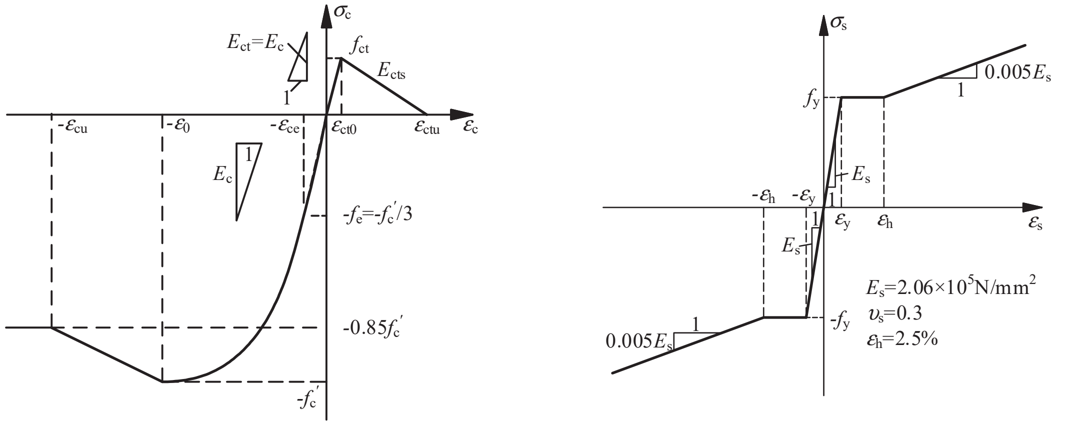

(a) Concrete (b) Steel

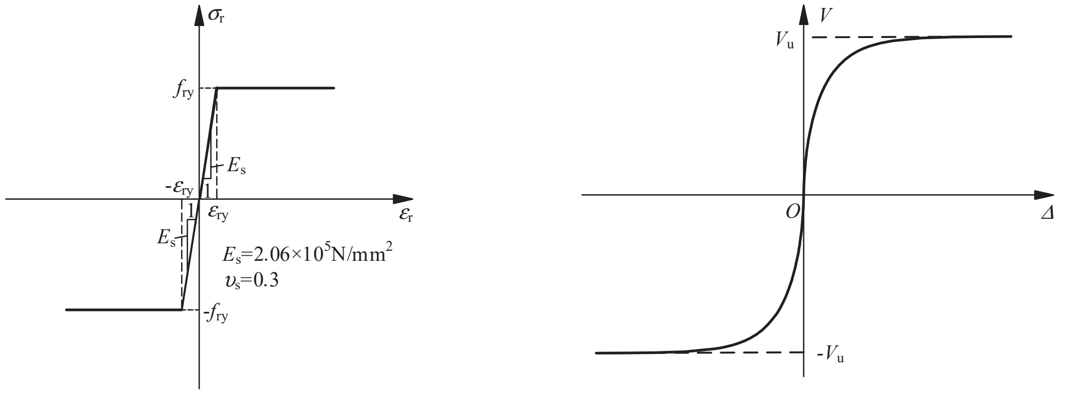

(c) Rebar in concrete slab (d) Shear studs at steel-concrete interface

**Figure 15.** The uniaxial constitutive relationship of the FE model.

According to the research of Guo [31], CEB-FIP 1990 [32], and Bazant and Oh [33], the uniaxial tensile stress–strain relationship of concrete is shown in Figure 15a. Equations (3)–(5) give the calculation formula of the curve in Figure 15a.

$$\frac{\sigma_c}{f_c'} = \begin{cases} 2\frac{\varepsilon_c}{\varepsilon_0} - \left(\frac{\varepsilon_c}{\varepsilon_0}\right)^2 & \varepsilon_c \le \varepsilon_{c0} \\ 1 - 0.85\left(\frac{\varepsilon_c - \varepsilon_{c0}}{\varepsilon_{cu} - \varepsilon_{c0}}\right) & \varepsilon_{c0} < \varepsilon_c \le \varepsilon_{cu} \end{cases} \tag{1}$$

$$f_c' = \begin{cases} 0.8f_{cu} & f_{cu} \le 50 \\ f_{cu} - 10 & f_{cu} > 50 \end{cases} \tag{2}$$

where $\varepsilon_{\mathrm{c}}$ is the strain of concrete; $\varepsilon_{\mathrm{c0}}$ is the peak compressive strain of concrete, taken as 0.002; $\varepsilon_{\mathrm{cu}}$ is the ultimate compressive strain of concrete, taken as 0.0033; $f_{\mathrm{c}}'$ is the compressive strength of the concrete cylinder; and $f_{\mathrm{cu}}$ is the compressive strength of the concrete cube, which can be obtained from the results of the material property tests in Table 4.

$$\frac{\sigma_{\mathrm{c}}}{f_{\mathrm{ct}}} = \begin{cases} \frac{\varepsilon_{\mathrm{c}}}{\varepsilon_{\mathrm{ct0}}} & \varepsilon_{\mathrm{c}} \le \varepsilon_{\mathrm{ct0}} \\ \frac{\varepsilon_{\mathrm{ctu}}-\varepsilon_{\mathrm{c}}}{\varepsilon_{\mathrm{ctu}}-\varepsilon_{\mathrm{ct0}}} & \varepsilon_{\mathrm{ct0}} < \varepsilon_{\mathrm{c}} \le \varepsilon_{\mathrm{ctu}} \end{cases} \tag{3}$$

$$f_{\mathrm{ct}} = \begin{cases} 0.26{f_{\mathrm{cu}}}^{2/3} & f_{\mathrm{cu}} \le 50 \\ 0.21{f_{\mathrm{cu}}}^{2/3} & f_{\mathrm{cu}} > 50 \end{cases} \tag{4}$$

$$\varepsilon_{\mathrm{ctu}} = \frac{2G_{\mathrm{f}}}{f_{\mathrm{ct}} l_{\mathrm{e}}} \tag{5}$$

where $f_{\mathrm{ct}}$ is the tensile strength of concrete; $\varepsilon_{\mathrm{ct0}}$ is the cracking strain of concrete; $\varepsilon_{\mathrm{ctu}}$ is the ultimate tensile strain of concrete; $G_{\mathrm{f}}$ is the fracture energy of concrete calculated according to CEB-FIP1990 [32]; and $l_{\mathrm{e}}$ is the characteristic length of elements of concrete calculated according to CEB-FIP1990 [32].

(2) Steel plate

For steel plates, the yield is represented by the von Mises yield surface, the hardening is represented by kinematic hardening, and the flow is represented by associated flow. The uniaxial stress–strain relationship of the steel is represented by the typical trilinear model according to the reference [34], as shown in Figure 15b. Equation 6 gives the calculation formula of the curve in Figure 15b.

$$\sigma_{\mathrm{s}} = \begin{cases} E_{\mathrm{s}}\varepsilon_{\mathrm{s}} & \varepsilon_{\mathrm{s}} \le \varepsilon_{\mathrm{y}} \\ f_{\mathrm{y}} & \varepsilon_{\mathrm{y}} < \varepsilon_{\mathrm{s}} \le \varepsilon_{\mathrm{h}} \\ f_{\mathrm{y}} + \frac{f_{\mathrm{u}}-f_{\mathrm{y}}}{\varepsilon_{\mathrm{su}}-\varepsilon_{\mathrm{h}}}(\varepsilon_{\mathrm{s}} - \varepsilon_{\mathrm{h}}) & \varepsilon_{\mathrm{s}} > \varepsilon_{\mathrm{h}} \end{cases} \tag{6}$$

where $\varepsilon_{\mathrm{y}}$ is the yield strain of the steel; $\varepsilon_{\mathrm{h}}$ is the strain when the steel begins to strengthen, taken as $12\varepsilon_{\mathrm{y}}$ according to Han's research [35]; $\varepsilon_{\mathrm{su}}$ is the ultimate strain of the steel; $f_{\mathrm{y}}$ is the yield strength of the steel, which can be obtained from the results of the material property tests in Table 2; and $f_{\mathrm{u}}$ is the ultimate strength of the steel.

(3) Rebar

For the rebar, the yield is represented by the von Mises yield surface, the hardening is represented by kinematic hardening, and the flow rule is represented by associated flow. The uniaxial stress–strain relationship of the steel is represented by the typical ideal elastoplastic model according to the reference [34], as shown in Figure 15c. Equation (7) gives the calculation formula of the curve in Figure 15c.

$$\sigma_{\mathrm{r}} = \begin{cases} E_{\mathrm{s}}\varepsilon_{\mathrm{r}} & \varepsilon_{\mathrm{r}} \le \varepsilon_{\mathrm{ry}} \\ f_{\mathrm{ry}} & \varepsilon_{\mathrm{r}} > \varepsilon_{\mathrm{ry}} \end{cases} \tag{7}$$

where $\varepsilon_{\mathrm{r}}$ is the strain of the rebar; $\sigma_{\mathrm{r}}$ is the stress of the rebar; $\varepsilon_{\mathrm{ry}}$ is the yield strain of the rebar; and $f_{\mathrm{ry}}$ is the yield strength of the rebar, which can be obtained from the results of the material property tests in Table 2.

(4) Stud

A three-dimensional nonlinear element is used to simulate the studs in ABAQUS, and the relationship of the shear force $V$-slip $\Delta$ specified by CEB-FIP2010 [36] is shown in Figure 15d. Equations (8) and (9) give the calculation formula of the curve in Figure 15d.

$$V = V_{\mathrm{u}}\left(1 - e^{-\alpha_2\Delta}\right)^{\alpha_1} \tag{8}$$

$$V_u = \left(5.3 - \frac{1.3}{\sqrt{n_s}}\right) A_{us} f_c'^{0.35} f_{ru}^{0.65} \left(\frac{E_c}{E_s}\right)^{0.4} \tag{9}$$

where $V_u$ is the shear bearing capacity of a single stud; $\alpha_1$ and $\alpha_2$ are the control parameters subjected to force, and according to CEB-FIP2010 [36], $\alpha_1$ = 0.75 and $\alpha_2$ = 1.1; $n_s$ is the number of studs in each group; $A_{us}$ is the area of a single stud; $E_c$ and $E_s$ are the elastic moduli of concrete and steel, respectively; and $f_{ru}$ is the tensile strength of the stud. The kinematic hardening model is used to simulate the hysteretic force behavior of studs.

For the FE model, the material and geometrical nonlinearities are considered. A modified arc-length approach is introduced to the algorithm with the auto-adaptive loading schedule. The boundary condition for the specimen is simply supported. As the concrete damage plastic model cannot simulate the concrete behavior subjected to shear, the abovementioned FE model can only simulate the flexural failure rather than shear failure of the curved composite beams.

### 4.2. Validation and Verification of Finite Element Modeling

The test observations and finite element simulation of the final loading shape of CCB-2 are presented in Figure 16. The curved composite box beam showed typical bending and torsion coupling force characteristics under vertical loading, and the final shapes of the other two specimens were similar. The figure shows that the results of the test observation were in good agreement with those of the finite element simulation.

**(a) Front view of test failure mode.**

**(b) Front view of FE failure mode.**

**(c) Side view of test failure mode.**

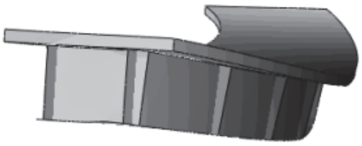

**(d) Side view of FE failure mode.**

**Figure 16.** Comparison of the failure modes from the test and finite element analyses of CCB-2.

Figure 17 shows a comparison between the test results and the finite element calculation results of the load–displacement curves of the midspan sections and 1/4-span sections of CCB-1–CCB-3. For the initial stiffness, ultimate bearing capacity, and the developing trend of the whole curve, the results of the test observation were in good agreement with those of the finite element calculations. However, in some partial sections of the load–displacement curves, the test results were slightly smaller than the results of the finite element calculation, which may be due to the welding residual stress decreasing the stiffness in the steel.

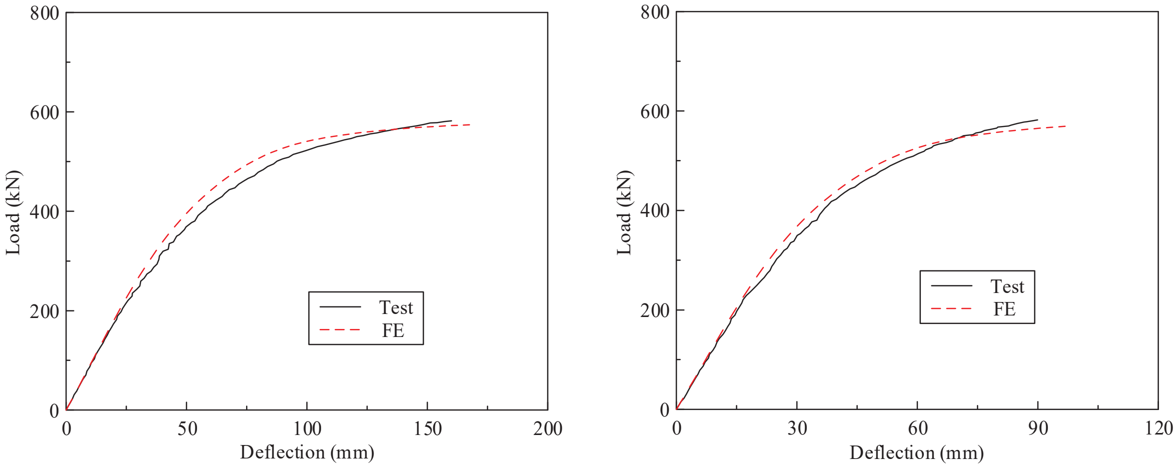

(a) Mid-span section of CCB-1 (b) 1/4-span section of CCB-1

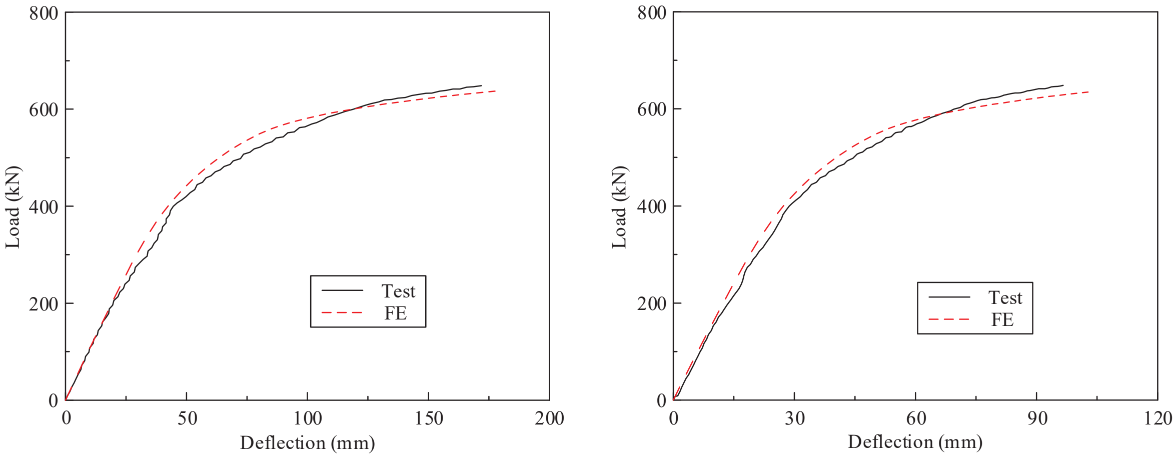

(c) Mid-span section of CCB-2 (d) 1/4-span section of CCB-2

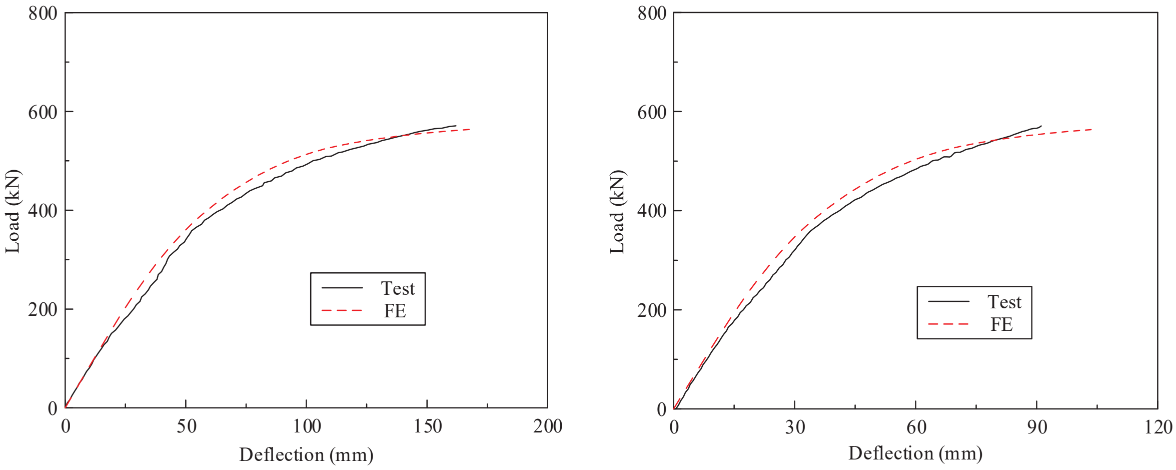

(e) Mid-span section of CCB-3 (f) 1/4-span section of CCB-3

**Figure 17.** Comparison of the load–deflection curves from the test and numerical analyses.

Figure 18 shows a comparison between the test results and the finite element calculation results for the load–torsion angle curves of the midspan sections and 1/4-span sections of CCB-1–CCB-3. Figure 19 gives a comparison between the test results and the finite element calculation results of the load–interface slip curves of the midspan sections and 1/4-span sections of CCB-1–CCB-3. Figures 18 and 19 show that the finite element model can simulate the development of the load–torsion angle curve and the load–interface slip curve of the specimen.

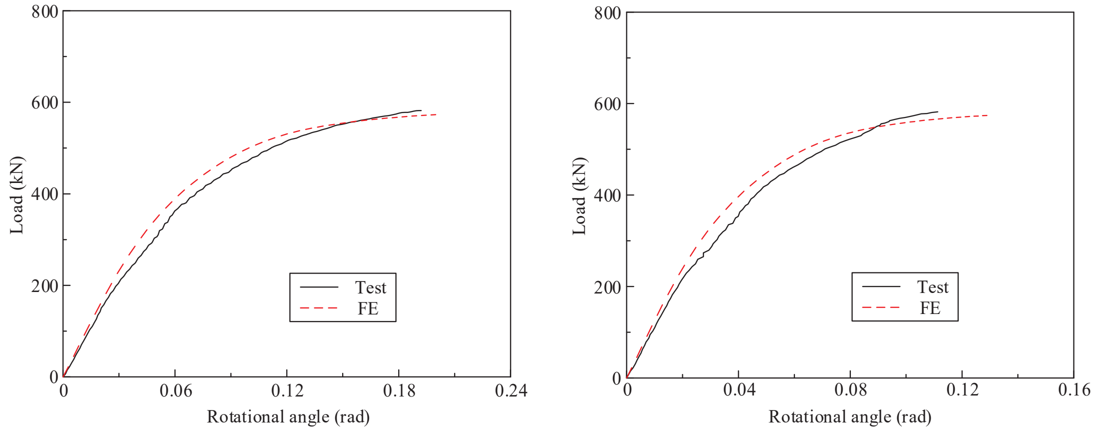

(a) Mid-span section of CCB-1 (b) 1/4-span section of CCB-1

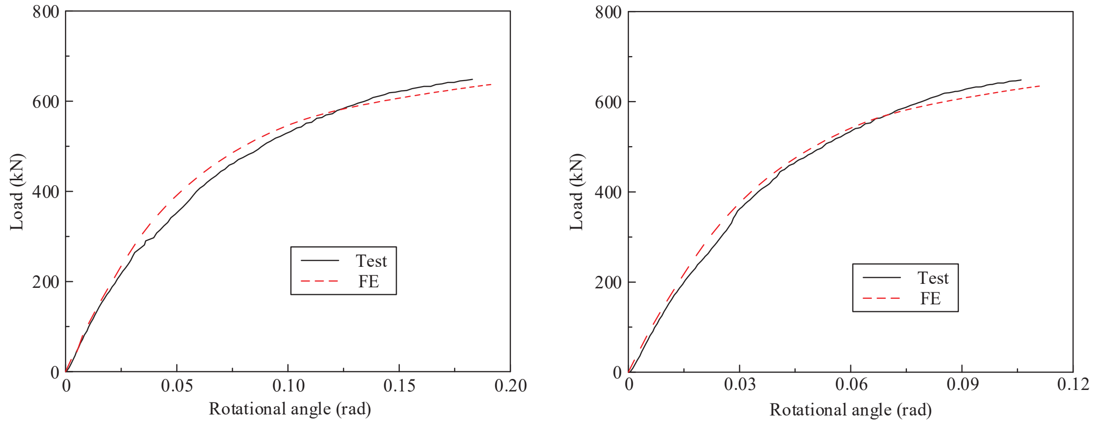

(c) Mid-span section of CCB-2 (d) 1/4-span section of CCB-2

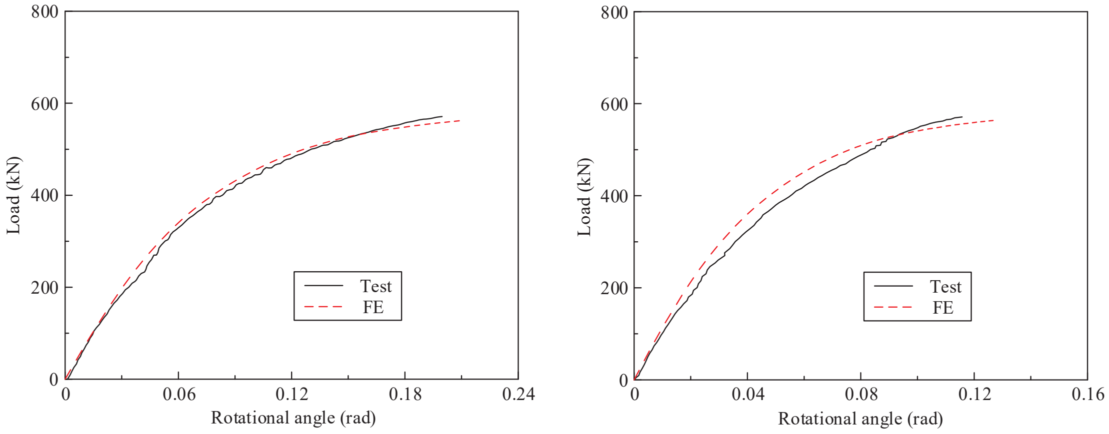

(e) Mid-span section of CCB-3 (f) 1/4-span section of CCB-3

**Figure 18.** Comparison of the load–rotational angle curves from the test and numerical analyses.

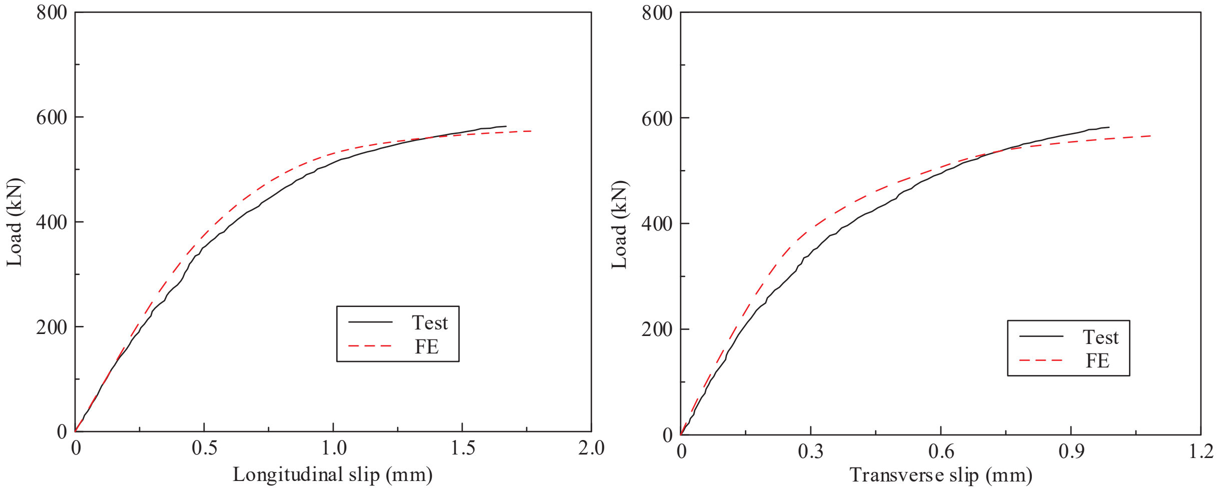

(a) Support section of CCB-1 (b) Mid-span section of CCB-1

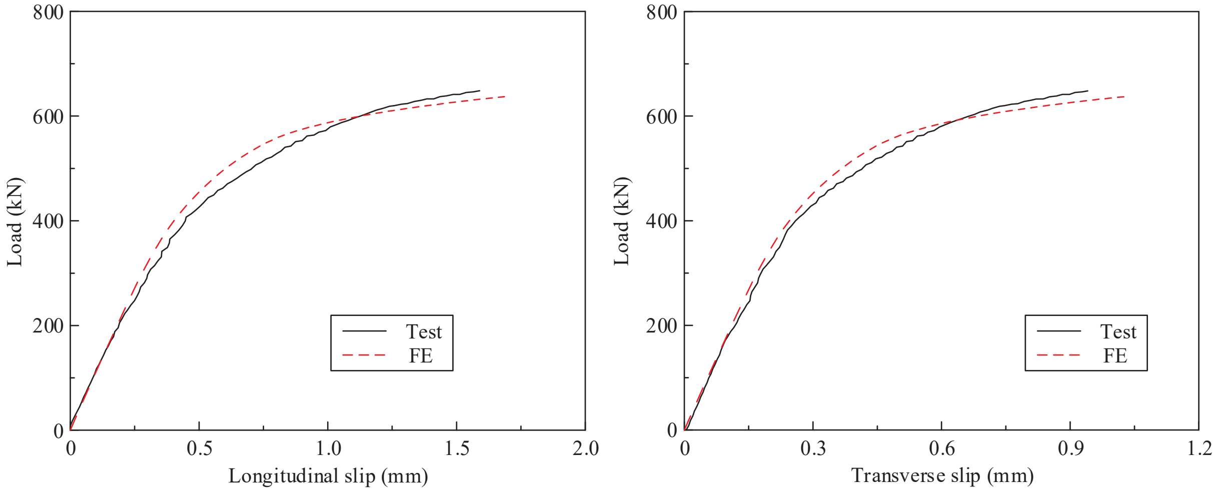

(c) Support section of CCB-2 (d) Mid-span section of CCB-2

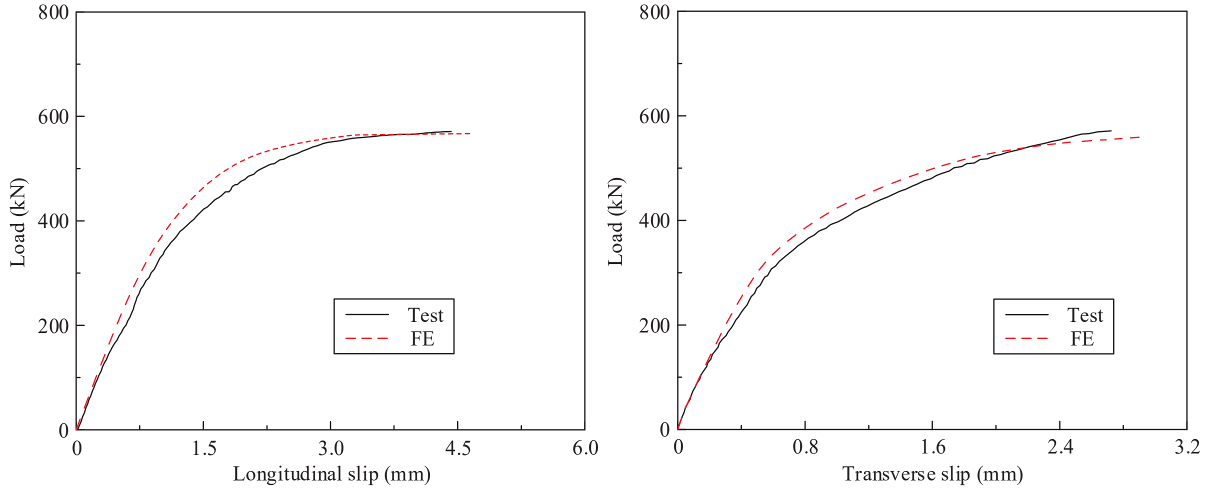

(e) Support section of CCB-3 (f) Mid-span section of CCB-3

**Figure 19.** Comparison of the load–interface slip curves from the test and numerical analyses.

Figure 20 shows a comparison between the test results and the finite element calculation results of the normal strain of the concrete slabs of the midspan sections and 1/4-span sections of CCB-1–CCB-3. Figure 21 gives a comparison between the test results and the finite element calculation results for the normal strain of the steel bottom plate of the midspan sections and 1/4-span sections of CCB-1–CCB-3. The finite element model simulates the strain distribution and trends of the structure during the loading process.

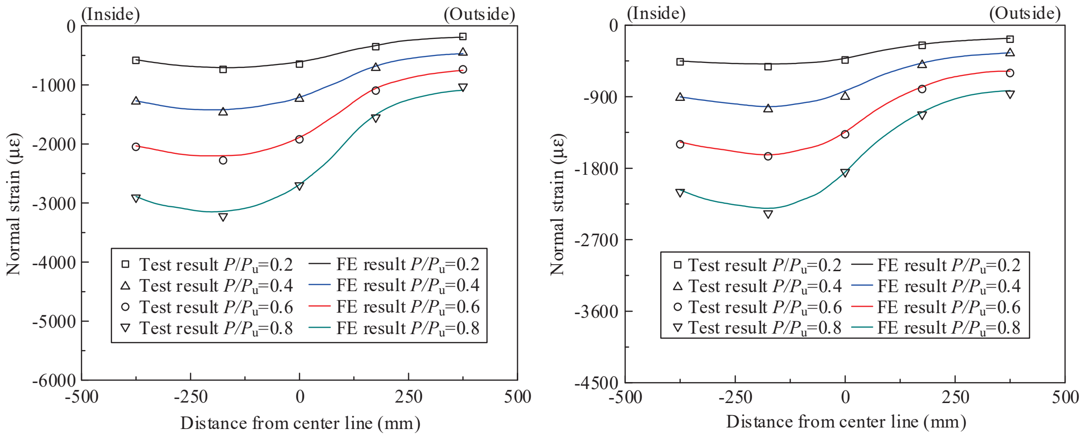

(a) Mid-span section of CCB-1

(b) 1/4-span section of CCB-1

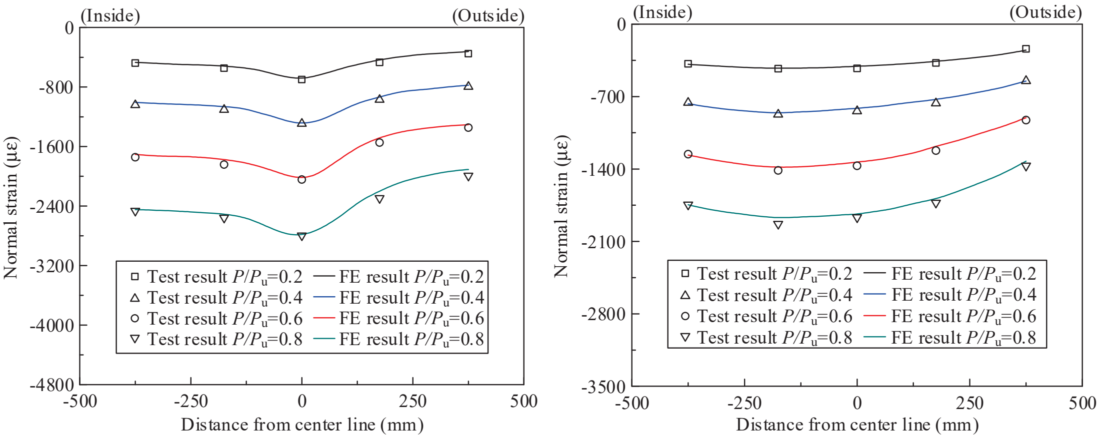

(c) Mid-span section of CCB-2

(d) 1/4-span section of CCB-2

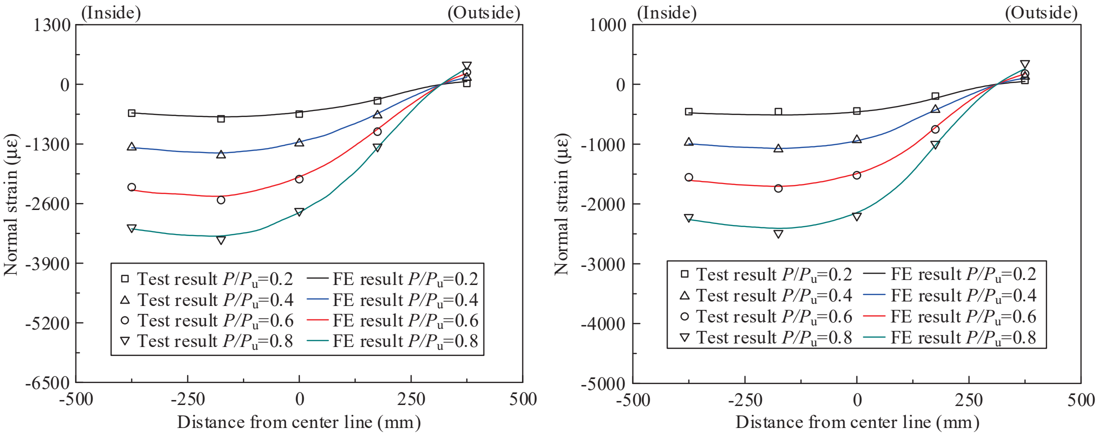

(e) Mid-span section of CCB-3

(f) 1/4-span section of CCB-3

**Figure 20.** Comparison of the normal strains of the concrete slabs from the test and numerical analyses.

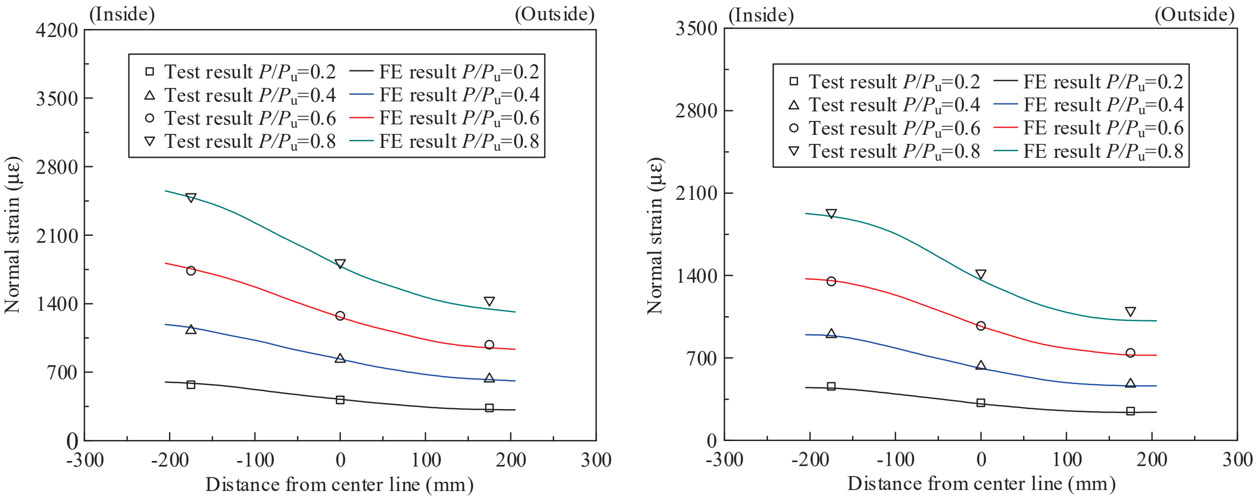

(a) Mid-span section of CCB-1 (b) 1/4-span section of CCB-1

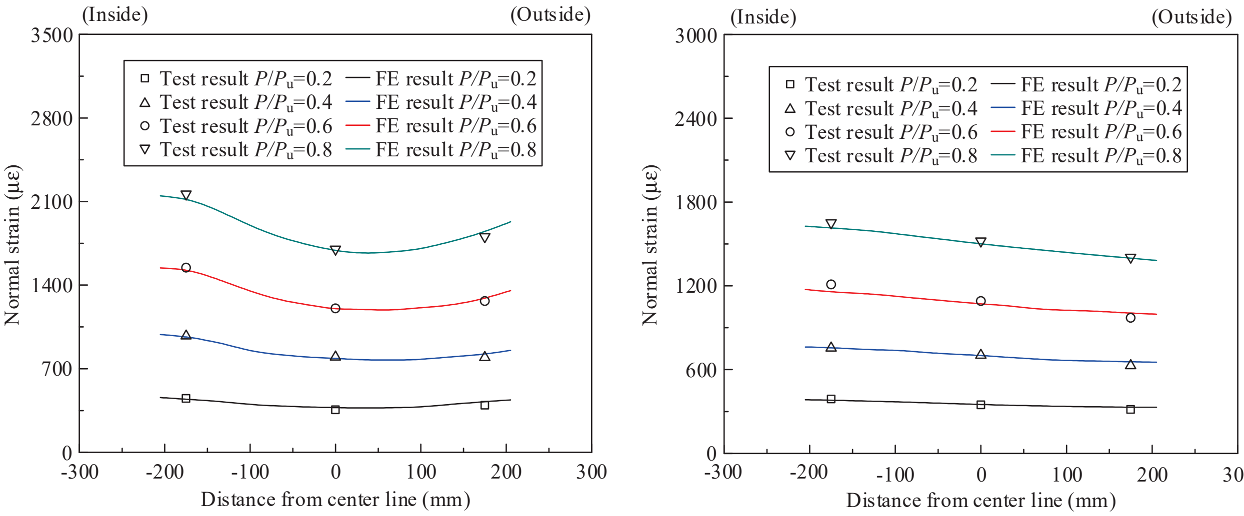

(c) Mid-span section of CCB-2 (d) 1/4-span section of CCB-2

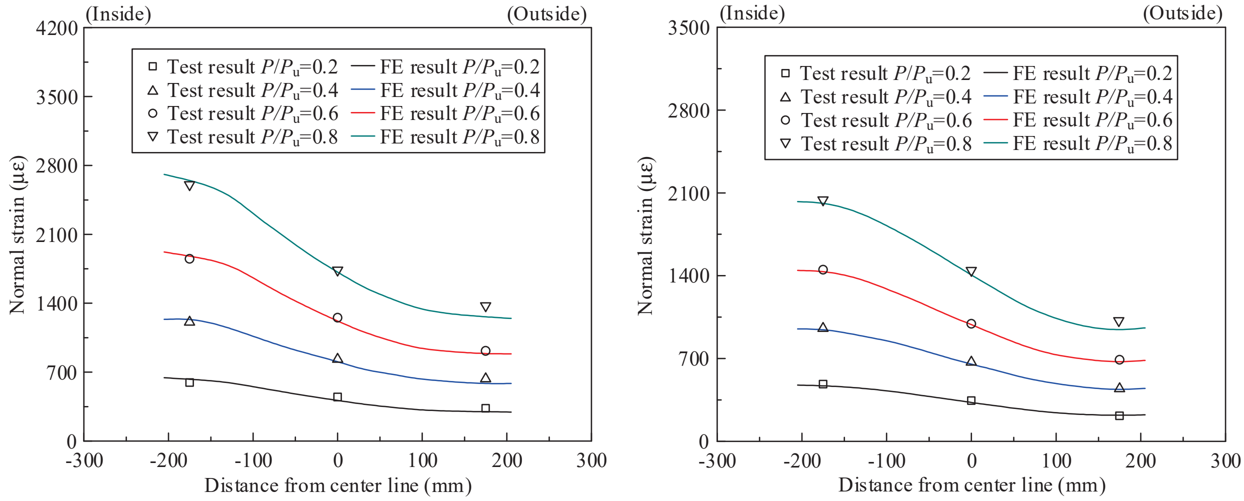

(e) Mid-span section of CCB-3 (f) 1/4-span section of CCB-3

**Figure 21.** Comparison of the normal strains of the steel bottom flanges from the test and numerical analyses.

In summary, the established fine finite element model can accurately simulate the developing trends of the force behavior of curved composite box beams during the whole loading process, which illustrates that the established fine finite element model can subsequently be used as a powerful numerical calculation tool for large-scale parameter analysis.

### *4.3. Comparison of Experimental, Numerical, and Theoretical Results*

The reference [37] gives the theoretical method to calculate the bearing capacity of composite beams. The method does not distinguish the cases of strong and weak shear connection at the interface. Table 6 gives the comparison among the bearing capacities of the three specimens obtained from the experimental, the numerical, and the theoretical results. It can be seen that there are good agreements among the results obtained from the test, the FEM, and the theoretical method.

**Table 6.** Bearing capacities obtained from experimental, numerical, and theoretical results (unit: kN).

| | **CCB-1** | **CCB-2** | **CCB-3** |
|---|---|---|---|
| Experimental | 582 | 648 | 571 |
| Numerical | 574 | 638 | 564 |
| Theoretical | 570 | 630 | 570 |

## 5. Conclusion

In this paper, static loading tests of three curved composite box beams with various central angles and interface shear connection degrees were carried out, and static performance indicators such as vertical displacement, rotational angle, interface slip, and strain of the critical sections were measured. In addition, three-dimensional elaborate finite element models were developed to simulate the test results. Based on the comparison between the finite element models and test results, the following three conclusions can be drawn:

(1) The ultimate bearing capacity and initial stiffness of the curved composite box beam specimens with large central angles were slightly lower than those with small central angles, but within the range of 25° to 45°; the central angle had a limited influence on the ultimate capacity and initial stiffness. Specifically, the ultimate bearing capacity of CCB-2 was 11.4% higher than that of CCB-1 and the ultimate bearing capacity of CCB-1 was 1.9% higher than that of CCB-3. The interface slip of the weak shear connection degree specimen was notably greater than that of the strong shear connection degree specimen. The ultimate interface slip of CCB-1 was twice more than that of CCB-3. The test results showed that the shear connection degree had a significant influence on the interface slip behavior and that the influence of the shear connection degree on the ultimate capacity and initial stiffness was weaker than that on the slip behavior.

(2) The positive strain of the top flange plate and the steel bottom plate of the curved composite box beam specimens was nonuniform along the transverse direction, and the inner side strain of the specimen was generally greater than the outer side strain under the combined effect of constrained torsion and distortion.

(3) The developed fine finite element model simulated well the deformation characteristics and macrocurves of the three curved composite box beam specimens under a positive moment, as well as the normal strain distributions and trends of the concrete plate, steel webs, and steel bottom plate. The constrained torsion and distortion effects of each specimen were accurately predicted; that is, the finite element model results could accurately simulate the full-process force behavior of the three curved composite box beams. This finite element model can be used as a powerful numerical tool for subsequent parameter analysis of the force behavior of curved composite box beams.

(4) The ultimate bearing capacities of the specimens obtained from the test, the numerical model, and the theoretical formula were compared. There were good agreements among the results obtained from the test, the numerical model, and the theoretical formula.

**Author Contributions:** Conceptualization: X.-J.H.; methodology: X.-J.H.; experiment: Z.-M.L.; validation: G.-M.W.; formal analysis: G.-M.W.; investigation, resources, data curation, writing: W.-Y.J. All authors have read and agreed to the published version of the manuscript.

**Funding:** This research was funded by the Technical and Development Project of Shuohuang Railway Development Co., Ltd., grant number SHTL-19-14.

**Institutional Review Board Statement:** Not applicable.

**Informed Consent Statement:** Not applicable.

**Data Availability Statement:** Not applicable.

**Conflicts of Interest:** The authors declare no conflict of interest.

## Abbreviations

| | |
|---|---|
| $\varepsilon_{\mathrm{c}}$ | Strain of concrete |
| $\varepsilon_{\mathrm{c0}}$ | Peak compressive strain of concrete |
| $\varepsilon_{\mathrm{cu}}$ | Ultimate compressive strain of concrete |
| $f_{\mathrm{c}}{}'$ | Compressive strength of concrete cylinder |
| $f_{\mathrm{cu}}$ | Compressive strength of concrete cube |
| $f_{\mathrm{ct}}$ | Tensile strength of concrete |
| $\varepsilon_{\mathrm{ct0}}$ | Cracking strain of concrete |
| $\varepsilon_{\mathrm{ctu}}$ | Ultimate tensile strain of concrete |
| $G_{\mathrm{f}}$ | Fracture energy of concrete calculated according to CEB-FIP1990 |
| $l_{\mathrm{e}}$ | Characteristic length of elements of concrete calculated according to CEB-FIP1990 |
| $\varepsilon_{\mathrm{y}}$ | Yield strain of steel |
| $\varepsilon_{\mathrm{h}}$ | Ultimate strain of steel |
| $\varepsilon_{\mathrm{su}}$ | Ultimate strain of steel |
| $f_{\mathrm{y}}$ | Yield strength of steel |
| $f_{\mathrm{u}}$ | Ultimate strength of steel |
| $\varepsilon_{\mathrm{r}}$ | Strain of rebar |
| $\sigma_{\mathrm{r}}$ | Stress of rebar |
| $\varepsilon_{\mathrm{ry}}$ | Yield strain of rebar |
| $f_{\mathrm{ry}}$ | Yield strength of rebar |
| $V_{\mathrm{u}}$ | Shear bearing capacity of a single stud |
| $\alpha_1$,$\alpha_2$ | Control parameters subjected to shear force calculated according to CEB-FIP2010 |
| $n_{\mathrm{s}}$ | Number of studs in each group |
| $A_{\mathrm{us}}$ | Area of a single stud |
| $E_{\mathrm{c}}$ | Elastic moduli of concrete |
| $E_{\mathrm{s}}$ | Elastic moduli of steel |
| $f_{\mathrm{ru}}$ | Tensile strength of stud |
| $K_{\mathrm{c}}$ | Parameter controlling the projection of yield surface onto the bias place for concrete |
| $\varphi$ | Expansive angle related to flow rule for concrete |
| $\lambda$ | Eccentricity of plastic potential function for concrete |
| $P_{\mathrm{u}}$ | Ultimate capacity of curved composite beams |

## References

1. Colville, J. Test of curved steel-concrete composite beams. *J. Struct. Div.* **1973**, *99*, 1555–1570. [CrossRef]
2. Brennan, P.J.; Mandel, J.A. Multiple configuration curved bridge model studies. *J. Struct. Div.* **1979**, *105*, 875–890. [CrossRef]
3. Jung, S. Inelastic strength behavior of horizontally curved composite I-girder bridge structural systems. Ph.D. Thesis, Georgia Institute of Technology, Atlanta, GA, USA, 2006.
4. Thevendran, V.; Shanmugam, N.E.; Chen, S.; Liew, J.Y.R. Experimental study on steel-concrete composite beams curved in plan. *Eng. Struct.* **2000**, *22*, 877–889. [CrossRef]
5. Krzmarzick, D.P.; Hajjar, J.F. *Load Rating of Composite Steel Curved I-Girder Bridges through Load Testing with Heavy Trucks*; Report MN/RC-2006-40; University of Minnesota: Minneapolis, MN, USA, 2006.
6. Tan, U.L.; Uy, B. Experimental study on curved composite beams subjected to combined flexure and torsion. *J. Constr. Steel Res.* **2009**, *65*, 1855–1863. [CrossRef]

7. Zhang, Y.L.; Ge, W.; Zhang, D.Y. Experimental research on bending-torsion characteristics of steel-concrete composite box beams. *Adv. Mater. Res.* **2012**, *594*, 785–790. [CrossRef]
8. Zhu, L.; Su, R.K.L.; Li, M.J. Finite beam element with 26 DOFs for curved composite box girders considering constrained torsion, distortion, shear lag and biaxial slip. *Eng. Struct.* **2021**, *232*, 111797. [CrossRef]
9. Zhu, L.; Wang, J.J.; Zhao, G.Y.; Huo, X.J.; Li, X. Experimental and numerical study on large-curvature curved composite box girder under hogging moment. *Steel Compos. Struct.* **2020**, *37*, 117–136.
10. El-Tawil, S.; Okeil, A.M. *Behavior and Design of Curved Composite Box Girder Bridges*; Report of Florida Department of Transportation; University of Central Florida: Orlando, FL, USA, 2002.
11. Samaan, M.; Kennedy, J.B.; Sennah, K. Impact factors for curved continuous composite multiple-box girder bridges. *J. Bridge Eng.* **2007**, *12*, 80–88. [CrossRef]
12. Samaan, M.; Sennah, K.; Kennedy, J.B. Distribution factors for curved continuous composite box-girder bridges. *J. Bridge Eng.* **2005**, *10*, 678–692. [CrossRef]
13. Sennah, K.M.; Kennedy, J.B. Load distribution factors for composite multicell box girder bridges. *J. Bridge Eng.* **1999**, *4*, 71–78. [CrossRef]
14. Sennah, K.M.; Zhang, X.; Kennedy, J.B. Impact factors for horizontally curved composite box girder bridges. *J. Bridge Eng.* **2004**, *9*, 512–520. [CrossRef]
15. Linzell, D.G.; Nadakuditi, V.P. Parameters influencing seismic response of horizontally curved, steel, I-girder bridges. *Steel Compos. Struct.* **2011**, *11*, 21–38. [CrossRef]
16. Nie, J.G.; Zhu, L. Beam-truss model of steel-concrete composite box-girder bridges. *J. Bridge Eng.* **2014**, *19*, 04014023. [CrossRef]
17. Lin, W.; Yoda, T. Numerical study on horizontally curved steel-concrete composite beams subjected to hogging moment. *Int. J. Steel Struct.* **2014**, *14*, 557–569. [CrossRef]
18. Fatemi, S.J.; Mohamed Ali, M.S.; Sheikh, A.H. Load distribution for composite steel-concrete horizontally curved box girder bridge. *J. Constr. Steel Res.* **2016**, *116*, 19–28. [CrossRef]
19. Zhu, L.; Wang, J.J.; Li, M.J.; Chen, C.; Wang, G.M. Finite beam element with 22 DOF for curved composite box girders considering torsion, distortion, and biaxial slip. *Arch. Civ. Mech. Eng.* **2020**, *20*, 101. [CrossRef]
20. Wang, G.M.; Zhu, L.; Ji, X.L.; Ji, W.Y. Finite beam element for curved steel-concrete composite box beams considering time-dependent effect. *Materials* **2020**, *13*, 3253. [CrossRef]
21. Sucharda, O.; Mateckova, P.; Bilek, V. Non-linear analysis of an RC beam without shear reinforcement with a sensitivity study of the material properties of concrete. *Slovak J. Civ. Eng.* **2020**, *28*, 33–43. [CrossRef]
22. Valikhnai, A.; Jahromi, A.J.; Mantawy, I.M.; Azizinamini, A. Numerical modelling of concrete-to-UHPC bond strength. *Materials* **2020**, *13*, 1379. [CrossRef] [PubMed]
23. China Ministry of Construction. *Code for Seismic Design of Buildings (GB 50011-2010)*; China Ministry of Construction: Beijing, China, 2010.
24. China Ministry of Construction. *Standard for Design of steel structures (GB50017-2017)*; China Ministry of Construction: Beijing, China, 2017.
25. China Ministry of Construction. *Standard for Test Methods of Long-Term Performance and Durability of Original Concrete (GB/T50082-2009)*; China Ministry of Construction: Beijing, China, 2009.
26. Nie, J.; Cai, C.S. Steel-concrete composite beams considering shear slip effects. *J. Struct. Eng.* **2003**, *129*, 495–506. [CrossRef]
27. Abaqus 6.14 Documentation. Available online: http://130.149.89.49:2080/v6.14/index.html (accessed on 28 May 2021).
28. Wang, Y.H.; Nie, J.G.; Cai, C.S. Numerical modeling on concrete structures and steel-concrete composite frame structures. *Compos. Part. B* **2013**, *51*, 58–67. [CrossRef]
29. Hognestad, E.; Hanson, N.W.; McHenry, D. Concrete stress distribution in ultimate strength design. *ACI J. Proc.* **1955**, *52*, 455–480.
30. Li, C.Q.; Li, K.F.; Chen, Z.Y. Numerical analysis of moisture influential depth in concrete and its application in durability design. *Tsinghua Sci. Technol.* **2008**, *13*, 7–12. [CrossRef]
31. Guo, Z.H. *Principles of Reinforced Concrete*; Butterworth-Heinemann: London, UK, 2014.
32. CEB-FIP (Comité Euro-International du Béton-Fédération International de la Précontrainte). *CEB-FIP Mode Code 1990: Design Code*; Thomas Telford: London, UK, 1993.
33. Bazant, Z.; Oh, B. Crack band theory for fracture of concrete. *Mater. Struct.* **1983**, *16*, 155–177.
34. Newman, J.C.; Loss, F.J. *Elastic-Plastic Fracture Mechanics Technology*; American Society for Testing and Materials: Philadelphia, PA, USA, 1986.
35. Han, L.H.; Yao, G.H.; Zhao, X.L. Tests and calculations for hollow structural steel (HSS) stub columns filled with self-consolidating concrete (SCC). *J. Constr. Steel Res.* **2005**, *61*, 1241–1269. [CrossRef]
36. CEB-FIP (Comité Euro-International du Béton-Fédération International de la Précontrainte). *CEB-FIP Model Code 2010, Design Code*; Thomas Telford: London, UK, 2010.
37. Johnson, R.P. *Composite structures of steel and concrete: Beams, slabs, columns and frames for buildings*; John Wiley & Sons, Inc.: Hoboken, NJ, USA, 2008.

materials

MDPI

*Article*

# Free Vibration Analysis of a Graphene-Reinforced Porous Composite Plate with Different Boundary Conditions

**Hong-Gang Pan [1], Yun-Shi Wu [1], Jian-Nan Zhou [2], Yan-Ming Fu [3,*], Xin Liang [1] and Tian-Yu Zhao [4,*]**

[1] Shenyang Institute of Engineering, School of Energy and Power, Shenyang 110136, China; phg666@163.com (H.-G.P.); Wuys0621@163.com (Y.-S.W.); lx18340158686@163.com (X.L.)
[2] Technology Center of Shenyang Customs, Shenyang 110016, China; tank261014@163.com
[3] Laboratory Management Center, Shenyang Sport University, Shenyang 110102, China
[4] School of Science, Northeastern University, Shenyang 110819, China
* Correspondence: fuym@syty.edu.cn (Y.-M.F.); zhaotianyu@mail.neu.edu.cn (T.-Y.Z.)

**Abstract:** Plates are commonly used in many engineering disciplines, including aerospace. With the continuous improvement in the capacity of high value-added airplanes, large transport aircrafts, and fighter planes that have high strength, high toughness, and corrosion resistance have gradually become the development direction of airplane plate structure production and research. The strength and stability of metal plate structures can be improved by adding reinforced materials. This paper studies graphene platelets (GPLs) reinforced with a free vibration porous composite plate. The porous plate is constructed with a multi-layer model in a metal matrix containing uniform or non-uniformly distributed open-cell internal pores. Considering the random and directional arrangement of graphene platelets in the matrix, the elastic modulus of graphene composites was estimated using the Halpin–Tsai micromechanical model, and the vibration frequencies of graphene composite were calculated using the differential quadrature method. The effects of the total number of layers, GPL distribution pattern, porosity coefficient, GPL weight fraction, and boundary conditions on the free vibration frequency of GPLs reinforced porous composite plates are studied, and the accuracy of the conclusions are verified by the finite element software.

**Keywords:** graphene platelets; free vibration frequency; porosity; boundary conditions

## 1. Introduction

Graphene is a material with one of the highest known strengths. The theoretical Young's modulus of graphene is up to 1.0 TPa and it has an inherent tensile strength of 130 GPa. The morphology of graphene is similar to the lamellar structure of thin paper and the thickness of a single layer is only 0.335 nm. It is the thinnest two-dimensional material presently known. Furthermore, it has good toughness, reproducibility, high dispersibility, and good chemical and biocompatibility [1]; thus, it has become an ideal reinforcement for composite materials. Additionally, a composite plate is made from a metal matrix plate, as a continuous phase, and has a sized graphene modifier as a dispersed phase. The modifier is dispersed in the matrix material through appropriate preparation methods in order to form a composite system that contains sized materials. Graphene reinforced porous composite plates have a lighter weight, higher stiffness, higher strength, and multi-functional properties that can meet the lightweight requirements of the aerospace field and inject new vitality into the development of aerospace materials.

Scholars have been paying more and more attention to the study of free vibration graphene reinforced porous composite plates. Rahman et al. [2] used molecular mechanics and molecular dynamic simulations to study graphene epoxy resin-based composites. The results showed that adding graphene platelet (GPL) to the epoxy resin matrix could significantly improve the Young's modulus and shear modulus of the matrix materials. King et al. [3] found that carbon-filled epoxy composites have high specific stiffness, which can be used for the structural components of fixed-wing aircrafts. Feng et al. [4] studied the vibration analysis of multi-layer graphene sheets using a continuum model. This paper confirms the use of the GNP aspect ratio and the two-dimensional randomly oriented filler Halpin–Tsai model, adjusted for platelet filler shapes, to predict the tensile modulus well for the GNP/epoxy composites, which provides a basic theory for our subsequent research. Alibeigloo [5] used non-local continuum mechanics to conduct a three-dimensional vibration analysis of multi-layer graphene platelets embedded in a polymer matrix. The numerical results show that the bending properties can be significantly improved by adding a small amount of GPLs into the polymer matrix. Yang et al. [6] studied the nonlinear bending and buckling behavior of graphene reinforced nanocomposite beams, based on the Timoshenko beam theory, and the results showed that composite beams doped with graphene platelets could exhibit better mechanical properties. Eringen [7–9], by the use of nonlocal thermodynamics and invariance under rigid motions, obtained constitutive equations for the nonlinear micromorphic elastic solids and differential equations of nonlocal elasticity and solutions for screw dislocation and surface waves. Polit et al. [10] analyzed the bending and elastic stability of thick beams with a hole based on the high-order shear deformation theory of the transverse tensile effect. The formula in this paper provides an important reference for the writing of this paper. Rafiee et al. [11] experimentally found that GPLs has the distinct advantage of reinforcing nanofillers over carbon nanotubes at a very low content, which has also been theoretically confirmed [12–15]. Zhao et al. [16] studied the rubbing of the mistuned bladed disk system with blades of variable thicknesses, and elastically supported shaft-variable thickness blades coupled with the finite element model was established. Sharma et al. [17,18] studied the reduction of sound pressure at the receiver location with a lumped mass at the optimal location, which was shown to be much more than what is achievable by a uniform distribution of the point mass over the plate. A novel concept of the local mitigation of the transmitted noise at a target receiver location is presented by controlling the directivity of the transmitted noise through a point mass attachment on the barrier surface. Zhao et al. [19–21] findings shed an important light on the design of the novel graphene reinforced blade-shaft system and remarkably improved its dynamic performance. Sharma et al. [22] studied the effect of uncertainties in material and geometric parameters on the acoustic performance of a viscoelastic coating. Zhao et al. [23–25] investigated the free vibration behaviors of a functionally graded (FG) disk-shaft rotor system, which was reinforced with a graphene nanoplatelet (GPL) that rested on elastic supports. Shafiei et al. [26] studied the size-dependent nonlinear vibration behavior of FG porous microbeams using the improved coupling of the stress and Euler–Bernoulli theory, and evaluated the effects of uniform and non-uniform porosity. Sharma et al. [27] studied the effect of strong and weak coupling of void resonances on the transmission characteristics and drew the conclusion that strong coupling of the resonance of voids results in broadband attenuation of sound. Davletshin et al. [28] found that an interlayer distance change leads to significant band gap size modulations and direct–indirect band gap transitions in the phosphorene–BN heterostructure. Babicheva et al. [29] found that a less dense structure may actually be stronger due to the fact that all the interatomic bonds in it are loaded more uniformly. Savin et al. [30] found that the thermal conductivity coefficient of the nanoribbon increases monotonically up to 10%, with an increasing twist angle; the regime of uniform twisting and twist deformation of nanoribbons can improve their mechanical and physical properties. Savin et al. [31] revealed that layered materials can support surface ripplocations that are highly mobile, topologically solitary waves that efficiently transport mass and energy. Chen et al. [32] conducted a numerical study on the crushing process of an FG porous structure, and pointed out that, under high-speed impact, a certain type of non-uniform asymmetric pore can significantly promote the energy absorption of foam metal. The above research results are very important and provide the basis for subsequent research. Before the porous composites can be applied to engineering applications, a large amount of corresponding research work is still needed in order to reveal the structural properties of porous composites.

In this paper, graphene platelets were mixed into copper-based, porous square plates to enhance the material properties of square copper-based plates. The study on the combination of a porous structure and graphene reinforced composites will better improve the performance of the copper substrate, and provide a reference for the preparation of a high performance graphene copper matrix composite material that is light weight, has a high modulus and high strength in the future. The Young's modulus and shear modulus of the porous graphene composite plate were calculated using the Halpin–Tsai micromechanical model, and the vibration equation of the plate was established. The free vibration frequencies under four boundary conditions were solved by the calculation. The effects of porous distribution, the distribution mode, content and geometric size of the free vibration frequency of the porous graphene composite plate were analyzed.

## 2. Material Properties Calculation and Model Establishment

The three pore distributions in the porous plate include two non-uniform symmetric pore distributions and one uniform pore distribution, as shown in Figure 1. The maximum pore size of the non-uniform distribution mode A is distributed on the middle plane, and the maximum pore size of the non-uniform distribution mode B is distributed on the top and bottom surfaces, which correspond to the changes in material properties and to Equations (1) and (2). The material properties of uniformly distributed pores correspond Equation (3). Meanwhile, the three distribution modes (X, O, and U) of the GPL dispersion pattern are shown in Figure 2.

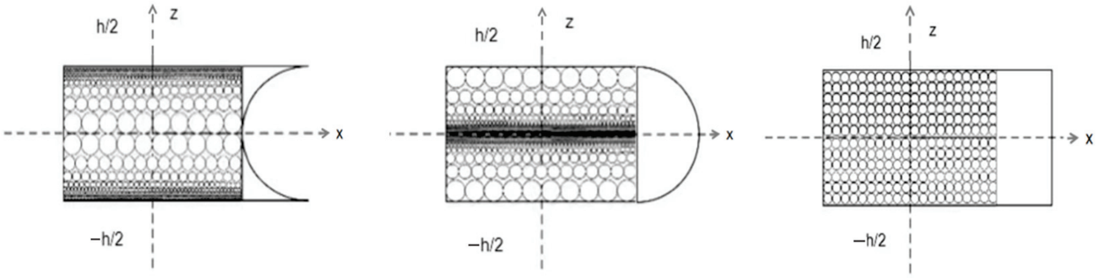

(**a**) Porosity distribution A (**b**) Porosity distribution B (**c**) Uniform porosity distribution

**Figure 1.** Three types of porosity distributions.

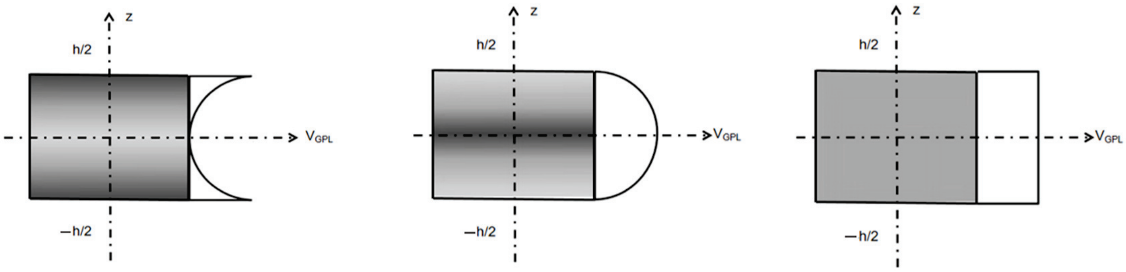

(**a**) GPL pattern X (**b**) GPL pattern O (**c**) GPL pattern U

**Figure 2.** Three types of GPL dispersion pattern.

Non-uniform porosity distribution A:

$$\begin{aligned} E(z) &= E^*[1 - e_0 \cos(\pi z/h)] \\ G(z) &= G^*[1 - e_0 \cos(\pi z/h)] \\ \rho(z) &= \rho^*[1 - e_m \cos(\pi z/h)] \end{aligned} \tag{1}$$

Non-uniform porosity distribution B:

$$\begin{aligned} E(z) &= E^*[1 - e_0^*(1 - \cos(\pi z/h))] \\ G(z) &= G^*[1 - e_0^*(1 - \cos(\pi z/h))] \\ \rho(z) &= \rho^*[1 - e_m^*(1 - \cos(\pi z/h))] \end{aligned} \tag{2}$$

Uniform porosity distribution:

$$\begin{aligned} E(z) &= E^*\alpha \\ G(z) &= G^*\alpha \\ \rho(z) &= \rho^*\alpha' \end{aligned} \tag{3}$$

where $\rho(z)$, $G(z)$, and $E(z)$ are the mass density, shear modulus, and Young's modulus of the porous composite plates, $\rho^*$, $G^*$, and $E^*$ are the corresponding properties of the GPLs reinforced porous composite plates without internal pores, $e_0$ and $e_0^*$ ($0 \le e_0(e_0^*) < 1$) in $G(z)$ and $E(z)$ are the porosity coefficients for distributions A and B, $e_m$ and $e_m^*$ in $\rho(z)$ are the corresponding coefficients of the mass densities, and $\alpha$ and $\alpha'$ are the parameters for the uniform porosity.

Based on Halpin–Tsai micromechanical model [33], the Young 's modulus $E^*$ of graphene nonporous composites was determined:

$$E^* = \frac{3}{8}\left(\frac{1 + \xi_L^{GPL}\eta_L^{GPL}V_{GPL}}{1 - \eta_L^{GPL}V_{GPL}}\right)E_\mathrm{m} + \frac{5}{8}\left(\frac{1 + \xi_\mathrm{W}^{\mathrm{GPL}}\eta_W^{GPL}V_{GPL}}{1 - \eta_W^{GPL}V_{GPL}}\right)E_\mathrm{m} \tag{4}$$

In which:

$$\begin{aligned} \xi_L^{GPL} &= \tfrac{2L_\mathrm{GPL}}{T_{GPL}} \\ \xi_W^{GPL} &= \tfrac{2W_{GPL}}{T_{GPL}} \\ \eta_L^{GPL} &= \tfrac{E_{GPL} - E_m}{E_{GPL} + \xi_L^{GPL}E_m} \\ \eta_W^{GPL} &= \tfrac{E_{GPL} - E_m}{E_{GPL} + \xi_W^{GPL}E_m} \end{aligned}$$

where $E_{GPL}$ and $E_m$ are the Young' s modulus of graphene and the metal matrix in the composites. The metal matrix material used in this paper was copper, $L_{GPL}$, $W_{GPL}$ and $T_{GPL}$ are the length, width, and thicknesses of the graphene platelets, and $V_{GPL}$ is the volume content of graphene. The density and Poisson's ratio of the composites were obtained according to the extended rule of the mixture [34]:

$$\begin{aligned} \rho^* &= \rho_{GPL}V_{GPL} + \rho_m(1 - V_{GPL}) \\ v^* &= v_{GPL}V_{GPL} + v_m(1 - V_{GPL}) \end{aligned} \tag{5}$$

where $\rho^*$ and $v^*$ are the mass density and Poisson s ratio of GPLs, and $\rho_m$ and $v_m$ are the corresponding parameters of the metal matrix. The Poisson's ratio for open metal foams was fixed. The shear modulus $G^*$ of the composite plate was:

$$G^* = \frac{E^*}{2(1 + v^*)} \tag{6}$$

The typical mechanical properties of open-cell metal foams, shown in Equation (7), were employed to establish the relationships, in Equation (8), between the mass density coefficients and the porosity coefficients for different porosity distributions.

$$\frac{E(z)}{E^*} = \left(\frac{\rho(z)}{\rho^*}\right)^2 \tag{7}$$

$$
\begin{aligned}
&1 - e_m \cos(\pi z/h) = \sqrt{1 - e_0 \cos(\pi z/h)} \\
&1 - e_m^*(1 - \cos(\pi z/h)) = \sqrt{1 - \cos(\pi z/h)} \\
&\alpha' = \sqrt{\alpha}
\end{aligned}
\tag{8}
$$

The mass and graphene distribution of porous composite plates with different porosity were considered to be equivalent. The formula is as follows:

$$
\begin{aligned}
&\int_0^{h/2} \sqrt{1 - e_0^*(1 - \cos(\pi z/h))}dz = \int_0^{h/2} \sqrt{1 - e_0 \cos(\pi z/h)}dz \\
&\int_0^{h/2} \sqrt{\alpha}dz = \int_0^{h/2} \sqrt{1 - e_0 \cos(\pi z/h)}dz
\end{aligned}
\tag{9}
$$

Formula (9) can determine $e_0^*$ and $\alpha$ by giving the value of $e_0$ [35], as shown in Table 1.

**Table 1.** Porosity coefficients for different distributions.

| $e_0$ | $e_0^*$ | $\alpha$ |
|---|---|---|
| 0.1 | 0.1738 | 0.9361 |
| 0.2 | 0.3442 | 0.8716 |
| 0.3 | 0.5103 | 0.8064 |
| 0.4 | 0.6708 | 0.7404 |
| 0.5 | 0.8231 | 0.6733 |
| 0.6 | 0.9612 | 0.6047 |

The 3D model of the multilayer thin plate (length a = 1 m, width b = 1 m, thickness h = 0.02 m) was established and defined in the Cartesian coordinate system (x, y, z), as shown in Figure 3. Each layer had the same thickness, and the internal pores and graphene were evenly distributed. Based on the following convergence analysis, the optimal total number of layers (n) was discussed and determined.

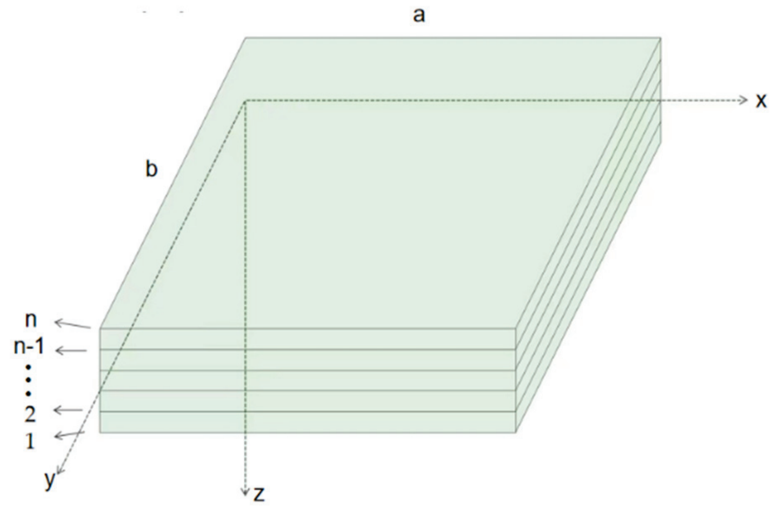

**Figure 3.** Configuration of a multi-layer plate model.

For different distribution patterns, the volume content $V_{GPL}$ was the graphene changes along the thickness direction.

$$
V_{GPL}(z) = \begin{cases} s_{i1}[1 - \cos(\pi z/h)] & GPL pattern X \\ s_{i2}\cos(\pi z/h) & GPL pattern O \\ s_{i3} & GPL pattern U \end{cases}
\tag{10}
$$

where $s_{i1}$, $s_{i2,}$ and $s_{\mathrm{i}3}$ are the maximum values of the volume content, and $i$ = 1, 2, 3 corresponding to the porosity distributions A and B and the uniform distribution. The total GPL volume content $V_{GPL}^{T}$ was calculated from the weight fraction $\wedge_{GPL}$ in Equation (11), and was then used to determine $s_{i1}$, $s_{i2}$ and $s_{i3}$ in Equation (12), with the aid of the multi-layer plate model.

$$V_{GPL}^{T} = \frac{\Lambda_{GPL}\rho_m}{\Lambda_{GPL}\rho_m + \rho_{GPL} - \Lambda_{GPL}\rho_{GPL}} \tag{11}$$

$$V_{GPL}^{T}\sum_{j=1}^{n}\frac{\rho(z_j)}{\rho^*} = \begin{cases} s_{i1}\sum_{j=1}^{n}\left\{[1-\cos(\pi z_j/h)]\frac{\rho(z_j)}{\rho^*}\right\} \\ s_{i2}\sum_{j=1}^{n}\left\{\cos(\pi z_j/h)]\frac{\rho(z_j)}{\rho^*}\right\} \\ s_{i3}\sum_{j=1}^{n}\frac{\rho(z_j)}{\rho^*} \end{cases} \tag{12}$$

In which: $z_j = \left(\frac{1}{2} + \frac{1}{2n} - \frac{j}{n}\right)h, j = 1, 2, 3, \ldots, n.$

## 3. Differential Equation of Thin Plate Vibration

The thin plate was an ideal mechanical model that satisfied certain assumptions. Generally, a certain actual problem is simplified on a thin plate model according to its actual size and force characteristics. For example, a thin plate model can be used for a structure with a thickness smaller than its length and width. According to the coordinate system in Figure 3, the relationship between stress, strain, and displacement is established. Set the position of any point a on the board and determine its coordinates x, y, and z before deformation. According to the classical theory of thin plates, the expression of the displacement components of any point a (x, y, and z) along the three directions can be obtained as:

$$\begin{aligned} u_a &= -z\frac{\partial w}{\partial x} \\ \nu_a &= -z\frac{\partial w}{\partial y} \\ w_a &= w \end{aligned} \tag{13}$$

According to the geometric relationship between strain and displacement, the three main strain components at each point can be calculated as:

$$\begin{aligned} \varepsilon_x &= \frac{\partial u_a}{\partial x} = -z\frac{\partial^2 w}{\partial x^2} \\ \varepsilon_y &= \frac{\partial \nu_a}{\partial y} = -z\frac{\partial^2 w}{\partial y^2} \\ \gamma_{xy} &= \frac{\partial u_a}{\partial y} + \frac{\partial \nu_a}{\partial x} = -2z\frac{\partial^2 w}{\partial x \partial y} \end{aligned} \tag{14}$$

Use Hooke's law to obtain the corresponding three main stress components as:

$$\begin{aligned} \sigma_x &= \frac{E}{1-\mu^2}(\varepsilon_x + \mu\varepsilon_y) = -\frac{Ez}{1-\mu^2}\left(\frac{\partial^2 w}{\partial x^2} + \mu\frac{\partial^2 w}{\partial y^2}\right) \\ \sigma_y &= \frac{E}{1-\mu^2}(\varepsilon_y + \mu\varepsilon_x) = \frac{Ez}{1-\mu^2}\left(\frac{\partial^2 w}{\partial y^2} + \mu\frac{\partial^2 w}{\partial x^2}\right) \\ \tau_{xy} &= G\gamma_{xy} = -\frac{Ez}{1+\mu}\frac{\partial^2 w}{\partial x \partial y} \end{aligned} \tag{15}$$

According to $\Sigma F_z = 0$, $\Sigma M_x = 0$, and $\Sigma M_y = 0$, in which $\Sigma F_z$ is the resultant force in the z direction and $\Sigma M_x$ and $\Sigma M_y$ are the resulting moments in the x and y direction.

$$\begin{gathered} Q_x dy + \tfrac{\partial Q_y}{\partial x} dydx - Q_x dy + Q_y dx + \tfrac{\partial Q_x}{\partial y} dxdy - Q_y dx \\ +P(x,y)f(t)dydx - \rho h \tfrac{\partial^2 w}{\partial t^2} dydx = 0 \\ (M_x dy + \tfrac{\partial M_x}{\partial x} dxdy) - M_x dy + (M_{yx} dx + \tfrac{\partial M_{yx}}{\partial y} dxdy) - M_{yx} dx \\ -(Q_x dy + \tfrac{\partial Q_x}{\partial x} dxdy) \cdot \tfrac{1}{2} dx - Q_x dy \cdot \tfrac{1}{2} dx = 0 \\ M_y dx - (M_y dx + \tfrac{\partial M_y}{\partial y} dydx) + \tfrac{1}{2} Q dxdy (Q_y dx + \tfrac{\partial Q_Y}{\partial y} dydx) \\ -M_{xy} dy - (M_{xy} dy + \tfrac{\partial M_{xy}}{\partial x} dxdy) = 0 \end{gathered} \tag{16}$$

$Q_x$ and $Q_y$ are the shear stresses in the x and y direction, *P* (x, y, t) =*P* (x, y) *f* (t) is the external load degree set along the z axis with a variable separation form. Reorganize the above formula in order to obtain the differential equation of the lateral free vibration of the rectangular plate:

$$D[\frac{\partial^4 w}{\partial x^4} + 2\frac{\partial^4 w}{\partial x^2 \partial y^2} + \frac{\partial^4 w}{\partial y^4}] + \rho h \frac{\partial^2 w}{\partial t^2} = 0 \tag{17}$$

*D* is the bending stiffness of the thin plate. The form of the solution is that the time variable and the coordinate variable can be separated:

$$w(x,y,t) = W(x,y)\cos\omega t \tag{18}$$

*w* (*x*, *y*, and *t*) is the transverse displacement, and the following can be obtained:

$$\nabla^4 W - k^4 W = 0 \tag{19}$$

where: $k^4 = \frac{\rho h}{D}\omega^2$.

The boundary conditions studied in this paper include fixed-supported edge and simply-supported edge, and their forms are:

$$w = 0, M_n = 0 \text{ Simple-support edge is represented by S} \tag{20}$$

$$w = 0, \frac{\partial w}{\partial n} = 0 \text{ The fixed edge is represented by C} \tag{21}$$

## 4. Finite Element Analysis

The free vibration frequency of the porous composite plates can be calculated using the above formula. The MATLAB 2018 software and ANSYS 19.0 software were used for analysis in this study. MATLAB integrates many powerful functions, such as numerical analysis, matrix calculation, scientific data visualization, and modeling and simulating nonlinear dynamic systems into an easy-to-use window environment. MATLAB contains a large set of computing algorithms. It has more than 600 mathematical operation functions used in engineering, which can easily realize the various calculation functions required by users. The algorithms used in the function are the latest research results in scientific research and engineering calculations and have been optimized and made fault tolerant. MATLAB programming of the formula in the third section into the software can make the calculation results more accurate and efficient. ANSYS software is a large general finite element analysis software that uses the mathematical approximation method to simulate the real physical system (geometry and load conditions), and the analysis results of ANSYS simulation software are more suitable for engineering practice. The ANSYS and MATLAB calculation method is different but can calculate the free vibration frequency and vibration pattern. The ANSYS software was used to analyze the vibration frequency and vibration pattern of the composite plate. The results from the MATLAB software and ANSYS software under the same conditions were compared. If the error was less than 5%, it indicated that the calculation of the graphene reinforced porous composite plate in this paper was correct, and the influence of other factors on the vibration frequency of the plate can be further discussed. Because the boundary conditions of plates in this paper only consider the clamped and simply-supported edges, we choose four classical boundary conditions: SSSS, SSCC, SCCC, and CCCC. From the results of these four boundary conditions, we can find the influence of boundary conditions on plate vibration frequency. The following data are the first four-order analysis results and graphical comparisons of MATLAB and ANSYS with the boundary conditions: SSSS, SSCC, SCCC, CCCC, Porosity distribution A, and GPL pattern X. Observation Table 2 shows that, under different boundary conditions of the porous composite plate, the difference between the four-order free vibration frequencies calculated by MATLAB and ANSYS was below 5%, which verified the accuracy of the calculated results. The ANSYS and MATLAB results of the first four vibration modes of the graphene-reinforced porous composite plate with the boundary conditions of SSSS, Porosity distribution A, and GPL pattern X are shown in the following figure.

**Table 2.** Comparison of free vibration frequency $\omega$ (rad/s) results between MATLAB and ANSYS.

| Boundary Conditions | Order | MATLAB Calculation Results | ANSYS Analysis Results |
|---|---|---|---|
| SSSS | 1 | 102.35 | 102.22 |
| | 2 | 255.87 | 255.77 |
| | 3 | 255.87 | 255.77 |
| | 4 | 409.40 | 406.96 |
| SSCC | 1 | 139.31 | 140.92 |
| | 2 | 313.95 | 314.80 |
| | 3 | 313.95 | 316.02 |
| | 4 | 480.47 | 480.43 |
| SCCC | 1 | 163.01 | 166.27 |
| | 2 | 326.93 | 329.72 |
| | 3 | 367.50 | 370.15 |
| | 4 | 520.77 | 522.59 |
| CCCC | 1 | 182.06 | 188.34 |
| | 2 | 377.99 | 382.58 |
| | 3 | 377.99 | 382.58 |
| | 4 | 557.23 | 561.92 |

It can be seen from Figure 4; Figure 5 that the first four orders are similar, and the finite element analysis verifies the accuracy of the calculation steps above. Next, the calculation results from MATLAB are directly applied to discuss the influence of the total number of layers, porous distribution mode, graphene platelets distribution, and graphene platelets' geometric size on the vibration frequency of the porous composite plate.

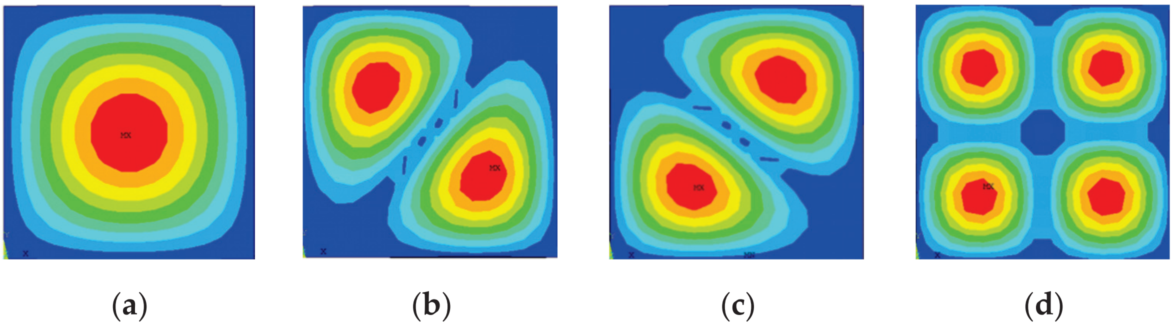

**Figure 4.** The first four-order vibration mode of ANSYS. (**a**) First order vibration mode, (**b**) Second order vibration mode, (**c**) third order vibration mode, and (**d**) fourth order vibration mode.

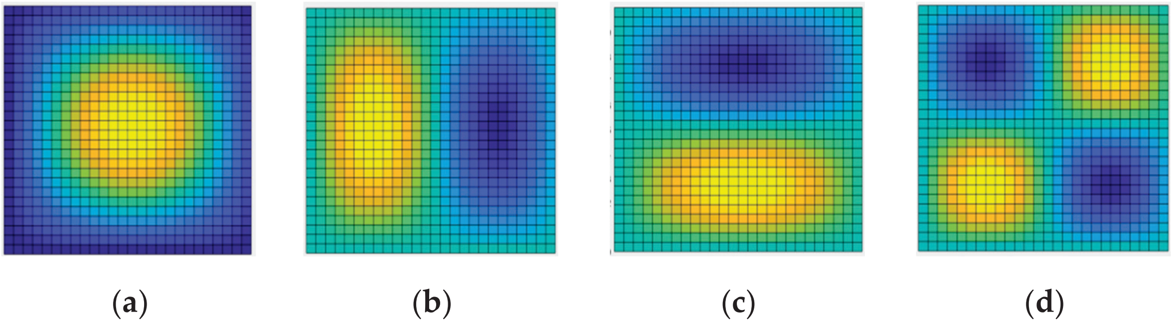

**Figure 5.** The first four-order vibration of MATLAB. (**a**) First order vibration mode, (**b**) second order vibration mode, (**c**) third order vibration mode, and (**d**) fourth order vibration mode.

## 5. Calculation and Discussion

### 5.1. Analysis of Stratified Convergence of GPL Reinforced Porous Composite Plate and the Influence of Boundary Conditions

The free vibration frequency of the composite plate with different layers and different boundary conditions when the porous distribution, with a porosity distribution A, is calculated, and the results are shown in Table 3.

**Table 3.** The free frequencies ω (rad/s) of GPL reinforced porous composite plates—effect of total layer number and the boundary condition.

| Boundary Conditions\Number of Layers | 2 | 4 | 6 | 8 | 10 | 12 | 100 |
|---|---|---|---|---|---|---|---|
| SSSS | 107.83 | 103.37 | 102.72 | 102.50 | 102.40 | 102.35 | 102.23 |
| SSCC | 146.77 | 140.70 | 139.81 | 139.52 | 139.38 | 139.31 | 139.15 |
| SCCC | 171.74 | 164.64 | 163.60 | 163.25 | 163.09 | 163.01 | 162.82 |
| CCCC | 191.81 | 183.88 | 182.72 | 182.33 | 182.16 | 182.06 | 181.85 |

By observing the influence of the total number of layers in Table 3 on the free vibration frequency of GPL reinforced porous composite plates, the optimal value can be determined, which is very important in ensuring excellent simulation accuracy and economical manufacturing efficiency at the same time. The results show that the free vibration frequency converged monotonously, with an increase in the total number of layers, and the difference was between $n = 12$ and $n = 100$, which was less than 5.0%. Therefore, $n = 12$ was used in the calculation below. When the boundary condition was CCCC, the vibration frequency of the composite plate was the largest. When the boundary condition was SSSS, the vibration frequency of the composite plate was the smallest. With the increase in the fixed edge (C), the vibration frequency of composite plate increased gradually.

### 5.2. Effect of Porosity Coefficient on Free Vibration Frequency of GPL Reinforced Porous Composite Plate

Calculate the influence of different porosity coefficients on the first four-order free vibration frequencies of the porous composite plates when there is a porosity distribution A and the GPL pattern X. Draw the result into a graph for a clearer expression, as shown in Figure 6. Specific data are shown in Table A1 of Appendix A.

It can be seen in Figure 6 that, with the increase in the porosity coefficient, the frequency of porous composite plates decreased. The increase in the internal porosity coefficient will reduce the stiffness of the porous composite plate.

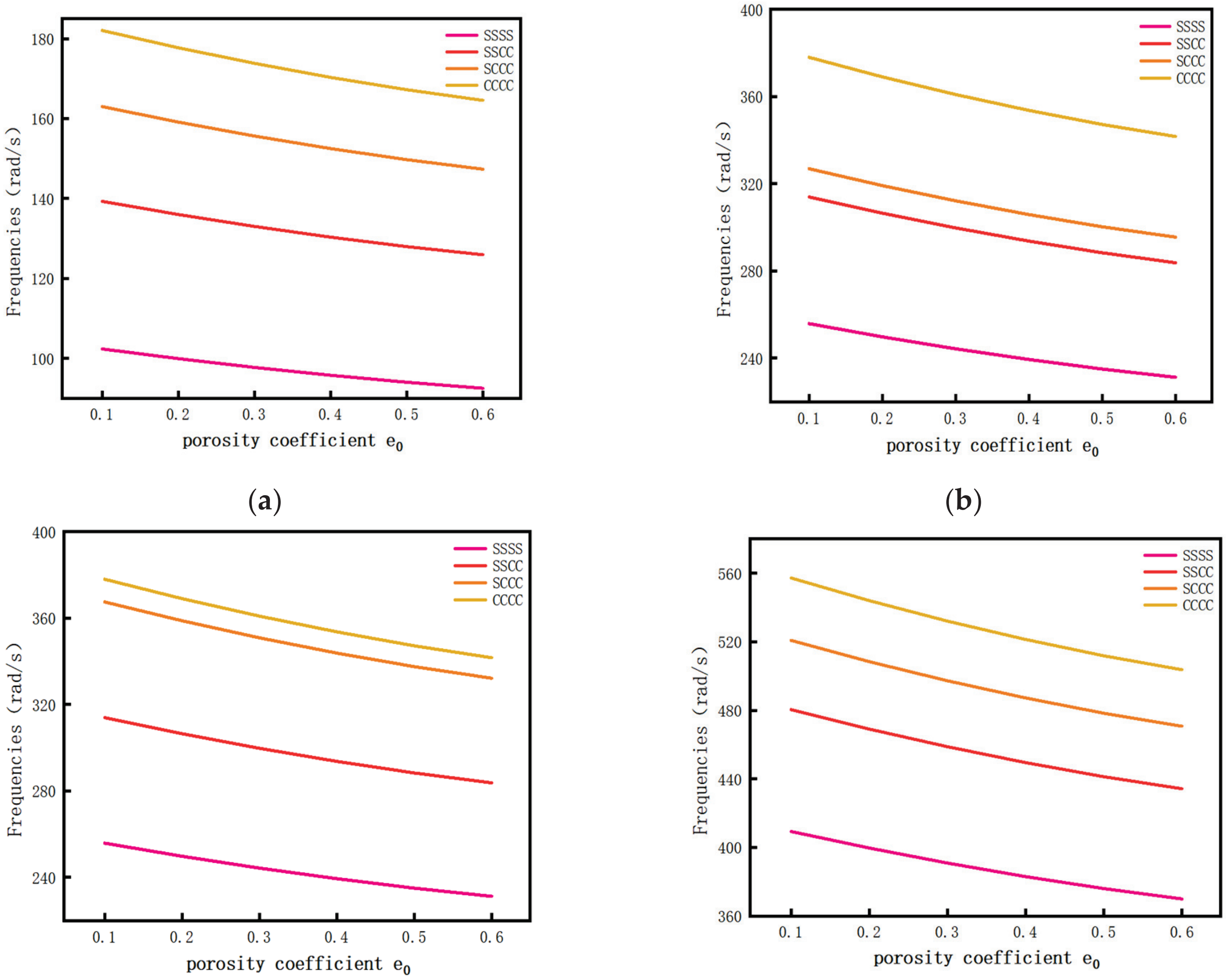

(**a**) (**b**)

(**c**) (**d**)

**Figure 6.** The relationship curve between the porosity coefficient and free vibration frequency. (**a**) First order vibration mode, (**b**) second order vibration mode, (**c**) third order vibration mode, and (**d**) fourth order vibration mode.

### *5.3. Effect of GPL Weight Fraction on Free Vibration Frequency of GPL Reinforced Porous Composite Plate*

Calculate the influence of different GPL weight fractions on the first four-order free vibration frequencies of the porous composite plates when there is a porosity distribution A and the GPL pattern X. A drawn curve is shown in Figure 7. Specific data are shown in Table A2 of Appendix A.

It can be seen from Figure 7 that the frequency of the porous composite plate increases with the increase in the GPL weight fraction under other conditions unchanged. Moreover, it can be seen that a small graphene content has a great influence on the vibration frequency of the porous composite plate.

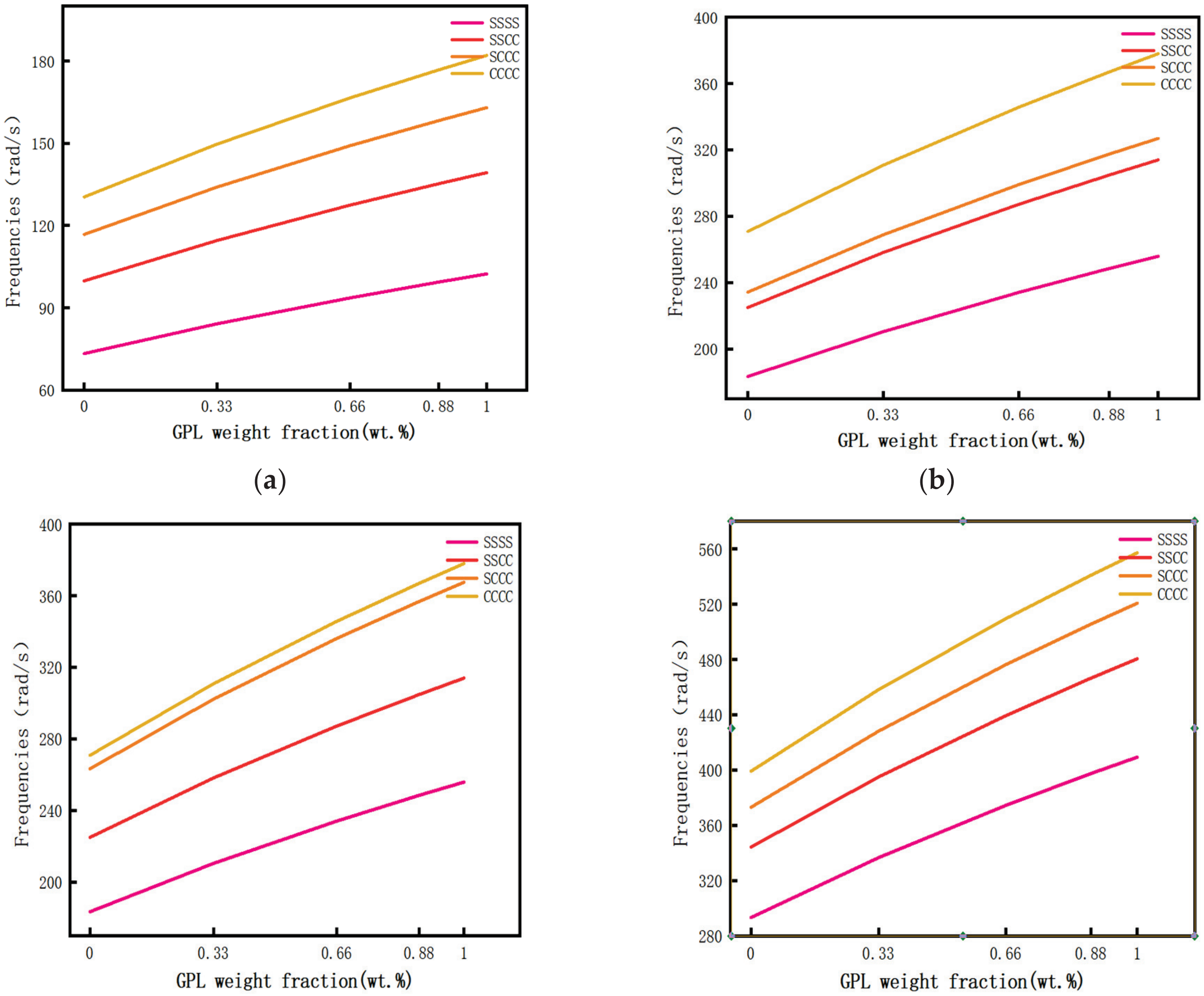

(**a**) (**b**)

(**c**) (**d**)

**Figure 7.** The relationship curve between GPL weight fraction and free vibration frequency. (**a**) First order vibration mode, (**b**) second order vibration mode, (**c**) third order vibration mode, and (**d**) fourth order vibration mode.

### *5.4. Effect of GPL Shape on Free Vibration Frequency of GPL Reinforced Porous Composite Plate*

Calculate the influence of different $L_{GPL}/T_{GPL}$ ratios on the first four-order free vibration frequency of the porous composite plate when there is a porosity distribution A and the GPL pattern X. A drawn curve is shown in Figure 8. Specific data are shown in Table A3 of Appendix A.

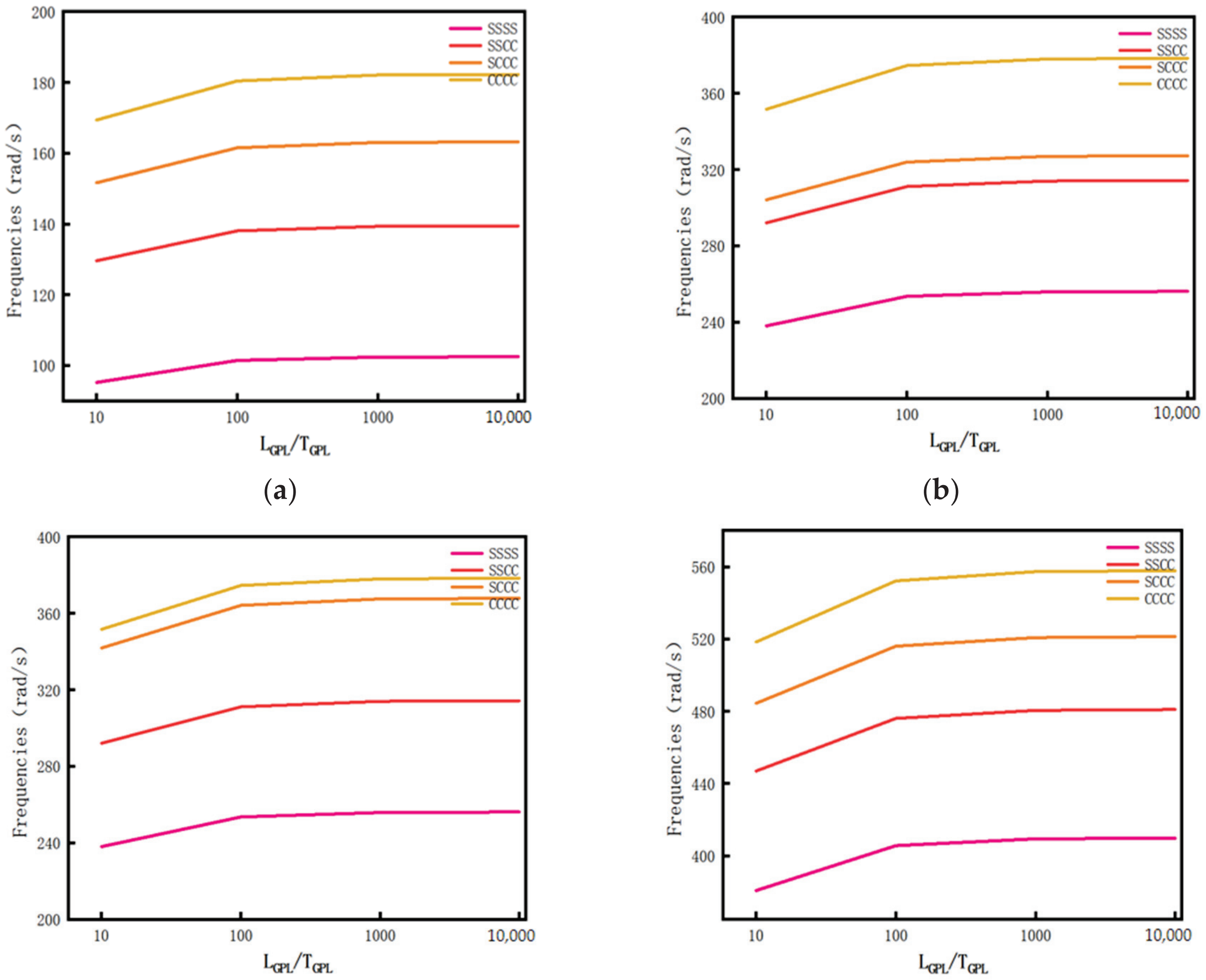

(**a**) (**b**)

(**c**) (**d**)

**Figure 8.** The relationship curve between $L_{GPL}/T_{GPL}$ fraction and vibration frequency. (**a**) First order vibration mode, (**b**) second order vibration mode, (**c**) third order vibration mode, and (**d**) fourth order vibration mode.

Figure 8 shows that the frequency of the GPL reinforced porous composite plate increases with the increase in $L_{GPL}/T_{GPL}$. As shown in the figure, when the ratio was 10 to 100 and the boundary condition was fixed for each order, the frequency increase amplitude was obvious, and the influence on the frequency of the GPL reinforced porous composite plate was obvious. When the ratio was greater than 100, the frequency change was very small.

Calculate the influence of different $L_{GPL}/W_{GPL}$ ratio on the first four-order free vibration frequencies of GPL reinforced porous composite plate when there is a porosity distribution A and the GPL pattern X. A drawn curve is shown in Figure 9. Specific data are shown in Table A4 of Appendix A.

It can be seen in Figure 9 that, with the fixed boundary conditions of each order, the free vibration frequency of the GPL reinforced porous composite plate decreased with the increase in the ratio of $L_{GPL}/W_{GPL}$, but it had a smaller impact.

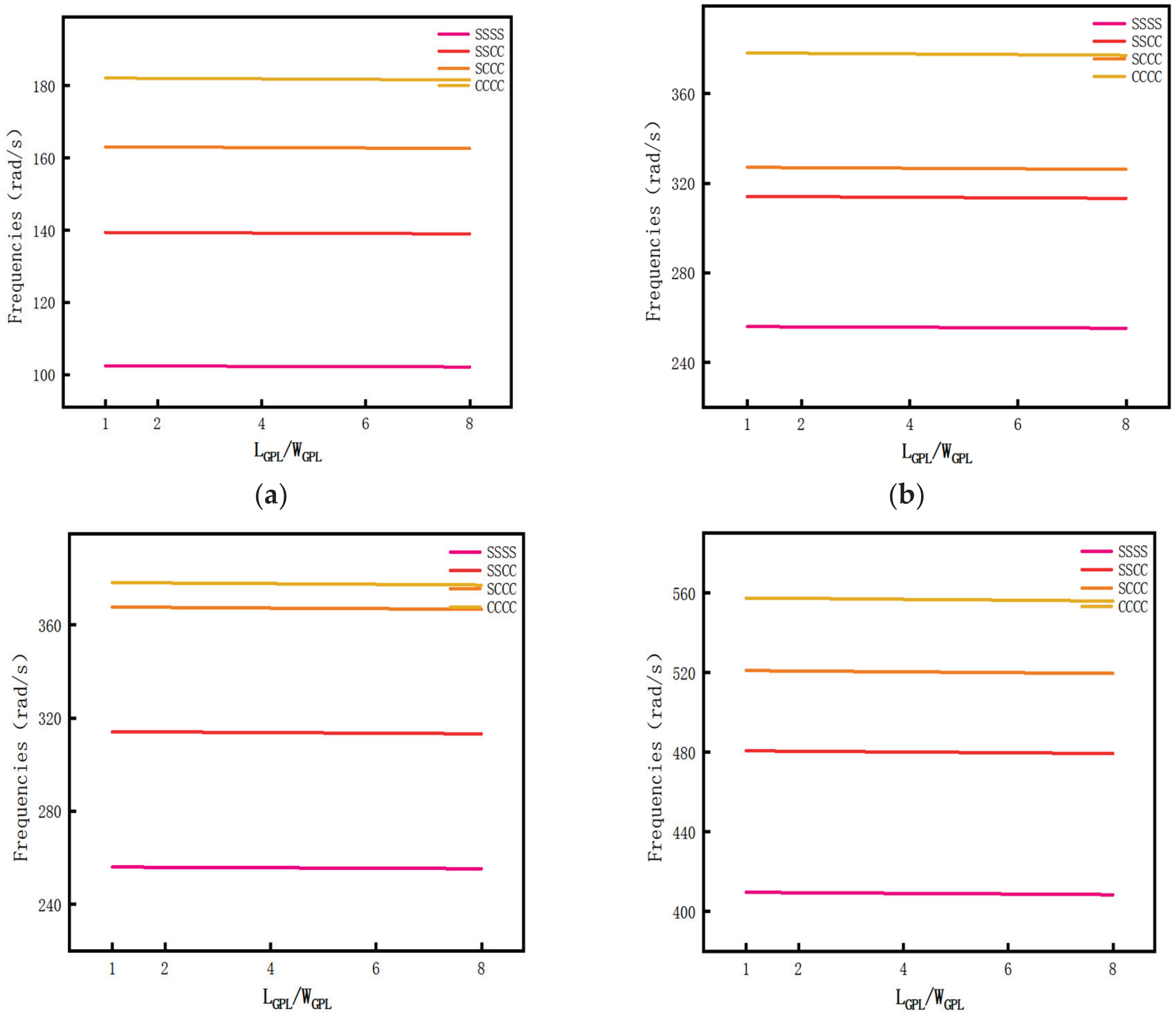

(**a**) (**b**)

(**c**) (**d**)

**Figure 9.** The relationship curve between $L_{GPL}/W_{GPL}$ fraction and vibration frequency. (**a**) First order vibration mode, (**b**) second order vibration mode, (**c**) third order vibration mode, and (**d**) fourth order vibration mode.

### *5.5. The Effect of Porous Distribution and GPL Distribution Pattern on the Free Vibration Frequency of GPL Reinforced Porous Composite Plate*

Calculate the free vibration frequency of GPL reinforced porous composite plate with different porous distributions and GPL distribution patterns. The results are shown in Table 4.

**Table 4.** Free vibration frequency $\omega$ (rad/s) of GPL reinforced porous composite plate with different porous distributions and GPL distribution patterns.

| Boundary Conditions | Porosity A/GPL X | Porosity A/GPL U | Porosity A/GPL O | Uniform/GPL X | Uniform/GPL U | Uniform/GPL O | Porosity B/GPL X | Porosity B/GPL U | Porosity B/GPL O |
|---|---|---|---|---|---|---|---|---|---|
| SSSS | 102.35 | 93.54 | 86.27 | 100.91 | 92.19 | 85.13 | 98.38 | 89.84 | 83.17 |
| SSCC | 139.31 | 127.32 | 117.43 | 137.35 | 125.48 | 115.87 | 133.91 | 122.28 | 113.20 |
| SCCC | 163.01 | 148.98 | 137.40 | 160.71 | 146.82 | 135.58 | 156.69 | 143.09 | 132.46 |
| CCCC | 182.06 | 166.39 | 153.47 | 179.50 | 163.98 | 151.43 | 175.01 | 159.81 | 147.94 |

In the case of fixed boundary conditions of each order, when the distribution mode of the GPL distribution pattern is fixed, the GPL reinforced porous composite plate free vibration frequency was the highest when the porous distribution was porosity distribution A, and the lowest when the GPL reinforced porous composite plate free vibration frequency was porosity distribution B, and the free vibration frequency of uniform porosity distribution was between them both. When the internal porous distribution of the plate was fixed, the free vibration frequency of the GPL reinforced porous composite plate was the highest, and when the GPL pattern was X, it was the lowest when the GPL pattern was O, and the free vibration frequency of the GPL reinforced porous composite plate was between them both when the GPL pattern was U. It can be concluded that the maximum free vibration frequency can be obtained by combining the porosity distribution A and with the distribution mode of the GPL pattern X.

## 6. Conclusions

The combination of porosity design and graphene reinforcement can improve the strength and stability of high value-added airplane plate structures, such as large transport aircrafts and fighters. In this work, the influences of the total number of layers, porous distribution patterns, GPL distribution patterns, porosity coefficients, GPL weight fractions, and GPL shape and boundary conditions on the free vibration frequency of GPL reinforced porous composite were studied, and a simulation analysis was conducted using finite element software in order to verify the accuracy of the conclusion. It is very important to analyze the structure of graphene reinforced composites and its application in engineering. The results show that:

1. The freer the vibration frequency of the GPL reinforced porous composite plate monotonically converged with the increase in the total number of layers, and $n = 12$ was the most suitable number of layers. With the increase in the fixed edge (C), the vibration frequency of composite plate increased gradually. When the boundary condition was CCCC, the vibration frequency of the porous composite plate at the maximum;
2. The freer the vibration frequency of the GPL reinforced porous composite plate decreased with the increase in the porosity coefficient, increased with the increase in the GPL weight fraction, increased with the increase in the $L_{GPL}/T_{GPL}$, and decreased with the increase in $L_{GPL}/W_{GPL}$. This can help us better select the size and content of graphene platelets to be applied to practice;
3. The maximum free vibration frequency can be obtained by combining the porosity distribution A and with the distribution mode of the GPL pattern X. This combination greatly verifies the properties of the reinforcement materials and the possibility of weight reduction in aircraft design, and can be applied to the aerospace industry, which can play a better role.

**Author Contributions:** Conceptualization, H.-G.P. and T.-Y.Z.; methodology, J.-N.Z. and Y.-S.W.; software, Y.-S.W. and Y.-M.F.; validation, X.L.; formal analysis, Y.-S.W.; investigation, H.-G.P. and T.-Y.Z.; resources, H.-G.P. and J.-N.Z.; data curation, Y.-S.W. and J.-N.Z.; writing—original draft preparation, H.-G.P.; writing—review and editing, Y.-S.W.; visualization, X.L. and J.-N.Z.; supervision, T.-Y.Z. and Y.-M.F.; project administration, H.-G.P. and T.-Y.Z. and Y.-M.F.; funding acquisition, H.-G.P. and T.-Y.Z. All authors have read and agreed to the published version of the manuscript.

**Funding:** This research was funded the National Natural Science Foundation of China, grant number 51775093, China Postdoctoral Science Foundation, grant number 2019M661125, Doctorate Start Foundation of Liaoning Provincial, grant number 20180540077, Scientific Research Funding Project of Liaoning Education Department, grant number Jl-2003, Science and Technology Program of Shenyang, grant number 20-206-4-16, Science and Technology Innovation Team Support Program of Shenyang middle-aged and young people, grant number RC190342.

**Institutional Review Board Statement:** Not applicable.

**Informed Consent Statement:** Not applicable.

**Data Availability Statement:** The data is available within the article and can be requested from the corresponding authors.

**Conflicts of Interest:** The authors declare no conflict of interest.

## Appendix A

**Table A1.** Free vibration frequency $\omega$ (rad/s) of GPL reinforced porous composite plate with different porosity coefficients.

| Boundary Conditions | Order | $e_0 = 0.1$ | $e_0 = 0.2$ | $e_0 = 0.3$ | $e_0 = 0.4$ | $e_0 = 0.5$ | $e_0 = 0.6$ |
|---|---|---|---|---|---|---|---|
| SSSS | 1 | 102.35 | 99.92 | 97.73 | 95.75 | 94.01 | 92.51 |
| | 2 | 255.87 | 249.81 | 244.32 | 239.39 | 235.02 | 231.28 |
| | 3 | 255.87 | 249.81 | 244.32 | 239.39 | 235.02 | 231.28 |
| | 4 | 409.40 | 399.70 | 390.91 | 383.02 | 376.03 | 370.05 |
| SSCC | 1 | 139.31 | 136.01 | 133.02 | 130.33 | 127.96 | 125.92 |
| | 2 | 313.95 | 306.51 | 299.78 | 293.72 | 288.37 | 283.78 |
| | 3 | 313.95 | 306.51 | 299.78 | 293.72 | 288.37 | 283.78 |
| | 4 | 480.47 | 469.09 | 458.78 | 449.51 | 441.32 | 434.29 |
| SCCC | 1 | 163.01 | 159.15 | 155.65 | 152.50 | 149.72 | 147.34 |
| | 2 | 326.93 | 319.19 | 312.17 | 305.87 | 300.29 | 295.51 |
| | 3 | 367.50 | 358.80 | 350.91 | 343.82 | 337.55 | 332.18 |
| | 4 | 520.77 | 508.43 | 497.26 | 487.21 | 478.33 | 470.72 |
| CCCC | 1 | 182.06 | 177.75 | 173.84 | 170.33 | 167.22 | 164.56 |
| | 2 | 377.99 | 369.03 | 360.92 | 353.63 | 347.19 | 341.66 |
| | 3 | 377.99 | 369.03 | 360.92 | 353.63 | 347.19 | 341.66 |
| | 4 | 557.23 | 544.03 | 532.07 | 521.33 | 511.82 | 503.68 |

**Table A2.** Free vibration frequency $\omega$ (rad/s) of GPL reinforced porous composite plate with different GPL weight fractions (wt.%).

| Boundary Conditions | Order | wt.% = 0 | wt.% = 0.33 | wt.% = 0.66 | wt.% = 0.88 | wt.% = 1 |
|---|---|---|---|---|---|---|
| SSSS | 1 | 73.33 | 84.15 | 93.61 | 99.37 | 102.35 |
| | 2 | 183.31 | 210.37 | 234.03 | 248.41 | 255.87 |
| | 3 | 183.31 | 210.37 | 234.03 | 248.41 | 255.87 |
| | 4 | 293.30 | 336.60 | 374.45 | 397.46 | 409.40 |
| SSCC | 1 | 99.80 | 114.54 | 127.42 | 135.25 | 139.31 |
| | 2 | 224.92 | 258.12 | 287.15 | 304.80 | 313.95 |
| | 3 | 224.92 | 258.12 | 287.15 | 304.80 | 313.95 |
| | 4 | 344.22 | 395.03 | 439.46 | 466.46 | 480.47 |
| SCCC | 1 | 116.78 | 134.02 | 149.09 | 158.26 | 163.01 |
| | 2 | 234.22 | 268.80 | 299.03 | 317.40 | 326.93 |
| | 3 | 263.29 | 302.15 | 336.13 | 356.79 | 367.50 |
| | 4 | 373.09 | 428.17 | 476.32 | 505.59 | 520.77 |
| CCCC | 1 | 130.43 | 149.69 | 166.52 | 176.75 | 182.06 |
| | 2 | 270.80 | 310.77 | 345.72 | 366.97 | 377.99 |
| | 3 | 270.80 | 310.77 | 345.72 | 366.97 | 377.99 |
| | 4 | 399.21 | 458.15 | 509.67 | 540.99 | 557.23 |

**Table A3.** Free vibration frequency $\omega$ (rad/s) of GPL reinforced porous composite plates with different $L_{GPL}/T_{GPL}$ ratios.

| Boundary Conditions | Order | $L_{GPL}/T_{GPL}$ = 10 | $L_{GPL}/T_{GPL}$ = 100 | $L_{GPL}/T_{GPL}$ = 1000 | $L_{GPL}/T_{GPL}$ = 10,000 |
|---|---|---|---|---|---|
| SSSS | 1 | 95.21 | 101.41 | 102.35 | 102.45 |
| | 2 | 238.03 | 253.52 | 255.87 | 256.12 |
| | 3 | 238.03 | 253.52 | 255.87 | 256.12 |
| | 4 | 380.85 | 405.63 | 409.40 | 409.79 |
| SSCC | 1 | 129.59 | 138.03 | 139.31 | 139.44 |
| | 2 | 292.06 | 311.06 | 313.95 | 314.26 |
| | 3 | 292.06 | 311.06 | 313.95 | 314.26 |
| | 4 | 446.97 | 476.05 | 480.47 | 480.94 |
| SCCC | 1 | 151.64 | 161.51 | 163.01 | 163.17 |
| | 2 | 304.13 | 323.93 | 326.93 | 327.25 |
| | 3 | 341.88 | 364.12 | 367.50 | 367.86 |
| | 4 | 484.45 | 515.98 | 520.77 | 521.27 |
| CCCC | 1 | 169.36 | 180.39 | 182.06 | 182.24 |
| | 2 | 351.63 | 374.51 | 377.99 | 378.36 |
| | 3 | 351.63 | 374.51 | 377.99 | 378.36 |
| | 4 | 518.38 | 552.11 | 557.23 | 557.77 |

**Table A4.** Free vibration frequency $\omega$ (rad/s) of GPL reinforced porous composite plates with different $L_{GPL}/W_{GPL}$ ratios.

| Boundary Conditions | Order | $L_{GPL}/W_{GPL}$ = 1 | $L_{GPL}/W_{GPL}$ = 2 | $L_{GPL}/W_{GPL}$ = 4 | $L_{GPL}/W_{GPL}$ = 6 | $L_{GPL}/W_{GPL}$ = 8 |
|---|---|---|---|---|---|---|
| SSSS | 1 | 102.39 | 102.35 | 102.27 | 102.18 | 102.10 |
| | 2 | 255.98 | 255.87 | 255.66 | 255.46 | 255.25 |
| | 3 | 255.98 | 255.87 | 255.66 | 255.46 | 255.25 |
| | 4 | 409.57 | 409.40 | 409.06 | 408.74 | 408.40 |
| SSCC | 1 | 139.37 | 139.31 | 139.19 | 139.08 | 138.97 |
| | 2 | 314.08 | 313.95 | 313.70 | 313.45 | 313.19 |
| | 3 | 314.08 | 313.95 | 313.70 | 313.45 | 313.19 |
| | 4 | 480.67 | 480.47 | 480.08 | 479.70 | 479.31 |
| SCCC | 1 | 163.07 | 163.01 | 162.87 | 162.75 | 162.61 |
| | 2 | 327.07 | 326.93 | 326.66 | 326.41 | 326.14 |
| | 3 | 367.66 | 367.50 | 367.20 | 366.91 | 366.61 |
| | 4 | 520.98 | 520.77 | 520.34 | 519.93 | 519.51 |
| CCCC | 1 | 182.14 | 182.06 | 181.91 | 181.77 | 181.62 |
| | 2 | 378.14 | 377.99 | 377.68 | 377.38 | 377.07 |
| | 3 | 378.14 | 377.99 | 377.68 | 377.38 | 377.07 |
| | 4 | 557.46 | 557.23 | 556.78 | 556.34 | 555.88 |

## References

1. Stankovich, S.; Dikin, D.A.; Dommett, G.H.B.; Kohlhaas, K.M.; Zimney, E.J.; Stach, E.A.; Piner, R.D.; Nguyen, S.B.T.; Ruoff, R.S. Graphene-based composite materials. *J. Nat.* **2006**, *442*, 282–286. [CrossRef] [PubMed]
2. Rahman, R.; Haque, A. Molecular modeling of crosslinked graphene–epoxy nanocomposites for characterization of elastic constants and interfacial properties. *J. Compos. Part B* **2013**, *54*, 353–364. [CrossRef]
3. Julia, A.; King, D.R.; Klimek, I.; Miskioglu, I.; Odegard, G.M. Mechanical properties of graphene nanoplatelet/epoxy composites. *J. Appl. Polym. Sci.* **2013**, *128*, 4217–4223.
4. Feng, C.; Kitipornchai, S.; Yang, J. Nonlinear bending of polymer nanocomposite beams reinforced with non-uniformly distributed graphene platelets (GPLs). *J. Compos. Part B* **2017**, *110*, 132–140. [CrossRef]
5. Alibeigloo, A.; Kari, M.R. Forced vibration analysis of antisymmetric laminated rectangular plates with distributed patch mass using third order shear deformation theory. *J. Thin-Walled Struct.* **2008**, *47*, 653–660. [CrossRef]
6. Yang, J.; Wu, H.; Kitipornchai, S. Buckling and postbuckling of functionally graded multilayer graphene platelet-reinforced composite beams. *J. Compos. Struct.* **2017**, *161*, 111–118. [CrossRef]
7. Eringen, A. Nonlocal polar elastic continua. *Int. J. Eng. Sci.* **1972**, *10*, 1–16. [CrossRef]
8. Eringen, A.C. On differential equations of nonlocal elasticity and solutions of screw dislocation and surface waves. *J. Appl. Phys.* **1983**, *54*, 4703–4710. [CrossRef]

9. Eringen, A.; Edelen, D. On nonlocal elasticity. *Int. J. Eng. Sci.* **1972**, *10*, 233–248. [CrossRef]
10. Polit, O.; Anant, C.; Anirudh, B.; Ganapathi, M. Functionally graded graphene reinforced porous nanocomposite curved beams: Bending and elastic stability using a higher-order model with thickness stretch effect. *Compos. Part B Eng.* **2019**, *166*, 310–327. [CrossRef]
11. Rafiee, M.A.; Rafiee, J.; Wang, Z.; Song, H.H.; Yu, Z.Z.; Koratkar, N. Enhanced mechanical properties of nanocomposites at low graphene content. *ACS Nano* **2009**, *3*, 3884–3890. [CrossRef]
12. Liu, D.Y.; Kitipornchai, S.; Chen, W.Q.; Yang, J. Three-dimensional buckling and free vibration analyses of initially stressed functionally graded graphene reinforced composite cylindrical shell. *Compos. Struct.* **2018**, *189*, 560–569. [CrossRef]
13. Reddy, R.M.R.; Karunasena, W.; Lokuge, W. Free vibration of functionally graded-GPL reinforced composite plates with different boundary conditions. *Aerosp. Sci. Technol.* **2018**, *78*, 147–156. [CrossRef]
14. Amirabadi, H.; Farhatnia, F.; Eftekhari, S.A.; Hosseini-Ara, R. Free vibration analysis of rotating functionally graded GPL-reinforced truncated thick conical shells under different boundary conditions. *Mech. Based Des. Struct. Mach.* **2020**, 1–32. [CrossRef]
15. Feng, C.; Kitipornchai, S.; Yang, J. Nonlinear free vibration of functionally graded polymer composite beams reinforced with graphene nanoplatelets (GPLs). *Eng. Struct.* **2017**, *140*, 110–119. [CrossRef]
16. Zhang, H.; Zhao, T.Y.; Zhang, H.Y.; Pan, H.G.; Yuan, H.Q.; Ma, H.; Yin, F.; Tai, X.; Kou, H.; Yuan, H.; et al. Dynamic characteristics of mistuned bladed disk system under rub-impact force. *Adv. Mech. Eng.* **2020**, *12*. [CrossRef]
17. Sharma, G.S.; Sarkar, A. Directivity based control of acoustic radiation. *J. Appl. Acoust.* **2019**, *154*, 226–235. [CrossRef]
18. Sharma, G.S.; Sarkar, A. Directivity-Based Passive Barrier for Local Control of Low-Frequency Noise. *J. Theor. Comput. Acoust.* **2018**, *26*, 1850012. [CrossRef]
19. Zhao, T.Y.; Ma, Y.; Zhang, H.Y.; Pan, H.G.; Cai, Y. Free vibration analysis of a rotating graphene nanoplatelet reinforced pre-twist blade-disk assembly with a setting angle. *Appl. Math. Model.* **2021**, *93*, 578–596. [CrossRef]
20. Zhao, T.Y.; Jiang, L.P.; Pan, H.G.; Yang, J.; Sritawat, K. Coupled free vibration of a functionally graded pre-twisted blade-shaft system reinforced with graphene nanoplatelets. *Compos. Struct.* **2020**, *262*, 113362. [CrossRef]
21. Zhao, T.Y.; Ma, Y.; Zhang, H.Y.; Yang, J. Coupled Free Vibration of Spinning Functionally Graded Porous Double-Bladed Disk Systems Reinforced with Graphene Nanoplatelets. *Materials* **2020**, *13*, 5610. [CrossRef] [PubMed]
22. Sharma, G.S.; Faverjon, B.; Dureisseix, D.; Skvortsov, A.; MacGillivray, I.; Audoly, C.; Kessissoglou, N. Acoustic Performance of a Periodically Voided Viscoelastic Medium with Uncertainty in Design Parameters. *J. Vib. Acoust.* **2020**, *142*. [CrossRef]
23. Zhao, T.Y.; Cui, Y.S.; Pan, H.G.; Yuan, H.Q.; Yang, J. Free vibration analysis of a functionally graded graphene nanoplatelet reinforced disk-shaft assembly with whirl motion. *Int. J. Mech. Sci.* **2021**, *197*, 106335. [CrossRef]
24. Zhao, T.Y.; Cui, Y.S.; Pan, H.G.; Yuan, H.Q.; Yang, J. Free vibration analysis of a spinning porous nanocomposite blade reinforced with graphene nanoplatelets. *J. Strain Anal. Eng. Des.* **2021**. [CrossRef]
25. Zhao, T.Y.; Jiang, Z.Y.; Zhao, Z.; Xie, L.Y.; Yuan, H.Q. Modeling and free vibration analysis of rotating hub-blade assemblies reinforced with graphene nanoplatelets. *J. Strain Anal. Eng. Des.* **2021**. [CrossRef]
26. Shafiei, N.; Mousavi, A.; Ghadiri, M. On size-dependent nonlinear vibration of porous and imperfect functionally graded tapered microbeams. *Int. J. Eng. Sci.* **2016**, *106*, 42–56. [CrossRef]
27. Sharma, G.S.; Skvortsov, A.; MacGillivray, I.; Kessissoglou, N. Sound transmission through a periodically voided soft elastic medium submerged in water. *Wave Motion* **2017**, *70*, 101–112. [CrossRef]
28. Davletshin, A.R.; Ustiuzhanina, S.V.; Kistanov, A.A.; Saadatmand, D.; Dmitriev, S.V.; Zhou, K.; Korznikova, E.A. Electronic structure of graphene– and BN–supported phosphorene. *J. Phys. B Phys. Condens. Matter* **2018**, *534*, 63–67. [CrossRef]
29. Babicheva, R.I.; Dmitriev, S.V.; Korznikova, E.A.; Zhou, K. Mechanical Properties of Two-Dimensional sp 2 -Carbon Nanomaterials. *J. Exp. Theor. Phys.* **2019**, *129*. [CrossRef]
30. Savin, A.; Korznikova, E.; Krivtsov, A.; Dmitriev, S. Longitudinal stiffness and thermal conductivity of twisted carbon nanoribbons. *Eur. J. Mech. A* **2020**, *80*. [CrossRef]
31. Savin, A.V.; Korznikova, E.; Dmitriev, S. Dynamics of surface graphene ripplocations on a flat graphite substrate. *Phys. Rev. B* **2019**, *99*, 235411. [CrossRef]
32. Chen, D.; Kitipornchai, S.; Yang, J. Dynamic response and energy absorption of functionally graded porous structures. *Mater. Des.* **2018**, *140*, 473–487. [CrossRef]
33. Hui-Shen, S.; Feng, L.; Xiang, Y. Nonlinear vibration of functionally graded graphene-reinforced composite laminated beams resting on elastic foundations in thermal environments. *J. Nonlinear Dyn.* **2017**, *90*, 899–914. [CrossRef]
34. Gibson, L.J.; Ashby, M.F. The Mechanics of Three-Dimensional Cellular Materials. *J. Proc. R. Soc. Lond. Ser. A* **1982**, *382*, 43–59.
35. Yang, J.; Chen, D.; Kitipornchai, S. Buckling and free vibration analyses of functionally graded graphene reinforced porous nanocomposite plates based on Chebyshev-Ritz method. *Compos. Struct.* **2018**, *193*, 281–294. [CrossRef]

materials

MDPI

*Article*

# Time-History Analysis of Composite Materials with Rectangular Microstructure under Shear Actions

**Marco Colatosti [1], Nicholas Fantuzzi [2] and Patrizia Trovalusci [1,*]**

[1] DISG Department, Sapienza University of Rome, Via A. Gramsci 53, 00197 Rome, Italy; marco.colatosti@uniroma1.it
[2] DICAM Department, University of Bologna, Viale del Risorgimento 2, 40136 Bologna, Italy; nicholas.fantuzzi@unibo.it
* Correspondence: patrizia.trovalusci@uniroma1.it

**Abstract:** It has been demonstrated that materials with microstructure, such as particle composites, show a peculiar mechanical behavior when discontinuities and heterogeneities are present. The use of non-local theories to solve this challenge, while preserving memory of the microstructure, particularly of internal length, is a challenging option. In the present work, composite materials made of rectangular rigid blocks and elastic interfaces are studied using a Cosserat formulation. Such materials are subjected to dynamic shear loads. For anisotropic media, the relative rotation between the local rigid rotation and the microrotation, which corresponds to the skewsymmetric part of strain, is crucial. The benefits of micropolar modeling are demonstrated, particularly for two orthotropic textures of different sizes.

**Keywords:** composite materials; multiscale procedures; micropolar continua; time-history analysis

## 1. Introduction

The most promising types of materials employed in numerous fields of inventive industry are modern composites. Materials such as ceramic [1–4] and metal composites, poly-crystals (e.g., alumina, zirconia) [5–8], masonry [9], porous rocks are examples of particle composites: their macroscopic behavior is strongly dependent on the internal microstructure, therefore, discontinuities and heterogeneities cannot be neglected. Detailed modeling is required for an appropriate mechanical description: a discrete model of the microstructure gives a high level of representation, but the drawback is the expensive computational cost [10–15] which increases with the scale reduction of the material [16], multiscale approaches are a viable option to derive equivalent homogenized continua [17–20], however, it has been shown that the classic Cauchy continuum is not reliable for those types of materials when the heterogeneities size has a prominent role, as in the presence of geometric discontinuities or high stress gradients [21–28]. For these reasons, a non-local description is necessary to take into account the microscopic effect on the macroscopic mechanical response. Continuum theories have a non-local character in the presence of internal length parameters (distance between particle in discrete structure, grain or cell size, correlation radius of at-a-distance force, etc.) and spatial dispersion properties (wave velocities depending on wavelength or frequency) [29–32]. It is worth mentioning that continua with additional degrees of freedom can be considered "implicitly" non-local [29,33].

Thanks to advances in nanostructures and nanotechnologies fields, nanomaterials are progressively commercialized. Materials with structure at the nanoscale generally have peculiar thermophysical and mechanical properties, and non-local theories, of an "explicit" or "implicit" kind, are usually applied to tackle the dynamical behavior of composites such as nanowires [34], nanobeams [35,36], nanorods [37], nanotubes [38–41], nanoplates [42] and composite beams [43] and plates [44,45].

Nonlocal theories have been used since 19th century (Voigt and Poincaré [29,46]) and applied in the "implicit" and "explicit" from the 1960s and 1970s . A comparison between the two non local approaches, the latter adopted in this paper, have been proposed for instance in [30,31].

The micropolar continuum can be considered as a micromorphic model, where the microdeformation is constrained to be a rotation (microrotation). The Cosserat model is a collection of rigid particles that undergo homogeneous displacements and rotations and interact via forces and couples. Instead, by way of example, for the second gradient and the Cauchy models, the particles are locally constrained to have the same rotation and to interact via forces and moments of forces; in particular, the continuum is a second gradient model if the displacements field is of the second order; while the continuum is a classical model if the field is homogeneous [28].

At different scale levels, micropolar models have already been adopted to describe materials made as an assembly of rigid particles which interacts through elastic interfaces. A typical example are masonry structures where the blocks have rectangular geometry and the mortar joints are modelled as linear elastic springs [23–26]. The micropolar theory takes into account extra degrees of freedom, which is referred to as microrotation (rotation of a point) to be distinguished from the macrorotation (local rigid rotation). It is worth noting that these rotations coincide in both the couple-stress and classical theories [24]. Micropolar effects become prominent in the presence of load or geometrical singularities, such as concentrated loads, voids or material inclusions. For anisotropic media, the additional strain measure of the so-called relative rotation, defined as the difference between microrotation and macrorotation, corresponding to the skew-symmetric part of the displacement gradient, makes an important contribution to the mechanical behavior [27,28].

In this work, two types of rectangular block textures at three different level scales are considered: the goal is to emphasize the advantages and the necessity of a description of these materials as micropolar continua compared to the classical continua even for dynamic conditions [47] not yet fully examined by the authors. For this purpose, a time-history analysis is used to determine the response of a structure under dynamic load. A homogenization technique, based on an energy equivalence criterion [23,24] between the discrete model, assumed as the benchmark, and the continuum model, is adopted to detect the anisotropic constitutive characteristics [48].

The paper is organized as follows: in Section 2, theoretical background on micropolar continua is presented for the two-dimensional case, in Section 3, the rectangular geometries, the reference volume elements and their relative constitutive properties of materials are reported; in Section 4, the numerical implementation of the structural problem is discussed, in Section 5, a brief review of time transient analysis is reported and the results are discussed and finally the conclusions are summarized in Section 6.

## 2. Micropolar Continuum

Let us consider a linearized kinematical framework. The displacement field for a two-dimensional micropolar continuum is made up of three degrees of freedom, two displacements $u_1$, $u_2$ and a microrotation $\omega$. In order to use the matrix notation, the displacement vector is defined as $\boldsymbol{u}^\top = \begin{bmatrix} u_1 & u_2 & \omega \end{bmatrix}$. The strain and stress vectors are respectively $\boldsymbol{\varepsilon}^\top = \begin{bmatrix} \varepsilon_{11} & \varepsilon_{22} & \varepsilon_{12} & \varepsilon_{21} & \kappa_1 & \kappa_2 \end{bmatrix}$, where the terms $\epsilon_{ij}$ are the normal and tangential strain components, with $\varepsilon_{12}$ and $\varepsilon_{21}$ not equal, and $\kappa_1$ and $\kappa_2$ are the microcurvatures, and $\boldsymbol{\sigma}^\top = \begin{bmatrix} \sigma_{11} & \sigma_{22} & \sigma_{12} & \sigma_{21} & \mu_1 & \mu_2 \end{bmatrix}$ where the terms $\sigma_{12}$, $\sigma_{21}$ are not equal and the terms $\mu_1$, $\mu_2$ represent the microcouples.

Defining the operator **D**:

$$\mathbf{D}^\top = \begin{bmatrix} \dfrac{\partial}{\partial x_1} & 0 & \dfrac{\partial}{\partial x_2} & 0 & 0 & 0 \\ 0 & \dfrac{\partial}{\partial x_2} & 0 & \dfrac{\partial}{\partial x_1} & 0 & 0 \\ 0 & 0 & 1 & -1 & \dfrac{\partial}{\partial x_1} & \dfrac{\partial}{\partial x_2} \end{bmatrix} \tag{1}$$

is possible to write the kinematic compatibility between the vectors $\boldsymbol{u}$ and $\boldsymbol{\varepsilon}$:

$$\boldsymbol{\varepsilon} = \mathbf{D}\,\boldsymbol{u} \tag{2}$$

The equilibrium of the body can be expressed using Hamilton's principle:

$$\delta \int_{t_1}^{t_2} (K - \Pi)\, dt = 0 \tag{3}$$

where $K$ is the kinetic energy and $\Pi$ is the total potential energy given by the sum of the strain energy $U$ and the potential of external loads $V$:

$$\Pi = U + V \tag{4}$$

The variation of the kinetic energy is:

$$\delta K = \int_V \rho \delta \dot{\boldsymbol{u}}^\top \dot{\boldsymbol{u}}\, dV = h \int_A \delta \dot{\boldsymbol{u}}^\top \mathbf{m} \dot{\boldsymbol{u}}\, dA = -h \int_A \delta \boldsymbol{u}^\top \mathbf{m} \ddot{\boldsymbol{u}}\, dA \tag{5}$$

where $h$ is the thickness of the body which can be assumed unitary and $\mathbf{m}$ is the equivalent mass matrix defined as:

$$\mathbf{m} = \begin{bmatrix} \rho h & 0 & 0 \\ 0 & \rho h & 0 \\ 0 & 0 & \rho J_c \end{bmatrix} \tag{6}$$

where $\rho$ is the material density and $J_c$ represents the rotary inertia of the material point. The variation of the strain energy is written in the form:

$$\delta U = \int_A \delta \boldsymbol{\varepsilon}^\top \boldsymbol{\sigma}\, dA \tag{7}$$

and using the Equation (1):

$$\delta U = \int_A \delta \boldsymbol{u}^\top \mathbf{D}^\top\, \boldsymbol{\sigma}\, dA \tag{8}$$

Finally, the variation of the potential of external loads is:

$$\delta V = -\int_A \delta \boldsymbol{u}^\top \boldsymbol{b}\, dA - \int_{\gamma_t} \delta \boldsymbol{u}^\top \boldsymbol{t}\, d\gamma \tag{9}$$

where the vectors $\boldsymbol{b}$ and $\boldsymbol{t}$ indicate the body and surface forces, respectively.

The micropolar anisotropic constitutive equation takes the form:

$$\boldsymbol{\sigma} = \mathbf{C}\,\boldsymbol{\varepsilon} \tag{10}$$

where

$$\mathbf{C} = \begin{bmatrix} A_{1111} & A_{1122} & A_{1112} & A_{1121} & B_{111} & B_{112} \\ & A_{2222} & A_{2212} & A_{2221} & B_{221} & B_{222} \\ & & A_{1212} & A_{1221} & B_{121} & B_{122} \\ & & & A_{2121} & B_{211} & B_{212} \\ & & & & D_{11} & D_{12} \\ sym & & & & & D_{22} \end{bmatrix} = \begin{bmatrix} \mathbf{A} & \mathbf{B} \\ \mathbf{B}^\top & \mathbf{D} \end{bmatrix} \tag{11}$$

The constitutive matrix is symmetric ($\mathbf{C} \in Sym$) when hyperelastic materials are considered: in particular $A_{ijhk} = A_{hkij}$; $B_{ijh} = B_{hij}$; $D_{ij} = D_{ji}$ [25]. From these assumptions, Hamilton's principle can be written as

$$\int_{t_1}^{t_2} \left( \int_A \delta \boldsymbol{u}^\top \left( \mathbf{m} \ddot{\boldsymbol{u}} + \mathbf{D}^\top \, \mathbf{C} \mathbf{D} \boldsymbol{u} \right) dA + \int_A \delta \boldsymbol{u}^\top \boldsymbol{b} \, dA + \int_{\gamma_t} \delta \boldsymbol{u}^\top \boldsymbol{t} \, d\gamma \right) dt = 0 \tag{12}$$

## 3. Rectangular Microstructure

Materials particle composites with rectangular microstructure are explored in this paper: masonry structures can be assumed as materials of this type. The masonry system is modeled as a discrete system in which the blocks can be considered as rigid bodies and the mortar joints can be assumed as elastic interfaces. Two different types of orthotropic textures that belong to the centrosymmetric class of material have been examined: texture 1 and texture 2 at three different scales (Figure 1). The reference block is 80 cm width and 20 cm high for the scale 1, for texture 2 the smaller block has a half width of the reference block. For the scale $s = 0.5$ and $s = 0.25$, all the geometries' lengths are obtained by multiplying the dimensions of the scale 1 for the considered scale factor. The aim is to study the dynamic response of the system in a 2D state plane of tension under a shear load modeled as a discrete system, considered as the benchmark, as a micropolar and a classical continuum. Because masonry is a system of rigid elements arranged according to a periodical texture, it possible to define a reference volume element (RVE) from which the constitutive properties of the equivalent continuum can be derived.

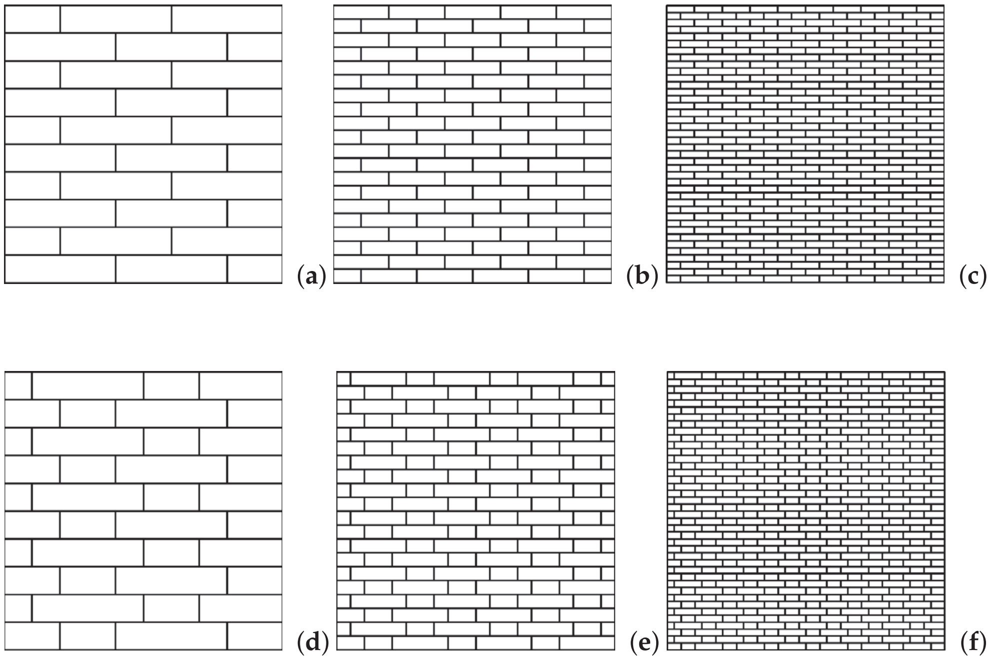

**Figure 1.** Rectangular microstructures. Texture 1: (**a**) $s = 1$ (**b**) $s = 0.5$ (**c**) $s = 0.25$. Texture 2: (**d**) $s = 1$ (**e**) $s = 0.5$ (**f**) $s = 0.25$.

### *Reference Volume Element*

Based on a generalization of the Cauchy–Born rule, starting from a kinematic correspondence map between discrete and continuous fields, an energy equivalence criterion is assumed. To apply the homogenization method to periodic assemblies, the Representative Volume Element (RVE) must first be identified [24].

The RVEs considered for the two textures are depicted in Figure 2: the RVE of texture 1 is made of four blocks and five elastic links which express the elasticity of bed and head joints; whereas the RVE of texture 2 is made of a central block and four smaller blocks with four elastic links. The material symmetries have to be preserved in the homogenization process [25,49] and as a consequence of the homogenization procedure adopted, it is possible to obtain the constitutive matrices of the materials. The procedure for the springs stiffness calculus of the RVE and the relative constitutive parameters is reported in detail in [28]. In short, homogenization is carried out by considering a RVE with a central block or interface and all the other links in the neighbourhood of such central entity. Elastic springs with normal, shear and rotational components are considered and included.

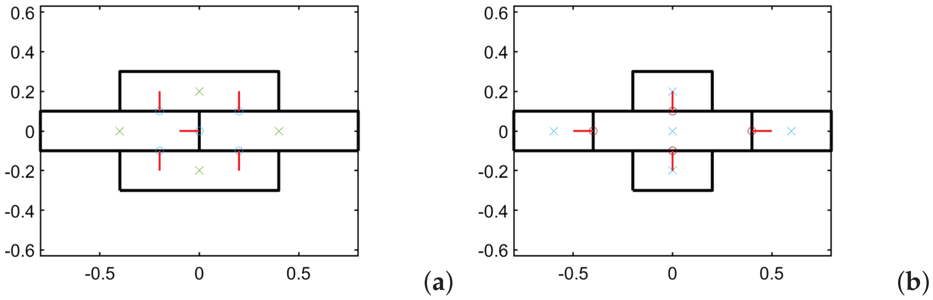

**Figure 2.** RVEs for the two microstures at scale $s = 1$: (**a**) texture 1 (**b**) texture 2.

The constitutive matrices for texture 1 are:

$$\mathbf{A}_{text1} = 10^{11}\begin{bmatrix} 9.00 & 0.0 & 0 & 0 \\ 0.0 & 2.00 & 0 & 0 \\ 0 & 0 & 0.80 & 0.0 \\ 0 & 0 & 0.0 & 3.60 \end{bmatrix} \qquad \mathbf{D}_{text_1}^{s=1} = 10^{11}\begin{bmatrix} 0.2340 & 0.0 \\ 0.0 & 0.0400 \end{bmatrix}$$
$$\mathbf{D}_{text_1}^{s=0.5} = 10^{11}\begin{bmatrix} 0.0585 & 0 \\ 0 & 0.0100 \end{bmatrix} \qquad \mathbf{D}_{text_1}^{s=0.25} = 10^{11}\begin{bmatrix} 0.0146 & 0 \\ 0 & 0.0025 \end{bmatrix} \tag{13}$$

The constitutive matrices for texture 2 are:

$$\mathbf{A}_{text_2} = 10^{12}\begin{bmatrix} 1.92 & 0.17 & 0 & 0 \\ 0.17 & 0.20 & 0 & 0 \\ 0 & 0 & 0.08 & 0.0 \\ 0 & 0 & 0.0 & 1.44 \end{bmatrix} \qquad \mathbf{D}_{text_2}^{s=1} = 10^{12}\begin{bmatrix} 0.0610 & 0.0015 \\ 0.0015 & 0.0112 \end{bmatrix}$$
$$\mathbf{D}_{text_2}^{s=0.5} = 10^{12}\begin{bmatrix} 0.0153 & 0.0004 \\ 0.0004 & 0.0028 \end{bmatrix} \qquad \mathbf{D}_{text_2}^{s=0.25} = 10^{12}\begin{bmatrix} 0.0038 & 0.0001 \\ 0.0001 & 0.0007 \end{bmatrix} \tag{14}$$

and, both textures being centrosymmetric, $\mathbf{B} = \mathbf{0}$ for both textures. The internal length of the material is taken into account by the sub matrix $\mathbf{D}$ where, approximately, $\mathbf{D}_{s=1} \approx 4\mathbf{D}_{s=0.5} \approx 16\mathbf{D}_{s=0.25}$. Note that the elements' size affects only the matrix $\mathbf{D}$.

The constitutive models for the Cauchy continuum are obtained from the previous constitutive matrices [27] as:

$$\mathbf{C} = \begin{bmatrix} A_{1111} & A_{1122} & 0 \\ A_{2211} & A_{2222} & 0 \\ 0 & 0 & \frac{1}{2}[A_{1212} + A_{2121}] + A_{1221} \end{bmatrix}$$

The classical model does not preserve a memory of the internal length of the microstructure.

## 4. Numerical Implementation

The differential equation problem for the classical and micropolar models are both solved through a MATLAB finite element method (FEM) code [50]. Newmark's method [51] is also implemented to investigate the dynamic response of a wall subjected to a dynamic shear load and the results are compared with a discrete model prepared with the FEM software ABAQUS (Dassault Systèmes, Johnston, RI, USA).

*Continuum Model*

To solve the continuum numerical problem, a mesh of 32 × 32 elements Q4 finite element with reduced integration is employed. The numerical problem is solved in terms of displacements and in order to apply reduced integration, the strain vector has to be rearranged by separating strain terms which are fully integrated and the ones for which reduced integration is applied [49,52].

The finite element method is based on the approximation of nodal displacements:

$$\boldsymbol{u} = \mathcal{N}\, \boldsymbol{d}^e \tag{15}$$

The kinematic displacement vector is arranged as follows:

$$\boldsymbol{d}^{eT} = \begin{bmatrix} u_1^1 & \dots & u_1^4 & u_2^1 & \dots & u_2^4 & \omega^1 & \dots & \omega^4 \end{bmatrix} \tag{16}$$

with 12 degrees of freedom overall (3 per node). The matrix of the shape functions is composed by the vector $\mathbf{N}$ that collects the Lagrangian shape functions:

$$\mathcal{N} = \begin{bmatrix} \mathbf{N} & \mathbf{0} & \mathbf{0} \\ \mathbf{0} & \mathbf{N} & \mathbf{0} \\ \mathbf{0} & \mathbf{0} & \mathbf{N} \end{bmatrix} \tag{17}$$

Including the above expression in the Hamilton principle, the kinetic energy becomes:

$$\delta K = -\delta \boldsymbol{d}^{eT} \int_A \mathbf{N}^\top \mathbf{m} \mathbf{N} \, dA \, \ddot{\boldsymbol{d}}^e \tag{18}$$

The mass matrix reads:

$$\mathbf{M}^e = \int_A \mathbf{N}^\top \mathbf{m} \mathbf{N} \, dA \tag{19}$$

The internal work takes the form:

$$\delta U = \delta \boldsymbol{d}^{eT} h \int_A (\mathbf{D}\mathcal{N})^\top \mathbf{C} (\mathbf{D}\mathcal{N}) \, dA \, \boldsymbol{d}^e = \delta \boldsymbol{d}^{eT} h \int_A \mathbf{B}^\top \mathbf{C}\, \mathbf{B} \, dA \, \boldsymbol{d}^e \tag{20}$$

where $\mathbf{B} = \mathbf{D}\mathcal{N}$, thus, the element stiffness matrix is:

$$\mathbf{K}^e = \int_A \mathbf{B}^\top \mathbf{C}\, \mathbf{B} \, dA \tag{21}$$

which has to be integrated according to a 2 × 2 Gauss integration for the normal components as well as microcouples, whereas reduced integration is applied on shear components. Finally, the potential of external forces is:

$$\delta V = -\delta \boldsymbol{d}^{eT} \int_A \mathbf{N}^\top \boldsymbol{b} \, dA - \delta \boldsymbol{d}^{eT} \int_{\gamma_t} \mathbf{N}^\top \boldsymbol{t} \, d\gamma = -\delta \boldsymbol{d}^{eT} \boldsymbol{F} \tag{22}$$

where $\boldsymbol{F}$ is the global vector of volume and surface forces.

## 5. Simulations

The results reported below investigate the behavior of a wall, clamped at the base and subjected to a distributed dynamic shear load applied at the top (Figure 3), in order to extend the numerical results already obtained for the static case [48] and to enrich the aspects related to the dynamic conditions [47]. Furthermore, a numerical evaluation, for the case in which blocks of different sizes are present in the masonry texture, wants to be performed, because in previous works, this aspect has been evaluated only in qualitative terms [25]. The footprint of the load is equal to $a = L_y/8$, where $L_y$ is the height of the panel and $L_x$ is the width. The data results are reported in terms of displacements; in particular, the displacements of the control point as a function of time are plotted for three different mechanical models: discrete, micropolar and classical. For texture 1, the panel has dimensions $L_x = 3.2$ m and $L_y = 4$ m, whereas for texture 2 the dimensions are $L_x = 3$ m and $L_y = 3.2$ m. The expression of the horizontal dynamic load is:

$$P(t) = q_0(1 - \cos(ft)); \tag{23}$$

where $q_0 = 100$ kN, the time domain is equal to 1000 s, the time step is equal to 5 s and the angular frequency $f = 0.02$ Hz (load case 1). Finally, further numerical simulations were carried out considering the same load type but with a frequency value equal to the frequency of the first free vibration mode of the structure in a time period of 0.01 (load case 2).

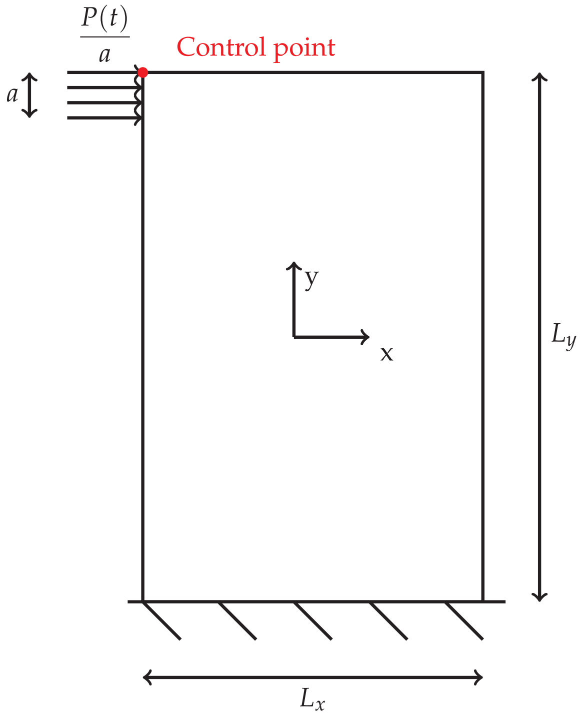

**Figure 3.** Schematic of the panel analyzed.

### 5.1. Time Transient Analysis

The Newmark method is briefly reported in [50]. The equation that must be solved is:

$$\mathbf{M}\ddot{\boldsymbol{d}} + \mathbf{K}\boldsymbol{d} = \boldsymbol{F} \tag{24}$$

where **M** is the mass matrix, **K** is the stiffness matrix, $\boldsymbol{d}$ is the displacement vector and $\boldsymbol{F}$ is the vector of the external loads, with the initial conditions $\boldsymbol{d} = \mathbf{0}$ and $\dot{\boldsymbol{d}} = \mathbf{0}$ at time $t = 0$. The time functions are approximated by Taylor's series arrested at the second-order derivative. The time increment is indicated as $dt = t_{s+1} - t_s$. The velocity and the acceleration vector can be written as

$$\dot{\boldsymbol{d}}_{s+1} = \dot{\boldsymbol{d}}_s + a_1\ddot{\boldsymbol{d}}_s + a_2\ddot{\boldsymbol{d}}_{s+1} \tag{25}$$

$$\ddot{\boldsymbol{d}}_{s+1} = a_3(\boldsymbol{d}_{s+1} - \boldsymbol{d}_s) - a_4\dot{\boldsymbol{d}}_s - a_5\ddot{\boldsymbol{d}}_s \tag{26}$$

The coefficients are

$$a_1 = (1-\alpha)\,dt,\;\; a_2 = \alpha\,dt,\;\; a_3 = 2/\gamma\,dt^2,\;\; a_4 = a_3\,dt,\;\; a_5 = (1-\gamma)/\gamma \tag{27}$$

The parameters $\alpha$ and $\gamma$ depend on the time integration scheme. For this study case, the constant average acceleration method has been used, thus, $\alpha = 1/2$, $\gamma = 1/2$. The algebraic system of equations at the generic time $t_{s+1}$ becomes:

$$\hat{\mathbf{K}}\boldsymbol{d}_{s+1} = \hat{\boldsymbol{F}},\ \boldsymbol{d}_{s+1} = \hat{\mathbf{K}}^{-1}\hat{\boldsymbol{F}} \tag{28}$$

where:

$$\hat{\mathbf{K}} = \mathbf{K}_{s+1} + a_3\mathbf{M}_{s+1} \tag{29}$$

$$\hat{\boldsymbol{F}} = \boldsymbol{F}_{s+1} + \mathbf{M}_{s+1}(a_3\boldsymbol{d}_s + a_4\dot{\boldsymbol{d}}_s + a_5\ddot{\boldsymbol{d}}_s) \tag{30}$$

All $\boldsymbol{d}$ quantities are known at the time $t_s$. The mass matrix, $\mathbf{M}$, and stiffness, $\mathbf{K}$, matrix remain constant. By using starting values for displacement and velocities at time $t = 0$, the initial acceleration can be carried out as:

$$\ddot{\boldsymbol{d}} = \mathbf{M}_0^{-1}(\boldsymbol{F}_0 - \mathbf{K}_0\boldsymbol{d}_0) \tag{31}$$

### *5.2. Texture 1*

In Figure 4a–c, the control point displacements along the $x$ direction are reported for the load case of Equation (23). The graphs depict three scales and three models: Figure 4a shows that both continuum models catch the same trend of the discrete model due the elasticity hypothesis, however, the Cauchy model underestimates the maximum displacement magnitude—in fact, the error is around 33%. In contrast, the Cosserat model shows greater accuracy in evaluating the values (around 12.78% for the first scale, until reaching approximately 3% for the smaller scale), therefore, the micropolar model converges to a discrete model with the scale reduction, whereas the classical continuum does not involve any improvement because it does not take into account the internal length of the material microstructure. Figure 4d shows the displacement of the control point (for the scale $s = 0.5$) at the resonance frequency and the differences between the continuum models are more evident: only the Cosserat model reproduces the result of the discrete system, whereas the Cauchy model presents a response with a phase shift and a gross estimation of the maximum amplitude.

### *5.3. Texture 2*

In Figure 5a–c, the horizontal displacements of the control point of the first load case are reported. For texture 2, the Cosserat model provides results with a very good approximation from the first scale $s = 1$, in fact, the error is around 4% for the larger scale and goes below 3% for the smaller one; instead, for the Cauchy model the maximum displacement evaluation gives an error around 30%. Once again, the difference between the discrete and the micropolar model improves by reducing the scale and this is very important since the smaller scale is the one that involves the highest computational burden for discrete models. In Figure 5, the displacement at resonance for the scale $s = 0.5$ is reported. The micropolar model matches with a good quality with the discrete system trend, whereas the classical model is not able to reproduce the response, there is no growth of the displacement values with the time increment.

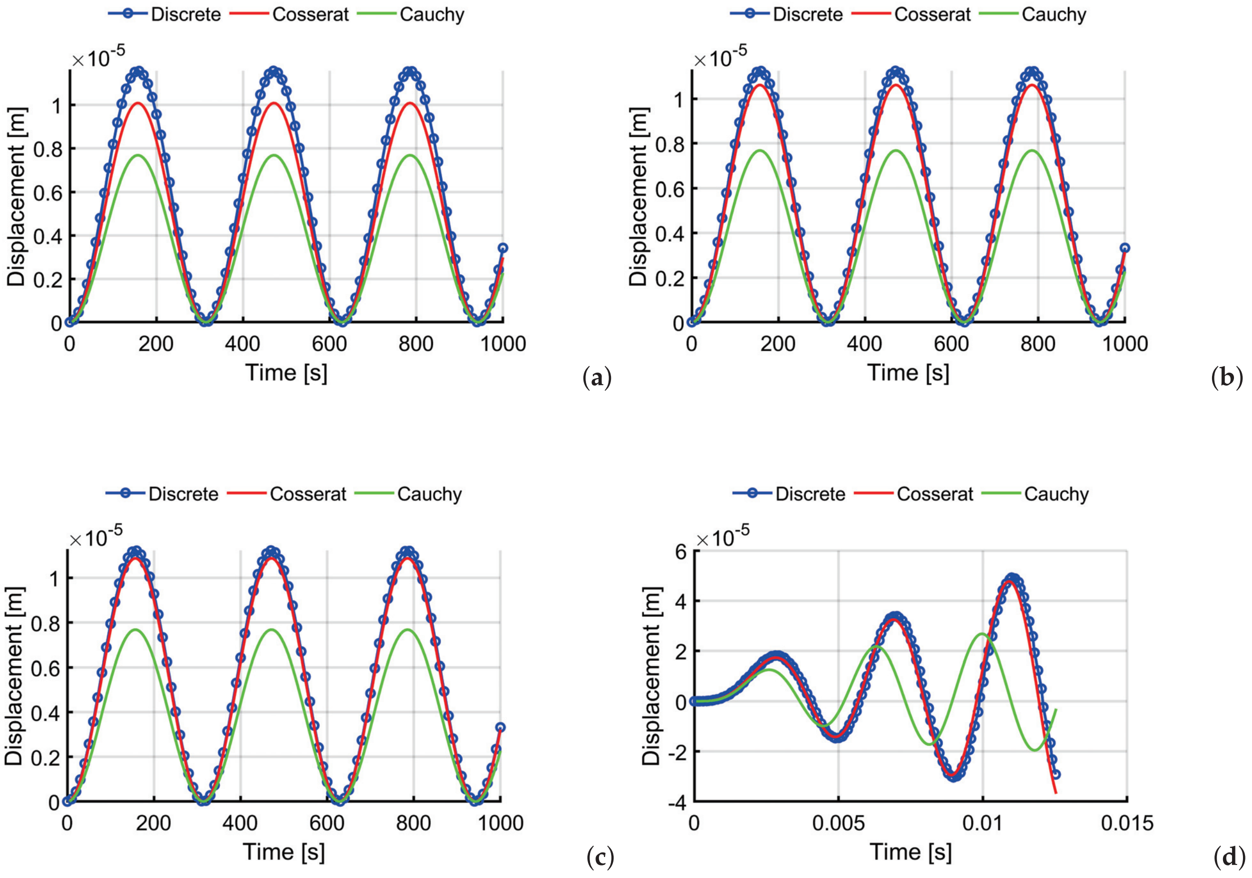

(**a**) (**b**) (**c**) (**d**)

**Figure 4.** Time-history analysis for texture 1: horizontal displacements for the three texture scales (**a**) $s = 1$ (**b**) $s = 0.5$ (**c**) $s = 0.25$ (load case 1) (**d**) mechanical resonance for the scale $s = 0.5$ (load case 2).

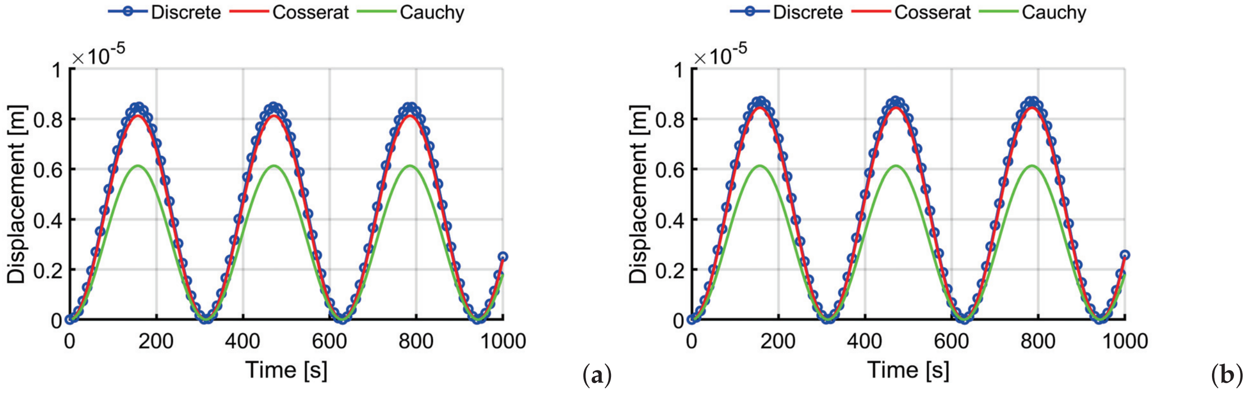

(**a**) (**b**)

**Figure 5.** *Cont.*

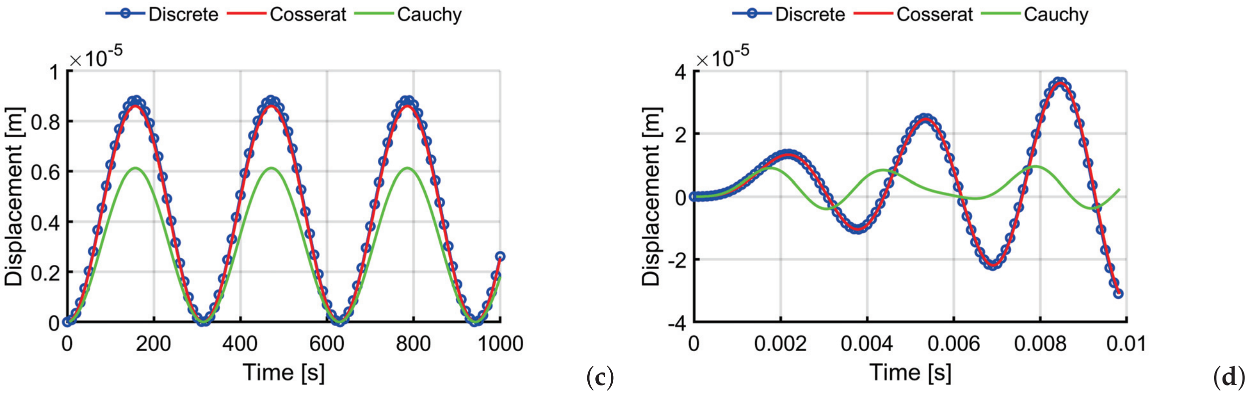

**Figure 5.** Time-history analysis for texture 2: horizontal displacements for the three texture scales (**a**) $s = 1$; (**b**) $s = 0.5$; (**c**) $s = 0.25$ (load case 1); (**d**) mechanical resonance for the scale $s = 0.5$ (load case 2).

## 6. Conclusions

This work investigates the dynamic response of particle composites with two different rectangular textures of the microstructure at three different scales. The usefulness of using continuous models for the representation of a complex material is well known, however, the goodness of the results strongly depends on the continuum theory adopted: the numerical analyses prove that the Cauchy continuum is not sufficient to describe the mechanical behavior of microstructured materials, for both textures and for all scales. On the other hand, the Cosserat model, which takes into account the scale effect, is accurate enough to reproduce the response of the discrete system, assumed as the benchmark of the problem, not only in static condition, but even under dynamic forced oscillations. Moreover, in the case of mechanical resonance, the differences are more noticeable: the micropolar continuum showed itself to be always reliable, whereas for the classical model a delay of the response is shown for texture 1 and the tendency of a mechanical system to respond at greater amplitude when the frequency of its oscillations matches the system natural frequency of vibration is completely missed for texture 2. The significant mechanical response discrepancy, between the classical and the micropolar model, may be related to the fact that for this microstructure, two blocks of different sizes were considered and the internal length plays an important role. Since the off-diagonal terms ($D_{12}$ and $D_{21}$) are non-zero, the micropolar contribution is remarkable, as seen for anisotropic materials, and this explains the major differences with the Cauchy model. Classical theory is not accurate enough to properly describe materials where the internal length has a prominent influence such as masonry, even if the simulations are limited to the elastic case only. In view of all these further analyses, which have not yet been addressed by the authors, new research will be conducted, considering nonlinear mechanical conditions such as crack and damage, as well as structural damping, for a more complete and exhaustive analysis of microstructured materials. Combining these last results with earlier analyses, it can be acknowledged that the Cosserat continuum is able to properly describe the response of the discrete system which is assumed as a micromodel for masonry-like systems.

**Author Contributions:** Conceptualization, N.F. and P.T.; methodology, N.F. and P.T.; software, N.F. and P.T.; validation, M.C. and N.F.; formal analysis, M.C.; investigation, M.C.; resources, P.T.; data curation, M.C.; writing—original draft preparation, M.C.; writing—and editing, M.C., reviewing P.T., N.F.; visualization, N.F. and P.T.; supervision, N.F. and P.T.; project administration, P.T.; funding acquisition, P.T. All authors have read and agreed to the published version of the manuscript.

**Funding:** This study is supported by: Italian Ministry of University and Research PRIN 2017, project No. 2017HFPKZY (B88D19001130001); Sapienza Research Grants "Progetti Grandi" 2018 (B81G19000060005).

**Institutional Review Board Statement:** Not applicable.

**Informed Consent Statement:** Not applicable.

**Data Availability Statement:** Some or all data, models, or code that support the findings of this study are available from the corresponding author upon reasonable request.

**Conflicts of Interest:** The authors declare no conflict of interest.

## References

1. Sadowski, T.; Samborski, S. Prediction of the mechanical behaviour of porous ceramics using mesomechanical modelling. *Comput. Mater. Sci.* **2003**, *28*, 512–517. [CrossRef]
2. Sadowski, T.; Samborski, S. Development of damage state in porous ceramics under compression. *Comput. Mater. Sci.* **2008**, *43*, 75–81. [CrossRef]
3. Samborski, S.; Sadowski, T. Dynamic fracture toughness of porous ceramics. *J. Am. Ceram. Soc.* **2010**, *93*, 3607–3609. [CrossRef]
4. Postek, E.; Sadowski, T. Assessing the influence of porosity in the deformation of metal–ceramic composites. *Compos. Interfaces* **2011**, *18*, 57–76. [CrossRef]
5. Sadowski, T.; Postek, E.; Denis, C. Stress distribution due to discontinuities in polycrystalline ceramics containing metallic inter-granular layers. *Comput. Mater. Sci.* **2007**, *39*, 230–236. [CrossRef]
6. Sadowski, T.; Marsavina, L. Multiscale modelling of two-phase ceramic matrix composites. *Comput. Mater. Sci.* **2011**, *50*, 1336–1346. [CrossRef]
7. Boniecki, M.; Sadowski, T.; Gołębiewski, P.; Węglarz, H.; Piątkowska, A.; Romaniec, M.; Krzyżak, K.; Łosiewicz, K. Mechanical properties of alumina/zirconia composites. *Ceram. Int.* **2020**, *46*, 1033–1039. [CrossRef]
8. Sadowski, T.; Łosiewicz, K.; Boniecki, M.; Szutkowska, M. Assessment of mechanical properties by nano-and microindentation of alumina/zirconia composites. *Mater. Today Proc.* **2021**, *45*, 4196–4201. [CrossRef]
9. Gatta, C.; Addessi, D.; Vestroni, F. Static and dynamic nonlinear response of masonry walls. *Int. J. Solids Struct.* **2018**, *155*, 291–303. [CrossRef]
10. Addessi, D.; Sacco, E. Enriched plane state formulation for nonlinear homogenization of in-plane masonry wall. *Meccanica* **2016**, *51*, 2891–2907. [CrossRef]
11. Addessi, D.; Sacco, E. Homogenization of heterogeneous masonry beams. *Meccanica* **2018**, *53*, 1699–1717. [CrossRef]
12. Baggio, C.; Trovalusci, P. Collapse behaviour of three-dimensional brick-block systems using non-linear programming. *Struct. Eng. Mech.* **2000**, *10*, 181. [CrossRef]
13. Godio, M.; Stefanou, I.; Sab, K.; Sulem, J.; Sakji, S. A limit analysis approach based on Cosserat continuum for the evaluation of the in-plane strength of discrete media: Application to masonry. *Eur. J. -Mech.-A/Solids* **2017**, *66*, 168–192. [CrossRef]
14. Baraldi, D.; Reccia, E.; Cecchi, A. In plane loaded masonry walls: DEM and FEM/DEM models. A critical review. *Meccanica* **2018**, *53*, 1613–1628. [CrossRef]
15. Reccia, E.; Leonetti, L.; Trovalusci, P.; Cecchi, A. A multiscale/multidomain model for the failure analysis of masonry walls: A validation with a combined FEM/DEM approach. *Int. J. Multiscale Comput. Eng.* **2018**, *16*, 325–343. [CrossRef]
16. Pepe, M.; Pingaro, M.; Trovalusci, P.; Reccia, E.; Leonetti, L. Micromodels for the in-plane failure analysis of masonry walls: Limit Analysis, FEM and FEM/DEM approaches. *Frat. Integrità Strutt.* **2020**, *14*, 504–516. [CrossRef]
17. Trovalusci, P.; Ostoja-Starzewski, M. Multiscale mechanical modelling of complex materials and engineering applications 2. *Int. J. Multiscale Comput. Eng.* **2011**, *9*, vii–ix. [CrossRef]
18. Sadowski, T.; Trovalusci, P.; Schrefler, B.; de Borst, R. Multi-scale and multi-physics modelling for complex materials. *Meccanica* **2014**, *49*, 2549–2550. [CrossRef]
19. Altenbach, H.; Sadowski, T. *Failure and Damage Analysis of Advanced Materials*; Springer: Berlin/Heidelberg, Germany, 2015.
20. Greco, F.; Leonetti, L.; Luciano, R.; Blasi, P.N. Effects of microfracture and contact induced instabilities on the macroscopic response of finitely deformed elastic composites. *Compos. Part Eng.* **2016**, *107*, 233–253. [CrossRef]
21. De Borst, R. Simulation of Strain Localization: A Reappraisal of the Cosserat Continuum. *Eng. Comp.* **1991**, *8*, 317–332. [CrossRef]
22. Sluys, L.; De Borst, R.; Mühlhaus, H.B. Wave propagation, localization and dispersion in a gradient-dependent medium. *Int. J. Solids Struct.* **1993**, *30*, 1153–1171. [CrossRef]
23. Masiani, R.; Rizzi, N.; Trovalusci, P. Masonry as structured continuum. *Meccanica* **1995**, *30*, 673–683. [CrossRef]
24. Masiani, R.; Trovalusci, P. Cosserat and Cauchy materials as continuum models of brick masonry. *Meccanica* **1996**, *31*, 421–432. [CrossRef]
25. Trovalusci, P.; Masiani, R. Material symmetries of micropolar continua equivalent to lattices. *Int. J. Solids Struct.* **1999**, *36*, 2091–2108. [CrossRef]
26. Trovalusci, P.; Masiani, R. A multifield model for blocky materials based on multiscale description. *Int. J. Solids Struct.* **2005**, *42*, 5778–5794. [CrossRef]
27. Pau, A.; Trovalusci, P. Block masonry as equivalent micropolar continua: The role of relative rotations. *Acta Mech.* **2012**, *223*, 1455–1471. [CrossRef]
28. Trovalusci, P.; Pau, A. Derivation of microstructured continua from lattice systems via principle of virtual works: The case of masonry-like materials as micropolar, second gradient and classical continua. *Acta Mech.* **2014**, *225*, 157–177. [CrossRef]

29. Trovalusci, P. Molecular Approaches for Multifield Continua: Origins and current developments. In *Multiscale Modeling of Complex Materials: Phenomenological, Theoretical and Computational Aspects*; Sadowski, T., Trovalusci, P., Eds.; Springer: Vienna, Austria, 2014; pp. 211–278. [CrossRef]
30. Tuna, M.; Trovalusci, P. Scale dependent continuum approaches for discontinuous assemblies: 'Explicit' and 'implicit' non-local models. *Mech. Res. Commun.* **2020**, *103*, 103461. [CrossRef]
31. Tuna, M.; Leonetti, L.; Trovalusci, P.; Kirca, M. 'Explicit' and 'implicit' non-local continuous descriptions for a plate with circular inclusion in tension. *Meccanica* **2020**, *55*, 927–944. [CrossRef]
32. Tuna, M.; Trovalusci, P. Stress distribution around an elliptic hole in a plate with 'implicit' and 'explicit' non-local models. *Compos. Struct.* **2021**, *256*, 113003. [CrossRef]
33. Eringen, A.C. Theory of micropolar elasticity. In *Microcontinuum Field Theories*; Springer: Berlin/Heidelberg, Germany, 1999; pp. 101–248.
34. Uzun, B.; Civalek, Ö. Nonlocal FEM formulation for vibration analysis of nanowires on elastic matrix with different materials. *Math. Comput. Appl.* **2019**, *24*, 38. [CrossRef]
35. Barretta, R.; Luciano, R.; de Sciarra, F.M. A Fully Gradient Model for Euler-Bernoulli Nanobeams. *Math. Probl. Eng.* **2015**, *2015*, 495095. [CrossRef]
36. Čanađija, M.; Barretta, R.; De Sciarra, F.M. A gradient elasticity model of Bernoulli–Euler nanobeams in non-isothermal environments. *Eur. J.-Mech.-A/Solids* **2016**, *55*, 243–255. [CrossRef]
37. Barretta, R.; Faghidian, S.A.; Luciano, R. Longitudinal vibrations of nano-rods by stress-driven integral elasticity. *Mech. Adv. Mater. Struct.* **2019**, *26*, 1307–1315. [CrossRef]
38. Barretta, R.; Marotti de Sciarra, F. A Nonlocal Model for Carbon Nanotubes under Axial Loads. *Adv. Mater. Sci. Eng.* **2013**, *2013*, 1–6. [CrossRef]
39. Eshraghi, I.; Jalali, S.K.; Pugno, N.M. Imperfection sensitivity of nonlinear vibration of curved single-walled carbon nanotubes based on nonlocal timoshenko beam theory. *Materials* **2016**, *9*, 786. [CrossRef]
40. Izadi, R.; Tuna, M.; Trovalusci, P.; Ghavanloo, E. Torsional characteristics of carbon nanotubes: Micropolar elasticity models and molecular dynamics simulation. *Nanomaterials* **2021**, *11*, 453. [CrossRef]
41. Civalek, Ö.; Dastjerdi, S.; Akbaş, Ş.D.; Akgöz, B. Vibration analysis of carbon nanotube-reinforced composite microbeams. *Math. Methods Appl. Sci.* **2021**. [CrossRef]
42. Tocci Monaco, G.; Fantuzzi, N.; Fabbrocino, F.; Luciano, R. Trigonometric solution for the bending analysis of magneto-electro-elastic strain gradient nonlocal nanoplates in hygro-thermal environment. *Mathematics* **2021**, *9*, 567. [CrossRef]
43. Akbaş, Ş.D.; Ersoy, H.; Akgöz, B.; Civalek, Ö. Dynamic Analysis of a Fiber-Reinforced Composite Beam under a Moving Load by the Ritz Method. *Mathematics* **2021**, *9*, 1048. [CrossRef]
44. Addessi, D. A 2D Cosserat finite element based on a damage-plastic model for brittle materials. *Comput. Struct.* **2014**, *135*, 20–31. [CrossRef]
45. Bacciocchi, M.; Tarantino, A. Natural Frequency Analysis of Functionally Graded Orthotropic Cross-Ply Plates Based on the Finite Element Method. *Math. Comput. Appl.* **2019**, *24*, 52. [CrossRef]
46. Capecchi, D.; Ruta, G.; Trovalusci, P. Voigt and Poincaré's mechanistic–energetic approaches to linear elasticity and suggestions for multiscale modelling. *Arch. Appl. Mech.* **2011**, *81*, 1573–1584. [CrossRef]
47. Colatosti, M.; Fantuzzi, N.; Trovalusci, P. Dynamic Characterization of Microstructured Materials Made of Hexagonal-Shape Particles with Elastic Interfaces. *Nanomaterials* **2021**, *11*, 1781. [CrossRef] [PubMed]
48. Colatosti, M.; Fantuzzi, N.; Trovalusci, P.; Masiani, R. New insights on homogenization for hexagonal-shaped composites as Cosserat continua. *Meccanica* **2021**. [CrossRef]
49. Fantuzzi, N.; Trovalusci, P.; Luciano, R. Material Symmetries in Homogenized Hexagonal-Shaped Composites as Cosserat Continua. *Symmetry* **2020**, *12*, 441. [CrossRef]
50. Ferreira, A.; Fantuzzi, N. *MATLAB Codes for Finite Element Analysis 2nd Edition: Solids and Structures*; Springer: Berlin/Heidelberg, Germany, 2020.
51. Newmark, N.M. A method of computation for structural dynamics. *J. Eng. Mech. Div.* **1959**, *85*, 67–94. [CrossRef]
52. Fantuzzi, N.; Trovalusci, P.; Luciano, R. Multiscale analysis of anisotropic materials with hexagonal microstructure as micropolar continua. *Int. J. Multiscale Comput. Eng.* **2020**, *18*, 265–284. [CrossRef]

materials

MDPI

*Article*

# Analysis of Fiber-Reinforced Concrete Slabs under Centric and Eccentric Load

**Zuzana Marcalikova [1,*], Vlastimil Bilek [2], Oldrich Sucharda [2] and Radim Cajka [1]**

[1] Department of Structures, Faculty of Civil Engineering, VSB-Technical University of Ostrava, Ludvíka Podéště 1875/17, 708 00 Ostrava, Czech Republic; radim.cajka@vsb.cz

[2] Department of Building Materials and Diagnostics of Structures, Faculty of Civil Engineering, VSB-Technical University of Ostrava, Ludvíka Podéště 1875/17, 708 00 Ostrava, Czech Republic; vlastimil.bilek@vsb.cz (V.B.); oldrich.sucharda@vsb.cz (O.S.)

* Correspondence: zuzana.marcalikova@vsb.cz; Tel.: +42-059-732-1396

**Abstract:** Research on the interaction between slabs and subsoil involves the field of materials engineering, concrete structures, and geotechnics. In the vast majority of cases, research focuses on only one of these areas, whereas for advanced study and computer simulations, detailed knowledge of the whole task is required. Among the new knowledge and information upon which this article focuses is the evaluation of subsoil stress using specialized pressure cells, along with detailed measurements of the deformation of a fiber-reinforced concrete slab. From a design point of view, this research is focused on the issue of the center of the cross section and the influence of eccentricity. Knowledge in this area is not yet comprehensively available for fiber-reinforced concrete slabs, where 2D deformation sections of the slab and 3D deformation surfaces of the slab are used in experiments. The experimental program includes a centrically and eccentrically loaded slab. These are structural elements that were tested on a specialized device. Both slabs had the same concrete recipe, with a dispersed reinforcement content of 25 kg/m$^3$. The dimensions of the slab were 2000 × 2000 × 150 mm. Laboratory tests assessed compressive strength, the modulus of elasticity, splitting tensile strength, and bending tensile strength. Based on approximate data from the 3D deformation surfaces, an evaluation of the load-displacement diagrams for the center of the slab and for the center of eccentricity was performed. In conclusion, an overall evaluation and discussion of the results relies on experiments and the mechanical properties of fiber-reinforced concrete.

**Keywords:** soil-structure interaction; fibers; fiber-reinforced concrete; slab; subsoil; experiments; mechanical properties

## 1. Introduction

One of the most used building materials is concrete [1,2]. However, current design codes and recommendations focus mainly on its basic mechanical properties. These include good compressive strength [3], modulus of elasticity, and, to a limited extent, tensile strength. However, more detailed analysis requires a comprehensive description based, for example, on the use of fracture mechanics [4]. Optimization of a specific concrete recipe is also often addressed [5,6]. Unfortunately, low tensile strength is a characteristic of concrete [7]. For this reason, one must reinforce concrete [8,9]. Reinforced concrete has significantly better tensile strength due to the use of steel and other materials [10,11]. However, the major disadvantage of reinforced concrete structures is the hard work required to make them, as it is necessary to ensure the correct position of the concrete reinforcement, sufficient coverage of the concrete reinforcement, the interaction of the concrete reinforcement and the concrete, and the requirements that arise for the reinforcement bond.

A variant of concrete where these specifics disappear is so-called fiber-reinforced concrete [12–15]. By inserting dispersed reinforcement into concrete, tensile strength is increased [13,16–19]. It is possible to choose both the size of the fiber dosing and the type/shape of the fibers themselves, which is important to ensure cohesion between concrete and dispersed reinforcement, where the shape of the fiber itself also has a significant effect on the residual tensile strength of concrete and a shape load–displacement diagram [12–19]. Inverse analysis and identification [20,21] can be used for a comprehensive description of the mechanical properties of fiber-reinforced concrete. Steel fiber can also have an effect on concrete abrasion resistance [22].

From the abovementioned works, the significant potential of fiber-reinforced concrete as a construction material for load-bearing structures is evident [12–21]. However, the many fiber-reinforced concrete variants that can be produced complicates its application. A suitable application often leads to an individual fiber-reinforced concrete recipe. The remaining issue is with the determination of a comprehensive description of the mechanical properties. There are a number of test variants, especially for determining tensile strength. With regard to the analyzed and presented works, a comprehensive experimental laboratory program was designed for the experimental program in Figure 1, focused mainly on comparative tests of three- and four-point bending tests.

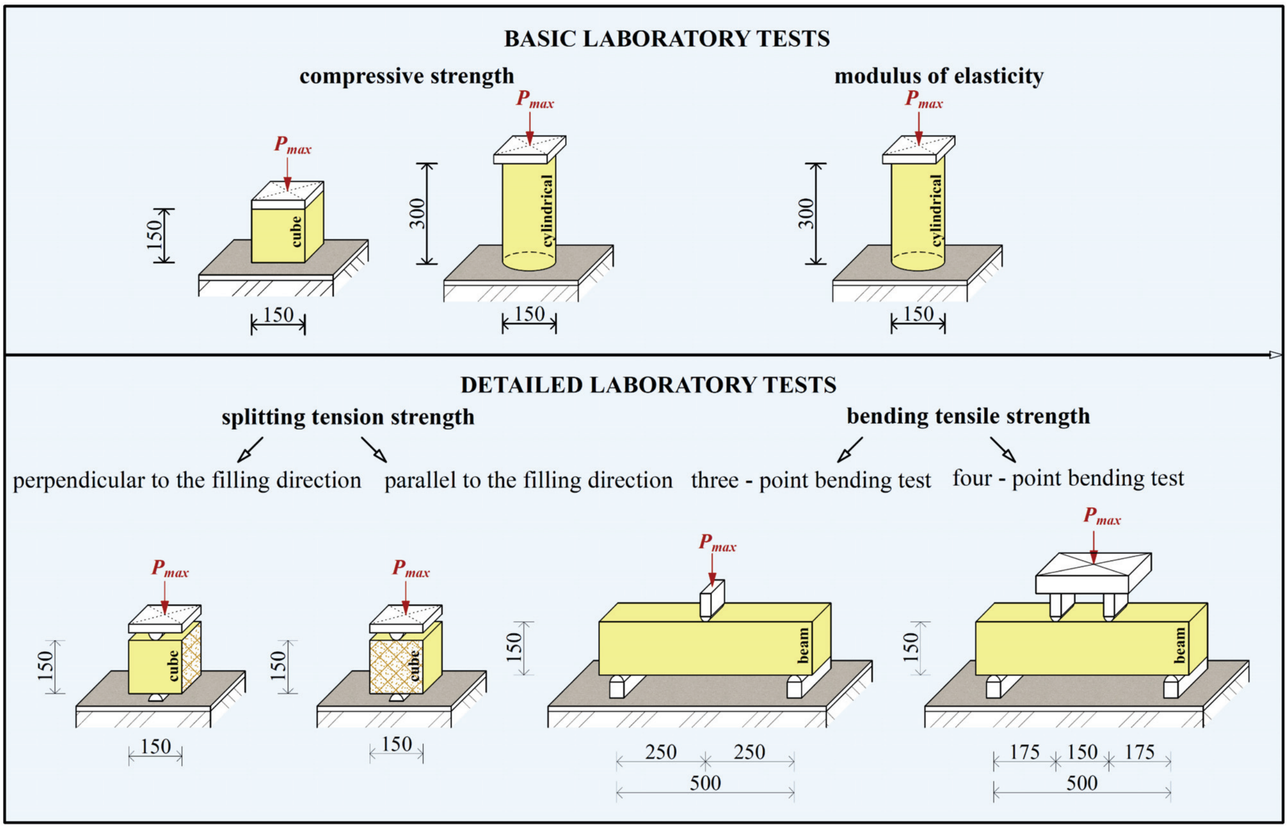

**Figure 1.** Set of laboratory tests performed.

One of the possible uses of fiber-reinforced concrete in construction is in foundation structures and floors [23–26]. Very interesting experiments in [23] deal in detail with selected tests of slabs and their collapse. However, slab tests are only performed with a limited laboratory simulation of the subsoil, when it is not possible, for example, to determine the active depth in more detail. The laboratory program for mechanical properties is also performed in the basic scope. One interesting experiment with slabs in interaction with subsoil is presented in [24]. The tests were performed for dosages of 20 and 30 kg/m$^3$. The experiments in [23–26] had a greater number of test variants, but were not focused on eccentric loading or monitoring of subsoil stress. The effect of the eccentric load on the slab in interaction with the subsoil is illustrated in Figure 2. The course of deformations is very different. The difference between the slab with centric and eccentric loads is also evident from Figure 3. Figure 3 also shows the size of the pressed and drawn cross-sectional area.

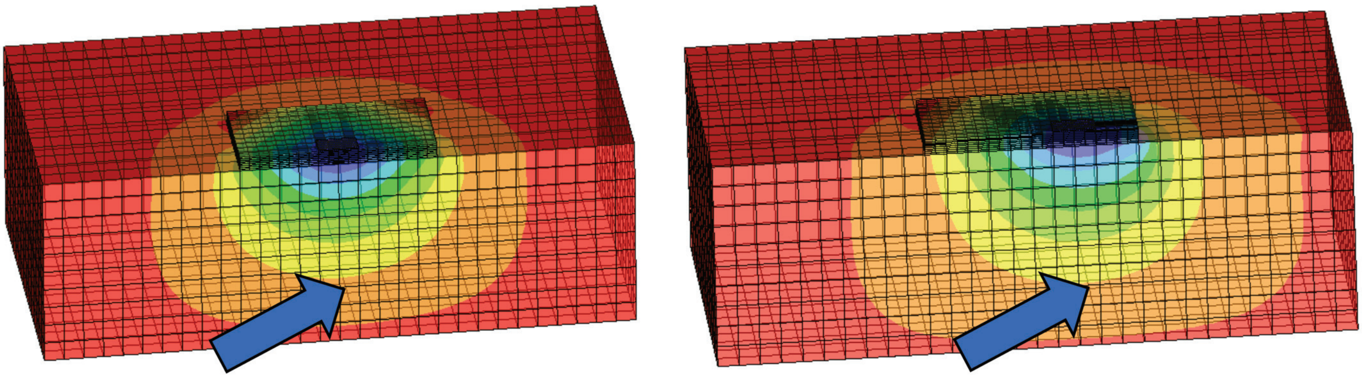

(**a**) (**b**)

**Figure 2.** Deformations for slab: (**a**) centrically loaded slab; (**b**) eccentrically loaded slab.

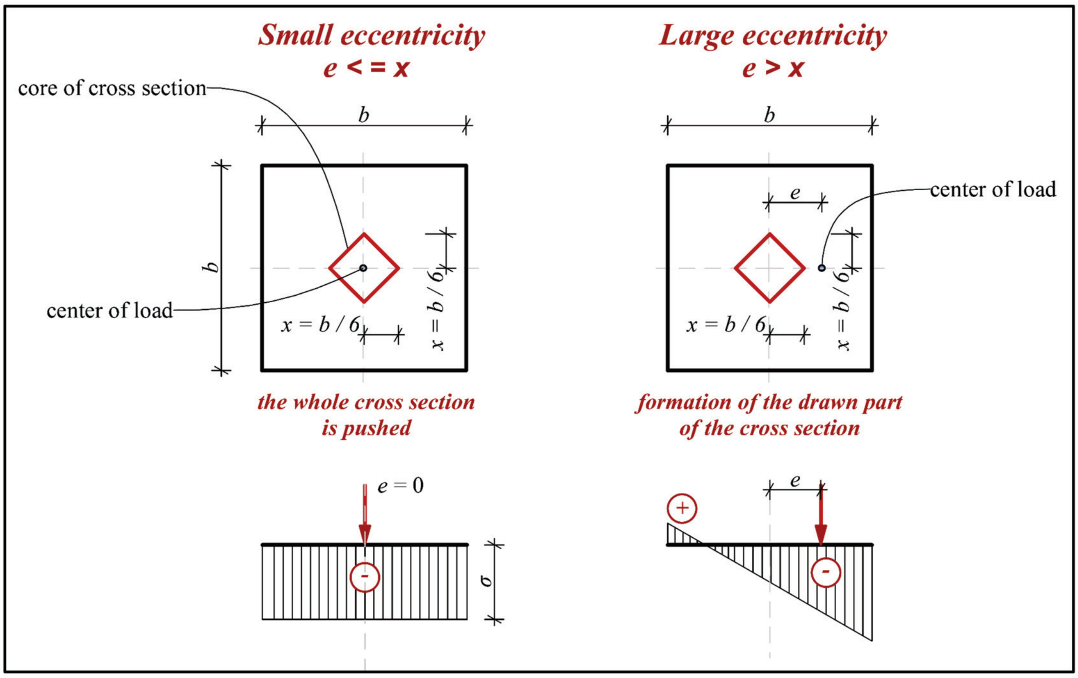

**Figure 3.** Core of cross section of slab ($e$ = eccentricity; $b$ = size of slab; $x$ = the distance of the load to the center of the slab.

Therefore, part of this research focuses on the laboratory testing of fiber-reinforced concrete to determine its mechanical properties, while another part of the research focuses on the experimental testing of fiber-reinforced concrete slabs to evaluate their behavior when exposed to the environmental effects of loading. This research builds on previous experiments on slabs in interaction with subsoil using numerical modeling [27,28]. The newly selected and presented research plan was conceived for significantly different subsoil, and the effect of load eccentricity on the overall course of deformations was also tested. It is also very important to expand the measurement and evaluation of specialized pressure cells in the subsoil.

In the case of solved tasks, it is necessary to take into account, among other things, the influence of the subsoil itself and the interactions between the foundation and the subsoil and between the structure and the foundation; we call such a task SSI (soil–

structure interaction). For this reason, it is also very important to determine the type of subsoil, e.g., by using a geological profile, where the individual subsoil layers and their mechanical properties, such as stiffness (rigid or flexible subsoil) and cohesion, are visible [29]. It is good to know the mechanical properties of the subsoil to a depth where the significant effect of external loads is evident, often referred to as the depth of the deformation zone. In case of unsuitable subsoil, it is possible to replace the subsoil via so-called subsoil homogenization. Determining the stiffness of the foundation also affects the overall behavior and interaction. Much attention is given to said area of slab experiments in interaction with the subsoil [30–37] and to numerical modeling [38,39]. However, detailed numerical modeling based on a non-linear analysis requires a comprehensive description of mechanical properties and the execution of full-scale experiments so that the results are of sufficient value. However, a large number of the listed experiments are devoted to concrete or reinforced concrete, and the behavior of fiber-reinforced concrete is significantly different than that of non-reinforced concrete.

The methodology and experimental program of research area were determined on the basis of current design-code approaches in the field of geotechnics [40] and concrete structures, which are based on the recommendations of the Model Code 1990 [1]. The Model Code 2010 [2] recommendation was also created by the wider application of concrete and its new variants. The summary information was used to design experiments that focused on the overall understanding of the problem of slab interaction with the subsoil. The test-specialized loading equipment Stand was designed especially for the resolution of the mentioned problem [41].

The presented research, as already mentioned, deals with the determination of the mechanical properties of fiber-reinforced concrete on the basis of laboratory testing and experimental testing of fiber-reinforced concrete slabs. Basic tests to determine the compressive strength and modulus of elasticity, as well as detailed tests to determine tensile strength, have been performed [42–45]. The set of basic and specialized tests is shown in Figure 1. The mechanical properties of concrete are also addressed [46–51]. However, in the case of fiber-reinforced concrete, it is more appropriate to perform our own specialized tests, where the above recommendations and standards cannot simply be modified for fiber-reinforced concrete.

Experimental testing of fiber-reinforced concrete slabs was carried out at the Faculty of Civil Engineering, VSB—Technical University of Ostrava, Czech Republic, where there is specialized loading equipment called Stand (Figure 4). It is possible to apply have a load of up to 1000 kN tested by the equipment, and it is connected to a universal bus system for measuring deformations and load forces. It is also possible to change the position of the slab load arbitrarily in one direction by means of a movable device mounted on the stand and a hydraulic press.

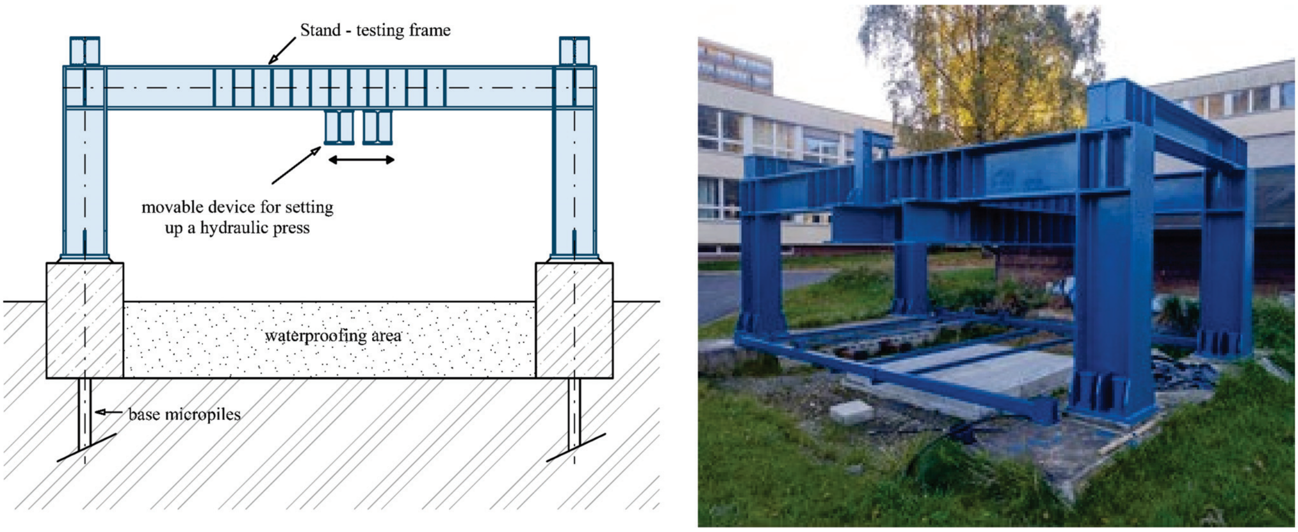

**Figure 4.** Specialized loading equipment Stand.

## 2. Experimental Program

Transport concrete was used for the production of slabs and laboratory samples, where the recipe and the content of individual components in the concrete mixture are given in Table 1. The concrete was reinforced with Dramix® 3D 65/60 BG fibers [52] with a dosage of 25 kg/m$^3$. The basic mechanical characteristics of the fibers are given in Table 2. The fibers have so-called end bends to ensure better cohesion with the concrete. The fibers are shown in Figure 5.

**Table 1.** Material properties of concrete for laboratory samples and slabs.

| **Concrete** | **Consistency** | **Cement** | **Min. Cement Content** | **Water–Cement Ratio: *v/c*** | **Aggregates 0/4 (Mined)** | **Aggregates 4/8 (Mined)** | **Aggregates 8/16 (Mined)** | **Water** | **Plasticizer** |
|---|---|---|---|---|---|---|---|---|---|
| Quantity per m$^3$ of concrete | S3 | CEM I 42.5 R | 300 kg | 0.6 | 870 kg | 150 kg | 820 kg | 189 l | 2.9 l |
| Quantity in % | - | - | 12.9% | - | 37.3% | 6.4% | 35.2% | 8.1% | 0.1% |

**Table 2.** Material properties of Dramix® 3D 65/60 BG.

| | |
|---|---|
| Fiber shape | Hooked ends |
| Bundling | Glued |
| Length (mm) | 60 |
| Diameter (mm) | 0.9 |
| Aspect ratio | 67 |
| Tensile strength (N/mm$^2$) | 1160 |
| Effect on consistence (s) | 8 |
| Effect on strength of concrete (kg/m$^3$) | 15 |
| Modulus of elasticity (GPa) | 200 |

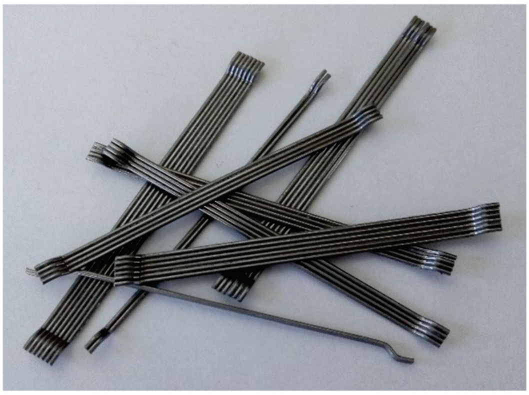

**Figure 5.** Fiber Dramix® 3D 65/60 BG.

The laboratory program included tests of samples to determine the compressive strength, modulus of elasticity, splitting tensile strength, and bending tensile strength [42–45]. Compressive strength was determined on cubes ($f_{c,\ cube}$) measuring 150 × 150 × 150 mm and on cylinders ($f_{c,\ cyl}$) with a diameter of 50 mm and a height of 300 mm. The test scheme is shown in Figure 1.

Very important properties also include tensile strength, which was determined by the splitting tensile test and the bending tensile strength test. Two sample loading variants were selected for the split tensile test. The first variant was for testing the splitting tensile strength perpendicular to the direction of filling. The second variant was for testing the splitting tensile strength parallel to the direction of filling. The schema is shown in

Figure 1. The splitting tensile strength was then determined according to the following equation [44]:

$$f_{ct,sp} = \frac{2 \cdot F}{\pi \cdot l \cdot d}, \tag{1}$$

where $F$ is the maximum load at failure of the sample, $l$ is the length of the line of contact, and $d$ is the transverse dimension of the body.

An alternative for determining tensile strength is a bending tensile test. The scheme and dimensions of the samples for both types of tests are shown in Figure 1. The span between the supports was 500 mm for both types of tests. Bending tensile strength can be determined according to the following equations:

- Three-point bending test [43]:

$$f_{c,fl,3B} = \frac{3 \cdot F \cdot L}{2 \cdot b \cdot h^2} \tag{2}$$

- Four-point bending test:

$$f_{c,fl,4B} = \frac{6 \cdot F \cdot e}{2 \cdot b \cdot h^2} \tag{3}$$

where $F$ is the maximum failure load of the sample, $L$ is the span, $b$ and $h$ are the transverse dimensions of the specimen, and $e$ is the distance between the support and the force.

From the test record, evaluations of the load–displacement diagrams for the three-point and four-point test were also performed; the diagrams are shown in Figure 6.

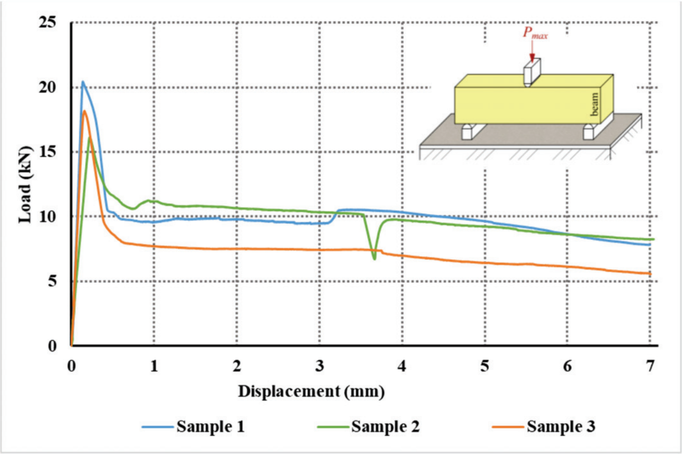

(**a**)

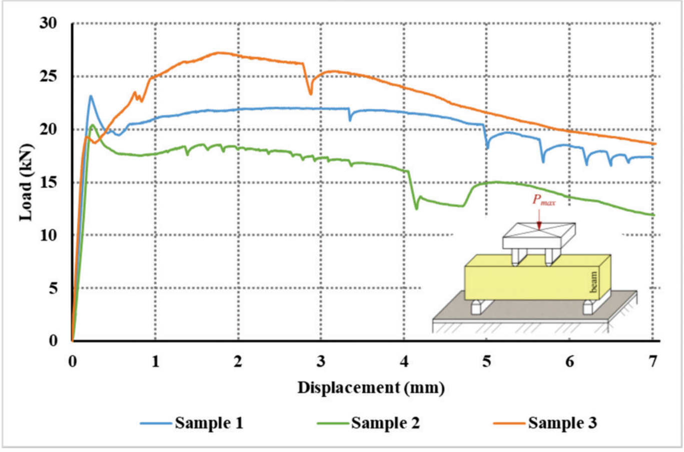

(**b**)

**Figure 6.** Load–displacement diagrams for: (**a**) three-point bending test; (**b**) four-point bending test.

In the case of a three-point bending test, the load–displacement curves are very similar. After the initialization of the crack, the load will decrease significantly to about 50–60% of the maximum load. The load gradually decreases with the development and opening of the crack. In the test, the crack was close to the load, i.e., at the point of maximum bending moment. In the four-point bending test, the results differ. In one of the selected tests, there was even tensile strengthening. In a four-point test, the location of the crack is not predefined. A crack can and did form between the loading forces. Gradually, the load decreased, and a crack opened up and increased deformations.

Based on all laboratory tests, the mechanical properties of fiber-reinforced concrete were determined, with the average values given in Table 3. The average cubic compressive strength of concrete was 24 MPa and the average cylindrical compressive strength was 20.5 MPa. The conversion coefficient between the cylindrical compressive strength, $f_{c,\,cyl}$, and the cubic compressive strength, $f_{c,\,cube}$, can be expressed as a mutual ratio of their values. The average value of this coefficient is 0.85, where this is the usual value. The split tensile strength was approximately 1/10 of the cylindrical strength. This is also the usual ratio.

**Table 3.** Strengths of fiber-reinforced concrete determined from laboratory tests.

| Type of Test | Number of Samples (pcs) | Min. (MPa/GPa) | Max. (MPa/GPa) | Average (MPa/GPa) | Coefficient of Variation (%) |
|---|---|---|---|---|---|
| Compressive strength—cube | 12 | 21.0 | 28.3 | 24.0 | 11.5 |
| Compressive strength—cylindrical | 11 | 18.6 | 22.9 | 20.5 | 8.2 |
| Splitting tensile strength—perpendicular to the filling direction | 12 | 1.8 | 2.5 | 2.2 | 9.5 |
| Splitting tensile strength—parallel to the filling direction | 12 | 1.4 | 2.2 | 1.8 | 15.0 |
| Modulus of elasticity | 5 | 17.0 | 23.0 | 20.3 | 13.7 |
| Three-point bending test | 5 | 3.5 | 4.4 | 4.0 | 8.0 |
| Four-point bending test | 4 | 3.1 | 4.1 | 3.7 | 13.0 |

A comparison was performed by conversion to uniaxial tensile strength. It is also possible to determine the value of the uniaxial tensile strength from the splitting tensile test as follows:

$$f_{ct} = f_{ct,sp} \tag{4}$$

or by conversion from a bending tensile test using the following equation:

$$f_{ct} = \frac{f_{ct,fl}}{1.65} \tag{5}$$

Figure 7 shows the recalculated values of uniaxial tensile strength. From the splitting tensile test, the value of uniaxial tensile strength was determined to be 2.17 MPa and 2.43 MPa and 2.23 MPa for the three- and four-point bending tests, respectively. The differences between the four-point test and the splitting tensile test are very small. On the other hand, for the three-point bending test, the tensile strengths are slightly higher.

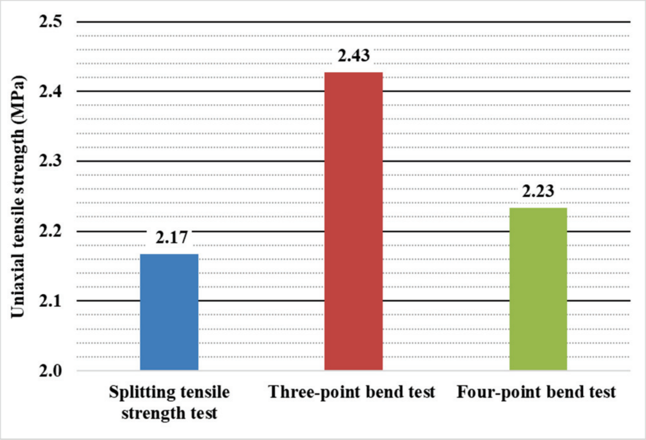

**Figure 7.** Uniaxial tensile strength for individual types of tests.

Furthermore, the functional dependence of the splitting tensile strength (perpendicular to the filling direction) and the bulk density was determined, as shown in Figure 8. The resulting functional dependence is:

$$\rho = 114.35 \cdot f_{ct,sp} + 1976.5. \tag{6}$$

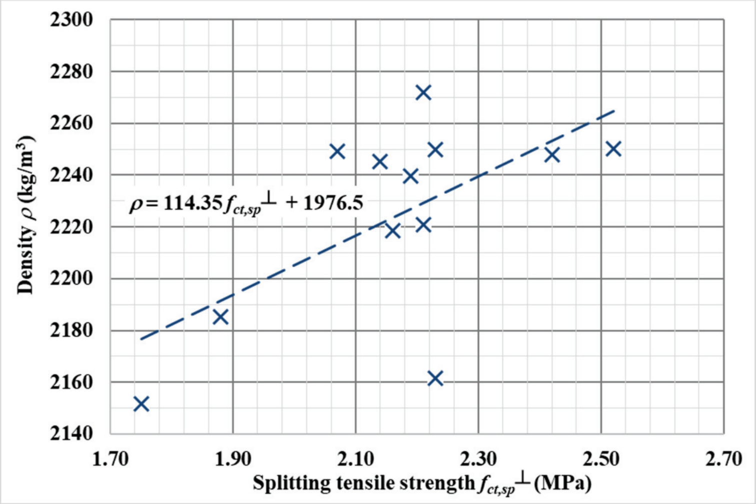

**Figure 8.** Functional dependence of splitting tensile strength (perpendicular to the filling direction) on density.

It is clear from Figure 8 that with a higher bulk density of concrete, the split tensile strength also increases. It can be assumed that the bulk density is affected by the larger proportion of steel fibers.

## 3. Parameters of Subsoil

Among other things, the parameters of the subsoil are also very important in slab experiments. In tests of slabs in interaction with the subsoil, soil was used that, before compaction, had the character of incoherent soil (approx. 55% sand, 15% gravel, and 30% clay). This soil can be globally classified, according to the already invalid standard CSN 731001 [53], as clayey sand SC (S5). The subsoil also had the characteristics given in Tables 4 and 5. The modulus of deformation of the subsoil was calculated on the basis of the following equation [54]:

$$E_{def} = \frac{1.5 \cdot r}{(a_1 + a_2 \cdot p_{max})} \tag{7}$$

where $r$ is the radius of the load plate (150 mm), $a_1$ and $a_2$ are the constants of the 2nd degree polynomial corresponding to the stress dependence of the plate loading (Figure 9), and $p_{max}$ is the maximum contact stress, i.e., 0.3 MPa.

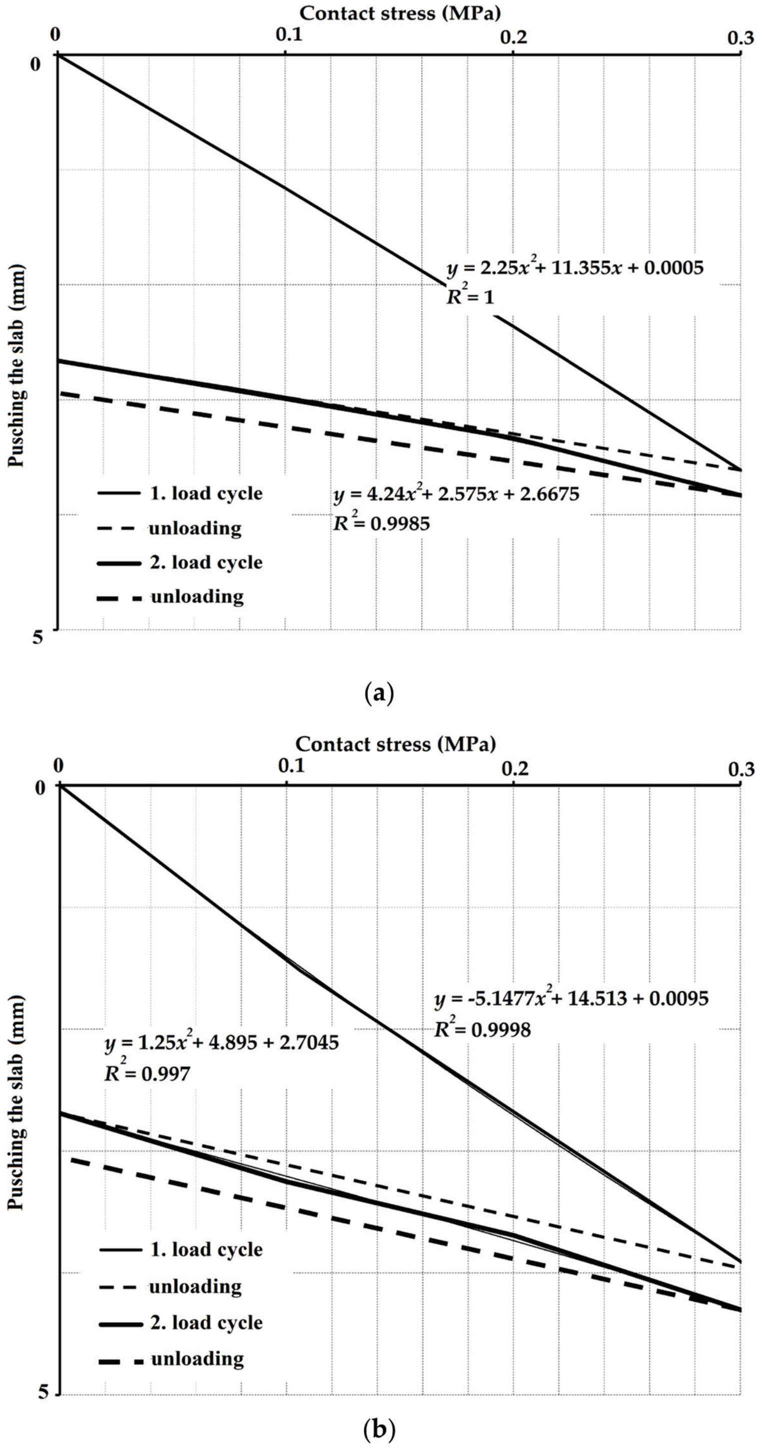

(**a**)

(**b**)

**Figure 9.** Dependence of pushing the slab on contact stress—hysteresis loops: (**a**) before concreting the centrically loaded slab G10, $e$ = 1.50 m; (**b**) before concreting the centrically loaded slab G10, $e$ = 0.75.

**Table 4.** Modulus of deformation—subsoil.

| Modulus of Deformation (MPa) | Place of Measurement | First Load Cycle $E_{def,1}$ | Second Load Cycle $E_{def,2}$ |
|---|---|---|---|
| Centrically loaded slab G10—before concreting the slab | $e$ = 1.50 m | 18.7 | 58.4 |
| Centrically loaded slab G10—before concreting the slab | $e$ = 0.75 m | 17.3 | 42.7 |
| Average | - | 18.0 | 50.55 |
| Eccentrically loaded slab G11—after the test | $e$ = 0.50 m | 16.6 | 32.6 |
| Eccentrically loaded slab G11—after the test | $e$ = 1.75 m (outside of slab) | 18.3 | 42.8 |
| Average | - | 17.45 | 37.7 |

**Table 5.** Soil properties.

| **Physical Characteristics** | | | |
|---|---|---|---|
| **Characteristics of Subsoil** | **Sample 1** | **Sample 2** | **Average** |
| Bulk density of soil in natural storage $\gamma_{\mathrm{i}}$ (kN/m$^3$) | 22.1 | 21.4 | 21.75 |
| Bulk density of dried soil $\gamma_{d,i}$ (kN/m$^3$) | 20.1 | 19.3 | 19.70 |
| Humidity $w_i$ (%) | 10.0 | 10.9 | 10.45 |
| Specific gravity of the skeleton using a pycnometer $\gamma_{\mathrm{s,i}}$ (kN/m$^3$) | | 25.71 | |
| **Strength characteristics** | | | |
| Cohesion $c$ (kPa) | | 0 | |
| Angle of internal friction $\varphi$ (°) | | 34.4 | |

When setting the modulus of deformation of the subsoil, it is appropriate to determine the $E_{def,2}/E_{def,1}$ ratio. In the case of pre-experiment measurements, the ratio of modulus of deformation averaged 2.8. From the above, it can be assumed that the soil has a relatively large deformation capacity. The modulus of deformation ratio determined after the tests decreased to 2.1. The measurement results also show that $E_{def,1}$ is very similar before and after the tests and is in the range of 16–19 MPa. The differences for the modulus of deformation $E_{def,2}$ are more pronounced, in the range of 32–58 MPa.

To determine the physical and descriptive characteristics of the soil, two samples were taken at different places under the base slab. The strength characteristics were determined on a reconstituted 100% sample on a box shear device (sample size: 100 × 100 × 20 mm).

## 4. Testing Equipment and Measurement

The experimental tests consisted of two fiber-reinforced concrete slabs that differed in the position of the load. The first slab, G10, was loaded in its center, so it was a centrically loaded slab (Figure 10a).

In the case of the eccentrically loaded slab G11, the position of the load was situated 400 mm from the center of the slab, i.e., it was an eccentrically loaded slab G11 (Figure 10b). Both fiber-reinforced concrete slabs had dimensions of 2000 × 2000 × 150 mm and were concreted into steel formwork. During the test, a constant increase in load was made possible by means of a hydraulic press. The loading of the slabs was performed in loading steps of 75 kN until complete collapse. Each loading step was performed after 30 min. To ensure load distribution, the hydraulic press was mounted on a steel plate measuring 400 × 400 mm. Sensor-layout schemata for a given type of slab are shown in Figure 11a,b. A total of 24 track sensors were installed.

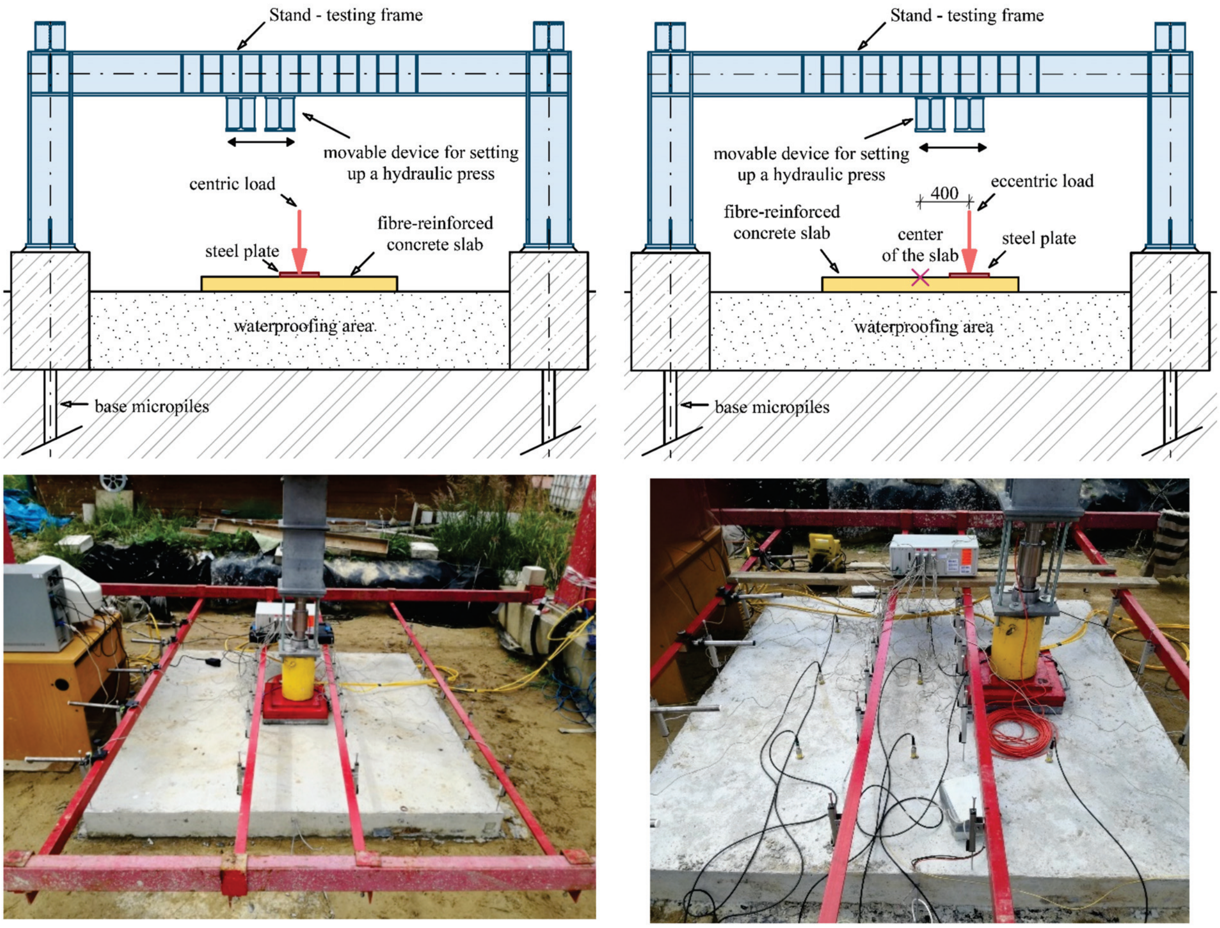

(**a**) (**b**)

**Figure 10.** Slab: (**a**) centrically loaded slab G10; (**b**) eccentrically loaded slab G11.

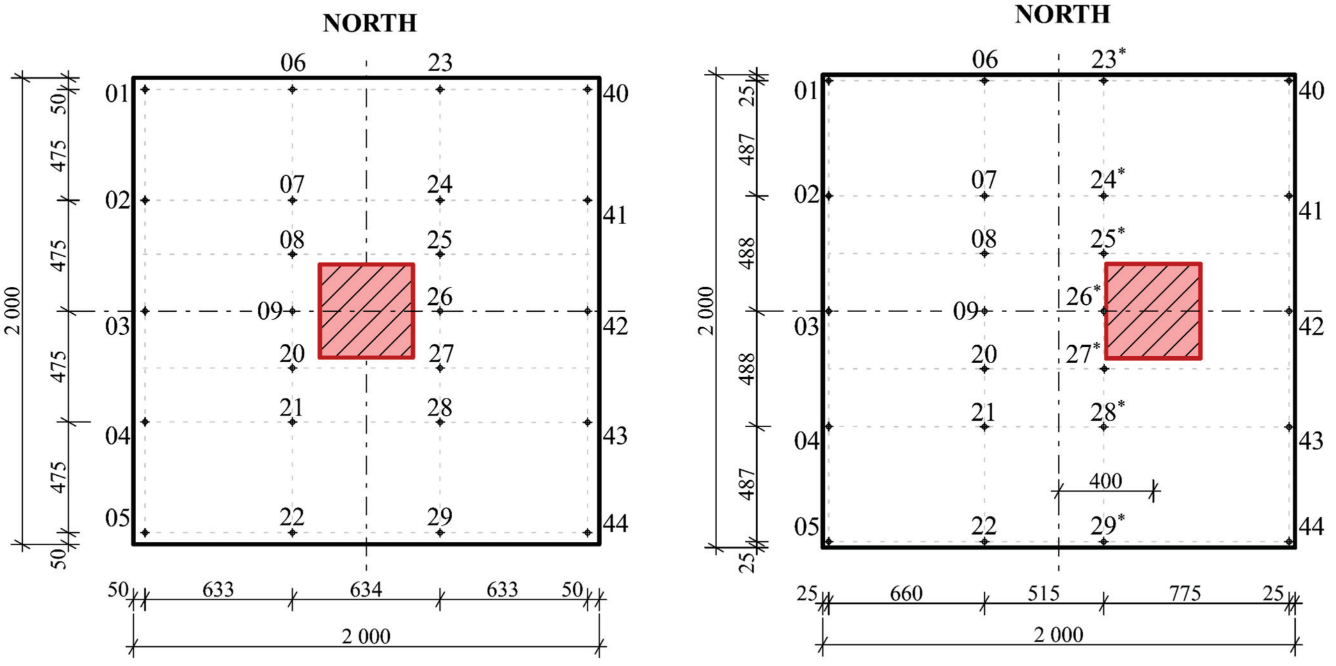

(**a**) (**b**)

**Figure 11.** Sensor layout schema: (**a**) centrically loaded slab G10; (**b**) eccentrically loaded slab G11.

## 5. Results of Experimental Tests of Slab

Based on the experimentally measured data, a diagram (Figure 12) was created showing the course of the test for a centrically (G10) and eccentrically loaded slab (G11). It can be seen from the diagram that the loading of both slabs was ended in the seventh loading step, when the pressure in the hydraulic press dropped, resulting in the destruction of both fiber-reinforced concrete slabs. The measurement of a centrically loaded slab (G10) was completed at a load of 499.2 kN, and for an eccentrically loaded slab (G11), at a load of 477.6 kN. The difference in the maximum achieved load value for both slabs is relatively small. It is clear from the graph that the relaxation of the slab is significantly smaller for the initial loading steps than for the loading before the end of the test. The decrease in the bending stiffness of the slab is also more pronounced when cracks in the fiber-reinforced concrete slab are already visible.

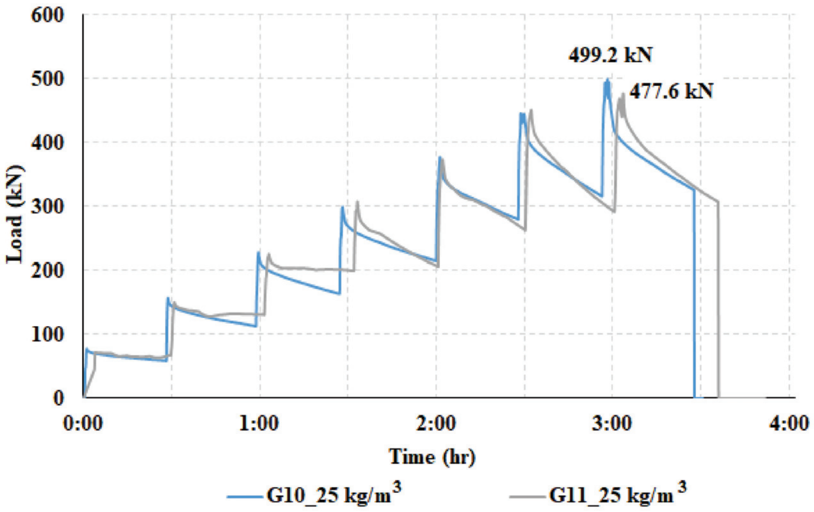

**Figure 12.** Loading in steps of the centrically loaded slab (G10) and eccentrically loaded slab (G11).

The first part of the experimental measurement of the slabs was monitoring the deformation behavior of the slab in the transverse direction. In the framework of this article, the sections correspond to track sensors 06–22 (Figure 13a), 23 | 23*–29 | 29* (Figure 13b). From the data read by the track sensors, the deformations of the slab at the locations of the track sensors were calculated.

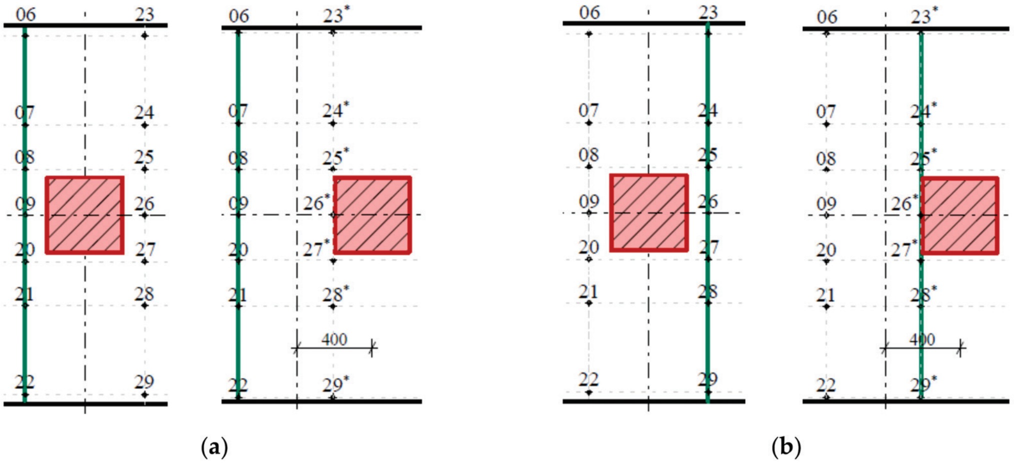

**Figure 13.** Monitored 2D sections: (**a**) first monitored 2D section for centrically loaded slab G10 (left) and eccentrically loaded slab G11 (right); (**b**) second monitored 2D section for centrically loaded slab G10 (left) and eccentrically loaded slab G11 (right).

The maximum negative deformations in the slabs of track sensors 06–22, which correspond to the lifted corners of the slabs, measured 13.93 mm (centrically loaded slab G10, sensor 06) and 20.01 mm (eccentrically loaded slab G11, sensor 22), respectively. The maximum positive deformations in the slabs of track sensors 06–22, which correspond to the pushing of the slabs into the subsoil, were measured at 26.72 mm (centrically loaded slab G10, sensor 09) and 8.24 mm (eccentrically loaded slab, sensor 20), respectively. Comparative 2D deformation sections at the locations of track sensors 06–22, which capture the behavior of both fiber-reinforced concrete slabs, are shown in Figure 14. Deformation values for selected loading steps and selected sensors in section 06–22 for centrically (G10) and eccentrically (G11) loaded slabs are shown in Table 6. In the case of eccentrically loaded slab G11, the lift of the corners of the slab (negative deformation) at track sensor of 22 was approximately triple compared to centrically loaded slab G10. The pushing of the slab (positive deformation) of centrically loaded slab G10 was approximately quadruple at track sensor of 09 in comparison with eccentrically loaded slab G11, as shown in Figure 14 and Table 6.

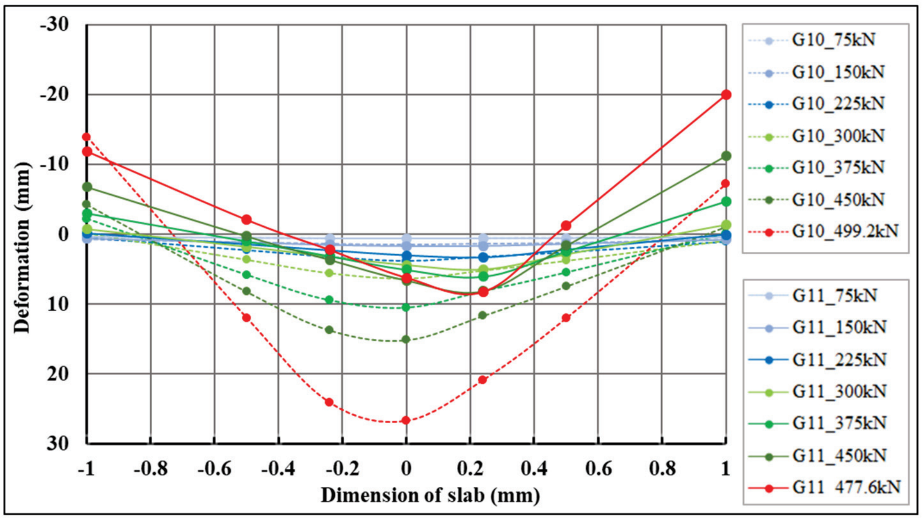

**Figure 14.** Comparison of 2D cross-deformation sections of centrically loaded slab G10 and eccentrically loaded slab G11 for sensors 06–22.

**Table 6.** Deformation of centrically loaded slab G10 and eccentrically loaded slab G11 for track sensors 06–22.

| **Load Step (kN)** | **Track Sensor** | | | | |
|---|---|---|---|---|---|
| | **06** | **07** | **09** | **21** | **22** |
| | **Deformation (mm) Centrically Loaded Slab G10 ǀ Eccentrically Loaded Slab G11** | | | | |
| 75 | 0.42 ǀ 0.39 | 0.53 ǀ 0.51 | 0.63 ǀ 0.61 | 0.53 ǀ 0.56 | 0.37 ǀ 0.46 |
| 225 | 0.47 ǀ −0.08 | 2.29 ǀ 1.5 | 3.85 ǀ 3.07 | 2.58 ǀ 2.26 | 1.05 ǀ 0.07 |
| 375 | −2.22 ǀ −2.97 | 5.8 ǀ 1.02 | 10.48 ǀ 5.08 | 5.44 ǀ 2.46 | −0.1 ǀ −4.68 |
| Maximum load | −13.93 ǀ −11.86 | 12.01 ǀ −2.06 | 26.72 ǀ 6.23 | 12.01 ǀ −1.28 | −7.2 ǀ −20.01 |

The maximum negative deformations at the locations of track sensors 23 ǀ 23*–29 ǀ 29*, which correspond to the lifted corners of the slabs, were 8.93 mm (centrically loaded slab G10, sensor 23) and 10.57 mm (eccentrically loaded slab G11, sensor 29*), respectively. Maximum positive deformations at the locations of track sensors 23 ǀ 23*–29 ǀ 29*, which correspond to the pushing of the slabs into the subsoil, were 24.36 mm (centrically loaded slab G10, sensor 26) and 18.79 mm (eccentrically loaded slab G11, sensor 27*), respectively.

Comparative 2D deformation sections at the locations of track sensors 23 ǀ 23*–29 ǀ 29*, which depict the behavior of both fiber-reinforced concrete slabs, are shown in Figure 15.

Deformation values for selected load steps and selected track sensors 23 | 23*–29 | 29* for centrically (G10) and eccentrically (G11) loaded slabs are shown in Table 7.

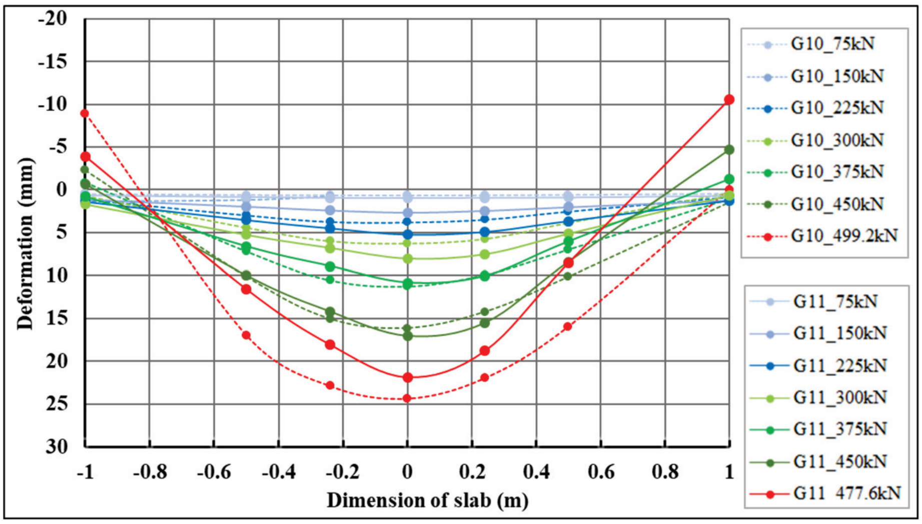

**Figure 15.** Comparison of 2D cross-deformation sections of centrically loaded slab G10 and eccentrically loaded slab G11 for track sensors 23 | 23*–29 | 29*.

**Table 7.** Deformation of centrically loaded slab G10 and eccentrically loaded slab G11 for track sensors 23 | 23*–29 | 29*.

| Load Step (kN) | Track Sensor | | | | |
|---|---|---|---|---|---|
| | 23 \| 23* | 24 \| 24* | 26 \| 26* | 28 \| 28* | 29 \| 29* |
| | Deformation (mm) Centrically Loaded Slab G10 \| Eccentrically Loaded Slab G11 | | | | |
| 75 | 0.45 \| 0.66 | 0.59 \| 0.83 | 0.66 \| 0.96 | 0.57 \| 0.89 | 0.41 \| 0.71 |
| 225 | 1.12 \| 1.37 | 2.97 \| 3.53 | 3.79 \| 5.25 | 2.53 \| 3.65 | 0.84 \| 1.23 |
| 375 | −0.85 \| 0.76 | 7.2 \| 6.59 | 11.27 \| 10.83 | 6.98 \| 6.03 | 1.06 \| −1.29 |
| Maximum load | −8.93 \| −3.92 | 16.96 \| 11.55 | 24.36 \| 21.84 | 15.94 \| 8.53 | −0.02 \| −10.57 |

In the longitudinal direction, the section corresponding to track sensors 03–42 was evaluated (Figure 16). From the measured data of the scanned track sensors, the deformations of the slabs in the places where the track sensors were mounted were calculated.

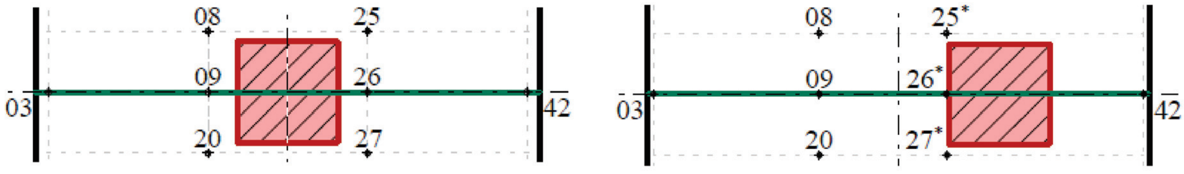

(**a**) (**b**)

**Figure 16.** Longitudinal sections: (**a**) centrically loaded slab G10; (**b**) eccentrically loaded slab G11.

The maximum negative deformations in the slabs of track sensors 03–42, which correspond to the lifted corners of the slabs, were 13.06 mm (centrically loaded slab G10, sensor 42) and 20.37 mm (eccentrically loaded slab G11, sensor 03), respectively. The maximum positive deformations in the slabs of track sensors 03–42, which correspond to the pushing of the slabs into the subsoil, were 26.72 mm (centrically loaded slab G10, sensor 09) and 21.84 mm (eccentrically loaded slab G11, sensor 26 *), respectively. Comparative 2D deformation sections in the slabs of track sensors 03–42, which capture the behavior of both fiber-reinforced concrete slabs, are shown in Figure 17. Deformation values for selected loading steps and track sensors in section 03–42 for centrically and eccentrically loaded slabs are shown in Table 8. At track sensor 03, located at the edge of the slab, the lifting of the corner for the maximum load case was twice that of eccentrically loaded slab G11, as is also evident from Figure 17 and Table 8. In the case of the track sensor 42, located on the opposite side of the slab, the deformations were of a different nature. In the case of centrically loaded slab G10, the slab was lifted (negative deformation). In the case of eccentrically loaded slab G11, the slab was pushed into the subsoil (positive deformation), as is evident from Figure 17.

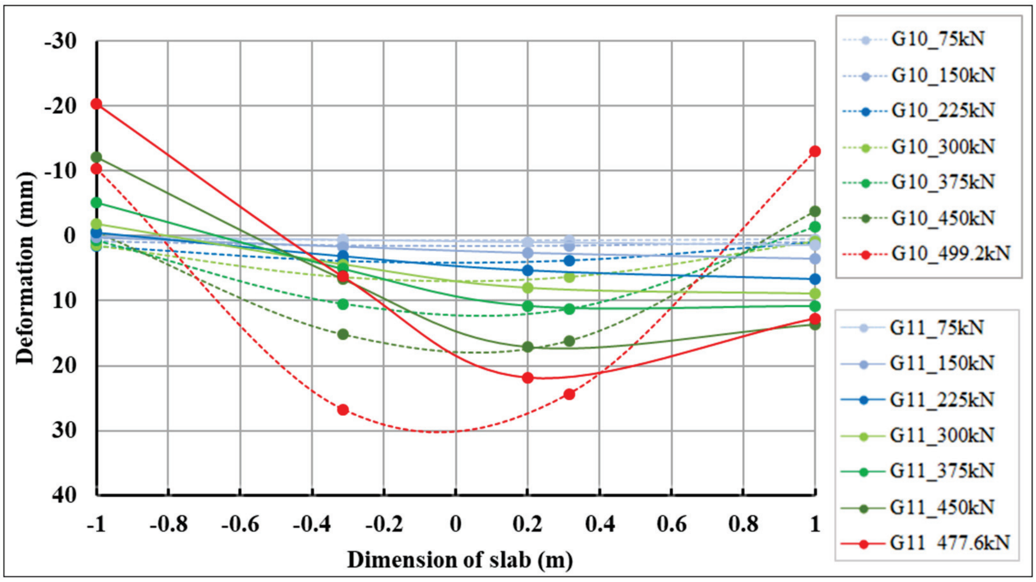

**Figure 17.** Comparison of 2D longitudinal-deformation sections of centrically loaded slab G10 and eccentrically loaded slab G11 for track sensors 03–42.

**Table 8.** Deformation of centrically loaded slab G10 and eccentrically loaded slab G11 for track sensors 03–42.

| Load Step (kN) | Track Sensor | | | |
|---|---|---|---|---|
| | 03 | 09 | 26 \| 26* | 42 |
| | Deformation (mm) Centrically Loaded Slab G10 \| Eccentrically Loaded Slab G11 | | | |
| 5 | 0.41 \| 0.11 | 0.63 \| 0.61 | 0.66 \| 0.96 | 0.48 \| 1.43 |
| 225 | 1.6 \| −0.57 | 3.85 \| 3.07 | 3.79 \| 5.25 | 1.01 \| 6.60 |
| 375 | 0.72 \| −5.19 | 10.48 \| 5.08 | 11.27 \| 10.83 | −1.37 \| 10.86 |
| Maximum load | −10.40 \| −20.37 | 26.72 \| 6.23 | 24.36 \| 21.84 | −13.06 \| 12.71 |

Centrically loaded slab G10 and eccentrically loaded slab G11 during loading are shown in Figure 18.

The 3D deformation surfaces of centrically loaded slab G10 and eccentrically loaded slab G11 were also evaluated for selected loading steps, i.e., for loading steps of 225 and 450 kN. Part of the evaluation of 3D deformation surfaces was the evaluation of the 3D deformation surface with transfer into the projection, where the maximum deformation area is clearly visible with regard to the applied load and eccentricity. The projections are shown only for the central part of the slab, i.e., for a slab strip of size 1 m. The evaluations of the 3D deformation surfaces of centrically loaded slab G10 and eccentrically loaded slab G11 and the projections of the 3D deformation surfaces for a loading step of 225 kN are shown in Figures 19 and 20. Based on the 3D approximation, the deformations in the center of the slab were determined for a load step of 225 kN. In the case of centrically loaded slab G10, the deformation in the center of the slab was 3.64 mm, while the deformation in the center was 4.26 mm for eccentrically loaded slab G11. Deformations of the slabs at the center of eccentricity were also evaluated for a load step of 225 kN. In the case of centrically loaded slab G10, the deformation in the center of the eccentricity was 3.37 mm, while it was 5.30 mm for eccentrically loaded slab G11.

The evaluations of the 3D deformation surfaces of centrically loaded slab G10 and eccentrically loaded slab G11 and the projections of the 3D deformation surfaces for a loading step of 450 kN are shown in Figures 21 and 22. Deformations at the center of the slabs and at the center of the eccentricity of the slabs were also evaluated for a load step of 450 kN. In the case of centrically loaded slab G10, the deformation was 14.71 mm at the center of the slab and 13.07 mm at the center of the slab eccentricity. Eccentrically loaded slab G11 had a deformation in the center of the slab with a value of 13.07 mm, and in the center of the eccentricity it had a value of 15.13 mm.

(**a**) (**b**)

**Figure 18.** Slab: (**a**) centrically loaded slab G10; (**b**) eccentrically loaded slab G11.

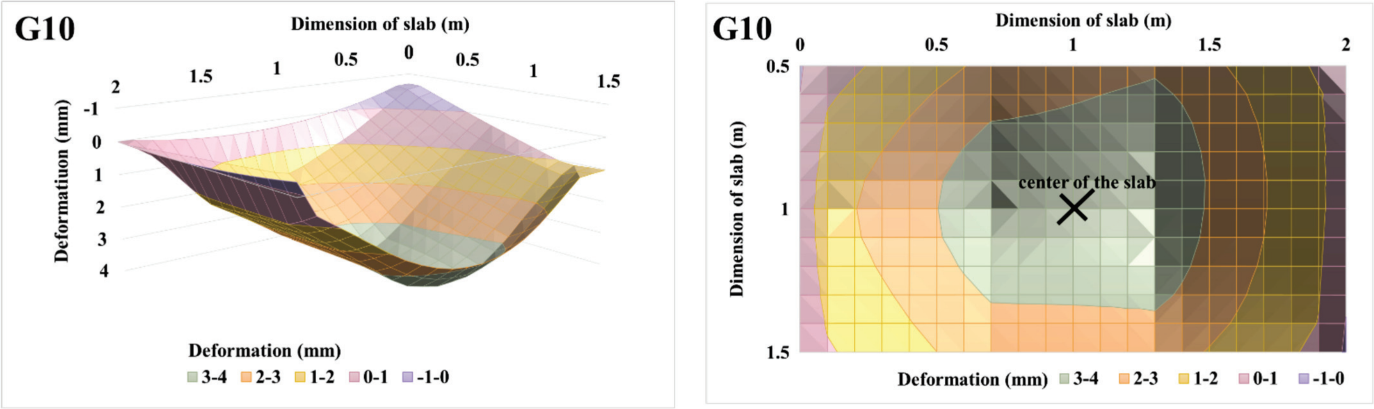

(**a**) (**b**)

**Figure 19.** Centrically loaded slab G10 with 225 kN load: (**a**) 3D deformation surface of the slab; (**b**) projection of 3D deformation surface of the slab.

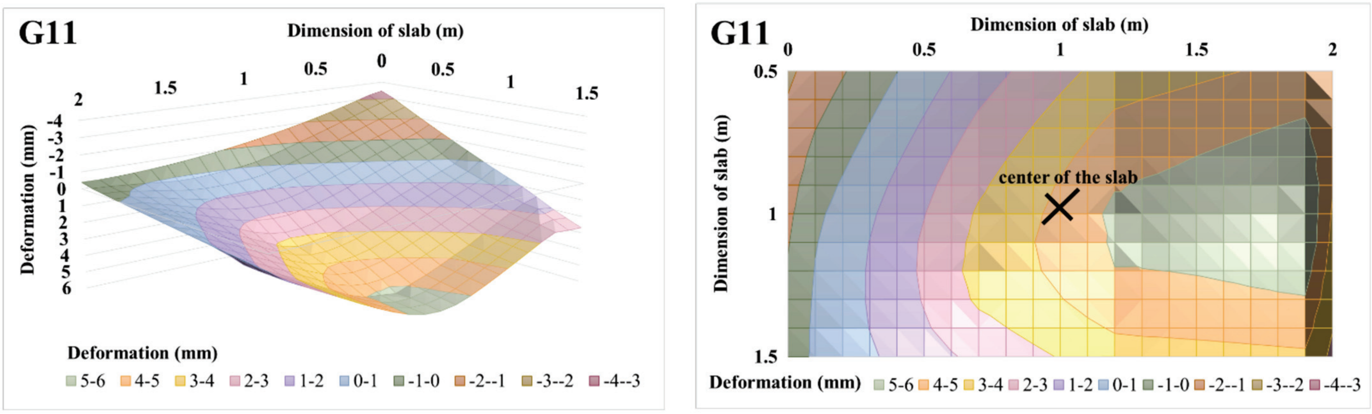

(**a**) (**b**)

**Figure 20.** Eccentrically loaded slab G11 with 225 kN load: (**a**) 3D deformation surface of the slab; (**b**) projection of 3D deformation surface of the slab.

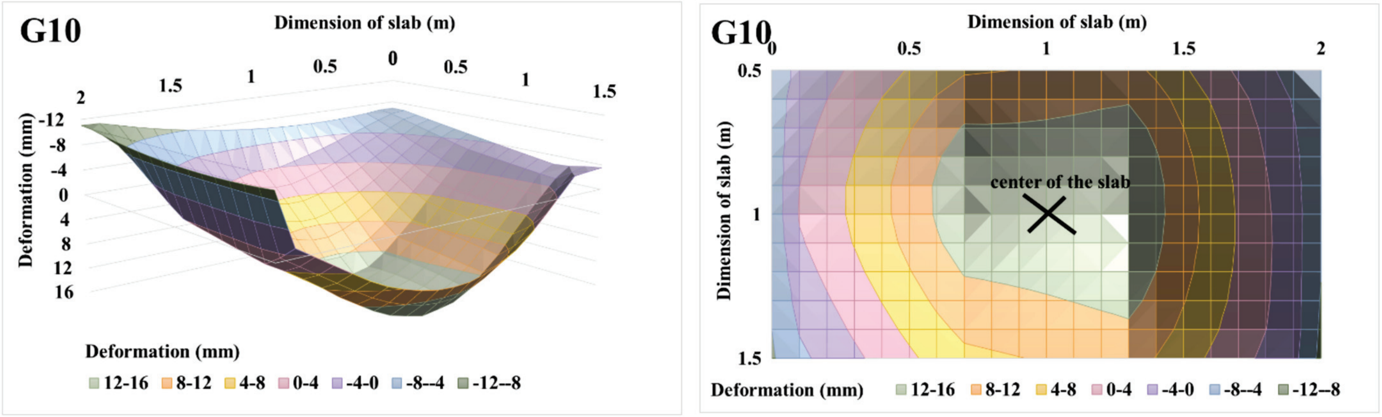

(**a**) (**b**)

**Figure 21.** Centrically loaded slab G10 with 450 kN load: (**a**) 3D deformation surface of the slab; (**b**) projection of 3D deformation surface of the slab.

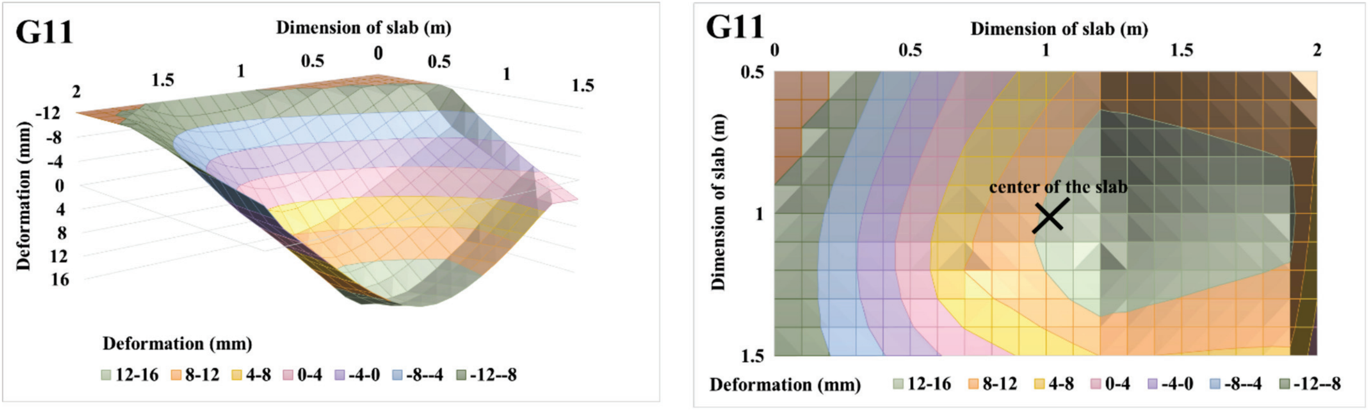

(**a**) (**b**)

**Figure 22.** Eccentrically loaded slab G11, with 450 kN load: (**a**) 3D deformation surface of the slab; (**b**) projection of 3D deformation surface of the slab.

Based on the approximation of the 3D deformation surfaces of the slabs, load–displacement diagrams were evaluated, as shown in Figure 23. From the load–displacement diagrams of slabs G10 and G11 in the middle of the slabs in Figure 23a, it can be stated that the course itself is very similar. The resulting deformation in the center of the slab was greater for centrically loaded slab G10. The maximum achieved load for centrically loaded slab G10 was 499.2 kN; this value corresponds to the approximate deformation of 24.09 mm. For the case of eccentrically loaded slab G11, the maximum load was reached at 477.6 kN, which corresponds to a 3D-approximated deformation of 14.92 mm. For eccentrically loaded slab G11, the approximate deformation was larger in the center of eccentricity than in the center of the slab. The approximate deformation in the center of the eccentricity was 17.95 mm, and in the center of the slab, it was 14.92 mm (Figure 23b).

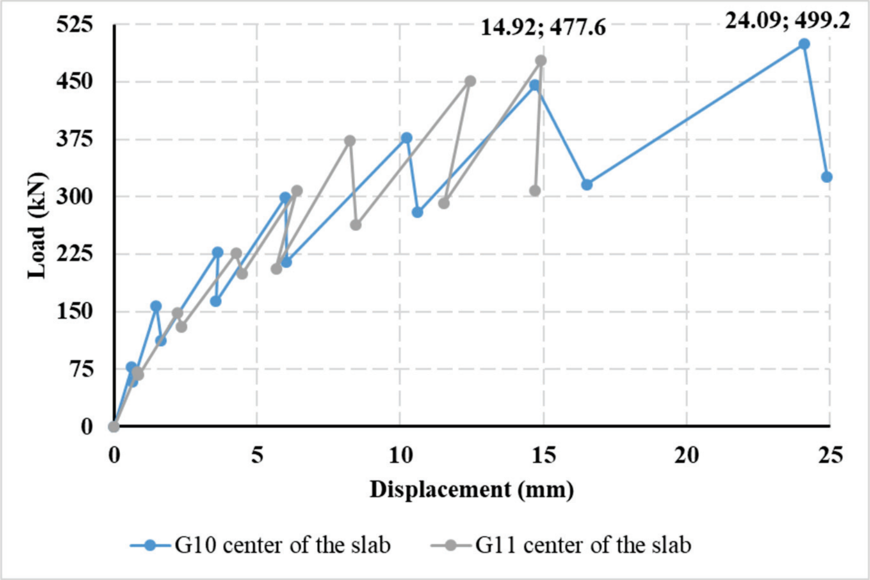

(**a**)

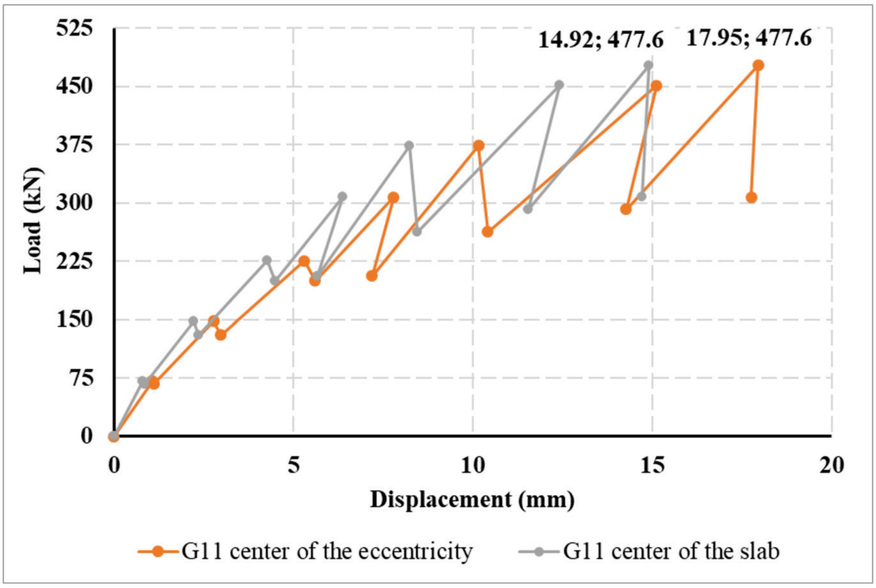

(**b**)

**Figure 23.** Load–displacement diagrams evaluated on the basis of the approximation of the 3D deformation surface: (**a**) in the center of centrically loaded slab G10 and eccentrically loaded slab G11; (**b**) in the center of the slab and the center of eccentricity of eccentrically loaded slab G11.

Based on the measured pressures in the subsoil during the load test of the slabs, the stresses in three layers at the locations of the stored pressure cells were evaluated. A diagram of the arrangement of the pressure cells is shown in Figure 24. The first layer of pressure cells is located at the location of the foundation joint. The other two layers with pressure cells are located 350 mm and 800 mm below the foundation joint. Three pressure cells are located in each layer. A total of nine pressure cells were located.

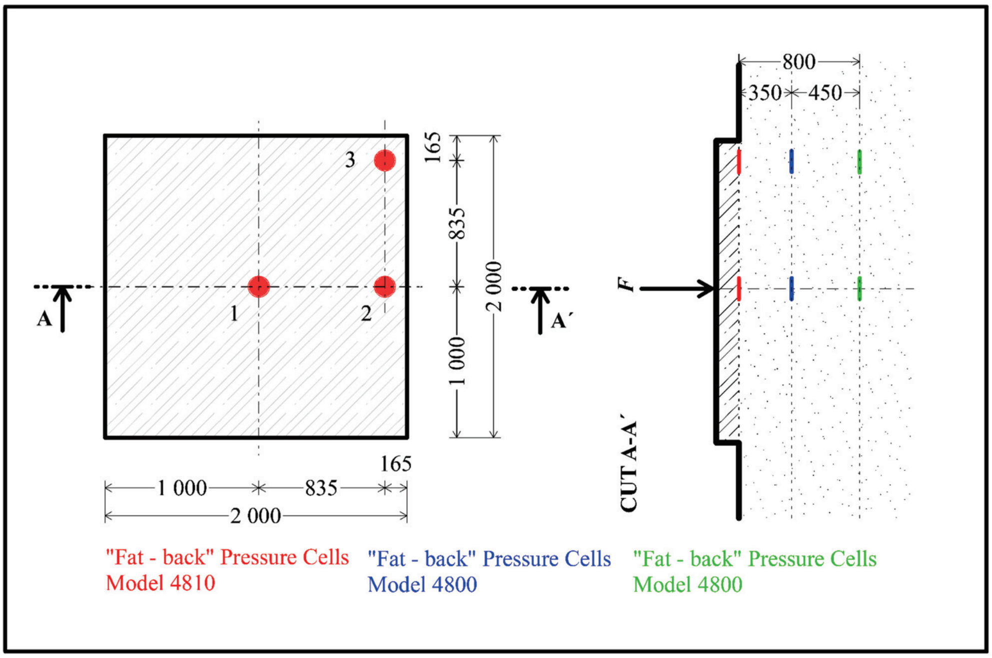

**Figure 24.** Schema of pressure cells in subsoil for centrically loaded slab G10 and eccentrically loaded slab G11.

Figure 25 shows the stress curves on the pressure cells for each layer. In the case of centrically loaded slab G10, the maximum values were reached for the pressure cells in the center of the slab. The maximum stress in the case of centrically loaded slab G10 reached values of 700 kPa. The effect of the load decreases significantly with the depth of the subsoil. For the deepest point, the stress at the edge of the slab and in the corner of the slab drops to a value corresponding to a maximum of 10% of the stress in the center of the slab. In the case of eccentrically loaded slab G11, measuring points 2 and 3 are closer to the load. For this reason, the measured stresses in the pressure cells are higher compared to centrically loaded slab G10. Again, for pressure cells located deeper, the stresses on the cells are significantly lower. The maximum stress approached 500 kPa.

The individual layers of the pressure cells or the stress curves in the pressure cells are differentiated by color in Figure 25. The color resolution of the individual layers is based on Figure 24. The layers of pressure cells in the foundation joint are marked by a red curve, the second layer of pressure cells (350 mm below the foundation joint) is shown by a blue curve, and the third and final layer of pressure cells (800 mm below the foundation joint) is represented by a green curve.

It can be seen from Figure 12 that the loading of the slabs took place in loading steps. Each loading step was 75 kN. After reaching the maximum load in a given loading step, the slab relaxed for 30 min. After this, another loading step followed, and there was time for the slab to relax. This was repeated until the maximum slab load was reached. Figure 26 has two stress curves showing the stress profile of a pressure cell. Figure 26 shows a different course of stress at the time of reaching the maximum load for a given load step (solid line—marked in the graph as peak load step) and at the time of load after 30 min of slab relaxation in a given load step (dashed line—marked in graph as a minimum load step). The stress on pressure cells after the slab relaxation time was lower.

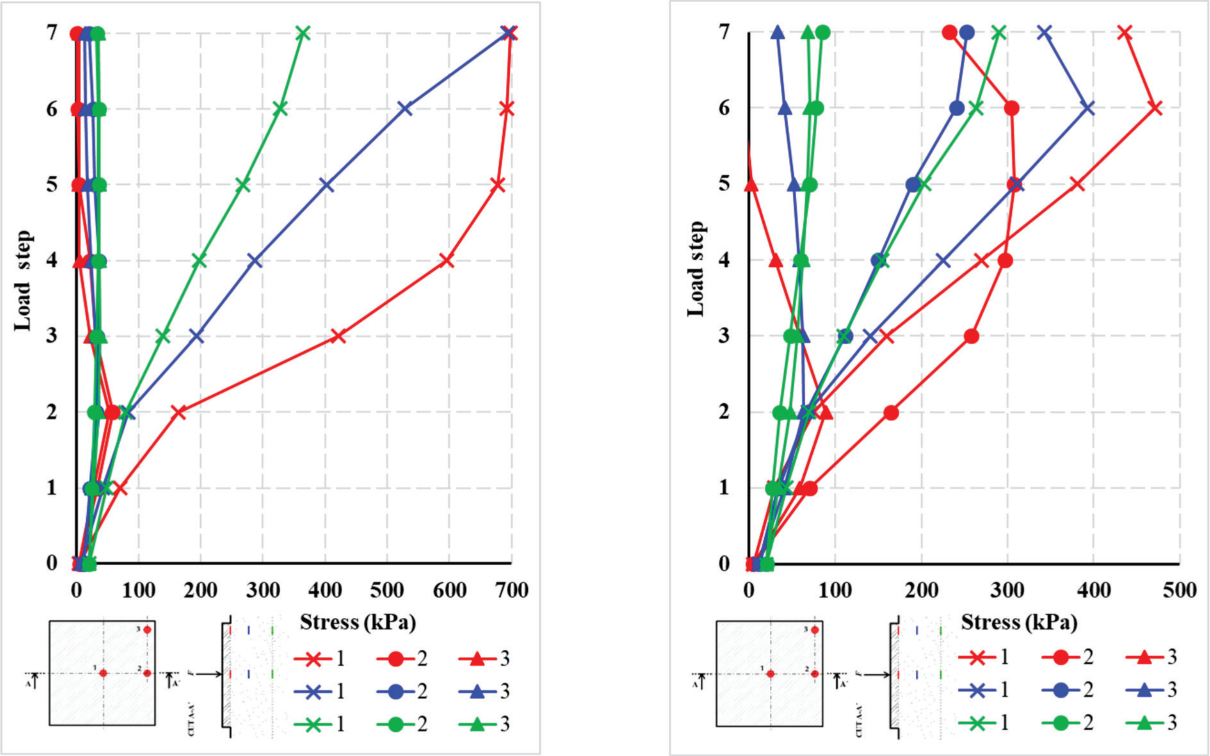

(**a**) (**b**)

**Figure 25.** Stress in individual pressure cells: (**a**) centrically loaded slab G10; (**b**) eccentrically loaded slab G11.

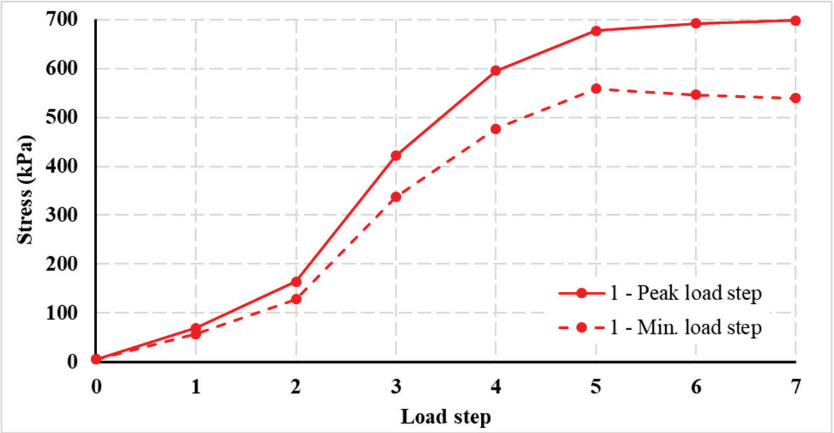

**Figure 26.** Example of stress for pressure cell 1 in the first layer (foundation joints)—centrically loaded slab G10.

## 6. Discussion

### 6.1. Fiber-Reinforced Concrete Slabs

The laboratory tests and tests of structural elements verified that fiber-reinforced concrete can significantly contribute to the structural and material optimization of the design of concrete structures. The use of fiber-reinforced concrete can significantly simplify the production of concrete structures. The selected dosing of fiber of 25 kg/m$^3$ is suitable with regard to concreting technology and financial costs. However, in comparison with previous experiments, it can be stated that the total load-bearing capacity of the fiber-reinforced concrete slab (usually around 500 kN) will typically be less than the traditional solution of a reinforced concrete slab with concrete reinforcement, where the load is up to 700 kN. However, the use of concrete reinforcement is more demanding on concreting and overall financial costs. However, the use of only plain concrete for slabs has the effect of creating a significantly lower load-bearing capacity of the slab than using a fiber-reinforced concrete slab. The collapse of a plain concrete slab is also marked by a significantly quasi-brittle nature.

The use of fiber-reinforced concrete also makes a significant contribution to increasing the ductility of the structure, i.e., to the safety of the structure as compared to the use of plain concrete. A broader evaluation of the presented experiments and tests already performed revealed that the overall load-bearing capacity of the slab in the subsoil interaction is influenced by the mechanical properties of the concrete rather than the subsoil. The mechanical parameters of the subsoil significantly affect the resulting deformations of the slab. These can be differences of up to tens of percentage points. From a design point of view, the experiment performed on a fiber-reinforced concrete slab with an eccentric load showed that the resulting load-bearing capacity was very similar to that of a slab with a centric load. This was mainly due to the fact that the slab remained whole throughout the test. However, the eccentric load significantly affected the course of deformations.

### *6.2. Fiber-Reinforced Concrete*

The selected fiber-reinforced concrete variant has a number of advantages over plain concrete. However, the quasi-brittle nature of fiber-reinforced concrete in itself requires a set of laboratory tests of the compressive strength of concrete, tensile strength under splitting, modulus of elasticity, and bending tensile strength. From the results of laboratory tests and a comparison with the available recommendations, we confirmed that it is appropriate to carry out specialized tests rather than using only the recommendations for modulus of elasticity and tensile strength under splitting.

It is clear from the tensile tests that the strengths different may be for test setup. However, the recalculated tensile strengths are relatively similar. In the three-point test, the strength values are slightly higher than in the four-point bending test. This is because the location of the crack is not predetermined in the four-point bending test. In the case of the modulus of elasticity, the results of the tests show a significantly lower modulus of elasticity than in Model Code 1990 [1]. In the splitting tensile test, it was shown that the higher the tensile strength, the higher the bulk density.

### *6.3. Subsoil*

Important information also includes knowledge about the subsoil, where our analysis revealed that the subsoil has the character of incoherent soil (approximately 55% sand, 15% gravel, and 30% clay). According to the percentage of individual fractions, this soil can be globally classified as clayey sand. The basic soil parameters are cohesion, $c$ (kPa), and angle of internal friction, $\varphi$ (°) 34.4. It is suitable to perform tests on the deformation modulus of soil, where the measurement values a relatively wide variance of measured values from 16 to 58 MPa; the resulting values depend on the actual history of loading and the specific climatic conditions. The mechanical properties of the soil are also often affected by the climate at the surface in particular. It is advisable to repeat this test several times to obtain a wider set of static data.

Simplified analytical/numerical models and experiments, such as symmetry, dimension, etc., can be used for typical cases of a slab in interaction with subsoil. Important aspects of the problem include the need to closely monitor the behavior and parameters of the fiber-reinforced slab and subsoil. In the case of fiber-reinforced concrete slabs, a network of vertical deformation sensors was used. In the case of subsoil, specialized pressure cells were used to measure stress. The comparison of the results allows for a detailed view of the behavior of the fiber-reinforced concrete slabs during a load test. A comparison of the results from the fiber-reinforced concrete slab and the subsoil showed that the initial formation of cracks at the lower surface of the slab were manifested by an increase in the contact stress in the middle of the slab. There was a significant increase in stress in the pressure cell in the middle of the slab closest to the surface. A more detailed study of data from soil pressure sensors in the lower layer (at a depth of 0.8 m) revealed that the stresses are significantly lower compared to the contact stresses at the surface. By approximating the stress results in the pressure cells in the individual layers, it was found that the concerned area of the subsoil and the deformation zone for maximum load is about 2 m deep. The specific values measured at the edges of the slab were significantly lower than below the center of the slab. The differences between the measured values were significant. With the achievement of the maximum load-bearing capacity of the fiber-reinforced concrete slab and the formation of significant cracks in the concrete, the stress in the pressure cells no longer increased and remained at the maximum values. This was due to the fact that there was a significant decrease in the bending stiffness of the slab. The differences in pressure cells in the subsoil for the centrically (G10) and eccentrically (G11) loaded slabs are relatively small. Only in the case of higher loading steps, when the corners of the slab were already being lifted, was it evident that the pressure cell was relieved, while the character itself was slightly different for the centrically (G10) and eccentrically (G11) loaded slabs. This is due to the different geometry and position of the load.

## 7. Conclusions

Research on slabs in interaction with subsoil is very demanding. This is because a number of factors enter into the analysis, which involves the use of advanced testing and diagnostic methods. The selected variant of fiber-reinforced concrete slab has a number of advantages in comparison with concrete and reinforced concrete slabs. However, the quasi-brittle nature of fiber-reinforced concrete itself requires an extensive set of laboratory tests. From the point of view of the design of concrete structures, it is important to monitor the deformations and cracks in the concrete of the fiber-reinforced concrete slab itself. By a more detailed study of the results from 2D deformation sections, it is possible to distinguish when the increase in deformations is no longer elastic and cracks have formed in the concrete. It is also clear from the graph that the deformation increment gradually increases within the loading step and the bending stiffness of the fiber-reinforced concrete slab decreases. The fiber-reinforced concrete slab remained whole in both tests; when the maximum load was reached, the cracks were over the entire thickness of the slab. During the test, the edges of the slab gradually began to rise. When analyzing the deformations of the slab with centric and eccentric load, it is also possible to use 3D graphs, which enable a clearer and more comparable display of deformations.

The results of the research can be presented in partial conclusions:

- The differences in the overall load capacity of slabs with centric and eccentric loads are relatively small. The center of the eccentric load was already outside the core of the cross section.
- For lower load steps, the difference in fiber-reinforced-concrete-slab behavior and deformation was relatively small. The differences began to increase, especially in the second half of the load experiment tests (loading).
- The position of the steel load plate affected the position of the cracks in the slab. For the slab with an eccentric load, the deformations were more pronounced on the load side. In the case of a slab with an eccentric load, there was also a more pronounced lifting of the corner on one side of the slab.
- In comparison with previous experiments, it can be stated that better deformation parameters of the subsoil mainly affected the magnitude of deformations of the slab and the subsoil rather than the overall load-bearing capacity.
- It is advisable to repeat the test several times when determining the deformation modulus of the subsoil and the ratio for the secondary and primary cycle, which are used to determine the deformation capacity of the subsoil. Pressure cells in at least two levels are suitable for determining the active deformation zone of the subsoil. By far, the most important are the pressure cells directly under the load in plan view.

- The laboratory experiments and tests of structural elements confirmed that dosing fibers at 25 kg/m$^3$ can significantly contribute to increasing the overall load-bearing capacity and eliminating cracks in the concrete.
- The use of fiber-reinforced concrete requires a more detailed determination of its mechanical properties. Tensile strength is especially important. It is also important to produce load–displacement diagrams, which can be used to identify fracture mechanical parameters.
- From laboratory tests in split tension, it was found that the position of concreting affects the mechanical properties in tension, i.e., the number of fibers along the cross-sectional height varies slightly.
- It is important to perform tests of the modulus of elasticity of concrete, where the values found are significantly different from those in the recommendations. Modulus of elasticity values were lower than those of the recommendations.
- When evaluating slab tests in subsoil interaction, it is appropriate to use 3D deformation graphs and to determine the load–displacement diagram for the entire structural element tests.

The benefits of this research include that a comprehensive set of information and knowledge with a detailed evaluation of laboratory tests and tests of structural elements can be further used for advanced numerical-modeling-based non-linear analysis, where an optimized structure solution is solved.

Among the important and new knowledge of the presented research is that the problem of the slab in the interaction of the subsoil can be further extended by the structural solution of the sliding joint. This area can be followed by laboratory research into the properties of sliding joints in the climate chamber and measurements on real structures of the base slab with a sliding joint on the subsoil. The authors will focus on this area in further research.

**Author Contributions:** Conceptualization, R.C. and V.B.; methodology and validation, Z.M. and O.S.; data curation, Z.M. and R.C.; writing—original draft preparation, Z.M.; visualization, O.S.; supervision, R.C. All authors have read and agreed to the published version of the manuscript.

**Funding:** This research was funded by VSB-TUO by the Ministry of Education, Youth and Sports of the Czech Republic.

**Data Availability Statement:** Data is contained within the article.

**Acknowledgments:** The work was supported by the Student Research Grant Competition of the VSB-Technical University of Ostrava under identification number SP2021/40. The writing of this paper was achieved with financial support by the means of the conceptual development of science, research, and innovation assigned to VSB-TUO by the Ministry of Education, Youth and Sports of the Czech Republic.

**Conflicts of Interest:** The authors declare no conflict of interest.

## References

1. FIB. *CEB-FIP Model Code 1990: Design Code*; Final Version; Thomas Telford Ltd.: London, UK, 1993.
2. Model Code 2010-Final Draft, fib, Bulletin Nos. 65 and 66. 1–2. 2012. Available online: https://www.fib-international.org/publications/fib-bulletins/model-code-2010-final-draft,-volume-1-detail.html (accessed on 26 March 2020).
3. Farzampour, A. Compressive Behavior of Concrete under Environmental Effects. In *Compressive Strength of Concrete*; IntechOpen: London, UK, 2019.
4. Bazant, Z.P.; Becq-Giraudon, E. Statistical prediction of fracture parameters of concrete and implications for choice of testing standard. *Cem. Concr. Res.* **2002**, *32*, 529–556. [CrossRef]
5. Chalangaran, N.; Farzampour, A.; Paslar, N. Nano Silica and Metakaolin Effects on the Behavior of Concrete Containing Rubber Crumbs. *CivilEng* **2020**, *1*, 264–274. [CrossRef]
6. Chalangaran, N.; Farzampour, A.; Paslar, N.; Fatemi, H. Experimental investigation of sound transmission loss in concrete containing recycled rubber crumbs. *Adv. Concr. Constr.* **2021**, *1*, 447–454. [CrossRef]
7. Sucharda, O.; Mateckova, P.; Bilek, V. Non-linear analysis of an RC beam without shear reinforcement with a sensitivity study of the material properties of concrete. *Slovak J. Civ. Eng.* **2020**, *28*, 33–43. [CrossRef]

8. Hegger, J.; Ricker, M.; Ulke, B.; Ziegler, M. Investigations on the punching behaviour of reinforced concrete footings. *Eng. Struct.* **2007**, *29*, 2233–2241. [CrossRef]
9. Hegger, J.; Sherif, G.A.; Ricker, M. Experimental investigations on punching behavior of reinforced concrete footings. *ACI Struct. J.* **2006**, *103*, 604–613.
10. AlAjarmeh, S.; Manalo, A.C.; Benmokrane, B.; Karunasena, K.; Ferdous, W.; Mendis, P. Hollow concrete columns: Review of structural behavior and new designs using GFRP reinforcement. *Eng. Struct.* **2020**, *203*, 109829. [CrossRef]
11. Al-Fakher, U.; Manalo, A.; Ferdous, W.; Aravinthan, T.; Zhuge, Y.; Bai, Y.; Edoo, A. Bending behaviour of precast concrete slab with externally flanged hollow FRP tubes. *Eng. Struct.* **2021**, *241*, 112433. [CrossRef]
12. Brandt, A.M. Fiber reinforced cement-based (FRC) composites after over 40 years of development in building and civil engineering. *Compos. Struct.* **2008**, *86*, 3–9. [CrossRef]
13. Pająk, M.; Ponikiewski, T. Flexural behavior of self-compacting concrete reinforced with different types of steel fibers. *Constr. Build. Mater.* **2013**, *47*, 397–408. [CrossRef]
14. Ponikiewski, T.; Katzer, J. Fresh mix characteristics of self-compacting concrete reinforced by fibre. *Period. Polytech. Civ. Eng.* **2017**, *61*, 226–231. [CrossRef]
15. Vandewalle, L.; Nemegeer, D.; Balazs, L.; Di Prisco, M.A. Rilem TC 162-TDF: Test and design methods for steel fibre reinforced concrete—Bending test. *Mater. Struct./Mater. Et Constr.* **2002**, *35*, 579–582.
16. EN 14651:2005+A1:2007(E). *Test Method for Metallic Fibre Concrete–Measuring the Flexural Tensile Strength (Limit of Proportionality (LOP), Residual)*; CEN—European Committee for Standardization: Brussels, Belgium, 2007.
17. Marcalikova, Z.; Cajka, R.; Bilek, V.; Bujdos, D.; Sucharda, O. Determination of mechanical characteristics for fiber-reinforced concrete with straight and hooked fibers. *Crystals* **2020**, *10*, 545. [CrossRef]
18. Alani, A.M.; Beckett, D. Mechanical properties of a large scale synthetic fibre reinforced concrete ground slab. *Constr. Build. Mater.* **2013**, *41*, 335–344. [CrossRef]
19. Katzer, J.; Domski, J. Quality and mechanical properties of engineered steel fibres used as reinforcement for concrete. *Constr. Build. Mater.* **2012**, *34*, 243–248. [CrossRef]
20. Sucharda, O.; Konecny, P.; Kubosek, J.; Ponikiewski, T.; Done, P. Finite Element Modelling and Identification of the Material Properties of Fibre Concrete. *Procedia Eng.* **2015**, *109*, 234–239. [CrossRef]
21. Sucharda, O.; Lehner, P.; Konečný, P.; Ponikiewski, T. Investigation of Fracture Properties by Inverse Analysis on Selected SCC Concrete Beams with Different Amount of Fibres. *Procedia Struct. Integr.* **2018**, *13*, 1533–1538. [CrossRef]
22. Mansouri, I.; Shahheidari, F.S.; Hashemi, S.M.A.; Farzampour, A. Investigation of steel fiber effects on concrete abrasion resistance. *Adv. Concr. Constr.* **2020**, *9*, 367–374. [CrossRef]
23. Sorelli, L.G.; Meda, A.; Plizzari, G.A. Steel fiber concrete slabs on ground: A structural matter. *ACI Struct. J.* **2006**, *103*, 551–558.
24. Chen, S. Strength of steel fibre reinforced concrete ground slabs. *Proc. Inst. Civ. Eng. Struct. Build.* **2004**, *157*, 157–163. [CrossRef]
25. Pazdera, L.; Cajka, R.; Topolář, L.; Mateckova, P.; Bilek, V.; Sucharda, O. Measurement and Utilization of Acoustic Emission for the Analysis and Monitoring of Concrete Slabs on the Subsoil. *Period. Polytech. Civ. Eng.* **2019**, *63*, 608–620. [CrossRef]
26. Alani, A.; Beckett, D.; Khosrowshahi, F. Mechanical behaviour of a steel fibre reinforced concrete ground slab. *Mag. Concr. Res.* **2012**, *64*, 593–604. [CrossRef]
27. Sucharda, O.; Smirakova, M.; Vaskova, J.; Mateckova, P.; Kubosek, J.; Cajka, R. Punching Shear Failure of Concrete Ground Supported Slab. *Int. J. Concr. Struct. Mater.* **2018**, *12*, 36. [CrossRef]
28. Cajka, R.; Marcalikova, Z.; Bilek, V.; Sucharda, O. Numerical Modeling and Analysis of Concrete Slabs in Interaction with Subsoil. *Sustainability* **2020**, *12*, 9868. [CrossRef]
29. Hrubesova, E.; Mohyla, M.; Lahuta, H.; Bui, T.Q.; Nguyen, P.D. Experimental Analysis of Stresses in Subsoil below a Rectangular Fiber Concrete Slab. *Sustainability* **2018**, *10*, 2216. [CrossRef]
30. Falkner, H.; Hunag, Z.; Teutsch, M. Comparative study of plain and steel fiber reinforced concrete ground slabs. *Concr. Int.* **1995**, *17*, 45–51.
31. Huang, X.; Liang, X.; Liang, M.; Deng, M.; Zhu, A.; Xu, Y.; Wang, X.; Li, Y. Experimental and theoretical studies on interaction of beam and slab for cast-in-situ reinforced concrete floor structure. *J. Build. Struct. (Jianzhu Jiegou Xuebao)* **2013**, *34*, 63–71.
32. Kueres, D.; Ricker, M.; Hegger, J. Improved Shear Reinforcement for Footings—Maximum Punching Strength. *ACI Struct. J.* **2018**, *115*, 1365–1377. [CrossRef]
33. Hoang, L.C.; Pop, A. Punching shear capacity of reinforced concrete slabs with headed shear studs. *Mag. Concr.* **2016**, *68*, 118–126. [CrossRef]
34. Beckett, D. Ground-supported slabs made from steel-fibre-reinforced concrete. *Concrete* **2004**, *38*, 30–31.
35. Meda, A.; Plizzari, G.A. New design approach for steel fiber-reinforced concrete slabs-on-ground based on fracture mechanics. *ACI Struct. J.* **2004**, *101*, 298–303.
36. Miltenberger, M.A.; Attiogbe, E.K.; Bissonnette, B. Behavior of conventional reinforcement and a steel-polypropylene fiber blend in slabs-on-grade. *Mater. Struct. Mater. Constr.* **2007**, *40*, 10. [CrossRef]
37. Kueres, D.; Schmidt, P.; Hegger, J. Punching strength of footings with varying shear reinforcement ratios [Durchstanztragverhalten von Einzelfundamenten mit variierenden Durchstanzbewehrungsgraden]. *Beton-Und Stahlbetonbau* **2019**, *114*, 231–241. [CrossRef]
38. Tomasovicova, D.; Jendzelovsky, N. Stiffness Analysis of the Subsoil under Industrial Floor. *Procedia Eng.* **2017**, *190*, 365–370. [CrossRef]

39. Kozielova, M.; Marcalikova, Z.; Mateckova, P.; Sucharda, O. Numerical Analysis of Reinforced Concrete Slab with Subsoil. *Civ. Environ. Eng.* **2020**, *16*, 107–118. [CrossRef]
40. CSN. *CSN 731004: Geotechnical Design—Foundations—Requirements for Calculation Methods*; Czech Standardization Agency: Praha, Czech Republic, 2020.
41. Cajka, R.; Krivy, V.; Sekanina, D. Design and Development of a Testing Device for Experimental Measurements of Foundation Slabs on the Subsoil. *Trans. VSB—Tech. Univ. Ostrav. Civ. Eng. Ser.* **2011**, *11*, 11–17. [CrossRef]
42. CSN. *CSN EN 12390-3:2020: Testing Hardened Concrete—Part 3: Compressive Strength of Test Specimens*; Czech Standardization Agency: Praha, Czech Republic, 2020.
43. CSN. *CSN EN 12390-5:2019: Testing Hardened Concrete—Part 5: Flexural Strength of Test Specimens*; Czech Standardization Agency: Praha, Czech Republic, 2019.
44. CSN. *CSN EN 12390-6:2010: Testing Hardened Concrete—Part 6: Tensile Splitting Strength of Test Specimens*; Czech Standardization Agency: Praha, Czech Republic, 2010.
45. CSN. *CSN ISO 1920-10:2016: Testing of Concrete–Part 10: Determination of Static Modulus of Elasticity in Compression*; Czech Standardization Agency: Praha, Czech Republic, 2016.
46. Ros, S.; Shima, H. Relationship between splitting tensile strength and compressive strength of concrete at early age with different types of cements and curing temperature histories. *Concr. Inst. Proc.* **2013**, *35*, 427–432.
47. JCI. *Guidelines for Control of Cracking of Mass Concrete*; Japan Concrete Institute: Tokyo, Japan, 2011.
48. JSCE. *Standard Specifications for Concrete Structures, Materials and Construction*; Japan Society of Civil Engineers: Tokyo, Japan, 2002.
49. JSCE. *Standard Specifications for Concrete Structures, Materials and Construction*; Japan Society of Civil Engineers: Tokyo, Japan, 2007.
50. ACI Committee 318. *Building Code Requirements for Structural Concrete (ACI 318-11) and Commentary*; American Concrete Institute: Farmington Hills, MI, USA, 2011; p. 111.
51. Raphael, J.M. Tensile strength of concrete. *ACI J. Proc.* **1984**, *81*, 158–165.
52. Concrete Reinforcement. Available online: http://www.bekaert.com/en/products/construction/concrete-reinforcement (accessed on 22 October 2020).
53. CSN. *CSN 73 1001: Subsoil under Shallow Foundations*; Czech Standardization Agency: Praha, Czech Republic, 1987.
54. CSN. *CSN 72 1006: Soil Compaction Control*; Czech Standardization Agency: Praha, Czech Republic, 1998.

materials

Article

# Rotational Stiffness and Carrying Capacity of Timber Frame Corners with Dowel Type Connections

**Marek Johanides [1,*], David Mikolasek [1], Antonin Lokaj [1], Petr Mynarcik [2], Zuzana Marcalikova [1] and Oldrich Sucharda [2,3]**

[1] Department of Structures, Faculty of Civil Engineering, VSB-Technical University of Ostrava, 708 00 Ostrava, Czech Republic; david.mikolasek@vsb.cz (D.M.); antonin.lokaj@vsb.cz (A.L.); zuzana.marcalikova@vsb.cz (Z.M.)

[2] Department Centre of Building Experiments, Faculty of Civil Engineering, VSB-Technical University of Ostrava, 708 00 Ostrava, Czech Republic; petr.mynarcik@vsb.cz (P.M.); oldrich.sucharda@vsb.cz (O.S.)

[3] Department of Building Materials and Diagnostics of Structures, Faculty of Civil Engineering, VSB-Technical University of Ostrava, 708 00 Ostrava, Czech Republic

* Correspondence: marek.johanides@vsb.cz

**Abstract:** With the development of wooden structures and buildings, there is a need to research physical and numerical tests of wood-based structures. The presented research is focused on construction and computational approaches for new types of joints to use in wooden structures, particularly glued lamella elements made of wood and wood-based composites. This article focuses on improving the frame connection of a wooden post and a beam with the use of fasteners to ensure better load-bearing capacity and stiffness of the structure. In common practice, bolts or a combination of bolts and pins are used for this type of connection. The aim is to replace these commonly used fasteners with modern ones, namely full thread screws. The aim is also to shorten and simplify the assembly time in order to improve the load-bearing capacity and rigidity of this type of frame connection. Two variations of the experimental test were tested in this research. The first contained bolts and pins as connecting means and the second contained the connecting means of a full threaded screw. Each experiment contained a total of two tests. For a detailed study of the problem, we used a 2D or 3D computational model that models individual components, including fasteners.

**Keywords:** rotational stiffness; wood; timber; frame connection; screws; glued laminated timber; numerical model; finite element method

## 1. Introduction

Wood is an important building material that can be used in all applications of construction tasks. However, in some respects, it requires specific approaches, such as testing of mechanical properties and classification [1,2]. It is also possible to use specific dynamic testing [3] or the vibration acoustic method [4]. The diagnostics of existing structures and the determination of mechanical properties are closely related to the testing of mechanical properties [5]. The current possibilities of wood processing technology and design of structures allow a wide range of applications from simple structures, through multi-story buildings [6] to long-span structures [7]. However, it is important to take into account the experience from previous accidents and structural failures in design and analysis [8]. For a correct understanding of the behavior and design of wooden structures, it is appropriate to use experimental tests of structural details [9–11] or structural parts, such as entire frames [12]. For example, the use of numerical modeling based on the finite element method is also very important [13–15]. It is most often used to determine rotational stiffness, overall load capacity, or failure mechanism. It is also possible to simulate dynamic loading [11]. Typical experiments include, in particular, frame corner [16], timber-to-timber joints [17], connection/joint [18], and detail [19] experiments.

In the Czech Republic and Slovakia, materials such as steel and reinforced concrete are used in construction more than wood. Of course, structural timber is also used but mainly for the construction of the roof structure or column structure of a building, for example, with a two by four system, or as formwork or visual elements [20].

Due to these facts, current standards are more focused on carpentry joints and the assessment of rod wooden structures produced from sawn wood. Therefore, no calculations or testing procedures have been developed for large joints or large elements made of glued laminated timber. Many production problems and questions associated with the calculation and assessment of such elements arose with the onset of the production of dimensional elements from glued laminated timber. New types of joints and dimensions of the structure brought new types of stresses that older standards for structural design did not identify.

Thanks to modern computer technology, mathematical models, and physical testing of structures on a real scale, it is now possible to design new types of structures, including their connections. Numerical modeling is a valuable and necessary tool in examining the nature of the structure as a whole; moreover, it enables clarification of the nature of various details of the structure, especially joints. It is possible to better understand the interaction between the material and the geometry of the structure by correctly designing and setting the numerical model. With the correct numerical model, we can save a lot of time, energy, and resources when designing the structure and details.

Today, with the emphasis on ecology and renewable resources, wooden structures have begun to appear in our region. Wood is a material with a high variability of properties and the only renewable raw material that comes from nature and disappears without a negative impact on the environment. Information on wood from the Czech Republic can be found in [21]. The most influential factors that cause a variance in wood properties include the type of wood and the locality in which the wood grew. Other influences on the properties of wood are the soil, climate, altitude, the season in which the tree was cut, and, last but not least, the method and quality of processing. In the case of wood as a construction material, we speak either of sawn wood, which is obtained by cutting from conifers or broad-leaved trees [22], or wood-based materials, such as glued laminated timber [23], which is produced by gluing wooden squares to the required size and shape. Wood shows different physical and mechanical properties in mutually perpendicular directions. This means that the properties observed parallel to the fibers are different from the properties observed perpendicular to the fibers. Wood has the greatest strength and stiffness and the least deformation due to moisture and temperature in the direction parallel to the fibers. The mechanical properties of wood define its ability to withstand external loads. In this context, it is necessary to distinguish between the properties of class A wood and structural timber. The properties of class A wood show a relatively large diffusion, which intensifies the most in the case of structural timber due to the influence of growth inhomogeneities. In terms of mechanical properties, wood is an anisotropic material, but for calculations or numerical modeling, it can be considered a material of rectangular or cylindrical orthotropy [21].

One of the uses of wood, among others, is the construction of hall buildings, which are very popular due to their design; moreover, they are of fundamental importance in the construction industry. In addition to the mentioned factors in the selection of construction material for indoor buildings, there is also a fundamental emphasis on the use of natural and aesthetic materials [24–26]. This is typical, for example, for the construction of sports facilities. For these reasons, wooden structures are being increasingly used for construction.

The designer cannot normally experimentally test a design. This is mainly due to the financial and time-consuming nature of the experiment. Therefore, the creation of a numerical model or analytical model based on the recommendations of applicable standards and academic literature is common for a design. In practice, however, selecting the wrong connection often leads to oversizing of structural elements, and thus, to an uneconomical design of the building.

The frame connection of these structural elements [27,28] is most often used between the beam and the post. Such connection of elements is one of the most important areas for the designing of wooden structures; the issue of design and assessment of joints of wooden structures fundamentally affects the overall composition of the supporting structure and the dimensions of the main supporting elements [29]. By optimizing this point, significant material savings can be achieved during construction, which will reduce the cost and complexity of the construction.

The load-bearing capacity and stiffness of joints are often a crucial factor for the design and operation of the structure as a whole, especially in structures with larger range, where the joint is heavily stressed. Joints of wooden frame elements can be addressed in several ways. One can use glued joints [30–32], for example, by means of glued steel bars. Another possibility is to form a frame connection from a post, which is arranged in a V-shape [33]. The most commonly used type of joint is the creation of a frame connection between a post and a beam by means of pin-type mechanical fasteners [34].

The subject of this paper is experiments focused on the frame connection of the post and the beam created by means of pin-type metal mechanical fasteners. Modern high-strength screws are currently also used as a semi-rigid coupling means for wood–concrete ceilings, as an alternative to fastening with a glued steel bar [35]. Correctly evaluating the behavior and load-bearing capacity of timber connections is important, for example, to evaluate structural timber connections with different distances between the fastener and the loaded end at different moisture contents [36]. The aim of this paper was also to create a more durable connection to the same structure, so the geometry, cross-section of structural elements, and the material of the strut and partition of both experiments were identical. Two types of experiments were created, each containing two tests. The connection was made in the first experiment from the standard mechanical pin-type fasteners that we encounter in common practice. This was a combination of bolts and pins. In the second experiment, the frame connection of the post and the beam was made of full threaded screws, which are not used for this type of connection in common practice. Therefore, the motivation was to analyze in detail this type of connection to determine how the structure functions as a whole, as well as the load-bearing capacity of the frame joint and the rotational stiffness, important for the redistribution of internal forces in the structural system of the bar model.

There is currently no standard for determining the load-bearing capacity and rotational stiffness of frame joints. Therefore, the analytical determination of these values was based on academic literature and articles [37,38], from which the bearing capacity and rotational stiffness of the joint were calculated. In addition, the translational stiffness and load-bearing capacity of the bonding agent were calculated from the standard [39] and current approaches to the design of wooden structures [40,41].

## 2. Materials and Methods

### 2.1. Description of Construction and Geometry

The construction system of the experiment consisted of a bending rigid connection of the frame post and the beam, which was formed from a metal mechanical connecting means of the pin type. The frame post had a cross section of 180/700 mm, with a wood class of GL24h. The frame beam had a cross section of 2 × 120/700 mm, wood class GL24h. The geometry and dimensions of the structural elements of the experimental tests were identical; the difference can be found in the connecting means, the number, and the geometries of the arrangement. The structural elements were connected by a bending rigid connection by means of a combination of bolts and pins with a diameter of 12 mm in experiment setup no. 1 (test no. 2 and test no. 4). In experiment setup no. 2 (test no. 1 and test no. 3), this connection consisted of an 11 mm diameter full thread screw. In order to perform this experiment, it was necessary to create the rigid boundary conditions of the structure. To ensure the correct boundary conditions, a steel structure was made, which was anchored by means of a threaded rod into a reinforced concrete ceiling slab 450 mm thick. The posts of the frame structure were attached to this structure by means of steel sheets and screws, which ensured the boundary conditions. The geometry of the frame corner structure and a sample of the steel structure are shown in Figure 1. The individual frame connections are described in the section below.

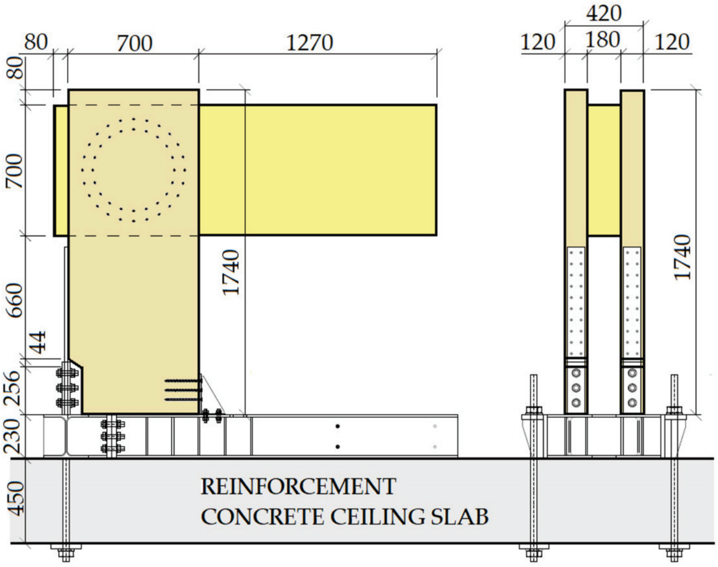

**Figure 1.** Design test system.

### 2.2. Experiment Setup No. 1—Joint Created from a Combination of Bolts and Pins

This experiment consisted of creating a frame connection between the post and the beam using bolts and pins with a diameter of 12 mm. The material of the fasteners was steel of class 8.8. The arrangement of the bolts and pins was on two symmetrically centered circles. Circle 1 had radius $r_1$ = 266 mm, and there were 22 fasteners on it. Circle 2 had radius $r_2$ = 206 mm, and there were 16 fasteners on it. The joint geometry and detailed arrangement of the screws is shown in Figure 2.

The arrangement of the fasteners from the loaded/unloaded edge and between the fasteners was not defined in [40] for a circular arrangement. Therefore, these distances were determined on the basis of recommendations given in the literature [41].

The ratio between the number of bolts and pins was chosen based on the recommendations of the literature [41].

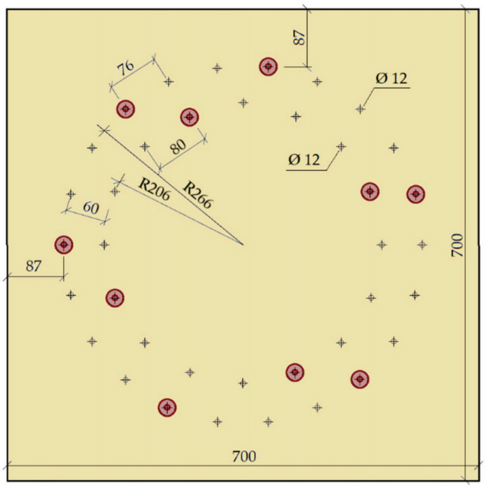

**Figure 2.** Location of fasteners, bolts, and pins (experiment setup no. 1).

### *2.3. Experiment Setup No. 2—Joint Created from Full Threaded Screws*

This experiment consisted of creating a frame connection of the post and the beam using full-threaded screws. The diameter was 11 mm, and the length of the screw was 400 mm. The material of the screw was steel class 10.9. The arrangement of the screws was on two symmetrically concentrated circles, where circle 1 had radius $r_1$ = 273 mm, and there were 24 screws on it. Circle 2 had radius $r_2$ = 218 mm, and there were 20 screws on it. The joint geometry and detailed arrangement of the screws are shown in Figure 3.

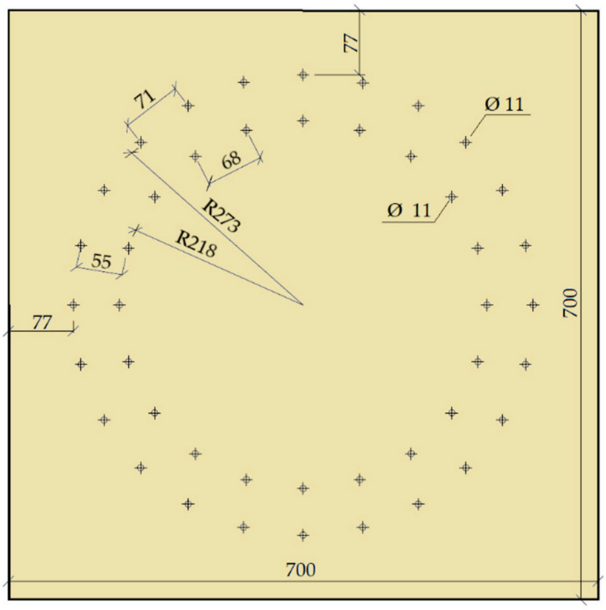

**Figure 3.** Location of fasteners, and full threaded screws (experiment setup no. 2).

The arrangement of the fasteners from the loaded/unloaded edge and between the fasteners was not defined in [40] for a circular arrangement. Therefore, these distances were determined on the basis of recommendations given in the literature [41].

### *2.4. Description of Sensor Location*

Three deformation sensors were mounted on the structure in order to be able to monitor the deformation of the structure, on the basis of which we later determined the value of rotational stiffness. Specifically, they were potentiometer sensors, which belong to the category of resistance sensors, Type TR–0100. The displacement tracer - the spring potentiometer linear position sensor, which had a linear deviation of 0.01 mm with a maximum stroke length of 100 mm, is shown in Figure 4.

Two sensors were placed on the cross-sectional axis of the beam. One was at the end of the free end of the beam, under the load (press head), and the other was placed in the middle of the frame corner (see the cross points in Figure 5). Due to the location of these two deformation sensors, we were able to measure and calculate the actual vertical deviation of the measured points. It was necessary to fit another deformation sensor to the structure. It was mounted on the post, specifically on the imaginary axis of the beam. This sensor recorded the horizontal tilt of the construction (see the full point in Figure 5).

Based on the arrangement of the deformation sensors, we were able to separate the individual components of deformation and tilt; thus, we calculated the actual value of the rotational stiffness of the frame connection of the post and the beam.

**Figure 4.** Displacement tracer—sensor from company Ahlborn [42].

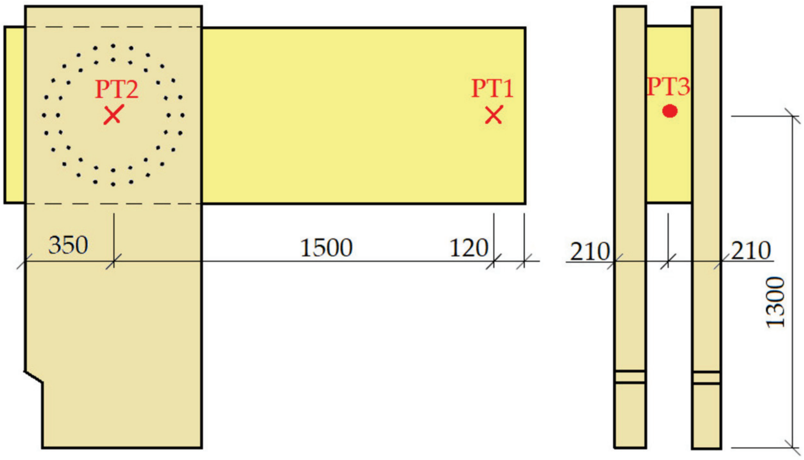

**Figure 5.** Deformation sensor location display, front view on the left, side view on the right.

### 2.5. Description of Test Equipment

The experiment was performed in the experimental construction center, Faculty of Civil Engineering VSB—Technical University of Ostrava, Czech Republic, on a hydraulic servo roller, which allowed tensile, pressure static, and dynamic tests. The maximum force that the electrohydraulic rollers of the test equipment could generate was 400 kN, which was sufficient for testing the frame system up to failure.

### 2.6. Description of the Loading Process

To perform experiments, it can be noted that the choice of loading (force/deformation) must be chosen individually with respect to a particular experiment (structure/part of the structure). From the point of view of design standards, the force load is more suitable for the linear area of loading. Deformation load, which is usually also used in numerical modeling in nonlinear analysis, is more suitable for determining the overall course of the experiment. It is possible to combine both approaches of loading (force/deformation), but this is suitable for tests that are repeated several times. The Newton Raphson Method and deformation load were used in the nonlinear calculation. Therefore, the same method was chosen for the experiments. The basic/initial process of loading was determined according to the standard in [43]. The structure was first loaded to about 40% of the characteristic load capacity, the value of which was calculated according to the standard in [40] and the professional literature [41]. Subsequently, the construction was lightened. This was followed by a second cycle in which the load was about 70% of the characteristic load capacity. This step was followed by loading until the structure was damaged. Table 1 shows the load values shows the load curve for experiment setup test no. 1 on bolts and pins fasteners, determined according to [44]. Table 2 shows the load values shows the load curve for experiment setup test no. 2 on screw fasteners, determined according to [44]. The resulting loading process is clearly visible in the resulting load–displacement diagrams.

**Table 1.** The course of test of the experiment setup no. 1, bolts and pins.

| Loading Step | From (kN) | | To (kN) |
|---|---|---|---|
| Step 1 | 0 = 0 | | $0.40 \times F_{\text{test}} = 40.80$ |
| Step 2 | | Hold | |
| Step 3 | $0.40 \times F_{\text{test}} = 40.80$ | | $0.10 \times F_{\text{test}} = 10.20$ |
| Step 4 | | Hold | |
| Step 5 | $0.10 \times F_{\text{test}} = 10.20$ | | $0.70 \times F_{\text{test}} = 71.40$ |
| Step 6 | $0.70 \times F_{\text{test}} = 71.40$ | | $F_{\text{test}} = 102.00$ |

**Table 2.** The course of test of the experiment setup no. 2, full threaded screws.

| Loading Step | From (kN) | | To (kN) |
|---|---|---|---|
| Step 1 | 0 = 0 | | $0.40 \times F_{\text{test}} = 52.80$ |
| Step 2 | | Hold | |
| Step 3 | $0.40 \times F_{\text{test}} = 52.80$ | | $0.10 \times F_{\text{test}} = 13.20$ |
| Step 4 | | Hold | |
| Step 5 | $0.10 \times F_{\text{test}} = 13.20$ | | $0.70 \times F_{\text{test}} = 92.40$ |
| Step 6 | $0.70 \times F_{\text{test}} = 92.40$ | | $F_{\text{test}} = 132.00$ |

Figure 6 shows the position of applying the load "*F*" to the structure. The position of loading into the structure was the same for both tests.

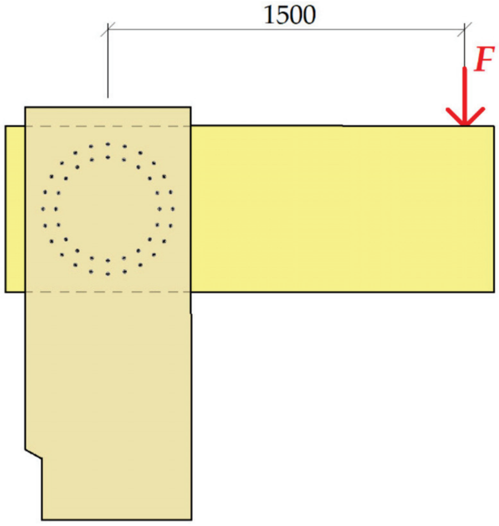

**Figure 6.** Position of the load *F*.

### 2.7. *Calculation of the Load-Bearing Capacity of the Frame Connection*

The literature [41] was used to determine the load-bearing capacity of the frame connection. The calculation of the bearing capacity was based on Johansen's relations. The frame connection was a double shear connection of the wood–wood type.

$$F_{v,Rk} = min\begin{cases} f_{h,1,k}\cdot t_1\cdot d \\ 0.5\cdot f_{h,2,k}\cdot t_2\cdot d \\ 1.05\cdot\frac{f_{h,1,k}\cdot t_1\cdot d}{2+\beta}\cdot\left[\sqrt{2\beta\cdot(1+\beta)+\frac{4\beta\cdot(2+\beta)\cdot M_{y,Rk}}{f_{h,1,k}\cdot d\cdot t_1^2}}-\beta\right]+\frac{F_{ax,Rk}}{4} \\ 1.15\cdot\sqrt{\frac{2\cdot\beta}{1+\beta}}\cdot\sqrt{2\cdot M_{y,Rk}\cdot f_{h,1,k}\cdot d}+\frac{F_{ax,Rk}}{4} \end{cases}, \quad (1)$$

with

$$\beta = \frac{f_{h,2,k}}{f_{h,1,k}}, \quad (2)$$

where:

$F_{v,Rk}$ is the characteristic load-bearing capacity of one cut of one fastener;
$t_i$ is the wood thickness 1 or 2;
$d$ is the diameter of the fasteners;
$M_{y,Rk}$ is the characteristic plastic moment of bearing capacity of the fastener;
$\beta$ is the ratio between the compressive strengths of the elements; and
$F_{ax,Rk}$ is the characteristic axial load capacity for pulling out the fasteners.

### 2.8. Calculation of Translational and Rotational Stiffness of a Frame Connection

To calculate the internal forces, it is important to correctly capture the rigidity of the connections. The main characteristic of the rigidity of the joint of wooden structures is the tempering module $K_{\mathrm{ser}}$; this value expresses the displacement of the fasteners from a given shear force in the shear surface and the axial force. The torsional spring stiffness $K_{\mathrm{r}}$ expresses the rotation from the moment. These displacement modules $K_{\mathrm{ser}}$ were calculated according to the standard in [40], and $K_{\mathrm{r}}$ was calculated according to literature [41].

### 2.9. Calculation of Translational Stiffness

The relationship applies to one cut of a transversely stressed bolt screw:

$$K_{\mathrm{ser}} = \frac{{\rho_{\mathrm{m}}}^{1.5}\cdot d}{23}, \quad (3)$$

where:

$\rho_{\mathrm{m}}$ is the average density of the connected wooden element; and
$d$ is the diameter of the fastener.

The literature [40,41] allows the value of $K_{\mathrm{ser}}$ to be doubled for the steel–wood joint:

$$K_{\mathrm{ser}} = 780\cdot d^{0.2}\cdot {l_{\mathrm{ef}}}^{0.4} \quad (4)$$

where:

$l_{\mathrm{ef}}$ is the effective length of screw penetration; and
$d$ is the screw diameter.

The design value of the release module is calculated as

$$K_{\mathrm{u}} = \frac{2}{3}\cdot K_{\mathrm{ser}}, \quad (5)$$

The translational stiffness of the joint is given by the sum of the slip modules of the individual fasteners. For a two-shear connection with $n$ fasteners in ULS, the following relation applies:

$$K_{\mathrm{t,u}} = 2\cdot n\cdot K_{\mathrm{u}}, \quad (6)$$

where:

$n$ is number of fasteners; and
$K_u$ is translational stiffness of the fasteners in Relation (5).

### 2.10. Calculation of Rotational Stiffness

The calculation of the torsional spring stiffness $K_r$ of the flexible joint can be determined by means of the slip module of the fastener in ULS $K_u$ or the slip module of the fastener in the SLS $K_{ser}$ according to the relation

$$K_{r,u} = \sum_{i=1}^{n} K_u \cdot r_i^2 \text{ resp } K_{r,ser} = \sum_{i=1}^{n} K_{ser} \cdot r_i^2, \tag{7}$$

where:

$K_u$ and $K_{ser}$ are the slip module in ULS and SLS, respectively in Relations (4) and (5).

Thus, for the torsional spring stiffness of a two-shear joint with $n$ same fasteners in ULS, the following relation applies (it can also be calculated analogously in SLS):

$$K_{r,u} = 2 \cdot \left( K_u \cdot r_1^2 + K_u \cdot r_2^2 + K_u \cdot r_3^2 + K_u \cdot r_n^2 \right). \tag{8}$$

### 2.11. Numerical Model

For the experiment of test sample no. 1, two concepts for the computational model were used for numerical modeling. Both approaches to numerical modelling are based on the finite element method. The first concept of numerical modelling is focused on verifying the stability calculation. The computational model consists of shell and beam (rod) finite elements. The detail of the computational model and the finite element mesh is shown in Figure 7. The computational model was processed down to the details of the connecting elements, which are evident in Figures 8 and 9. The connection between the connecting elements and the wood was in the form of stiffening springs (beam), as can be seen in Figure 10b. *SCIA Engineer* software [45] was used for the calculations. The computational model had 82,793 2D finite elements and 3970 1D finite elements. In total, the computational model had 80,277 nodes, and 481,662 equations were solved. The performed calculations were used to verify the stability of the whole system before the experiment.

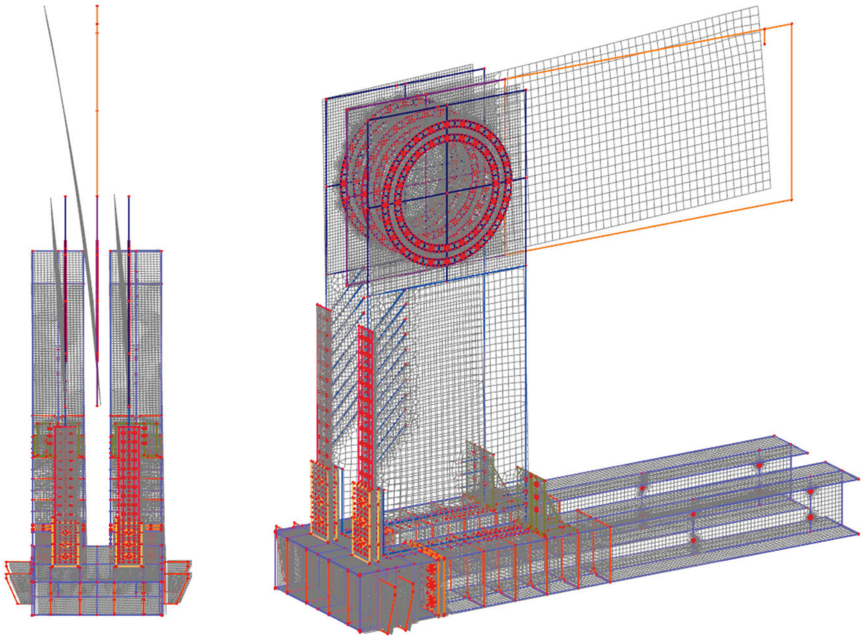

**Figure 7.** Computational model (global stability)—mesh finite elements.

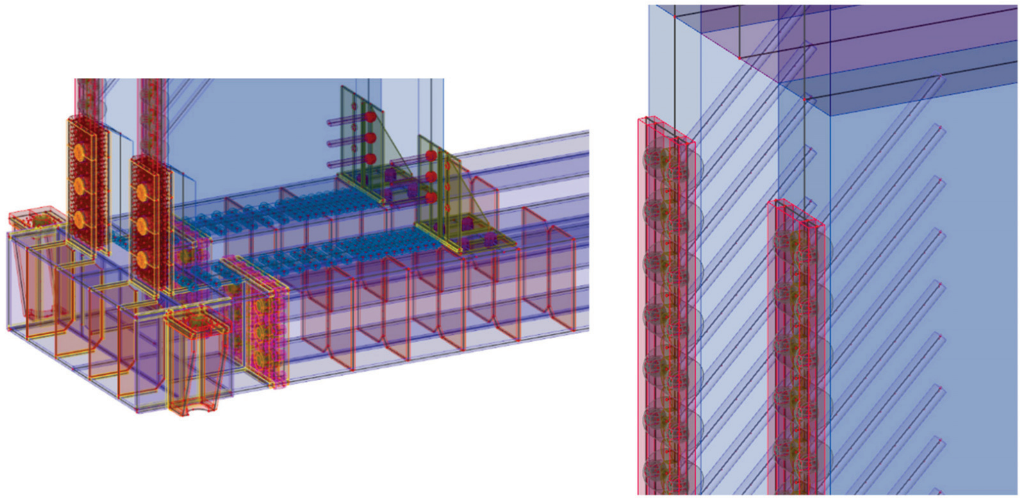

**Figure 8.** Computational model—detail of the mesh of finite elements of the frame.

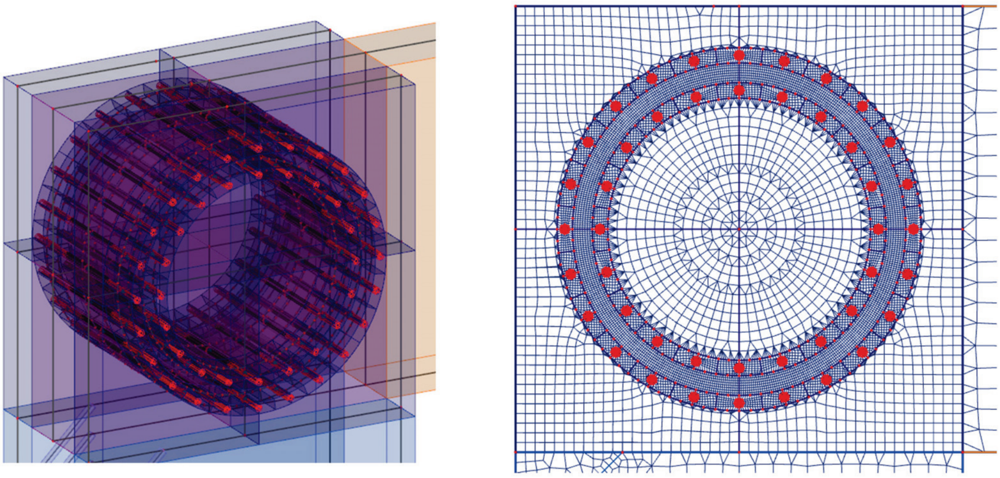

**Figure 9.** Computational model—detail of the mesh of finite elements of the frame.

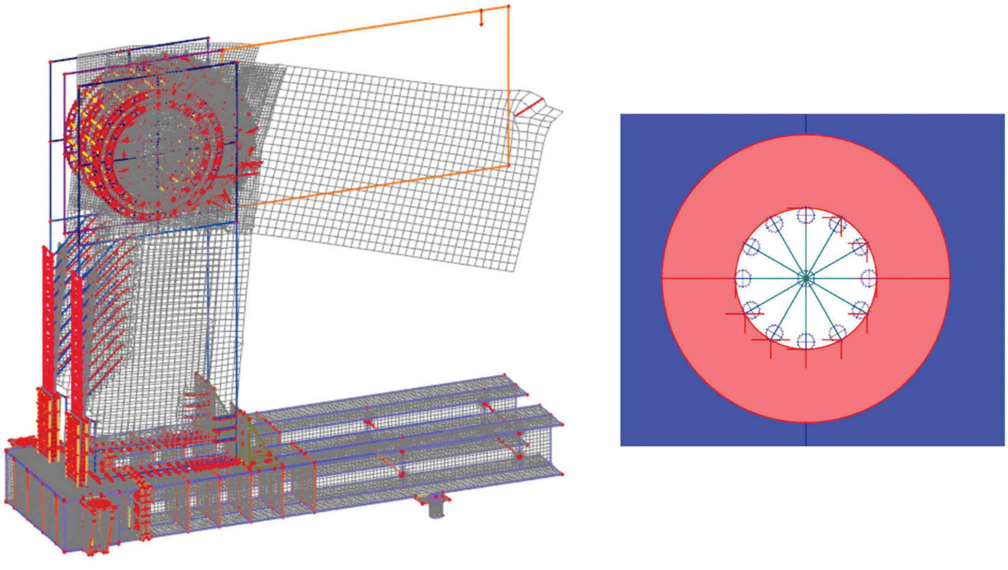

(**a**) (**b**)

**Figure 10.** Computational model: (**a**) local stability; (**b**) detail of the mesh of finite elements.

Calculations of nonlinear stability were performed. Figure 10a shows the local loss of stability. The global loss of stability is shown in Figure 7. The orthotropy of wood was taken into account in the calculations; the input parameters for the element with thickness are given in Table 3. For elements with a different thickness, the procedure was similar using the recommendations of the *SCIA Engineer* software [45]. The force in stability was calculated with a value of 132 kN, which corresponds to ultimate limit state. The first shape (Figure 10a) was 4.41, representing local buckling under force.

The second chosen concept of numerical modeling is based on the 3D computational model, which is shown in Figure 11. In the computational model, solid, shell, and beam finite elements were used, supplemented by contacts at the interface. *ANSYS*$^{\text{TM}}$ software [46] was used for the calculations. The computational model used finite elements: shell181, steel chassis base and frame corner; beam188, eccentricity exchanges and connections; and solid45, timber. Targe170 and conta174 elements were used for contacts. In total, the computational model had 543,939 nodes and 3,026,939 elements, and 1,693,955 equations were solved.

**Table 3.** Input parameters of wood elements.

| Element Width | Modulus of Elasticity of Wood | | Modulus of Elasticity in Torsion | | | Poisson's Ratio | |
|---|---|---|---|---|---|---|---|
| | Parallel to the Fibers | Perpendicular to the Fibers | | | | | |
| $h$ | $E_{\mid\mid}$ | $E_{\perp}$ | $G_{13}$ | $G_{23}$ | $G_{12}$ | $\nu_{12}$ | $\nu_{21}$ |
| (m) | (GPa) | | (GPa) | | | (-) | |
| 0.12 | 11 | 1 | 0.7 | 0.7 | 1.5 | 0.34 | 0.031 |
| 0.18 | 11 | 1 | 0.7 | 0.7 | 1.5 | 0.34 | 0.031 |

The goal of the computational models was to simulate the behavior during the test experiment. Again, the computational model was processed down to the detail of the fasteners, as shown in Figure 12a,b.

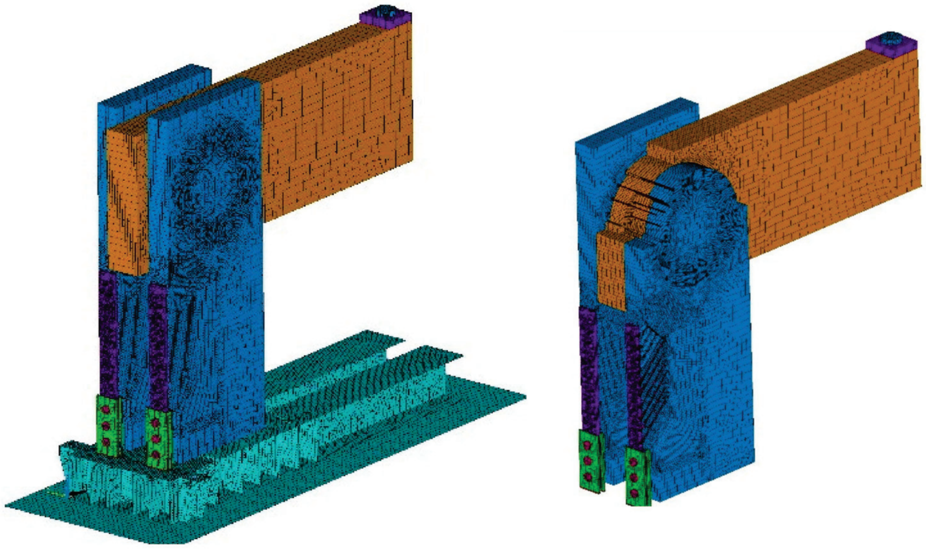

(**a**) (**b**)

**Figure 11.** The 3D computational model: (**a**) total model; (**b**) part of the model.

Wood behaves as a strong anisotropic material, but simplification to orthotropic behavior can be considered using numerical methods. When considering orthotropic material, it is possible to use a cylindrical model, which considers the curvature of annual rings, or a rectangular one, which does not consider the curvature of annual rings. We used a numerical orthotropic model, and the effects of annual rings were neglected, namely, the difference between spring and summer wood, local defects of wood such as bumps or cracks, and the variable structure of wood. Table 4 shows elastic constants of the material model of wood in the *ANSYS*$^{\text{TM}}$ program [46].

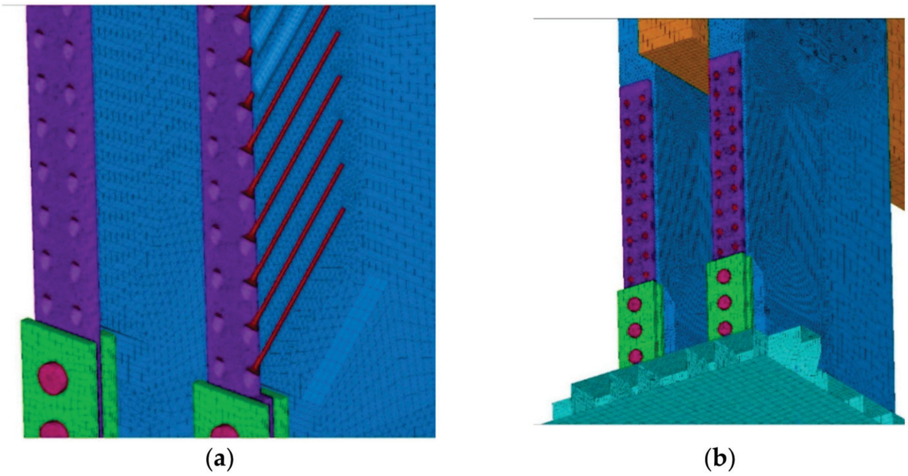
(**a**) (**b**)

**Figure 12.** The 3D computational model: (**a**) detail no. 1; (**b**) detail no. 2.

**Table 4.** Elastic constants of the material model of wood in the *ANSYS*$^{\text{TM}}$ program.

| Orthotropic Elasticity | Value | Units |
|---|---|---|
| Young's Modulus *X* direction | 11,000 | MPa |
| Young's Modulus *Y* direction | 821 | MPa |
| Young's Modulus *Z* direction | 455 | MPa |
| Poisson's Ratio *XY* | 0.44 | - |
| Poisson's Ratio *YZ* | 0.57 | - |
| Poisson's Ratio *XZ* | 0.56 | - |
| Shear Modulus *XY* | 555 | MPa |
| Shear Modulus *YZ* | 500 | MPa |
| Shear Modulus *XZ* | 677 | MPa |

The material model of wood was defined in the system of rectangular coordinates L, T, and R (see Figure 13) by nine elastic constants, which were the modulus of elasticity in the direction of fibers $E_L$; modulus of elasticity in tangential direction $E_T$; modulus of elasticity in radial direction $E_R$; modulus of elasticity in shear $G_{LT}$, $G_{LR}$, and $G_{TR}$; and the Poisson factors of transverse deformation $\nu_{LT}$, $\nu_{LR}$, and $\nu_{TR}$ (see Figure 13).

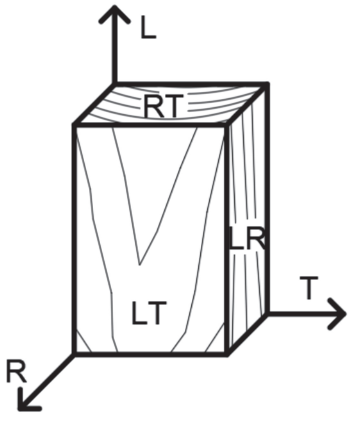

**Figure 13.** Planes of elastic symmetry of wood.

To illustrate the performed calculations, two graphic outputs were selected from the calculation in Figures 14 and 15. Figure 14 shows the total deformations on a 3D computational model. Figure 15 show the part of the computational with the strain $\varepsilon_{XZ}$. The 3D computational model allows a detailed study of the stress of the connecting elements; the illustrative results are shown in Figure 16.

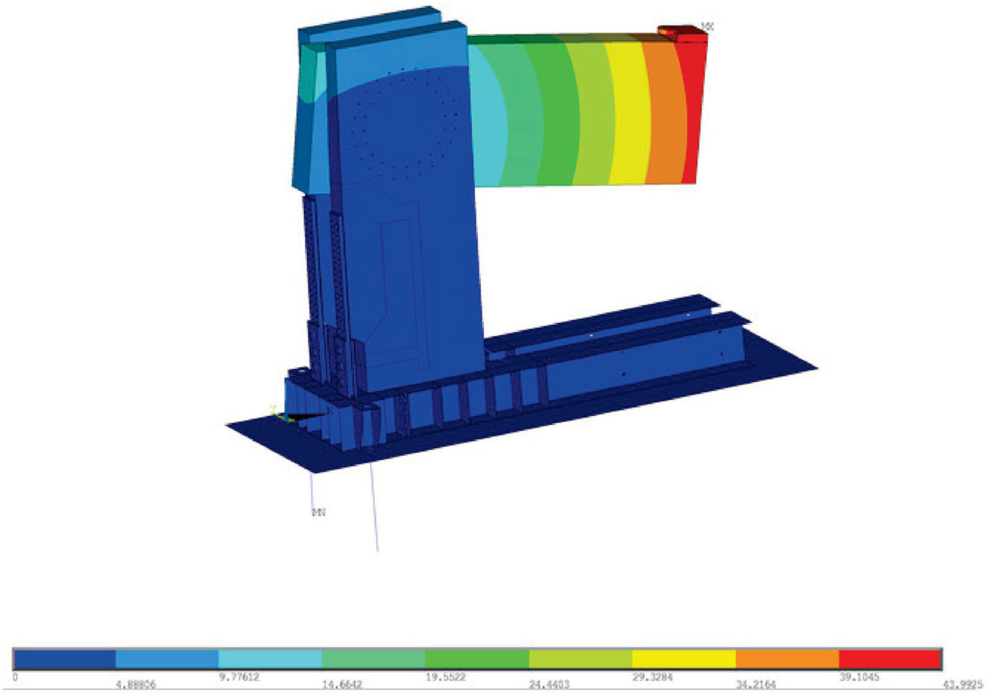

**Figure 14.** Total deformation of the computational model.

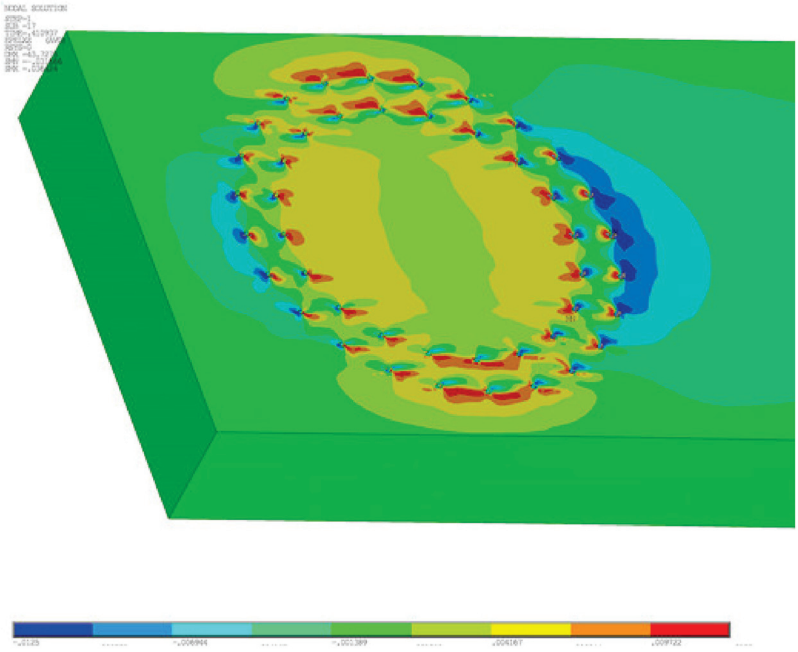

**Figure 15.** Computational model—strain $\varepsilon_{XZ}$.

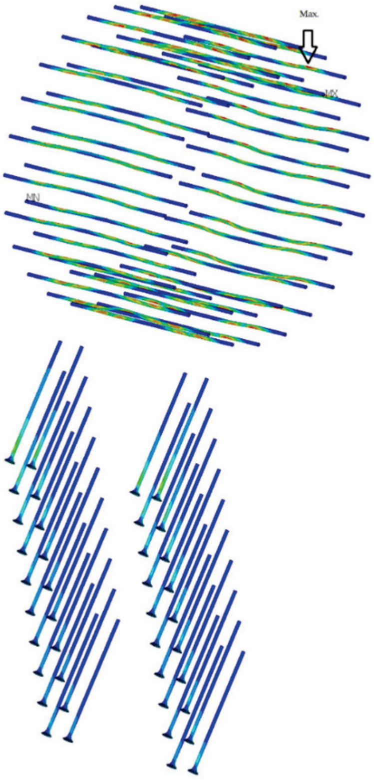

**Figure 16.** Connecting elements—max. stress.

### *2.12. Experimental Testing*

Individual samples of the frame connection were tested in the experimental construction center, Faculty of Civil Engineering VSB—Technical University of Ostrava, Czech Republic. Figure 17 shows a sample for experimental testing test sample no. 4 and no. 1.

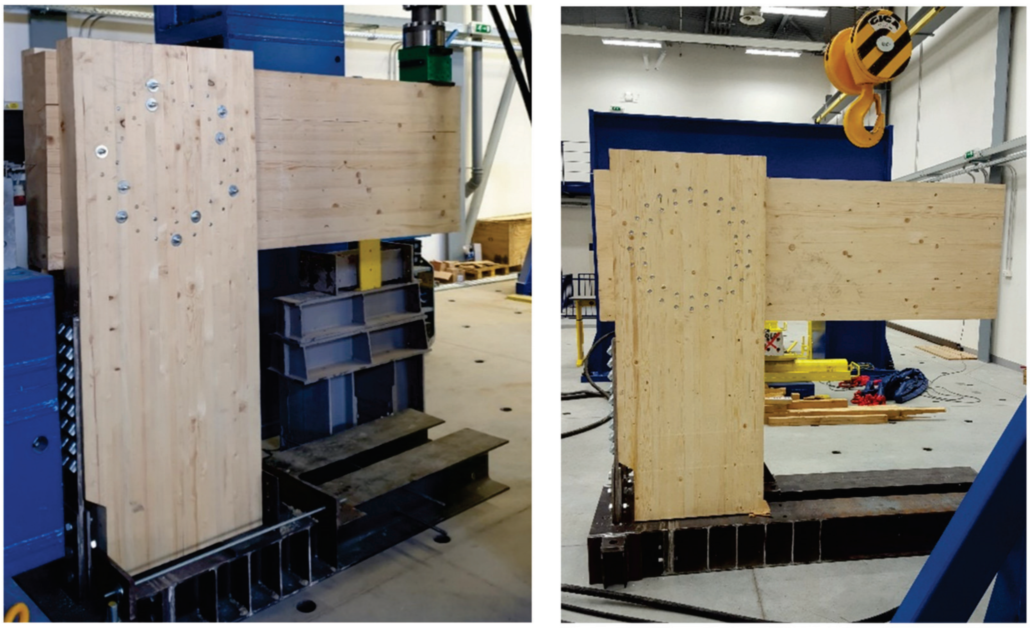
(**a**) (**b**)

**Figure 17.** Experimental sample: (**a**) test sample no. 4; (**b**) test sample no. 1.

Figure 18 shows the arrangement of the deformation sensors, according to the diagram shown in Figure 5.

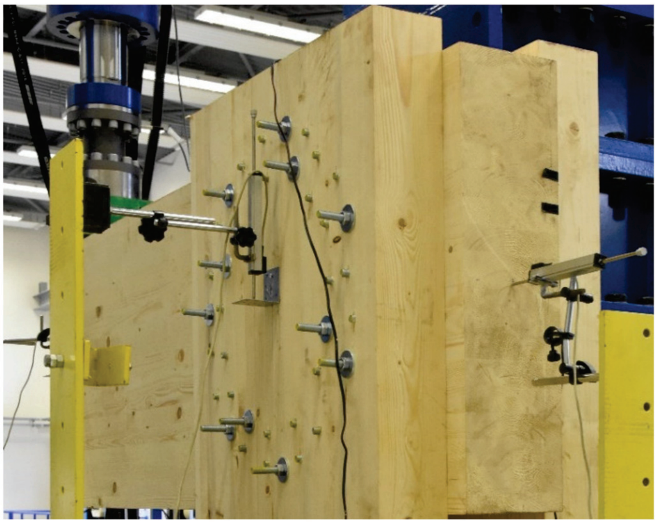

**Figure 18.** Placement of the deformation sensors.

The following figures show the damage modes of the individual samples. Figures 19 and 20 show the damage of the experimental test sample no. 1 and test sample no. 3, where the frame connections were made of full threaded screws. In these samples, the structure was broken by pulling perpendicular to the fibers at the top of the beam.

Figure 21 shows the damage of the experimental testing for test sample no. 2 and test no. 4, where the frame connections were made from a combination of bolts and pins. In these samples, the structure was broken by pulling perpendicular to the fibers in the upper part of the beam, which spread downwards.

(**a**) (**b**)

**Figure 19.** Experiment no. 2: (**a**) damage test sample no. 1; (**b**) damage test sample no. 3.

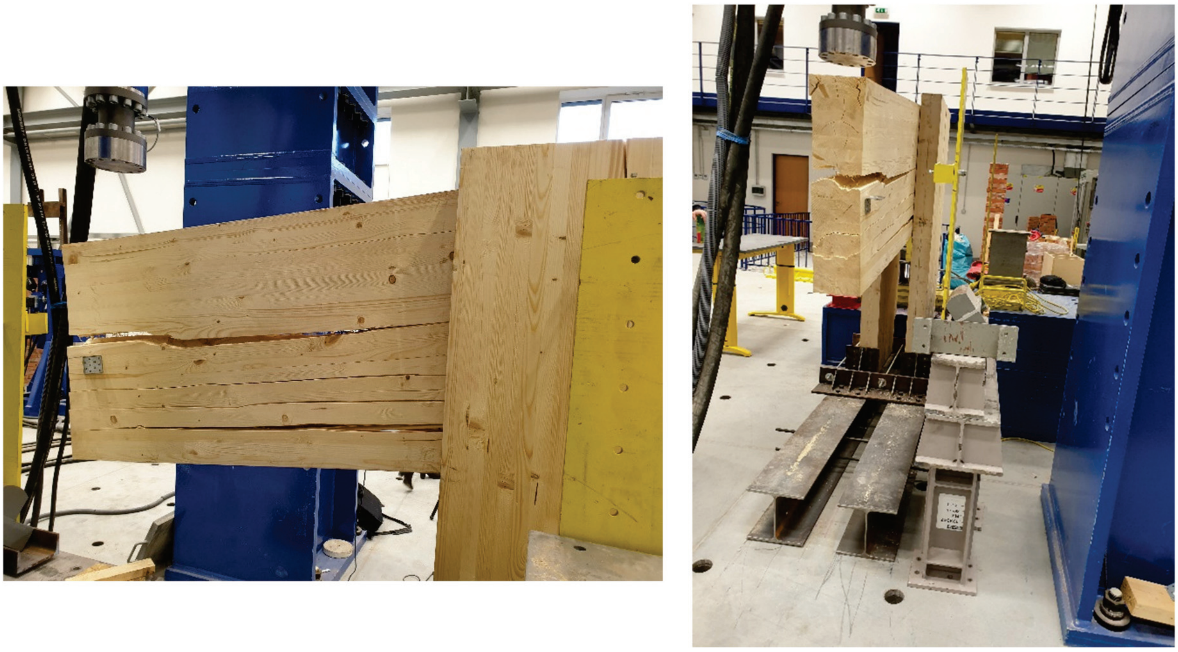

(**a**) (**b**)

**Figure 20.** Experiment no. 2: (**a**) damage test sample no. 3; (**b**) damage test sample no. 3.

(**a**) (**b**)

**Figure 21.** Experiment no. 1: (**a**) damage test sample no. 2; (**b**) damage test sample no. 4.

## 3. Results

### *3.1. Determination of Bearing Capacity and Rotational Stiffness of Joints for Test Sample No. 1 and No. 3, Full Threaded Screws, on the Basis of Standard and the Literature*

The load-bearing capacity of the connection was calculated according to [40,41]. To use the connection to about 100%, a force of 132 kN was used, which was located on the arm 1.50 m (spot of applying force, Figure 6). Table 5 shows the calculation of the load-bearing capacity of the connection for test no. 2 on screws. The table shows the load-bearing capacity of the outer circle, which contained 24 fasteners.

**Table 5.** Results of calculation of the characteristic load and capacity of the connection according to [40,41] for test sample no. 1 and test sample no. 3, full threaded screws.

| *N* | $\alpha$ | *r* | *x* | *y* | (*g*) | (*h*) | (*j*) | (*k*) | $F_{\mathrm{ax}}$ | $F_{\mathrm{v.Rk}}$ | $F_{\mathrm{v.E}}$ | **Use** |
|---|---|---|---|---|---|---|---|---|---|---|---|---|
| 19 | 270.00 | 273.00 | −273.00 | 0.00 | 38.64 | 20.57 | 13.11 | 6.06 | 5.32 | 22.77 | 22.73 | 99.79 |

$\alpha$ is the angle between the force and the direction of the fibers; *r* is the radius of the circle where the fasteners are located; *x* is the horizontal coordinate; *y* is the vertical coordinate; (*g*) is Johansen's relation (*g*)—Relation (1); (*h*) is Johansen's relation (*h*)—Relation (1); (*j*) is Johansen's relation (*j*)—Relation (1); (*k*) is Johansen's relation (*k*)—Relation (1); $F_{\mathrm{ax}}$ is the switching effect according to [41]; $F_{\mathrm{v,Rk}}$ is the characteristic load-bearing capacity of one cut of one fastener, Relation (1); $F_{\mathrm{v,E}}$ is a force acting on one cut of one fastener; and "Use" is the percentage utilization of the connection.

The Relations (3)–(8) were used to calculate the rotational stiffness, and we obtained the value $k_{\mathrm{r}}$ = 15.03 MNm/rad.

### *3.2. Determination of Bearing Capacity and Rotational Stiffness of Joints for Test Sample No. 2 and No. 4, Bolts and Pins, on the Basis of Standard and Literature*

According to [40,41] the load capacity of the connection was calculated. To use the connection to about 100%, the force of 102 kN was used, which was located on the arm 1.50 m (spot of applying force Figure 6). Table 6 shows the calculation of the load-bearing capacity of the connection for test no. 1, bolts and pins. The table shows the load-bearing capacity of the outer circle, which contained 22 fasteners. The fastening effect was neglected in this type of connection.

**Table 6.** Results of calculation of the characteristic capacity of the connection according to [40,41] for test sample no. 2 and sample no. 4, bolts and pins.

| *N* | $\alpha$ | *r* | *x* | *Y* | (g) | (*h*) | (*j*) | (*k*) | $F_{\mathrm{ax}}$ | $F_{\mathrm{v,Rk}}$ | $F_{\mathrm{v,E}}$ | **Use** |
|---|---|---|---|---|---|---|---|---|---|---|---|---|
| 18 | 278.18 | 266.00 | −263.29 | 37.85 | 39.71 | 20.37 | 14.13 | 10.44 | 1.08 | 20.89 | 20.88 | 99.95 |

$\alpha$ is the angle between the force and the direction of the fibers; *r* is the radius of the circle where the fasteners are located; x is the horizontal coordinate; *y* is the vertical coordinate; (*g*) is Johansen's relation (*g*)—Relation (1); (*h*) is Johansen's relation (*h*)—Relation (1); (*j*) is Johansen's relation (*j*)—Relation (1); (*k*) is Johansen's relation (*k*)—Relation (1); $F_{\mathrm{ax}}$ is the switching effect according to [41]; $F_{\mathrm{v,Rk}}$ is the characteristic load-bearing capacity of one cut of one fastener, Relation (1); $F_{\mathrm{v,E}}$ is a force acting on one cut of one fastener; and "Use" is the percentage utilization of the connection.

The Relations (3)–(8) were used to calculate the rotational stiffness, and we obtained the value $k_{\mathrm{r}}$ = 13.39 MNm/rad.

### *3.3. Comparison of Numerical Model and Experimental Testing*

Figure 22 shows a load–displacement diagram from the performed testing experiment of sample no. 1 and the calculations performed. Analyzed displacement is at the end of the beam. As part of the testing of the frame corner, two load tests were performed. The first load test marked with a yellow curve included two load steps with relief. The hysteresis of behavior during unloading is clearly visible on the curve. The structure (frame corner) did not collapse during testing. For clarity and comparison, a linearized approximation of the behavior of the tested frame for the elastic loading was performed for the first testing; the black dashed line with dots in the graph denotes the estimation of rigidity by linear segmenting. Furthermore, a second loading of the frame corner was performed, which is marked in orange, when the experiment was terminated by the collapse of the frame corner. The black dashed curve was created according to the analytical relationship of the force method with the simple rod/beam model using the rotational stiffness $K_{\mathrm{r,ser}}$ = 22.55 MNm/rad (calculated as a characteristic value according to the standard [40]). For the above simplified calculation by the force method, the difference in stiffness with the experiment was the largest. Furthermore, the calculation (blue curve) was performed using a numerical model created in *ANSYS*$^{\mathrm{TM}}$ and a linear calculation. The difference between an experiment and a calculation is smaller than for a simplified calculation. A more advanced variant in *ANSYS*$^{\mathrm{TM}}$ of the calculation taking into account the nonlinear character of the problem is indicated by a red curve. When comparing the load–displacement curve testing of a numerical model with a nonlinear solution, it can be stated that there was a relatively good agreement between the course and rotational stiffness.

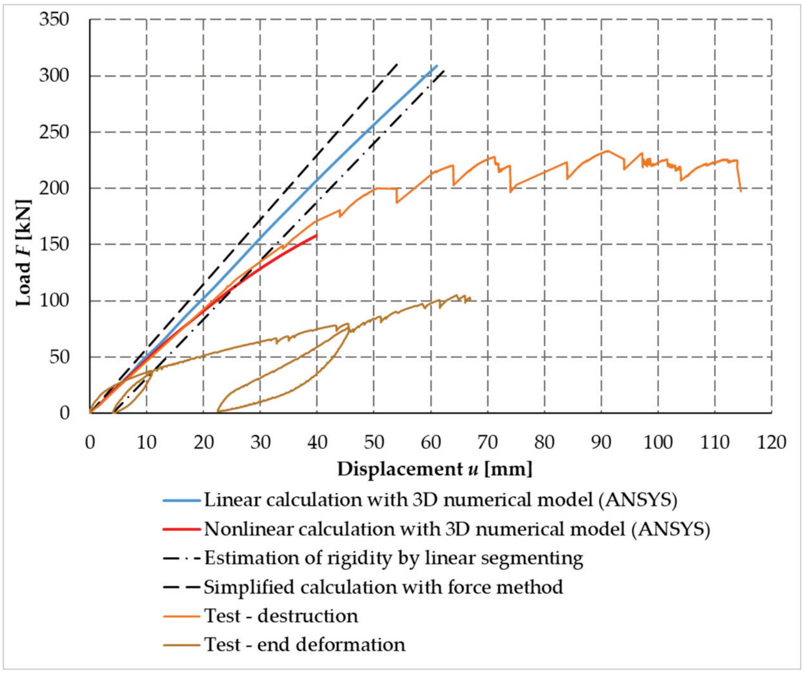

**Figure 22.** Load–displacement diagram with experiment sample no. 1 and calculations.

The individual research results (simplified calculation, numerical finite element models, and experimental testing) were compared with each other using some parameters, such as the collapse force of the wooden frame structure and deformation.

Testing also aimed to determine the mode of failure and the force causing the frame connection to collapse. Based on numerical and analytical calculations, it was assumed that the failure was the transverse tensile failure perpendicular to the fibers. This hypothesis was confirmed in experimental testing.

The corner connection of the frame was broken in tensile perpendicular to the fibers in the upper part of the beam at a force $F$ = 150.40 kN. It is possible to see the damage of the frame corner face in the pull perpendicular to the fibers in Figure 19.

The values of the maximum loading force of the experimental test were compared with the calculation methods given in Table 7. The value of the calculation according to [40] represented the force at the load-bearing capacity limit for the given frame connection. This value of [40] represented 1.14 times greater resistance than the load-bearing capacity based on experimental testing, showing relatively good agreement of the results. The highest load value came from a linear numerical model created in the *ANSYS*$^{\text{TM}}$ program; however, it was not confirmed in experimental testing. On the contrary, the best agreement was represented by a nonlinear numerical model in the *ANSYS*$^{\text{TM}}$ program, whose value of the failure force was closest to the force from the experimental testing. This agreement also suggested a fairly accurate numerical model.

**Table 7.** Comparison of results of individual computational approaches.

| Method of Calculation | Force Causing Collapse $F$ (kN) | Bending Moment Causing Collapse (kNm) | Multiplier $M$ (−) |
|---|---|---|---|
| Standard calculation EC5 [40] | 132.00 | 198.00 | - |
| *ANSYS*$^{\text{TM}}$—linear calculation | 308.89 | 469.51 | 1.96 |
| *ANSYS*$^{\text{TM}}$—nonlinear calculation | 157.94 | 240.07 | 1.20 |
| Experimental test | 150.40 | 225.60 | 1.14 |

### 3.4. Determination of Bearing Capacity Based on Experimental Testing

As already mentioned in the introduction, a total of four tests were created for experimental testing. Two frame connection structures were made of bolts and pins (test sample no. 2 and test sample no. 4) and the remaining two were made of screws (test sample no. 1 and test sample no. 3).

The maximum load-bearing capacities of the frame connection structure were found based on experimental testing, listed in Table 8. This table also shows the calculated load capacities from the analytical solution and these load capacities were mutually divided to obtain the load capacity ratio in the last column.

**Table 8.** Load-bearing capacity of individual frame connections.

| Test No. | Capacity Experimental Testing (kN) | Capacity Analytical Calculation (kN) | Ratio (−) |
|---|---|---|---|
| 1 | 233.30 | 132.00 | 1.767 |
| 2 | 161.30 | 102.00 | 1.581 |
| 3 | 150.40 | 132.00 | 1.139 |
| 4 | 133.00 | 102.00 | 1.304 |

Figure 23 shows the working curves of the experimental testing, which illustrate the dependence between the applied load and the deformation of the free end in the frame connection formed from bolts and pins for test sample no. 2 and test sample no. 4.

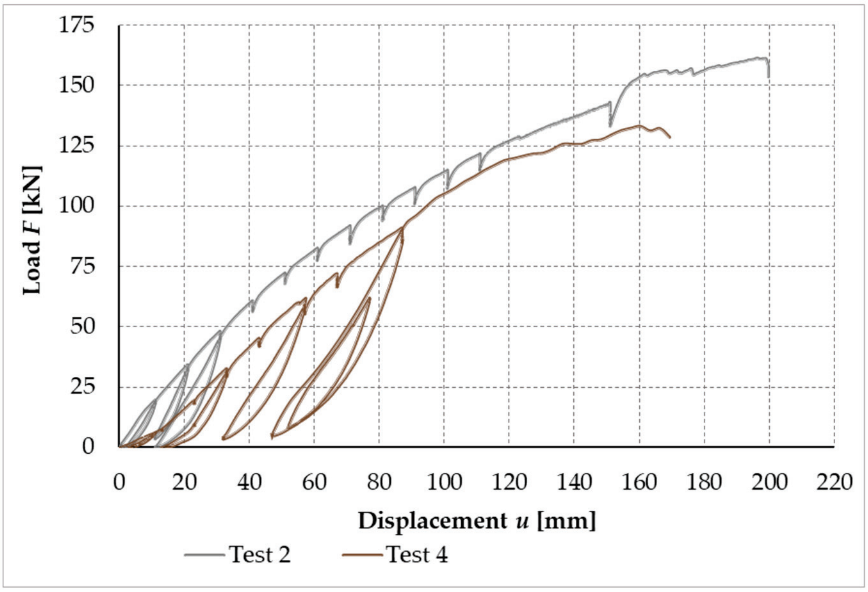

**Figure 23.** Load–displacement curves of experimental testing, test sample no. 2 and test sample no. 4 (experiment setup no. 1).

Figure 24 shows the working curves of the experimental testing, which illustrate the dependence between the applied load and the deformation of the free end in the frame connection formed from full-threaded screws for test sample no. 1 and test sample no. 3. Test sample no. 1 consists of two working curves. This is due to the fact that during the experimental measurement, it was necessary to readjust the path sensors at a force of about 100 kN.

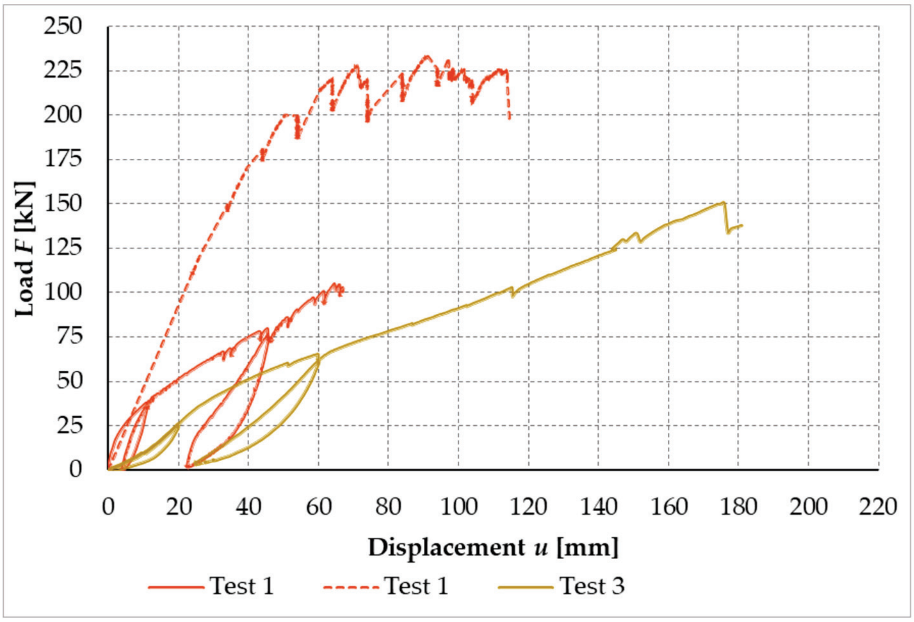

**Figure 24.** Load–displacement curves of experimental testing, test sample no. 1 and test sample no. 3 (experiment setup no. 2).

Figure 25 shows the load–displacement curves of all performed experimental tests.

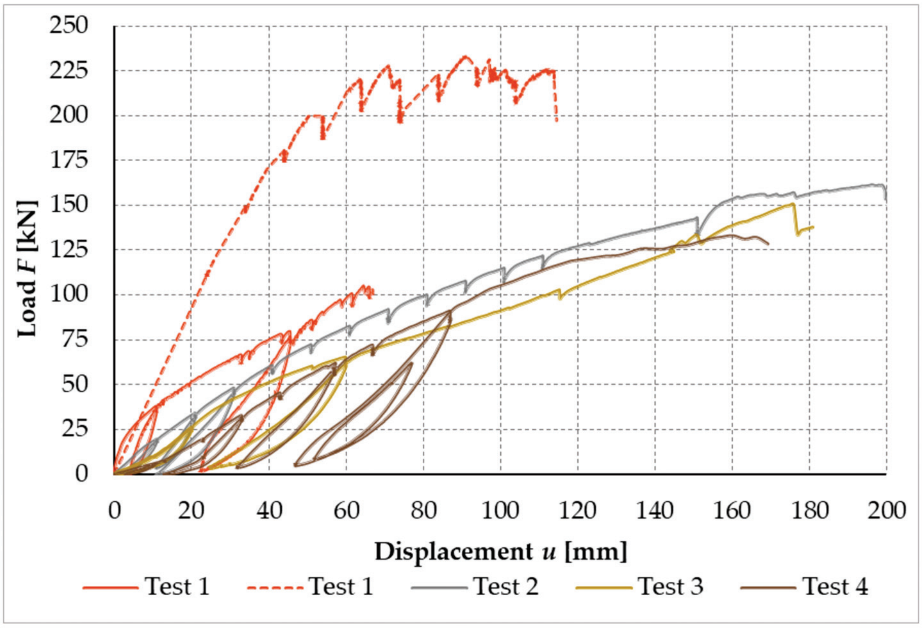

**Figure 25.** Load–displacement curves of experimental sample tests.

### *3.5. Determination of Rotational Stiffness Based on Experimental Testing*

Firstly, it was necessary to calculate all the experimental variables to determine the rotational stiffness of the frame joint. The variables were primarily detected as vertical deformations based on the applied load, from deformation sensors PT1 and PT2. When subtracting these two sensors, we found the actual vertical displacement of the scanned points. However, the section between these points was not a segment but a curve, the path of which was determined by the deformation of the cross-section of the beam by the bending moment and the shear force. Therefore, this value had to be calculated and brought into the calculation of the rotational stiffness of the joint. The vertical displacement of the points, under the sensors PT1 and PT2, was also influenced by the horizontal inclination of the structure due to the load. A deformation sensor PT3 was placed to measure this displacement. The last component that needed to be separated to calculate the rotational stiffness was the deformation of the cross-section of the post, which was caused by the bending moment and the shear force. For the location of said sensors, see Figure 5. After finding all the necessary variable deformations, it was possible to perform the separation of the rotational stiffnesses and thus, to calculate the actual value of the rotational stiffness of the fasteners in the frame connection.

Figure 26 shows the deformation value of the frame joint after subtracting all the mentioned deformation components. Based on the deformation components separated in this way, it was possible to determine the actual value of the rotational stiffness of the frame joint.

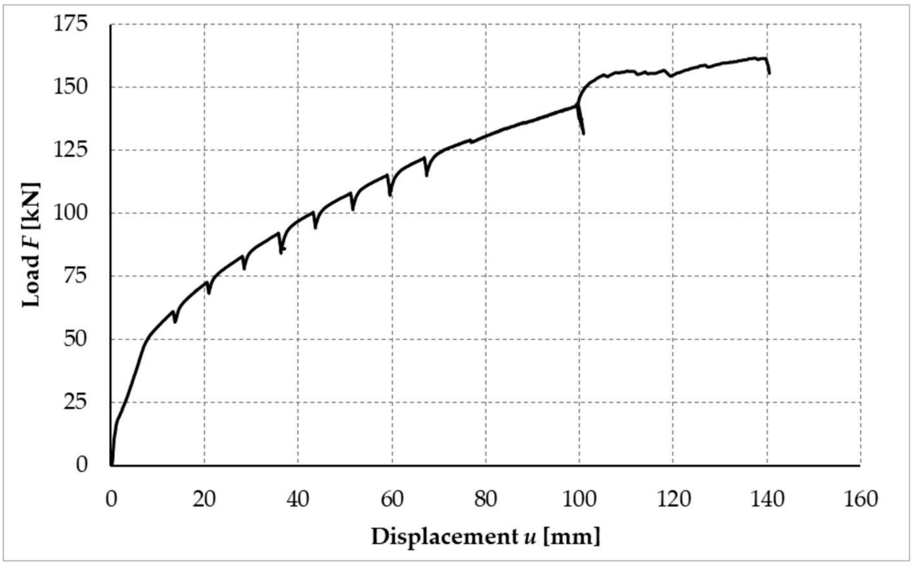

**Figure 26.** Deformation of the frame joint after separation of deformation components, test sample no. 2.

Figure 27 shows the calculated process of the rotational stiffness of the fasteners. The blue solid curve shown in Figure 27 is the course of rotational stiffness, the value of which is influenced by the magnitude of the applied load. The orange dashed line represents the value of rotational stiffness calculated for the ultimate limit (ULS) state according to [40,41]. The green solid line shows the actual measured value for 90% of the ultimate limit state (ULS) load capacity limit value. The black dashed line with one dot shows the calculated value for the serviceability limit state (SLS) and the blue dotted line shows the actual rotational stiffness value measured for 40% of the SLS load value for the serviceability limit state.

### 3.6. Measured Rotational Stiffness from Experimental Testing

Due to the fact that the PT3 deformation sensor was not fitted when performing test sample no. 1, it was not possible to determine the rotational stiffness of this test.

Table 9 shows the calculated values of rotational stiffness according to [40,41] and the actual measured values of rotational stiffness, which were measured and calculated for test sample no. 2 (bolts, pins) and test sample no. 3 (full thread screws).

The values given in Table 9 were determined based on [40], which recommends determining the value of rotational stiffness for the limit state of serviceability at a load of approximately 40% and for the limit state of ultimate at a load of approximately 90%.

Based on the values given in Table 9, the joint formed from the screws appears to be more rigid compared to the stiffness ratios between the measured values and the values calculated according to [40].

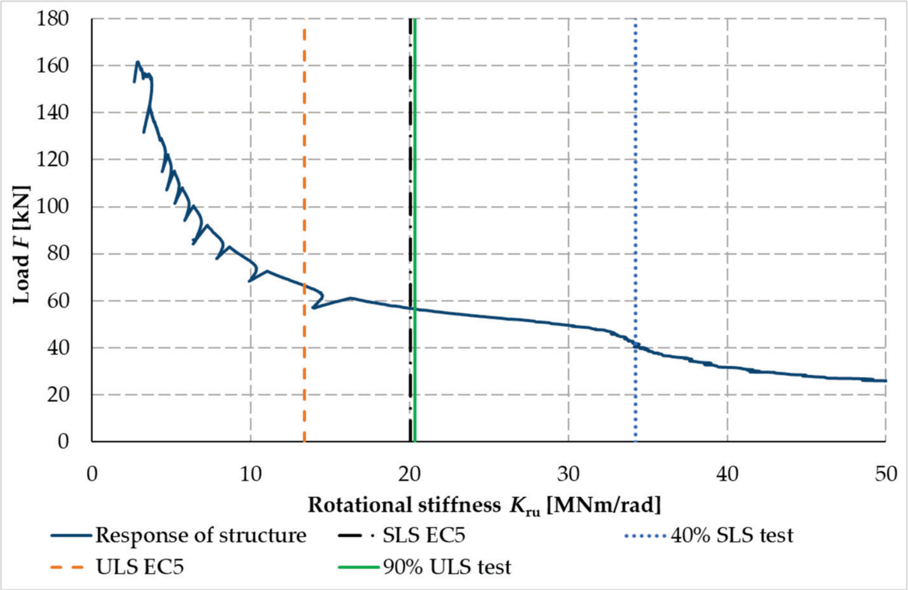

**Figure 27.** Process of rotational stiffness of frame connection, test sample no. 2.

**Table 9.** Table of stiffness.

| Frame Connection | $F$ (kN) | Serviceability Limit State $K_r$ (MNm/rad) | EC5 | $F$ (kN) | Ultimate Limit State $K_r$ (MNm/rad) | EC5 | Load Value (%) | Ratio (−) |
|---|---|---|---|---|---|---|---|---|
| Bolt | 40.80 | 34.258 | 20.081 | - | - | - | 40 | 1.706 |
| | - | - | - | 56.44 | 20.338 | 13.387 | 90 | 1.519 |
| Screws | 52.49 | 36.902 | 22.552 | - | - | - | 40 | 1.636 |
| | - | - | - | 73.28 | 21.617 | 15.033 | 90 | 1.438 |

### *3.7. Graphical Comparison of the Results of Numerical Modeling and Experimental Testing*

Figure 28 shows the deformed fasteners from the numerical model created in the *ANSYS*$^{TM}$ software and the experimental testing. Figure 29 shows these deformed fasteners in detail after the end of the experimental testing.

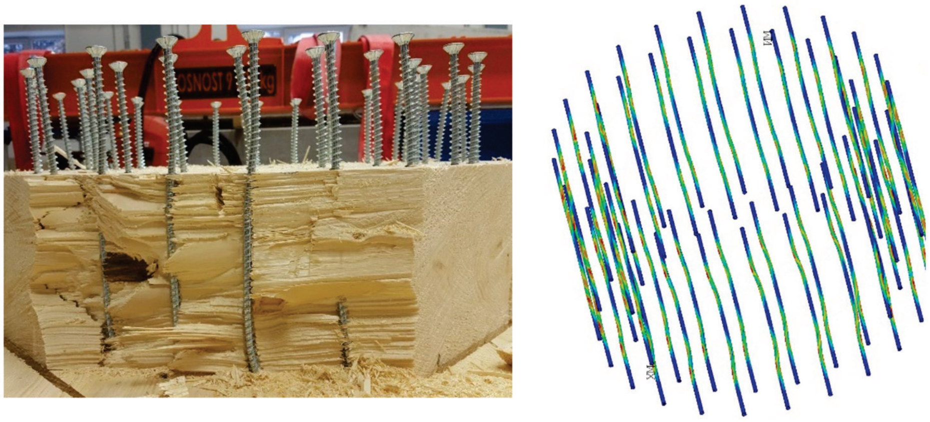

(**a**) (**b**)

**Figure 28.** (**a**) Deformed fasteners after experimental testing. (**b**) Deformed fasteners in numerical model *ANSYS*$^{TM}$.

**Figure 29.** Deformed fastener after experimental testing.

## 4. Discussion

This article focuses on the issue of a flexural rigid connection of wooden beams and posts connected by means of pin-type mechanical fasteners. Specifically, two samples were made with full threaded screws and two with bolts and pins. The task required the creation of numerical models and analytical assumptions, which were the basis for the design of experimental tests and were then used to compare the results.

Experimental testing has shown that screws, which are not commonly used to make this type of frame connection, have sufficient load-bearing capacity and rotational stiffness for the purpose of use as standard bolt-and-pin mechanical means.

In addition to the good agreement of the rotational stiffness of the sample with the full-threaded screws, such a connection also provides a load-bearing capacity with a certain margin in comparison with the determination of the load-bearing capacity according to the standard in [41,44] and the literature [40]. Such an assumption was considered because the standards assume a certain margin of bearing capacity before the collapse of a structural element or joint.

Experimental testing of samples formed from bolts and pins confirmed the safety and reliability of the use of these standardly used fasteners [40]. These samples showed a slightly higher value of the ratio between the result of bearing capacity and rotational stiffness of experimental testing and calculation according to standard [41,44] compared to samples formed from full threaded screws.

Frame connections formed of full threaded screws were broken during testing by pulling perpendicular to the fibers at the top of the beam (see Figure 19). This type of damage is predetermined and described in the literature [40] on analytical calculations and, which supports the correctness of the created numerical model.

Frame connections formed of bolts and pins were broken during testing by pulling perpendicular to the fibers at the top of the post (see Figure 21). This different type of damage, compared to samples with full threaded bolts, could occur because bolt and pin fasteners have only a minimal effect of closing the structural elements. Therefore, the stress was concentrated in the cross-section of the post. Damage occurred in it because the cross-section of the post is smaller than the beam. However, in order to verify such a hypothesis, it would be necessary to perform additional experimental tests of identical dimensions and connections.

The tested structure was not reinforced at the damage points, for example, by the use of screws or other additional reinforcements. It is possible to expect an increased escalation in load-bearing capacity by such reinforcement, as determined by the literature [41]. However, in order to verify this hypothesis, it would be necessary to perform experimental tests of samples that would be amplified in this way.

In addition to examining the possibility of using full-threaded screws to create a frame connection in terms of load-bearing capacity and reliability, it is possible to state the following based on these experiments. The frame connection made of full-threaded screws was approximately 1.29 times more durable and approximately 1.10 times stiffer than the connection made on the same surface of the frame connection from bolts and pins. In terms of the diameter and arrangement of bolts and pins, several alternatives were investigated before choosing such a number. The higher load-bearing capacity of the full-threaded screw connection could also save wood mass. This would be an excellent benefit of this connection, as it would save material and money. Moreover, there would be easier manipulation of structural elements, and, last but not least, it would reduce the environmental impact. To confirm this idea, it would be necessary to create further experimental samples having the same diameter and arrangement of the fasteners on the same surface of the frame connection. Therefore, the continuation of experimental measurements is in progress, in cooperation with practice and research activities at the Faculty of Civil Engineering VSB—Technical University of Ostrava, Czech Republic. In particular, experimental measurements of reduced frame connections are underway. The connections are also made of full-thread screws and bolts and pins. The aim of these experimental tests is to support and disseminate the results presented in this article.

## 5. Conclusions

Experimental testing is the most concise way to verify the structural details of wooden structures. It is possible to obtain sufficiently complex knowledge about the action of the joint at a certain nature of the load and the arrangement of the joint in terms of materials, geometry, and design by load tests. The issue of determining the load-bearing capacity of joints of wooden structures according to European standards for the design of wooden structures [41] is constantly evolving. Our experiments, which were aimed at determining the load-bearing capacity and rotational stiffness of the frame connection of a wooden beam and a post using mechanical pin-type fasteners, should also contribute to this trend.

Our experiments have demonstrated the suitability of using high-strength full-thread bolts in the frame connection of the cross member and the strut. The experiments have also demonstrated the reliability and safety of using bolts and pins as fasteners to create a frame connection. In terms of load-bearing capacity, all tested experiments showed a higher load-bearing capacity than the assumption for the ultimate limit state [41]; the connections show safety and reliability with a certain margin. The data of experiments can be advantageously used to calculate rotational stiffness for the purpose of calculating numerical bar models. For a detailed study of the problem, it is also appropriate to use a 2D or 3D computational model that models individual components, including fasteners. The use of experiments can then be applied to 3D numerical modelling using an analysis that takes into account the orthotropic properties of wood. The created computational model enables detailed study of the construction details of pin-type fasteners. The performed calculations sufficiently simulated the plastic behavior of the fasteners.

**Author Contributions:** Conceptualization, D.M. and M.J.; validation, D.M. and A.L.; data curation, M.J., O.S. and P.M.; methodology, O.S.; visualization, Z.M.; formal analysis and writing—original draft, M.J.; supervision, A.L; writing—review and editing, M.J. and Z.M. All authors have read and agreed to the published version of the manuscript.

**Funding:** This research was funded by VSB-TUO by the Ministry of Education, Youth and Sports of the Czech Republic. The supported project has the number SP2021/120 of Student Research Grant Competition of the VSB-Technical University of Ostrava.

**Institutional Review Board Statement:** Not applicable.

**Informed Consent Statement:** Not applicable.

**Data Availability Statement:** Data are contained within the article.

**Acknowledgments:** Experimental measurements and research were carried out thanks to VSB Technical University of Ostrava and the financial support of the following companies: EXTEN CZ spol. s.r.o., ROTHOBLAAS, and INGENIA. The work was supported by the Student Research Grant Competition of the VSB-Technical University of Ostrava under identification number SP2021/120.

**Conflicts of Interest:** The authors declare no conflict of interest.

## References

1. Mirski, R.; Dziurka, D.; Chuda-Kowalska, M.; Kawalerczyk, J.; Kuliński, M.; Łabęda, K. The Usefulness of Pine Timber (*Pinus sylvestris* L.) for the Production of Structural Elements. Part II: Strength Properties of Glued Laminated Timber. *Materials* **2020**, *13*, 4029. [CrossRef]

2. Mirski, R.; Dziurka, D.; Chuda-Kowalska, M.; Wieruszewski, M.; Kawalerczyk, J.; Trociński, A. The Usefulness of Pine Timber (*Pinus sylvestris* L.) for the Production of Structural Elements. Part I: Evaluation of the Quality of the Pine Timber in the Bending Test. *Materials* **2020**, *13*, 3957. [CrossRef]
3. Bragov, A.; Igumnov, L.; dell'Isola, F.; Konstantinov, A.; Lomunov, A.; Iuzhina, T. Dynamic Testing of Lime-Tree (Tilia Europoea) and Pine (Pinaceae) for Wood Model Identification. *Materials* **2020**, *13*, 5261. [CrossRef]
4. Olaoye, K.; Aguda, L.; Ogunleye, B. Prediction of Mechanical Properties of Hardwood Species Using the Longitudinal Vibration Acoustic Method. *For. Prod. J.* **2021**, *71*, 391. [CrossRef]
5. Nowak, T.; Patalas, F.; Karolak, A. Estimating Mechanical Properties of Wood in Existing Structures—Selected Aspects. *Materials* **2021**, *14*, 1941. [CrossRef]
6. Malo, K.A.; Abrahamsen, R.B.; Bjertnæs, M.A. Some structural design issues of the 14-storey timber framed building "Treet" in Norway. *Eur. J. Wood Prod.* **2016**, *74*, 407–424. [CrossRef]
7. Crocetti, R. Large-span timber structures. In Proceedings of the World Congress on Civil, Structural and Environmental Engineering (CSEE′16), Prague, Czech Republic, 30–31 March 2016; pp. 1–23. [CrossRef]
8. Frühwald, E. Analysis of structural failures in timber structures: Typical causes for failure and failure modes. *Eng. Struct.* **2011**, *33*, 2978–2982. [CrossRef]
9. Steiger, R.; Serrano, E.; Stepinac, M.; Rajčić, V.; O'Neill, C.; McPolin, D.; Widmann, R. Strengthening of timber structures with glued-in rods. *Constr. Build. Mater.* **2015**, *97*, 90–105. [CrossRef]
10. Vavrusova, K.; Mikolasek, D.; Lokaj, A.; Klajmonova, K.; Sucharda, O. Determination of carrying capacity of steel-timber joints with steel rods glued-in parallel to grain. *Wood Res.* **2016**, *61*, 733–740.
11. Solarino, F.; Giresini, L.; Chang, W.-S.; Huang, H. Experimental Tests on a Dowel-Type Timber Connection and Validation of Numerical Models. *Buildings* **2017**, *7*, 116. [CrossRef]
12. Zhou, S.R.; Li, Z.Y.; Feng, S.Y.; Zhu, H.; Kang, S.B. Effects of bolted connections on behaviour of timber frames under combined vertical and lateral loads. *Constr. Build. Mater.* **2021**, *293*, 123542. [CrossRef]
13. Bouchaïr, A.; Racher, P.; Bocquet, J.F. Analysis of dowelled timber to timber moment-resisting joints. *Mater. Struct.* **2007**, *40*, 1127–1141. [CrossRef]
14. Wang, M.; Song, X.; Gu, X.; Tang, J. Bolted glulam beam-column connections under different combinations of shear and bending. *Eng. Struct.* **2019**, *181*, 281–292. [CrossRef]
15. Johanides, M.; Kubincova, L.; Mikolasek, D.; Lokaj, A.; Sucharda, O.; Mynarcik, P. Analysis of Rotational Stiffness of the Timber Frame Connection. *Sustainability* **2021**, *13*, 156. [CrossRef]
16. Wang, X.T.; Zhu, E.C.; Niu, S.; Wang, H.J. Analysis and test of stiffness of bolted connections in timber structures. *Constr. Build. Mater.* **2021**, *303*, 124495. [CrossRef]
17. Noguchi, M.; Komatsu, K. A new method for estimating stiffness and strength in bolted timber-to-timber joints and its verification by experiments (II): Bolted cross-lapped beam to column joints. *J. Wood Sci.* **2004**, *50*, 391–399. [CrossRef]
18. Glišovíc, I.; Stevanovíc, B.; Kočetov-Mišulić, T. Embedment test of wood for dowel-type fasteners. *Wood Res.* **2012**, *57*, 639–650.
19. Karagiannis, V.; Málaga-Chuquitaype, C.; Elghazouli, A.Y. Modified foundation modelling of dowel embedment in glulam connections. *Constr. Build. Mater.* **2016**, *102*, 1168–1179. [CrossRef]
20. Blass, H.J.; Sandhaas, C. *Timber Engineering—Principles for Design*; Karlsruher Institut für Technologie: Karlsruhe, Germany, 2017; ISBN 978-3-7315-0673-7.
21. Požgaj, A.; Kürjatko, S. Wood properties of spruce from forests affected by pollution in Czechoslovakia. *IAWA J.* **1986**, *7*, 405–410. [CrossRef]
22. Widmann, R.; Fernandez-Cabo, J.L.; Steiger, R. Mechanical properties of thermally modified beech timber for structural purposes. *Eur. J. Wood Wood Prod.* **2012**, *70*, 775–784. [CrossRef]
23. Gao, S.; Xu, M.; Guo, N.; Zhang, Y. Mechanical properties of glued-laminated timber with different assembly patterns. *Adv. Civ. Eng.* **2019**, *2019*, 9495705. [CrossRef]
24. Smiroldo, F.; Giongo, I.; Piazza, M. Use of timber panels to reduce the seismic vulnerability of concrete frame structures. *Eng. Struct.* **2021**, *244*, 112797. [CrossRef]
25. Yaremchuk, L.; Olyanyshen, T.; Hogaboam, L. Selection of coating materials for wood finishing based on a hierarchical analysis method of their technological, economic and ecological criteria. *Int. J. Energy Technol. Policy* **2016**, *12*, 295–311. [CrossRef]
26. Lindfors, N.C.; Salo, J. New ecological wood–plastic composite materials for scaphoid-type casting: Material properties and clinical evaluation. *Hand Ther.* **2014**, *19*, 67–72. [CrossRef]
27. Jorissen, A.J.M.; Leijten, A.J.M. Tall timber buildings in the netherlands. *Struct. Eng. Int. J. Int. Assoc. Bridge Struct. Eng.* **2008**, *18*, 133–136. [CrossRef]
28. Leijten, A.J.M.; Brandon, D. Advances in moment transfering dvw reinforced timber connections—Analysis and experimental verification, part 1. *Constr. Build. Mater.* **2013**, *43*, 614–622. [CrossRef]
29. Kasal, B.; Pospisil, S.; Jirovsky, I.; Heiduschke, A.; Drdacky, M.; Haller, P. Seismic performance of laminated timber frames with fiber-reinforced joints. *Earthq. Eng. Struct. Dyn.* **2004**, *33*, 633–646. [CrossRef]
30. Aruova, L.B.; Ospanova, Z.N.; Aruov, B.B.; Alibekova, N.T.; Shashpan, Z.A.; Kyrgizbaev, A.T. Cyclic tests of joints of glued wooden structures. *IOP Conf. Ser. Mater. Sci. Eng.* **2020**, *829*, 012017. [CrossRef]

31. Bachtiar, E.V.; Clerc, G.; Brunner, A.J.; Kaliske, M.; Niemz, P. Static and dynamic tensile shear test of glued lap wooden joint with four different types of adhesives. *Holzforschung* **2017**, *71*, 391–396. [CrossRef]
32. Jung, K.; Murakami, S.; Kitamori, A.; Chang, W.; Komatsu, K. Improvement of glued-in-rod joint system using compressed wooden dowel. *Holzforschung* **2010**, *64*, 799–804. [CrossRef]
33. Candelas-Gutierrez, A. The power of geometric relationships in mudéjar timber roof frames. *Nexus Netw. J.* **2017**, *19*, 521–545. [CrossRef]
34. Blaß, H.J.; Schädle, P. Ductility aspects of reinforced and non-reinforced timber joints. *Eng. Struct.* **2011**, *33*, 3018–3026. [CrossRef]
35. Cajka, R.; Burkovic, K. Coupled timber-concrete ceiling using bonded shear connectors. *Adv. Mater. Res.* **2013**, *772*, 130–135. [CrossRef]
36. Lokaj, A.; Dobes, P.; Sucharda, O. Effects of Loaded End Distance and Moisture Content on the Behavior of Bolted Connections in Squared and Round Timber Subjected to Tension Parallel to the Grain. *Materials* **2020**, *13*, 5525. [CrossRef] [PubMed]
37. Winter, S.; Dietsch, P. Eurocode 5—Design of timber structures. [Eurocode 5—Bemessung und konstruktion von holzbauwerken]. *Bauingenieur* **2011**, *86*, 348–355.
38. Kleinhenz, M.; Winter, S.; Dietsch, P. Eurocode 5—A halftime summary of the revision process. In Proceedings of the WCTE 2016—World Conference on Timber Engineering, Vienna, Austria, 22–25 August 2016.
39. Bemessung Nach Eurocode 5. *Holz Kurier* **2001**, *56*, 15.
40. *ČSN EN 1995-1-1. Eurocode 5: Design of Timber Structures—Part 1-1: General—Common Rules and Rules for Buildings*; Czech Standards Institute: Praha, Czech Republic, 2006.
41. *Wooden Structures According to Eurocode 5. STEP 1: Design and Construction Materials*; Bohumil, K., Translator; KODR: Zlin, Czech Republic, 1998; ISBN 80-238-2620-4. (In Czech)
42. Ahlborn. Available online: https://www.ahlborn.com/ (accessed on 25 November 2021).
43. *EN 26891:1991. Timber Structures—Joints Made with Mechanical Fasteners—General Principles for the Determination of Strength and Deformation Characteristics (ISO 6891-1983)*; ISO: Geneva, Switzerland, 1999.
44. *Wooden Structures According to Eurocode 5; STEP 2: Design of Details and Load-Bearing Systems*; Koželouh, B., Translator; ČKAIT Information Center: Prague, Czech Republic, 2004; ISBN 80-86769-13-5. (In Czech)
45. SCIA Engineer Software. Available online: https://www.scia.net/en/software/scia-engineer (accessed on 26 March 2021).
46. ANSYSTM Software. Available online: https://www.ansys.com (accessed on 26 March 2021).

materials

MDPI

*Article*

# Effect of Various Types of Superplasticisers on Consistency, Viscosity, Structure and Long-Term Strength of Geopolymer Products

**Łukasz Anaszewicz**

Faculty of Civil Engineering and Geodesy, Military University of Technology in Warsaw, 00-908 Warsaw, Poland; lukasz.anaszewicz@wat.edu.pl

**Abstract:** This article presents the results of research on the effect of plasticisers made based on four different compounds—melamine (M), naphthalene (NF), acrylic polymers (AP) and polycarboxylic ethers (PC)—added to the tested mixes in the amount of 2% of the fly ash (FA). The influence of superplasticisers (SPs) on the consistency of the fresh concrete was investigated using a flow table and a penetrometer, and the air voids content was determined by means of a porosimeter. Additionally, the influence of plasticisers on the viscosity of the paste was investigated using a rheometer. Hardened mortar that matured under two different conditions was also tested at elevated and room temperatures. The tested properties were 7-, 28- and 90-days compressive strength and internal microstructure viewed under a microscope. NF had the greatest viscosity-reducing effect while it increased the air void volume in the mix at the same time. The highest early and late strengths were obtained after curing in elevated temperature samples with an acrylic-polymer-based superplasticiser. However, the increased curing temperature of the samples only influenced the early strength results. Its effect was not visible after 90 days. The AP addition also had a significant impact on improving the consistency of the mixture. The addition of plasticisers did not affect the microstructure of the specimens.

**Keywords:** plasticisers; geopolymer; consistency; viscosity; strength; microstructure

## 1. Introduction

In the era of increasing demand for cement, we have reached the point where there are shortages of this product on the market. This situation increases the need for the quick phasing in of products that could replace cement-based concrete. Dusty industrial waste materials are an increasingly well-researched alternative material in this application. The energy economy, so far based to a large degree on coal, has provided us with fly ash (FA) deposits, which require disposal and at the same time are a promising alternative to cement. This is clearly demonstrated by the results of research on geopolymer mortars [1–3], concretes [4–7] and even models of structural elements [8–10].

However, even though geopolymeric materials intended for use in construction have been studied for a long time, there is still a need for well-tested and dedicated workability-improving agents. Until they are developed, we must rely on agents designed for cement concrete available on the market.

One of the first studies in this area is presented in [11], where granular blast furnace slag (GGBFS) geopolymer products were supplemented with 1% plasticiser additive (SP) based on four different compounds: polycarboxylic ethers (PC), melamine (M), naphthalene (NF) and vinyl copolymers (V). The tests demonstrated a slight effect on the 28-day compressive strength of the test specimens (in relation to cement concrete controls), no increase in slump for PC, M and V and a considerable increase in slump in the case of NF specimens. GGBFS appeared in the study reported in [12], in which from 2% to 6% addition of a plasticiser of an unknown basis was used, and the specimens were cured in a room-temperature environment. In this case, the results show an increase in cone slump ranging from 3.7% to 40.7%, depending on the amount of plasticiser, and an increase in compressive strength from 0.4% to 6.1%. Additionally, in [13], the results obtained for geopolymers of variable amounts in the composition of GGBFS and FA were compared. From 1% to 4% of PC- and NF-based plasticisers were added, and the specimens were cured under room-temperature conditions. The study demonstrated that the flow of specimens made with the addition of PC is not only greater, but also lasts longer in relation to the specimens containing N. Additionally, the authors observed that PC improves the 7-day compressive strength of cement base. Another study which presents the results of the geopolymer tests based on GGBFS and on the mix of GGBFS with FA is [14]. The specimens contained 1%, 2% and 3% of PC-based SP. The test results presented by the authors were 7- and 28-day strength data. Both in the case of compressive strength and tensile strength by splitting, higher strengths were obtained for specimens with a higher SP content.

One of the first papers to study fly ash (FA) geopolymers was [15]. Plasticisers based on lignosulfonates (L), melamine (M) and polycarboxylic ethers (PC) were used for the tests. In their conclusions, the authors pointed out that the viscosity of all the specimens was lower than the viscosity of the control, but higher than the viscosity of the specimen containing Portland cement. Moreover, the plasticising properties disappeared in less than 10 min. Additionally, the correlation between the obtained slump and the viscosity data was investigated. According to the authors, using a viscometer for measurements is a more accurate method for studying the influence of admixtures on the behaviour of geopolymers. On the other hand, the slump cone test is only suitable for Portland cement specimens. Studies [16,17] investigated the influence of PC on FA-based geopolymers. Their objective was to obtain self-compacting concrete, and therefore, the amount of plasticiser was between 3% and 7%. The specimens were heated at 70 °C for 24 h and 48 h, respectively. The results show that a higher amount of admixture increased the strength. In addition, the use of an activator with a higher $NaOH_{sol}$ molarity and increasing the amount of the SP additive reduced cracking at the matrix–aggregate interface. The results of tests on specimens containing similar amounts of PC and NF plasticisers, i.e., 1% to 5%, are presented in [18]. Viscosity was tested by means of a viscometer at 5 rpm for a period of 30 min. It was demonstrated that PC plasticiser slightly reduced the viscosity of the paste, in contrast to NF, which increased the viscosity and accelerated the setting time. However, the authors did not investigate the effect of SP on the strength. Rheological properties were also examined in [19]. L- and PC-based plasticisers were used in the tests, added at 1% and 1.5%, respectively. $NaOH_{sol}$ was changed in addition. According to the authors, the molarity of the $NaOH_{sol}$ solution above 4M affects the rheological parameters of the fresh concrete and reduces slump. Better workability results were obtained for L-based plasticisers. The effect of 1% addition of M-, NF- and PC-based plasticisers was examined in [20]. The strength test specimens were heated for 24 h at 60 °C before the test. The slump of specimens in which the two-component activator was used was the greatest, in the range of 39–45% for the PC-based plasticiser; for the NF plasticiser, the increase was of 6–8%. On the other hand, M-based plasticiser gave a 3% reduction in the slump value as compared to the control. At the same time, there was a loss in the strength of the specimens with the SP addition compared to the control. The effect of NF and PC added at 0.5% to 2% was also investigated in [21]. Two types of fly ash were used in this study, i.e., with low and high limestone content (class F and C, respectively). The results show that in the case of low-calcareous ash, the use of a naphthalene plasticiser results in a greater paste plasticisation as compared to PC. In the case of high-calcareous ash, the situation is opposite. Better results were obtained with PC. Additionally, it was observed that in the specimen containing class F ash, the relationship between shear stresses and shear rate was the same for each of the tested superplasticisers. In the case of class C ash, the curve decreased along with the increasing fluidity of the mix. Unfortunately, the authors did not test the specimens for strength. There are publications in the literature that deal with the influence of plasticisers on geopolymers made of less common materials. Study [22] gives the results of specimens from oil palm fibre ash with a 10% addition of an NF-based plasticiser. On the other hand, study [23] gives the results of research regarding one-component geopolymeric concrete. It was prepared by mixing the dry ingredients, including FA, GGBFS and various types of powdered sodium silicate, and then adding water and other liquid additives. PC and NF plasticisers added at 1% were used for the tests, and the strength test specimens were heated prior to testing. The results demonstrate a positive effect of plasticisers on the flow, along with simultaneous reduction in the strength of most of the specimens. Table 1 compiles the plasticisers and the above-mentioned studies. Part of the consistency testing was carried out using the slump cone method, and some was performed using the flow table method.

**Table 1.** Plasticisers used and the studies described in the referenced publications. Designations: PC—polycarboxylic ethers, M—melamine, NF—naphthalene, V—vinyl copolymers, L—lignosulfonates, + tested, − not tested, nd—no data.

| Publication | Plasticiser | | | | | Slump | Viscosity | Curing Temperature | | Strength | | | | |
|---|---|---|---|---|---|---|---|---|---|---|---|---|---|---|
| | PC | M | NF | V | L | /Flow | | Room | Elevated | 1–3 | 7 | 14 | 28 | 90 |
| Palacios, 2005 | + | + | + | + | - | + | - | + | - | + | + | - | + | - |
| Criado, 2009 | + | + | - | - | + | + | + | - | - | - | - | - | - | - |
| Nurrudin, 2011 | + | - | - | - | - | + | - | - | + | + | + | - | + | - |
| Nurrudin, 2012 | + | - | - | - | - | + | - | - | + | + | + | - | + | - |
| Montes, 2012 | + | - | + | - | - | - | + | - | - | - | - | - | - | - |
| Laskar, 2013 | + | - | - | - | + | + | + | - | - | - | - | - | - | - |
| Nematollahi, 2014 | + | + | + | - | - | + | - | - | + | + | - | - | - | - |
| Jang, 2014 | + | - | + | - | - | + | - | + | - | + | + | + | + | - |
| Xie, 2016 | + | - | + | - | - | - | + | - | - | - | - | - | - | - |
| Salami, 2016 | - | - | + | - | - | - | - | - | + | + | + | + | + | - |
| Jithendra, 2018 | nd | nd | nd | nd | nd | + | - | + | - | + | - | - | + | - |
| Bong, 2019 | + | - | + | - | - | + | - | - | + | + | - | - | - | - |
| Gupta, 2021 | + | - | - | - | - | - | - | nd | nd | - | - | - | + | - |

The review of all these publications makes it possible to narrow down the choice of plasticisers depending on the produced mix. However, none of them are comprehensive enough to define the influence of plasticisers on the consistency and viscosity, as well as the short- and long-term strength of the material depending on the curing conditions. This being so, this article presents the results of laboratory tests on the influence of the four types of plasticisers on the consistency and viscosity of the geopolymer paste and on the 7-, 28- and 90-day strength of the specimens of mortar maturing both at room temperature and heated after moulding for 24 h at the temperature of 70 °C.

## 2. Materials and Production Methodology

### *2.1. Matrix*

The specimens contained fly ash (FA) classified as class F as per ASTM C618 or class V ash as per EN 197-1. A mix of sodium silicate aqueous solution and sodium hydroxide solution was used as the activator. The commercial version of water glass R140 with a $SiO_2/Na_2O$ molar modulus of 2.9–3.1 was used as the sodium silicate solution ($SS_{sol}$); $Na_2O+SiO_2$ content min. 36% and viscosity (at 20 °C) 0.05 Pa·s. A sodium hydroxide ($NaOH_{sol}$) solution with a molarity of 12 M was mixed with $SS_{sol}$ at a 1:2.5 ratio.

### *2.2. Admixtures*

Four plasticisers, each with different base components, were chosen for use in the tests. Table 2 gives the designations of the specimens along with information on the base component of the plasticiser and the specimen curing conditions. All the tested plasticisers were added at 2% of fly ash by weight.

**Table 2.** Designations of the specimens and admixtures and specimen curing conditions.

| Specimen Designation | Plasticiser Base | Curing Conditions |
|---|---|---|
| Ma | melamine (M) | 20° |
| Me | | 70° |
| NFa | naphtalene (NF) | 20° |
| NFe | | 70° |
| APa | acrylic polymers (AP) | 20° |
| APe | | 70° |
| PCa | polycarboxylic ethers (PC) | 20° |
| PCe | | 70° |

Melamine and naphthalene-based plasticisers employ an electrostatic effect to fluidise the paste. In simple terms, the process consists of inducing negative charges on the surface of the cement grains, which cause the grains to repel each other. On the other hand, the action of acrylic polymer and polycarboxylic ether-based plasticisers is based on the steric effect. It is associated with long side chains of polymers that make it difficult for the particles to get closer to each other.

### 2.3. Production of the Test Specimens

The specimens were produced using 0–2 mm excavated sand as a filler. For 1 $m^3$ of each type of specimen, 160 kg of sand, 53 kg of fly ash, 27 kg of activator, 6 kg of water and 1.06 kg of additives were used to test the consistency, air void content, strength and for a part of the microscopic tests. For the viscosity tests and other microscopic tests, paste of the same proportions was made, except sand was not added to the mix. First, dry ingredients were mixed for 3 min, and then, the prior-mixed liquid ingredients were added to the mix. Then, the whole batch was mixed for another 10 min.

### 2.4. Specimen Curing Conditions

The specimens were divided into two groups. Half of them were cured in a laboratory environment (i.e., at about 20 °C), and the other half were cured at an elevated temperature. The latter were placed in moulds and vibrated and then immediately placed in a lab oven heated up to 70 °C and were kept there for 24 h.

### 2.5. Consistency Testing

The consistency of the fresh concrete was determined in two ways: using a flow table, as per EN 12350-5, and by means of a penetrometer, as per EN 1015-4. The mix was used up within 10 min from the end of mixing. For the flow test, the mix was placed in a truncated-cone-shaped mould, and then, after quick demoulding, the table made 10 strokes and the flow diameter was measured. The penetrometer test consisted of filling the mould with fresh concrete, then lowering the penetrometer's penetration piston and reading the immersion depth on the gauge. Each mix was subjected to three tests, from which the average value was drawn.

### 2.6. Air Void Content

The air void content was determined upon completion of the mixing. The method prescribed by EN 1015-7 was applied. A 1 L porosimeter was used in the test.

### 2.7. Viscosity

The viscosity test was carried out using a rheometer. The tested paste was composed of activator, water, plasticiser and ash mixed in proportions as for the mortar. Additionally, the test was performed using comparative paste without plasticiser. The ingredients were mixed for 3 min immediately before testing. The test procedure for this test consisted of

10 revolutions of the spindle at speeds from 50 rpm to 200 rpm, and back to 50 rpm at 10 rpm steps. The average result of 10 revolutions for each speed was recorded.

### *2.8. Compressive and Flexural Strength*

Mortar strength was tested after 7, 28 and 90 days on 40 mm × 40 mm × 160 mm beam-shaped specimens. The test method of EN 196-1 was used. Four batches that differed with respect to plasticiser were made. Half of the specimens in each batch were cured under laboratory conditions, while the other half were subjected to additional heating immediately after placement in moulds. Each variant was tested for flexural strength on five specimens and for compressive strength on ten specimens.

## 3. Results and Discussion

### *3.1. Consistency Testing*

Figure 1 shows that the highest flow of 206 mm was observed on the specimens containing AP acrylic polymers. Still, the difference in flow was not significant when compared to the M specimens—200 mm—and NF specimens—198 mm—containing first-generation plasticisers. The only significantly different result, 166 mm, was obtained for the PC specimen containing a polycarboxylic ether-based plasticiser. The same results for M, NF and PC were obtained in the studies [18,19,21], the last of which indicates that it was related to the use of low-calcareous ash. Opposite results were obtained for high-calcareous ashes.

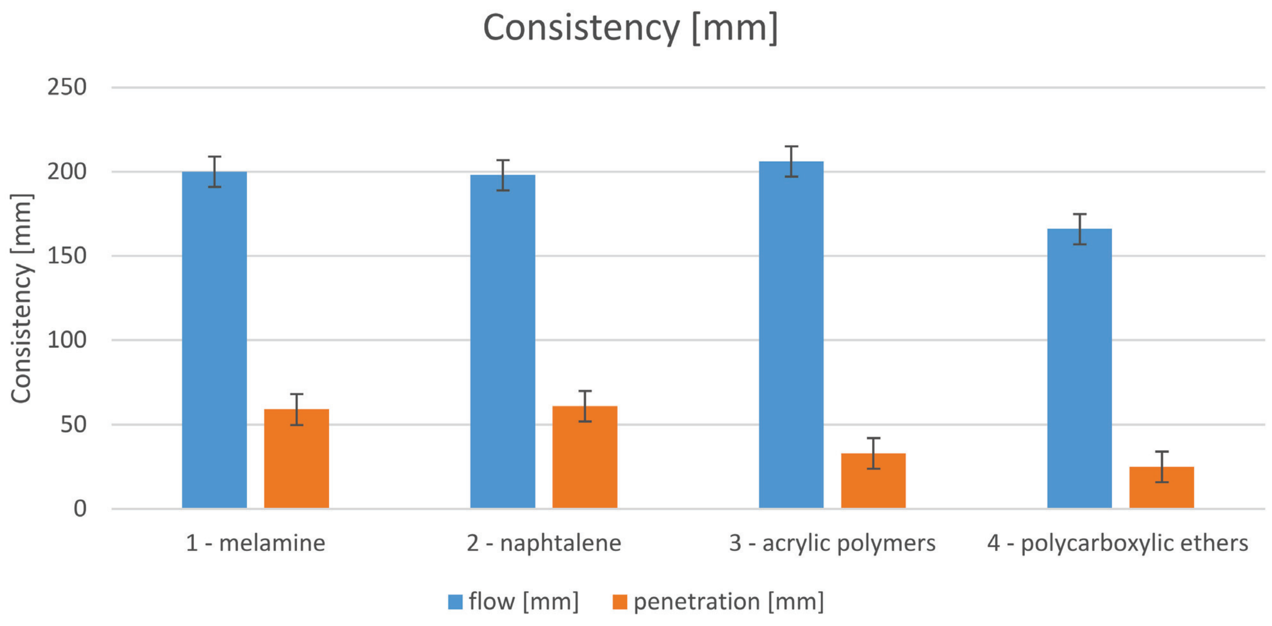

**Figure 1.** Flow and penetration testing results.

In the penetration test, the M specimens with 59 mm and NF specimens with 61 mm again achieved a similar rod penetration. On the other hand, the specimens containing AP and PC plasticisers had lower results, i.e., 33 mm and 25 mm in the case of AP and PC, respectively. In the case of M and NF specimens, the penetration rod would easily sink into the fresh concrete, while in the case of the AP and PC specimens, the pressure exerted by the rod pushed the mix sideways and upwards out of the container, and the rod only slightly penetrated the mix.

The above results indicate a lack of a direct correlation between the two methods of fresh mortar consistency testing for different geopolymeric materials. The addition of plasticisers has a desirable effect on the flow of the mix, yet easier penetration was only obtained in the case of M and NF plasticisers.

### 3.2. Air Void Content

The same conditions were ensured in the preparation of each of the respective mixes. Despite this, Figure 2 shows significant variations in the air void volumes. The AP specimen with 4.9% air void content was the most effectively deaerated specimen. The greatest air void volume, of 11%, was obtained from the NF specimen. No correlation was found with the consistency test results.

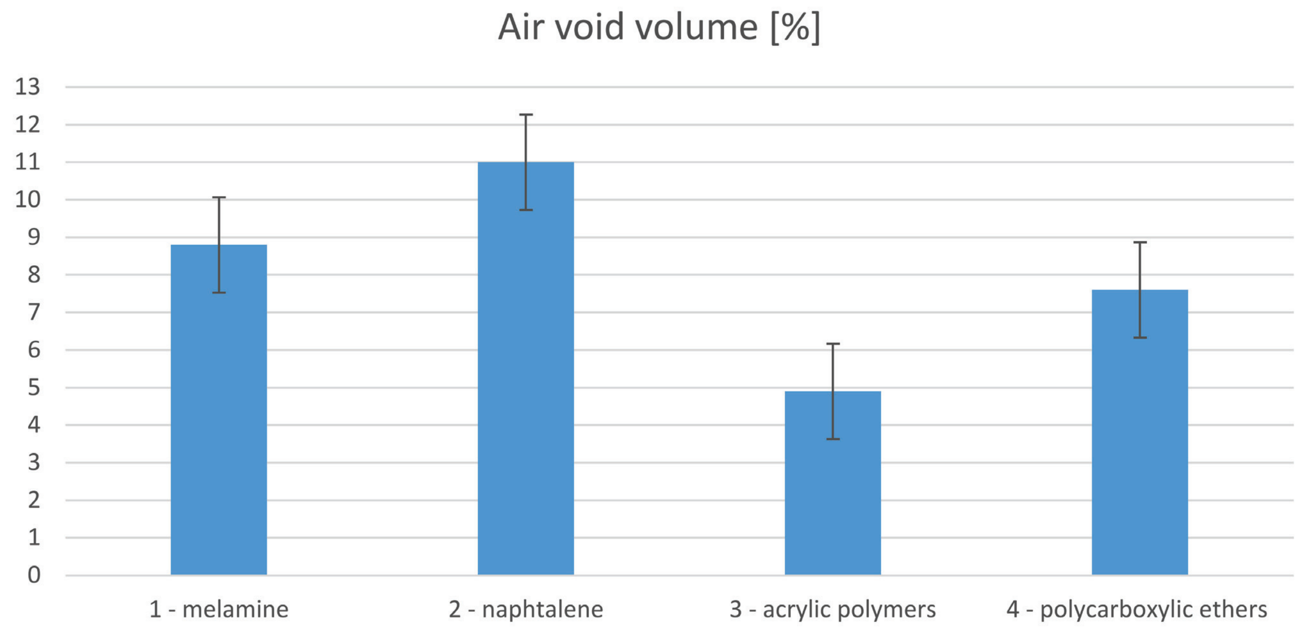

**Figure 2.** Volume of air voids.

### 3.3. Viscosity

The results given in Figure 3 show that the viscosity of all the mixes containing plasticiser was lower than the control. N had the greatest impact on viscosity reduction, two times the value obtained for M. The differences in comparison to the controls for 200 rpm were 172 and 407 mPa·s for M and N, respectively. The PC curve overlapped most of the range with the AP curve. The only curve slightly different in course than the reference one was the AP curve. It changed its course while reducing the spindle revolutions. For 130 rpm, the difference was over 100 mPa·s. This indicates the effect of shear on bonds being formed. Note that this is not evident for high spindle revolution speeds.

A relationship between viscosity and the degree of air entrainment in the mix can be seen: the lower the viscosity, the greater the volume of air voids in the fresh concrete. A relationship between extending the mixing time and increasing the air entrainment of the fresh concrete is known both for cement and asphaltic concretes. As far as geopolymer material is concerned, we can see that the use of additives that strongly lower the viscosity have a significant effect on air entrainment, increasing it considerably. On the other hand, an attempt to reduce air entrainment by shortening the mixing time may lower the strength, which was presented in [4].

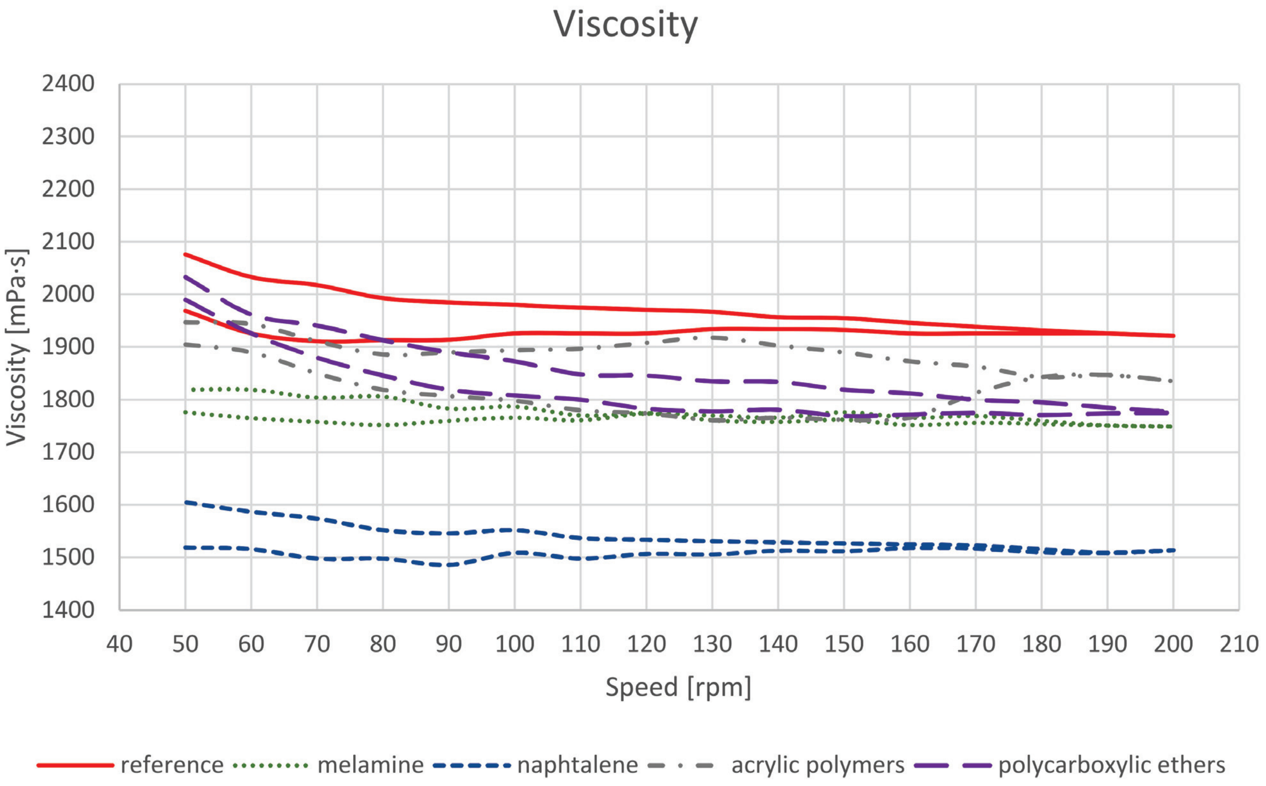

**Figure 3.** Results of the viscosity tests.

### *3.4. Microscopic Testing*

The microscopic examination of the structure of the test specimens was carried out on paste specimens prepared in the same way as for viscosity tests and on hardened mortar specimens.

The internal structures of the control and of the paste containing the additives were homogeneous throughout. In Figure 4, there are no distinguishable clusters of homogeneous particles or segregation and precipitation of the liquid components of the test mixes.

Figure 5 shows mortars at 7× magnification, and even distribution of the aggregate, the same for all additives, can be seen on the images. In the case of N, numerous air voids can be seen. In addition, no shrinkage or interfacial cracking can be seen in Figure 6 at 45× magnification.

Heating the specimens for 24 h at 70 °C had no visible effect on the appearance of the internal structure of the tested specimens. Elevated temperature and faster evaporation did not result in the formation of cracks within the matrix or at the interface between the matrix and the aggregate. None of the specimens showed any signs of precipitation on the surface of the paste specimen, excessive vibration or stratification of the mix components. These results are consistent with observations [24] on the stability of the geopolymer structure at elevated temperatures. The difference in the hues of the pictures is due to the white balance setting.

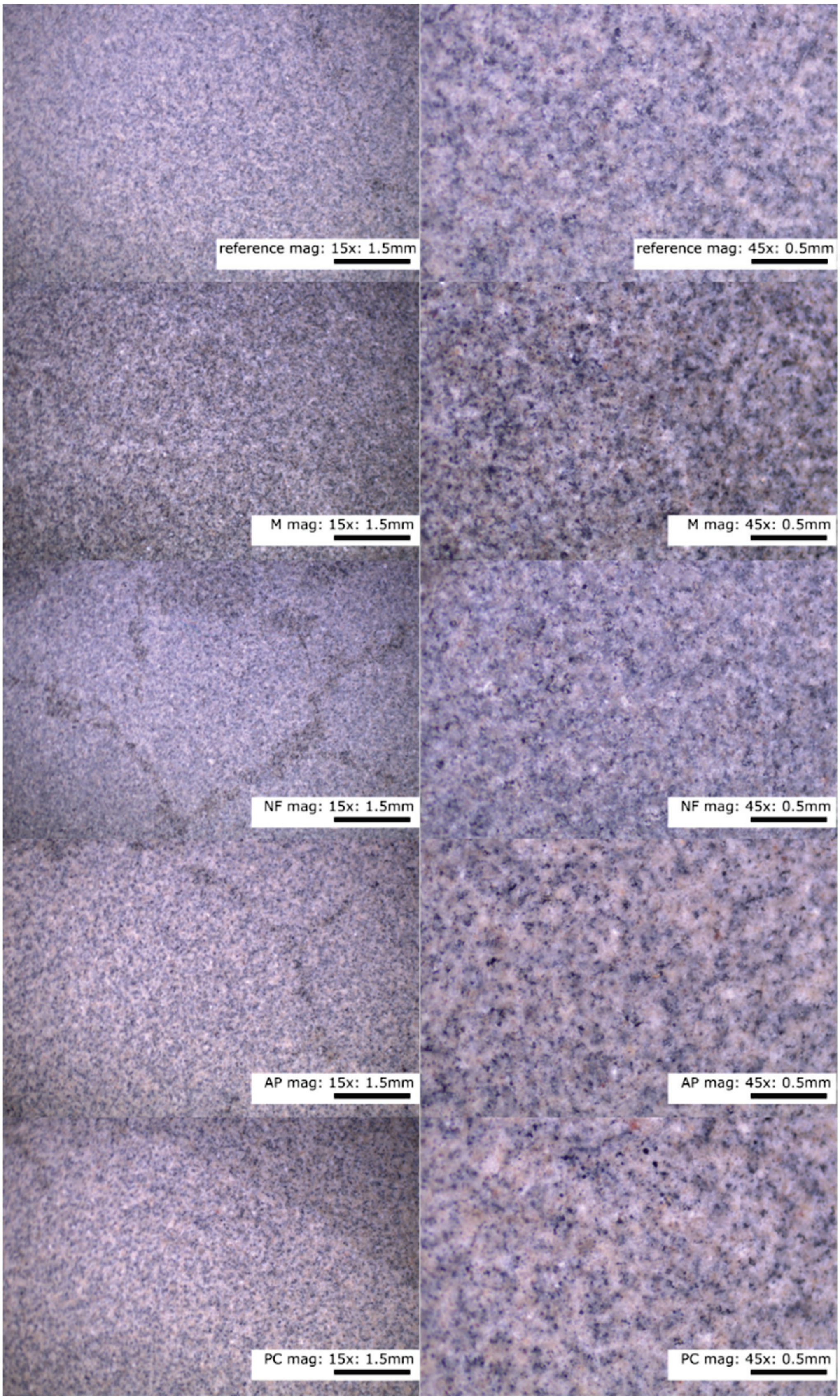

**Figure 4.** Microscope photographs of the paste at 15× and 45× magnification. Designations: M—melamine, NF—naphthalene, AP—acrylic polymers, PC—polycarboxylic ethers.

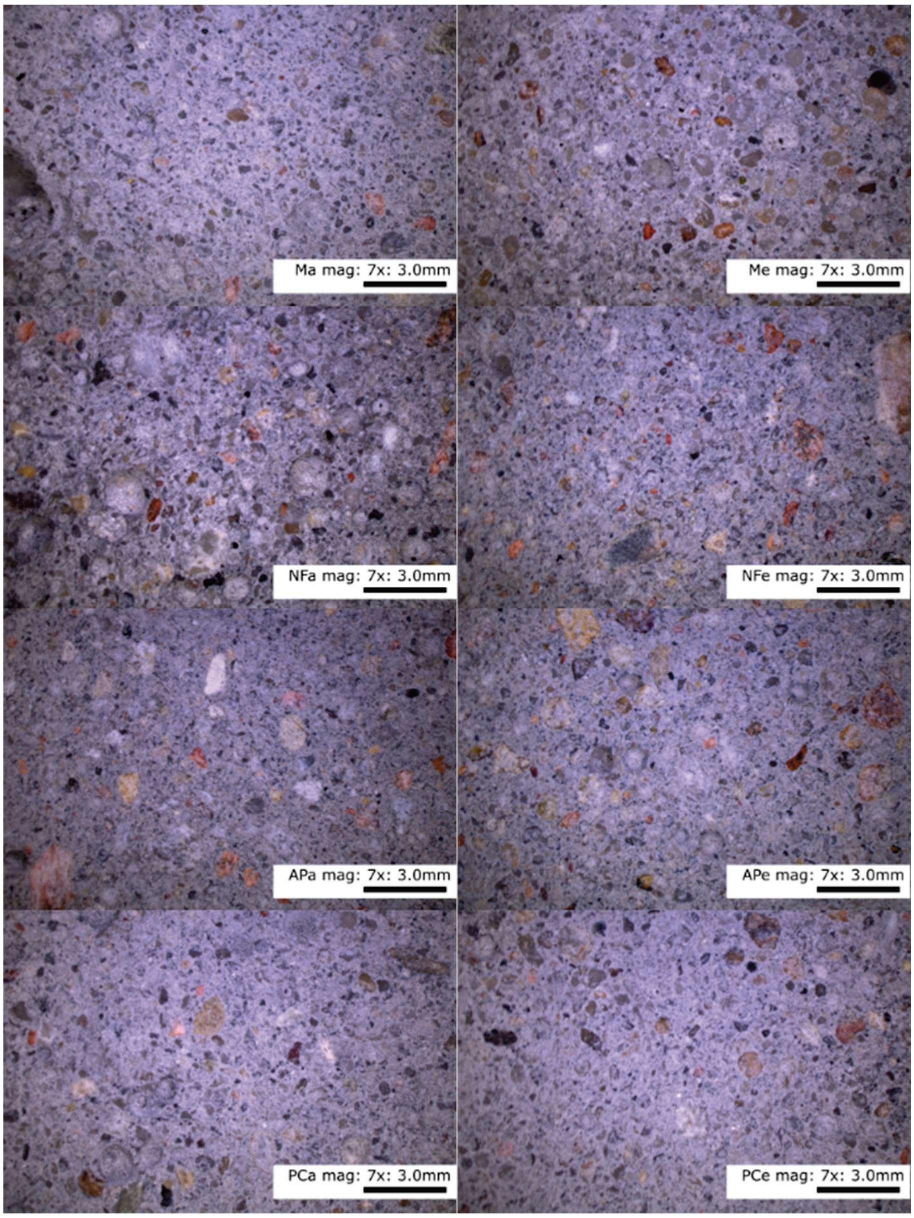

**Figure 5.** Mortars cured in lab ambient conditions and heated, imaged at 7× magnification. Designations: M—melamine, NF—naphthalene, AP—acrylic polymers, PC—polycarboxylic ethers.

### *3.5. Compressive and Flexural Strength*

The results shown in Figure 7 indicate a greater increase in 7-day strength for specimens cured at an elevated temperature. Later on, the differences between the obtained strengths tended to decrease. Figure 8 shows the percentage difference in compressive strengths assuming that the strengths achieved by the heated specimens are 100%. After 7 days, the differences ranged from 78.5% to 66.1%. The results for the AP and PC specimens show greater differences. After 28 days, the differences in compressive strength decreased, falling within the 24.7% to 17.7% range. After this time, greater differences occurred in the compressive strength of the M and NF specimens. After 90 days, the difference in the strength of specimens cured at room temperature and those that were heated disappeared for the AP and PC specimens. For the M and NF specimens, they remained at the level of 27% to 30%.

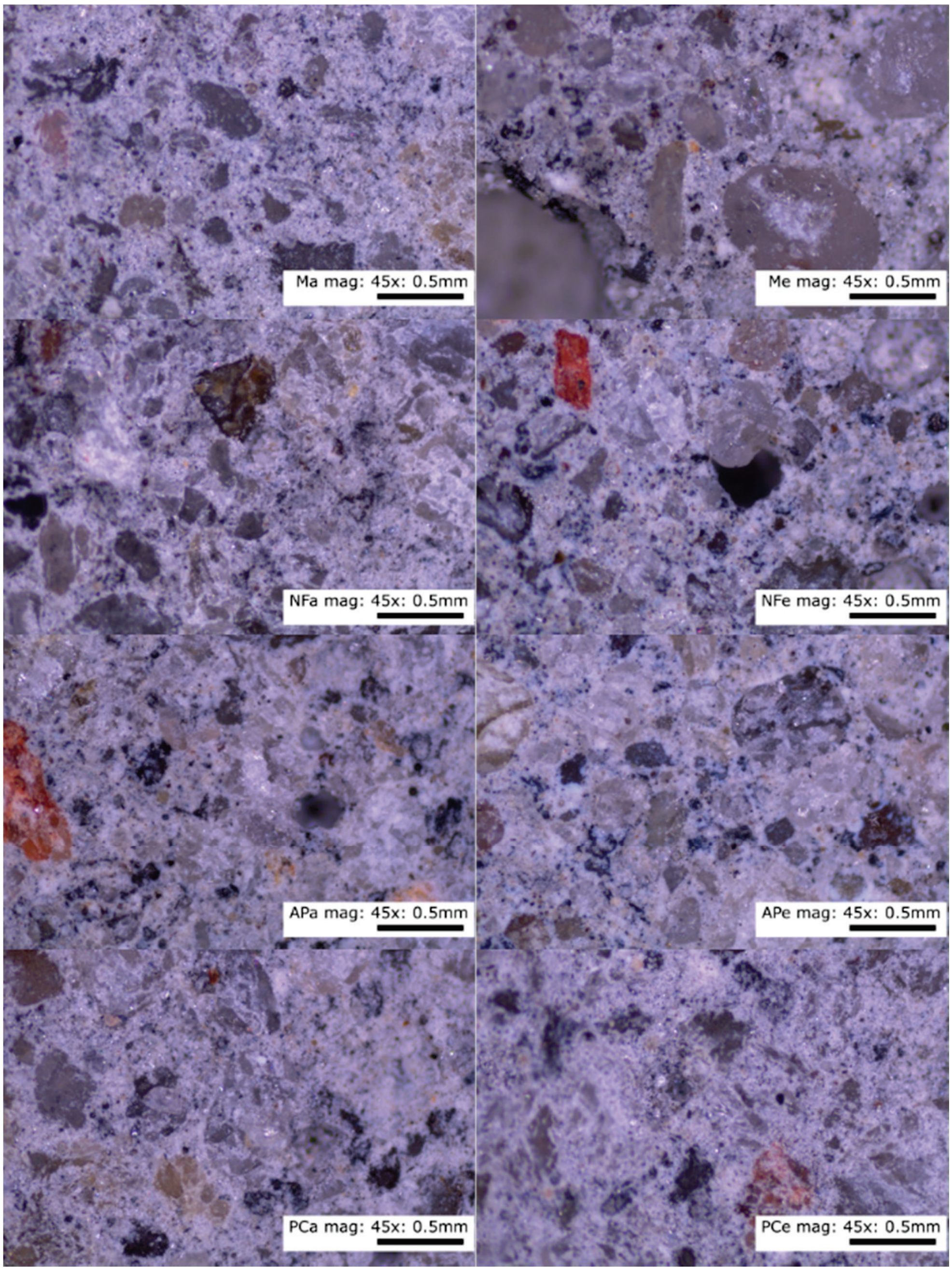

**Figure 6.** Mortars cured in lab ambient conditions and heated, imaged at 45× magnification. Designations: M—melamine, NF—naphthalene, AP—acrylic polymers, PC—polycarboxylic ethers.

At the same time, it is clear that the highest compressive strength results were obtained at each stage for the specimens in which the AP-based plasticiser was used. One of the reasons behind this result may be that they contained the smallest volume of air voids that weakened the matrix. Moreover, the strength of the APa and APe specimens reached similar values after 90 days. The same phenomenon can be observed in the case of the PCa and PCe specimens. It is also visible that the remaining specimens (M, N and PC) cured under the same conditions achieved similar strengths.

The gain in strength between the 7th and the 28th day and between the 28th and the 90th day, shown in Figure 9, is also worth noting. It is clear that the gains observed for the specimens subjected to heating are more balanced. However, despite larger strength gains up to the 7th day for heated specimens and strength gains reaching 545% achieved by the unheated specimens between the 7th and 28th day, microscopic examination did not reveal any shrinkage cracks in any of the specimens.

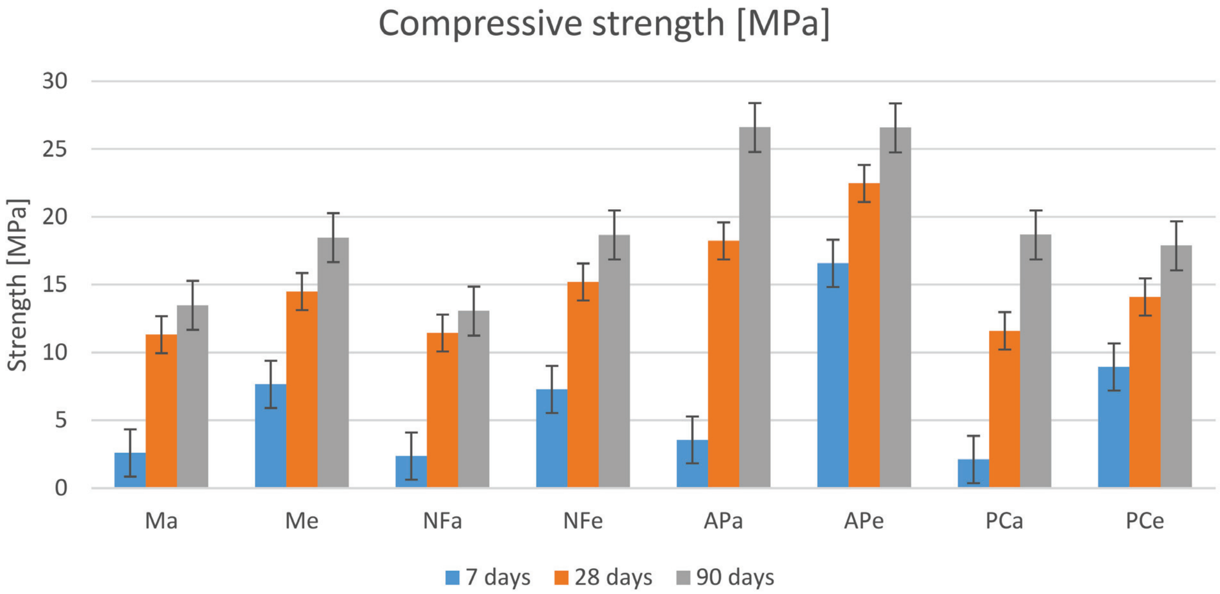

**Figure 7.** Compressive strength results.

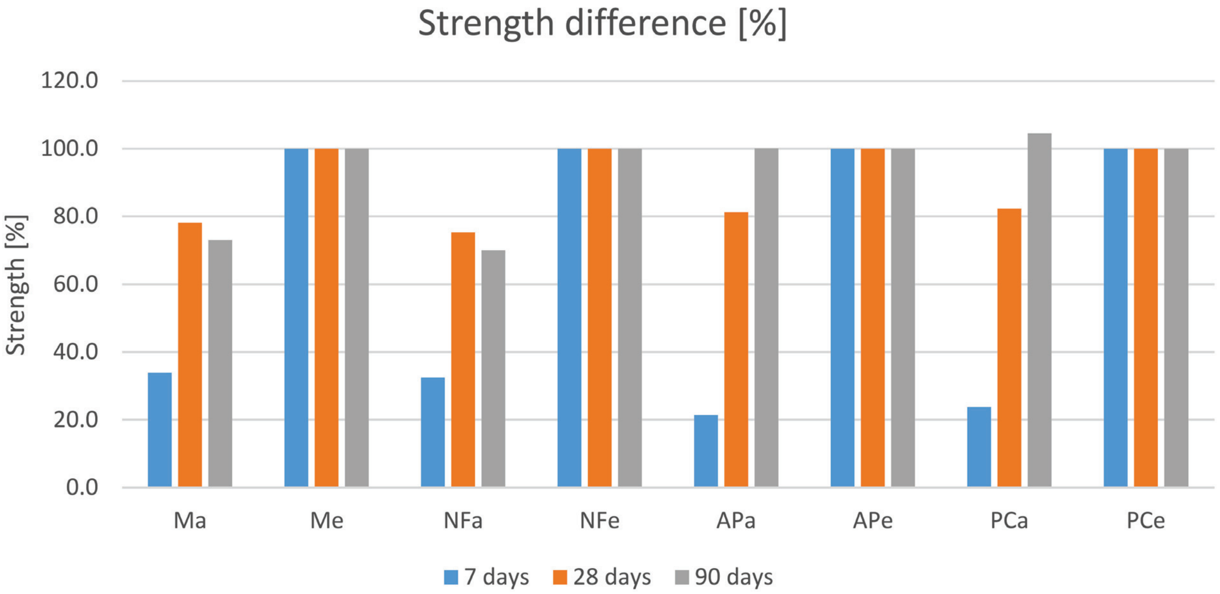

**Figure 8.** The percentage difference in compressive strength between the heated specimens and the specimens cured under room conditions. To be considered in pairs: Ma-Me, NFa-NFe, APa-Ape and PCa-PCe.

Similarly to the results of the compressive strength tests, the highest value of flexural strength (Figure 10) was obtained for the mortar containing AP. The result for heated and unheated specimens after 90 days was identical—4.6 MPa. Additionally, the PC specimens achieved the same flexural strength values. In the case of the other additives, the results obtained for heated specimens were higher by 35%. The heated specimens tended to gain higher strength after 7 days as compared to those cured under laboratory conditions: Me—58%, NFe—50%, APe—80% and PCe—79%.

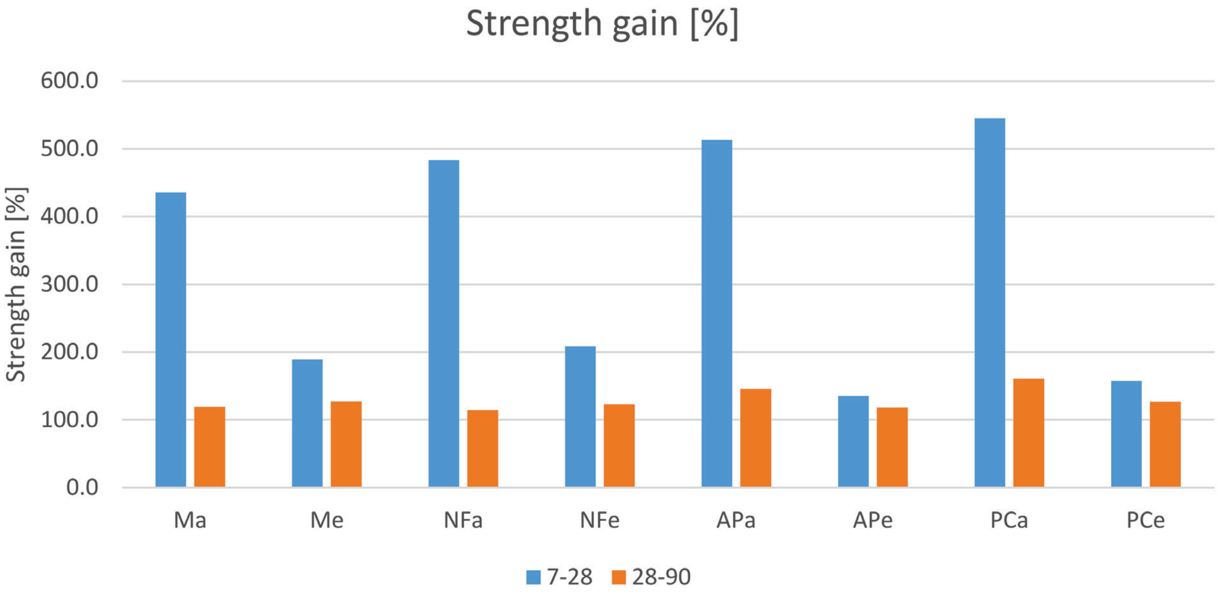

**Figure 9.** Percentage gain in compressive strength between the 7th and the 28th day and between the 28th and the 90th day.

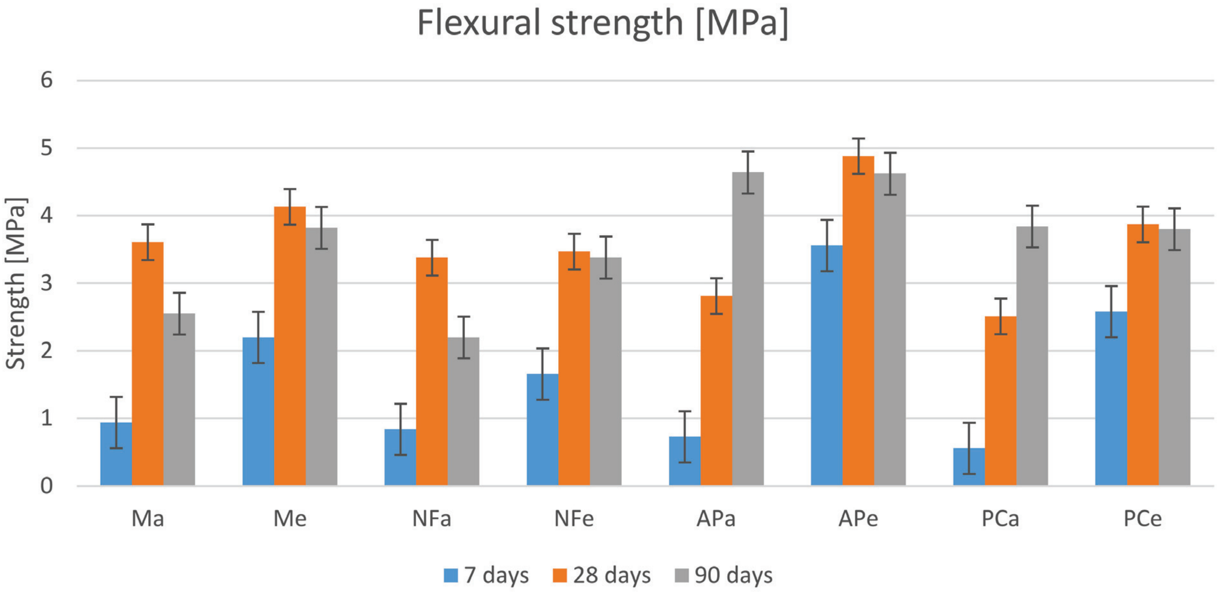

**Figure 10.** Flexural strength results.

A phenomenon that did not occur in the case of compressive strength is the decrease in flexural strength of the specimens after 90 days. The reason behind this phenomenon requires further research. The loss of strength noted between the 28th and the 90th day for heated specimens is less than 8%; for Ma, it is 29.5% and for NFa, it is 35%. A stable gain in strength was only observed for the unheated APa and PCa specimens. Despite that, the results of the flexural strength test after 90 days ranged from 16.8% to 21.3% of the compressive strength test.

## 4. Conclusions

This study supplements the earlier results presented in the literature with regard to the outcome of research on the effect of plasticisers and their heating on the long-term strength results. Additionally, it investigates another acrylic-polymer-based additive which has not been considered in the literature thus far.

Among the plasticisers available on the domestic market, admixtures based on melamine, naphthalene and acrylic polymers had the greatest influence on the flow. The greatest penetration was observed for the M and NF specimens. The naphthalene-based additive had also the greatest impact on reducing the viscosity of the paste, but at the same time, it significantly increased the volume of air voids, which could result in strength loss. The highest compressive and flexural strengths were gained by specimens with an acrylic-polymer-based admix. Heating increased the early strength significantly; however, it had no effect on the compressive strength after 90 days for AP and PC additives. Nevertheless, the heating procedure increased the compressive strength of the M and NF specimens.

It is difficult to compare the research results obtained in this study with the results given in previous publications. This is due to imprecisely defined base components of the plasticisers. This, in turn, is due to the reluctance of manufacturers to share detailed information about their products. In most of the international literature, we can find polycarboxylate-based plasticisers. However, these can be either polycarboxylate compounds (acrylates) or polycarboxylic ethers. The same applies to the term acrylic, which can be given without specifying whether it refers to acrylates, acrylic acid copolymers or cross-linked acrylic polymers. All the published research results allow us to pick a plasticiser to achieve the expected results. The highest early and late strengths were obtained after curing samples acrylic-polymer-based superplasticiser in elevated temperatures. However, the increased curing temperature of the samples only influenced the early strength results. Its effect was not visible after 90 days. The AP addition also had a significant impact on improving the consistency of the mixture. However, further development in the area of geopolymer concrete additives requires additional studies that take into account the exact compositions of superplasticising agents currently available on the market.

**Funding:** This research received no external funding.

**Institutional Review Board Statement:** Not applicable.

**Informed Consent Statement:** Not applicable.

**Data Availability Statement:** The data presented in this study are available on request from the corresponding author.

**Acknowledgments:** The work was prepared taking into account the results of the engineering work written by Maciej Kłysiak at the Faculty of Civil Engineering and Geodesy.

**Conflicts of Interest:** The author declares no conflict of interest.

## References

1. Dudek, M.; Sitarz, M. Analysis of Changes in the Microstructure of Geopolymer Mortar after Exposure to High Temperatures. *Materials* **2020**, *13*, 4263. [CrossRef]
2. Ukrainczyk, N.; Muthu, M.; Vogt, O.; Koenders, E. Geopolymer, Calcium Aluminate, and Portland Cement-Based Mortars: Comparing Degradation Using Acetic Acid. *Materials* **2019**, *12*, 4321. [CrossRef] [PubMed]
3. Pawluczuk, E.; Kalinowska-Wichrowska, K.; Soomro, M. Alkali-Activated Mortars with Recycled Fines and Hemp as a Sand. *Materials* **2021**, *14*, 4580. [CrossRef] [PubMed]
4. Hardjito, D.; Rangan, B.V. *Development and Properties of Low-Calcium Fly Ash-Based Geopolymer Concrete*; Curtin University of Technology: Perth, Australia, 2005.
5. Nagaraj, V.K.; Venkatesh Babu, D.L. Assessing the performance of molarity and alkaline activator ratio on engineering properties of self-compacting alkaline activated concrete at ambient temperature. *J. Build. Eng.* **2018**, *20*, 137–155. [CrossRef]
6. Nguyen, K.T.; Ahn, N.; Le, T.A.; Lee, K. Theoretical and experimental study on mechanical properties and flexural strength of fly ash-geopolymer concrete. *Constr. Build. Mater.* **2016**, *106*, 65–77. [CrossRef]
7. Anaszewicz, Ł.; Rekucki, R.; Stolarski, A. Effects of Portland cement addition on Young's modulus of geopolymer concrete cured at ambient conditions. *Bull. Mil. Univ. Technol.* **2018**, *67*, 71–82. [CrossRef]
8. Yost, J.R.; Radlińska, A.; Ernst, S.; Salera, M.; Martignetti, N.J. Structural behavior of alkali activated fly ash concrete. Part 2: Structural testing and experimental findings. *Mater. Struct.* **2013**, *46*, 449–462. [CrossRef]
9. Visintin, P.; Mohamed Ali, N.; Albitar, M.; Lucas, W. Shear behaviour of geopolymer concrete beams without stirrups. *Constr. Build. Mater.* **2017**, *148*, 10–21. [CrossRef]

10. Mathew, G.; Joseph, B. Flexural behaviour of geopolymer concrete beams exposed to elevated temperatures. *J. Build. Eng.* **2018**, *15*, 311–317. [CrossRef]
11. Palacios, M.; Puertas, F. Effect of superplasticiser and shrinkage-reducing admixes on alkali-activated slag pastes and mortars. *Cem. Concr. Res.* **2005**, *35*, 1358–1367. [CrossRef]
12. Jithendra, C.; Elavenil, S. Role of Superplasticiser on GGBS based Geopolymer Concrete under ambient curing. *Mater. Today Proc.* **2019**, *18*, 148–154. [CrossRef]
13. Jang, J.G.; Lee, N.K.; Lee, H.K. Fresh and hardened properties of alkali-activated fly ash/slag pastes with superplasticisers. *Constr. Build. Mater.* **2014**, *50*, 169–176. [CrossRef]
14. Gupta, N.; Gupta, A.; Saxena, K.K.; Shukla, A.; Goyal, S.K. Mechanical and durability properties of geopolymer concrete composite at varying superplasticiser dosage. *Mater. Today Proc.* **2021**, *44*, 12–16. [CrossRef]
15. Criado, M.; Palomo, A.; Fernández-Jiménez, A.; Banfill, P.F.G. Alkali activated fly ash: Effect of admixes on paste rheology. *Rheol. Acta* **2009**, *48*, 447–455. [CrossRef]
16. Nuruddin, F.M.; Demie, S.; Ahmed, F.M.; Shafiq, N. Effect of Superplasticiser and NaOH Molarity on Workability, Compressive Strength and Microstructure Properties of Self-Compacting Geopolymer Concrete. *Int. J. Geol. Environ. Eng.* **2011**, *5*, 187–194.
17. Memon, F.A.; Nuruddin, M.F.; Demie, S.; Shafiq, N. Effect of Superplasticiser and Extra Water on Workability and Compressive Strength of Self-Compacting Geopolymer Concrete. *Res. J. Appl. Sci. Eng. Technol.* **2012**, *4*, 407–414.
18. Montes, C.; Zang, D.; Allouche, E.N. Rheological behavior of fly ash-based geopolymers with the addition of superplasticisers. *J. Sustain. Cem. Based Mater.* **2012**, *1*, 179–185. [CrossRef]
19. Laskar, A.I.; Bhattacharjee, R. Effect of Plasticiser and Superplasticiser on Rheology of Fly-Ash-Based Geopolymer Concrete. *ACI Mater. J.* **2013**, *110*, 513–518.
20. Nematollahi, B.; Sanjayan, J. Efficacy of available superplasticisers on geopolymers. *Res. J. Appl. Sci. Eng. Technol.* **2014**, *7*, 1278–1282. [CrossRef]
21. Xie, J.; Kayali, O. Effect of superplasticiser on workability enhancement of Class F and Class C fly ash-based geopolymers. *Constr. Build. Mater.* **2016**, *122*, 36–42. [CrossRef]
22. Salami, B.A.; Megat, J.M.; Ahmad, Z.A.; Maslehuddin, M. Impact of added water and superplasticiser on early compressive strength of selected mixes of palm oil fuel ash-based engineered geopolymer composites. *Constr. Build. Mater.* **2016**, *109*, 198–206. [CrossRef]
23. Bong, S.H.; Nematollahi, B.; Nazari, A.; Xia, M.; Sanjayan, J. Efficiency of Different Superplasticisers and Retarders on Properties of 'One-Part' Fly Ash-Slag Blended Geopolymers with Different Activators. *Materials* **2019**, *12*, 3410. [CrossRef] [PubMed]
24. Nguyen, H. Microstructure Stability and Thermal Resistance of Ash-Based Geopolymer with Sodium Silicate Solution at High Temperature. *Int. J. Eng. Res. Afr.* **2021**, *53*, 101–111. [CrossRef]

materials

MDPI

Article

# Experimental Study of Single-Lap, Hybrid Joints, Made of 3D Printed Polymer and Aluminium Adherends

**Przemysław Golewski, Marek Nowicki *, Tomasz Sadowski and Daniel Pietras**

Department of Solid Mechanics, Faculty of Civil Engineering and Architecture, Lublin University of Technology, Nadbystrzycka 38, 20-618 Lublin, Poland; p.golewski@pollub.pl (P.G.); t.sadowski@pollub.pl (T.S.); d.pietras@pollub.pl (D.P.)
* Correspondence: marek.nowicki@pollub.pl

**Abstract:** This paper presents the results of an experimental study into single-lap joints. One part of the joint was made as a 3D printed polymer and had cylindrical tenons, while the other part was made of an aluminium flat bar having mortises whose diameter and distribution corresponded to the polymer tenons. In addition to the mechanical joint, a layer of double-sided VHB (Very High Bond) adhesive tape was also placed in the lap, thus creating a hybrid joint. In total, 80 specimens were made, which were divided into four groups: A—specimens with one tenon of different diameters, B—specimens with different number of tenons of the same diameter, C—specimens characterised by multi-stage operation and R—reference specimens, connected only by double-sided adhesive tape. The joints were subjected to uniaxial tensile tests. The force–displacement characteristics obtained and the energy required, up to the point of the failure of the joints, have been analysed in this paper. The four and six-stage joints designed can significantly increase the safety of the structures in which they will be used.

**Keywords:** hybrid joints; single lap joints; 3D printing

## 1. Introduction

The use of 3D printing is becoming increasingly popular, not only for the fabrication of mock-ups and prototypes, but also for industrial scale products. 3D printing technology facilitates production for multi-material products [1], reduces defects and lowers both production costs [2] and the need for repairs [3]. Considering the statistics, the Compound Annual Growth Rate (CAGR) for the next few years averages 23.5%. This means that the market will double every three years. Such significant growth also results in the greater involvement of researchers to improve this technology. However, not all parts can be replaced by printed products, since they may not be cost-effective, hence the problem of joining them with other materials arises. There are many joining techniques such as riveting [4], welding, spot-welding [5], friction stir welding (FSW) [6], friction stir interlocking (FSI) [7,8] and clinching [9]. The authors in [7] used micro-texturing by ablative laser pre-treatment on the surface of an aluminium alloy. In this case, the polymer–aluminium bonding was done using the FSW method, which produced high strength. In the paper [10], the authors used the Injection Clinching Joining (ICJ) method in which a pre-formed polymeric tenon is melted and formed in the mortise of a metal part. This type of mechanical joint is free of clearance. A similar technique is presented in [11], but in this case an aluminium tenon, made by a printing technique on the surface of a thin-walled profile, is used. At present, the laser-assisted technique is also used for joining metal-printed polymer structures [12,13]. During this process, the polymer is melted under the influence of laser beam energy and penetrates the structure of the metal surface under the application of a specific joining pressure. The advantage of this type of solution is that there is no correlation between the surface roughness Ra and the shear strength of the joint. A similar technique is ultrasonic welding [14], which allows thermoplastic composites to be joined with aluminium alloys. In the work [15], the authors used a clinched metal-polymer type joint. Experimental studies were conducted by varying the main process parameters such as heating time, the temperature of the air and moulding pressure.

A common feature of these types of mechanical connections is that they invade the structure of the parts being joined. In many cases, they are also a source of concentrated stress. Therefore, another group of joints that can be used to connect polymer 3D prints are adhesive joints, either using liquid adhesives [16,17], tapes [18] or dual-adhesive [19,20]. Their advantage is that the load is transferred over a considerable area and thus distribution of the stress, in the joined parts, is in many cases free of concentration.

Currently, the study of the adhesive bonding of polymer 3D prints has been carried out in many directions. The works [21,22] analysed the effect of surface topography on peel and shear strength. The surface topography can also be designed, for example, by introducing undulation [23]. When using adhesive joints, the thickness of the adhesive plays a large role. In the paper [24], three adhesive thicknesses were analysed: 0.2 mm, 0.3 mm and 0.4 mm. It was shown that the 0.2 mm thickness was the best and led to higher mechanical performance and tensile strength compared to the other two. The bonding strength also depends on the adhesive used. When bonding polymer 3D prints, it is more beneficial to use cyanoacrylate adhesive than epoxy adhesive [25]. Surface wettability, which is another parameter, can be modified by sandblasting or by employing atmospheric plasma treatment; using the second, an increase of 200% in shear strength can be achieved [26].

In recent years, connections using double-sided adhesive tapes have received increasing attention [27–31]. In many cases, they allow traditional liquid adhesives or mechanical joints to be replaced. From a researcher's point of view, the soft and relatively thick (0.4–1.6 mm) layer of double-sided adhesive tape also comes with some challenges. The acrylic-based polymer used in VHB tapes is highly deformable, highly visco-elastic and very sensitive to temperature changes, hence the numerical modelling of this type of bond is difficult.

The simultaneous use of two techniques: mechanical and adhesive joints lead to a hybrid joint [32,33]. In this case, research is usually conducted using a single-lap scheme and various types of mechanical fasteners such as screws [34–36], embossing [37] and spot-welding [38].

To sum up, many techniques are used to join polymer 3D prints. Authors most often aim to increase their strength and often the energy used, up to the point of the failure of the joint, is also analysed. However, there is not much call to use the two simplest solutions: double-sided adhesive tape and mechanical connection of the "mortise and tenon" type. This type of hybrid solution is the subject of this paper. Its advantage is the rapidity with which the joints can be produced, since no adhesive curing time is needed and also, by properly selecting the ratio of the surface of the mechanical joint to the surface of the double-sided adhesive tape, it is possible to design the characteristics of the joint. In this paper, the results of the laboratory tests for innovative joints, with multi-stage characteristics, are also presented.

## 2. Materials and Methodology

Testing of the hybrid joints was performed using the popular and currently most widely used single-lap model. The dimensions of the joints, which are shown in Figures 1–3, were designed so that there would be no fracturing of the connected parts.

The hybrid joints were divided into 3 groups:

- group A—single-lap joints with one tenon having 5 different diameters "D": 5 mm, 8 mm, 11 mm, 14 mm and 19 mm (Figure 1),
- group B—joints with different numbers of tenons of the same diameter D = 5 mm (Figure 2),

- group C—special joints, characterised by multi-stage operations with tenons of diameter D = 5 mm (Figure 3).

In addition, reference joints "R" were made, using only double-sided adhesive tape, having the same dimensions as in Figure 1. In each case, 5 specimens were used per batch, hence the total number of specimens was 80.

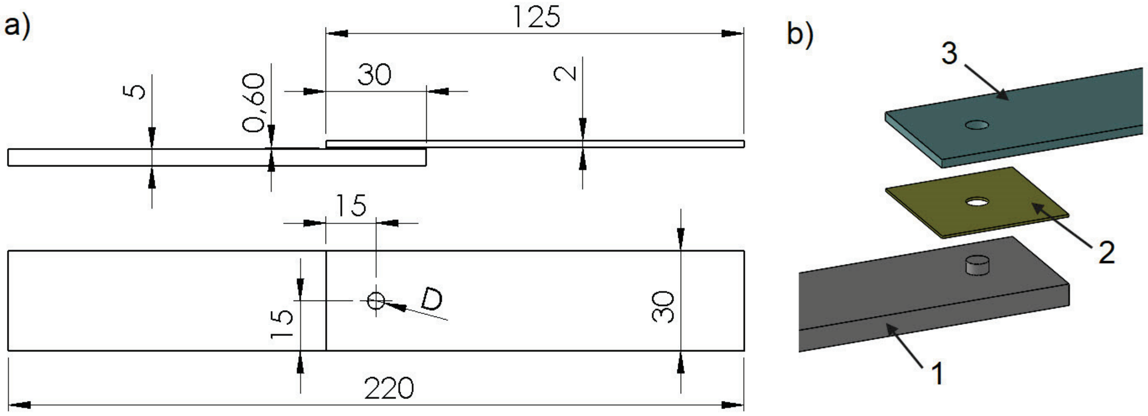

**Figure 1.** Joints with one tenon: (**a**) joint diagram; (**b**) perspective view (1—polymer lap, 2—double-sided adhesive tape, 3—aluminium lap).

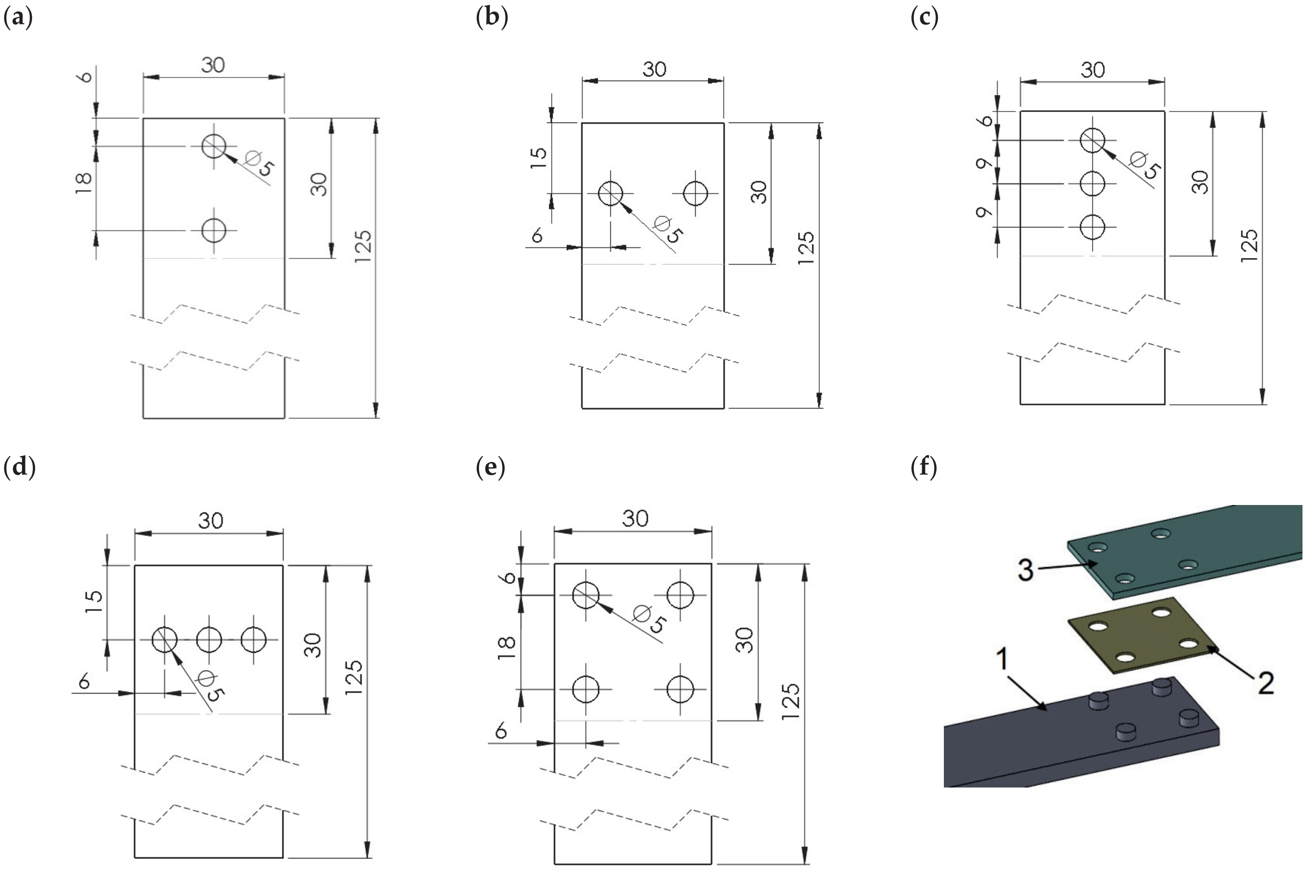

**Figure 2.** Types of joints with different numbers of tenons of the same diameter D = 5 mm: (**a**) model B1; (**b**) model B2; (**c**) model B3; (**d**) model B4; (**e**) model B5; (**f**) model B5 in perspective view (1—polymer lap, 2—double-sided adhesive tape, 3—aluminium lap).

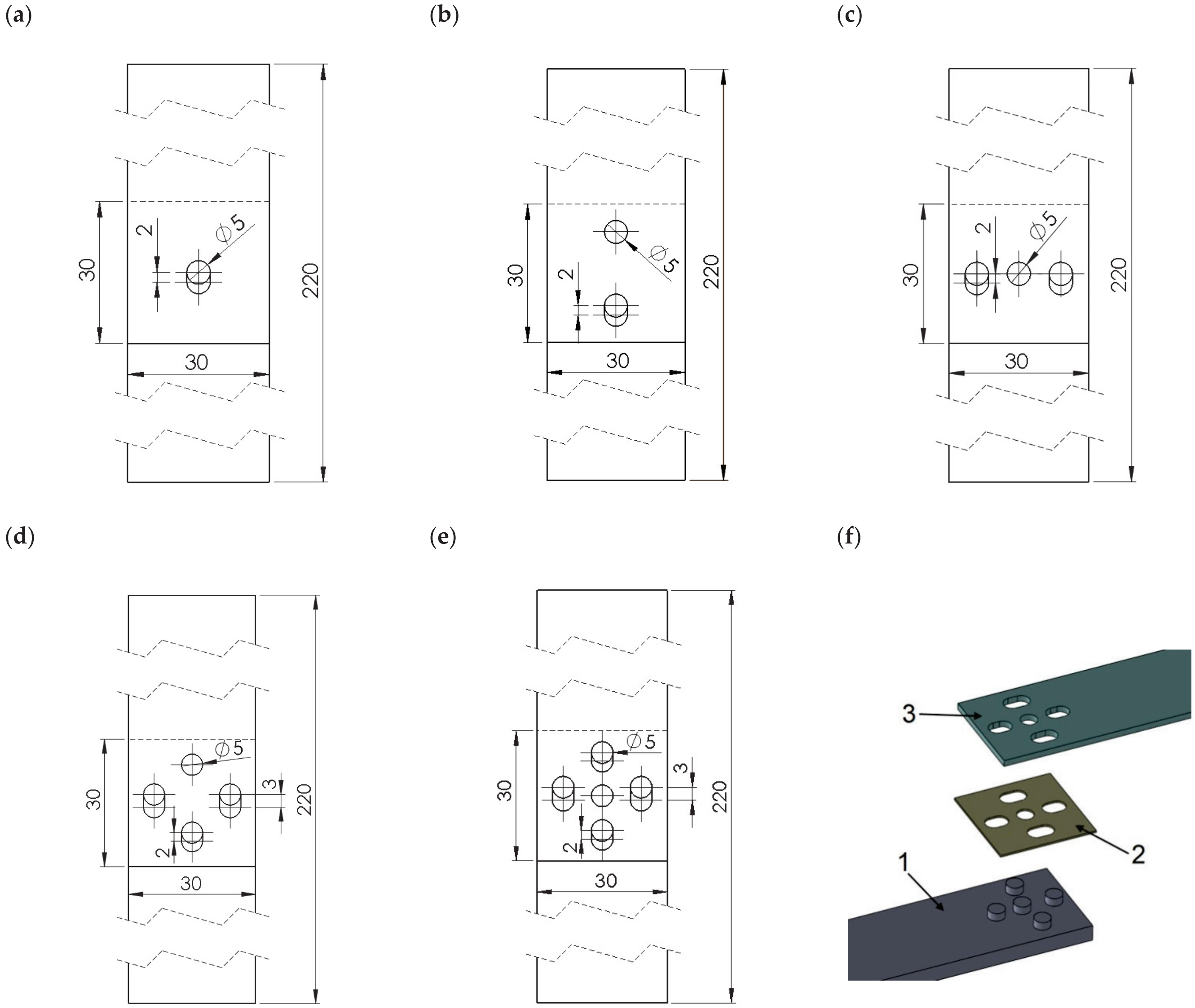

**Figure 3.** Special joints characterised by multi-stage operation using tenons of diameter D = 5 mm: (**a**) model C1; (**b**) model C2; (**c**) model C3; (**d**) model C4; (**e**) model C5; (**f**) model C5 in perspective view (1—polymer lap, 2—double-sided adhesive tape, 3—aluminium lap).

3D prints of polymer laps, made of Z-ABS material including the tenons, were made on a Zortrax M300 printer. The print parameters and material data of the filament are shown in Table 1.

Although the tensile strength of the ABS material according to Table 1 is 29.6 MPa, tests conducted on dog bone samples with a cross section of 10 × 5 mm, showed a print tensile strength of 13.25 MPa.

The second laps were made of an aluminium flat bar, made of AW-6060 T4 alloy, with the following properties: yield strength—65 MPa, tensile strength 130 MPa, elongation at break 13%. The holes in the aluminium laps were made by milling on a CNC machine.

To connect the aluminium and polymer parts, 3 M VHB 5925 double-sided adhesive tape with a thickness of 0.6 mm and a width of 38 mm was used. The tape is designed for permanent bonding to irregular surfaces or to powder-skin coated materials and provides good adhesion, with high and medium surface energy to various surfaces, including plastics, paints, metals and glass. One of the mechanisms of adhesion of VHB tape to laps is intermolecular force. This is an electrical interaction that occurs when two molecules are in close proximity to each other. The two surfaces do not stick to each other regardless of how close they are. The reason for this is that the surfaces are rough at the nano level and the molecules cannot get close to each other. The VHB tape causes these roughnesses to fill in, resulting in intermolecular forces.

**Table 1.** Printing parameters and properties of ABS and 3D-printed specimens.

| Printing Parameters | Values | ABS Parameters | Values |
|---|---|---|---|
| Raster angle (°) | ±45 | Density (g/cm$^3$) | 1.06 |
| Raster width (mm) | 0.4 | Young modulus (GPa) | 2.24 |
| Print tolerance (%) | ±0.2 | Poisson ratio | 0.38 |
| Infill percentage (%) | 100 | Yield point (MPa) | 20 |
| Layer thickness (mm) | 0.09 | Tensile strength (MPa) | 29.6 |
| Bed temperature (°C) | 80 | Filament diameter (mm) | 1.75 |
| Nozzle diameter (mm) | 0.4 | Diameter tolerance (mm) | ±0.05 |
| Printing speed (mm/s) | 30 | Melting point (°C) | ∼250 |
| Nozzle temperature (°C) | 275 | Thermal conductivity (W/mK) | 0.16 |

The manufacturing process of the joints consists of the following steps:

1. A check was done to make sure that all mechanical joints would be able to fit together. If there was significant compression, the geometry had to be corrected.
2. The surface of the aluminium laps was cleaned with Loctite 7061 because coolant and oil were to be used during milling.
3. UNI UV 0.23 primer for VHB tapes was applied to the surfaces of the aluminium and polymer laps.
4. The tape was unrolled and placed on a flat surface with the adhesive side up and then five aluminium laps were placed on it, next to each other, at intervals of a few millimetres.
5. Cutting the tape for each lap was done using a scalpel and a punch of appropriate diameter; holes were made in the tape to match the corresponding holes in the aluminium lap.
6. The protective layer was removed from the tape and bonded to the other polymer lap.
7. The tape was 38 mm wide and the overlay was 30 mm wide. The excess tape on the aluminium part was trimmed with a scalpel and then removed from the surface. In this way, the tape's geometry perfectly matched the geometry of the lap.
8. The tape manufacturer requires a low clamping pressure of 100 kPa, hence the laps were clamped by hand without any additional tooling. The specimens were tested more than 72 h after they were made, which, according to the manufacturer, ensures that maximum strength is achieved.

For this type of connection, the strength of the laps exceeded the strength of the connection, hence there was no risk of breakage nor was there any need for bonding the tabs at the ends of the laps. The completed connections (one specimen from each batch) are shown in Figures A1–A3.

Uniaxial tensile tests were performed on an MTS 25 kN testing machine. In order to avoid pre-bending, the specimens due to the geometry of the single-lap model, a sufficient thickness of inserts was used between the grips and the ends of the tabs. The specimens were loaded at a constant displacement increment of 5 mm/min. Tests were conducted at a temperature of 23 °C ± 2.

## 3. Results and Discussion

### *3.1. Mechanical Response of Reference Specimens "R" Joined by VHB Double-Sided Adhesive Tape*

Although VHB double-sided adhesive tapes are characterised by low maximum stress, high strains to failure result in impressive fracture energy. The failure process often starts with the nucleation of microscopic cracks inside the layer. The failure model is usually cohesive, with a layer of tape remaining on both adherends. Operation of the adhesive tape, as shown in Figure 4 for the reference specimens, has several stages. Initially, the force increases linearly; the graph then becomes curved and flattened. This stage continues until about the middle of the strain range, culminating in failure. The final stage is the tape failure process, which initially occurs quite rapidly; however, at about 30% of the maximum force, the graph begins to smoothly move towards zero. The average maximum force, achieved for the joints made with the VHB tape, was 333 N, which corresponds to a stress of 2.22 MPa in the 3D printed laps. The average energy required to failure, calculated as the area under the force–displacement diagram, was 3 J. These values will be considered as reference and the average values of force and energy for each batch of specimens and work stage will be referred to. The samples after the test are shown in Figure A4. The failure is mainly cohesive in nature. There is also a loss of adhesion between the tape and the aluminum surface and between the tape and the polymer 3D print. The percentages of adhesion failure are 8% and 17.4%, respectively, considering all samples in the batch.

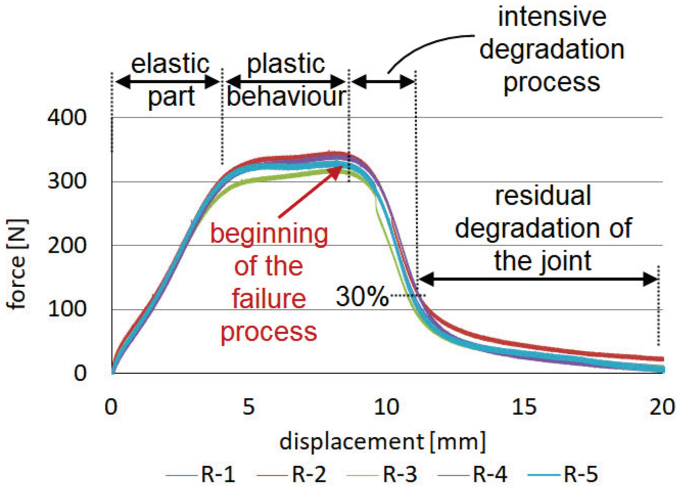

**Figure 4.** Force–displacement diagrams for reference specimens "R" joined by VHB double-sided adhesive tape.

### 3.2. Mechanical Response of the Single—Lap Joints with One Tenon—Group "A"

The first type of hybrid joint, labelled "A", was concerned with analysing the effect of the diameter of the mechanical joint. In this case, only one tenon was used, whose diameter varied from 5 mm to 19 mm. In batches A1 to A4, there was shearing of the mechanical joint and subsequent gradual degradation up to the final failure of the adhesive joint. In the case of specimen A5, the mechanical joint was so strong that the lap breakage occurred at the location of the tenon. By properly selecting the ratio of the area of the tenon and the adhesive tape, not only can different levels of maximum force and energy be obtained, but different characteristics can also be obtained. An analogous phenomenon occurs here, as in [19], where double-sided adhesive tape was also used, while the role of rigid connection was achieved by the point bond of epoxy adhesive. Thus, the "A" type joints are characterised by a two-stage operation (Figure 5), which is schematically shown in Figure 5f. In the first stage, the rigid mechanical joint works and the load are mainly transferred through the polymeric tenon reaching the $F_1$ force. When the tenon is cut by shear loading, the force drops rapidly to $F_2$, while the joint does not lose integrity. The load is taken up by the adhesive joint and the force increases, reaching $F_3$ again.

The purpose of using polymeric tenons is to increase the strength and stiffness of the joint. For the A1 group of specimens, the maximum force achieved by the mechanical connection is about 26% lower than the maximum force achieved by reference connection "R".

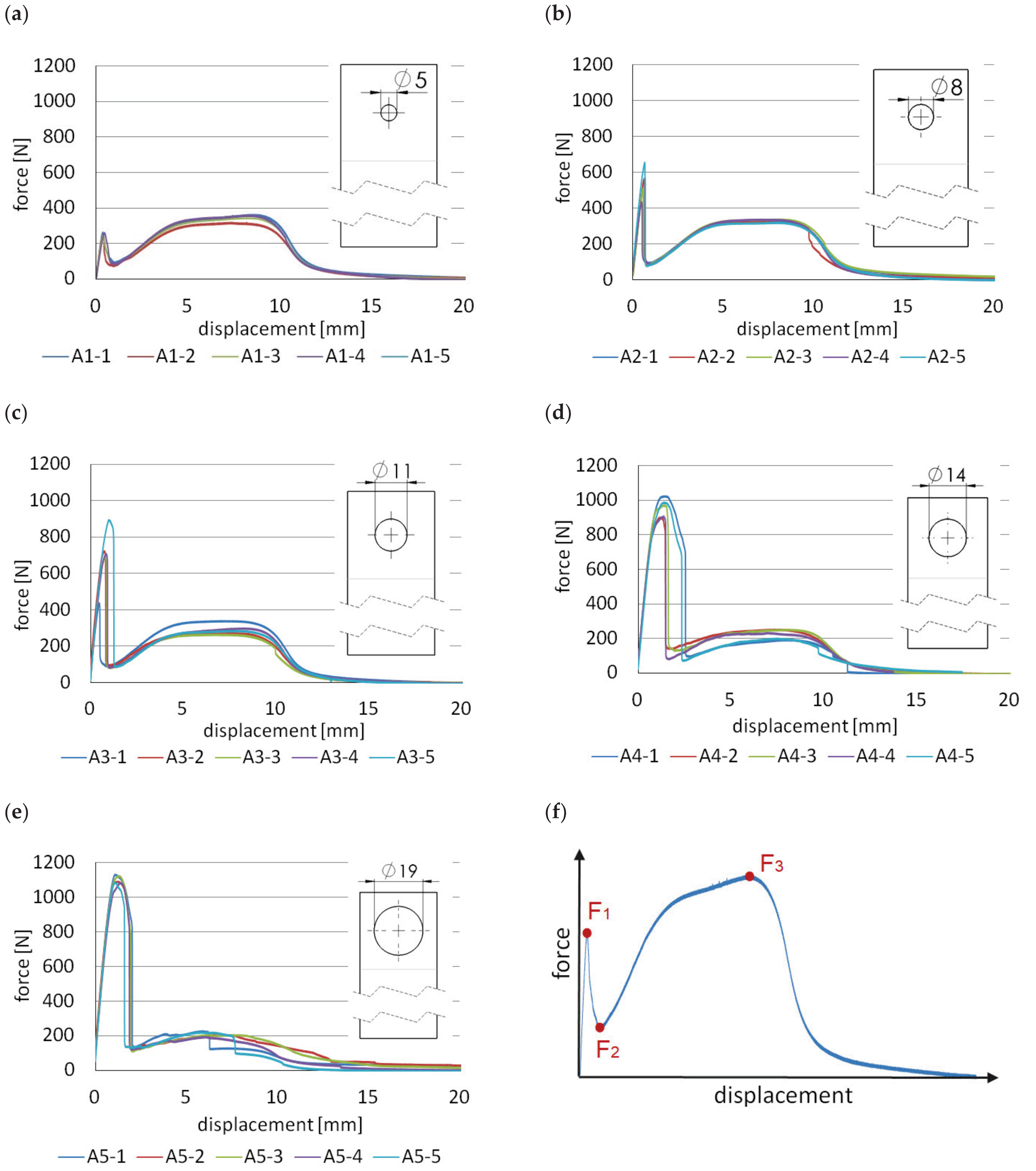

**Figure 5.** Force–displacement diagrams for models "A": (**a**) models A1; (**b**) models A2; (**c**) models A3; (**d**) models A4; (**e**) models A5; (**f**) working diagram.

When the diameter is increased to 8 mm, the mechanical joint achieves a higher strength, by 46.5%, compared to the reference connection. For A3 series specimens, having a tenon diameter of 11 mm, the mechanical joint achieves about 123% of the maximum strength of the reference connection "R".

Although for the subsequent A4 group, this ratio is even more favourable and the connection has a higher strength, it should be noted that the strength decreases quite sharply in the working stage of the adhesive joint. For the A1 and A2 series, the work of the adhesive tape is similar to that of reference joint "R". There is no noticeable decrease in strength, in this case. The reason for this is that the area occupied by the tenon is small (11%) relative to the area of the entire lap. For A4 and A5, the adhesive area of the tape decreases by about 17.1% and 31.5%, respectively.

Table 2 collects the force values $F_1$–$F_3$ and the corresponding stress values $\sigma_1$–$\sigma_3$ in the 3D printed lap outside the joint zone, assuming that it is only in tension.

**Table 2.** Summary of average $F_1$, $F_2$, and $F_3$ forces and the corresponding stresses $\sigma_1$, $\sigma_2$ and $\sigma_3$ in the printed lap outside the joint zone as well as energies for Type A specimens.

| | Model A1 | Model A2 | Model A3 | Model A4 | Model A5 |
|---|---|---|---|---|---|
| $F_1$ [N], ($\sigma_1$ [MPa]) | 246 (1.64) | 488 (3.25) | 744 (4.96) | 953 (6.35) | 1094 (7.29) |
| $F_2$ [N], ($\sigma_2$ [MPa]) | 83 (0.55) | 89 (0.59) | 90 (0.6) | 123 (0.82) | 126 (0.84) |
| $F_3$ [N], ($\sigma_3$ [MPa]) | 342 (2.28) | 329 (2.19) | 277 (1.85) | 219 (1.46) | 207 (1.38) |
| energy [J] | 3.1 | 3.2 | 2.8 | 3.1 | 3.3 |

Group A2 should be considered as the best model because, in this case, we obtain a significant increase in stiffness in the initial stage of operation, which does not come at the expense of a decrease in the strength of the adhesive joint. Considering the energy which is needed to the point of the failure of the joint, the A2 model is also, in this respect, the best. An increase of about 6.6% is obtained compared to the reference model. In general, the highest energy was obtained for model A5, but it should be noted that, in this case, there was no shear failure of the mechanical connections, but rather a fracture of the lap at the tenon location. The samples after the test are shown in Figures A5–A9. As in the reference samples, there is mainly cohesive failure in the tape. There is also a loss of adhesion between the tape and the aluminium surface and between the tape and the polymer 3D print. For example, for samples A1 (Figure A5), the percentage of adhesive failure is 16% and 15%, respectively, considering all samples in the batch.

### *3.3. Mechanical Response of the Joints Having Different Numbers of Tenons—Group B*

Type B specimens, for which the force-displacement diagrams are shown in Figure 6, were made and tested to determine the effect of the number of mechanical joints on their mechanical response. In this case, the polymeric tenon was 5 mm in diameter for each specimen, having two, three and four tenons. Models B1 (Figure 2a) and B2 (Figure 2b) had two tenons. In the first case, the line on which the tenons were placed, coincided with the axis of the specimen and thus the line of load action. In the second case, the line connecting the two pivots was perpendicular to the line of load action and was located at the midpoint of the lap length (Figure 2b). Failure of single-lap joints often starts at the free edge of the joint between two materials, where there is a stress singularity leading to cracks developing exponentially [39]. Hence, mechanical fasteners are most advantageously placed near the end of the lap region [18]. It is also common to introduce an additional pre-stressing force from the mechanical fastener [40].

Table 3 collects the force values $F_1$–$F_3$ and the corresponding stress values $\sigma_1$–$\sigma_3$ in the 3D printed lap outside the joint zone, assuming that it is only in tension.

In the tests conducted, similar values of $F_1$ forces were obtained for B1 and B2 specimens; however, a higher value of $F_3$ force and energy in relation to B2 specimens favours placement along the line of force action.

The next batches of samples to be analysed are groups of specimens B3 and B4. These are analogous to series B1 and B2, the only difference being the introduction of an additional third tenon.

In this case, it is more advantageous to place the row of mechanical joints, perpendicularly to the loading direction. This results in an increase of approximately 19.5% in the $F_1$ force level, compared to specimen B3. Both $F_2$ and $F_3$ force and energy levels remain the same for both series types.

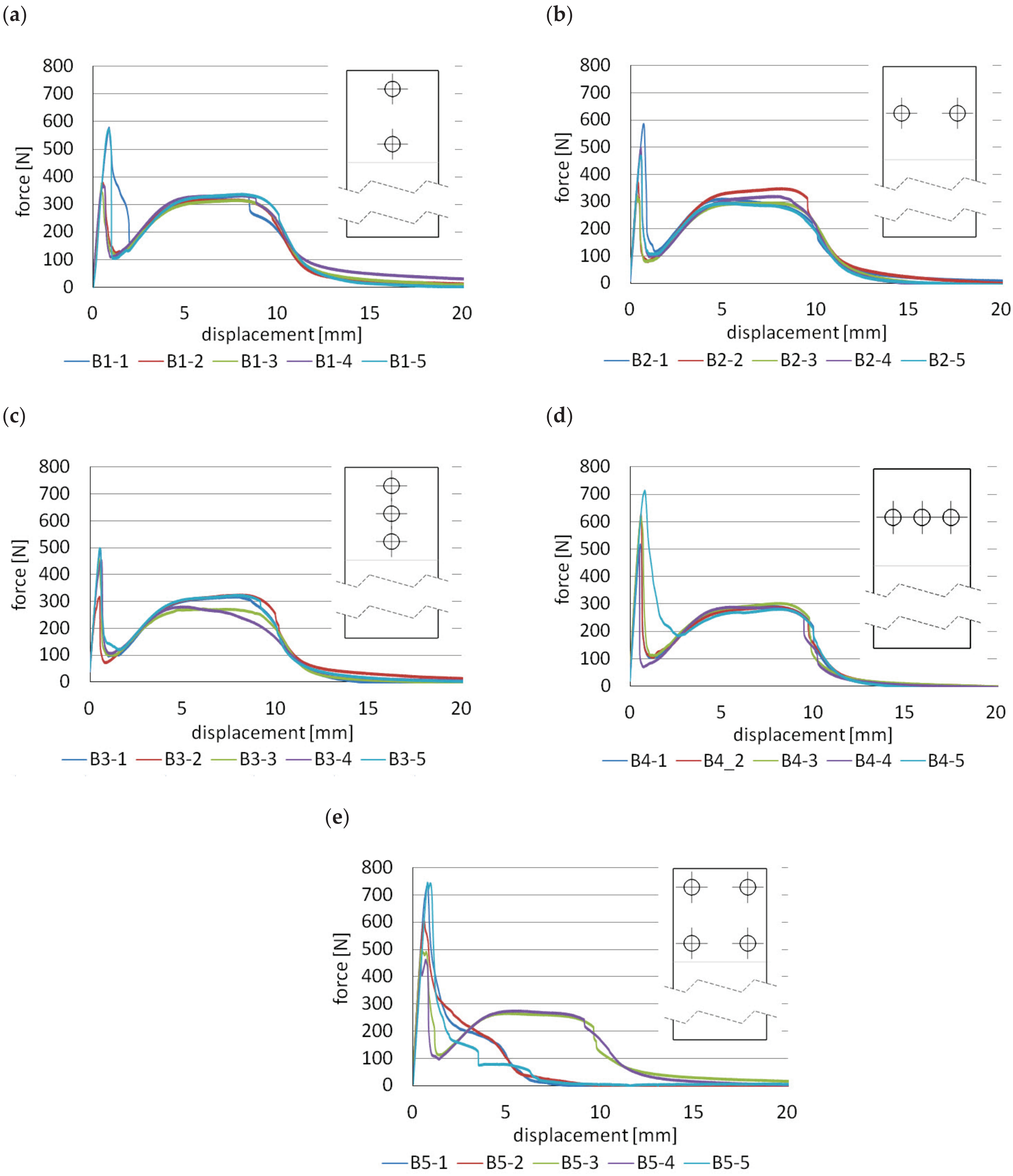

**Figure 6.** Force-displacement diagrams for "B" models: (**a**) B1 models; (**b**) B2 models; (**c**) B3 models; (**d**) B4 models; (**e**) B5 models.

**Table 3.** Summary of average $F_1$, $F_2$, and $F_3$ forces and the corresponding stresses $\sigma_1$, $\sigma_2$, and $\sigma_3$ in the printed lap outside the joint zone as well as energies for Type B specimens.

| | **Model B1** | **Model B2** | **Model B3** | **Model B4** | **Model B5** |
|---|---|---|---|---|---|
| $F_1$ [N], ($\sigma_1$ [MPa]) | 380 (2.53) | 395 (2.63) | 451 (3.01) | 539 (3.59) | 591 (3.94) |
| $F_2$ [N], ($\sigma_2$ [MPa]) | 147 (0.98) | 101(0.67) | 137 (0.91) | 144 (0.96) | 104 (0.69) |
| $F_3$ [N], ($\sigma_3$ [MPa]) | 325 (2.16) | 305 (2.03) | 287 (1.91) | 288 (1.92) | 270 (1.8) |
| energy [J] | 3.3 | 2.8 | 2.8 | 2.7 | 2.8 |

A different model is that of the B5 group of specimens in which one additional mechanical joint was introduced. These were also repositioned so that they were located at the corners of the overlap. There is an increase in $F_1$ force of about 77% over the reference model. Although specimen B5 had the smallest adhesive tape area, the energy required to failure is at a level similar to that for models B2, B3 and B4. To the disadvantage of model B5 is the fact that three specimens in this series failed in an unusual way, consisting in the absence of the working stage of the double-sided adhesive tape. Once the maximum $F_1$ force is reached, there is a decrease in its value with varying speed. Initially, the decrease is rapid—to about half of the $F_1$ value—but then the graphs become smoother. From this, it can be concluded that the greater the number of mechanical joints, the greater the influence of defects, both in the making of the holes in the tape and in the influence of clearances in the mechanical joints. In order to prevent clearances between tenon and mortise, the authors in [15] proposed an original method by heating a metal lap and forming the heated tenon under pressure. This type of technology can eliminate the clearance; however, its application, in many cases, may be limited because the heating process itself takes a certain amount of time and must be strictly controlled. In order to obtain proper pressure and the plasticisation of the tenon in the groove, the joint must be supported on the other side. Manufacturing this type of specimen and applying it in engineering may be difficult to achieve, especially due to lack of available space.

In conclusion, the most advantageous solution from the group of B models is model B1. In this case, both an increase in the value of $F_1$ force by about 14% in comparison with the reference model "R" and an increase in the energy required to failure of the joint by 10%, are obtained. In addition, the joint shows significant stiffness at the stage of reaching the $F_1$ value, while operation of the double-sided adhesive tape provides high safety, since its degradation consumes the most energy. The samples after the test are shown in Figures A10–A14. The cohesive nature of the failure that is characteristic of double-sided VHB tape is most disturbed for samples B5 (Figure A14). In this case, the cohesive failure covers about 46% of the total surface area, the adhesive failure between the tape and the aluminium surface is as high as 41%, and the adhesive failure between the tape and the 3D printed polymer is 13%, considering all the samples in the batch.

### *3.4. Mechanical Response of Hybrid Joints Characterised by Multi-Stage Operation—C Group*

The last type of "C" models is the most original and advanced. The idea of this type of connection is to achieve multi-stage operation and specific characteristics, through the use of mechanical joints that take part in load transfer in a controlled manner. This is realised by an appropriately sized clearance in one of the laps, by making an elongated hole. In this type of model, there can be different solutions:

(a) all mechanical joints have the same diameter and the holes with which they engage are equally elongated (e.g., C1 Figure 3a),
(b) both tenons are seated in holes of the same diameter and tenons engage with elongated holes of the same length (e.g., C2 Figure 3b, C3 Figure 3c),
(c) there are tenons embedded in holes of the same diameter and tenons engaging with elongated holes of different lengths (e.g., C4 Figure 3d, C5 Figure 3e).

Figure 7 shows the force–displacement diagrams obtained from the laboratory tests, while Figure 8 shows the three different characteristics that correspond to them. The samples after the test are shown in Figures A14–A19. For example, for specimen C1 (Figure A15), the cohesive failure covers 71% of the lap area, the adhesive failure between the tape and the aluminum surface is 19%, and the adhesive failure between the tape and the 3D printed polymer is 10%, considering all specimens in the series.

For specimen C1, the scheme of operation is similar to models A and B, whose characteristics are shown in Figure 5f. In specimen C1, there is an elongated hole, and it is only after some time, with the joint beginning to stretch, that the tenon engages with the hole. Therefore, there is a change in stiffness as indicated by the SC (stiffness change) point in Figure 8a. By changing the length of the hole, it is possible to design which displacement (load) the joint starts to resist more. Further operation takes place as for models A and B and three levels of forces $F_1$, $F_2$, and $F_3$ can be distinguished.

The second group of models are C2 and C3. Their operating characteristics are shown in Figure 8b.

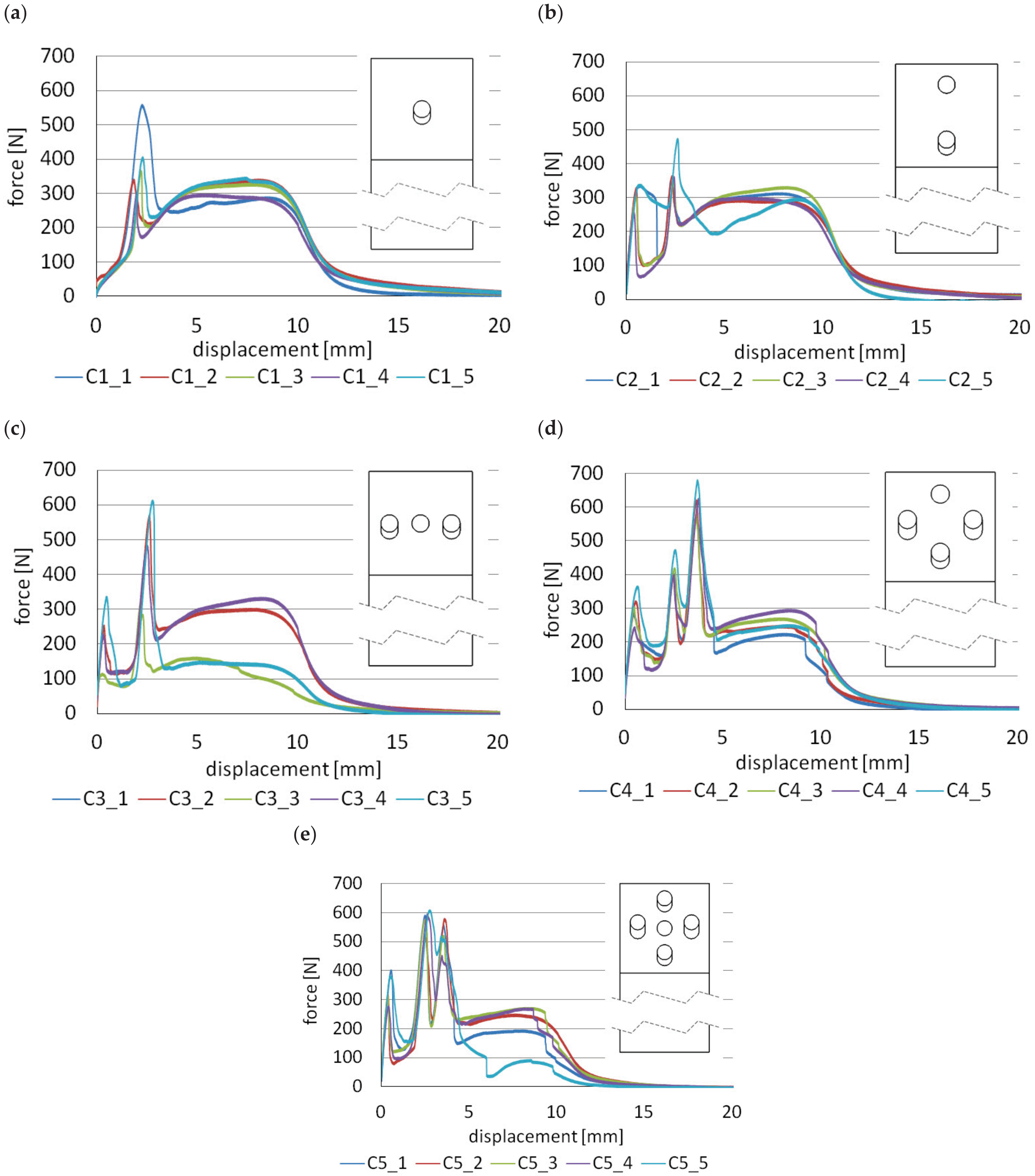

**Figure 7.** Force–displacement diagrams for "C" models: (**a**) C1 models (Figure 3a); (**b**) C2 models (Figure 3b); (**c**) C3 models (Figure 3c); (**d**) C4 models (Figure 3d); (**e**) C5 models (Figure 3e).

Already, from the beginning of the load, with these models, one of the tenons engages with the hole. The joint therefore has a much higher stiffness than if only the double-sided adhesive tape was working i.e., model "R". In the next stage, when force $F_1$ is reached, the tenon is cut due to shear and the force drops to $F_2$, the load being carried by the adhesive tape. In the third stage, other mechanical joints engage with the holes and the force increases again to $F_3$. The fourth and final stage occurs after all tenons have been sheared and the load is again taken up by the adhesive tape. Of course, force levels $F_1$ and $F_2$ can differ, depending on the diameter value and the number of tenons for each stage.

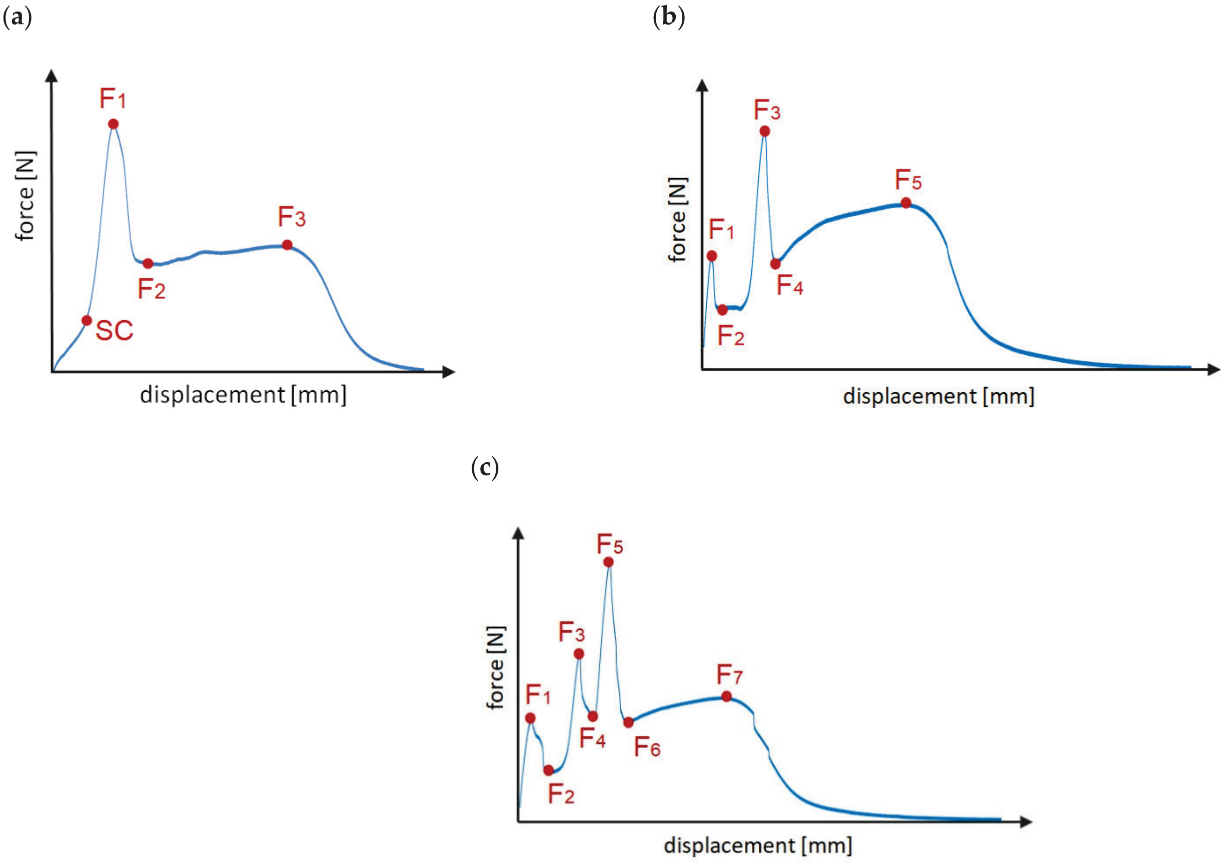

**Figure 8.** Schematics of connections: (**a**) C1; (**b**) C2; C3; (**c**) C4; C5.

The last group of joints C4 and C5 (Figure 8c) is the most advanced because there are as many as six stages of operation—three stages of mechanical joint operation and three stages of adhesive tape operation. To achieve this effect, one of the laps must have both holes with diameters corresponding to the mating tenons and two types of enlarged holes. By properly selecting the diameters of the tenons and the length of the enlarged holes, it is possible to obtain different force ratios $F_1$, $F_3$, $F_5$ and $F_7$. The disadvantage of this type of solution is that more effort is required to drill the holes and high precision must be exercised.

Table 4 collects the force values $F_1$–$F_7$ and the corresponding stress values $\sigma_1$–$\sigma_7$ in the 3D printed lap outside the joint zone, assuming that it is only in tension. Analysis and discussion of the results for the C series will begin with a comparison of the A1 and C1 models. Both types of connections have one tenon with the same diameter of 5 mm. According to Tables 2 and 4, the $F_1$ forces are 246 N and 340 N, respectively. Thus, the application of additional clearance in the hole allows an increase in the $F_1$ force of about 38%. This large increase can be explained by the fact that, in the case of model A1, the double-sided adhesive tape is completely relieved when it is loaded. In the case of model C1, there is already considerable deformation in the tape and the mechanical fastener engages smoothly with the whole joint. However, there is a question as to what the value of the $F_1$ force would be if the mechanical fastener were to come into contact with the hole, at the stage where the double-sided adhesive tape reached its maximum force value, i.e., in the displacement range of about 4–9 mm. This type of model will be the subject of on-going laboratory tests. Note, however, that, for model C1, there is a change in stiffness (point SC of Figure 8a).

**Table 4.** Summary of average $F_1$–$F_7$ forces and the corresponding stresses $\sigma_1$–$\sigma_7$ in the printed lap outside the joint zone as well as energies for Type C specimens.

| | Model C1 | Model C2 | Model C3 | Model C4 | Model C5 |
|---|---|---|---|---|---|
| $F_1$ [N], ($\sigma_1$ [MPa]) | 340 (2.32) | 285 (1.90) | 219 (1.46) | 291 (1.94) | 310 (2.07) |
| $F_2$ [N], ($\sigma_2$ [MPa]) | 233 (1.55) | 151 (1.01) | 98 (0.65) | 156 (1.04) | 124 (0.83) |
| $F_3$ [N], ($\sigma_3$ [MPa]) | - | 347 (2.31) | 420 (2.8) | 411 (0.27) | 552 (3.68) |
| $F_4$ [N], ($\sigma_4$ [MPa]) | - | 241 (1.61) | 184 (1.23) | 246 (1.64) | 329 (2.19) |
| $F_5$ [N], ($\sigma_5$ [MPa]) | - | - | - | 598 (3.99) | 514 (3.43) |
| $F_6$ [N], ($\sigma_6$ [MPa]) | - | - | - | 221 (1.47) | 197 (1.31) |
| $F_7$ [N], ($\sigma_7$ [MPa]) | 313 (2.09) | 300 (2.00) | 226 (1.51) | 251 (1.67) | 212 (1.41) |
| energy [J] | 3 | 3 | 2.3 | 2.8 | 2.5 |

In the four-stage C3 model, the predicted effect of giving a larger $F_3$ force was obtained compared to the C2 model. This effect was achieved by having two tenons come into contact with a delay rather than one, as is the case in model C2. The percentage difference in this case is approximately 21%.

The common feature of C4 and C5 models is that, in the initial stage, one tenon is working; therefore, $F_1$ forces are at a similar level. The second and third stages of the mechanical connections are already different, due to the different number of tenons, coming in contact with the holes; hence, forces $F_3$ and $F_5$ are different. For the C5 models, the lowest value of force $F_7$ is also obtained and is 36% lower compared to the reference model "R". The explanation for this decrease is related to the making of as many as five holes in the adhesive tape, which results in a weakening of the tape. The use of one or two tenons in the lap does not reduce the energy required for them to fail. For models C1 and C2, the same values were obtained as for the reference model "R". However, the energy reduction is very negatively affected by placing three tenons in one row, perpendicular to the direction of the load action. In this case, the decrease of this parameter is as much as 23%. Similarly, for model B4, the lowest energy value in the entire "B" series was also obtained.

### 3.5. Scatter Analysis of the Results

Figure 9 shows the relative standard deviation for all series for maximum force. The "R" reference samples achieved a value of 13.3%. This is not a large value considering that operations such as cutting the double-sided tape and joining the laps were performed manually, without the use of special positioning devices. Therefore, one cannot have any objections to the "A" series. In this case, the maximum value was obtained for model A2 and was 13.2%. Samples A5 have a very low % RSD parameter because, in this case, there was a breakage of the polymer laps. The "B" group is dominated by values of 20%; only samples B3 obtained a % RSD level of almost 33%. The increase in value of this parameter is associated with a higher degree in the complexity of the geometry, making more holes, which must be fitted properly. Interesting results were obtained for the "C" group; on the one hand, there is a very low repeatability of results in relation to the maximum force for C3 samples (45% RSD). On the other hand, there is also a very low value of 2% for specimen C5, which can be explained by the fact that the fasteners are uniformly distributed in the lap and come into contact with the holes in a smooth manner.

The nature of the joint failure using VHB tape may also influence the scatter in results. Theoretically, only cohesive failure should occur in the tape volume, but, regardless of the type of specimen, there is additionally adhesive failure between the tape and the surface of the aluminium adherend and between the tape and the surface of the 3D printed polymer. The largest share of cohesive failure (about 74.6%) occurs in the reference samples. After the insertion of tenons in the B and C series samples, the percentage of cohesive failure decreases. The reason may be the fragments of tenons after their failure, which, moving together with the lap, cause tearing of the tape and change the nature of its failure to adhesive.

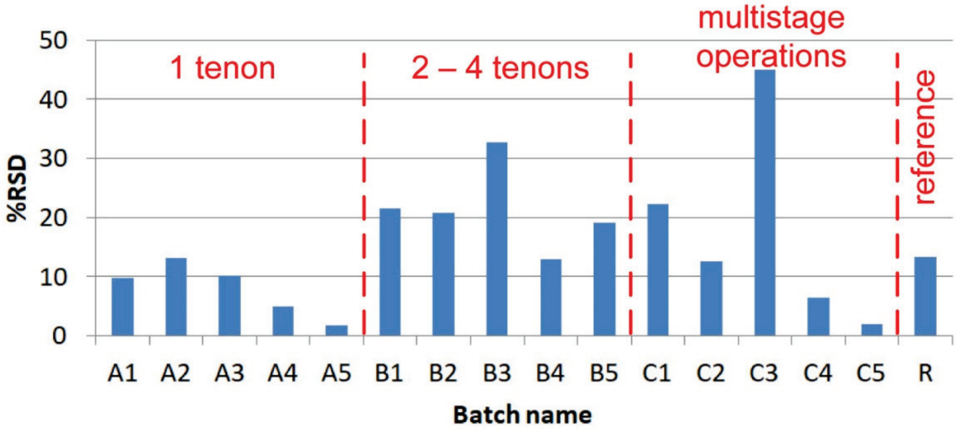

**Figure 9.** Relative standard deviation.

The results of the laboratory tests obtained can be a valuable source of data for calibrating numerical models, which is necessary because, as shown in the current paper, the number of combinations of the use of mechanical joints can be very large.

## 4. Conclusions

This paper presents three groups of original and innovative single-lap joints that are made using double-sided adhesive tape and mechanical joints by tenons. The manner in which their manufacture is implemented is described in detail. The study of lap joints was carried out on a total of 80 samples in which one of the laps was 3D printed, Z-ABS material and the other was made of aluminium. Joining of 3D printouts is a new issue and has been put into practice in many ways. However, no connections as advanced as those presented in this paper have been encountered. As the results of the tests illustrate, the following conclusions can be formulated:

- the introduction of mechanical joints, depending on the number and diameter of tenons, does not cause too high an increase in the energy required to cause the joints to fail, in comparison to the reference model R (maximum 10%). More often, there is a decrease of this parameter even by as much as 23%. This is because the polymeric tenon is much stiffer than the VHB tape, but it fails at small strains, hence the total energy is similar in each case,
- the introduction of mechanical connections significantly increases joint stiffness and maximum force. The largest increase was obtained for model A4 and was equal to 186%, compared to the reference model,
- the proportional increase of the tenon area, in the group A specimens, also results in a proportional increase in maximum force, with the operation of these joints being a two-stage process,
- increasing the tenon area, in the group A specimens, decreases the force transferred by the double-sided adhesive tape in the second stage, but all joints, regardless of tenon area, fail at the same displacement,
- the most advantageous solution from group B is model B1 which achieves both an increase in $F_1$ force of about 14% in comparison to reference model R and above a 10% increase in the energy required to cause the joint to fail.

- specimens of the group C have the greatest potential for the arbitrary shaping of the characteristics of lap joints. The four- and six-stage joints, as designed, can significantly increase the safety of the structural elements,
- Four types of failure were observed during the study. The first is the cohesive failure that occurs in the volume of the VHB tape; the effect is that it remains on both surfaces of the laps. The second type consists of deformation and finally shearing of the polymeric tenons. The third type of failure, which occurs in almost every sample, is the loss of adhesion between the VHB tape and the laps. The last type of failure, which occurred in two A4 series specimens and all A5 series specimens, is cracking of the polymer laps at the tenon location.

**Author Contributions:** Conceptualization, P.G.; Methodology, P.G.; Software, D.P., P.G. and M.N.; Validation, P.G. and T.S.; Formal Analysis, M.N. and T.S.; Investigation, D.P. and M.N.; Resources, T.S. and M.N.; Data Curation, D.P. and P.G.; Writing—Original Draft Preparation, P.G.; Writing—Review and Editing, M.N., P.G. and T.S.; Visualization, D.P. and P.G.; Supervision, T.S.; Project Administration, M.N.; Funding Acquisition, M.N. All authors have read and agreed to the published version of the manuscript.

**Funding:** The project/research was financed within the framework of the project of the Lublin University of Technology-Regional Excellence Initiative, funded by the Polish Ministry of Science and Higher Education (contract no. 030/RID/2018/19) and Polish Ministry of Science and Higher Education (Poland—contract FN 20/ILT/2021).

**Institutional Review Board Statement:** Not applicable.

**Informed Consent Statement:** Not applicable.

**Data Availability Statement:** The data presented in this study are available on request from the corresponding author.

**Conflicts of Interest:** The authors declare no conflict of interest.

## Appendix A

**Figure A1.** Samples A before the test.

**Figure A2.** Samples B before the test.

**Figure A3.** Samples C before the test.

## Appendix B

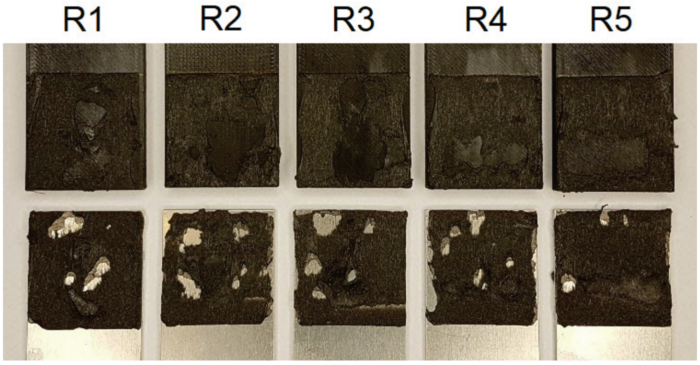

**Figure A4.** Reference samples after the tensile test.

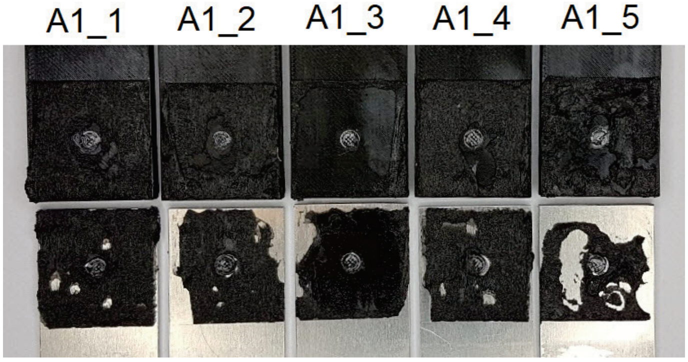

**Figure A5.** Samples A1 after the tensile test.

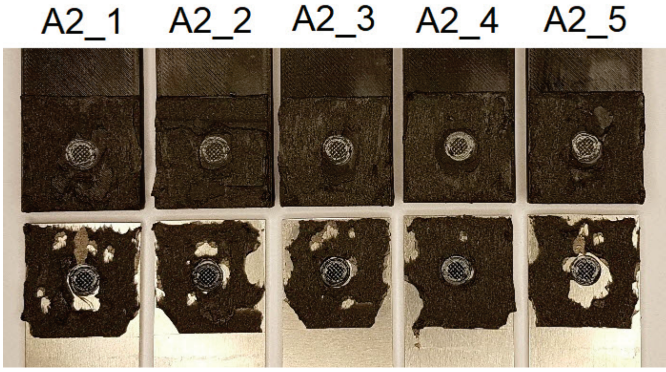

**Figure A6.** Samples A2 after the tensile test.

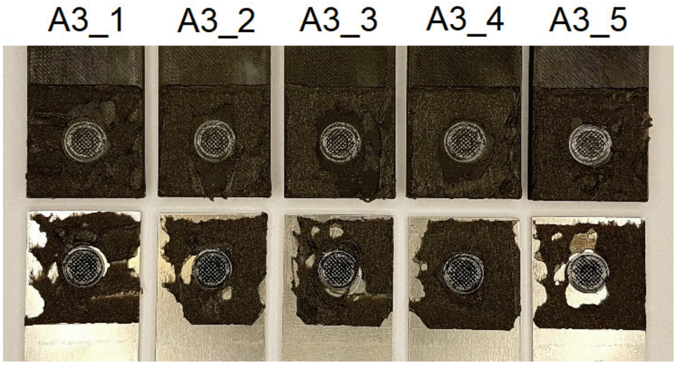

**Figure A7.** Samples A3 after the tensile test.

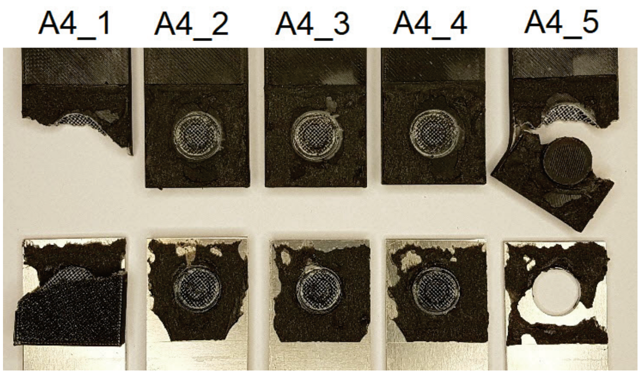

**Figure A8.** Samples A4 after the tensile test.

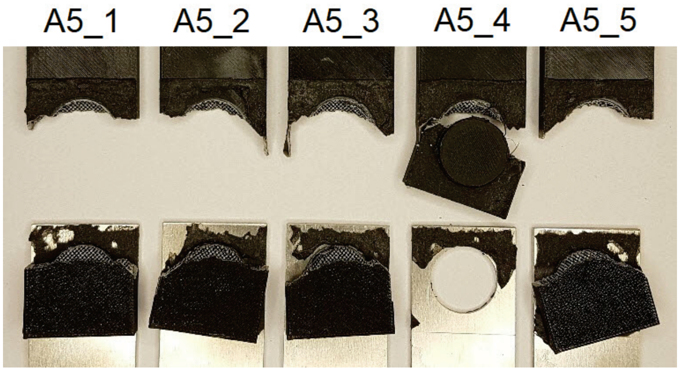

**Figure A9.** Samples A5 after the tensile test.

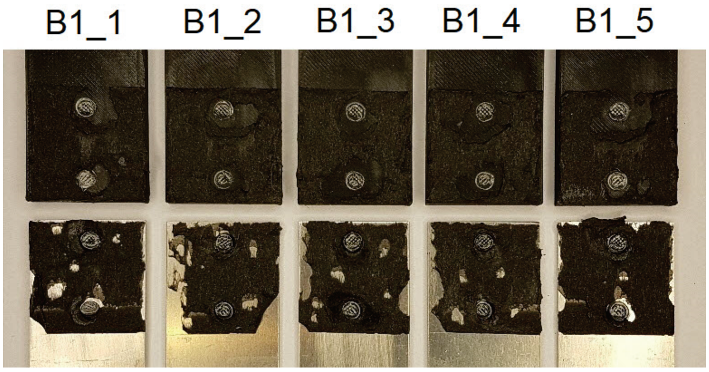

**Figure A10.** Samples B1 after the tensile test.

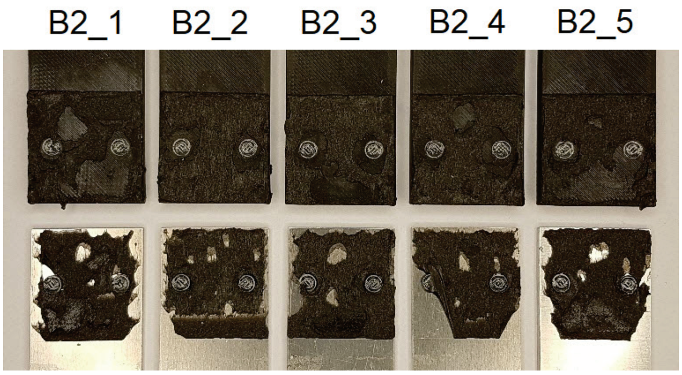

**Figure A11.** Samples B2 after the tensile test.

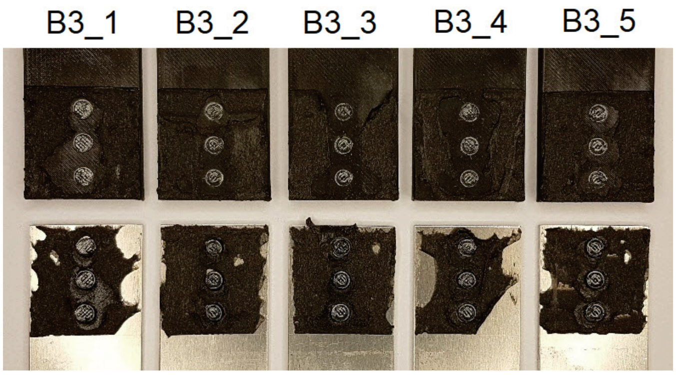

**Figure A12.** Samples B3 after the tensile test.

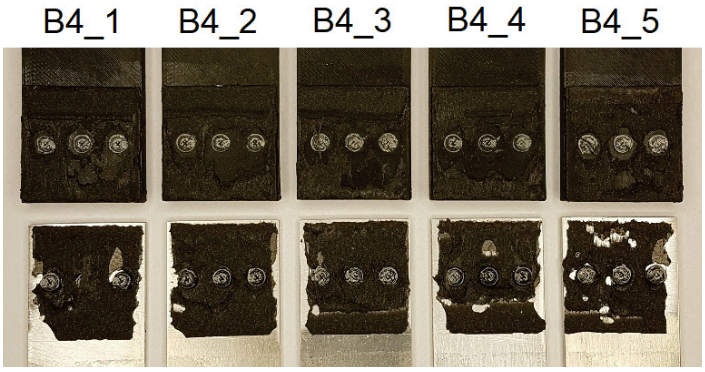

**Figure A13.** Samples B4 after the tensile test.

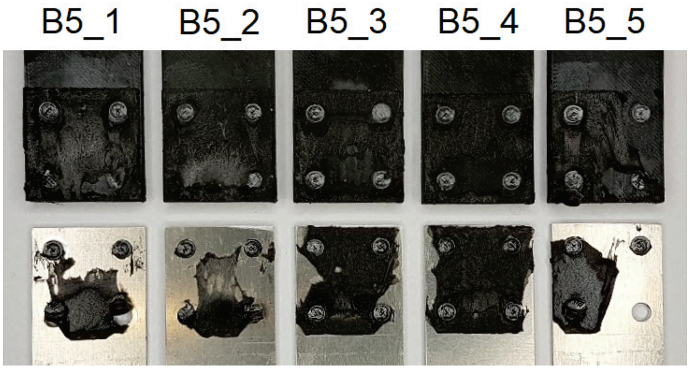

**Figure A14.** Samples B5 after the tensile test.

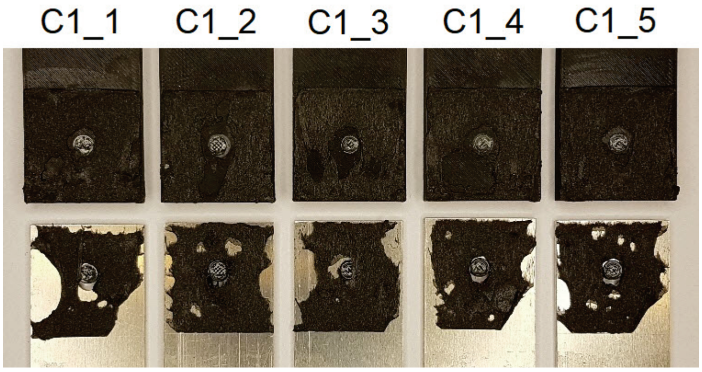

**Figure A15.** Samples C1 after the tensile test.

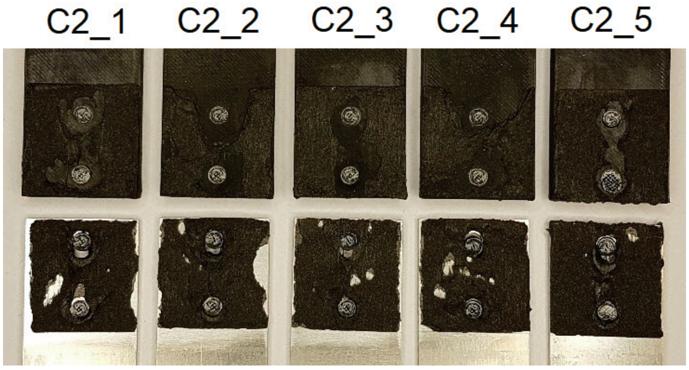

**Figure A16.** Samples C2 after the tensile test.

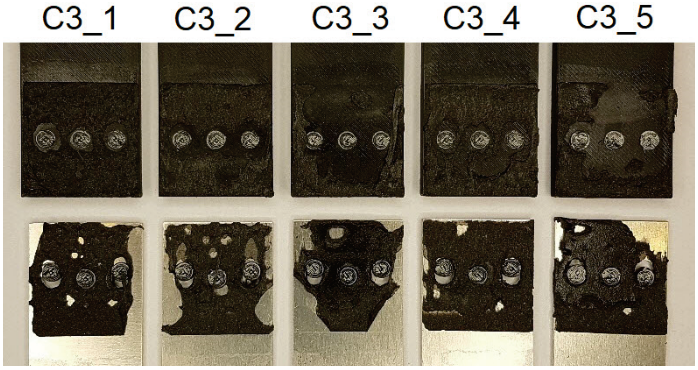

**Figure A17.** Samples C3 after the tensile test.

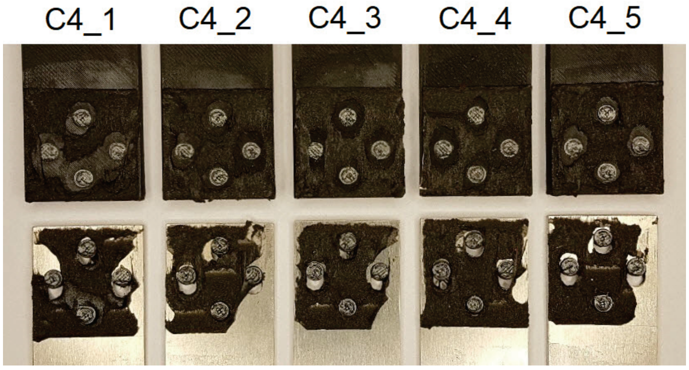

**Figure A18.** Samples C4 after the tensile test.

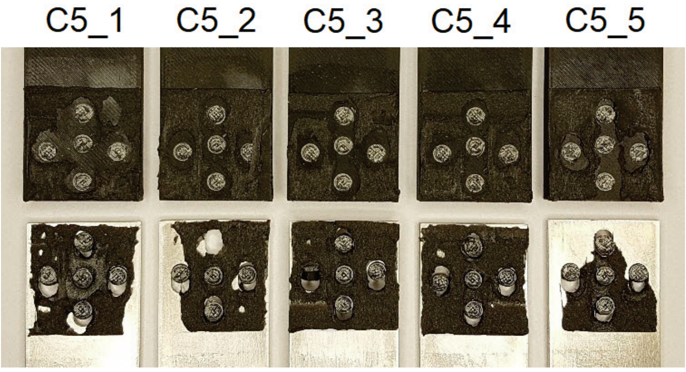

**Figure A19.** Samples C5 after the tensile test.

## References

1. Garcia, R.; Prabhakar, P. Bond interface design for single lap joints using polymeric additive manufacturing. *Compos. Struct.* **2017**, *176*, 547–555. [CrossRef]
2. Dahmen, V.; Redmann, A.J.; Austermann, J.; Quintanilla, A.L.; Mecham, S.J.; Osswald, T.A. Fabrication of hybrid composite T-joints by co-curing with 3D printed dual cure epoxy. *Compos. Part B Eng.* **2020**, *183*, 107728. [CrossRef]
3. Albahri, R.; Yoon, H.-I.; Lee, J.D.; Yoon, S.-N.; Lee, S.J. Shear bond strength of provisional repair materials bonded to 3D printed resin. *J. Dent. Sci.* **2021**, *16*, 261–267. [CrossRef]
4. Sadowski, T.; Golewski, P. Effect of Tolerance in the Fitting of Rivets in the Holes of Double Lap Joints Subjected to Uniaxial Tension. *Key Eng. Mater.* **2014**, *607*, 49–54. [CrossRef]
5. Sadowski, T.; Kneć, M.; Golewski, P. Fatigue Response of the Hybrid Joints Obtained by Hot Spot Welding and Bonding Techniques. *Key Eng. Mater.* **2014**, *601*, 25–28. [CrossRef]
6. Więckowski, W.; Lacki, P.; Adamus, J. Examinations of steel overlap joints obtained using the friction stir welding technology. *Arch. Metall. Mater.* **2019**, *64*, 393–399. [CrossRef]
7. Wang, W.; Wang, S.; Zhang, X.; Xu, Y.; Tian, Y.; Huang, H. Enhanced aluminum alloy-polymer friction stir welding joints by introducing micro-textures. *Mater. Lett.* **2021**, *295*, 129872. [CrossRef]
8. Wang, T.; Upadhyay, P.; Rabby, R.-E.; Li, X.; Li, L.; Soulami, A.; Kappagantula, K.S.; Whalen, S. Joining of thermoset carbon fiber reinforced polymer and AZ31 magnesium alloy sheet via friction stir interlocking. *Int. J. Adv. Manuf. Technol.* **2020**, *109*, 689–698. [CrossRef]
9. Balawender, T. The Ability to Clinching as a Function of Material Hardening Behavior. *Acta Met. Slovaca* **2018**, *24*, 58–64. [CrossRef]
10. Abibe, A.B.; Amancio-Filho, S.T.; dos Santos, J.; Hage, E. Mechanical and failure behaviour of hybrid polymer–metal staked joints. *Mater. Des.* **2013**, *46*, 338–347. [CrossRef]
11. Baptista, R.; Pragana, J.; Bragança, I.; Silva, C.; Alves, L.; Martins, P. Joining aluminium profiles to composite sheets by additive manufacturing and forming. *J. Mater. Process. Technol.* **2020**, *279*, 116587. [CrossRef]
12. Bergmann, J.P.; Stambke, M. Potential of Laser-manufactured Polymer-metal hybrid Joints. *Phys. Procedia* **2012**, *39*, 84–91. [CrossRef]
13. Schricker, K.; Stambke, M.; Bergmann, J.P.; Bräutigam, K.; Henckell, P. Macroscopic Surface Structures for Polymer-metal Hybrid Joints Manufactured by Laser Based Thermal Joining. *Phys. Procedia* **2014**, *56*, 782–790. [CrossRef]
14. Konchakova, N.; Balle, F.; Barth, F.; Mueller, R.; Eifler, D.; Steinmann, P. Finite element analysis of an inelastic interface in ultrasonic welded metal/fibre-reinforced polymer joints. *Comput. Mater. Sci.* **2010**, *50*, 184–190. [CrossRef]
15. Lambiase, F.; Di Ilio, A. Mechanical clinching of metal–polymer joints. *J. Mater. Process. Technol.* **2015**, *215*, 12–19. [CrossRef]
16. Golewski, P.; Sadowski, T.; Pietras, D.; Dudzik, S. The influence of aging in salt chamber on strength of aluminum—CFRP single lap joints. *Mater. Today Proc.* **2021**, *45*, 4264–4267. [CrossRef]
17. Negru, R.; Marsavina, L.; Hluscu, M. Experimental and numerical investigations on adhesively bonded joints. *IOP Conf. Series Mater. Sci. Eng.* **2016**, *123*, 012012. [CrossRef]
18. Golewski, P.; Sadowski, T. The Influence of Single Lap Geometry in Adhesive and Hybrid Joints on Their Load Carrying Capacity. *Materials* **2019**, *12*, 1884. [CrossRef]
19. Golewski, P.; Sadowski:, T. The influence of dual adhesive in single lap joints on strength and energy absorption. *Mater. Today Proc.* **2021**, *45*, 4280–4285. [CrossRef]
20. Gajewski, J.; Golewski, P.; Sadowski, T. The Use of Neural Networks in the Analysis of Dual Adhesive Single Lap Joints Subjected to Uniaxial Tensile Test. *Materials* **2021**, *14*, 419. [CrossRef] [PubMed]
21. Xu, Y.; Huettig, F.; Schille, C.; Schweizer, E.; Geis-Gerstorfer, J.; Spintzyk, S. Peel bond strength between 3D printing tray materials and elastomeric impression/adhesive systems: A laboratory study. *Dent. Mater.* **2020**, *36*, e241–e254. [CrossRef] [PubMed]
22. Khosravani, M.R.; Soltani, P.; Reinicke, T. Fracture and structural performance of adhesively bonded 3D-printed PETG single lap joints under different printing parameters. *Theor. Appl. Fract. Mech.* **2021**, *116*, 103087. [CrossRef]
23. Nash, R.J.; Li, Y. Experimental and numerical analysis of 3D printed suture joints under shearing load. *Eng. Fract. Mech.* **2021**, *253*, 107912. [CrossRef]
24. Khosravani, M.R.; Soltani, P.; Weinberg, K.; Reinicke, T. Structural integrity of adhesively bonded 3D-printed joints. *Polym. Test.* **2021**, *100*, 107262. [CrossRef]
25. Yap, Y.L.; Toh, W.; Koneru, R.; Lin, R.; Chan, K.I.; Guang, H.; Chan, W.Y.B.; Teong, S.S.; Zheng, G.; Ng, T.Y. Evaluation of structural epoxy and cyanoacrylate adhesives on jointed 3D printed polymeric materials. *Int. J. Adhes. Adhes.* **2020**, *100*, 102602. [CrossRef]
26. Li, W.; Sang, L.; Jian, X.; Wang, J. Influence of sanding and plasma treatment on shear bond strength of 3D-printed PEI, PEEK and PEEK/CF. *Int. J. Adhes. Adhes.* **2020**, *100*, 102614. [CrossRef]
27. Jucienė, M.; Dobilaitė, V. Impact of climatic effects and various surfaces on the tack of adhesive tapes for building & construction. *J. Build. Eng.* **2021**, *42*, 102825. [CrossRef]
28. Biel, A.; Alfredsson, K.S.; Carlberger, T. Adhesive Tapes; Cohesive Laws for a Soft Layer. *Procedia Mater. Sci.* **2014**, *3*, 1389–1393. [CrossRef]
29. Fufa, S.M.; Labonnote, N.; Frank, S.; Rüther, P.; Jelle, B.P. Durability evaluation of adhesive tapes for building applications. *Constr. Build. Mater.* **2018**, *161*, 528–538. [CrossRef]

30. Liao, Z.; Hossain, M.; Yao, X.; Mehnert, M.; Steinmann, P. On thermo-viscoelastic experimental characterization and numerical modelling of VHB polymer. *Int. J. Non-Linear Mech.* **2020**, *118*, 103263. [CrossRef]
31. Zhu, Z.; Xia, Y.; Jiang, C.; Yang, Z.; Jiang, H. Investigation of zero-degree peeling behavior of visco-hyperelastic highly stretchable adhesive tape on rigid substrate. *Eng. Fract. Mech.* **2021**, *241*, 107368. [CrossRef]
32. Sadowski, T.; Nowicki, M.; Golewski, P. The influence of the use of fasteners with different stiffness in hybrid joints subjected to complex mechanical loads. *Arch. Metall. Mater.* **2019**, *64*, 1263–1268. [CrossRef]
33. Sadowski, T.; Golewski, P. Modelling and Experimental Testing of Hybrid Joints Made of: Aluminium Adherends, Adhesive Layers and Rivets for Aerospace Applications. *Arch. Met. Mater.* **2017**, *62*, 1577–1583. [CrossRef]
34. Elzaroug, M.; Kadioglu, F.; Demiral, M.; Saad, D. Experimental and numerical investigation into strength of bolted, bonded and hybrid single lap joints: Effects of adherend material type and thickness. *Int. J. Adhes. Adhes.* **2018**, *87*, 130–141. [CrossRef]
35. Li, X.; Cheng, X.; Cheng, Y.; Wang, Z.; Huang, W. Tensile properties of a composite–metal single-lap hybrid bonded/bolted joint. *Chin. J. Aeronaut.* **2021**, *34*, 629–640. [CrossRef]
36. Romanov, V.S.; Heidari-Rarani, M.; Lessard, L. A parametric study on static behavior and load sharing of multi-bolt hybrid bonded/bolted composite joints. *Compos. Part B Eng.* **2021**, *217*, 108897. [CrossRef]
37. Huang, Z.; Sugiyama, S.; Yanagimoto, J. Hybrid joining process for carbon fiber reinforced thermosetting plastic and metallic thin sheets by chemical bonding and plastic deformation. *J. Mater. Process. Technol.* **2013**, *213*, 1864–1874. [CrossRef]
38. Marques, G.; Campilho, R.; Silva, F.; Moreira, R.D.F. Adhesive selection for hybrid spot-welded/bonded single-lap joints: Experimentation and numerical analysis. *Compos. Part B Eng.* **2016**, *84*, 248–257. [CrossRef]
39. Marsavina, L.; Nurse, A.D.; Braescu, L.; Craciun, E.M. Stress singularity of symmetric free-edge joints with elasto-plastic behaviour. *Comput. Mater. Sci.* **2012**, *52*, 282–286. [CrossRef]
40. Sadowski, T.; Golewski, P. Numerical Study of the Prestressed Connectors and Their Distribution on the Strength of a Single Lap, a Double Lap and Hybrid Joints Subjected to Uniaxial Tensile Test. *Arch. Met. Mater.* **2013**, *58*, 579–585. [CrossRef]

materials

MDPI

*Article*

# Analytical Solution for Forced Vibration Characteristics of Rotating Functionally Graded Blades under Rub-Impact and Base Excitation

**Tianyu Zhao [1], Yuxuan Wang [1], Xinze Cui [2] and Xin Wang [2,*]**

[1] Key Laboratory of Structural Dynamics of Liaoning Province, School of Science, Northeastern University, Shenyang 110819, China; zhaotianyu@mail.neu.edu.cn (T.Z.); sqwyx95@163.com (Y.W.)
[2] Department of Kinesiology, Shenyang Sport University, Shenyang 110102, China; cuixinze0323@163.com
* Correspondence: wangxin@syty.edu.cn

**Abstract:** This paper presents an analytical investigation on the forced vibration characteristics of a rotating functionally graded material (FGM) blade subjected to rub-impact and base excitation. Based on the Kirchhoff plate theory, the rotating blade is modelled theoretically. The material properties of the FGM blade are considered to vary continuously and smoothly along the thickness direction according to a volume fraction power-law distribution. By employing Hamilton's principle, the equations of motion are derived. Then, the Galerkin method and the small parameter perturbation method are utilized to obtain the analytical solution for the composite blade under a combined action of radial force, tangential force and displacement load. Finally, special attention is given to the effects of power-law index, rub-impact location, friction coefficient, base excitation amplitude and blade aspect ratio on the vibration characteristics of the FGM structure. The obtained results can play a role in the design of rotating FGM blades to achieve significantly improved structural performance.

**Keywords:** functionally graded material; rotating blades; rub-impact; base excitation; analytical solution

## 1. Introduction

Rotating blades [1–3] with a low aspect ratio can compresses gas effectively; hence, they are widely used in real-world engineering applications, such as in a gas turbine or an aeroengine. In order to improve the performance of aeroengine, the radial clearance between the rotor blade and the casing needs to be as small as possible. However, the probability of rub-impact between the casing and blade tip increases with a decrease in radial clearance. A rub-impact fault may cause the complex vibration of blades and very high contact stresses that lead to blade fracture and degradation of system performance. Many major accidents have happened over an extended period. For instance, in 1973, an engine fan disintegrated in flight owing to rub-impact, as reported by the National Transportation Safety Board (NTSB). From 1994 to 1996, four F16 aircraft accidents happened due to rub-impact fault. A homemade carrier aircraft that was equipped with a WJ5A aircraft engine was grounded on account of the touch between the stator and rotor. This problem has received extensive attention from the scholars around the world.

Ma et al. [4] established improved rubbing models between a rotating blade and casing based on different methods. Liu et al. [5] focused on the dynamic responses of the whole aeroengine with a blade-casing rubbing. Hou et al. [6] studied the mechanism of a complex bifurcation behavior caused by flight maneuvers in an aircraft rub-impact rotor system with Duffing-type nonlinearity. Xiao et al. [7] developed a nonlinear dynamic model of the single-stage reciprocating compressor system with a rub-impact fault caused by subsidence, considering the piston rod's flexibility. Tchomeni et al. [8] developed a two-dimensional model of the Navier–Stokes equations for incompressible flow for the viscous fluid motion around the spinning rotor under high fluctuations induced by unbalance, rotor–stator rub and a crack. Wang et al. [9] considered rub-impact forces, eccentricity of the rotor, and nonlinear stiffness of the armature shaft, and built a dynamic differential equation to investigate the bifurcation and chaos behavior of the locomotive traction system. Ebrahim et al. [10] investigated nonlinear dynamics due to rub-impact within tilting pad journal bearings supporting a flexible rotor. In theory, thin blades are generally established as elastic plate models. It is noted that few studies focus on the analytical analysis of forced vibrations of a rotating plate subject to the combined loads of rub-impact and base excitation.

With the rapid development of modern material science [11–13], a trend to substitute advanced lightweight materials in aerorotor systems has emerged. In the mid-1980s, a new concept of FGMs was first introduced by a group of Japanese scientists [14] in the context of high-performance demand of composite materials for aerospace applications. FGM is a material with continuously varying compositions from one surface to the other. Therefore, its material properties and microstructure are not uniform. In general, FGM is constructed as follows: one surface is ceramic which is designed to withstand severe external loads, such as high temperature, wear and corrosion; the other surface is attached to another material that is designed to ensure excellent toughness and thermal conductivity. The composition changes gradually along the thickness direction according to a designed law. The most significant advantages of FGM are not only improving the bonding strength, material hardness, abrasion resistance and corrosion resistance between the two materials, but also reducing the thermal stress and residual stress. Therefore, FGM is an excellent material for today’s engineering applications. It has been researched widely as FGM has excellent performances compared with traditional materials.

Shen et al. [15] presented free and forced vibration analyses for initially stressed FGM plates in a thermal environment. Kumar et al. [16] proposed two new higher-order transverse shear deformation plate theories with five variables. Singh et al. [17] investigated the buckling responses of FGM plates subjected to uniform, linear and nonlinear in-plane loads. Do et al. [18] analyzed the buckling responses of FGM plates under diverse types of thermal loadings. Wang et al. [19] analyzed the vibration of FGM beams through critical examination of midplane and neutral plane formulations. To perform further analyses, Chen et al. [20] proposed a novel FGM porous plate in which the continuous gradient in material properties based on a graded porosity offers a smooth stress distribution along the plate thickness. Yang and Zhao et al. [21–29] made a systematic and extensive analysis of an FGM graphene-reinforced composite structure. Li et al. [30] focused on the elastic structural stability analysis of the pressurized thin-walled FGM arches in a temperature variation field. Bourada and Bousahla et al. [31–33] studied the buckling and vibration of several FGM structures. Sobhy et al. [34,35] investigated the bending and wave propagation of FGM graphene-reinforced structures. To sum up, the vibration behaviors of many FGM structures have been studied. However, to the best of our knowledge, almost no study has been performed on the forced vibration of FGM plates subjected to rub-impact and base excitation.

The increasing flight speed of spacecraft has necessitated higher requirements for high-performance blades. Traditional homogeneous metal alloys no longer meet the requirement. FGM is more widely applicable in this industry due to its excellent mechanical properties, such as mitigating thermal stress, residual stress and stress concentration. Thus, the blade structure is considered as a rotating FGM plate in this paper. In addition, its forced vibration behaviors when subjected to rub-impact and base excitation need to be investigated in detail. The differential equations of motion are derived based on Hamilton’s principle. Moreover, the analytic solutions are obtained by employing the Galerkin method and the small parameter perturbation method. Finally, the effects of power-law index, rub-impact location, friction coefficient, base excitation amplitude and plate aspect ratio on the forced vibration responses are highlighted. Consequently, this paper can provide theoretical guidance and technical support for the further development and application of rotating FGM structure design.

## 2. Theoretical Formulations

### *2.1. Modeling*

A rotating FGM plate model subject to rub-impact force and base excitation is established as shown in Figure 1. For the convenience of the subsequent analysis, two coordinate systems are proposed. $O_1$-$X_1Y_1Z_1$ is the fixed coordinate system, where $X_1$ is the radial direction, $Y_1$ is the axial direction and $Z_1$ is the radial direction. The plate rotates at the angular velocity $\Omega$ along the $Y_1$-axis. $O$-$XYZ$ is the rotating coordinate system, in which the origin $O$ is fixed at the corner of the plate. The angle between the $X_1$-axis and the $X$-axis is $\Omega\, t$. The sizes of the plate along three directions are $a$, $b$ and $h$, respectively.

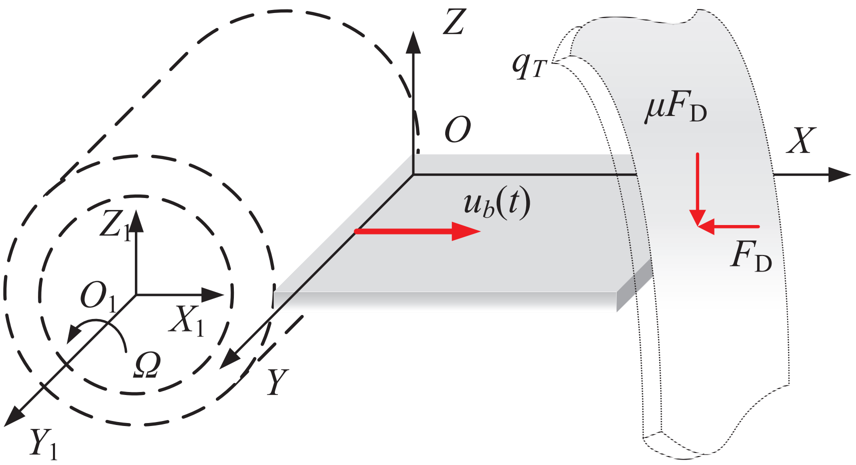

**Figure 1.** The rotating FGM plate.

The presented plate is considered as a functionally gradient material structure whose material properties have the following forms:

$$\begin{cases} E(z) = (E_1 - E_2)\left(\frac{2z+h}{2h}\right)^n + E_2 \\ v(z) = (v_1 - v_2)\left(\frac{2z+h}{2h}\right)^n + v_2 \\ \rho(z) = (\rho_1 - \rho_2)\left(\frac{2z+h}{2h}\right)^n + \rho_2 \end{cases} \tag{1}$$

where $n$ is the power-law index that dictates the material variation profile through the plate thickness. The above formulas mean that for $z = -h/2$, $E(z) = E_2$, $v\ (z) = v_2$, $\rho(z) = \rho_2$, while for $z = h/2$, $E(z) = E_1$, $v(z) = v_1$, $\rho(z) = \rho_1$. The material properties vary continuously and smoothly from $z = -h/2$ to $z = h/2$ along the thickness direction of the FGM structure.

A sine harmonic excitation along the $X$-axis direction is taken into account as the base excitation [36], expressed as:

$$\begin{cases} u_b(t) = u_0 \sin \omega_0 t \\ \dot{u}_b(t) = u_0 \omega_0 \cos \omega_0 t \\ \ddot{u}_b(t) = -u_0 \omega_0^2 \sin \omega_0 t \end{cases} \tag{2}$$

where $u_0$ and $\omega_0$ are the amplitude and frequency of base excitation, respectively.

The rub-impact fault consists of an impact force FD, located at the point of contact, and the resulting friction $\mu F_D$, in which $\mu$ is the friction coefficient. The impact force, shown in Figure 2, is assumed as a segmental periodic sinusoidal pulse excitation in the form of [37]:

$$F_D(t) = \begin{cases} 0 & (n-1)T_c + t_p < t < nT_c \\ F_{\max} \sin\left[\frac{\pi}{t_p}(t - (n-1)T_c)\right] & (n-1)T_c \le t \le (n-1)T_c + t_p \end{cases} \tag{3}$$

where $n$ = 1, 2, 3, . . . ; $t_p$ is the impact time of one period; $T_c$ is the periodic time; $F_{\max}$ is the amplitude of impact force.

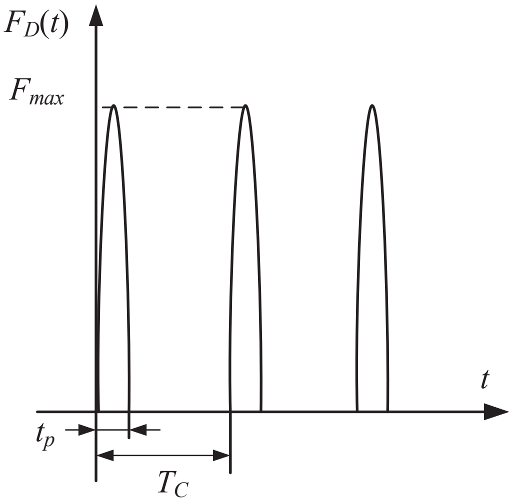

**Figure 2.** Sinusoidal pulse rub-impact force.

According to the principle of Fourier expansion, Equation (3) can be rewritten as:

$$F_D(t) = a_0 + \sum_{k=1}^{\infty}\left(a_k \cos\frac{2k\pi}{T_c}t + b_k \sin\frac{2k\pi}{T_c}t\right) \tag{4}$$

where

$$\begin{cases} a_0 = \frac{1}{T_c}\int_0^{t_p}\left[F_{\max}\sin\left(\frac{\pi}{t_p}t\right)\right]\mathrm{d}t \\ a_k = \frac{2}{T_c}\int_0^{t_p}\left[F_{\max}\sin\left(\frac{\pi}{t_p}t\right)\cos\left(\frac{2k\pi}{T}t\right)\right]\mathrm{d}t \\ b_k = \frac{2}{T_c}\int_0^{t_p}\left[F_{\max}\sin\left(\frac{\pi}{t_p}t\right)\sin\left(\frac{2k\pi}{T}t\right)\right]\mathrm{d}t \end{cases} \tag{5}$$

### *2.2. Energy Functionals*

The position vector of an arbitrary point $M$ is:

$$\mathbf{r}_{\mathrm{OM}} = x\mathbf{i} + y\mathbf{j} + w\mathbf{k} \tag{6}$$

where **i**, **j** and **k** are the unit vectors of the rotating coordinate system in the $X$-axis, $Y$-axis and $Z$-axis directions, respectively; $w$ is the transverse deformation of the plate.

The position relation between the rotating and fixed coordinate system is:

$$\mathbf{r}_{\mathrm{O_1O}} = u_b\mathbf{i} \tag{7}$$

From this, the position vector of point $M$ in the fixed coordinate system can be determined by:

$$\mathbf{r}_{\mathrm{O_1M}} = \mathbf{r}_{\mathrm{O_1O}} + \mathbf{r}_{\mathrm{OM}} = (x + u_b)\mathbf{i} + y\mathbf{j} + w\mathbf{k} \tag{8}$$

According to the vector and velocity relationship between the rotating and fixed coordinate system:

$$\begin{cases} \mathbf{i} = \mathbf{i}_1\cos\Omega t - \mathbf{k}_1\sin\Omega t \\ \mathbf{j} = \mathbf{j}_1 \\ \mathbf{k} = \mathbf{i}_1\sin\Omega t + \mathbf{k}_1\cos\Omega t \end{cases} \begin{cases} \mathbf{i}' = -\Omega\mathbf{i}_1\sin\Omega t - \Omega\mathbf{k}_1\cos\Omega t = -\Omega\mathbf{k} \\ \mathbf{j}' = 0 \\ \mathbf{k}' = \Omega\mathbf{i}_1\cos\Omega t - \Omega\mathbf{k}_1\sin\Omega t = \Omega\mathbf{i} \end{cases} \tag{9}$$

in which $\mathbf{i}_1$, $\mathbf{j}_1$ and $\mathbf{k}_1$ are the unit vectors of fixed coordinate system, then:

$$\begin{aligned} \dot{\mathbf{r}}_{\mathrm{O_1M}} &= (x+u_b)\mathbf{i}' + \dot{u}_b\mathbf{i} + w\mathbf{k}' + \dot{w}\mathbf{k} \\ &= \left(w\Omega + \dot{u}_b\right)\mathbf{i} + \left(\dot{w} - x\Omega - u_b\Omega\right)\mathbf{k} \end{aligned} \tag{10}$$

The kinetic energy of the plate can be derived as:

$$\begin{aligned} T_M &= \tfrac{1}{2}\int_{-h/2}^{h/2}\int_0^b\int_0^a \rho\dot{\mathbf{r}}_{\mathrm{O_1M}}{}^2\mathrm{d}x\mathrm{d}y\mathrm{d}z \\ &= \tfrac{1}{2}\int_{-h/2}^{h/2}\int_0^b\int_0^a \rho\begin{bmatrix} \dot{u}_b{}^2 + w^2\Omega^2 + 2\dot{u}_b w\Omega + \left(\frac{\partial w}{\partial t}\right)^2 + \\ (u_b+x)^2\Omega^2 - 2\frac{\partial w}{\partial t}(u_b+x)\Omega \end{bmatrix}\mathrm{d}x\mathrm{d}y\mathrm{d}z \end{aligned} \tag{11}$$

Based on the Kirchhoff plate theory [38], the constitutive relations are:

$$\begin{cases} \varepsilon_x = -\frac{\partial^2 w}{\partial x^2}z \\ \varepsilon_y = -\frac{\partial^2 w}{\partial y^2}z \\ \gamma_{xy} = -2\frac{\partial^2 w}{\partial x\partial y}z \end{cases},\quad \begin{cases} \sigma_x = -\frac{Ez}{1-v^2}\left(\frac{\partial^2 w}{\partial x^2} + v\frac{\partial^2 w}{\partial y^2}\right) \\ \sigma_y = -\frac{Ez}{1-v^2}\left(\frac{\partial^2 w}{\partial y^2} + v\frac{\partial^2 w}{\partial x^2}\right) \\ \tau_{xy} = -\frac{Ez}{1+v}\frac{\partial^2 w}{\partial x\partial y} \end{cases} \tag{12}$$

The deformation potential energy of the plate is given by:

$$\begin{aligned} U_1 &= \tfrac{1}{2}\int_{-h/2}^{h/2}\int_0^b\int_0^a \left(\sigma_x\varepsilon_x + \sigma_y\varepsilon_y + \tau_{xy}\gamma_{xy}\right)\mathrm{d}x\mathrm{d}y\mathrm{d}z \\ &= \tfrac{1}{2}\int_{-h/2}^{h/2}\int_0^b\int_0^a Dz^2\begin{bmatrix} \left(\frac{\partial^2 w}{\partial x^2}\right)^2 + \left(\frac{\partial^2 w}{\partial y^2}\right)^2 + \\ 2v\left(\frac{\partial^2 w}{\partial x^2}\right)\left(\frac{\partial^2 w}{\partial y^2}\right) + 2(1-v)\left(\frac{\partial^2 w}{\partial x\partial y}\right)^2 \end{bmatrix}\mathrm{d}x\mathrm{d}y\mathrm{d}z \end{aligned} \tag{13}$$

where $D = E/(1-v^2)$.

When the instantaneous coordinates of an arbitrary point are taken as $(x, y)$, the centrifugal force per unit volume of the plate is:

$$F_1 = \rho\Omega^2(u_b + x) \tag{14}$$

The inertia force per unit volume of the plate is:

$$F_2 = \rho\ddot{u}_b \tag{15}$$

According to the d'Alembert principle, the total force caused by rotation is:

$$F_3 = \rho\Omega^2(u_b + x) - \rho\ddot{u}_b \tag{16}$$

The corresponding displacement can be calculated by:

$$\mathrm{d}s - \mathrm{d}x = \sqrt{(\mathrm{d}x)^2 + \left(\frac{\partial w}{\partial x}\mathrm{d}x\right)^2} - \mathrm{d}x = \frac{\left(\frac{\partial w}{\partial x}\mathrm{d}x\right)^2}{\sqrt{(\mathrm{d}x)^2 + \left(\frac{\partial w}{\partial x}\mathrm{d}x\right)^2} + \mathrm{d}x} \approx \frac{1}{2}\left(\frac{\partial w}{\partial x}\right)^2\mathrm{d}x \tag{17}$$

The work that is done by $F_3$ is:

$$\overline{U}_2 = \int_x^a F_3(\mathrm{d}s - \mathrm{d}x) = \frac{1}{2}\left[\rho\Omega^2 u_b(a-x) + \frac{1}{2}\rho\Omega^2\left(a^2 - x^2\right) - \rho\ddot{u}_b(a-x)\right]\left(\frac{\partial w}{\partial x}\right)^2 \tag{18}$$

The centrifugal potential energy of the plate is stated as:

$$\begin{aligned} U_2 &= \int_{-h/2}^{h/2}\int_0^b\int_0^a \overline{U}_2\mathrm{d}x\mathrm{d}y\mathrm{d}z \\ &= \tfrac{1}{2}\int_{-h/2}^{h/2}\int_0^b\int_0^a\left\{\begin{bmatrix} \rho\Omega^2 u_b(a-x) + \frac{1}{2}\rho\Omega^2(a^2 - x^2) \\ -\rho\ddot{u}_b(a-x) \end{bmatrix}\left(\frac{\partial w}{\partial x}\right)^2\right\}\mathrm{d}x\mathrm{d}y\mathrm{d}z \end{aligned} \tag{19}$$

As a result, the total potential energy of the plate is:

$$\begin{aligned} U_M &= \tfrac{1}{2}\int_{-h/2}^{h/2}\int_0^b\int_0^a D\left\{\begin{array}{l} \left(\frac{\partial^2 w}{\partial x^2}+\frac{\partial^2 w}{\partial y^2}\right)^2 - \\ 2(1-v)\left[\frac{\partial^2 w}{\partial x^2}\frac{\partial^2 w}{\partial y^2}-\left(\frac{\partial^2 w}{\partial x\partial y}\right)^2\right] \end{array}\right\} z^2 \mathrm{d}x\mathrm{d}y\mathrm{d}z \\ &+\tfrac{1}{2}\int_{-h/2}^{h/2}\int_0^b\int_0^a \left\{\left[\begin{array}{l} \frac{1}{2}\rho\Omega^2\left(a^2-x^2\right)+ \\ \rho\left(\Omega^2 u_b-\ddot{u}_b\right)(a-x) \end{array}\right]\left(\frac{\partial w}{\partial x}\right)^2\right\}\mathrm{d}x\mathrm{d}y\mathrm{d}z \end{aligned} \tag{20}$$

The virtual work done by the rub-impact force is:

$$\delta W_D = q(x,y,t)\delta w \tag{21}$$

where

$$q(x,y,t) = \mu F_D(t)\delta(x-x_D)\delta(y-y_D) \tag{22}$$

in which $x_D$ and $y_D$ are the rotating coordinates of an arbitrary rub-impact point $D$.

### 2.3. Governing Equations

Applying Hamilton's principle:

$$\delta\int_{t_0}^{t_1}(T_M-U_M)\mathrm{d}t+\int_{t_0}^{t_1}\int_0^a\int_0^b \delta W_D \mathrm{d}x\mathrm{d}y\mathrm{d}t = 0 \tag{23}$$

and substituting Equations (11), (20) and (21) into Equation (23) lead to the governing equation of motion, expressed as:

$$\begin{aligned} &\int_{-h/2}^{h/2}\left[\rho\left(w\Omega^2+\ddot{w}\right)\right]dz-\int_{-h/2}^{h/2}\left\{\rho(a-x)\left[\Omega^2\left(\frac{a+x}{2}+u_b\right)-\ddot{u}_b\right]\frac{\partial^2 w}{\partial x^2}\right\}\mathrm{d}z \\ &-\int_{-h/2}^{h/2}\left\{D\left[\frac{\partial^4 w}{\partial x^4}+\frac{\partial^4 w}{\partial y^4}+v\left(\frac{\partial^4 w}{\partial x^2\partial y^2}+\frac{\partial^4 w}{\partial y^2\partial x^2}\right)+2(1-v)\frac{\partial^4 w}{\partial x\partial y\partial x\partial y}\right]z^2\right\}\mathrm{d}z \\ &= -q(x,y,t) \end{aligned} \tag{24}$$

When the rub-impact and base excitation are ignored, Equation (30) can be given by

$$\begin{aligned} &\int_{-h/2}^{h/2}\left[\rho\left(w\Omega^2+\ddot{w}\right)\right]\mathrm{d}z-\tfrac{1}{2}\int_{-h/2}^{h/2}\left[\rho\Omega^2\left(a^2-x^2\right)\frac{\partial^2 w}{\partial x^2}\right]\mathrm{d}z \\ &-\int_{-h/2}^{h/2}\left\{D\left[\frac{\partial^4 w}{\partial x^4}+\frac{\partial^4 w}{\partial y^4}+v\left(\frac{\partial^4 w}{\partial x^2\partial y^2}+\frac{\partial^4 w}{\partial y^2\partial x^2}\right)+2(1-v)\frac{\partial^2 w}{\partial x\partial y}\frac{\partial^2 w}{\partial x\partial y}\right]z^2\right\}\mathrm{d}z = 0 \end{aligned} \tag{25}$$

The deformation is assumed as:

$$w(x,y,t) = W(x,y)\sin(\omega t+\phi) \tag{26}$$

where:

$$w(x,y) = \sum_{m=1}^{M}\sum_{n=1}^{N} A_{mn}\phi_m(x)\phi_n(y) \tag{27}$$

in which [39]:

$$\phi_m(x) = \cosh(\alpha_m x)-\cos(\alpha_m x)-c_m[\sinh(\alpha_m x)-\sin(\alpha_m x)] \tag{28}$$

$$\left\{\begin{array}{l} \varphi_1(y) = 1, \varphi_2(y) = 1-\frac{2y}{b} \\ \varphi_n(y) = \cosh(\beta_n y)+\cos(\beta_n y)-d_n[\sinh(\beta_n y)+\sin(\beta_n y)] \end{array}\right. \tag{29}$$

where

$$\left\{\begin{array}{l} \cosh(\alpha_m a)\cos(\alpha_m a) = -1 \\ c_m = \frac{\cos(\alpha_m a)+\cosh(\alpha_m a)}{\sin(\alpha_m a)+\sinh(\alpha_m a)} \\ m = 1,2,\cdots,M \end{array}\right., \left\{\begin{array}{l} \cosh(\beta_n b)\cos(\beta_n b) = 1 \\ d_n = \frac{\cos(\beta_n b)-\cosh(\beta_n b)}{\sin(\beta_n b)-\sinh(\beta_n b)} \\ n = 3,4,\cdots,N \end{array}\right. \tag{30}$$

Substituting Equations (32) and (33) into Equation (31), the Galerkin method leads to

$$\int_{-h/2}^{h/2}\int_0^b\int_0^a\left\{\begin{array}{l} D(1-v)\left[-2\sum\limits_{m=1}^{M}\sum\limits_{n=1}^{N}\sum\limits_{i=1}^{M}\sum\limits_{j=1}^{N}A_{mn}\varphi_m{}'(x)\varphi_n{}'(y)\phi_i{}'(x)\varphi_j{}'(y)\right]z^2 \\ -Dvz^2\left[\begin{array}{l}\sum\limits_{m=1}^{M}\sum\limits_{n=1}^{N}\sum\limits_{i=1}^{M}\sum\limits_{j=1}^{N}A_{mn}\varphi_m{}''(x)\varphi_n(y)\phi_i(x)\varphi_j{}''(y) \\ +\sum\limits_{m=1}^{M}\sum\limits_{n=1}^{N}\sum\limits_{i=1}^{M}\sum\limits_{j=1}^{N}A_{mn}\varphi_m(x)\varphi_n{}''(y)\phi_i(x)''\varphi_j(y)\end{array}\right] \\ +\rho\left(\Omega^2-\omega^2\right)\sum\limits_{m=1}^{M}\sum\limits_{n=1}^{N}\sum\limits_{i=1}^{M}\sum\limits_{j=1}^{N}A_{mn}\varphi_m(x)\varphi_n(y)\phi_i(x)\varphi_j(y) \\ -\frac{1}{2}\rho\Omega^2\left(a^2-x^2\right)\sum\limits_{m=1}^{M}\sum\limits_{n=1}^{N}\sum\limits_{i=1}^{M}\sum\limits_{j=1}^{N}A_{mn}\varphi_m{}'(x)\varphi_n(y)\varphi_i{}'(x)\varphi_j(y) \\ -Dz^2\left[\begin{array}{l}\sum\limits_{m=1}^{M}\sum\limits_{n=1}^{N}\sum\limits_{i=1}^{M}\sum\limits_{j=1}^{N}A_{mn}\varphi_m{}''(x)\varphi_n(y)\phi_i(x)''\varphi_j(y) \\ +\sum\limits_{m=1}^{M}\sum\limits_{n=1}^{N}\sum\limits_{i=1}^{M}\sum\limits_{j=1}^{N}A_{mn}\varphi_m(x)\varphi_n{}''(y)\phi_i(x)\varphi_j{}''(y)\end{array}\right]\end{array}\right\}\mathrm{d}x\mathrm{d}y\mathrm{d}z=0 \tag{31}$$

Eliminating the coefficient $A_{mn}$, then:

$$\left[\begin{array}{l}\mathbf{E}\int_{-h/2}^{h/2}\rho\Omega^2\mathrm{d}z-(\mathbf{H}+\mathbf{G}-2\mathbf{K})\int_{-h/2}^{h/2}Dvz^2\mathrm{d}z \\ -(\mathbf{I}+\mathbf{F}+2\mathbf{K})\int_{-h/2}^{h/2}Dz^2\mathrm{d}z-\frac{\Omega^2}{2}\mathbf{L}\int_{-h/2}^{h/2}\rho\mathrm{d}z\end{array}\right]-\omega^2\mathbf{E}\int_{-h/2}^{h/2}\rho\mathrm{d}z=0 \tag{32}$$

where, **E**, **F**, **G**, **H**, **I**, **K** and **L** are in the same form of:

$$\boldsymbol{X}=\begin{bmatrix} X_{11} & \cdots & X_{1j} & \cdots & X_{1(M\times N)} \\ \vdots & \ddots & \vdots & & \vdots \\ X_{i1} & \cdots & X_{ij} & \cdots & X_{i(M\times N)} \\ \vdots & & \vdots & \ddots & \vdots \\ X_{(M\times N)1} & \cdots & X_{(M\times N)j} & \cdots & X_{(M\times N)(M\times N)}\end{bmatrix} \tag{33}$$

in which $Xij$ is the corresponding element in each matrix, determined by:

$$\begin{cases} E_{[(i-1)N+j][(m-1)N+n]}=\int_0^b\int_0^a\phi_m(x)\varphi_n(y)\phi_i(x)\varphi_j(y)\mathrm{d}x\mathrm{d}y \\ F_{[(i-1)N+j][(m-1)N+n]}=\int_0^b\int_0^a\phi_m{}''(x)\varphi_n(y)\phi_i{}''(x)\varphi_j(y)\mathrm{d}x\mathrm{d}y \\ G_{[(i-1)N+j][(m-1)N+n]}=\int_0^b\int_0^a\phi_m(x)\varphi_n{}''(y)\phi_i{}''(x)\varphi_j(y)\mathrm{d}x\mathrm{d}y \\ H_{[(i-1)N+j][(m-1)N+n]}=\int_0^b\int_0^a\phi_m{}''(x)\varphi_n(y)\phi_i(x)\varphi_j{}''(y)\mathrm{d}x\mathrm{d}y \\ I_{[(i-1)N+j][(m-1)N+n]}=\int_0^b\int_0^a\phi_m(x)\varphi_n{}''(y)\phi_i(x)\varphi_j{}''(y)\mathrm{d}x\mathrm{d}y \\ K_{[(i-1)N+j][(m-1)N+n]}=\int_0^b\int_0^a\phi_m{}'(x)\varphi_n{}'(y)\phi_i{}'(x)\varphi_j{}'(y)\mathrm{d}x\mathrm{d}y \\ L_{[(i-1)N+j][(m-1)N+n]}=\int_0^b\int_0^a\left(a^2-x^2\right)\phi_m{}'(x)\varphi_n(y)\phi_i{}'(x)\varphi_j(y)\mathrm{d}x\mathrm{d}y \end{cases} \tag{34}$$

The natural frequencies $\omega_{mn}$ and coefficients $A_{mn}$ can be obtained by solving the standard eigenvalue problem in Equation (34).

### *2.4. Analytic Solution for Forced Vibration*

The analytic solution for Equation (30) is assumed as:

$$w(x,y,t)=\sum_{m=1}^{M}\sum_{n=1}^{N}B_{mn}(t)W_{mn}(x,y) \tag{35}$$

where

$$W_{mn}(x,y)=A_{mn}\phi_m(x)\varphi_n(y) \tag{36}$$

Applying the free vibration theory and substituting Equation (36) into Equation (30) leads to:

$$\frac{\mathrm{d}^2 B_{mn}(t)}{\mathrm{d}t^2} + \omega_{mn}^2 B_{mn}(t) + \left[\ddot{u}_b(t) - \Omega^2 u_b(t)\right] \frac{C_{mn}}{M_{mn}} B_{mn}(t) = \frac{P_{mn}(t)}{M_{mn}} \tag{37}$$

in which

$$\begin{cases} P_{mn} = \int_0^b \int_0^a q(x,y,t) W_{mn}(x,y) \mathrm{d}x\mathrm{d}y \\ M_{mn} = \int_{-h/2}^{h/2} \int_0^b \int_0^a \rho W_{mn}^2(x,y) \mathrm{d}x\mathrm{d}y\mathrm{d}z \\ C_{mn} = \int_{-h/2}^{h/2} \int_0^b \int_0^a \rho (a-x) \frac{\partial^2 W_{mn}(x,y)}{\partial x^2} W_{mn}(x,y) \mathrm{d}x\mathrm{d}y\mathrm{d}z \end{cases} \tag{38}$$

The base excitation and rub-impact are considered as first-order small quantities in the form of:

$$\begin{cases} u_b = \varepsilon u_0 \sin(\omega_0 T_0) \\ q(x,y,t) = \varepsilon q(x,y,t) \end{cases} \tag{39}$$

The response is set as a second-order small quantity, expressed as:

$$B_{mn}(T_0, T_1) = \varepsilon B_{mn}^1(T_0, T_1) + \varepsilon^2 B_{mn}^2(T_0, T_1) \tag{40}$$

Substituting Equations (38) and (39) into Equation (37), the first-order equation can be derived as:

$$\frac{\partial^2 B_{mn}^1(t)}{\partial T_0^2} + \omega_{mn}^2 B_{mn}^1(t) = \frac{P_{mn}(t)}{M_{mn}} \tag{41}$$

Based on the forced vibration theory, the analytic solution for Equation (41) can be given by:

$$\begin{aligned} B_{mn}^1(x,y,t) = {} & a_{mn} \sin(\omega_{mn} t) + b_{mn} \cos(\omega_{mn} t) + \mu \frac{W_{mn}(x_D, y_D)}{M_{mn}} \frac{a_0}{\omega_{mn}^2} \\ & + \mu \frac{W_{mn}(x_D, y_D)}{M_{mn}} \sum_{k=1}^{\infty} \left[ \frac{a_k}{\omega_{mn}^2 - \omega_d^2} \cos(\omega_d t) + \frac{b_k}{\omega_{mn}^2 - \omega_d^2} \sin(\omega_d t) \right] \end{aligned} \tag{42}$$

in which $\xi$ = a means that the rub-impact occurs at the edge of the plate; $a_{\mathrm{mn}}$ and $b_{\mathrm{mn}}$ are constants determined by initial conditions; and $\xi d$ = 2k$\xi$/Tc is the rub-impact frequency.

Similarly, substituting (45) and (46) into Equation (43), the second-order equation can be obtained as:

$$\frac{\partial^2 B_{mn}^2(t)}{\partial T_0^2} + \omega_{mn}^2 B_{mn}^2(t) = -2 \frac{\partial^2 B_{mn}^1(t)}{\partial T_0 \partial T_1} + \left[\Omega^2 u_b(t) - \ddot{u}_b(t)\right] \frac{C_{mn}}{M_{mn}} B_{mn}^1(t) \tag{43}$$

Then, eliminating the secular term of Equation (43), namely

$$\frac{\partial^2 B_{mn}^1(t)}{\partial T_0 \partial T_1} = 0 \tag{44}$$

gives:

$$\frac{\partial^2 B_{mn}^2(t)}{\partial T_0^2} + \omega_{mn}^2 B_{mn}^2(t) = \left[\Omega^2 u_b(t) - \ddot{u}_b(t)\right] \frac{C_{mn}}{M_{mn}} B_{mn}^1(t) \tag{45}$$

Based on the principle of linear superposition, the analytic solution for Equation (45) can be written as:

$$\begin{aligned} B_{mn}^2(t) = {} & AA_{mn}^1 \cos[(\omega_0 - \omega_{mn})t] - AA_{mn}^2 \cos[(\omega_0 + \omega_{mn})t] \\ & + BB_{mn}^1 \sin[(\omega_0 + \omega_{mn})t] + BB_{mn}^2 \sin[(\omega_0 - \omega_{mn})t] \\ & + CC_{mn}^1 \sum_{k=1}^{\infty} \left\{ \frac{a_k}{\omega_{mn}^2 - \omega_d^2} \sin[(\omega_0 + \omega_d)t] \right\} + CC_{mn}^2 \sum_{k=1}^{\infty} \left\{ \frac{a_k}{\omega_{mn}^2 - \omega_d^2} \sin[(\omega_0 - \omega_d)t] \right\} \\ & + DD_{mn}^1 \sum_{k=1}^{\infty} \left\{ \frac{b_k}{\omega_{mn}^2 - \omega_d^2} \cos[(\omega_0 - \omega_d)t] \right\} - DD_{mn}^2 \left\{ \frac{b_k}{\omega_{mn}^2 - \omega_d^2} \cos[(\omega_0 + \omega_{mn})t] \right\} \end{aligned} \tag{46}$$

where:

$$\begin{cases} AA_{mn}^{1/2} = u_0\left(\Omega^2 + {\omega_0}^2\right)\frac{C_{mn}}{M_{mn}}\frac{a_{mn}}{2}\frac{1}{{\omega_{mn}}^2-(\omega_0-/+\omega_{mn})^2} \\ BB_{mn}^{1/2} = u_0\left(\Omega^2 + {\omega_0}^2\right)\frac{C_{mn}}{M_{mn}}\frac{b_{mn}}{2}\frac{1}{{\omega_{mn}}^2-(\omega_0+/-\omega_{mn})^2} \\ CC_{mn}^{1/2} = u_0\left(\Omega^2 + {\omega_0}^2\right)\frac{C_{mn}}{M_{mn}}\frac{\mu S_{mn}}{2M_{mn}}\frac{1}{{\omega_{mn}}^2-(\omega_0+/-\omega_{mn})^2} \\ DD_{mn}^{1/2} = u_0\left(\Omega^2 + {\omega_0}^2\right)\frac{C_{mn}}{M_{mn}}\frac{\mu S_{mn}}{2M_{mn}}\frac{1}{{\omega_{mn}}^2-(\omega_0-/+\omega_{mn})^2} \end{cases} \tag{47}$$

Consequently, the analytical solution for forced vibration is:

$$w(x,y,t) = \sum_{m=1}^{M}\sum_{n=1}^{N}\left[B_{mn}^1(t)W_{mn}(x,y) + B_{mn}^2(t)W_{mn}(x,y)\right] \tag{48}$$

## 3. Results and Discussion

### 3.1. Validation Study

As there are no existing solutions available in the open literature for the problem being considered, the free vibrations are investigated to validate the accuracy of the present analysis. In Table 1, the results given by Yoo [40] and Zhao [41] are provided for a direct comparison with the present results. The material and structural parameters in this example are plate length $a$ = 1 m, width $b$ = 1 m, thickness $h$ = 0.01 m, Young's modulus $E$ = 71 GPa, mass density $\rho$ = 2750 kg/m$^3$, and Poisson's ratio $v$ = 0.3.

**Table 1.** Comparison of first five natural frequencies with different rotating speeds.

| Dimensionless Rotating Speed | Frequency | Present | Yoo [40] | Zhao [41] |
|---|---|---|---|---|
| $\gamma$ = 1 | 1st | 3.478 | 3.516 | 3.639 |
| | 2nd | 8.514 | 8.533 | 8.571 |
| | 3rd | 21.325 | 21.520 | 21.469 |
| | 4th | 27.208 | 27.353 | 27.194 |
| | 5th | 31.013 | 31.206 | 31.068 |
| $\gamma$ = 2 | 1st | 3.493 | 3.596 | 4.101 |
| | 2nd | 8.517 | 8.551 | 8.755 |
| | 3rd | 21.388 | 21.865 | 21.877 |
| | 4th | 27.214 | 27.384 | 27.284 |
| | 5th | 31.062 | 31.477 | 31.379 |

As can be observed from Table 1, the present results agree well with those in the literature. The errors among those results are very small, which indicates that the proposed model is sufficiently accurate.

### 3.2. Forced Vibration Analysis

In this section, an analytical analysis is performed on the rotating FGM plate under rub-impact and base foundation. A detailed parametric study in graphical form is conducted to investigate the influence of volume fraction index and rotating speed on frequency field and the effects of base excitation, rub-impact and plate size on displacement fields of the FGM structure, which is made of Al and $Al_2O_3$. Unless otherwise stated, the material parameters of the plate are $E_1$ = 70,000 MPa, $\nu_1$ = 0.317756, $\rho_1$ = 2707 kg/m$^{-3}$, $E_2$ = 380,000 MPa, $\nu_2$ = 0.31, $\rho_2$ = 3800 kg/m$^{-3}$, $n$ = 0.1; the dimension parameters are $a$ = 1 m, $b$ = 0.3 m, and $h$ = 0.01 m; and the load parameters are $T_c$ = $2\pi/\Omega$, $t_p$ = 0.01 $T_c$, $F_{\max}$ = 6400 N, $\mu$ = 0.3, $\xi$ = $a$, $\eta$ = $b/2$, $\omega_0$ = $\Omega$ = 300 rad/s, $u_0$ = 0.1.

The forced vibration responses of the rotating FGM plate are presented in Figure 3. It can be seen that the vibration responses along the plate length direction have obvious irregularity, while those along plate direction are relatively uniform. In addition, it is found that the time–domain response of the FGM plate at the rubbing point ($a$, $b/2$) is periodic, while the main frequencies of its responses are in the low frequency region.

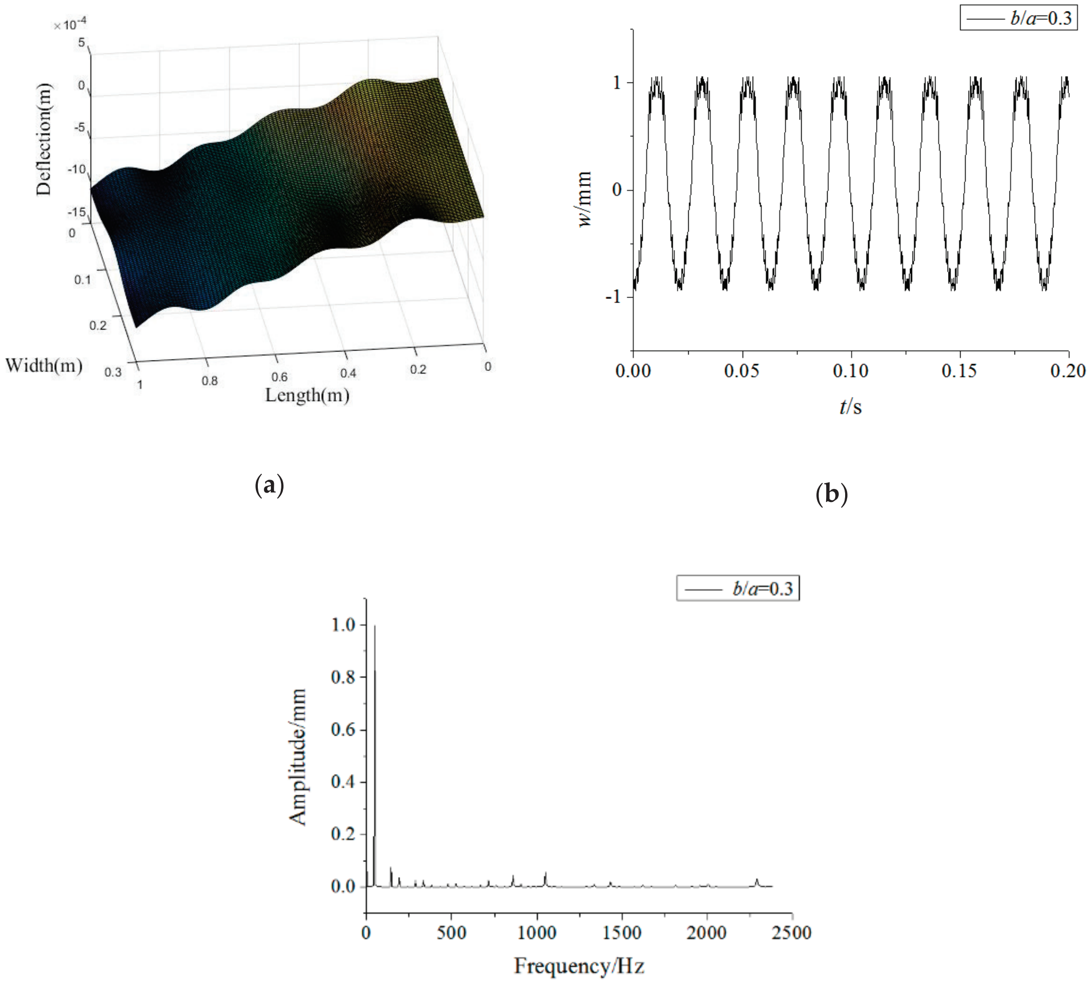

(**a**) (**b**)

(**c**)

**Figure 3.** Forced vibration responses of the rotating FGM plate (**a**) vibration mode, (**b**) time-domain response, (**c**) frequency-domain response.

Figure 4 plots the variations of the forced vibration responses of the rotating FGM plate for different power-law indices. The results show that increasing the power-law index leads to a rise in the vibration amplitudes, while the main frequencies of the responses are less affected by the power-law index. This implies that more $Al_2O_3$ in the FGM plate can enhance the structural stiffness. Moreover, it can be found from Figures 3a and 4a,b that the vibration differences along the plate length direction decrease significantly with an increase in the power-law index. This means a rise in the power-law index tends to improve the vibration stationarity of the rotating FGM plate.

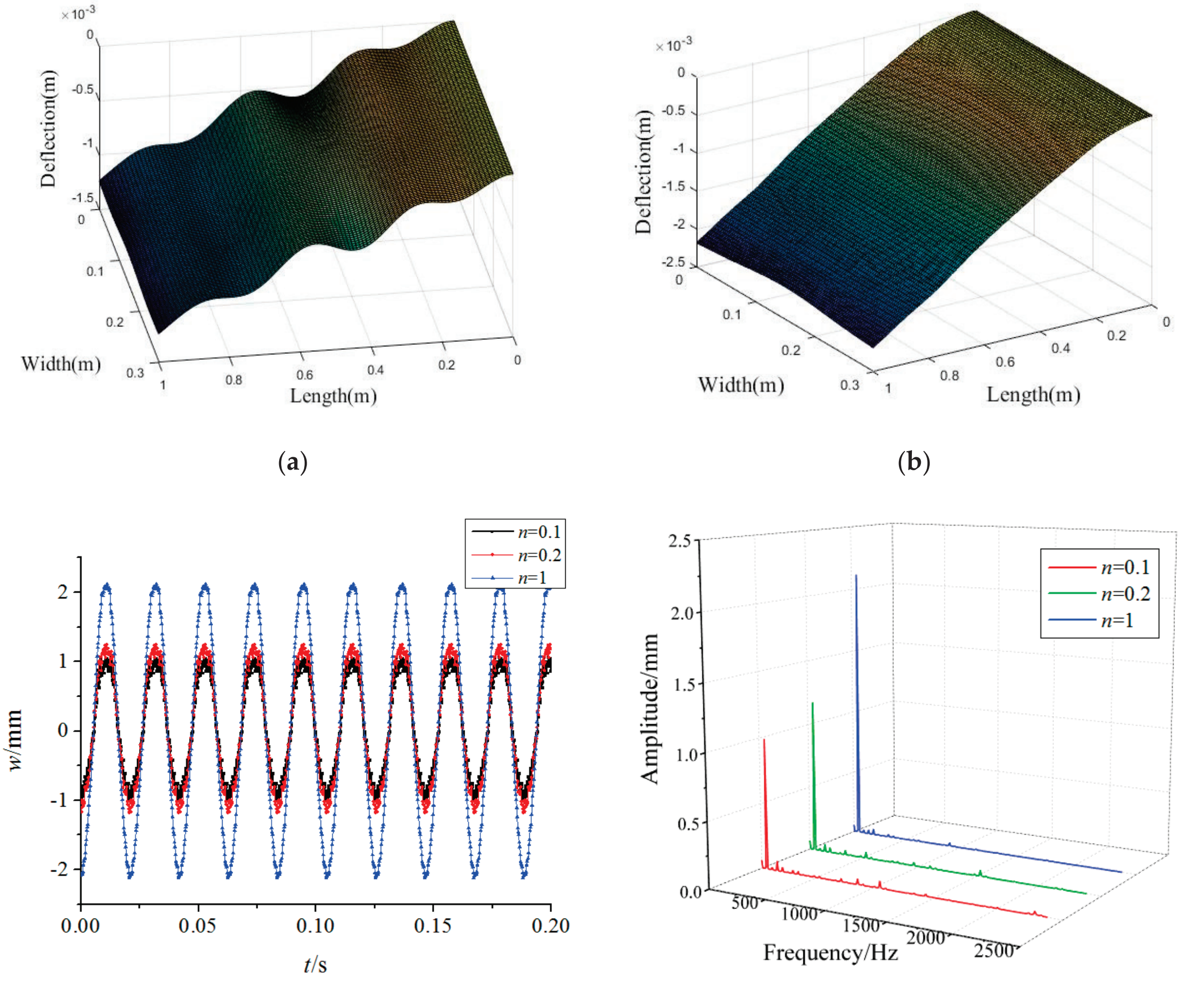

(**a**) (**b**)

(**c**) (**d**)

**Figure 4.** Effects of power-law indices on forced vibration responses of the rotating FGM plate (**a**) $n$ = 0.2, (**b**) $n$ = 1, (**c**) time-domain response, (**d**) frequency-domain response.

Figure 5 plots the variations in the forced vibration responses of the rotating FGM plate for different base excitation amplitudes. One can find that increasing base excitation amplitudes tends to achieve higher vibration amplitudes. Besides, the base excitation can cause a high frequency vibration of the rotating FGM plate, especially for 1000 Hz and 2400 Hz. This indicates that decreasing the foundation vibration plays an important role in achieving better mechanical performance. By comparing the vibration modes from Figures 3 and 5, it can be seen that the vibration differences along the plate width direction decrease with an increase in base excitation amplitudes.

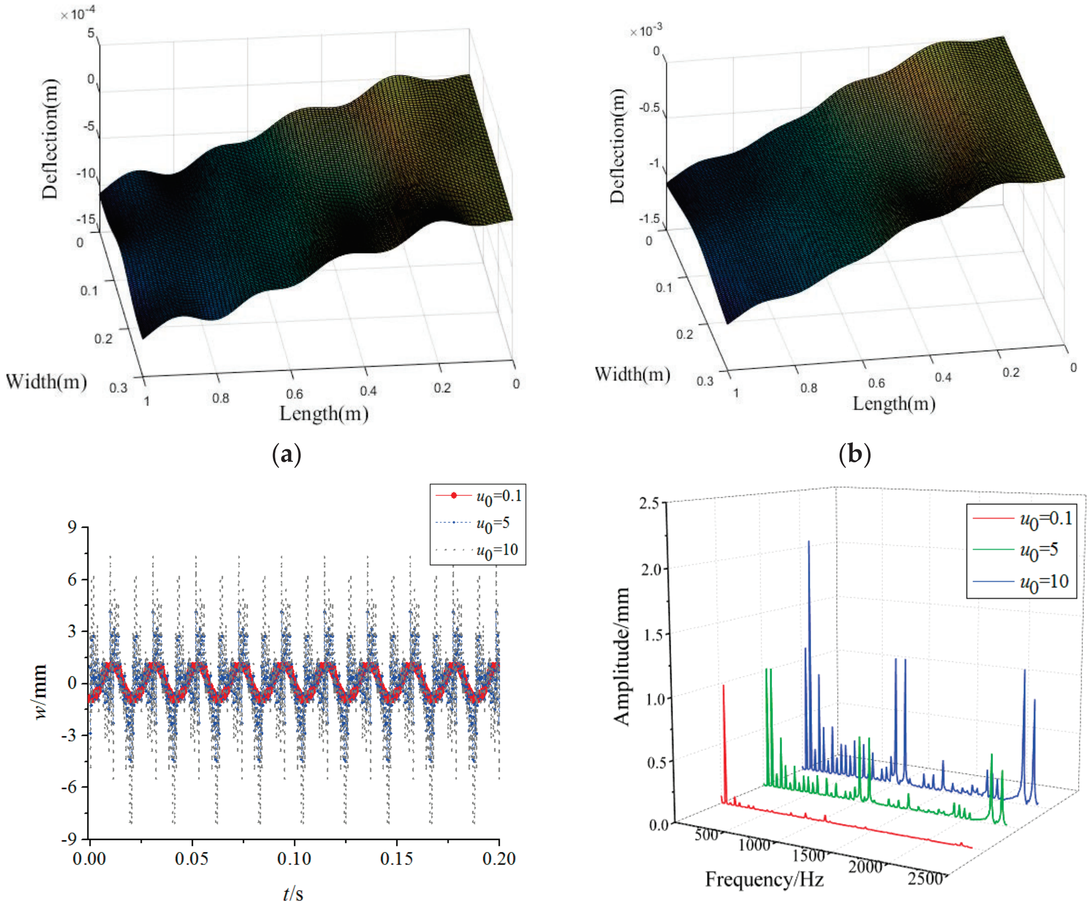

(**a**) (**b**)

(**c**) (**d**)

**Figure 5.** Effects of base excitation on forced vibration responses of the rotating FGM plate (**a**) $u_0 = 5$, (**b**) $u_0 = 10$, (**c**) time-domain response, (**d**) frequency-domain response.

In Figure 6, the variations of the forced vibration responses of the rotating FGM plate for different rub-impact locations are presented where $u_0 = 10$. It is obvious that the vibration amplitudes of the FGM plate for different rub-impact locations differ very little. However, the vibration amplitudes corresponding to 1000 Hz increase considerably when the rub-impact location is close to the midpoint of the plate edge. This shows that the high-frequency vibrations may occur in the case of the rub-impact course near the midpoint of the plate edge. Besides, the vibration differences along the plate width direction increase markedly as the rub-impact location approaches the midpoint the of plate edge. Due to the vibration differences along the width direction, the two-dimensional plate model has more advantages than a one-dimensional beam model.

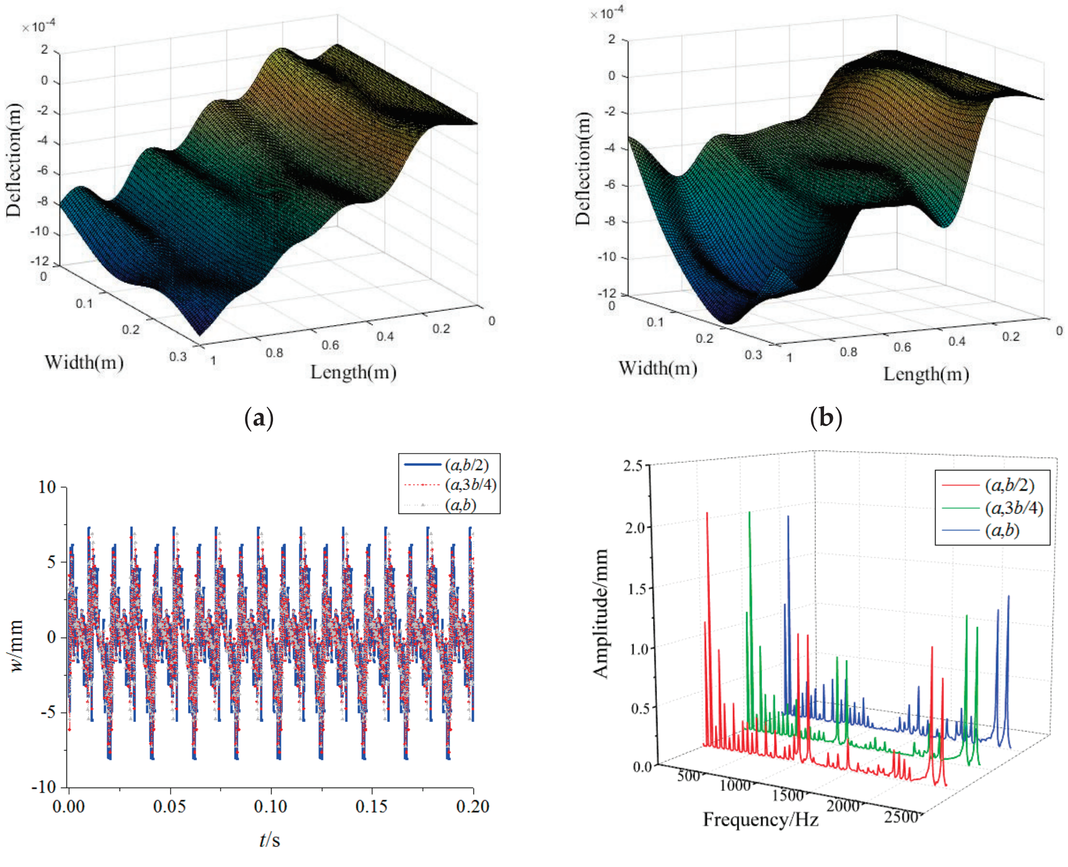

(**a**) (**b**) (**c**) (**d**)

**Figure 6.** Effects of rub-impact locations on forced vibration responses of the rotating FGM plate (**a**) $(\xi, \eta) = (a, 3b/4)$, (**b**) $(\xi, \eta) = (a, b)$, (**c**) time-domain response, (**d**) frequency-domain response.

Figure 7 illustrates the variations of the forced vibration responses of the rotating FGM plate for different friction coefficients. It can be seen that the main frequencies of the responses and the vibration modes change little for the different friction coefficients. On the contrary, the vibration amplitudes increase steadily with the increase in friction coefficients, which indicates that a higher friction coefficient would exacerbate the vibrations caused by rub-impact. For the purpose of preventing damage, we can decrease the friction by reducing the surface roughness between the tip of the plate and the casing during production.

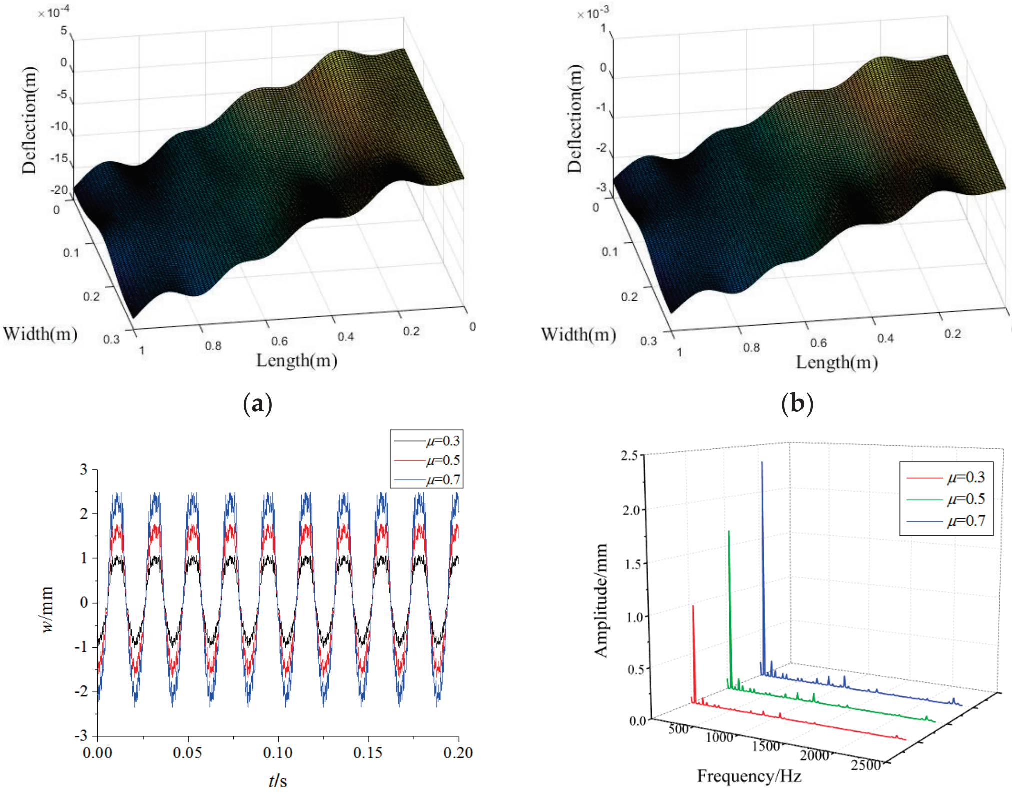

(**c**) (**d**)

**Figure 7.** Effects of friction coefficients on forced vibration responses of the rotating FGM plate (**a**) $\mu = 0.5$, (**b**) $\mu = 0.7$, (**c**) time-domain response, (**d**) frequency-domain response.

Figure 8 illustrates the variations in the forced vibration responses of the rotating FGM plate for different plate width-to-length ratios in which the plate length remains constant. One can see that the vibration amplitudes decrease obviously with the increase of the plate width-to-length ratio. Therefore, the FGM plate with a higher plate width-to-length ratio should be designed to reduce vibrations in actual engineering. Moreover, it can be told from the vibration modes that the vibration fluctuation along the plate length direction decreases with an increase in the plate width-to-length ratio. This implies that a higher plate width-to-length ratio can improve the vibration stationarity of a rotating FGM plate.

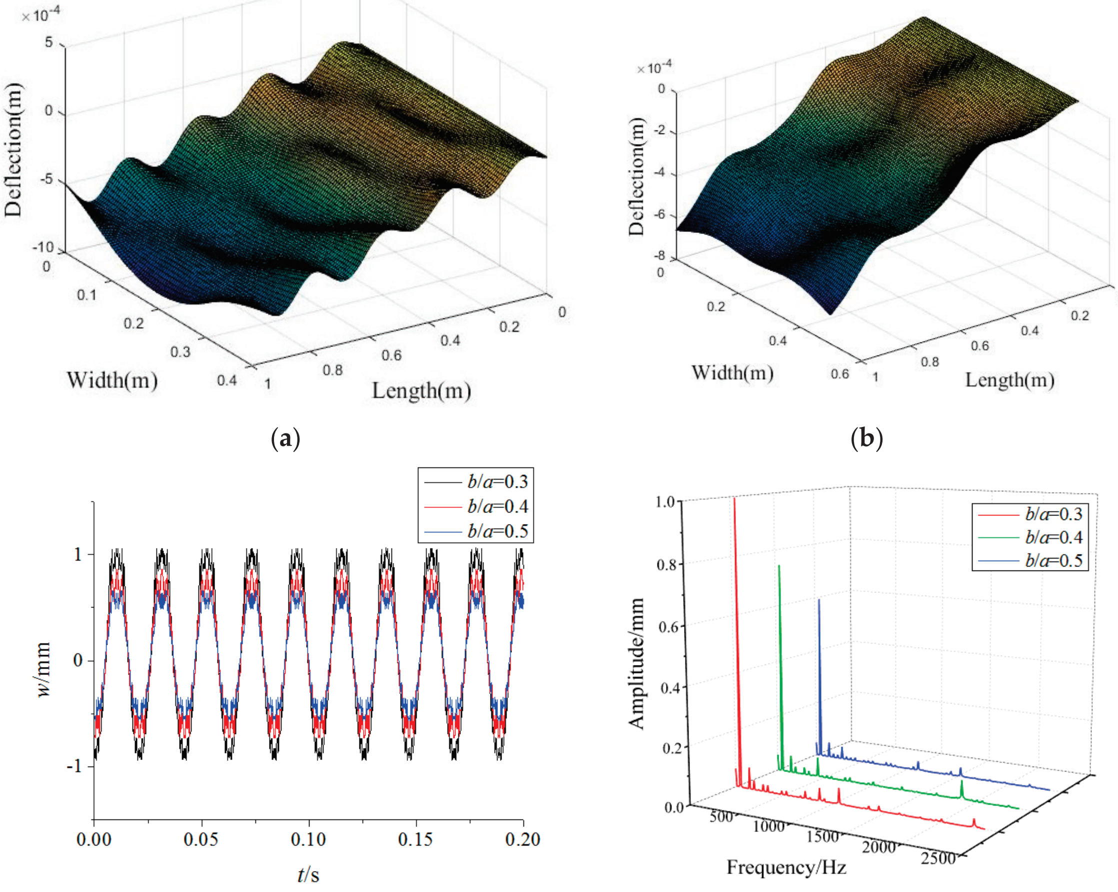

(**a**) (**b**)

(**c**) (**d**)

**Figure 8.** Effects of plate width-to-length ratios on forced vibration responses of the rotating FGM plate (**a**) $b/a = 0.4$, (**b**) $b/a = 0.5$, (**c**) time-domain response, (**d**) frequency-domain response.

## 4. Conclusions

By employing the Kirchhoff plate theory, this paper examines a rotating FGM plate subjected to rub-impact force and base excitation. The equations of motion are derived by Hamilton's principle. Then, the analytical solutions are obtained by adopting the Galerkin method and the small parameter perturbation method. Furthermore, the effects of the power-law index, base excitation amplitude, rub-impact location, friction coefficient and plate width-to-length ratio on vibration characteristics of the rotating FGM plate are examined in detail.

The results show: (1) decreasing the power-law index leads to a decline in the vibration amplitudes, which means that setting more $Al_2O_3$ in the FGM plate can enhance the structural stiffness; (2) the base excitation can cause larger vibration amplitudes and the generated vibrations are almost in the high frequency region; (3) the vibration amplitude corresponding to high frequency increases markedly when the rub-impact location is close to the midpoint of the plate edge; (4) a greater friction coefficient would exacerbate the vibrations caused by rub-impact; (5) and FGM plates with larger width-to-length ratios should be designed to reduce vibration and improve vibration stationarity in actual engineering.

**Author Contributions:** Conceptualization, T.Z. and Y.W. methodology, T.Z.; software, X.W.; validation, Y.W.; formal analysis, Y.W.; investigation, X.W. resources, X.W.; data curation, X.C.; writing—original draft preparation, Y.W.; writing—review and editing, T.Z.; supervision, X.C.; All authors have read and agreed to the published version of the manuscript.

**Funding:** This research was funded by the key R&D plan of China for the Winter Olympics (2021YFF0306401), the major project of aeroengine and gas turbine of China (HT-J2019-IV-0016-0084), the National Natural Science Foundation of China (No. 51805076, No. U1708255 and No. 51775093), the National Science and Technology Major Project of China (J2019-I-0008-0008) and the Fundamental Research Funds for the Central Universities of China (N2105013).

**Conflicts of Interest:** The authors declare no conflict of interest in preparing this article.

## References

1. Zhang, J.; Shaw, A.D.; Wang, C.; Gu, H.; Amoozgar, M.; Friswell, M.I.; Woods, B.K.S. Aeroelastic Model and Analysis of an Active Camber Morphing Wing. *Aerosp. Sci. Technol.* **2021**, *111*, 106534. [CrossRef]
2. Yu, X.; Sun, Y.; Zhao, D.; Wu, S. A Revised Contact Stiffness Model of Rough Curved Surfaces Based on the Length Scale. *Tribol. Int.* **2021**, *164*, 107206. [CrossRef]
3. Arefi, M.; Loghman, A.; Mohammad Hosseini Mirzaei, M. Thermoelastic Analysis of a Functionally Graded Simple Blade Using First-Order Shear Deformation Theory. *Mech. Adv. Compos. Struct.* **2019**, *7*, 147–155.
4. Ma, H.; Tai, X.Y.; Han, H.K.; Wu, Z.Y.; Wang, D.; Wen, B.C. A revised model for rubbing between rotating blade and elastic casing. *J. Sound Vib.* **2015**, *337*, 301–320. [CrossRef]
5. Wang, N.F.; Liu, C.; Jiang, D.X.; Behdinan, K. Casing vibration response prediction of dual–rotor–blade-casing system with blade-casing rubbing. *Mech. Syst. Signal. Process.* **2019**, *118*, 61–77. [CrossRef]
6. Hou, L.; Chen, H.Z.; Chen, Y.S.; Lu, K.; Liu, Z.S. Bifurcation and stability analysis of a nonlinear rotor system subjected to constant excitation and rub-impact. *Mech. Syst. Signal Process.* **2019**, *125*, 65–78. [CrossRef]
7. Xiao, S.G.; Liu, S.L.; Jiang, F.; Song, M.M.; Cheng, S.G. Nonlinear dynamic response of reciprocating compressor system with rub-impact fault caused by subsidence. *J. Vib. Control.* **2019**, *25*, 1737–1751. [CrossRef]
8. Tchomeni, B.X.; Alugongo, A. Modelling and numerical simulation of vibrations induced by mixed faults of a rotor system immersed in an incompressible viscous fluid. *Adv. Mech. Eng.* **2018**, *10*, 1–21. [CrossRef]
9. Wang, J.G.; Zhang, J.; Bai, R.S.; Yang, X.F.; Zhao, Y.X. Nonlinear analysis of the locomotive traction system with rub-impact and nonlinear stiffness. *Adv. Mech. Eng.* **2018**, *10*, 1–11. [CrossRef]
10. Ebrahim, T.N.; Pouya, A.S.; Hamid, A. Nonlinear dynamics of a flexible rotor on tilting pad journal bearings experiencing rub-impact. *Nonlinear Dyn.* **2018**, *94*, 2937–2956.
11. Zhang, Z.; Yang, F.; Zhang, H.; Zhang, T.; Wang, H.; Xu, Y.; Ma, Q. Influence of $CeO_2$ Addition on Forming Quality and Microstructure of TiC-Reinforced $CrTi_4$-Based Laser Cladding Composite Coating. *Mater. Charact.* **2021**, *171*, 110732. [CrossRef]
12. Zhang, C.; Ali, A.; Sun, L. Investigation on Low-Cost Friction-Based Isolation Systems for Masonry Building Structures: Experimental and Numerical Studies. *Eng. Struct.* **2021**, *243*, 112645. [CrossRef]
13. Hu, Y.; Qing, J.X.; Liu, Z.H.; Conrad, Z.J.; Cao, J.N.; Zhang, X.P. Hovering Efficiency Optimization of the Ducted Propeller with Weight Penalty Taken into Account. *Aerosp. Sci. Technol.* **2021**, *117*, 106937. [CrossRef]
14. Minoo, N.; Kamyar, S. Functionally graded materials: A review of fabrication and properties. *Appl. Mater. Today* **2016**, *5*, 223–245.
15. Yang, J.; Shen, H.S. Vibration characteristics and transient response of shear-deformation functionally graded plates in thermal environments. *J. Sound Vib.* **2002**, *255*, 579–602. [CrossRef]
16. Kumar, R.; Lal, A.; Singh, B.N.; Singh, J. New transverse shear deformation theory for bending analysis of FGM plate under patch load. *Compos. Struct.* **2019**, *208*, 91–100. [CrossRef]
17. Singh, S.J.; Harsha, S.P. Buckling analysis of FGM plates under uniform, linear and non-linear in-plane loading. *J. Mech. Sci. Technol.* **2019**, *33*, 1761–1767. [CrossRef]
18. Do, V.N.V.; Ong, T.H.; Lee, C.H. Isogeometric analysis for nonlinear buckling of FGM plates under various types of thermal gradients. *Thin-Walled Struct.* **2019**, *137*, 448–462. [CrossRef]
19. Wang, C.M.; Ke, L.L.; Chowdhury, A.N.R.; Yang, J.; Kitipornchai, S.; Fernando, D. Critical examination of midplane and neutral plane formulations for vibration analysis of FGM beams. *Eng. Struct.* **2017**, *130*, 275–281. [CrossRef]
20. Chen, D.; Yang, J.; Kitipornchai, S. Buckling and bending analyses of a novel functionally graded porous plate using Chebyshev-Ritz method. *ScienceDirect* **2019**, *19*, 157–170. [CrossRef]
21. Zhao, T.Y.; Yang, Y.F.; Pan, H.G.; Zhang, H.Y.; Yuan, H.Q. Free vibration analysis of a spinning porous nanocomposite blade reinforced with graphene nanoplatelets. *Materials* **2022**, *56*, 574–586. [CrossRef]
22. Zhao, T.Y.; Jiang, Z.Y.; Zhao, Z.; Xie, L.Y.; Yuan, H.Q. Modeling and free vibration analysis of rotating hub-blade assemblies reinforced with graphene nanoplatelets. *J. Strain Anal. Eng.* **2021**, *56*, 563–573. [CrossRef]
23. Zhao, T.Y.; Ma, Y.; Zhang, H.Y.; Yang, J. Coupled Free Vibration of Spinning Functionally Graded Porous Double-Bladed Disk Systems Reinforced with Graphene Nanoplatelets. *Materials* **2020**, *13*, 5610. [CrossRef] [PubMed]
24. Zhao, T.Y.; Liu, Z.F.; Pan, H.G.; Zhang, H.Y.; Yuan, H.Q. Vibration Characteristics of Functionally Graded Porous Nanocomposite Blade-disk-shaft Rotor System Reinforced with Graphene Nanoplatelets. *Appl. Compos. Mater.* **2021**, *28*, 717–731. [CrossRef]
25. Zhao, T.Y.; Jiang, L.P.; Pan, H.G.; Yang, J.; Kitipornchai, S. Coupled free vibration of a functionally graded pre-twisted blade-shaft system reinforced with graphene nanoplatelets. *Compos. Struct.* **2021**, *262*, 113362. [CrossRef]

26. Zhao, T.Y.; Ma, Y.; Zhang, H.Y.; Pan, H.G.; Cai, Y. Free vibration analysis of a rotating graphene nanoplatelet reinforced pre-twist blade-disk assembly with a setting angle. *Appl. Math. Model.* **2021**, *93*, 578–596. [CrossRef]
27. Zhao, T.Y.; Cui, Y.S.; Pan, H.G.; Yuan, H.Q.; Yang, J. Free vibration analysis of a functionally graded graphene nanoplatelet reinforced disk-shaft assembly with whirl motion. *Int. J. Mech. Sci.* **2021**, *197*, 106335. [CrossRef]
28. Zhao, T.Y.; Cui, Y.S.; Wang, Y.Q.; Pan, H.G. Vibration characteristics of graphene nanoplatelet reinforced disk-shaft rotor with eccentric mass. *Mech. Adv. Mater.* **2021**, 1–25. [CrossRef]
29. Zhao, T.Y.; Jiang, L.P.; Yu, Y.X.; Wang, Y.Q. Study on theoretical modeling and mechanical performance of a spinning porous graphene nanoplatelet reinforced beam attached with double blades. *Mech. Adv. Mater. Struct.* **2022**, 1–12. [CrossRef]
30. Li, Z.C.; Zheng, J.X.; Sun, Q.; He, H.T. Nonlinear structural stability performance of pressurized thin-walled FGM arches under temperature variation field. *Int. J. Non-Linear Mech.* **2019**, *113*, 86–102. [CrossRef]
31. Bakora, A.; Bourada, F.; Bousahla, A.A.; Tounsi, A.; Benrahou, K.H.; Tounsi, A.; I-Zahrani, M.M.A.; Mahmoud, S.R. Buckling analysis of functionally graded plates using HSDT in conjuction with the stress function method. *Comput. Concr.* **2021**, *27*, 73–83.
32. Guellil, M.; Saidi, H.; Bourada, F.; Bousahla, A.A.; Tounsi, A.; I-Zahrani, M.M.A.; Hussain, M.; Mahmoud, S.R. Influences of porosity distributions and boundary conditions on mechanical bending response of functionally graded plates resting on Pasternak foundation. *Steel Compos. Struct.* **2021**, *38*, 1–15.
33. Bekkaye, T.H.L.; Fahsi, B.; Bousahla, A.A.; Bourada, F.; Tounsi, A.; Benrahou, K.H.; Tounsi, A.; I-Zahrani, M.M.A. Porosity-dependent mechanical behaviors of FG plate using refined trigonometric shear deformation theory. *Comput. Concr.* **2020**, *26*, 439–450.
34. Sobhy, M. Size dependent hygro-thermal buckling of porous FGM sandwich microplates and microbeams using a novel four-variable shear deformation theory. *Int. J. Appl. Mech.* **2020**, *12*, 2050017. [CrossRef]
35. Sobhy, M.; Zenkour, A.M. Vibration analysis of functionally graded graphene platelet-reinforced composite doubly curved shallow shells on elastic foundations. *Steel Compos. Struct.* **2019**, *33*, 195–208.
36. Guégan, A. *Parameter Study of Bladed Disk/Casing Interactions through Direct Contact in Aero-Engine Assemblies. Structural Dynamics and Vibration Laboratory*; McGill University Press: Montreal, QC, Canada, 2015.
37. Padova, C.; Barton, J.; Dunn, M.G.; Manwaring, S.; Young, G.; Adams, M. Development of an Experimental Capability to Produce Controlled Blade Tip/Shroud Rubs at Engine Speed. *J. Turbomach. Trans. Asme* **2005**, *127*, 726–735. [CrossRef]
38. Amabili, M. *Nonlinear Vibrations and Stability of Shells and Plate*; Cambridge University Press: Cambridge, UK, 2008.
39. Yao, M.H.; Ma, L.; Zhang, W. Nonlinear Dynamics of the High-Speed Rotating Plate. *Int. J. Aerosp. Eng.* **2018**, *2018*, 5610915. [CrossRef]
40. Yoo, H.H.; Pierre, C. Modal Characteristic of a Rotating Rectangular Cantilever Plata. *J. Sound Vib.* **2003**, *259*, 81–96. [CrossRef]
41. Zhao, J.; Tian, Q.; Hu, H.Y. Modal Analysis of a Rotating Thin Plate via Absolute Nodal Coordinate Formulation. *J. Comput. Nonlinear Dyn.* **2020**, *6*, 041013. [CrossRef]

materials

MDPI

*Article*

# Steady-State Thermal Analysis of Functionally Graded Rotating Disks Using Finite Element and Analytical Methods

**M. M. Shahzamanian [1,2,*], A. Shahrjerdi [3], B. B. Sahari [4] and P. D. Wu [1]**

[1] Department of Mechanical Engineering, McMaster University, Hamilton, ON L8S 4L7, Canada
[2] Department of Mechanical Engineering, Texas A&M University, College Station, TX 77843-3123, USA
[3] Mechanical Engineering Department, Malayer University, Malayer, Iran
[4] Faculty of Engineering and Built Environment, UCSI University, Kuala Lumpur 56000, Malaysia
* Correspondence: mehdi@tamu.edu or mmshahzamanian@gmail.com

**Abstract:** A steady-state thermal analysis for a hollow and axisymmetric functionally graded (FG) rotating disk with a uniform thickness was performed in this study. In the studied FG disk, metal and ceramic materials were considered for the inner and outer surfaces, respectively, when the material properties varied along the radial direction but not through material thickness variations. A power law distribution was employed to represent the material properties. Three different methods were used to present the temperature distribution along the radial direction of the FG disk, namely (1) an in-house finite element (FE) program, (2) the ANSYS parametric design language (APDL), and (3) an analytical solution. Furthermore, the in-house FE program presented the thermal stress and thermal strain of the FG disk. The weighted residual method in the FEM was used to present the temperature distribution when the material properties along an element are varying in contrast with using a commercial finite element software when the material properties are constant within an element to simulate FGMs. The accuracy of the in-house FE program was tested, and it was shown that the temperature distributions obtained by using the abovementioned methods were exactly the same. A parametric material gradation study was performed to understand the effects on the temperature, thermal strain, and stress. The material gradation was found to have a significant effect in this regard. The in-house finite element program enables one to perform a post-processing analysis in a more efficient and convenient manner than that through simulations in a finite element software program such as ANSYS. Lastly, this in-house code can be used to perform an optimization analysis to minimize the thermal strain and stress while the stiffness of the plate is maintained when the material properties within an element vary.

**Keywords:** finite element method (FEM); functionally graded materials (FGMs); steady-state thermal analysis

## 1. Introduction

The material properties vary smoothly and continuously based on a specified function along direction(s) in functionally graded materials (FGMs) [1–3]. Thus, the thermal and mechanical properties can vary from metals to ceramics in FG rotating disks. FGMs are mainly fabricated to operate in high-temperature environments such as in ultra-light, temperature-resistant materials used for space vehicles [4]. FGMs offer an advantage because the thermal stresses are smooth compared with when the disk is coated [5] (Figure 1a,b for a coated disk and Figure 1c,d for an FGM). As such, the steady-state temperature distributions in FG rotating disks are analyzed in this study. The results presented here were obtained using the finite element method (FEM), the commercial software ANSYS, the in-house written code in MATLAB, and an analytical method. The material properties along an element vary using the in-house FE code in contrast with using the commercial FE software when the material properties are constant within an element when simulating FGMs.

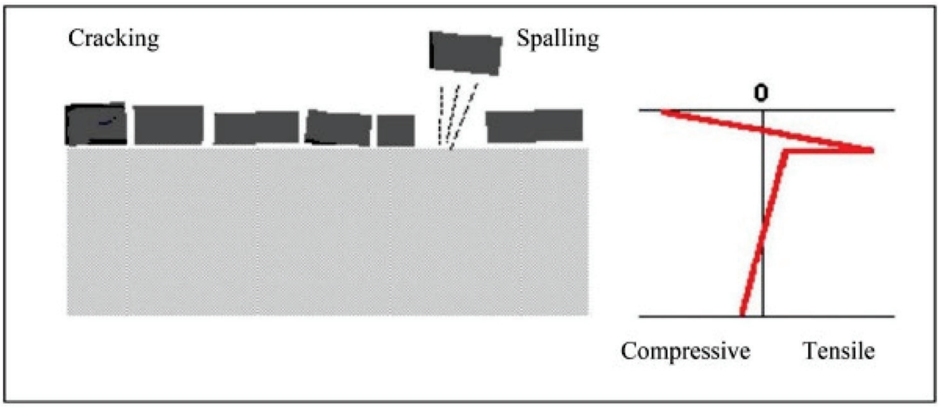

**(a)** Conventional thermal barrier coating and related failure modes

**(b)** Thermal stress distribution

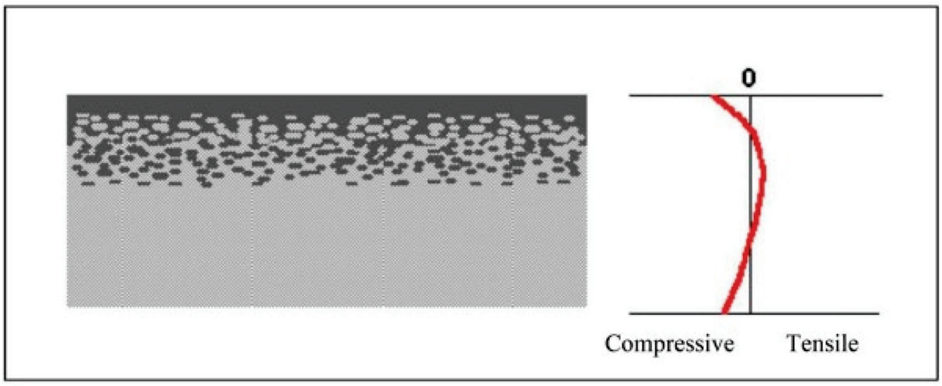

**(c)** FGM Thermal Barrier Coating

**(d)** Thermal stress distribution

**Figure 1.** Comparison between a coated material and FGM used to resist thermal loads [5].

Many researchers have performed thermoelastic analyses on FG rotating disks using analytical methods [6–15]. Bayat et al. [6,7] performed a thermoelastic analysis of FG rotating disks considering the small and large deflections under constant and variable thicknesses. In another study by Jabbari et al. [8,9], a thermoelastic analysis of short and long thick hollow FG cylinders was performed. Zenkour [10] performed a numerical analysis of the stress distribution of the rotating composite structures of FG disks. Eldeeb et al. [11] performed a thermoelastic analysis for a rotating sandwich disk made of temperature dependent FGMs. Erdogan and Wu [12] analyzed the crack problems for FGMs under thermal stresses. Duc et al. [13] performed an analysis to investigate the non-linear dynamic response of shear deformable FGM plates. In all mentioned works, the analytical methods were found useful in analyzing the responses of FGMs and in investigating the effect of material gradation under various conditions.

The FEM is an applicable tool for simulating FGMs and analyzing their responses under various conditions [16–26]. FG rotating disks can be simulated using the FEM to analyze the thermomechanical results [18–21]. FGMs have been simulated using the FEM by Durodola and Attia [22], and the deformation and stresses have been analyzed. Shahzamanian et al. [23–25] performed a simulation for FG brake disks using the APDL. The material properties of FG brake disks vary in radial [23] and thickness [25] directions. The thermomechanical results of FG brake disks under pressure and heat sources due to friction between the pads and disks have been analyzed. The effects of various contact parameters in FG brake disks were studied in [24]. Genao et al. [26] used a non-linear FEM to perform a thermoelastic analysis of temperature dependent FGMs. Overall, the material gradation has been found to have a significant effect on the thermomechanical responses of FGMs [27–31].

Steady-state thermal analyses of FGMs have been performed by many researchers. Functionally graded materials (FGMs) can resist high temperatures and can reduce the thermal stresses [32]. Jabbari et al. [33,34] presented the steady-state thermal and mechanical stresses for functionally graded piezo-electric porous material (FGPPM) hollow spheres. Bayat et al. [35] performed an analytical and numerical analysis to present the thermal and mechanical response of an FGM under combined pressure and temperature loading. Delouei et al. [36] presented the steady-state two-dimensional temperature distribution for an FGM. In their analysis, a Fourier transform was used.

In the present study, an FG hollow rotating disk was considered, and the material properties of the FG rotating disk were assumed via the power law distribution with respect to the radial direction. The inner and outer surfaces were completely metal and ceramic, respectively. The temperature distribution of the FG disks with various material gradations was calculated and presented using three methods: a simulation in ANSYS software, an analytical solution, and an in-house FE program. The thermal stress and thermal strain of the FG rotating disk were determined using the in-house FEM. The results using the ANSYS software were verified, and a parametric study was performed to understand the effects of each material gradation on the temperature distribution, thermal strain, and stress distributions. The in-house finite element code makes the post-processing analysis more convenient and efficient than that performed using ANSYS software.

## 2. Material Gradation Relation

In this study, as mentioned previously, the material properties of the FG disk vary along the radial direction using the power law distribution [8]:

$$P(r) = P_{\bullet} r^{m} \tag{1}$$

where P is the material property at radius r and $P_{\bullet}$ and m are material constants. $E_{\bullet}$, $\alpha_{\bullet}$, and $K_{\bullet}$ are constant parameters for the Young's modulus, thermal expansion coefficient, and thermal conductivity, respectively to create the material variation in FG disks. Moreover, $m_{YM}$, $m_{TE}$, and $m_{TC}$ are the power parameters for the Young's modulus, thermal expansion, and thermal conductivity, respectively.

## 3. Methodology and Problem Formulation

As mentioned previously, first the temperature distribution of the FG rotating disk was presented for validation and accuracy testing in to present the thermoelastic results for the three different methods. The three different methods are as follows [37]:

1. In-house finite element program;
2. APDL;
3. Analytical solution.

In this section, each method will be described in detail and in a stepwise manner. We describe how these methods calculate the temperature distribution of an FG disk when all material properties, such as the Young's modulus, thermal conductivity, and thermal expansion coefficient, vary along the radius. The thermal conductivity varies along an element using the in-house FE code in contrast with using the FE commercial software when the thermal conductivity is constant within an element to simulate FGMs.

### 3.1. Method #1: In-House FE Program

In an FG disk, the temperature distribution can be stated as [38,39]:

$$\frac{1}{r}\left(\frac{\partial}{\partial r}\right)\left(rk(r)\frac{\partial T}{\partial r}\right) + \frac{\partial}{\partial z}\left(k(r)\frac{\partial T}{\partial z}\right) = 0 \tag{2}$$

The following expressions are given by expanding Equation (2):

$$\left(\left[\frac{k(r)}{r} + k\prime(r)\right]\frac{\partial T}{\partial r} + k(r)\frac{\partial^2 T}{\partial r^2}\right) + k(r)\frac{\partial^2 T}{\partial z^2} = 0 \tag{3}$$

$$\left[\frac{1}{r} + \frac{k\prime(r)}{k(r)}\right]\frac{\partial T}{\partial r} + \frac{\partial^2 T}{\partial r^2} + \frac{\partial^2 T}{\partial z^2} = 0 \tag{4}$$

The following equation is obtained using Equation (1):

$$\frac{k\prime(r)}{k(r)} = \frac{m_{TC}}{r} \tag{5}$$

The following equations are obtained by substituting Equation (5) into Equation (4):

$$\left[\frac{1}{r} + \frac{m_{TC}}{r}\right]\frac{\partial T}{\partial r} + \frac{\partial^2 T}{\partial r^2} + \frac{\partial^2 T}{\partial z^2} = 0 \tag{6}$$

$$\frac{\partial^2 T}{\partial r^2} + \frac{1}{r}\frac{\partial T}{\partial r} + \frac{\partial^2 T}{\partial z^2} + \left(\frac{m_{TC}}{r}\right)\frac{\partial T}{\partial r} = 0 \tag{7}$$

The element matrix integral is calculated by applying the weighted residual method [40]:

$$\int_{\Omega} \omega\left(\frac{\partial^2 T}{\partial r^2} + \frac{1}{r}\frac{\partial T}{\partial r} + \frac{\partial^2 T}{\partial z^2} + \left(\frac{m_{TC}}{r}\right)\frac{\partial T}{\partial r}\right)d\Omega \tag{8}$$

where "ω" is the weighted residual. Equation (8) can be rewritten as follows:

$$\int_{\Omega} \omega\left(\frac{1}{r}\frac{\partial}{\partial r}\left(\frac{\partial T}{\partial r}\right) + \frac{\partial^2 T}{\partial z^2} + \left(\frac{m_{TC}}{r}\right)\frac{\partial T}{\partial r}\right)d\Omega \tag{9}$$

Thereafter, the domain integral can be expressed as an axisymmetric cylindrical, as shown in Equation (10):

$$\begin{aligned} &\int_{\Omega} \omega\left(\frac{1}{r}\frac{\partial}{\partial r}\left(\frac{\partial T}{\partial r}\right) + \frac{\partial^2 T}{\partial z^2} + \left(\frac{m_{TC}}{r}\right)\frac{\partial T}{\partial r}\right)d\Omega \\ &= 2\pi\int_r\int_z r\left(\omega\left(\frac{1}{r}\frac{\partial}{\partial r}\left(\frac{\partial T}{\partial r}\right) + \frac{\partial^2 T}{\partial z^2} + \left(\frac{m_{TC}}{r}\right)\frac{\partial T}{\partial r}\right)\right)dr\,dz \end{aligned} \tag{10}$$

Equation (10) is rewritten based on Equation (11):

$$2\pi\int_r\int_z \omega\left(\frac{\partial}{\partial r}\left(\frac{\partial T}{\partial r}\right) + r\frac{\partial^2 T}{\partial z^2} + m_{TC}\frac{\partial T}{\partial r}\right)dr\,dz \tag{11}$$

The weak formulation of the first two terms in Equation (11) using the integration parts is replaced in Equation (12) [40]:

$$2\pi\int_r\int_z r\left(-\frac{\partial \omega}{\partial r}\frac{\partial T}{\partial r} + \frac{\partial \omega}{\partial z}\frac{\partial T}{\partial z} + \frac{m_{TC}}{r}\frac{\partial T}{\partial r}\right)dr\,dz \tag{12}$$

In the in-house FE method, 80 axisymmetric triangular elements were used. A mesh study was performed and the number of elements was selected in order to not have a significant effect on the results, and in the meantime to minimize the computational effort. Figure 2 shows the mesh division by the triangular elements.

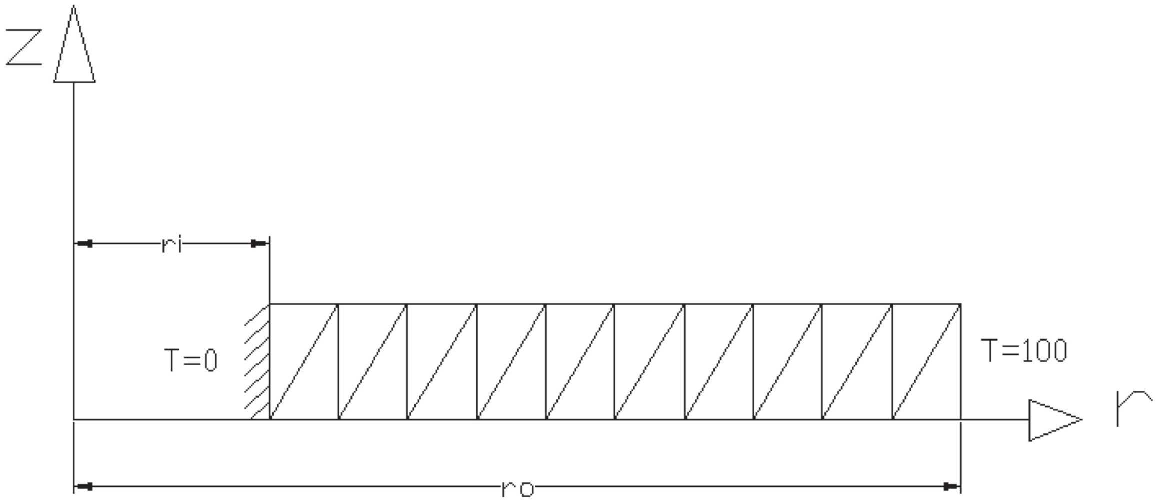

**Figure 2.** Element distribution of the FG disk using an axisymmetric triangular element.

For the axisymmetric triangular element, the element matrix is stated as presented in Equation (13).

$$
\begin{aligned}
[\mathrm{k}] = 2\pi \int_{\mathrm{z}} \int_{\mathrm{r}} \Bigg\{ \mathrm{r} \Bigg( - \begin{Bmatrix} \frac{\partial \mathrm{H}_1}{\partial \mathrm{r}} \\ \frac{\partial \mathrm{H}_2}{\partial \mathrm{r}} \\ \frac{\partial \mathrm{H}_3}{\partial \mathrm{r}} \end{Bmatrix} \begin{Bmatrix} \frac{\partial \mathrm{H}_1}{\partial \mathrm{r}} & \frac{\partial \mathrm{H}_2}{\partial \mathrm{r}} & \frac{\partial \mathrm{H}_3}{\partial \mathrm{r}} \end{Bmatrix} - \begin{Bmatrix} \frac{\partial \mathrm{H}_1}{\partial \mathrm{z}} \\ \frac{\partial \mathrm{H}_2}{\partial \mathrm{z}} \\ \frac{\partial \mathrm{H}_3}{\partial \mathrm{z}} \end{Bmatrix} \begin{Bmatrix} \frac{\partial \mathrm{H}_1}{\partial \mathrm{z}} & \frac{\partial \mathrm{H}_2}{\partial \mathrm{z}} & \frac{\partial \mathrm{H}_3}{\partial \mathrm{z}} \end{Bmatrix} \\
+ \frac{\mathrm{m}_{\mathrm{TC}}}{\mathrm{r}} \begin{Bmatrix} \mathrm{H}_1 \\ \mathrm{H}_2 \\ \mathrm{H}_3 \end{Bmatrix} \begin{Bmatrix} \frac{\partial \mathrm{H}_1}{\partial \mathrm{r}} & \frac{\partial \mathrm{H}_2}{\partial \mathrm{r}} & \frac{\partial \mathrm{H}_3}{\partial \mathrm{r}} \end{Bmatrix} \Bigg) \Bigg\} \mathrm{dzdr}
\end{aligned} \tag{13}
$$

Shape functions for an axisymmetric triangular element are denoted by $\mathrm{H}_1, \mathrm{H}_2,$ and $\mathrm{H}_3$.

Lastly, Equation (14) is solved to determine the vector of the temperature (T) as follows:

$$
[\mathrm{K}]\{\mathrm{T}\} = \{\mathrm{F}\} \tag{14}
$$

In Equation (14), F is a matrix representing the force vector.

A MATLAB code was implemented, and the nodes and elements were created in an algorithm. Then, the element matrix of every element ([k] : small "k") was calculated, and they were considered in [K] (Capital "K") to solve Equation (14). The temperature boundary conditions were applied, and finally the temperature distribution was calculated. The implemented in-house code has been shared for public use and can be downloaded from [41].

### *3.2. Method #2: APDL*

For the validation and accuracy testing of method #1, the FG rotating disk was divided into 40 elements along the radius, as shown in Figure 3, using ANSYS. The APDL was used to simulate the FG disk. Again, a mesh study was performed and the number of elements was selected in a manner so as to not have a significant effect on the results, and in the meantime to minimize the computational effort. The Plane42 element in ANSYS was used to obtain the temperature distribution. Shahzamanian et al. [23–25] have explained the simulation of FGMs in ANSYS. However, the material properties of the FG rotating disk were calculated at the mean radius of each element. By applying the temperature at the inner and outer surfaces of disks, the temperature distribution will be given by ANSYS.

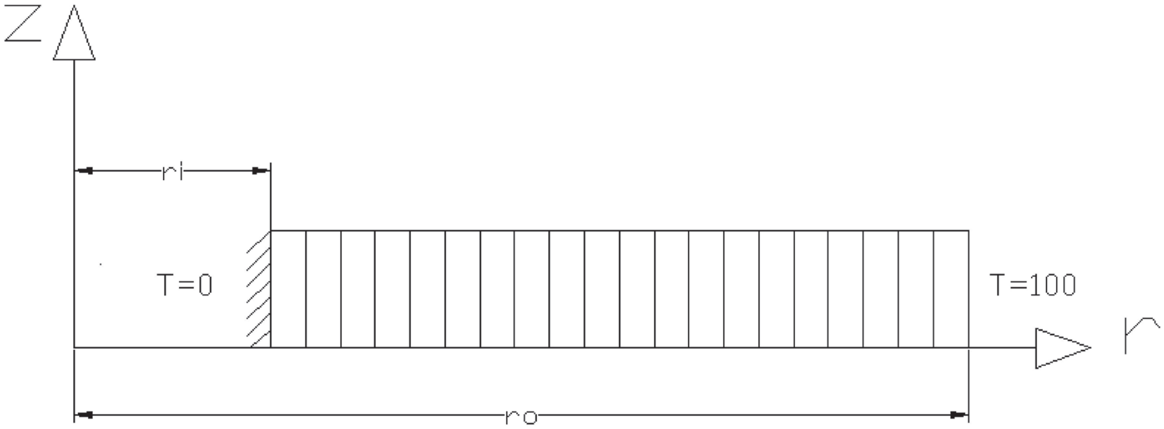

**Figure 3.** Element distribution of an FG disk using ANSYS software.

### 3.3. Method #3: Analytical Solution

An analytical solution also was used to determine the temperature distribution and the obtained results were compared with those presented by the previous methods. In this study, the variation in temperature distribution was only along the radius. Therefore, neglecting the terms in the thickness (z) direction in Equation (2) leads to obtaining Equations (15) and (16).

$$\frac{\partial^2 T}{\partial r^2} + \left(\frac{m_{TC} + 1}{r}\right)\frac{\partial T}{\partial r} = 0 \tag{15}$$

$$r^2\frac{\partial^2 T}{\partial r^2} + Ar\frac{\partial T}{\partial r} = 0 \tag{16}$$

where, $A = m_{TC} + 1$. By considering, $r = e^t$ or $t = \ln(r)$, the following expressions are presented sequentially:

$$\frac{dT}{dr} = \frac{dT}{dt}\frac{dt}{dr} = \frac{dT}{rdt} \tag{17}$$

$$\begin{aligned}\frac{d^2T}{dr^2} &= \frac{d}{dr}\left(\frac{dT}{dr}\right) = \frac{d}{dr}\left[\frac{dT}{dt}\frac{1}{r}\right] = \frac{d}{dr}\left[\frac{dT}{dr}e^{-t}\right] = \frac{d\left[\frac{dT}{dr}e^{-t}\right]}{dt}\frac{dt}{dr} \\ &= \frac{d\left[\frac{dT}{dr}e^{-t}\right]}{dt}\frac{1}{r} = \left[\frac{d^2T}{dt^2}e^{-t} - \frac{dT}{dt}e^{-t}\right]e^{-t}\end{aligned} \tag{18}$$

By substituting Equations (17) and (18) into Equation (16), one obtains:

$$\begin{aligned}\frac{d^2T}{dt^2}e^{-2t} - \frac{dT}{dt}e^{-2t} + Ae^{-t}\frac{dT}{dr}e^{-t} &= \frac{d^2T}{dt^2}e^{-2t} - \frac{dT}{dt}e^{-2t} + A\frac{dT}{dr}e^{-2t} \\ &= \frac{d^2T}{dt^2}e^{-2t} + (A-1)\frac{dT}{dt}e^{-2t} = 0\end{aligned} \tag{19}$$

or Equation (19) can be rewritten as follows:

$$T'' + (A - 1)T' = 0 \tag{20}$$

$$\frac{d\left(\frac{dT}{dt}\right)}{dt} = (1 - A)\frac{dT}{dt} \tag{21}$$

By considering $\frac{dT}{dt} = X$, the following equations are expressed sequentially.

$$X = e^{(1-A)t + c_1} \tag{22}$$

$$T'(t) = e^{(1-A)t+c_1} \tag{23}$$

$$T(t) = \frac{e^{(1-A)t+c_1}}{(1 - A)} + c_2 \tag{24}$$

$$T(r) = \frac{e^{(1-A)\ln r + c_1}}{(1 - A)} + c_2 \tag{25}$$

Finally, the temperature distribution is:

$$T(r) = \frac{e^{-m_{TC}\ln r + c_1}}{-m_{TC}} + c_2 \tag{26}$$

where $c_1$ and $c_2$ are constants, which are found by applying the boundary condition.

## 4. Thermal Stress and Strain Relations

The thermal stress and strain were determined using the in-house FE code, and the effect of the material gradation was studied as well. Equations (27) and (28) present the thermal strain and stress in an FG disk, respectively [42].

$$\varepsilon^T = \alpha(r)T(r) \tag{27}$$

$$\sigma^T = \frac{E(r)}{(1 - \upsilon^2)}[(1 + \upsilon)\alpha(r)T(r)] \tag{28}$$

where $E(r) = E_\bullet r^{m_{YM}}$ and $\alpha(r) = \alpha_\bullet r^{m_{TE}}$. $\alpha_\bullet$, $m_{TE}$, $E_\bullet$ and $m_{YM}$ are material parameters, and $\upsilon$ is Poisson's ratio.

## 5. Numerical Results and Discussion

### 5.1. Material Property Variations in an FG Disk

In this case, the values of $\frac{r_i}{r_o} = 0.2$ and $\frac{r_i}{h} = 0.2$ were used, where $r_i$ and $r_o$ are the inner and outer radii, respectively, and h is the thickness of a hollow FG brake disk. The material properties of the inner and outer surfaces as metals and ceramics are shown in Table 1 [8], and the FG gradation material properties were calculated and are shown in Table 2. Poisson's ratio was constant in the rotating disk.

**Table 1.** Material properties of the inner and outer surfaces [8].

| **Material Properties** | **E (GPa)** | $\upsilon$ | $\alpha\left(\frac{1}{K}\right)$ | $K\left(\frac{W}{mK}\right)$ |
|---|---|---|---|---|
| Ceramic (outer surface) | 117.0 | 0.3 | $7.11 \times 10^{-6}$ | 2.036 |
| Metal (inner surface) | 66.2 | 0.3 | $10.3 \times 10^{-6}$ | 18.1 |

**Table 2.** FG gradation material properties.

| $K_\bullet$ | $m_{TC}$ | $\alpha_\bullet$ | $m_{TE}$ | $E_\bullet$ | $m_{YM}$ |
|---|---|---|---|---|---|
| 2.036 | −1.3575 | $7.11 \times 10^{-6}$ | −0.23 | 117 | 0.3539 |

Figure 4 shows the variations in non-dimensional material properties along the non-dimensional radius ($r/r_o$). The material properties were non-dimensionalized by dividing the material properties at the outer surface of the FG rotating disk. Young's modulus increases, and the thermal properties decrease along the radius of the disk when $m_{YM} = 0.3539$, $m_{TE} = -0.23$, and $m_{TC} = -1.3575$. These values correspond to the FGM used in this study. However, a material gradation study was performed, and the effects of each parameter on the material properties are shown in Figure 4. The effects of $m_{TC}$, $m_{TE}$, and $m_{YM}$ on the temperature distribution, thermal strain, and thermal stress will be discussed later in this section.

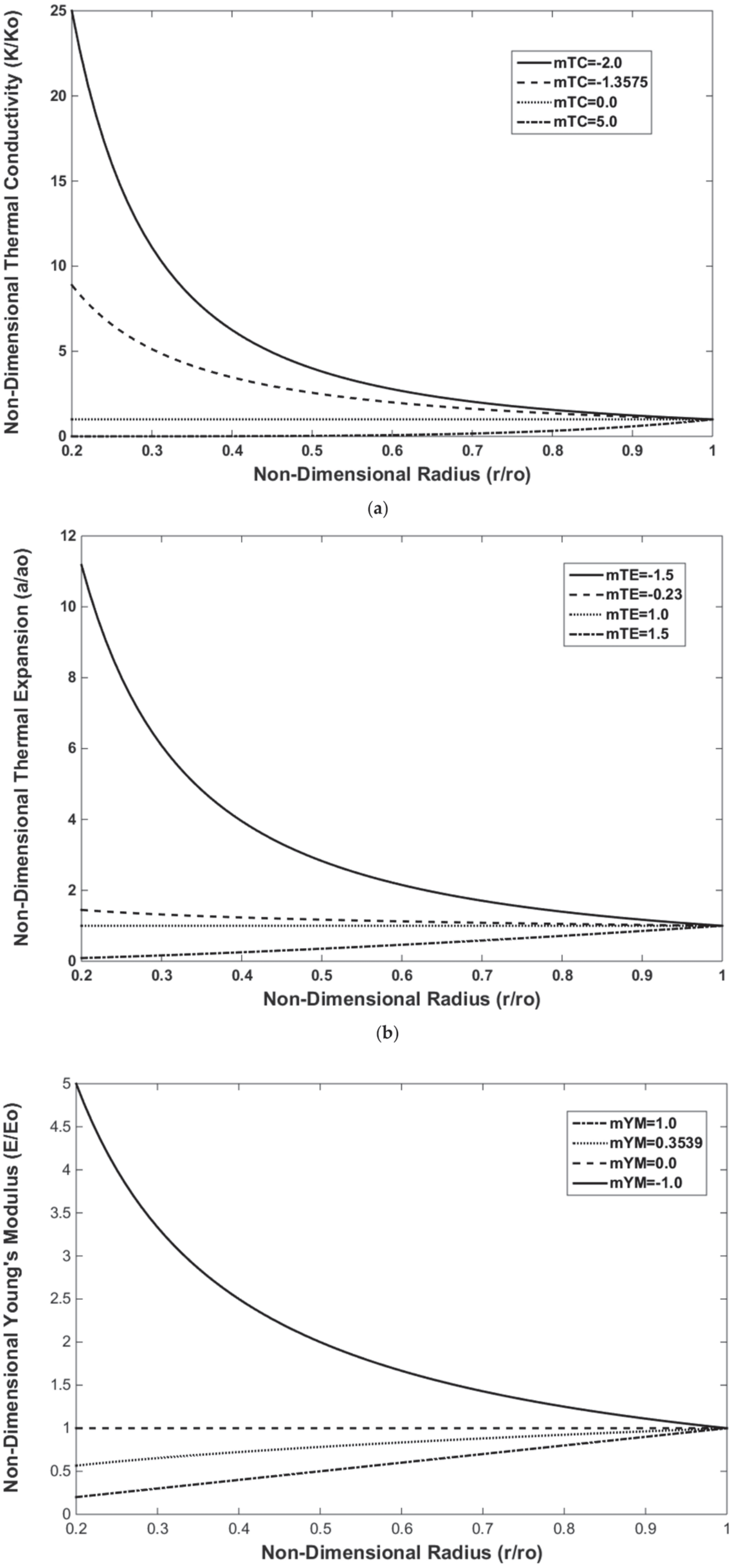

(**a**)

(**b**)

(**c**)

**Figure 4.** Variations in material properties in FG rotating disks along the radius: (**a**) thermal conductivity; (**b**) thermal expansion; (**c**) Young's modulus.

### *5.2. Numerical Results of the Three Methods*

At the inner surface, the temperature was zero (T = 0 °C); at the outer surface, the temperature was 100 °C (T = 100 °C). Figure 5 shows the temperature distribution of the FG disk, which was determined by the three mentioned methods, namely the in-house finite element program, ANSYS, and analytical solution. Figure 5 shows that the values of $m_{YM} = 0.3539$, $m_{TE} = -0.23$, and $m_{TC} = -1.3575$ were used. As observed, the results were compared and demonstrate the accuracy of the FEMs used in this study. Figure 5 shows that the results presented by the in-house code compared well with the other two methods, and the accuracy of the in-house code was also tested.

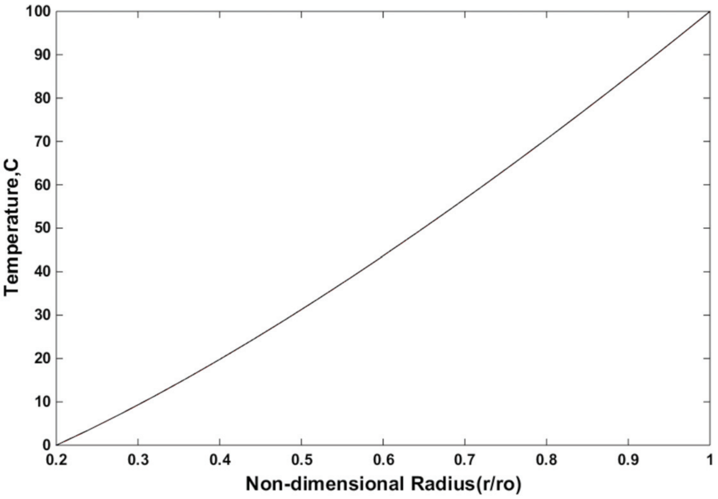

**Figure 5.** Temperature distribution using three methods for $m_{YM} = 0.3539$, $m_{TE} = -0.23$, and $m_{TC} = -1.3575$.

The thermal strain and thermal stress of the FG disk are presented in Figures 6 and 7, respectively. The thermal strain and thermal stress were assessed using the in-house finite element program. The thermal strain and stress have the same trend that exists for temperature along the radius. As expected, and observed in Figures 6 and 7, the maximum values of thermal strain and thermal stress were obtained at the outer surface, where the maximum temperature was applied.

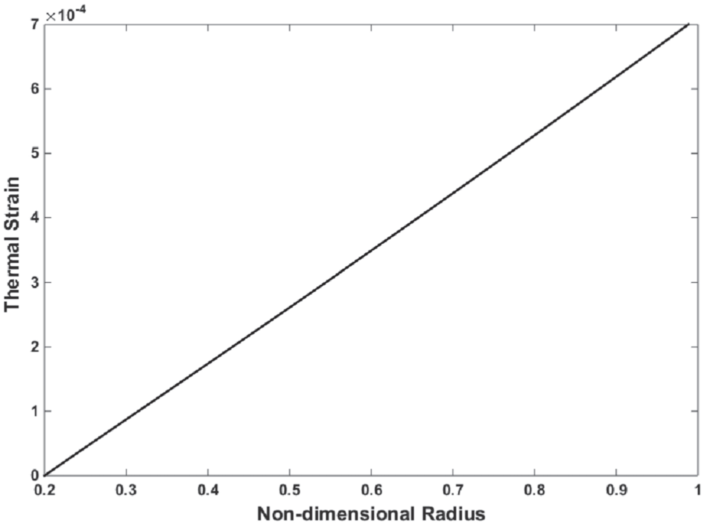

**Figure 6.** Thermal strain of the FG disk versus the non-dimensional radius for $m_{YM} = 0.3539$, $m_{TE} = -0.23$, and $m_{TC} = -1.3575$.

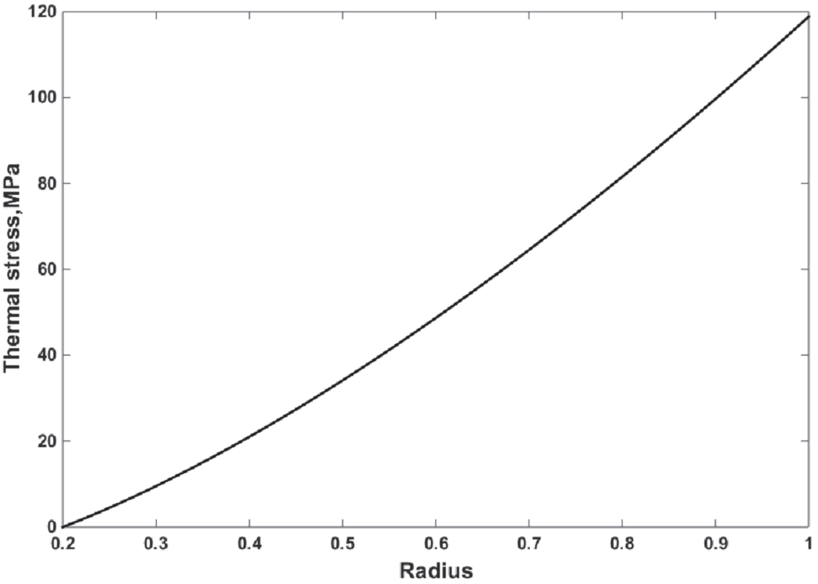

**Figure 7.** Thermal stress of the FG disk versus the non-dimensional radius for $m_{YM} = 0.3539$, $m_{TE} = -0.23$, and $m_{TC} = -1.3575$.

### *5.3. Material Gradation Parametric Study*

The effects of $m_{TC}$, $m_{TE}$, and $m_{YM}$ were investigated on the distributions of the temperature, thermal strain, and thermal stress, respectively. The in-house FEM was used, and the results are shown in Figures 8–10. The effect of the $m_{TC}$ on the temperature distribution is shown in Figure 8. The temperature from zero at the inner surface rises to 100 °C at the outer surface of the FGMs. The thermal conductivity coefficient decreases with increasing $m_{TC}$ (Figure 4a). As observed, the temperature distribution decreases with the decrease in $m_{TC}$. This trend can be justified following Equation (14), whereby the temperature decreases with the increasing thermal conductivity coefficient. Notably, $m_{TC} = 0.0$ is attributed to the non-FGM and when the thermal conductivity is distributed uniformly along the radius.

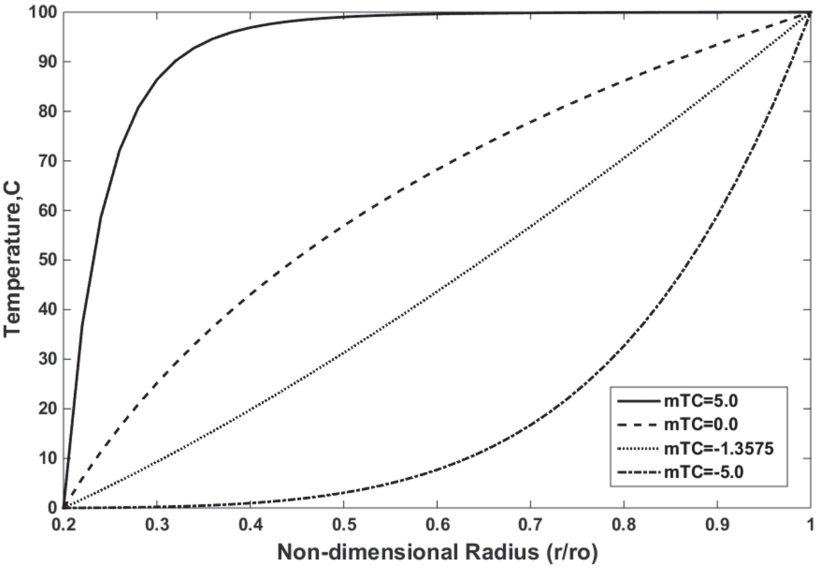

**Figure 8.** Effect of the $m_{TC}$ on the temperature distribution in FGMs for $m_{YM} = 0.3539$ and $m_{TE} = -0.23$.

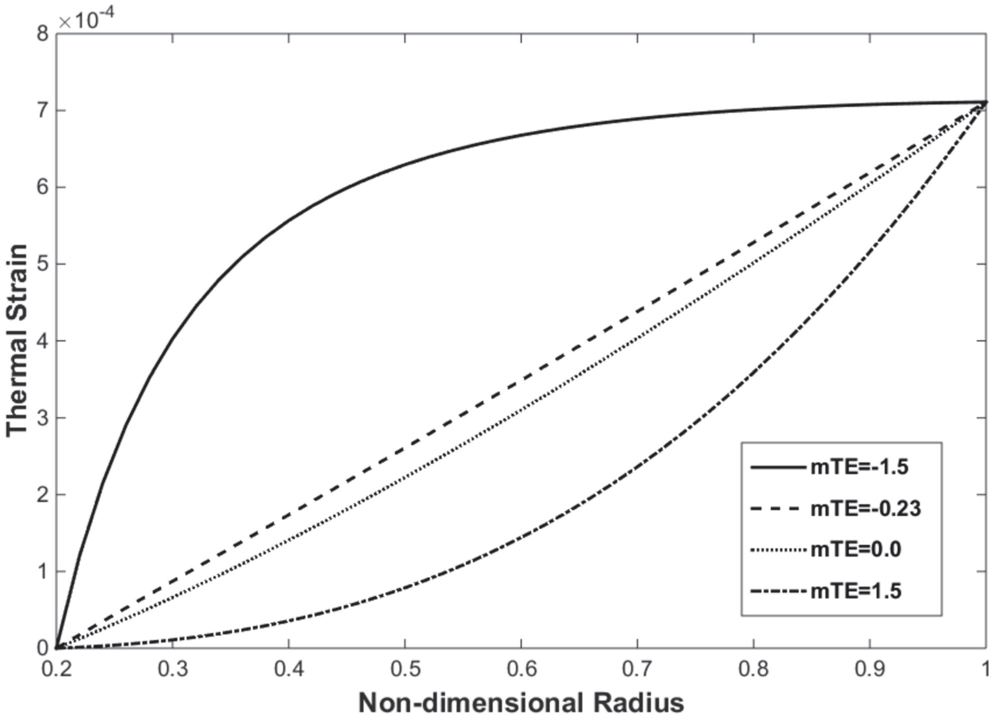

**Figure 9.** Effect of the $m_{TE}$ on the thermal strain distribution for $m_{YM} = 0.3539$ and $m_{TC} = -1.3575$.

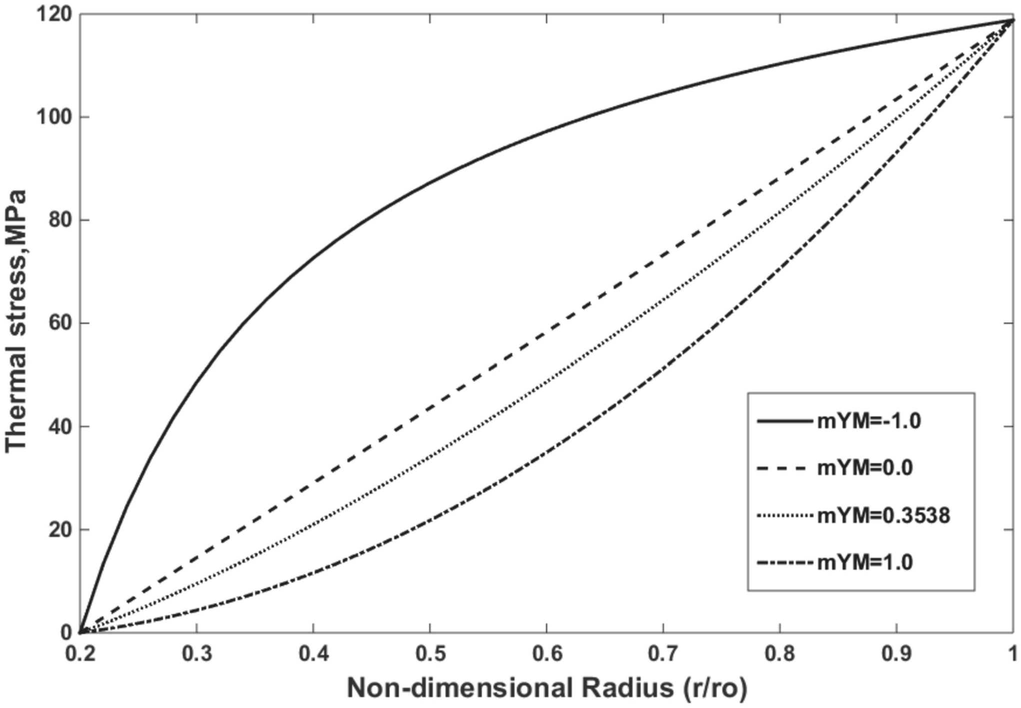

**Figure 10.** Effect of the $m_{YM}$ on the thermal stress distribution for $m_{TE} = -0.23$ and $m_{TC} = -1.3575$.

The effect of the $m_{TE}$ on the thermal strain distribution is shown in Figure 9. The thermal strain decreases with increasing $m_{TE}$. As observed in Figure 4b, the thermal expansion coefficient decreases with increasing $m_{TE}$ along the radius in the FG rotating disks. This trend helps decrease the thermal strain with the increase in $m_{TE}$ following Equation (27). The thermal expansion coefficient is constant along the radius when $m_{TE} = 0.0$, but this value does not correspond to the non-FGM because other material properties such as Young's modulus and coefficient of thermal conductivity vary along the radius.

The effect of the $m_{YM}$ on the thermal stress distribution is shown in Figure 10. The thermal stress decreases with the increasing $m_{YM}$. As observed in Figure 4c, the Young's modulus decreases with the increasing $m_{YM}$ along the radius in the FG rotating disks. This phenomenon helps decrease the thermal stress with the increase in $m_{YC}$ following Equation (28). The Young's modulus is constant along the radius when $m_{YM} = 0.0$, but this value does not correspond to the non-FGM because other properties such as the thermal conductivity and thermal expansion coefficients vary along the radius.

The in-house finite element program performs a post-processing analysis in a more efficient and convenient manner than through a simulation in a finite element software program such as ANSYS. For example, an optimization analysis can be carried out to minimize the thermal strain and stress while the stiffness of the plate is maintained. Such an algorithm can be used to calculate the thermal strain and stress, as well as the stiffness, for various ranges of material properties in an FG disk. Appropriate criteria to select the most suitable properties can be applied to present the material properties.

## 6. Conclusions

In this study, the temperature, thermal stress, and strain distributions of an FG disk were determined under an applied thermal condition. The material properties of the FG disk varied along the radial direction following the power law distribution. The inner and outer surfaces of the disk were assumed to be fully metal and fully ceramic, respectively. Three methods were used, namely (i) an in-house finite element program, (ii) the APDL, and (iii) an analytical solution to present the temperature distribution and compare the results for the sake of validation. The thermal conductivity in an FGM varies along an element when using the in-house FE code in contrast with using a commercial FE software when the thermal conductivity is constant within an element. The thermal strain and thermal stress were determined using the in-house finite element program. The temperature distributions obtained using these methods were exactly the same. Thus, in the steady thermal analysis of the FG rotating disk, these three methods are worthwhile because the effect of every material gradation parameter on the results can be investigated when the material properties within an element vary. These findings can lead to improved designs in the future for the fabrication of FGMs subject to thermal loads. The in-house code can be used to perform an optimization analysis to minimize the thermal strain and stress while the stiffness of the plate is maintained. Several numerical examples can be run in a short time to identify the optimized values under various thermal conditions.

**Author Contributions:** Conceptualization, M.M.S., B.B.S. and P.D.W.; Formal analysis, M.M.S., A.S., B.B.S. and P.D.W.; Funding acquisition, P.D.W.; Investigation, M.M.S., A.S., B.B.S. and P.D.W.; Methodology, M.M.S. and A.S.; Resources, P.D.W.; Software, B.B.S.; Supervision, B.B.S. and P.D.W.; Visualization, M.M.S., B.B.S., A.S. and P.D.W.; Writing—original draft, M.M.S., B.B.S. and P.D.W.; Writing—review & editing, M.M.S., B.B.S. and P.D.W. All authors have read and agreed to the published version of the manuscript.

**Funding:** Natural Sciences and Engineering Research Council of Canada (NSERC, Project No: RGPIN-2016-06464).

**Institutional Review Board Statement:** Not applicable.

**Informed Consent Statement:** Not applicable.

**Data Availability Statement:** Not applicable.

**Acknowledgments:** This work was supported by the Natural Sciences and Engineering Research Council of Canada (NSERC, Project No: RGPIN-2016-06464).

**Conflicts of Interest:** The authors declare no conflict of interest.

## References

1. Suresh, S.; Mortensen, A. *Fundamentals of Functionally Graded Materials*; Massachusetts Institute of Materials; IOM Communications Ltd.: London, UK, 1998.
2. Reddy, J. Analysis of functionally graded plates. *Int. J. Numer. Methods Eng.* **2000**, *47*, 663–684. [CrossRef]
3. Saleh, B.; Jiang, J.; Fathi, R.; Al-Hababi, T.; Xu, Q.; Wang, L.; Song, D.; Ma, A. 30 Years of functionally graded materials: An overview of manufacturing methods, Applications and Future Challenges. *Compos. Part B Eng.* **2020**, *201*, 108376. [CrossRef]
4. Koizumi, M. The concept of FGM. *Ceram. Trans.* **1993**, *34*, 3–10.
5. Aerospace Specification Metals, Inc. Titanium Ti–6Al–2Sn–4Zr–2Mo, Duplex Annealed. Available online: http://asm.matweb.com/search/SpecificMaterial.asp?bassnum\protect$\relax\protect{\begingroup1\endgroup\@@over4}$MTA641 (accessed on 3 December 2003).
6. Bayat, M.; Saleem, M.; Bin Sahari, B.; Hamouda, A.M.; Mahdi, E. Thermo elastic analysis of a functionally graded rotating disk with small and large deflections. *Thin Walled Struct.* **2007**, *45*, 677–691. [CrossRef]
7. Bayat, M.; Saleem, M.; Sahari, B.; Hamouda, A.; Mahdi, E. Analysis of functionally graded rotating disks with variable thickness. *Mech. Res. Commun.* **2008**, *35*, 283–309. [CrossRef]
8. Jabbari, M.; Bahtui, A.; Eslami, M. Axisymmetric mechanical and thermal stresses in thick short length FGM cylinders. *Int. J. Press. Vessel. Pip.* **2009**, *86*, 296–306. [CrossRef]
9. Jabbari, M.; Bahtui, A.; Eslami, M.R. Axisymmetric Mechanical and Thermal Stresses in Thick Long FGM Cylinders. *J. Therm. Stress.* **2006**, *29*, 643–663. [CrossRef]
10. Zenkour, A. Stress distribution in rotating composite structures of functionally graded solid disks. *J. Mater. Process. Technol.* **2009**, *209*, 3511–3517. [CrossRef]
11. Eldeeb, A.; Shabana, Y.; Elsawaf, A. Thermo-elastoplastic behavior of a rotating sandwich disc made of temperature-dependent functionally graded materials. *J. Sandw. Struct. Mater.* **2021**, *23*, 1761–1783. [CrossRef]
12. Erdogan, F.; Wu, B.H. Crack problems in FGM layers under thermal stresses. *J. Therm. Stress.* **1996**, *19*, 237–265. [CrossRef]
13. Duc, N.D.; Bich, D.H.; Cong, P.H. Nonlinear thermal dynamic response of shear deformable FGM plates on elastic foundations. *J. Therm. Stress.* **2016**, *39*, 278–297. [CrossRef]
14. Yaghmourali, Y.V.; Ahmadi, N.; Abbaspour-Sani, E. A thermal-calorimetric gas flow meter with improved isolating feature. *Microsyst. Technol.* **2017**, *23*, 1927–1936. [CrossRef]
15. Choudhur, R.; Das, U.J.; Ceruti, A.; Piancastelli, L.; Frizziero, L.; Zanuccoli, G.; Ahmadpour, V. Visco-elastic effects on the three dimensional hydrodynamic flow past a vertical porous plate. *Int. Inf. Eng. Technol. Assoc.* **2013**, *31*, 1–8.
16. Shahzamanian, M.M.; Partovi, A.; Wu, P.D. Finite element analysis of elastic-plastic and fracture behavior in functionally graded materials (FGMs). *SN Appl. Sci.* **2020**, *2*, 2135. [CrossRef]
17. Swaminathan, K.; Sachin, H.; Rajanna, T. Buckling analysis of functionally graded materials by dynamic approach. *Mater. Today Proc.* **2021**, *45*, 172–178. [CrossRef]
18. Hirane, H.; Belarbi, M.-O.; Houari, M.S.A.; Tounsi, A. On the layerwise finite element formulation for static and free vibration analysis of functionally graded sandwich plates. *Eng. Comput.* **2021**, 1–29. [CrossRef]
19. Sweidan, F.B.; Ryu, H.J. One-step functionally graded materials fabrication using ultra-large temperature gradients obtained through finite element analysis of field-assisted sintering technique. *Mater. Des.* **2020**, *192*, 108714. [CrossRef]
20. Shivay, O.N.; Mukhopadhyay, S. A complete Galerkin's type approach of finite element for the solution of a problem on modified Green-Lindsay thermoelasticity for a functionally graded hollow disk. *Eur. J. Mech. A Solids* **2020**, *80*, 103914. [CrossRef]
21. Trabelsi, S.; Zghal, S.; Dammak, F. Thermo-elastic buckling and post-buckling analysis of functionally graded thin plate and shell structures. *J. Braz. Soc. Mech. Sci. Eng.* **2020**, *42*, 233. [CrossRef]
22. Durodola, J.; Attia, O. Deformation and stresses in functionally graded rotating disks. *Compos. Sci. Technol.* **2000**, *60*, 987–995. [CrossRef]
23. Shahzamanian, M.; Sahari, B.; Bayat, M.; Mustapha, F.; Ismarrubie, Z. Finite element analysis of thermoelastic contact problem in functionally graded axisymmetric brake disks. *Compos. Struct.* **2010**, *92*, 1591–1602. [CrossRef]
24. Shahzamanian, M.; Sahari, B.; Bayat, M.; Ismarrubie, Z.; Mustapha, F. Transient and thermal contact analysis for the elastic behavior of functionally graded brake disks due to mechanical and thermal loads. *Mater. Des.* **2010**, *31*, 4655–4665. [CrossRef]
25. Shahzamanian, M.M.; Sahari, B.B.; Bayat, M.; Mustapha, F.; Ismarrubie, Z.N. Elastic Contact Analysis of Functionally Graded Brake Disks Subjected to Thermal and Mechanical Loads. *Int. J. Comput. Methods Eng. Sci. Mech.* **2013**, *14*, 10–23. [CrossRef]
26. Genao, F.Y.; Kim, J.; Żur, K.K. Nonlinear finite element analysis of temperature-dependent functionally graded porous micro-plates under thermal and mechanical loads. *Compos. Struct.* **2021**, *256*, 112931. [CrossRef]
27. Najibi, A.; Alizadeh, P.; Ghazifard, P. Transient thermal stress analysis for a short thick hollow FGM cylinder with nonlinear temperature-dependent material properties. *J. Therm. Anal.* **2021**, *146*, 1971–1982. [CrossRef]
28. Babaee, A.; Jelovica, J. Nonlinear transient thermoelastic response of FGM plate under sudden cryogenic cooling. *Ocean Eng.* **2021**, *226*, 108875. [CrossRef]
29. Bidgoli, M.O.; Arefi, M.; Loghman, A. Thermoelastic behaviour of FGM rotating cylinder resting on friction bed subjected to a thermal gradient and an external torque. *Aust. J. Mech. Eng.* **2021**, *19*, 1–9. [CrossRef]
30. Sarkar, P.R.; Rahman, A.S. Effect of magnetic field on the thermo-elastic response of a rotating FGM Circular disk with non-uniform thickness. *J. Strain Anal. Eng. Des.* **2022**, *57*, 116–131. [CrossRef]

31. Bezzie, Y.M.; Woldemichael, D.E.; Chekol, E.T.; Admass, S.A.; Selvaraj, S.K.; Paramasivam, V. Effect of volumetric fraction index on temperature distribution in thick-walled functionally graded material made cylinder. *Mater. Today Proc.* **2021**, *46*, 7442–7447. [CrossRef]
32. Swaminathan, K.; Sangeetha, D. Thermal analysis of FGM plates—A critical review of various modeling techniques and solution methods. *Compos. Struct.* **2017**, *160*, 43–60. [CrossRef]
33. Jabbari, M.; Karampour, S.; Eslami, M.R. Steady state thermal and mechanical stresses of a poro-piezo-FGM hollow sphere. *Meccanica* **2013**, *48*, 699–719. [CrossRef]
34. Jabbari, M.; Karampour, S.; Eslami, M.R. Radially Symmetric Steady State Thermal and Mechanical Stresses of a Poro FGM Hollow Sphere. *ISRN Mech. Eng.* **2011**, *2011*, 1–7. [CrossRef]
35. Bayat, Y.; Ghannad, M.; Torabi, H. Analytical and numerical analysis for the FGM thick sphere under combined pressure and temperature loading. *Ingenieur-Archiv* **2012**, *82*, 229–242. [CrossRef]
36. Delouei, A.A.; Emamian, A.; Karimnejad, S.; Sajjadi, H.; Jing, D. Two-dimensional temperature distribution in FGM sectors with the power-law variation in radial and circumferential directions. *J. Therm. Anal.* **2021**, *144*, 611–621. [CrossRef]
37. Shahzamanian, M.M.; Sahari, B.B.; Bayat, M.; Mustapha, F.; Ismarrubie, Z.N.; Shahrjerdi, A. Steady state and thermoelastic analysis of a functionally graded rotating disk. In Proceedings of the World Engineering Congress 2010, Malaysia Conference on Aerospace and Mechanical Engineering, Kuching, Sarawak, Malaysia, 2–5 August 2010; pp. 222–228.
38. Kordkheili, S.H.; Naghdabadi, R. Thermoelastic analysis of a functionally graded rotating disk. *Compos. Struct.* **2007**, *79*, 508–516. [CrossRef]
39. Delouei, A.A.; Emamian, A.; Karimnejad, S.; Sajjadi, H.; Jing, D. Asymmetric Conduction in an Infinite Functionally Graded Cylinder: Two-Dimensional Exact Analytical Solution Under General Boundary Conditions. *J. Heat Transf.* **2020**, *142*, 044505. [CrossRef]
40. Kwon, Y.W.; Bang, H. *The Finite Element Method Using MATLAB*; CRC Press: Boca Raton, FL, USA, 2018.
41. Available online: https://github.com/mmshahzamanian/FGM-disc_FEM_thermal-analysis/tree/main (accessed on 22 July 2022).
42. Bayat, M.; Saleem, M.; Bin Sahari, B.; Hamouda, A.M.; Mahdi, E. Mechanical and thermal stresses in a functionally graded rotating disk with variable thickness due to radially symmetry loads. *Int. J. Press. Vessel. Pip.* **2009**, *86*, 357–372. [CrossRef]

materials

MDPI

Article

# Hybrid Data-Driven Deep Learning Framework for Material Mechanical Properties Prediction with the Focus on Dual-Phase Steel Microstructures

**Ali Cheloee Darabi [1], Shima Rastgordani [1], Mohammadreza Khoshbin [2], Vinzenz Guski [1] and Siegfried Schmauder [1,*]**

[1] Institute for Materials Testing, Materials Science and Strength of Materials, University of Stuttgart, Pfaffenwaldring 32, 70569 Stuttgart, Germany
[2] Department of Mechanical Engineering, Shahid Rajaee Teacher Training University, Lavizan, Tehran 1678815811, Iran
* Correspondence: siegfried.schmauder@imwf.uni-stuttgart.de

**Abstract:** A comprehensive approach to understand the mechanical behavior of materials involves costly and time-consuming experiments. Recent advances in machine learning and in the field of computational material science could significantly reduce the need for experiments by enabling the prediction of a material's mechanical behavior. In this paper, a reliable data pipeline consisting of experimentally validated phase field simulations and finite element analysis was created to generate a dataset of dual-phase steel microstructures and mechanical behaviors under different heat treatment conditions. Afterwards, a deep learning-based method was presented, which was the hybridization of two well-known transfer-learning approaches, ResNet50 and VGG16. Hyper parameter optimization (HPO) and fine-tuning were also implemented to train and boost both methods for the hybrid network. By fusing the hybrid model and the feature extractor, the dual-phase steels' yield stress, ultimate stress, and fracture strain under new treatment conditions were predicted with an error of less than 1%.

**Keywords:** deep learning; material properties; dual-phase steel; micromechanical modeling; phase field simulation

## 1. Introduction

Dual-phase (DP) steels are a family of high-strength low-alloy steels that exhibit high strength and good formability. They have, therefore, found extensive use in the automotive industry [1]. Their promising properties can be attributed to their microstructure, which consists of hard martensite islands and a soft ferrite matrix. This microstructure leads to high formability, continuous yielding behavior, high strength, high strain hardening rate, and low yield stress-to-tensile strength ratio [2].

One of the fundamental objectives of materials science and engineering is the development of reliable working models which connect process parameters, microstructures, and material properties. Many models have been developed for analyzing each individual domain. For example, phase field modeling (PFM) can simulate the phase transformations during heat treatment [3,4], and finite element analysis (FEA), can be used to obtain the mechanical response of a microstructure [5]. These have also been combined [6,7]. This generally takes the form of a PFM analysis obtaining a representative volume element (RVE) of a multiphase material that has undergone heat treatment and the resulting microstructure being loaded with specific boundary conditions to obtain its fracture stress using FEA.

These models have an inherent deficiency that they only work on a limited part of the problem and connecting all the effects can be very challenging. Furthermore, they can only be used to analyze a particular configuration after it has been conceived. They do not have any predictive power and must be run many times to obtain a suitable model. Currently, using these approaches for designing new materials is very costly, time-consuming, and requires substantial lab work.

These problems can be avoided by assigning the modern advancements of machine learning methods [8]. Machine learning and deep learning, and especially their subcategories, such as artificial neural networks (ANN) and convolutional neural networks (CNN), are being introduced in materials science and engineering because they can accelerate the processes and, in some cases, reduce the required physical experiments [9–11]. These models can also automate different layers of material characteristic investigations [12]. Different scaled microstructure studies, from macro and continuum levels to the atomic and micro scales, could benefit from the recent developments in ANN techniques [13,14]. Additionally, methods such as phase field modeling could assist the researchers in 2D and 3D simulations, enhancing the dataset for further steps to an ANN model [15,16]. These new tools make the final aim of tailoring the material features achievable and within reach.

The classic paradigm of microstructural behavior studies needs to be revised. Recent material informatics developments could magnify machine learning approaches' vital role in quantitative microstructural subjects [17–19]. Thus, the need to expand the knowledge of neural network applications in materials science and engineering is evident. In the last decade, various methods have been implemented to predict the characteristics of different materials [20].

This work represents a timely, advanced computational methodology with a wide range of implications to help the materials community [21]. The novelty of this work is twofold: we use validate and utilize simulations of heat treatment to generate microstructures, which reduces the cost associated with creating a machine learning dataset. Additionally, we introduce a hybrid machine learning model and apply it to a materials science problem. In the first step of this study, since having an extensive data set for training is the prerequisite of a deep neural network, about 1000 images were generated with a phase field model. About 10 percent of the whole data set was randomly chosen for the testing set. For this study, different models, including simple CNN and transfer learning methods, were investigated and two algorithms with faster optimization behavior, VGG16 [22] and ResNet [23], were paralleled and named "Hybrid Model". Not every model showed promising results regarding the prediction of tensile stress and fracture strain. However, with an error of less than 1% for the prediction of ultimate stress and yield stress for the testing data, and about 0.5% for the training set, this model could respond ideally. This fast and accurate technique could be applied to different alloy data sets, giving scientists a better overview of the metal characteristics.

## 2. Data Generation

### 2.1. Overview

In this study, a large number of phase field (PF) heat treatment simulations were performed to generate artificial DP steel microstructures. These microstructures were then analyzed using finite element analysis (FEA) to obtain the mechanical response of those steels. Consequently, a dataset containing process parameters, resulting microstructure, and mechanical properties was created, which was then used in Section 3 to train a machine learning system. A high-level illustration of the process is shown in Figure 1.

The following sections describe and validate the PF and FEA models and then explain how the two data pipelines work together to create the final dataset.

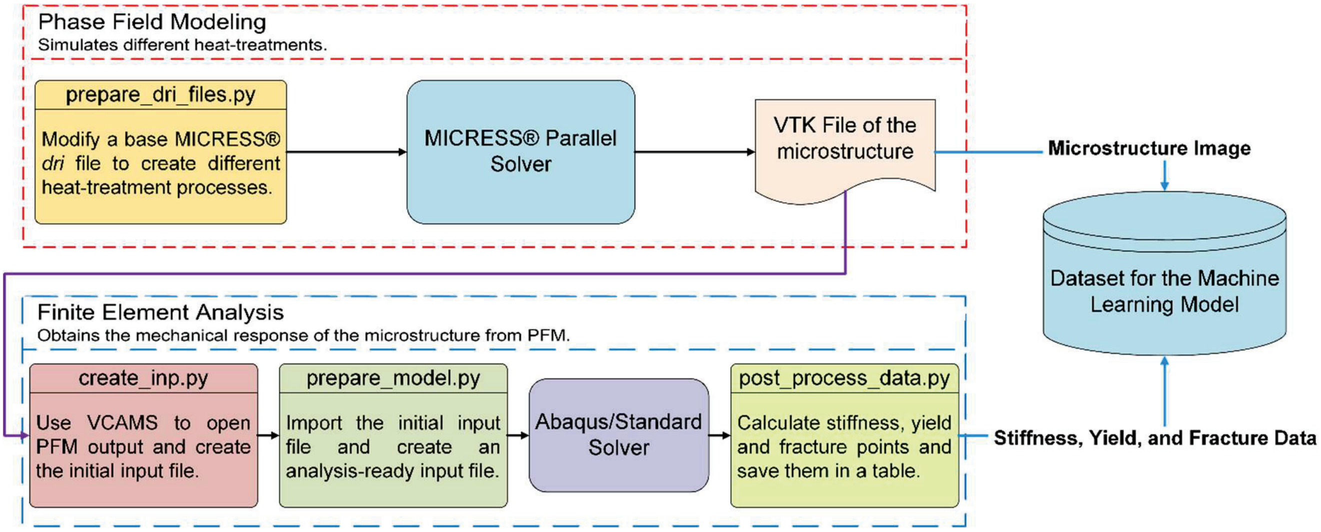

**Figure 1.** Workflow of the microstructure data generation with different heat treatment conditions.

## 2.2. Multiphase Field Simulation

### 2.2.1. Basic Theory

The phase field equation was implemented by Steinbach et al. [24,25] to predict microstructure evolution. In this approach, a phase field parameter $\varphi$ is defined for each phase, which changes between 0 and 1 during the process. Parameter $\varphi_\alpha$ indicates the local fraction of phase ($\alpha$) in a grain, which means the sum of the local fraction of phases is equal 1 ($\sum \varphi_\alpha = 1$). In this paper, MICRESS® software, version 7, was used for the phase field simulation, and the rate of parameter $\varphi$ during the process is shown as Equation (1) [26]:

$$\dot{\varphi}_\alpha = \sum_{\alpha\neq\beta}^{n} M^{\varphi}_{\alpha\beta}\left[b\Delta G_{\alpha\beta} - \sigma_{\alpha\beta}\left(K_{\alpha\beta}+A_{\alpha\beta}\right) + \sum_{\alpha\neq\beta\neq\gamma}^{\upsilon} j_{\alpha\beta\gamma}\right], \tag{1}$$

where the parameters $\alpha$, $\beta$, and $\gamma$ show the different phases, and n is the number of phases in the simulation. Parameter $M^{\varphi}_{\alpha\beta}$, given as Equation (2), is related to the interface mobility between phases $\alpha$ and $\beta$, which is a function of the kinetic coefficient in the Gibbs–Thomson equation:

$$M^{\varphi}_{\alpha\beta} = \frac{\mu^G_{\alpha\beta}}{1 + \frac{\mu^G_{\alpha\beta}\eta\Delta s_{\alpha\beta}}{8}\left\{\sum_i m^l_i \sum_i \left[\left(D^{ij}_\alpha\right)^{-1}(1-k_j)c_{j\alpha}\right]\right\}}, \tag{2}$$

where $\eta$ and $\Delta s_{\alpha\beta}$ are the thickness of the interface and entropy of fusion between the phases, respectively. Additionally, the parameters $m^l_i$ and $D^{ij}_\alpha$ represent the liquidus line slop for component $i$ and the diffusion matrix, respectively, and $k_j$ is related to the partition coefficient.

The expression inside the brackets represents the required force for moving the interface between phases $\alpha$ and $\beta$. Parameter $b$ is a pre-factor and is calculated using Equation (3). The parameters $\Delta G_{\alpha\beta}$ and $K_{\alpha\beta}$ show the difference in Gibbs energy and pairwise curvature between the two phases, as indicated in Equations (4) and (5), respectively. $J_{\alpha\beta\gamma}$ is related to the triple junction between three phases through Equation (6):

$$b = \frac{\pi}{\eta}\left(\varphi_\alpha + \varphi_\beta\right)\sqrt{\varphi_\alpha\varphi_\beta}, \tag{3}$$

$$\Delta G_{\alpha\beta} = \frac{1}{\nu^m}\left(\mu^0_\beta - \mu^0_\alpha\right), \tag{4}$$

$$K_{\alpha\beta} = \frac{\pi^2}{2\eta^2}\left(\varphi_\beta - \varphi_\alpha\right) + \frac{1}{2}\left(\nabla^2\varphi_\beta - \nabla^2\varphi_\alpha\right), \tag{5}$$

$$J_{\alpha\beta\gamma} = \frac{1}{2}(\sigma_{\beta\gamma} - \sigma_{\alpha\gamma})\left(\frac{\pi^2}{\eta^2}\varphi_\gamma + \nabla^2\varphi_\gamma\right). \tag{6}$$

### 2.2.2. Validation of PF Simulations

Before using the PF model for generating microstructures under different heat treatment conditions, the model's accuracy for simulating the basic heat treatment must be validated against experiments. Here, the step quenching heat treatment process routine for the production of DP steel from low carbon steel, shown in Figure 2, is simulated using phase field simulation in MICRESS software. Afterwards, the same heat treatment procedure is also carried out experimentally, and the resulting microstructures are compared.

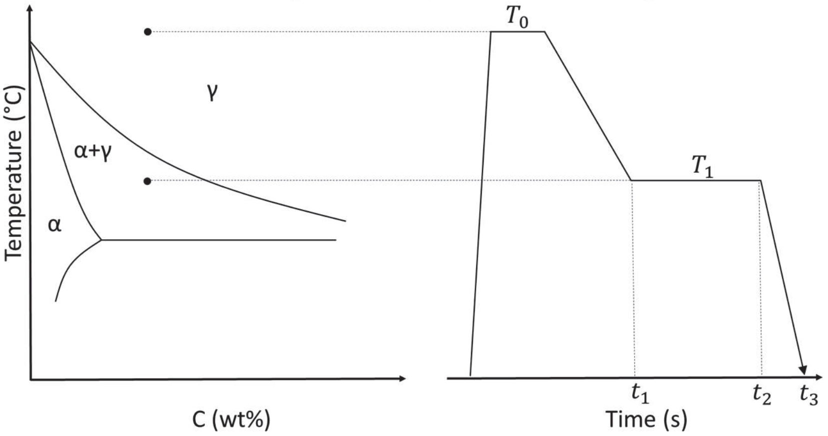

**Figure 2.** Schematic view of the step-quenching heat treatment process routine.

The base material used in the PF simulations was a ferritic–pearlitic steel with the chemical composition given in Table 1. To reduce computational costs, the heat treatment simulations started from the fully austenitic microstructure and the morphology for this state was calculated using MatCalc software, version 6.03 [27]. Afterwards, the step quenching heat treatment was simulated, resulting in the formation of ferrite and martensite phases. It was assumed that the remaining austenite phase is wholly transformed into martensite below the martensite temperature. Additionally, based on the chemical composition given in Table 1 and using the equation in the study [28], the martensite starting temperature ($M_s$) was calculated to be 417.34 °C. For this particular heat treatment based on the step quenching shown in Figure 2, first the fully austenitic microstructure was cooled from 1100 °C to 770 °C, then held for 10 min, and finally quenched in water to room temperature.

**Table 1.** Chemical composition of the low-carbon steel used for validating the PF model.

| Element | C | Mn | Si | P | S | Cr | Mo | V | Cu | Co |
|---|---|---|---|---|---|---|---|---|---|---|
| wt% | 0.2 | 1.1 | 0.22 | 0.004 | 0.02 | 0.157 | 0.04 | 0.008 | 0.121 | 0.019 |

In this study, a binary phase diagram was implemented for the simulation. Table 2 provides information on carbon and magnesium concentration and proportionality driving pressure ($L_{ij}$) at $T_1$, which were calculated using MatCalc. Some other phase interaction properties, such as interface kinetic coefficient and interface mobility, were extracted from the literature and are shown in Table 3. For carbon's diffusion properties, the maximal diffusion coefficient ($D_0$) in ferrite and austenite were set to $2.20 \times 10^{-4}$ and $0.15 \times 10^{-4}$ m$^2$/s; and the activation energy for diffusion ($Q$) were set to 122.5 and 142.1 KJ/mol, respectively [29–31]. The diffusion of magnesium was ignored in this study and the "phase concentration" model in MICRESS and periodic boundary conditions (named PPPP in MICRESS) were used. Figure 3a–e illustrates the sample progression of the heat treatment.

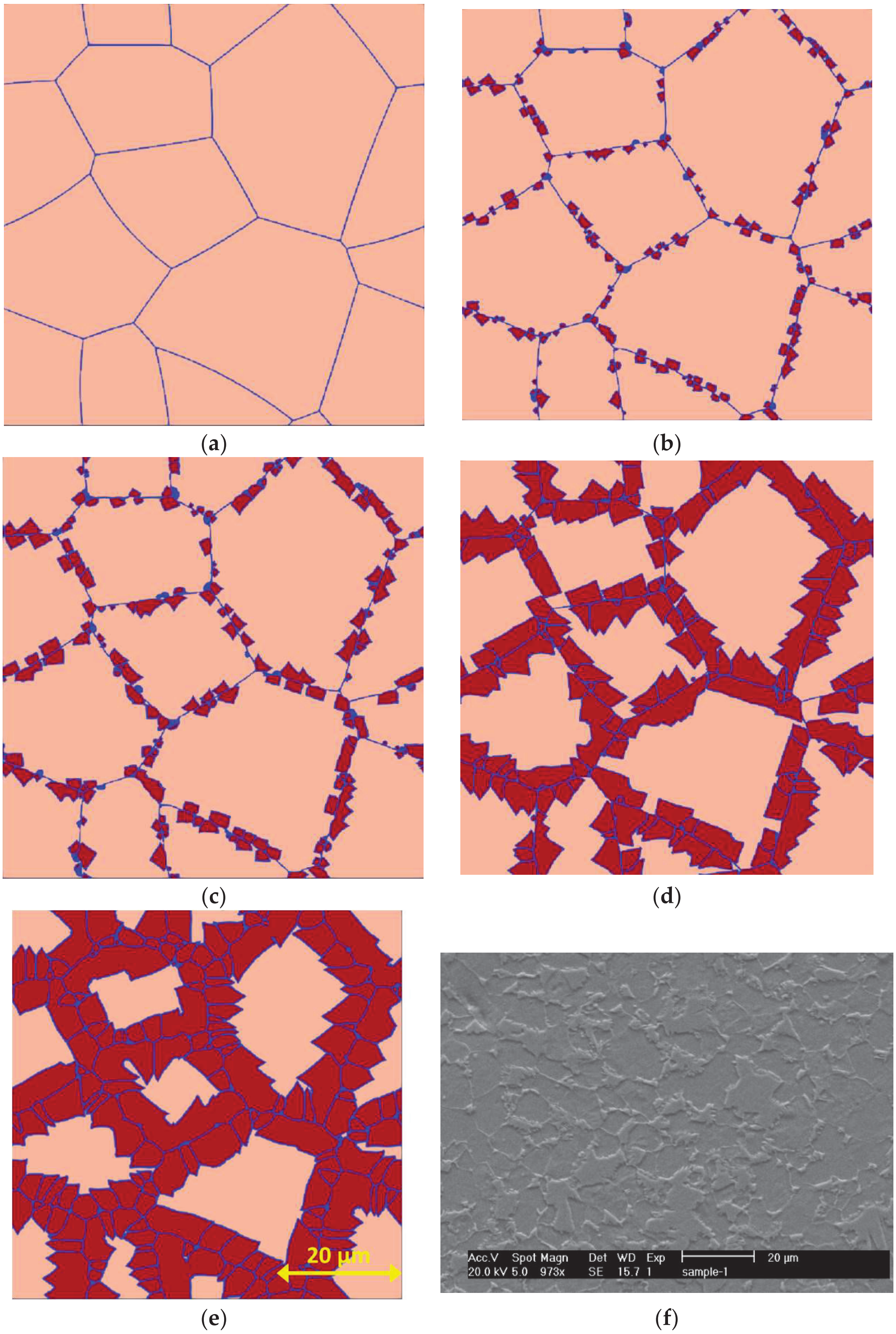

(**a**) (**b**)

(**c**) (**d**)

(**e**) (**f**)

**Figure 3.** Progression of the results of the PF simulation: (**a**) initial state, (**b**) 15 s, (**c**) 1 min, (**d**) 10 min, and (**e**) after quenching; and (**f**) SEM image of a sample undergoing the same heat treatment.

**Table 2.** Linearized data for the phase diagram at $T_1 = 1043$.

| | Phase Boundary | $\alpha/\gamma + \alpha$ | $\gamma/\alpha + \gamma$ |
|---|---|---|---|
| **Carbon ($C_{ij}$)** | **Concentration (wt%)** | 0.0048 | 0.365 |
| | **Slope (°K/wt%)** | −13,972.00 | −188.80 |
| **Manganese ($Mn_{ij}$)** | **Concentration (wt%)** | 1.58 | 3.78 |
| | **Slope (°K/wt%)** | −100.03 | −23.55 |
| | $L_{ij}$ **(J cm$^{-3}$)** | 0.238 | |

**Table 3.** Interfacial parameters between ferrite (α) and austenite (γ) [3,32].

| Interface | α/α | α/γ | γ/γ |
|---|---|---|---|
| **Interfacial energy (J cm$^{-2}$)** | $7.60 \times 10^{-5}$ | $7.20 \times 10^{-5}$ | $7.60 \times 10^{-5}$ |
| **Mobility (cm$^4$J$^{-1}$s$^{-1}$)** | $5.00 \times 10^{-6}$ | $2.40 \times 10^{-4}$ | $3.50 \times 10^{-6}$ |

The only output taken from the PF models for the FEA is the final microstructure geometry. This means that to validate the PF models, it is only necessary to make sure they predict martensite volume fraction, average phase size, and morphology (banded or equiaxed) correctly. Figure 3e,f shows the simulated and experimental microstructures resulting from the described heat treatment. There is a good agreement between the results, as both microstructures have the same martensite volume fraction (34%), average phase size (15 μm) and morphology (equiaxed). This means that the utilized multiphase model can accurately predict the experimental results. Therefore, this validated model is used for simulating the final microstructure after undergoing heat treatment under different conditions.

### *2.3. FEM Simulation*

#### 2.3.1. FEA Parameters

This section describes the process of creating, analyzing, and validating micromechanical FEA models based on the PF simulations. After a microstructure is generated using PFM, it can be used as a representative volume element (RVE). The parameters for a single simulation are explained here, and the next section explains how a large number of simulations is performed.

The material properties of the ferrite and martensite phases are essential factors to consider. It is well known that they change with the process parameters [33,34], but to simplify the process, the flow curves were taken from DP600 steel, as shown in Figure 4, which was reported in a previous study [2]. Damage in the martensite phase was ignored, and the Johnson–Cook damage model was used for the ferrite phase. Since the test was executed at room temperature with constant strain rates, $D_4$ and $D_5$ were ignored and local fracture strain under uniaxial loading was predicted by [2] to be 0.4. Finally, $D_1$, $D_2$, and $D_3$ were found to be 0.17, 0.80, and −0.7, respectively. Darabi et al. [35] showed that there is no difference in stress–strain curves of RVEs loaded under periodic and symmetric boundary conditions. Therefore, symmetric (linear displacement) boundary conditions were applied to the RVE.

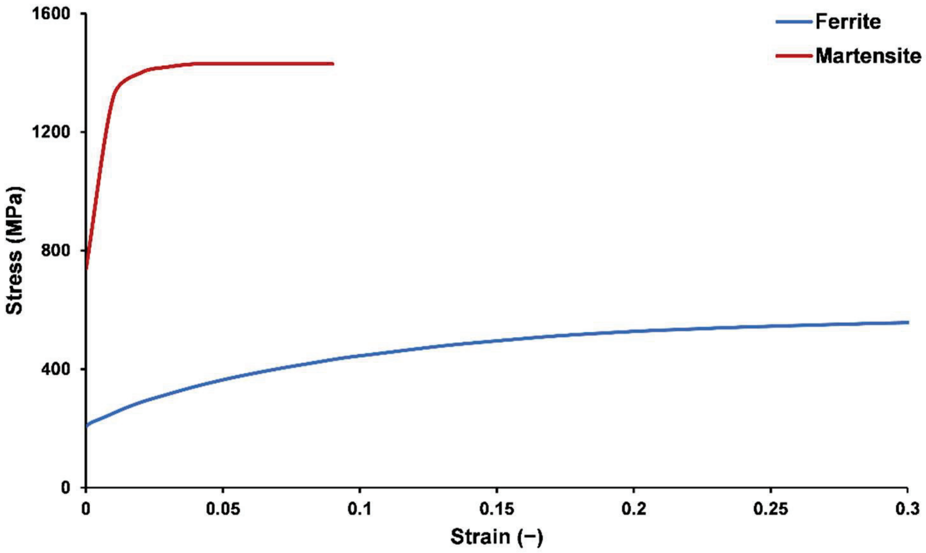

**Figure 4.** Flow curves of the ferrite and martensite phases used in micromechanical FEA [2].

### 2.3.2. Validation of the FE Simulation

The main outputs of the analysis were the yield strength, UTS, and fracture points. To obtain the mentioned properties, the model's equivalent plastic strain and von Mises stress were homogenized using the method described in our previous work [2] to obtain the stress–strain curve. Afterward, the model's Young's modulus was calculated based on the 2% offset method, and finally, the yield strength, UTS, and fracture points were found based on the curve.

Table 4 compares the experimental and numerical results, showing that the numerical model can predict the mechanical behavior of the simulated microstructure. Therefore, this micromechanical model can predict the mechanical behavior of microstructures generated using PF simulations.

**Table 4.** Comparison of mechanical behavior and experimental results.

| | Yield Stress (MPa) | Ultimate Stress (MPa) | Fracture Strain (−) |
|---|---|---|---|
| **Numerical** | 314.36 | 517.9 | 0.127 |
| **Experimental** | 323.7 | 530.1 | 0.131 |

## *2.4. Data Pipelines*

The main goal of PFM and FEA is to generate a large amount of reliable data for training and testing the machine learning models. Since the model parameters are determined and the validity of the models is examined, we can automate the process for each of the PFM and FEA data pipelines and connect them together to create the full dataset.

### 2.4.1. PFM Data Pipeline

The PFM parameters are based on the various points in Figure 2. Table 5 shows them with a short description and selected values. There is a total of four variable heat treatment parameters, which result in 1188 different data points. To automate such a large number of PFM analyses, a base MICRESS® driving (.dri) file was created and extensively tested. Afterwards, scripts were written that changed the parameters and saved new .dri files. Additionally, the PFM process was divided into two steps to reduce computational time. The first step was heat treatment, which was until the time $t_2$ in Figure 2 was reached, and the second step restarted the PFM analysis and quenched the microstructure. This procedure greatly reduces computational time because, although the second step had to be performed 1188 times, the first step was performed only 396 times. In the end, the microstructures were saved as VTK files, which were used as input for creating FEA models in Section 2.4.2. They were also saved as images to be directly used by the machine learning model. The PFM data pipeline is shown in the red section of Figure 1.

**Table 5.** Heat treatment parameters and their values. The units for temperatures, times, and cooling rates are Kelvin, seconds, and $\frac{K}{s}$, respectively.

| Parameter | Description | Values |
|---|---|---|
| $T_0$ | Initial temperature of the microstructure. | 1250 |
| $CR_{01}$ | Cooling rate between points 0 and 1. Not used directly. | −10, −5, −1 |
| $t_{01}$ | Number of seconds it takes to cool down from point 1 to point 2. | Calculated based on $CR_{01}$ |
| $T_1$ | Temperature of the microstructure in point 1. | 1000, 1010, 1020, 1030, 1040, 1050, 1060, 1070, 1080, 1090, 1100, 1110 |
| $t_{12}$ | Holding time between points 1 and 2 in seconds. | 10, 20, 30, 60, 300, 600, 900, 1800, 3600, 7200, 10,800 |
| $T_2$ | Temperature of the microstructure in point 2. | Equal to $T_1$ |
| $CR_{23}$ | Cooling rate between points 2 and 3 based on the quench media. Not used directly. | $Brine = -220$<br>$Water = -130$<br>$Oil = -50$ |
| $t_{23}$ | Number of seconds it takes to cool down from point 1 to point 2. | Calculated based on $QM$ |
| $T_3$ | Room temperature. | 298 |

### 2.4.2. FEA Data Pipeline

MICRESS® PFM software allows output to a number of different file formats. To enable the easy creation of FEA models, output is requested in The Visualization Toolkit (VTK) file format, which can be read using readily available software libraries. The output used for modeling was the “phas” variable, which shows the phase of each element, i.e., each element was either ferrite, martensite, or part of the phase interface. Interface elements were converted to ferrite in subsequent operations.

A Python script was written that extracted the phase distribution from the VTK file and passed it to the open-source VCAMS library, which created an Abaqus® input file containing the elements with the proper phase labels, as well as linear displacement boundary conditions. Another script was written for the Abaqus Python environment that opened the input file and defined the rest of the simulation parameters, such as the material assignment, etc. described in Section 2.3.1.

The main script then submitted the analysis and passed the final ODB to an Abaqus Python script that post-processed the results. This included homogenization of stress and strains using the method described in Ref. [2] to obtain the stress–strain curve, determine the elastic modulus based on the 2% offset method, and find the yield strength, UTS, in addition to fracture strains. These were then written to a file that mapped each model with its output. Pictures of the microstructure and the stress–strain curve were also saved so they can be audited if necessary. The FEA data pipeline is illustrated in the blue section of Figure 1.

## 3. Deep Learning Approaches

### *3.1. Introduction and Overview*

Inspired by brain biology, artificial neural networks (ANNs) allow for the modeling of complex patterns. Nowadays, various methods have also been applied to compare the different performances of AN networks in computational mechanics [36–38]. The attention paid to ANN in recent years has led to the flourishing of methods such as transfer learning, which allows for loading new datasets onto pre-trained models, greatly reducing the effort required for training the neural network [39].

In order to design safe and functional parts, we need information about the material's mechanical properties, such as ultimate stress (UTS), stiffness (E), yield stress (Y), fracture strain (F), elongation, fatigue life, etc. The same properties are also expected when we are designing a new material. Naturally, experimental tests are the gold standard for obtaining this information, but they are costly and time-consuming. The field of material informatics presents an excellent alternative, offering to learn and then predict these properties based on suitable datasets. It is worth mentioning that when mechanical properties are discussed, researchers are dealing with numeric values, leading us to see the mechanical features prediction more as a regression problem. In recent years, applying machine learning approaches to predict material behavior has attracted great attention [40–44].

The prerequisite of material informatics is a trustworthy dataset used as the input for the next steps, such as the one that has been thoroughly explained in the previous sections. This dataset can then be used for quantitative predictions. The next step is identifying features and labels in the dataset. In the context of machine learning, feature refers to the parameters used as the input and label refers to the output corresponding to a set of features [45]. In neural networks, both features and labels must be numeric, meaning that even images are represented by numbers. The act of mapping specific features to labels is called learning, and the choice of how to map these relationships opens the door to learning algorithms [36]. This paper aims to predict three mechanical properties of DP steels, namely UTS, Y, and F, based on PFM-generated microstructures, making them the labels and the feature, respectively.

This research tries to train a hybrid deep-learning model for predicting these mechanical properties based on 1188 PFM-generated microstructure images of DP steel. An overview of the deep learning model is as follows. In this study, the input parameters defined as "labels", used to train a network for prediction of mechanical properties, are ultimate stress, yield stress and fracture strain for each microstructure. After a deep research study on different transfer learning architectures such as LeNet, Xception, and Inceptionv3 [22] for the material informatics, and having in mind the resemblance of medical images to microstructure images [46], two transfer learning models ResNet50 and VGG16 were trained, and their output was used independently in conjunction with microstructure images to perform deep feature extraction. The Adam optimizer has been implemented as one of the best adaptive gradient-based methods while discussing the optimization functions with the stochastic objective [47]. In order to use it for future estimations, this method saves an exponentially decaying average of previously squared gradients [20]. What makes the Adam optimizer remarkable is the ability to keep the momentum of previous gradients, resulting in a better estimation of the following behavior orders [48]. In addition, it is worth mentioning that Adam's adaptability to different learning rates is superior and its stability in the convergence process cannot be disputed. This resulted in two feature vectors for each microstructure image, which were then merged to form a stacked feature matrix, which was finally used as the input for the Adaboost and Random Forest (RF) algorithms. Figure 5 illustrates this hybrid deep learning model.

All implementations were performed in Python via the Google Colaboratory platform utilizing an NVIDIA Tesla K80. The Keras, Tensorflow, and SKlearn packages were used to build the final deep network. Training the whole grid with the feature extraction section takes about 2 h, and with access to more advanced hardware and clusters, this could decrease to below one hour.

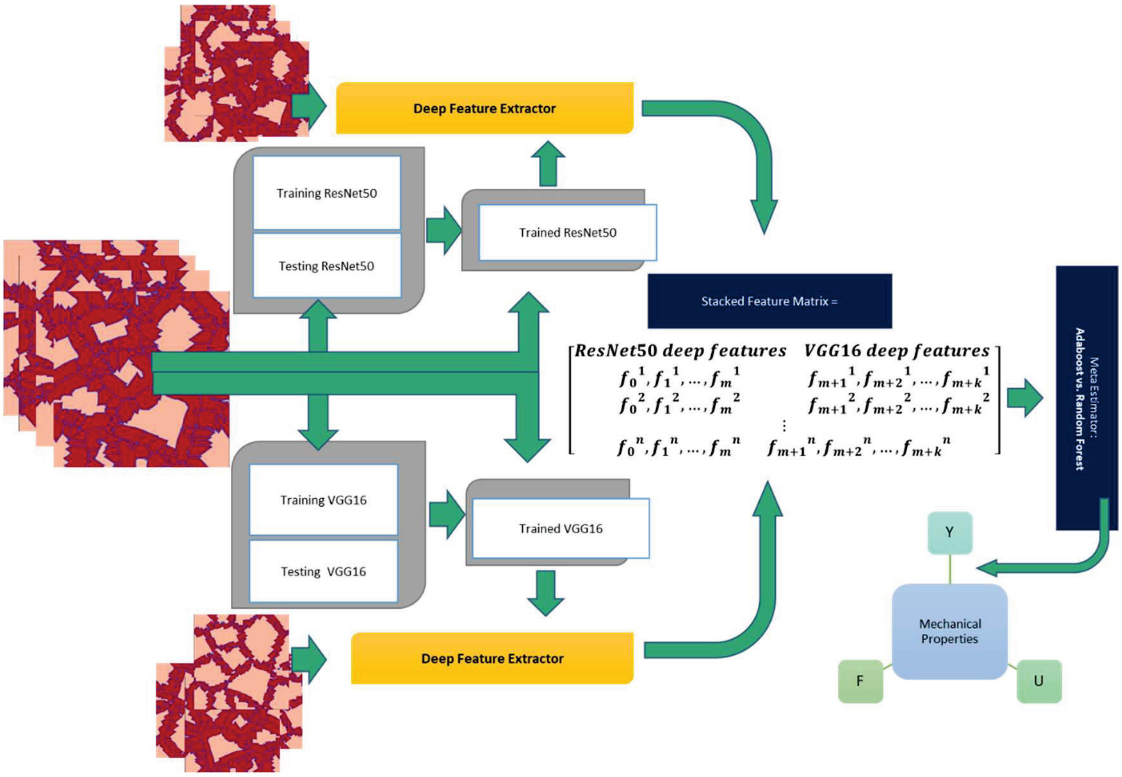

$$\begin{bmatrix} \textit{ResNet50 deep features} & \textit{VGG16 deep features} \\ f_0{}^1, f_1{}^1, \ldots, f_m{}^1 & f_{m+1}{}^1, f_{m+2}{}^1, \ldots, f_{m+k}{}^1 \\ f_0{}^2, f_1{}^2, \ldots, f_m{}^2 & f_{m+1}{}^2, f_{m+2}{}^2, \ldots, f_{m+k}{}^2 \\ & \vdots \\ f_0{}^n, f_1{}^n, \ldots, f_m{}^n & f_{m+1}{}^n, f_{m+2}{}^n, \ldots, f_{m+k}{}^n \end{bmatrix}$$

**Figure 5.** General framework of the hybrid model.

### *3.2. VGG16*

The model was proposed by Andrew Zisserman and Karen Simonyan at Oxford Visual Geometry Group [49]. Compared to most convolutional neural networks (CNN), the network is simple and works with a simple 3 × 3 stacked layer. VGG is a promising CNN model based on an ImageNet dataset that is trained by over 14 million images to nearly 22,000 categories. To train the model, all images were downsized to 256 × 256. RGB images with a size of 224 × 224 were the inputs for the VGG16 model. Then, the convolutional layers were applied to the images. The whole setup can differ, although the stride, padding, and down-sampling layers can be distinguished. Five max-pooling layers were applied following some of the CNN layers in the very first architecture of the model [50]. The last layer was also equipped with a soft-max layer. An optimum batch size of 16 was selected for the model. It is worth mentioning that the Rectifier Linear Unit (ReLU) function was used in all hidden layers, as depicted below. Other activation functions were also considered. Since we only deal with positive values, ReLU showed the best performance in the case of speed of the convergence, following the mathematical formula in Equation (7) [51]:

$$R'(z) = \begin{cases} z & z \geq 0 \\ 0 & z < 0 \end{cases}. \tag{7}$$

### *3.3. ResNet50 (Deep Residual Learning)*

Another transfer learning architecture used in the current study was initially designed due to the problematic subject of losing accuracy by adding more layers. The model is called ResNet since it deals with residual learning. The model's algorithm could justify the superb performance of ResNet in that, instead of modeling the intermediate output, it tries to model the residual of the output of each layer [50]. ResNet50, as the structure has been displayed in Figure 6, is the enhanced model with 48 CNN layers, a max pool, and an average pool. Similar to the VGG16 model, all layers are passed through a ReLU activation function. What matters here is the shortcut connections that skip every three layers in the new ResNet50 model. In comparison to the classic ResNet, every two layers are removed [52], which means that each block of 2 CNN layers in a network of 34 layers was replaced with a bottleneck block of 3 layers. Despite the fact that the ResNet model could be time-consuming, it showed promising performance on the microstructure images.

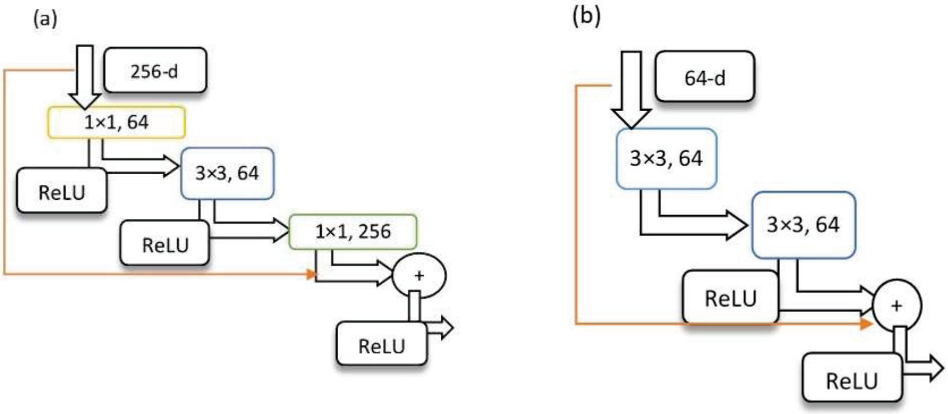

**Figure 6.** (**a**) ResNet50 model vs. (**b**) ResNet classic model.

### *3.4. Study of Hyper Parameters*

Several hyper parameters have different effects on the network, such as learning rate, the number of nodes, dense layers, batch size, or even iteration number. To enhance each model, a set of three hyper parameters, as listed below, is optimized in a deep network with the help of a Keras Tuner, and it will be fixed for the other trials. Until tuning all hyper parameters in a model, this process will go on. The effect of the learning rate, dense layers, and the number of nodes has been investigated and will be discussed in the next section.

The global optimization framework, called Bayesian Optimization [10], is applied to select optimal values. The posterior distribution of this function provides insights into the reliability of the function's values in the hyper parameter space [53]. With the previously tested values of each iteration, this function tries to take advantage of the variance effect of every defined hyper parameter.

Building a search space [54] for each effective parameter is the main idea behind the Bayesian formulation. With the help of a Keras Tuner in this study, how the performance varies could be detected with the alteration of the values of each hyper parameter. Before applying an automated approach for tuning, a manual grid search was also investigated. Since the process was costly time- and budget-wise, the Keras tuner was a better alternative with the possibility of creating a search space. The same values for three categories of hyper parameters were considered for both models.

#### 3.4.1. Learning Rate (lr)

The learning rate is among the top three in the list of significant hyper parameters in stochastic gradient descent. This factor controls how much the model alters every time weights are updated according to the calculated error of each iteration [55]. Higher learning rates were chosen to accelerate the training at the initial step. Then, lower amounts were applied to avoid any sudden cross-domain fluctuations, especially at the optimal neighborhood. The quantities of $lr = (1e-2.1e-3.1e-4.1e-5)$ were the selected values to test the performance of each model, and the best performance was detected with the implementation of an optimizer. This will be discussed in the Results and Discussion section.

#### 3.4.2. Dense Layers

The most common layer in the ANNs is the dense layer, where the multiplication of matrix vectors occurs. One, two, and three layers were implemented for both VGG16 and ResNet50 networks. Dense units, defined as the output size of each dense layer, were also considered as a hyper parameter. All three models were tested by the change of dense unit numbers. For this study, the range of 16 to 2048 with a step of 32 was considered for tuning the units of the dense layer for both models. The results will be reported in the next part. While discussing the effect of dense layers on the network, the number of layers was also studied. One to three layers were simulated, the most common number of dense layers [56] as one of the most influential parameters in the whole network. The ReLU function for the activation function, which plays the role of neuron transformation for each layer, was designated.

#### 3.4.3. Regression Ensemble Learning Method

Keeping in mind that the regression part of the model could also be a turning point in the simulation, two main methods based on the decision tree algorithm were nominated for the learning method in the last part of the model to predict the mechanical properties. Adaboost and Random Forest architectures are illustrated in Figure 7. In the first method, which is quite a famous method called Random Forest (RF), every decision tree for the optimal splits takes a random volume of features according to the bagging method, meaning that each tree is trained individually with a random subset of data but with equal weights. However, in the following method, which we are focused on, called Adaboost, each tree takes its own weight by analyzing the mistakes of the previous one and increases the weight of misclassified data points, which is called the boosting method. The ordering of the trees in the Adaboost method could affect the subsequent layers, although each tree performs independently with RF. The algorithms of both models are sketched in the demo below.

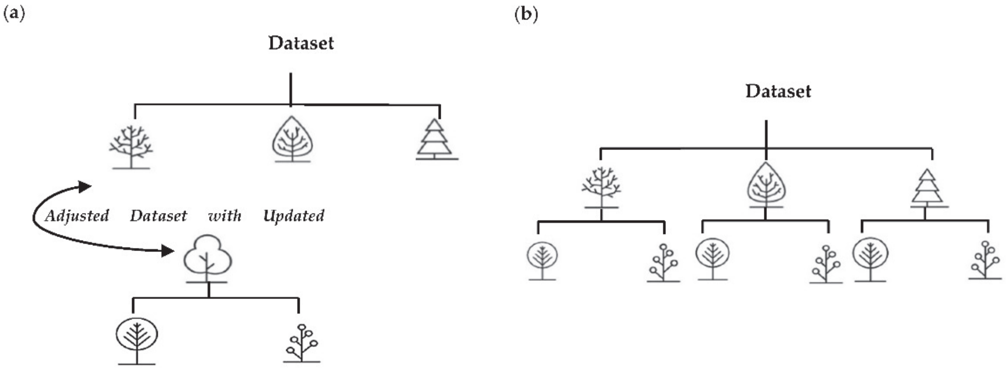

**Figure 7.** (**a**) Decision stumps in Adaboost based on the boosting method; (**b**) decision trees in RF with the bagging method.

### *3.5. Models' Performance Analysis*

Different types of errors could be considered to have a mutual understanding of the performance of a model. Different methods were considered to analyze the model's performance and calculation of accuracy. To visualize each model's performance, training loss and validation loss, abbreviated as "loss" and "val_loss", respectively, were calculated as evaluation measures according to mean square error (MSE). Training loss, formulated with the cost function, is the measurement that is calculated after each batch, depicting how accurately a deep model can fit the training dataset. In contrast, validation loss is defined for assessing the performance of the dataset that was put aside. Root mean square error (*RMSE*) is the second approach for monitoring the error in the current study, reported in some studies as the error that can outperform some other types, such as weighted MSE [20]:

$$MSE = \frac{1}{N}\sum_{i}^{N}(y_i - \hat{y}_i)^2, \tag{8}$$

$$RMSE = \sqrt{\frac{1}{N}\sum_{i}^{N}(y_i - \hat{y}_i)^2}, \tag{9}$$

where $y_i$, $\hat{y}_i$, and N are the ground truth practical values, the predicted effective values of the mechanical property (UTS, Y, and F in this study), and the number of selected data in a set for which error is calculated, respectively. In addition, $y_{average}$ is the average value of the aforementioned property in the dataset [13].

As we are dealing with a regression algorithm, two mathematical errors are also calculated during the prediction of mechanical properties, enabling us to have a perspective of how to compare the final results of the regression step. For both categories of training and testing datasets, mean absolute error (*MAE*) and mean absolute scaled error (*MASE*) (Ref. [57]) are estimated as:

$$MAE = \frac{1}{N}\sum\nolimits_{i}^{N} |y_i - \hat{y}_i|, \tag{10}$$

$$RMASE = \frac{1}{N}\sum\nolimits_{i}^{N} \left|\frac{y_i - \hat{y}_i}{y_{average}}\right| \times 100\%, \tag{11}$$

## 4. Results and Discussion

Some traditional approaches are presented in different micromechanical studies, though not every microstructure output after augmentation can lead to the same mechanical properties, which seems to be ignored in some studies. Flipping up to down, abbreviated as Flip UD, flipping left to right (LR), and rotating clockwise (CC) and counterclockwise (CCW) approaches were investigated, respectively, and each time, about 2000 to 4000 images were produced. Additionally, according to some studies [58] with the shear approach for data generation, this method with $-16 <$ shear angle $< +16$ also was studied.

This could be significant evidence of how microstructure investigation is a criterion that needs more consideration while being on data generation. In many datasets, machine-learning networks could be problem solvers, for either classification or regression problems, and the criteria for boosting the dataset Table 6 still shows a good amount of error values; however, this study's primary dataset had better results without boosting with traditional methods. The presence of two phases of ferrite and martensite and, more importantly, the interface of phases means that methods such as cropping could change the mechanical properties. Among them, flipping is the method with a minimum error of 2 percent; however, it is still not as low as the genuine dataset itself with no augmentation.

**Table 6.** MASE comparison for three labels of mechanical properties with different methods of traditional augmentation, such as flipping, rotating, and shearing.

| **Rotate 90 CC** | | **MASE Y** | **MASE U** | **MASE F** |
|---|---|---|---|---|
| **Hybrid Model Error Report (%)** | Train | 10.196 | 6.681 | 11.215 |
| | Test | 10.209 | 6.308 | 11.440 |
| Rotate 90 CCW | | **MASE Y** | **MASE U** | **MASE F** |
| **Hybrid Model Error Report (%)** | Train | 10.89 | 6.502 | 12.002 |
| | Test | 11.01 | 6.401 | 11.928 |
| Random Shear | | **MASE Y** | **MASE U** | **MASE F** |
| **Hybrid Model Error Report (%)** | Train | 1.232 | 0.943 | 2.9172 |
| | Test | 3.534 | 2.346 | 8.134 |
| Flip UD | | **MASE Y** | **MASE U** | **MASE F** |
| **Hybrid Model Error Report (%)** | Train | 1.4474 | 1.0802 | 3.0451 |
| | Test | 4.623 | 2.971 | 8.677 |
| Flip LR | | **MASE Y** | **MASE U** | **MASE F** |
| **Hybrid Model Error Report (%)** | Train | 1.0306 | 0.8930 | 2.744 |
| | Test | 2.692 | 2.195 | 7.025 |

The performance of the two models individually, as discussed in the previous section, is reported in Figure 8, demonstrating the decreasing trends of performance evaluation errors. As discussed in studies including the deep learning keywords, if validation loss shows a big difference in value to training loss, overfitting occurs, which did not happen in this model, as can be evidently seen in the diagram below. To avoid the occurrence of under-fitting, each epoch was carefully monitored with the illustration of MSE for both training data and validation. The ResNet50 model shows smoother behavior, while the VGG16 model results in fewer error values sooner. The analysis of both models and other deep learning approaches emphasizes the advantages of both models in combination.

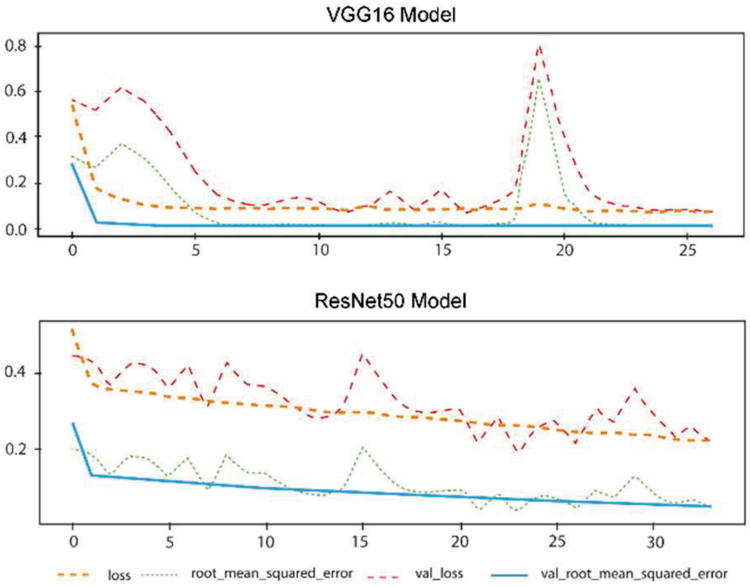

**Figure 8.** Loss and validation loss diagram for two approaches, ResNet50 and VGG16.

With a fixed batch size of 16 for both models, the results after the optimization are depicted below. While it has been reported by [59] that 32 is a better value for the batch size, before the optimization process for other values, it was studied manually with different iterations, and in this case, a batch size of 16 showed better performance, as was also reported in some other studies [60]. The details of the parametric study are listed in Table 7. The epochs represent each time the model and the whole training dataset were trained. The batches were picked randomly for each epoch, and the testing dataset (10 percent of the dataset) was randomly separated to see the model validation performance. This must be done to avoid further overfitting while running the subsequent simulations. On 52 simulations, each epoch was performed, and the number of epochs was fixed to 200 and manually optimized. We might obtain better results with more epochs, though overfitting is more probable and time-consuming. The HP optimization section of the ResNet50 model could take less than 40 min, and the VGG16 optimization could take less than an hour.

Regarding the timing issue and monitoring the running epochs, it needs to be pointed out that the training time since Callback defined in the model could be less than 15 min. Callbacks in the Keras library help in periodically saving the model and monitoring the metrics after each batch, and EarlyStopping Callback could stop training after it is triggered. Along with the ModelCheckpoint Callback, the best model while training the network with a defined measurement factor for the validation data performance could be saved.

**Table 7.** Parameters choice list for the optimization of two methods of transfer learning, VGG16 and ResNet50.

| Parameter | Description | Values | VGG16 Optimized Values | ResNet50 Optimized Values |
|---|---|---|---|---|
| *E* | Epoch numbers | 200 | 200 | 200 |
| *lr* | Learning rate | $1 \times 10^{-2}$, $1 \times 10^{-3}$, $1 \times 10^{-4}$, $1 \times 10^{-5}$ | $1 \times 10^{-4}$ | $1 \times 10^{-3}$ |
| *Conv2D* | Number of filters in the convolution layer | min = 16, max = 512, step = 32 | 336 | 16 |
| *Dense Units* (layer1) | Output size of each dense layer | min = 32, max = 1024, step = 64 | 992 | 992 |
| *Dense Units* (layer2) | | | - | 672 |
| *Dense Units* (layer3) | | | - | 32 |

MASE, as the main error for the overview of each simulation, is reported in Table 8. Adaboost and RF errors are also reported for the three mechanical properties in this study. According to the authors' knowledge, this is the first study that gives an optimization performance analysis to investigate the effect of more than three hyper parameters. Table 8 tries to report the errors for the ResNet50 optimized trial, which showed acceptable performance for the prediction of ultimate and yield stress with about 3 percent MASE error. The other model's performance was also investigated, and the optimized trial errors were reported, respectively. Unfortunately, VGG16, as reported the results in the Table 9, with an approximate error of 15 and 11 percent for ultimate and yield stresses, respectively, could not perform more accurately.

**Table 8.** ResNet50 error report for training and testing data after the HP optimization.

| | | MASE Y | MASE U | MASE F |
|---|---|---|---|---|
| **Resnet50 Model Error Report (%)** | Train | 5.559 | 3.713 | 8.092 |
| | Test | 5.465 | 3.610 | 10.448 |

It is worth noting that the two models could reasonably identify stress characteristics. However, in the case of reporting the strain performance, they could not correspond better than 10 percent with the testing samples. This could result from the scarcity of data that is needed when it comes to fracture strain investigation, such as crack initiation or crack propagation pattern. The dependence of the amount of strain on morphology is more than that of stress values, which could also explain why better results were obtained in the case of stress investigation [2].

**Table 9.** VGG16 error report for training and testing data after the HP optimization.

| | | MASE Y | MASE U | MASE F |
|---|---|---|---|---|
| **VGG16 Model Error Report (%)** | Train | 13.043 | 16.071 | 36.67 |
| | Test | 11.292 | 15.001 | 41.963 |

The optimized model proved its best performance with an error of 1.3% for the testing dataset for the prediction of ultimate stress, 0.9% for the yield stress, and 6% for the prediction of fracture strain of the same data (stated in the following table for each parameter).

The errors for each model for both regression approaches are listed in Table 10. It is worth noting that while each model works individually, the hybrid model outperforms them. The results in every step are compared to the ground truth and are depicted in Figures 9 and 10 for both applied regressors, Adaboost and RF, respectively.

**Table 10.** Hybrid model error report for training and testing data after the HP optimization, while considering two approaches, Adaboost and RF regressors.

| **Hybrid Model Error Report** | | **MASE Y** | **MASE U** | **MASE F** |
|---|---|---|---|---|
| **Adaboost (%)** | *Train* | 2.532 | 1.625 | 6.323 |
| | *Test* | 2.387 | 2.172 | 6.881 |
| | | **MASE Y** | **MASE U** | **MASE F** |
| **Random Forest (%)** | *Train* | 0.386 | 0.494 | 2.432 |
| | *Test* | 0.924 | 0.574 | 6.670 |

As it is evident in the fluctuation plots in Figures 9 and 11. The hybrid model, after running the feature extraction [61] with the adaptively fusing loss function as discussed in [62], could grasp most of the fluctuations and predict the values of peaks and bottoms better.

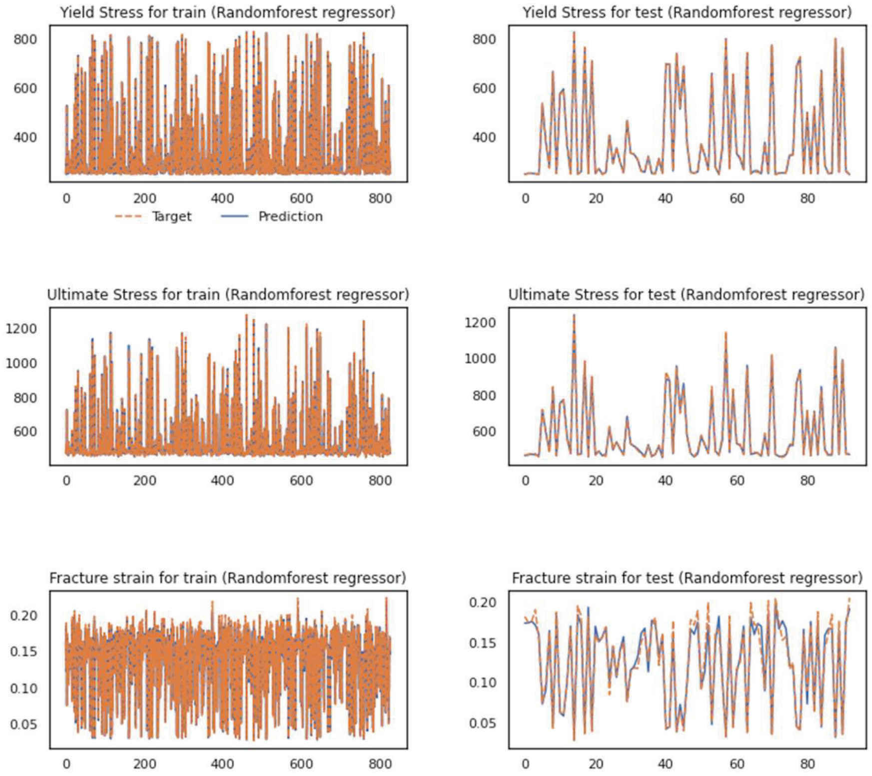

**Figure 9.** Performance of the proposed hybrid model while using the RF regressor for the training set (left diagrams) and test set (right figures).

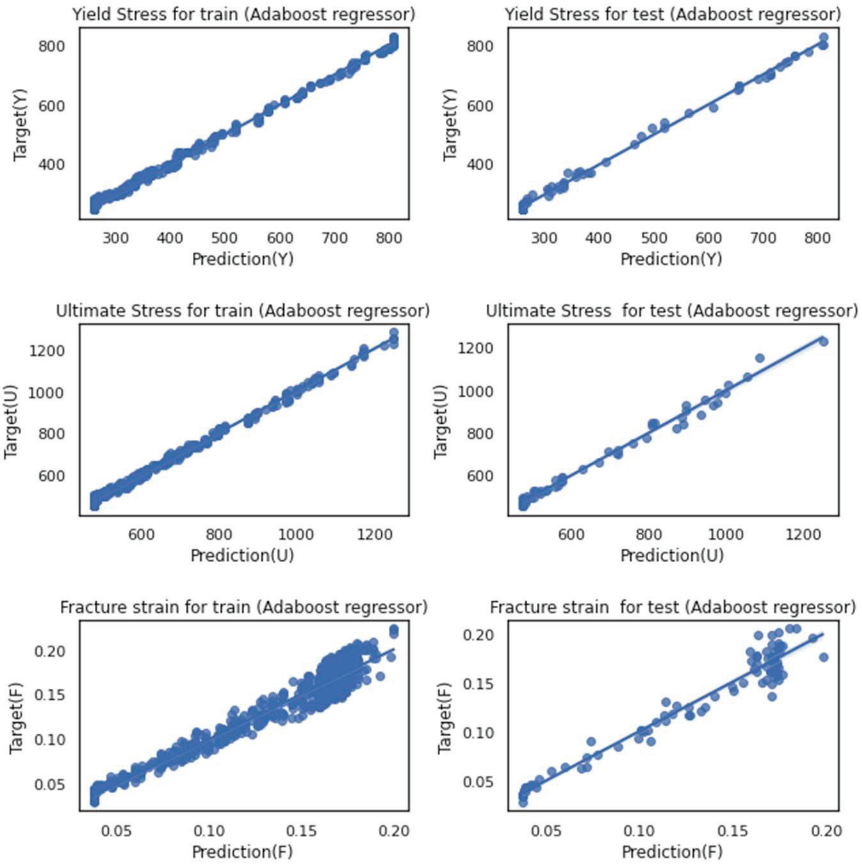

**Figure 10.** Dataset parity plot while using the Adaboost regressor for training (right figures) and testing (left figures) datasets for three mechanical properties: yield stress (Y), ultimate stress (U), fracture strain (F).

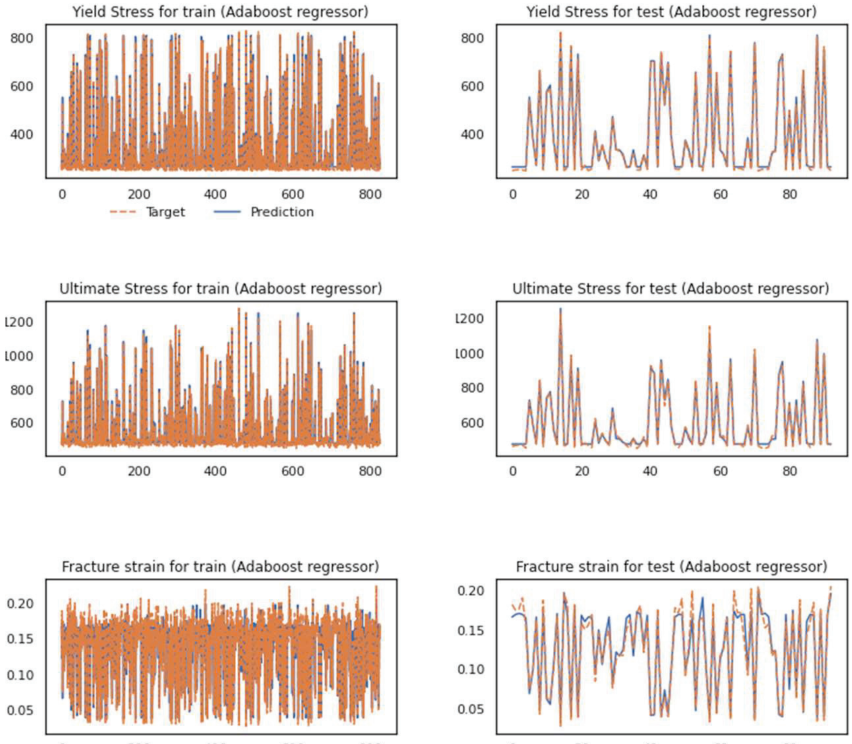

**Figure 11.** Performance of the proposed hybrid model while using the Adaboost regressor.

As discussed for each model in previous section, the same characteristics could be detected in the hybrid model while talking about the fracture strain. The parity plots in Figures 11 and 12 could be good representatives of how the prediction of strain behavior could still be challenging. Even though each model benefits from less time-consuming simulations, running the feature extraction section in the hybrid model could satisfy us with the difference in the outputs for the testing trials. Considering the model's excellent performance in analyzing all three mechanical properties, we can ignore the fact that it could be tedious. Neither the testing dataset nor the training set shows significant deviation to either side of the ideal regression line (r = 1).

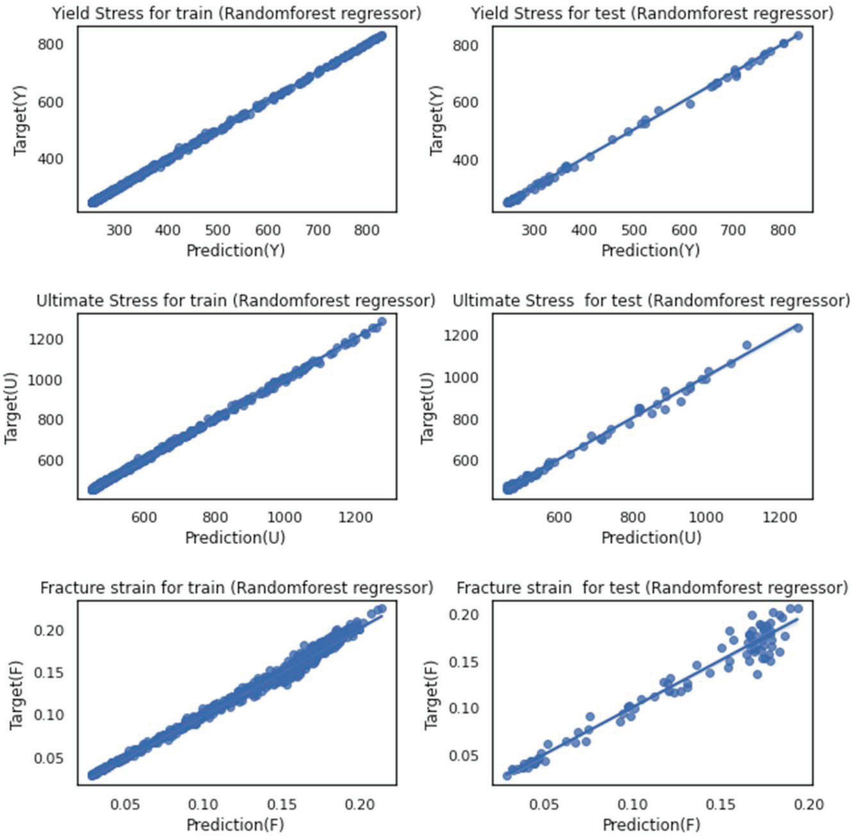

**Figure 12.** Scatter diagram of training and testing microstructure images while using the RF regressor for training (right figures) and testing (left figures) datasets for three mechanical properties: yield stress (Y), ultimate stress (U), fracture strain (F).

Last but not least is this model's outstanding performance of RF regression. More evidently, in the scatter plots, this could be recognized. Machine learning at this moment proves its significant role in eliminating costly experiments, especially regarding topics such as material characteristics which, for a substantial amount of time, could only be validated against experiments.

## 5. Conclusions

In the presented work, a dataset of microstructures using Phase Field Modeling based on the experimental microstructures was created, containing 1188 RVEs of dual-phase steel in different heat treatment conditions. The FEA technique labeled the entire dataset with three mechanical properties. This aims to feed a deep learning approach that was implemented with the help of two transfer learning approaches, VGG16 and ResNet50, called the hybrid model. Before building the final model, a parametric study was performed to optimize each model to access the best features of both VGG16 and ResNet50 models. Moreover, a comparison of decreasing trends of performance evaluation errors between the two models was also explored. The results show that with the implementation of tuning, which leads to the optimization of hyper parameters, each model independently could not show a fair prediction of mechanical properties. In contrast, the hybrid model claims to predict the mechanical properties, including the ultimate and yield stresses, with less than two percent of mean absolute squared error (MASE). However, in the case of fracture strain, some challenges still exist due to the relationship between this parameter and the morphology, which is more than that of stress values.

To optimize the model, we used three dense layers for the ResNet50 model with 992, 671 and 32 nodes, and one layer for the VGG16 model with 992 nodes. The learning rate effect was investigated and optimum values of $1 \times 10^{-4}$ for VGG16 and $1 \times 10^{-3}$ for ResNet50 were nominated. The number of convolutional layers was the third hyper parameter that we focused on and the best number of filters was 16 for the VGG16 model and 16 for the ResNet50 model, respectively.

Two regressors' performances (Random Forest (RF) and Adaboost) were also observed, and at each evaluation, the RF showed promising results, with about 1 to 3 percent of enhanced error. Data augmentation was also investigated carefully to determine how approaches such as flipping, rotation, or shearing could boost the dataset numerically but not the results of the prediction step. Finally, we proposed an optimized model with a great accuracy of 98% to predict the mechanical properties, which is an excellent demonstration of how applicable ANN could be in the field of material informatics.

**Author Contributions:** Conceptualization, A.C.D.; methodology, A.C.D. and M.K.; software, A.C.D., S.R. and M.K.; validation, A.C.D. and S.R.; formal analysis, A.C.D. and M.K.; investigation, A.C.D. and M.K.; resources, A.C.D., S.R. and V.G.; data curation, S.R. and M.K.; writing—original draft preparation, A.C.D., S.R. and M.K.; writing—review and editing, V.G. and S.S.; visualization, S.R. and M.K.; supervision, V.G. and S.S.; project administration, A.C.D., V.G. and S.S.; funding acquisition, S.S. All authors have read and agreed to the published version of the manuscript.

**Funding:** The authors would like to thank the German Research Foundation (DFG) for financial support of the project at the University of Stuttgart (SCHM 746/248-1), with the title "Integrative material and process model for the correlation of phase morphology and flow behavior of spheroidization annealed low-alloyed carbon steels".

**Institutional Review Board Statement:** Not applicable.

**Informed Consent Statement:** Not applicable.

**Data Availability Statement:** The data set of this study was generated at "Institut für Materialprüfung, Werkstoffkunde und Festigkeitslehre" (IMWF). Data could be made available upon reasonable request under the supervision of the IMWF institute. The proposed model is available upon reasonable request to the corresponding author.

**Conflicts of Interest:** The authors declare no conflict of interest.

## References

1. Rana, R.; Singh, S.B. (Eds.) *Automotive Steels: Design, Metallurgy, Processing and Applications*; Woodhead Publishing Series in Metals and Surface Engineering; Elsevier/Woodhead Publishing: Amsterdam, The Netherlands; Boston, MA, USA; Heidelberg, Germany, 2017; ISBN 978-0-08-100653-5.
2. Cheloee Darabi, A.; Kadkhodapour, J.; Pourkamali Anaraki, A.; Khoshbin, M.; Alaie, A.; Schmauder, S. Micromechanical Modeling of Damage Mechanisms in Dual-Phase Steel under Different Stress States. *Eng. Fract. Mech.* **2021**, *243*, 107520. [CrossRef]
3. Rudnizki, J.; Böttger, B.; Prahl, U.; Bleck, W. Phase-Field Modeling of Austenite Formation from a Ferrite plus Pearlite Microstructure during Annealing of Cold-Rolled Dual-Phase Steel. *Metall. Mater. Trans. A* **2011**, *42*, 2516–2525. [CrossRef]
4. Zhu, B.; Militzer, M. Phase-Field Modeling for Intercritical Annealing of a Dual-Phase Steel. *Metall. Mater. Trans. A* **2015**, *46*, 1073–1084. [CrossRef]
5. Rastgordani, S.; Ch Darabi, A.; Kadkhodapour, J.; Hamzeloo, S.R.; Khoshbin, M.; Schmauder, S.; Mola, J. Damage Characterization of Heat-Treated Titanium Bio-Alloy (Ti–6Al–4V) Based on Micromechanical Modeling. *Surf. Topogr. Metrol. Prop.* **2020**, *8*, 045016. [CrossRef]

6. Yamanaka, A. Prediction of 3D Microstructure and Plastic Deformation Behavior in Dual-Phase Steel Using Multi-Phase Field and Crystal Plasticity FFT Methods. *Key Eng. Mater.* **2015**, *651–653*, 570–574. [CrossRef]
7. Laschet, G.; Apel, M. Thermo-Elastic Homogenization of 3-D Steel Microstructure Simulated by the Phase-Field Method. *Steel Res. Int.* **2010**, *81*, 637–643. [CrossRef]
8. Guo, K.; Yang, Z.; Yu, C.-H.; Buehler, M.J. Artificial Intelligence and Machine Learning in Design of Mechanical Materials. *Mater. Horiz.* **2021**, *8*, 1153–1172. [CrossRef]
9. Liu, R.; Yabansu, Y.C.; Agrawal, A.; Kalidindi, S.R.; Choudhary, A.N. Machine Learning Approaches for Elastic Localization Linkages in High-Contrast Composite Materials. *Integr. Mater. Manuf. Innov.* **2015**, *4*, 192–208. [CrossRef]
10. Hertel, L.; Collado, J.; Sadowski, P.; Ott, J.; Baldi, P. Sherpa: Robust Hyperparameter Optimization for Machine Learning. *SoftwareX* **2020**, *12*, 100591. [CrossRef]
11. Chowdhury, A.; Kautz, E.; Yener, B.; Lewis, D. Image Driven Machine Learning Methods for Microstructure Recognition. *Comput. Mater. Sci.* **2016**, *123*, 176–187. [CrossRef]
12. Khorrami, M.S.; Mianroodi, J.R.; Siboni, N.H.; Goyal, P.; Svendsen, B.; Benner, P.; Raabe, D. An Artificial Neural Network for Surrogate Modeling of Stress Fields in Viscoplastic Polycrystalline Materials. *arXiv* **2022**, arXiv:2208.13490. [CrossRef]
13. Yang, Z.; Yabansu, Y.C.; Al-Bahrani, R.; Liao, W.; Choudhary, A.N.; Kalidindi, S.R.; Agrawal, A. Deep Learning Approaches for Mining Structure-Property Linkages in High Contrast Composites from Simulation Datasets. *Comput. Mater. Sci.* **2018**, *151*, 278–287. [CrossRef]
14. Peivaste, I.; Siboni, N.H.; Alahyarizadeh, G.; Ghaderi, R.; Svendsen, B.; Raabe, D.; Mianroodi, J.R. Accelerating Phase-Field-Based Simulation via Machine Learning. *arXiv* **2022**, arXiv:2205.02121. [CrossRef]
15. Li, X.; Liu, Z.; Cui, S.; Luo, C.; Li, C.; Zhuang, Z. Predicting the Effective Mechanical Property of Heterogeneous Materials by Image Based Modeling and Deep Learning. *Comput. Methods Appl. Mech. Eng.* **2019**, *347*, 735–753. [CrossRef]
16. Li, Y.; Hu, S.; Sun, X.; Stan, M. A Review: Applications of the Phase Field Method in Predicting Microstructure and Property Evolution of Irradiated Nuclear Materials. *npj Comput. Mater.* **2017**, *3*, 16. [CrossRef]
17. Gu, G.X.; Chen, C.-T.; Buehler, M.J. De Novo Composite Design Based on Machine Learning Algorithm. *Extreme Mech. Lett.* **2018**, *18*, 19–28. [CrossRef]
18. Peivaste, I.; Siboni, N.H.; Alahyarizadeh, G.; Ghaderi, R.; Svendsen, B.; Raabe, D.; Mianroodi, J.R. Machine-Learning-Based Surrogate Modeling of Microstructure Evolution Using Phase-Field. *Comput. Mater. Sci.* **2022**, *214*, 111750. [CrossRef]
19. Jung, J.; Na, J.; Park, H.K.; Park, J.M.; Kim, G.; Lee, S.; Kim, H.S. Super-Resolving Material Microstructure Image via Deep Learning for Microstructure Characterization and Mechanical Behavior Analysis. *Npj Comput. Mater.* **2021**, *7*, 96. [CrossRef]
20. Rabbani, A.; Babaei, M.; Shams, R.; Da Wang, Y.; Chung, T. DeePore: A Deep Learning Workflow for Rapid and Comprehensive Characterization of Porous Materials. *Adv. Water Resour.* **2020**, *146*, 103787. [CrossRef]
21. Kautz, E.; Ma, W.; Baskaran, A.; Chowdhury, A.; Joshi, V.; Yener, B.; Lewis, D. Image-Driven Discriminative and Generative Methods for Establishing Microstructure-Processing Relationships Relevant to Nuclear Fuel Processing Pipelines. *Microsc. Microanal.* **2021**, *27*, 2128–2130. [CrossRef]
22. Banerjee, D.; Sparks, T.D. Comparing Transfer Learning to Feature Optimization in Microstructure Classification. *iScience* **2022**, *25*, 103774. [CrossRef] [PubMed]
23. Tsutsui, K.; Matsumoto, K.; Maeda, M.; Takatsu, T.; Moriguchi, K.; Hayashi, K.; Morito, S.; Terasaki, H. Mixing Effects of SEM Imaging Conditions on Convolutional Neural Network-Based Low-Carbon Steel Classification. *Mater. Today Commun.* **2022**, *32*, 104062. [CrossRef]
24. Steinbach, I.; Pezzolla, F. A Generalized Field Method for Multiphase Transformations Using Interface Fields. *Phys. Nonlinear Phenom.* **1999**, *134*, 385–393. [CrossRef]
25. Eiken, J.; Böttger, B.; Steinbach, I. Multiphase-Field Approach for Multicomponent Alloys with Extrapolation Scheme for Numerical Application. *Phys. Rev. E* **2006**, *73*, 066122. [CrossRef] [PubMed]
26. ACCESS, e.V. MICRESS Microstructure Simulation Software Manual, Version 7.0. Available online: https://micress.rwth-aachen.de/download.html#manuals (accessed on 21 November 2022).
27. Kozeschnik, E. *MatCalc Software*, version 6.03 (rel 1.000); Materials Center Leoben Forschungsgesellschaft; Materials Cener Leoben MatCalc: Leoben, Austria, 2020.
28. Krauss, G. Quench and Tempered Martensitic Steels. In *Comprehensive Materials Processing*; Elsevier: Amsterdam, The Netherlands, 2014; pp. 363–378. ISBN 978-0-08-096533-8.
29. Steinbach, I.; Pezzolla, F.; Nestler, B.; Seeßelberg, M.; Prieler, R.; Schmitz, G.J.; Rezende, J.L.L. A Phase Field Concept for Multiphase Systems. *Phys. Nonlinear Phenom.* **1996**, *94*, 135–147. [CrossRef]
30. Bréchet., Y. (Ed.) *Solid-Solid Phase Transformations in Inorganic Materials*; Solid State Phenomena; Trans Tech Publications: Durnten-Zuerich, Switzerland; Enfield, NH, USA, 2011; ISBN 978-3-03785-143-2.
31. Azizi-Alizamini, H.; Militzer, M. Phase Field Modelling of Austenite Formation from Ultrafine Ferrite–Carbide Aggregates in Fe–C. *Int. J. Mater. Res.* **2010**, *101*, 534–541. [CrossRef]
32. Steinbach, I.; Apel, M. The Influence of Lattice Strain on Pearlite Formation in Fe–C. *Acta Mater.* **2007**, *55*, 4817–4822. [CrossRef]

33. Pierman, A.-P.; Bouaziz, O.; Pardoen, T.; Jacques, P.J.; Brassart, L. The Influence of Microstructure and Composition on the Plastic Behaviour of Dual-Phase Steels. *Acta Mater.* **2014**, *73*, 298–311. [CrossRef]
34. Alibeyki, M.; Mirzadeh, H.; Najafi, M.; Kalhor, A. Modification of Rule of Mixtures for Estimation of the Mechanical Properties of Dual-Phase Steels. *J. Mater. Eng. Perform.* **2017**, *26*, 2683–2688. [CrossRef]
35. Ch.Darabi, A.; Chamani, H.R.; Kadkhodapour, J.; Anaraki, A.P.; Alaie, A.; Ayatollahi, M.R. Micromechanical Analysis of Two Heat-Treated Dual Phase Steels: DP800 and DP980. *Mech. Mater.* **2017**, *110*, 68–83. [CrossRef]
36. Ramprasad, R.; Batra, R.; Pilania, G.; Mannodi-Kanakkithodi, A.; Kim, C. Machine Learning in Materials Informatics: Recent Applications and Prospects. *Npj Comput. Mater.* **2017**, *3*, 54. [CrossRef]
37. Azimi, S.M.; Britz, D.; Engstler, M.; Fritz, M.; Mücklich, F. Advanced Steel Microstructural Classification by Deep Learning Methods. *Sci. Rep.* **2018**, *8*, 2128. [CrossRef] [PubMed]
38. Smokvina Hanza, S.; Marohnić, T.; Iljkić, D.; Basan, R. Artificial Neural Networks-Based Prediction of Hardness of Low-Alloy Steels Using Specific Jominy Distance. *Metals* **2021**, *11*, 714. [CrossRef]
39. Agrawal, A.; Gopalakrishnan, K.; Choudhary, A. Materials Image Informatics Using Deep Learning. In *Handbook on Big Data and Machine Learning in the Physical Sciences*; World Scientific Publishing Co.: Singapore, 2020; pp. 205–230.
40. Kwak, S.; Kim, J.; Ding, H.; Xu, X.; Chen, R.; Guo, J.; Fu, H. Machine Learning Prediction of the Mechanical Properties of $\gamma$-TiAl Alloys Produced Using Random Forest Regression Model. *J. Mater. Res. Technol.* **2022**, *18*, 520–530. [CrossRef]
41. Gajewski, J.; Golewski, P.; Sadowski, T. The Use of Neural Networks in the Analysis of Dual Adhesive Single Lap Joints Subjected to Uniaxial Tensile Test. *Materials* **2021**, *14*, 419. [CrossRef]
42. Kosarac, A.; Cep, R.; Trochta, M.; Knezev, M.; Zivkovic, A.; Mladjenovic, C.; Antic, A. Thermal Behavior Modeling Based on BP Neural Network in Keras Framework for Motorized Machine Tool Spindles. *Materials* **2022**, *15*, 7782. [CrossRef]
43. Valença, J.; Mukhandi, H.; Araújo, A.G.; Couceiro, M.S.; Júlio, E. Benchmarking for Strain Evaluation in CFRP Laminates Using Computer Vision: Machine Learning versus Deep Learning. *Materials* **2022**, *15*, 6310. [CrossRef]
44. Azarafza, M.; Hajialilue Bonab, M.; Derakhshani, R. A Deep Learning Method for the Prediction of the Index Mechanical Properties and Strength Parameters of Marlstone. *Materials* **2022**, *15*, 6899. [CrossRef]
45. Liu, H.; Motoda, H. *Feature Selection for Knowledge Discovery and Data Mining*; Springer: Boston, MA, USA, 1998; ISBN 978-1-4613-7604-0.
46. Rasool, M.; Ismail, N.A.; Boulila, W.; Ammar, A.; Samma, H.; Yafooz, W.M.S.; Emara, A.-H.M. A Hybrid Deep Learning Model for Brain Tumour Classification. *Entropy* **2022**, *24*, 799. [CrossRef]
47. Zou, F.; Shen, L.; Jie, Z.; Zhang, W.; Liu, W. A Sufficient Condition for Convergences of Adam and RMSProp. *arxiv* **2018**, arXiv:1811.09358. [CrossRef]
48. Ramstad, T.; Idowu, N.; Nardi, C.; Øren, P.-E. Relative Permeability Calculations from Two-Phase Flow Simulations Directly on Digital Images of Porous Rocks. *Transp. Porous Media* **2012**, *94*, 487–504. [CrossRef]
49. Simonyan, K.; Zisserman, A. Very Deep Convolutional Networks for Large-Scale Image Recognition. *arxiv* **2014**, arXiv:1409.1556. [CrossRef]
50. Patel, A.; Cheung, L.; Khatod, N.; Matijosaitiene, I.; Arteaga, A.; Gilkey, J.W. Revealing the Unknown: Real-Time Recognition of Galápagos Snake Species Using Deep Learning. *Animals* **2020**, *10*, 806. [CrossRef] [PubMed]
51. Pengtao, W. Based on Adam Optimization Algorithm: Neural Network Model for Auto Steel Performance Prediction. *J. Phys. Conf. Ser.* **2020**, *1653*, 012012. [CrossRef]
52. He, K.; Zhang, X.; Ren, S.; Sun, J. Deep Residual Learning for Image Recognition. *arxiv* **2015**, arXiv:1512.03385. [CrossRef]
53. Xu, M.; Wang, S.; Guo, J.; Li, Y. Robust Structural Damage Detection Using Analysis of the CMSE Residual's Sensitivity to Damage. *Appl. Sci.* **2020**, *10*, 2826. [CrossRef]
54. Pedersen, M.E.H. Available online: https://github.com/Hvass-Labs/TensorFlow-Tutorials/blob/master/11_Adversarial_Examples.ipynb (accessed on 2 April 2020).
55. Brownlee, J. Loss and Loss Functions for Training Deep Learning Neural Networks. *Machine Learning Mastery*, 23 October 2019. Available online: https://machinelearningmastery.com/loss-and-loss-functions-for-training-deep-learning-neural-networks/ (accessed on 21 November 2022).
56. Ritter, C.; Wollmann, T.; Bernhard, P.; Gunkel, M.; Braun, D.M.; Lee, J.-Y.; Meiners, J.; Simon, R.; Sauter, G.; Erfle, H.; et al. Hyperparameter Optimization for Image Analysis: Application to Prostate Tissue Images and Live Cell Data of Virus-Infected Cells. *Int. J. Comput. Assist. Radiol. Surg.* **2019**, *14*, 1847–1857. [CrossRef] [PubMed]
57. Hyndman, R.J.; Koehler, A.B. Another Look at Measures of Forecast Accuracy. *Int. J. Forecast.* **2006**, *22*, 679–688. [CrossRef]
58. Medghalchi, S.; Kusche, C.F.; Karimi, E.; Kerzel, U.; Korte-Kerzel, S. Damage Analysis in Dual-Phase Steel Using Deep Learning: Transfer from Uniaxial to Biaxial Straining Conditions by Image Data Augmentation. *JOM* **2020**, *72*, 4420–4430. [CrossRef]
59. Bengio, Y. Practical Recommendations for Gradient-Based Training of Deep Architectures. *arxiv* **2012**, arXiv:1206.5533. [CrossRef]
60. Ibrahim, M.M. The Design of an Innovative Automatic Computational Method for Generating Geometric Islamic Visual Art with Aesthetic Beauty. University of Bedfordshire. 2021. Available online: https://uobrep.openrepository.com/handle/10547/625007 (accessed on 21 November 2022).

61. Brownlee, J. *Data Preparation for Machine Learning: Data Cleaning, Feature Selection, and Data Transforms in Python*; Machine Learning Mastery: San Francisco, CA, USA, 2020. Available online: https://machinelearningmastery.com/data-preparation-for-machine-learning/ (accessed on 21 November 2022).
62. Wang, Y.; Oyen, D.; Guo, W.G.; Mehta, A.; Scott, C.B.; Panda, N.; Fernández-Godino, M.G.; Srinivasan, G.; Yue, X. StressNet—Deep Learning to Predict Stress with Fracture Propagation in Brittle Materials. *npj Mater. Degrad.* **2021**, *5*, 6. [CrossRef]

materials

Article

# Assessment of the Specimen Size Effect on the Fracture Energy of Macro-Synthetic-Fiber-Reinforced Concrete

**Mohammad Daneshfar [1], Abolfazl Hassani [1], Mohammad Reza Mohammad Aliha [2] and Tomasz Sadowski [3,*]**

[1] School of Civil and Environmental Engineering, Tarbiat Modares University, Tehran 14115-111, Iran
[2] School of Industrial Engineering, Iran University of Science and Technology, Tehran 16846-13114, Iran
[3] Department of Solid Mechanics, The Lublin University of Technology, Nadbystrzycka 40 Str., 20-2618 Lublin, Poland
* Correspondence: t.sadowski@pollub.pl

**Abstract:** The most frequently used construction material in buildings is concrete exhibiting a brittle behaviour. Adding fibers to concrete can improve its ductility and mechanical properties. To this end, a laboratory study was conducted to present an experimental model for the specimens' size effect of on macro-synthetic fiber-reinforced concrete using variations in fracture energy. Composite concrete beams with different thicknesses and widths were made and tested under mode I to obtain (1) fracture toughness, (2) fracture energy, and (3) critical stress intensity factor values. Results indicated that by increasing the thickness and the width, fracture toughness and fracture energy were enhanced. Moreover, increasing the thickness and width of the beam led to critical stress intensity factors enhancement respectively by 35.01–41.43% and 7.77–8.09%.

**Keywords:** concrete; twisted fiber; fracture energy; mode I fracture toughness; size effect

## 1. Introduction

Fiber-reinforced concrete is a type of composite material made of concrete mixed with fibers of various types and sizes, which can additionally include glass, polymer, carbon, and steel [1].

Studies have been conducted to investigate the effect of fibers on concrete, such as its mechanical properties, fatigue life, and durability, which indicate the positive effect of fibers on concrete performance [2–5]. Ahmad ([6]) indicated that polypropylene fiber improves the mechanical strength and durability of concrete (particularly tensile capacity) but decreases the flowability of concrete. The optimum dose is important, as a higher dose adversely affects strength and durability due to a lack of flowability. Scanning electronic microscopy results indicate that polypropylene fibers restrict the propagation of cracks, which improves the strength and durability of concrete [6]. Wang et al. reported that with the increase in the steel fiber volume fraction, some fracture parameters increase gradually and maintain a certain linear growth [7].

Pakravan et al. focused on the use of hybrid fibers in concrete and reported that combining various types of fibers would yield better results in terms of concrete toughness and energy absorption [8]. Bordelon and Roesler studied fiber-reinforced concrete pavements using steel, synthetic, and steel mesh fibers. They reported that the use of fibers leads to increased bearing capacity and reduces the thickness of the concrete pavement [9]. Chari et al. investigated the mode I fracture behavior of high-strength steel-fiber-reinforced concrete, the results of which indicated that increased beam size leads to enhanced fracture energy [10]. The shear stress of three beams with different sizes was analyzed by Gustafsson et al. [11]. Their results showed that a concrete mixture containing steel fibers yields better strength. Kreiger [12] conducted a study on a model to explain the mode I rupture of high-performance steel-fiber-reinforced concrete and concluded that increasing the fiber percentage leads to higher fracture energy. In addition, by increasing the span-length-to-depth ratio of the beam, the maximum rupture force significantly reduced. Rao and Rao conducted a study on the toughness change in steel-fiber-reinforced concrete, estimated by mode II loading. Adding fibers to the concrete significantly influenced the concrete's toughness and shear strength [13]. Different methods were used to rank the toughness of fiber-reinforced concrete, toughness optimization, and the properties of the reinforced concrete.

A summary of recent studies on the effects of different types of fibers on concrete's mechanical properties is presented in Table 1.

**Table 1.** A summary of fibers' effects on mechanical properties, as reported in the literature (increase ↑, decrease ↓, not significant, N.S.).

| **Authors** | **Year** | **Fiber Properties** | | | **Concrete Type** | **Compressive Strength** | **Splitting Tensile Strength** | **Flexural Strength** | **Energy Absorption** |
|---|---|---|---|---|---|---|---|---|---|
| | | **Type** | **Length (mm)** | **Fiber Volume Fraction (%)** | | | | | |
| Valdez et al. [14] | 2021 | Steel fibers | 50 | 0.25, 0.5 | Normal concrete | - | - | - | ↑ |
| Blazy et al. [15] | 2021 | Polypropylene | 48, 54 | 0.22, 0.33 | Normal concrete | - | - | 5.55–13.5% ↑ | - |
| Daneshfar et al. [16] | 2017 | Polypropylene | 38 | 0.2, 0.4, 0.6 | Normal concrete | 4.57–26.32% ↓ | 0.84–34.29% ↑ | 19.6–81.69% ↑ | - |
| Fallah and Nematzadeh [17] | 2017 | Polypropylene | 39 | 0.25, 0.75, 1.25 | High-strength concrete | 8% ↑, 3% ↑, 4% ↓ | 8, 9, 27% ↑ | - | - |
| Lee et al. [18] | 2017 | Steel fibers | 20, 30, 40 | 0.25, 0.375, 0.5 | Normal concrete | - | - | At least 20.8% ↑ | ↑ |
| Alberti et al. [19] | 2017 | Steel fibers (hooked) | 35 | 0.33 | Self-compacting concrete | ↓ | ↑ | ↑ | ↑ |
| | | Polypropylene | 60 | 0.5 | | | | | |
| Hesami et al. [20] | 2016 | Polypropylene | 60 | 0.10, 0.12 | Self-compacting concrete | 2% ↑, 5% ↓ | 19, 27% ↑ | 26, 33% | - |
| Saidani et al. [21] | 2016 | Steel fibers | 50 | 4% (by cement volume) | Normal concrete | 2% ↓ | 98% ↑ | - | - |
| | | Polypropylene | 50 | 4% (by cement volume) | | 5% ↓ | 65%↑ | - | - |
| Afroughsabet and Ozbakkaloglu [22] | 2015 | Hooked-end steel | 60 | 0.25, 0.5, 0.45, 1 | High-strength concrete | 12, 14, 15, 19% ↑ | 15, 22, 38, 57% ↑ | 14, 28, 36, 61% ↑ | - |
| Yew et al. [23] | 2015 | Polypropylene (twisted bundle) | 54 | 0.25, 0.375, 0.5 | Lightweight concrete | 5, 11, 15% ↑ | 8, 24, 33% ↑ | 29, 31, 40%↑ | - |
| | | | 30 | 0.25, 0.375, 0.5 | | 3, 10, 14% ↑ | 10, 19, 27% ↑ | 18, 22, 30%↑ | - |
| | | Polypropylene (straight) | 20 | 0.25, 0.375, 0.5 | | 4, 10, 14% ↑ | 13, 14, 21%↑ | 6, 10, 20%↑ | - |
| Karadelis and Yougui [24] | 2015 | Steel | 50 | 1.5 | Roller-compacted concrete | N.S | - | 24%↑ | - |
| Hesami et al. [25] | 2014 | Steel | 36 | 0.5 | Previous concrete | 24% ↑ | 33%↑ | 19%↑ | - |
| | | PPS | 54 | 0.3 | | 28% ↑ | 37%↑ | 21%↑ | - |
| | | Glass | 12 | 0.2 | | 32% ↑ | 28%↑ | 17%↑ | - |

**Table 1.** *Cont.*

| Authors | Year | Fiber Properties | | | Concrete Type | Compressive Strength | Splitting Tensile Strength | Flexural Strength | Energy Absorption |
|---|---|---|---|---|---|---|---|---|---|
| | | Type | Length (mm) | Fiber Volume Fraction (%) | | | | | |
| Pajak and Ponikiewski [26] | 2013 | Hooked-end steel | 30 | 0.5, 1, 1.5 | Self-compacting concrete | 34, 32, 20% ↑ | - | 55, 151, 339% ↑ | - |
| Singh et al. [27] | 2010 | Steel fibers (corrugated) | 35 | 1 | Normal concrete | 18% ↑ | - | 80%↑ | ↑ |
| | | Polypropylene (fibrillated) | 60 | | | | | | |
| Silva and Thaumaturgo [28] | 2002 | Wollastonite | 20 | 2, 3, 5 | Geopolymer concrete | - | - | - | 80% ↑ |

There are numerous studies on the mechanical properties of fiber-reinforced concrete and the size effect of concrete specimens. However, most of the studies related to the size effect increased the thickness and span of the beam specimens. This approach does not describe the effect of thickness or width variations independently.

In this study, we evaluated the effect of the size of a macro-synthetic-fiber-reinforced concrete specimen on the variations in fracture energy. The studied parameters were the fracture energy of notched concrete beams and the stress intensity factor. We used twisted fibers, which were added to the concrete mix with a volume fraction of 0.4%. Three samples were developed for each specimen, and the results were averaged and recorded in tables.

This research was conducted to achieve the following goals:

- The experimental model of variations in concrete fracture energy considers thickness, width, and macro-synthetic fiber content.
- The effect of specimen size on the fracture energy of concrete specimens is explained.
- The effect of fibers on the stress intensity factor of concrete specimens with three different thicknesses and widths is described.

## 2. Materials and Methods

### 2.1. Test Variables

To evaluate the fracture energy and stress intensity factor of notched concrete beams, a concrete mixture was designed based on the ACI 211 standard [29]. All the concrete samples were developed with the same mix design and 0, 0.4, and 0.6 volume percentages of twisted fibers. In this research, concrete mix designs were coarse aggregate 880 (kg/m$^3$), fine aggregate 789 (kg/m$^3$), cement 442 (kg/m$^3$), water 199 (kg/m$^3$), superplasticizer 2.2 (kg/m$^3$) m$^3$), and fibers with two doses of 3.6 and 5.4 (kg/m$^3$). The fibers used in this research were selected according to the specifications of ASTM D7508/D7508M-10, with a length of 3.8 cm [30]. Figure 1 shows the fibers used in this research.

### 2.2. Specimen Preparation

To evaluate the fracture energy and critical stress intensity factor ($K_{Ic}$) of fiber-reinforced concrete, concrete beam samples were fabricated based on the JCI-S-001-2003 standard [31]. First, cement was mixed with sand, gravel, and fibers; then water was mixed with a superplasticizer accordingly; and finally, several rectangular beam specimens with and without twisted fibers were manufactured. Table 2 shows the geometrical properties of the prepared specimens.

**Figure 1.** Twisted fibers used in the manufacturing of fiber-reinforced concrete.

**Table 2.** Specifications of tested specimens.

| Specimen No. | Shape of Fiber | Fiber Volume Fraction (%) | Specimen Size (mm) | Notch Length (mm) | Notch Width (mm) |
|---|---|---|---|---|---|
| E1 | Twisted | 0.4, 0.6 | 80 × 120 × 450 | 30 | 2 |
| E2 | Twisted | 0.4, 0.6 | 100 × 120 × 450 | 30 | 2 |
| E3 | Twisted | 0.4, 0.6 | 150 × 120 × 450 | 30 | 2 |
| E4 | Twisted | 0.4, 0.6 | 100 × 50 × 350 | 30 | 2 |
| E5 | Twisted | 0.4, 0.6 | 100 × 100 × 350 | 30 | 2 |
| E6 | Twisted | 0.4, 0.6 | 100 × 150 × 350 | 30 | 2 |
| N1 | - | 0 | 80 × 120 × 450 | 30 | 2 |
| N2 | - | 0 | 100 × 120 × 450 | 30 | 2 |
| N3 | - | 0 | 150 × 120 × 450 | 30 | 2 |
| N4 | - | 0 | 100 × 50 × 350 | 30 | 2 |
| N5 | - | 0 | 100 × 100 × 350 | 30 | 2 |
| N6 | - | 0 | 100 × 150 × 350 | 30 | 2 |

### *2.3. Fracture Energy Tests*

Fracture energy is defined as the amount of energy required for crack growth per unit area along the ligament. The fracture energy of the manufactured concrete specimens was measured based on the Japan Concrete Institute’s standard [31]. In this research, the geometry of specimens was as shown in Figure 2. Next, using a three-point bend test, the diagram of load–crack mouth opening displacement (CMOD) was obtained. The area under the curve was measured, and fracture energy $G_F$ was calculated using Equations (1) and (2).

$$G_F = \frac{0.75\ W_0 + W_1}{A_{lig}} \quad (1)$$

$$W_1 = 0.75\ (\frac{S}{L} m_1 + 2m_2)\ g\ CMOD_C \quad (2)$$

where

$G_F$—the fracture energy (N/mm$^2$),
$W_0$—the area below the CMOD curve up to rupture of the specimen (Nmm),
$W_1$—the work done by the deadweight of the specimen and loading jig (a piece between the testing machine and the specimen; Nmm),
$A_{lig}$—the area of the broken ligament (b × h; mm$^2$),
$m_1$—the mass of the specimen (kg),

$S$—the loading span (mm),
$L$—the total length of the specimen (mm),
$m_2$—the mass of the jig not attached to the testing machine but placed on the specimen.

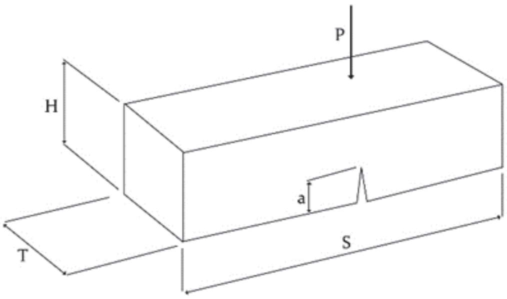

**Figure 2.** The geometry of the tested specimen [28].

The adjustment of the device and specimen is presented in Figure 3.

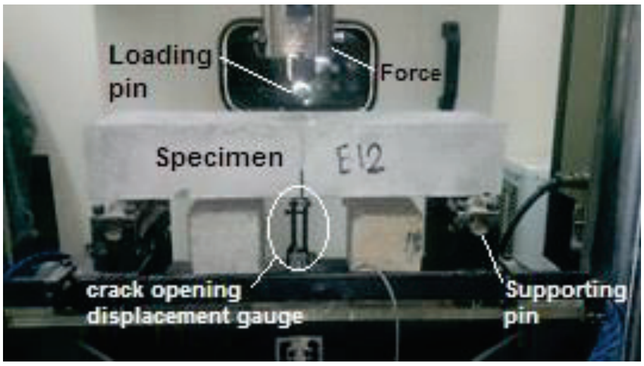

**Figure 3.** Adjustment of the device and specimen to measure the load–CMOD.

### 2.4. Critical Stress Intensity Factor

As an important parameter in fracture mechanics, the critical value of the stress intensity factor shows the resistance of a material to crack growth. When a cracked specimen is exposed to remote load, high-stress intensity occurs around the tip of the crack, and when this stress reaches its critical value, the fracture process is initiated in the specimen. The value of the stress intensity coefficient, which is calculated based on this critical stress, is known as the critical stress intensity factor ($K_{\mathrm{Ic}}$) [31,32]. The stress intensity factor $k_I$ for a notched beam subjected to three-point bend loading is obtained from Equation (3).

$$k_I = \frac{PS}{TH^{1.5}}\left[2.9\left(\frac{a}{H}\right)^{0.5} - 4.6\left(\frac{a}{H}\right)^{1.5} + 21.8\left(\frac{a}{H}\right)^{2.5} - 37.6\left(\frac{a}{H}\right)^{3.5} + 38.7\left(\frac{a}{H}\right)^{4.5}\right] \tag{3}$$

where $P$, $H$, $T$, and $S$ are shown in Figure 2.

## 3. Results and Discussion

### 3.1. Fracture Energy

To calculate the fracture energy of fiber-reinforced concrete specimens, notched specimens with three different thicknesses (8, 10, and 15 cm) and widths (5, 10, and 15 cm) were manufactured based on the JCI-S-001-2003 standard [31] and loaded by three-point bend loading. The P-CMOD diagrams were obtained from the experiments, and the fracture energy of each concrete specimen was calculated by measuring the area under the curve using Equations (1) and (2). Figure 4 depicts an example of load–CMOD curves of the tested notched fiber-reinforced concrete specimens with a 0.4% fiber volume fraction with different thicknesses.

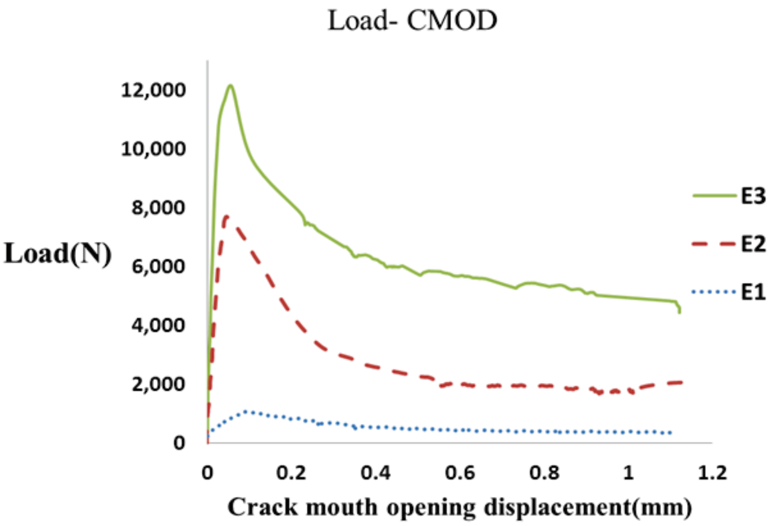

**Figure 4.** The load–CMOD curve obtained for fiber-reinforced concrete specimens with different thicknesses.

To study the effect of independent variables, including the thickness of concrete specimens, and fiber dosage on fracture energy, multiple linear regressions were used. The initial equation considered for analysis is shown in Equation (4).

$$GF = \beta_1 H + \beta_2 Fiberdosage + \beta_3 H^2 + \beta_4 Fiberdosage^2 + \beta_5 H.Fiberdosage \quad (4)$$

where:

$G_F$—fracture energy (N/mm$^2$)
$H$—thickness of concrete specimens (CM)
*Fiberdosage*—fiber volume fraction (%) $\beta_1, \beta_2, \beta_3, \beta_4, \beta_5$ are regression coefficients.

After fitting, coefficients of their significance values were less than the present significance level and were eliminated by the stepwise regression and backward elimination method, and the final model was obtained according to Tables 3 and 4. Following Table 4, the quadratic term for thickness ($H$) and the linear term for fiber dosage was meaningful if the $p$-values were less than 0.05 with 95% reliability. In the final model, the interactive term was eliminated due to insignificance, which means that the thickness ($H$) and percentage of the fibers do not interact with each other. According to Table 3, the high value of F indicates the overall significance of the model at a high confidence level. However, the adjusted $R^2$ value of 0.98 indicates that two variables, thickness ($H$) and fiber dosage, explain about 98% of the fracture energy variations; hence, the model is suitable to predict fracture energy.

As shown in Table 4, the coefficient H$^2$ was equal to 0.00122. Therefore, if the change in fracture energy for thickness ($H$), holding other factors fixed, is considered, the equation $\Delta GF = 2 \times 0.00122 \times H \times \Delta H$ would show the fracture energy change value by thickness change (which is plotted for changes from 1 to 6 cm in Figure 5). These diagrams can be used for optimal design and economic evaluation. However, considering fiber dosage coefficients, each 1% increase in the amount of fiber increases the fracture energy by 0.09. To investigate the effect of two variables, thickness and fiber dosage, on fracture energy, considering that the units of these two variables are not the same, the effects of these variables cannot be compared with each other according to their coefficients. For this purpose, the coefficients must first be standardized so that it is possible to compare. The values of these standard coefficients are presented in the last column of Table 4. As can be seen, the higher the value of the coefficient H$^2$, the greater the effect of the thickness variable ($H$) relative to the fiber dosage on the fracture energy.

**Table 3.** ANOVA table.

| | DF | SS | MS | F-Value | *p*-Value |
|---|---|---|---|---|---|
| Total | 8 | 0.06862 | 0.008578 | - | - |
| Model | 2 | 0.06757 | 0.033786 | 192.98 | 0.0000 |
| Residual error | 6 | 0.00105 | 0.000175 | - | - |
| $R^2$ | 0.985 | - | - | - | - |
| Adjusted $R^2$ | 0.980 | - | - | - | - |

**Table 4.** Values of regression coefficients of $G_F$.

| Independent Variable | Regression Coefficient | *p*-Value | *t*-Value | Standard Error | Standardized Coefficients |
|---|---|---|---|---|---|
| Constant | 0.01781 | 0.159 | 1.61 | 0.0000639 | - |
| $H^2$ | 0.00122 | 0 | 19.02 | 0.0012159 | 0.9607599 |
| Fiber dosage | 0.0869 | 0.003 | 4.92 | 0.011086 | 0.2482591 |

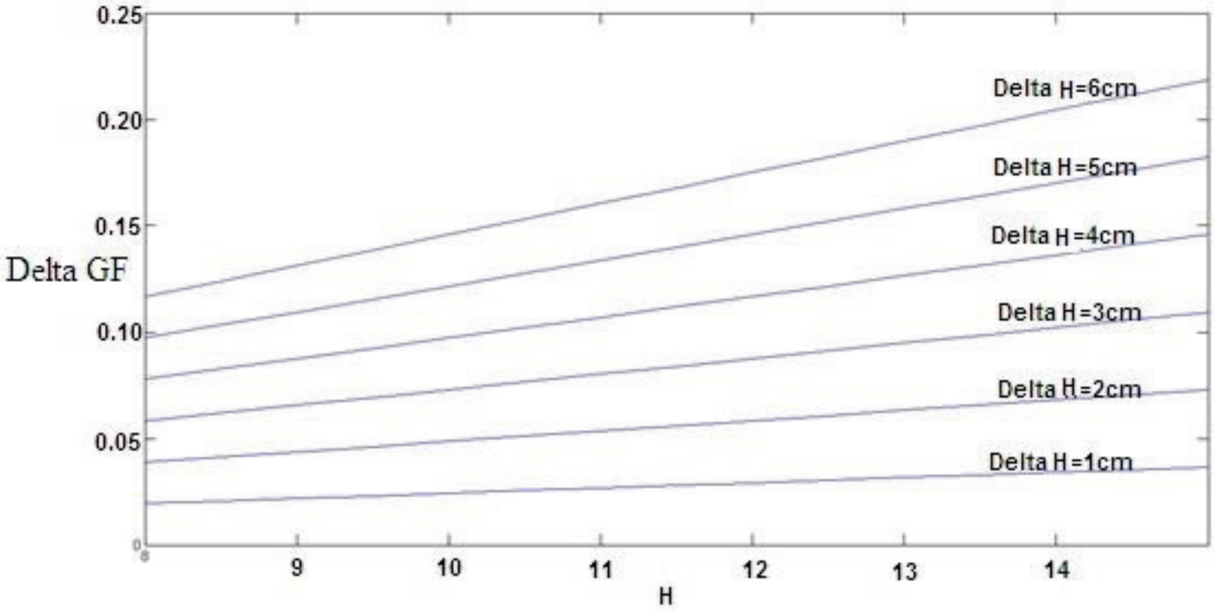

**Figure 5.** The effect of thickness *H* change on fracture energy $G_F$.

According to the model, the relationship between the three mentioned variables is graphically plotted in Figure 6, which is parabolic. As shown in Figure 6, the thickness and fiber dosage had a positive effect on the fracture energy, and by increasing each, the fracture energy increased, and the highest fracture energy occurred at the highest values of thickness and fiber dosage.

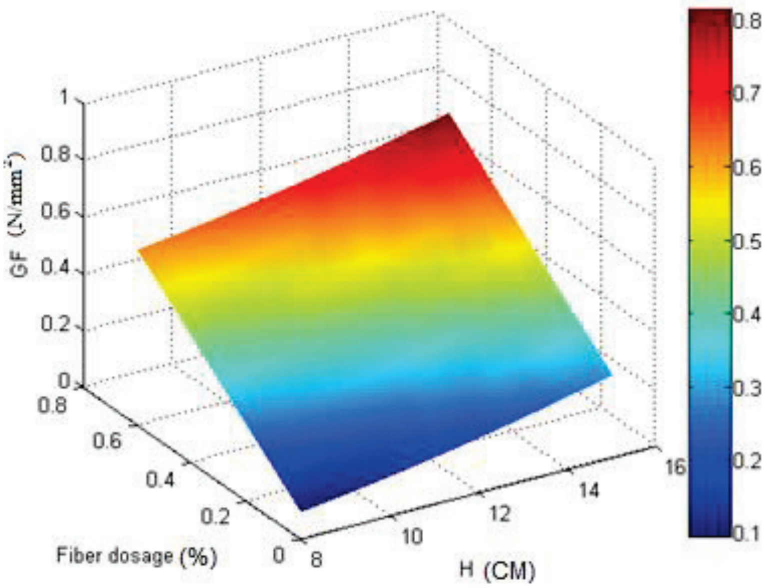

**Figure 6.** The relationship between $G_F$, $H$, and *Fiberdosage*.

Figure 7 shows an example of the load–CMOD curve of the notched fiber-reinforced concrete specimens with different widths and a 0.4% volume fraction.

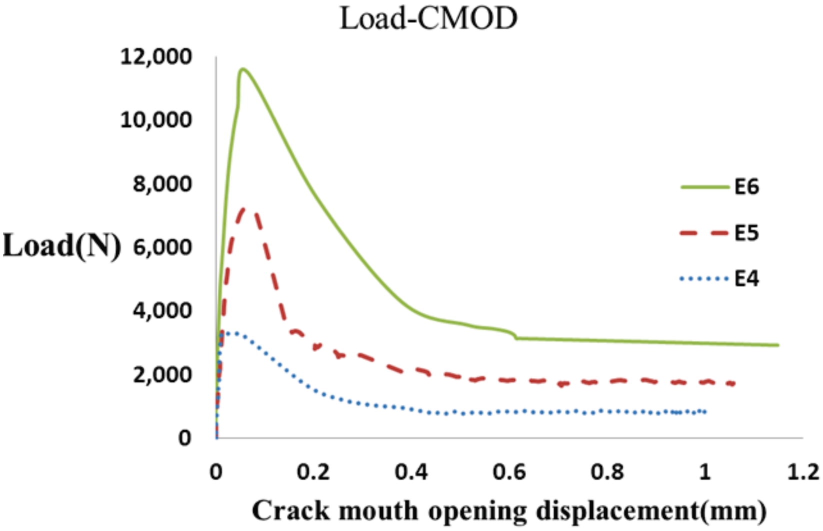

**Figure 7.** The load–CMOD curve of fiber-reinforced concrete specimens with different widths $T$.

To study the effect of independent variables, including the width of concrete specimens and fiber dosage, on fracture energy, multiple linear regressions were used. The initial equation considered for analysis is shown in Equation (4) by replacing $T$ with $H$.

Similar to the method used for thickness variations, a width change was also made and the final model was obtained according to Tables 5 and 6. According to Table 5, the high value of $F$ indicates the overall significance of the model at a high confidence level. However, the adjusted $R^2$ value of 0.98 indicates that two variables, width ($T$) and *Fiberdosage*, explain about 96% of the fracture energy variations; hence, the model is suitable to predict fracture energy.

**Table 5.** ANOVA table.

| Total | DF | SS | MS | F-Value | *p*-Value |
|---|---|---|---|---|---|
| Model | 8 | 0.0584 | 0.007302 | - | - |
| Residual error | 2 | 0.0569 | 0.028428 | 109.12 | 0 |
| $R^2$ | 6 | 0.0016 | 0.00026 | | |
| Adjusted $R^2$ | 0.9732 | - | - | - | - |
| | 0.9643 | - | - | - | - |

**Table 6.** Values of regression coefficients of $G_F$.

| Independent Variable | Regression Coefficient | *p*-Value | *t*-Value | Standard Error | Standardized Coefficients |
|---|---|---|---|---|---|
| Constant | 0.1438929 | 0 | 12.23 | 0.0117701 | - |
| T2 | 0.0005169 | 0 | 7.93 | 0.0003574 | 0.5293087 |
| Fiber dosage | 0.2588928 | 0 | 12.47 | 0.2161148 | 0.8325113 |

As shown in Table 6, the coefficient $T^2$ was equal to 0.00051. Therefore, if the change in fracture energy for width ($T$), holding other factors fixed, is considered, the equation $\Delta GF = 2 \times 0.00051 \times T \times \Delta T$ would show the fracture energy change value by width change (which is plotted for changes from 1 to 6 cm in Figure 8). These diagrams can be used for optimal design and economic evaluation. However, considering fiber dosage coefficients, each 1% increase in the amount of fiber increases the fracture energy by 0.26. To investigate the effect of two variables, width and fiber dosage, on fracture energy, considering that the units of these two variables are not the same, the effects of these variables cannot be compared with each other according to their coefficients. For this purpose, the coefficients must first be standardized so that it is possible to compare. The values of these standard coefficients are presented in the last column of Table 6. As can be seen, the higher the value of the fiber dosage coefficient, the greater effect of the fiber dosage relative to the width variable ($T$) on the fracture energy.

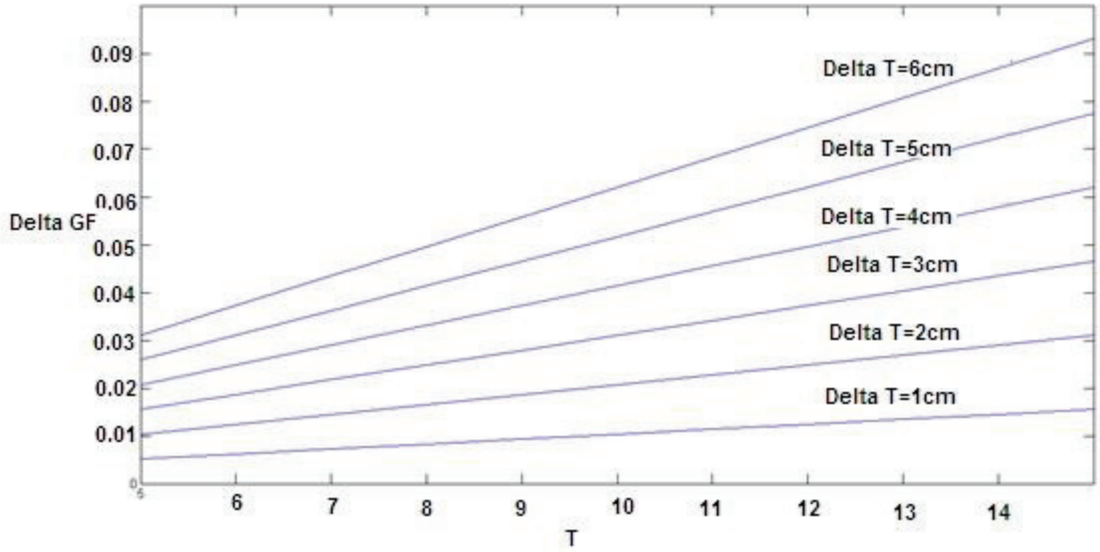

**Figure 8.** The effect of width change on fracture energy.

According to the model, the relationship between the three mentioned variables is graphically plotted in Figure 9, which is parabolic. The width and fiber dosage had a positive effect on the fracture energy, and by increasing each, the fracture energy increased, and the highest fracture energy occurred at the highest values of width and fiber dosage.

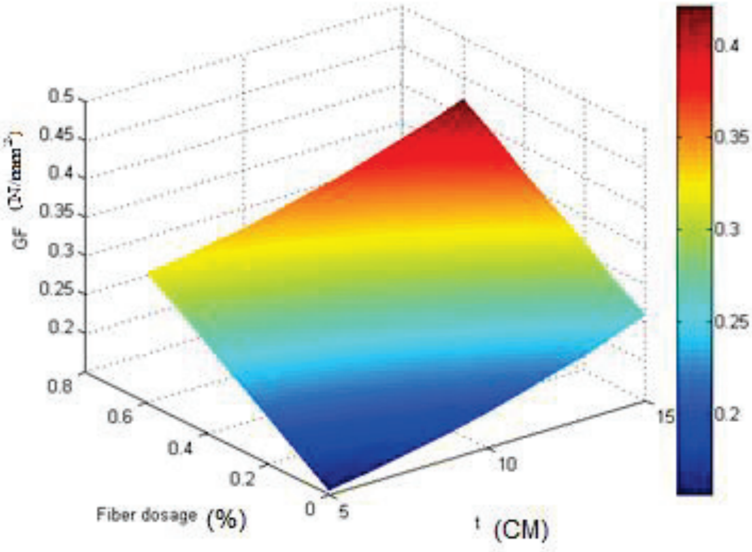

**Figure 9.** The relationship between $G_F$, $T$, and *Fiberdosage*.

### *3.2. Critical Stress Intensity Factor*

The critical stress intensity factors of different notched macro-synthetic fiber-reinforced concrete specimens were calculated based on Equation (3) and are presented in Tables 7 and 8.

**Table 7.** Critical stress intensity factor for different thicknesses *H*.

| Specimen | PAVE (N) | a (mm) | H (mm) | a/H | T (mm) | K (MPa × $\sqrt{}$m) | Percentage Change w.r.t Plane Concrete (%) |
|---|---|---|---|---|---|---|---|
| N1 | 2080 | 30 | 80 | 0.375 | 120 | 17.48972 | 0 |
| N2 | 5082.9 | 30 | 100 | 0.3 | 120 | 25.15605 | 0 |
| N3 | 13,211.2 | 30 | 150 | 0.2 | 120 | 27.3126 | 0 |
| E1-0.4 | 2880.1 | 30 | 80 | 0.375 | 120 | 24.21737 | 38.46 |
| E2-0.4 | 6701.5 | 30 | 100 | 0.3 | 120 | 33.16676 | 31.84 |
| E3-0.4 | 16,821.1 | 30 | 150 | 0.2 | 120 | 34.77565 | 27.32 |
| E1-0.6 | 3164.6 | 30 | 80 | 0.375 | 120 | 26.60959 | 52.14 |
| E2-0.6 | 7704.7 | 30 | 100 | 0.3 | 120 | 38.13175 | 51.58 |
| E3-0.6 | 19,099.6 | 30 | 150 | 0.2 | 120 | 39.48618 | 44.57 |

**Table 8.** Critical stress intensity factor for different widths *T*.

| Specimen | PAVE (N) | a (mm) | H(mm) | a/H | T (mm) | K (MPa × $\sqrt{}$m) | Percentage Change w.r.t Plane Concrete (%) |
|---|---|---|---|---|---|---|---|
| N4 | 3318.9 | 30 | 100 | 0.3 | 50 | 30.32 | 0 |
| N5 | 7240.6 | 30 | 100 | 0.3 | 100 | 33.08 | 0 |
| N6 | 11,505.8 | 30 | 100 | 0.3 | 150 | 35.04 | 0 |
| E4-0.4 | 3587.3 | 30 | 100 | 0.3 | 50 | 32.78 | 8.09 |
| E5-0.4 | 7774.1 | 30 | 100 | 0.3 | 100 | 35.52 | 7.37 |
| E6-0.4 | 12,400 | 30 | 100 | 0.3 | 150 | 37.77 | 7.77 |
| E4-0.6 | 3752.1 | 30 | 100 | 0.3 | 50 | 34.28 | 13.05 |
| E5-0.6 | 8101.4 | 30 | 100 | 0.3 | 100 | 37.01 | 11.88 |
| E6-0.6 | 12,691.8 | 30 | 100 | 0.3 | 150 | 38.65 | 10.3 |

As seen from these results, generally, the value of $K_{Ic}$ increases by increasing the thickness *H* and width *T* of concrete beams.

### *3.3. Assessment of Ruptured Cross Section and Fibers*

After the tests, the cross-sectional area of the sample was broken and the tip of the fiber was examined.

Figure 10 shows the number of broken sections of the fiber. A cross-sectional analysis of the broken sample showed that most of the sample failure was from aggregates and the mixture design was suitable. In addition, according to the figure, the tip of the fiber shows that the fibers did not rupture due to elongation and were not pulled out, which indicates good performance of the fibers.

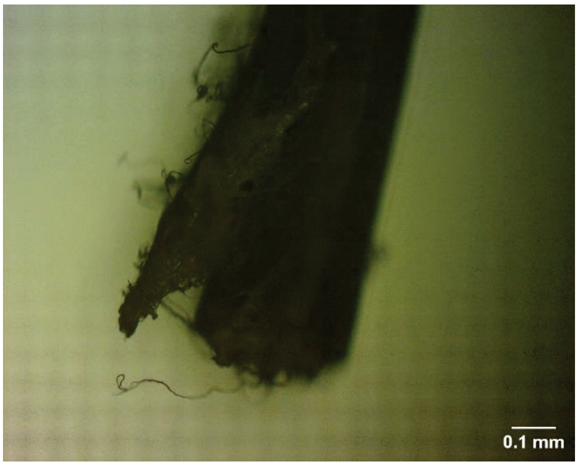

**Figure 10.** The cross-sectional area of a fiber.

## 4. Conclusions

In this study, we calculated the fracture energy for macro-synthetic fiber-reinforced concrete specimens with different thicknesses and widths tested using notched beam specimens. The main concluding remarks are:

- The experimental model of the effect of specimen size was presented by testing specimens with three different thicknesses and widths for normal and fiber-reinforced concrete.
- The results in Tables 4 and 6 show the relationship between the fracture energy and the thickness and width of the parabola.
- The results in Table 4 and Figures 5 and 6 indicate that adding fibers and increasing the thickness will increase the fracture energy.
- The results in of Table 6 and Figures 8 and 9 indicate that adding fibers and increasing the width will increase the fracture energy.
- The results in Tables 4 and 6 show that by assuming constant fracture energy, the thickness of fiber-reinforced concrete samples is lower than that of conventional concrete, which can be considered in the design of concrete structures, especially concrete pavement.
- The results in Table 7 indicate that adding fibers and increasing the thickness will increase the critical stress intensity factor up to 52.14%.
- The results in Table 8 indicate that adding fibers and increasing the width will increase the critical stress intensity factor up to 13.05%.

**Author Contributions:** Conceptualization, M.D., A.H. and M.R.M.A.; Methodology, M.D., A.H., M.R.M.A. and T.S.; Validation, M.R.M.A. and T.S.; Formal analysis, A.H.; Investigation, M.D.; Writing—original draft, M.D.; Writing—review & editing, A.H., M.R.M.A. and T.S.; Supervision, A.H., M.R.M.A. and T.S. All authors have read and agreed to the published version of the manuscript.

**Funding:** This work was financially supported by the Ministry of Education and Science of the Republic of Poland within the statutory research numbers: FD-20/IL-4/018.

**Conflicts of Interest:** The authors declare no conflict of interest.

## References

1. Zongjin, L.J.H. *Advanced Concrete Technology*; John Wiley & Sons: Hoboken, NJ, USA, 2011.
2. Lee, M.G.; Wang, W.C.; Wang, Y.C.; Hsieh, Y.C.; Lin, Y.C. Mechanical Properties of High-Strength Pervious Concrete with Steel Fiber or Glass Fiber. *Buildings* **2022**, *12*, 620. [CrossRef]
3. Abd Elmoaty, A.E.M.; Morsy, A.M.; Harraz, A.B. Effect of Fiber Type and Volume Fraction on Fiber Reinforced Concrete and Engineered Cementitious Composite Mechanical Properties. *Buildings* **2022**, *12*, 2108. [CrossRef]
4. Li, L.; Li, B.; Wang, Z.; Zhang, Z.; Alselwi, O. Effects of Hybrid PVA–Steel Fibers on the Mechanical Performance of High-Ductility Cementitious Composites. *Buildings* **2022**, *12*, 1934. [CrossRef]
5. Daneshfar, M.; Hassani, A.; Aliha, M.R.; Berto, F. Investigating Flexural Performance of Fiber-Reinforced Concrete with Different Contents and Types of Macrosynthetic Fiber. *Strength Mater.* **2022**, *54*, 650–661. [CrossRef]
6. Ahmad, J.; Burduhos-Nergis, D.D.; Arbili, M.M.; Alogla, S.M.; Majdi, A.; Deifalla, A.F.J.B. A Review on Failure Modes and Cracking Behaviors of Polypropylene Fibers Reinforced Concrete. *Buildings* **2022**, *12*, 1951. [CrossRef]
7. Wang, Z.; Gou, J.; Gao, D. Experimental study on the fracture parameters of concrete. *Materials* **2020**, *14*, 129. [CrossRef]
8. Pakravan, H.; Latifi, M.; Jamshidi, M.J.C. Hybrid short fiber reinforcement system in concrete: A review. *Constr. Build. Mater.* **2017**, *142*, 280–294. [CrossRef]
9. Bordelon, A.; Roesler, J.R. Fiber-reinforced concrete pavement design and material requirements. In Proceedings of the 8th International Conference on the Bearing Capacity of Roads, Railways and Airfields (BCR2A'09), Urbana, IL, USA, 29 June–2 July 2009; pp. 717–727.
10. Chari, K.B.; Research, I. Investigation on Mode–I Fracture Parameters Using Steel Fibers in High Strength Concrete. *Int. J. Sci. Eng. Res.* **2015**, *3*, 2347–3878.
11. Gustafsson, J.; Noghabai, K. Steel fibers as shear reinforcement in high strength concrete beams. *Nord. Concr. Res. Publ.* **1999**, *22*, 35–52.
12. Kreiger, E.L. A Model to Describe the Mode I Fracture of Steel Fiber Reinforced Ultra-High Performance Concrete. Master's Thesis, Michigan Technological University, Houghton, MI, USA, 2012.
13. Rao, G.A.; Rao, A.S. Toughness indices of fiber reinforced concrete subjected to mode II loading. *Proc. Fract. Mech. Concr. Struct.* **2010**, 112–117.
14. Valdez Aguilar, J.; Juárez-Alvarado, C.A.; Mendoza-Rangel, J.M.; Terán-Torres, B.T.J.M. Effect of the notch-to-depth ratio on the post-cracking behavior of steel-fiber-reinforced concrete. *Materials* **2021**, *14*, 445. [CrossRef]
15. Blazy, J.; Drobiec, Ł.; Wolka, P.J.M. Flexural tensile strength of concrete with synthetic fibers. *Materials* **2021**, *14*, 4428. [CrossRef]
16. Daneshfar, M.; Hassani, A.; Aliha, M.R.M.; Berto, F. Evaluating mechanical properties of macro-synthetic fiber-reinforced concrete with various types and contents. *Strength Mater.* **2017**, *49*, 618–626. [CrossRef]
17. Fallah, S.; Nematzadeh, M. Mechanical properties and durability of high-strength concrete containing macro-polymeric and polypropylene fibers with nano-silica and silica fume. *Constr. Build. Mater.* **2017**, *132*, 170–187. [CrossRef]
18. Lee, J.-H.; Cho, B.; Choi, E.J.C. Flexural capacity of fiber reinforced concrete with a consideration of concrete strength and fiber content. *Constr. Build. Mater.* **2017**, *138*, 222–231. [CrossRef]
19. Alberti, M.G.; Enfedaque, A.; Gálvez, J.C. Fibre reinforced concrete with a combination of polyolefin and steel-hooked fibres. *Compos. Struct.* **2017**, *171*, 317–325. [CrossRef]
20. Hesami, S.; Hikouei, I.S.; Emadi, S.A.A. Mechanical behavior of self-compacting concrete pavements incorporating recycled tire rubber crumb and reinforced with polypropylene fiber. *J. Clean. Prod.* **2016**, *133*, 228–234. [CrossRef]
21. Saidani, M.; Saraireh, D.; Gerges, M.J.E.S. Behaviour of different types of fibre reinforced concrete without admixture. *Eng. Struct.* **2016**, *113*, 328–334. [CrossRef]
22. Afroughsabet, V.; Ozbakkaloglu, T.J.C. Mechanical and durability properties of high-strength concrete containing steel and polypropylene fibers. *Constr. Build. Mater.* **2015**, *94*, 73–82. [CrossRef]
23. Yew, M.K.; Mahmud, H.B.; Ang, B.C.; Yew, M.C.J.C. Influence of different types of polypropylene fibre on the mechanical properties of high-strength oil palm shell lightweight concrete. *Constr. Build. Mater.* **2015**, *90*, 36–43. [CrossRef]
24. Karadelis, J.N.; Lin, Y. Flexural strengths and fibre efficiency of steel-fibre-reinforced, roller-compacted, polymer modified concrete. *Constr. Build. Mater.* **2015**, *93*, 498–505. [CrossRef]
25. Hesami, S.; Ahmadi, S.; Nematzadeh, M.J.C. Effects of rice husk ash and fiber on mechanical properties of pervious concrete pavement. *Constr. Build. Mater.* **2014**, *53*, 680–691. [CrossRef]
26. Pająk, M.; Ponikiewski, T.J.C. Flexural behavior of self-compacting concrete reinforced with different types of steel fibers. *Constr. Build. Mater.* **2013**, *47*, 397–408. [CrossRef]
27. Singh, S.; Singh, A.; Bajaj, V. Strength and flexural toughness of concrete reinforced with steel-polypropylene hybrid fibres. *Asian J. Civ. Eng.* **2010**, *11*, 495–507.
28. Silva, F.J.; Thaumaturgo, C. Fibre reinforcement and fracture response in geopolymeric mortars. *Fatigue Fract. Eng. Mater. Struct.* **2003**, *26*, 167–172. [CrossRef]
29. *ACI 211.1-91*; Standard Practice for Selecting Proportions for Normal. Heavyweight, and Mass Concrete. American Concrete Institute: Farmington Hills, MI, USA, 2009.

30. *D7508/D7508M-10*; Standard Specification for Polyolefin Chopped Strands for Use in Concrete. ASTM International: West Conshohocken, PA, USA, 2015.
31. *JCI-S-001e2003*; Japan Concrete Institute Standard. Method of Test for Fracture Energy of Concrete by Use of Notched Beam. Japan Concrete Institute: Tokyo, Japan, 2003.
32. Zhu, X.K.; Joyce, J.A. Review of fracture toughness (G, K, J, CTOD, CTOA) testing and standardization. *Eng. Fract. Mech.* **2012**, *85*, 1–46. [CrossRef]

materials

Article

# Application of an Eco-Friendly Adhesive and Electrochemical Nanostructuring for Joining of Aluminum A1050 Plates

**George C. Papanicolaou *, Lykourgos C. Kontaxis, Nikolaos Kouris and Diana V. Portan**

Composite Materials Group, Department of Mechanical Engineering and Aeronautics, University of Patras, Rio, GR 265 04 Patras, Greece
* Correspondence: gpapan@upatras.gr

**Abstract:** In adhesive joints used in several industrial applications, the adherends' bonding is made using an adhesive, which is usually an epoxy resin. However, since these adhesives are derived from petroleum fractions, they are harmful to the environment, due to the pollutants produced both during their manufacture and subsequent use. Thus, in recent years, effective steps have been made to replace these adhesives with ecological (green) ones. The present work focuses on the study of aluminum A1050 joints bonded with a green adhesive; the study also involves the electrochemical anodization method applied to adherends for nano-functionalization. The nanostructured aluminum adherends allow the formation of an expanded surface area for adhesion, compared to the non-anodized adherends. For comparison reasons, two different adhesives (Araldite LY1564 and Green Super Sap) were used. In addition, for the same reasons, both anodized and non-anodized aluminum adherends were joined with both types of adhesives. The lap joints were subsequently tested under both shear-tension and three-point bending conditions. The major findings were that aluminum A1050 anodization in all cases resulted in shear strength enhancement of the joints, while joints with both aluminum anodized and non-anodized adherends and bonded with the eco-friendly adhesive showed a superior shear behavior as compared to the respective joints bonded with Araldite adhesive.

**Keywords:** eco-friendly adhesive; aluminum A1050; single-lap joint (SLJ); tensile-shear testing; three-point bending; electrochemical anodization; alumina nanotubes

## 1. Introduction

In industrial load-bearing components manufacture, adhesives are used in joining both similar and dissimilar materials (e.g., metal-to-metal, metal-to-composite, metal-to-rubber, metal-to-glass, metal-to-wood, etc.) together [1]. The use of adhesives for joining materials is targeting to the development of cheaper and lighter products. Adhesive joining is a tried-and-true fastening technique in the industrial industry that expands the present range of traditional joints. Elastic adhesives were first utilized to assemble and join elements of automobiles in the early 1980s. Regardless of whether the joint is elastic or stiff, the adhesive joining method differs fundamentally from mechanical joining techniques. Structural adhesives are frequently used in the industry as joining techniques because flexible adhesives, as opposed to rigid ones, may bend when subjected to stress. Welding issues frequently include deformation and thermal distortion. To fix these flaws, sanding and polishing procedures are used. Moreover, some metals, such as some varieties of ultra-high strength steel, deteriorate in the presence of heat [2]. By more uniformly spreading stresses, adhesive bonding prolongs the useful life of a component or thins out the material. In contrast to stiff structural adhesive-bonded structures, which distribute stress along the bond line, elastic adhesives offer a stress distribution over the whole bonded region.

In addition to joining two parts, adhesives also act as a sealant. The protection against galvanic and crevice corrosion provided by adhesive bonding has been demonstrated to be superior to that of traditional fastening techniques. Unlike mechanical joints, adhesive joints need some time to reach their maximum or ultimate strength. Assembly handling and advancement to the following manufacturing stage, however, typically occurs before assemblies attain their peak performance. Although it is well-established in the industrial sector, structural adhesive bonding has a lot of potential applications. An outdated joining technique is replaced and much improved by adhesive bonding.

However, although adhesive bonding looks like a promising solution for cheap and lighter product manufacture, there are some serious problems that must be overcome. The main problem is that adhesives must fulfill the performance requirements of the product while, at the same time, they must be eco-friendly so that they do not harm the global environment. For example, adhesives based on phthalates and formaldehyde release emissions as they dry, which can significantly affect air quality, resulting in human skin and eye irritation as well as liver and kidney damage. The same, or worse, problems can occur when using other adhesives containing several harmful chemicals [3].

This aspect is becoming more significant while developing novel polymers because of rising environmental consciousness [4–7]. A rising variety of environmentally friendly epoxies have been created recently, and these materials are now made from natural and renewable resources including epoxidated oils (soybean oil, cottonseed oil, etc.), furans, sorbitol, and others [8–10]. Several of these are already offered commercially [11,12]. Depending primarily on their green carbon content, level of toxicity, environmental effect throughout their life cycle (greenhouse emissions, energy consumption, etc.), and end-of-life possibilities, these materials can be eco-friendly (recyclability, biodegradability, compostability). A variety of green materials have been designed and developed to employ as adhesives [13–18]. However, further study is required to investigate the environmental impact and enhance the mechanical performance of eco-friendly adhesives.

Depending on which component (i.e., adhesive or adherend) of the lap joint plays the primary role when the joint is loading, one can use adhesives belonging to one of the following four main categories, namely, (a) sealants, (b) low-strength adhesives, (c) medium-strength adhesives, and (d) high-strength adhesives.

Adhesive bonding is an interdisciplinary area of research since, depending on the specific application, it combines knowledge coming out from different sciences, such as chemistry, mechanical engineering, medical and medicine, biology, and other sciences. The main areas of application adhesive joints being used comprise aeronautics, aerospace, and medicine. On the base of their geometrical characteristics, adhesively bonded joints, are classified into many categories the basic types of which are (a) single-lap joints, (b) scarf joints, and (c) butt joints (Figure 1). In any case, the choice of the appropriate joining technique is of cardinal importance to lead in a high-strength structure. Each one of the three types of joints mentioned has its own advantages and disadvantages. Single-lap joints (SLJs) are the simplest ones to adhesively join two materials together. In the case of scarf joints, there is an inclined section the slope of which dictates the stress field developed upon loading. Finally, a disadvantage of butt joints is the small overlap area.

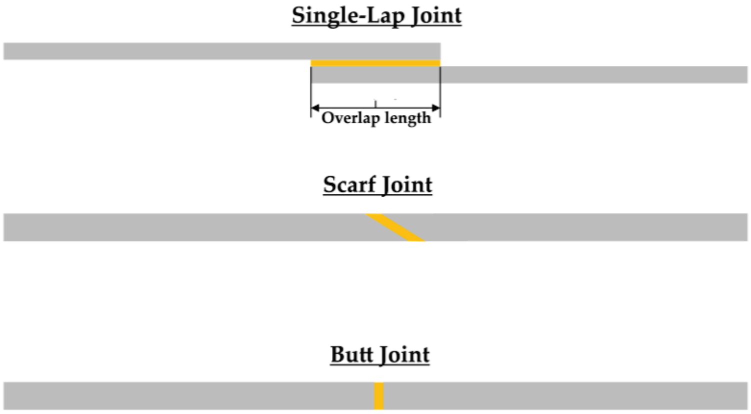

**Figure 1.** Basic types of adhesively bonded joints.

There are numerous factors affecting the mechanical performance of adhesive joints. Amongst them, except for the joint geometry and the adhesive type, one can mention the mechanical properties of the adherends/adhesive, the overlap length, the thicknesses of the adherends/adhesive, the adherends' surface roughness in the overlap area, etc. Testing and modelling of SLJs under tension has been extensively examined and presented in the literature [19–21]. Based on the pioneering works of Volkersen [22] and Goland and Reissner [23] as well as the Hart Smith modified model [24], the effect of different factors such as adherends properties [25], stress fields developed [26], plasticity effects [27] and adhesive fillet [28], affecting the SLJs behavior, have also been studied and presented.

Except for the above-mentioned parameters, a parameter of cardinal importance affecting the overall mechanical performance of adhesively bonded SLJs is the adherends' surface pre-treatments by applying special techniques such as sol–gel, wet chemical, electrochemical deposition, and mussel-inspired chemistry [29]. Adherends' surface pre-treatment is used, amongst others, for surface contaminants removal, surface roughness control, and surface wetting characteristics enhancement, thus leading to a better mechanical interlocking and/or adhesive/adherends' chemical bonding. Generally, research on the electrochemical anodization of metals is conducted on standard plates provided by well-known suppliers. Anyhow, most of the metals that are used in the industrial sectors, such as aeronautics, shipbuilding, and automotive, are low-cost and alloyed; this is because the low-cost metals allow the acquisition of large parts. In the laboratory research, results are influenced by very small changes in the metal's structure and composition (i.e., alloying or impurities). Thus, small differences in the metal's structure (purity, density, and porosity) modify the anodization results. This makes it difficult to realize the transfer of the process from the lab to the industries/market. Investigations are required to manage the shifting of the new nano-functionalized joints to applications, which is the purpose of previous and the present studies [30].

The electrochemical anodization has several advantages, such as, simplicity in application and low-cost processing. Anodizing is an electrochemical process to passivate metals. The process is carried out by electrolysis (direct current channeling), in an acid solution bath, under strict conditions of control of the concentrations of the chemical components, the temperature, the density of the metal, etc. This process is difficult to compare with any other surface treatment, since during anodizing aluminum has an active role. As part of this process, a thin layer of aluminum oxidation is created that is fully integrated into the outer surface of the profiles, thus offering remarkable features. This method allows the formation of highly organized nanostructures (i.e., oxide nanotubes) and the functionalization of metallic surfaces for specific applications [31–33]. However, two main challenges are accounted for in this method. The first mentioned above is that it shows some difficulties when applied to industrial grade surfaces of complex geometry and big sizes, and the second one, is that depending on the metallic surfaces to be adhesively bonded together, a specific anodization recipe is needed. In our previous publications, the anodization method was used to both titanium-titanium [34] and aluminum-aluminum adhesively bonded SLJs with very promising results [35].

Although tensile-shear testing of SLJs is well documented and a lot of works on this topic can be found in literature, there are only few papers dealing with SLJ performance when under three-point bending conditions. However, since under real conditions, joints are loaded both in tension and bending, SLJs three-point bending testing is very important. Three-point bending, and tension loading are very similar in the way in which they affect the adhesive while the four-point bending does not cause failure because the metallic substrates yield before the joint fails [2]. In addition, due to the complex stress field developed within the joint, analytical models that have been developed to predict joints' failure when under bending conditions, proved unsuccessful [36,37].

In the present work, the mechanical performance of single-lap aluminum adhesive joints using both non-anodized and anodized adherends were investigated and compared. Also, two different adhesives, the Araldite LY1564 resin and the eco-friendly Super Sap®

INR epoxy resin were used as adhesives. The later uses technology that reduces the environmental impact of the epoxies production, ultimately reducing the carbon footprint of the epoxy itself. Results of both tensile-shear testing and three-point bending showed that there is a considerable improvement of the joints' mechanical performance when using nanostructured adherends, while in all cases, specimens with the eco-friendly adhesive showed superior shear performance as compared to respective specimens with Araldite adhesive. These results are very promising in replacing the standard epoxy resin adhesives with more eco-friendly adhesives, while at the same time, improving the aluminum SLJs mechanical behavior.

## 2. Materials and Methods

### *2.1. Materials*

Low-cost aluminum A1050 of 99.6% purity was purchased from Manousaridis Bros OE (Athens, Greece). Compared to most metals, it generally shows a ductile behavior, low mechanical strength, good electrical and thermal conductivity, low density (2.79 g/cm$^3$), annealing temperature of 350–500 °C, and melting temperature of 650 °C (Table 1).

**Table 1.** Aluminum A1050 properties [38].

| Property | Value |
|---|---|
| Density (Kg/m$^3$) | 2.79 |
| Modulus of Elasticity (GPa) | 73 |
| Tensile Strength (MPa) | 75 |
| Proof Stress 0.2% (MPa) | 35 |
| Fatigue Strength 50 mil. Cycles (MPa) | 20 |
| Shear Strength (MPa) | 50 |
| Hardness Vickers (HV) | 22 |
| Hardness Brinell | 20 |
| Elongation 50 mm (%) | 32 |
| Melting Point (°C) | 640 |
| Thermal Conductivity (W/m·K) | 121–193 |
| Thermal Expansion | $23.1 \times 10^{-6}$ grad$^{-1}$ |

Two different types of resins were used. The first adhesive used was the Super Sap® INR Epoxy combined with hardener Super Sap® INF. As opposed to traditional epoxies that are composed primarily of petroleum-based materials, Super Sap® formulations contain biobased renewable materials sourced as co-products or from waste streams of other industrial processes, such as wood pulp and bio-fuels production. These natural components have excellent elongation and exceptionally high adhesion properties. The Super Sap INR/INS epoxy system was prepared by mixing the two parts with a ratio of 100:33. The system underwent an initial cure at room temperature for 24 h and post cure at 120 °C for 2 h. The adhesive material used in the second epoxy resin system for the SLJs was a traditional resin type, Araldite LY 1564 (bisphenol A) combined with Aradur 2954 (cycloaliphatic polyamine) as curing agent at a ratio 100:35 parts by weight. The curing time was of 1 h at 80 °C followed by 8 h at 140 °C. The properties of the two resins used can be seen in Table 2.

### *2.2. Electrochemical Anodization of the Adherends*

An alumina nanotube layer has been created on the surface of aluminum plates using the electrochemical anodization technique. The objective was to create a stronger interlock in the interphase between adherends and adhesive, as well as to improve the adherends' surface roughness and increase their contact area with the adhesive. A graphite bar served as the cathode and the metallic plate served as the anode. The anodization was performed only in the joining region of the aluminum adherend. The electrodes were spaced approximately 2.5 to 3 cm apart. There are main parameters influencing the results of the aluminum anodization: (i) the electrolyte type, (ii) the anodization duration, and (iii) the applied voltage.

**Table 2.** Applied adhesives properties [39,40].

| Property | Super Sap INR/INS | Araldite LY1564/Aradur 2954 |
|---|---|---|
| Viscosity at 25 °C (mPas) | 2200/25 | 1200–1400/70–120 |
| Density (g/cm$^3$) | 1.1 (mixed) | 1.1–1.2/0.94–0.95 |
| Mix ratio (PBW) | 100:33 | 100:35 |
| Cure cycle | 24 h at 25 °C + 2 h at 120 °C | 1 h at 80 °C + 8 h at 140 °C |
| Tensile Modulus (GPa) | 3.38 [1] | 2.55–2.65 [4] |
| Tensile Strength (MPa) | 68.9 [1] | 71–77 [4] |
| Elongation (%) | 3–4 [1] | 4.5–5.5 [4] |
| Flexural Modulus (GPa) | 2.62 [2] | 2.6–2.8 [5] |
| Flexural Strength (MPa) | 105.5 [2] | 120–124 [5] |
| Ultimate Tg by DSC (°C) | 104.4 [3] | 148 [6] |

[1] ASTM D638; [2] ASTM D790; [3] ASTM D3418; [4] ISO 527; [5] ISO 178; [6] IEC 1006, 10 K/min.

Using electrochemical anodization on the metal substrates it is possible, by applying a specific anodization recipe, to control the geometrical characteristics of nanotubes developed on the adherends surface and thus producing nanotubes of specific height and diameter, as well as surface density. Although this method is based on a trial-and-error procedure, once the recipe is found, then a pronounced increase in adhesive joints strength can be achieved. To find the best method for producing structured alumina nanotubes, many combinations of these variables were investigated until we reached the final anodizing formula, summarized in three steps. Prior to the anodization procedure, specimens were polished with sandpaper, starting from 320 grits for few seconds, followed by polishing with an intermediate sandpaper of 600 grits for 2 min, and ending with 5 min methanol bath cleaning. Some publications mention a two-steps anodization process applied on industrial alumina [41,42]. The protocol within the present investigation is formed of one preparation step and two steps of effective anodization. The three steps were found to be necessary to obtain the desired results. The protocol was previously developed as described in [35]: (i) Electropolishing: which is an exothermic process and it needs temperature control by freezing part of the electrolyte; (ii) Pre-anodization: allows a field-assisted dissolution of the oxide under a higher electric potential which is considered a prerequisite for the controlled formation of a porous alumina oxide; and (iii) Anodization: performed for an extended time (4 h) compared to the pre-anodization, which enables a guided self-building of the nanotube architecture.

The electrolytes were sulfuric and oxalic acids-based. Sulfuric acid is used for Type III Hard Anodizing, also known as hard coat anodize, meant for components that are subject to extreme wear or highly corrosive environments to create a more durable coating needed in applications like blast shields, hinge mechanisms, valves, and joints [43]. Oxalic acid is commonly used in aluminum anodization and is appropriate for industrial aluminum too [41,42].

In the first anodization step, the electrolyte was a water solution of a half-frozen 3% (*w*/*w*) hydrofluoric acid (HF), while the anodization had a duration of 20 min and the applied voltage was 20 V. In step 2, the specimen was anodized in a solution of 15.12 mL $H_2C_2O_4$ (oxalic acid) in 344.88 mL $H_2O$ and 40 mL $(CH_2OH)_2$ (ethylene glycol) for 10 min at a 40 V potential difference. Finally, in step 3, the aluminum was anodized in a solution of 15.12 mL $H_2C_2O_4$ (oxalic acid) in 344.88 mL $H_2O$ and 40 mL $(CH_2OH)_2$ (ethylene glycol) for 240 min at a 60 V potential difference. Between the anodization steps, the samples were cleaned with deionized water, ethanol and dried before proceeding to the next step. After the anodization process, the adherends were put in ultra-sonic bath for 25 min, in a solution of $H_3PO_4$ 3 wt.%, to remove the chemical traces of the electrolytes [35]. The ultrasonication was applied as described after the last anodization step and was a pore widening step.

### 2.3. Specimens' Manufacturing

Two types of specimens were manufactured for each test that was conducted, due to the different dimensional requirements. The joints designed for tensile testing were prepared according to the ASTM-D1002. The aluminum adherends had dimensions of 94 × 25.4 × 2 mm as shown in Figure 2a. The aluminum adherends for the three-point bending test had different dimensions of 140 × 18 × 2 mm as shown in Figure 2b. For each test, four different combinations of anodized/non-anodized aluminum adherends bonded with Araldite/Super Sap adhesives were manufactured (Figure 3).

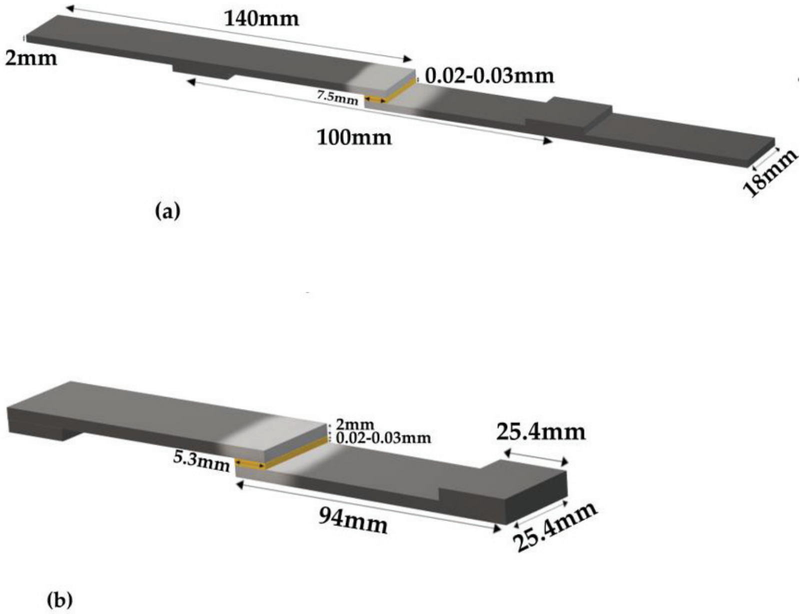

**Figure 2.** Adhesive single-lap joint specimens (**a**) for three-point bending test (**b**) for tensile test.

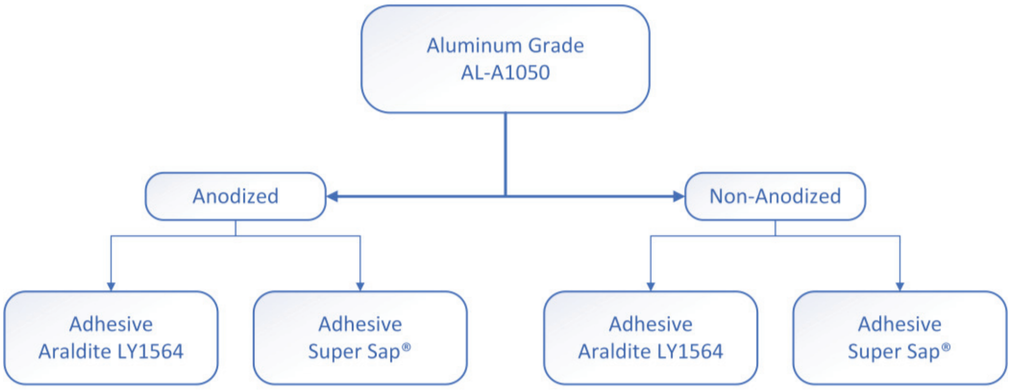

**Figure 3.** The four different types of single-lap joints manufactured and tested.

The preparation of the Araldite LY-1564/Aradure 2954 epoxy system began by mixing them at a ratio of 100:35, then stirring the mixture for a few minutes and putting it in an air-vacuum chamber for 5–7 min. After that, the epoxy adhesive was applied to the overlap area, with the overlap lengths presented in Figure 2 and the adherents were bonded under controlled pressure at room temperature conditions. Subsequently, the SLJs were put in the oven for 1 h at 80 °C and then for 8 h at 140 °C. The Super Sap INR/INS epoxy system was prepared by mixing the two parts at a ratio of 100:33, same precured process had been followed except that the specimens were left for 24 h in ambient conditions and then were put in the oven for 2 h at 120 °C. After the adhesive was cured the specimens were kept in air-sealed plastic bags.

### 2.4. Surface Analysis and Mechanical Characterization

A Scanning Electron Microscope (SEM) device, Model Zeiss SUPRA 35VP (Jena, Germany) was used to observe the adherends' contact area micro/nanostructure.

The apparent shear strength of the adhesive was determined through tensile loading of the joint, as indicated by ASTM D1002-01, using an Instron 8872-25 kN servohydraulic (High Wycombe, UK) universal mechanical testing machine. In all cases, a constant crosshead speed of 1 mm/min was applied. Based on the maximum tensile forces recorded for each tested joint, the adhesive shear strength $\tau$ was calculated as the maximum shear stress attained in an adhesive layer using the formula:

$$\tau = \frac{P}{w \cdot l_0} \quad (1)$$

where $\tau$ is the adhesive shear strength, $P$ is the load, $w$ is the width, and $l_0$ is the overlap length. Five or more specimens per type (i.e., anodized/non-anodized and Araldite/Super Sap) were tested to ensure the repeatability of the results.

The flexural behavior of the manufactured SLJs was studied through a series of quasi-static three-point bending tests using an Instron 4301 (High Wycombe, UK) universal mechanical testing machine. A schematic representation of the three-point bending test as executed in all types of joints tested is shown in Figure 4. The tests were performed at room temperature with a constant crosshead speed of 1 mm/min. Five or more specimens per type (i.e., anodized/non-anodized and Araldite/Super Sap) were tested to ensure the repeatability of the results. The experimental setups used are shown in Figure 5.

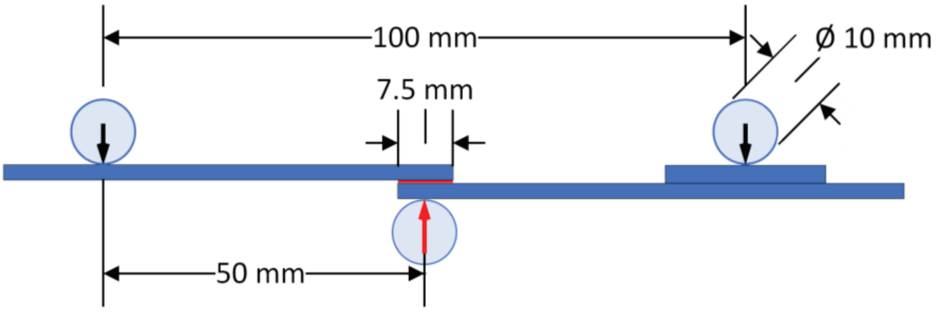

**Figure 4.** Schematic representation of the joints flexural loading as applied.

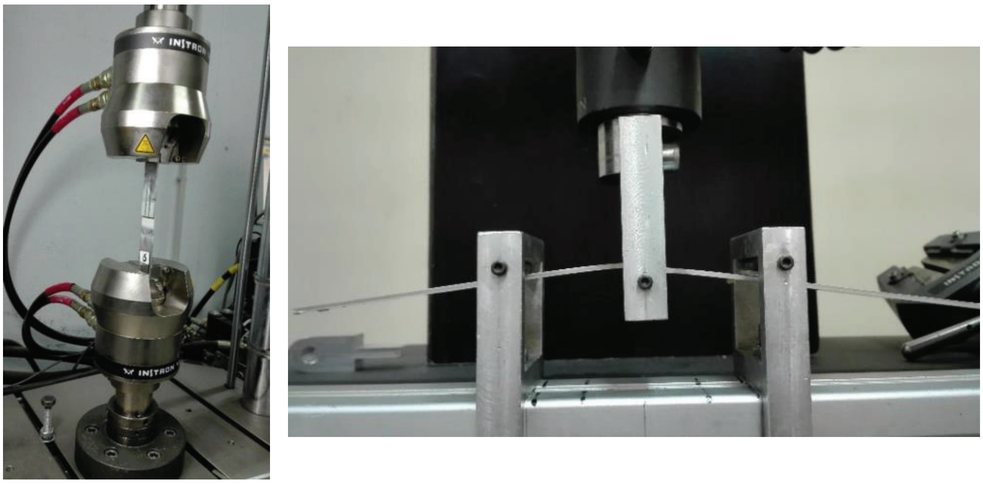
(**a**) (**b**)

**Figure 5.** Experimental setup of a single-lap joint for (**a**) tensile-shear loading, (**b**) flexural loading.

### *2.5. Data Analysis*

The experimental results for the tensile-shear tests were obtained as described in the previous sub-chapter and the maximum apparent shear strength was calculated using Equation (1). The individual specimens' values for each case (i.e., anodized/non-anodized and Araldite/Super Sap) were used to calculate the mean maximum shear strength, the standard deviation, and the coefficient of variation of these experimental values. The coefficient of variation never exceeded 10%.

For the three-point bending tests the same procedure was followed. The mean values, the standard deviation, and the coefficient of variation for failure load, failure deflection, and load-deflection slope were calculated.

## **3. Results and Discussion**

### *3.1. Scanning Electron Microscopy*

In the present work, a specific protocol of hard anodization of aluminum plates was applied for the development of surface alumina nanotubes layers. The aluminum plates are intended to be used subsequently for the manufacture of adhesive SLJs. The main anodizing parameters affecting the nanotubes size and morphology are the aluminum alloy composition, the anodizing voltage, the type of electrolyte, and the duration of the anodization process. Therefore, the anodization process is a highly controlled oxidation phenomenon. For the present investigation, electrolytes and voltage intensities were combined until the ideal recipe for the employed aluminum was found. It was previously stated that anodizing in sulfuric acid results in small pore sizes and interpore distances compared to the ones obtained by anodizing in phosphoric and oxalic acids [44]. Three-step anodization method has been utilized before to prepare anodic alumina templates with various pore morphologies (e.g., arched-shape, tree-like, branched-shape) and tunable interpore distances and it was affirmed that such structures are not found within the more traditional alumina templates fabricated by a two-step anodization of aluminum films [45]. Recently, it was found that the optimal etching effect on alumina is obtained with 1 wt% HF, which is the reason why a three-step anodization procedure has been chosen [46]. However, the previously mentioned concentration of hydrofluoric acid was low for the type of aluminum used in the present investigation and consequently it needed to be adjusted to 3 wt%.

The aluminum plates topography at the different protocol anodization stages is shown in Figure 6. To achieve both, chemical traces elimination and pore widening, ultrasonication of anodized aluminum plates was applied in a 3 wt% $H_3PO_4$ water solution. Prior to applying ultrasonication, nanotubes were not clearly observed (Figure 6c).

Figure 6b shows the obtained roughness after the second anodization step (20 V for 20 min) is completed. After the third anodization step is accomplished, a continuous distribution of pores may be observed on the entire analyzed surface, with pore diameter around 80–90 nm (Figure 6c). However, upon the completion of the last stage of anodization pores may not be clearly observed (Figure 6c). After ultrasonication the impurities layer is removed, and pores are widened (Figure 6d).

These findings prove that parameters such as electrolyte type, applied voltage and electrochemical anodization duration strongly affect the nanotubes size and morphology while, at the same time, they are in complete agreement with respective results found in Araoyinbo et al. [47]. Our findings are in agreement with other bibliographic studies; it has been stated that the formation of the aluminum oxide layer and the control of the anodization process is a challenge, since the presence of alloying elements affects not only the rate of oxide growth but also the microstructure of the anodic film. Furthermore, it was found that pore circularity and regularity of pore arrangement in AAO membranes formed on the AA1050 alloy were always worse than those observed on the pure Al substrate. The structural features, such as pore diameter, interpore distance, wall thickness, barrier layer thickness, porosity, and pore density of porous anodic alumina formed on AA1050 are a little different from those obtained for high purity aluminum [41]. That is why an adapted protocol consisting of one preparation procedure by electropolishing and two anodization steps are needed.

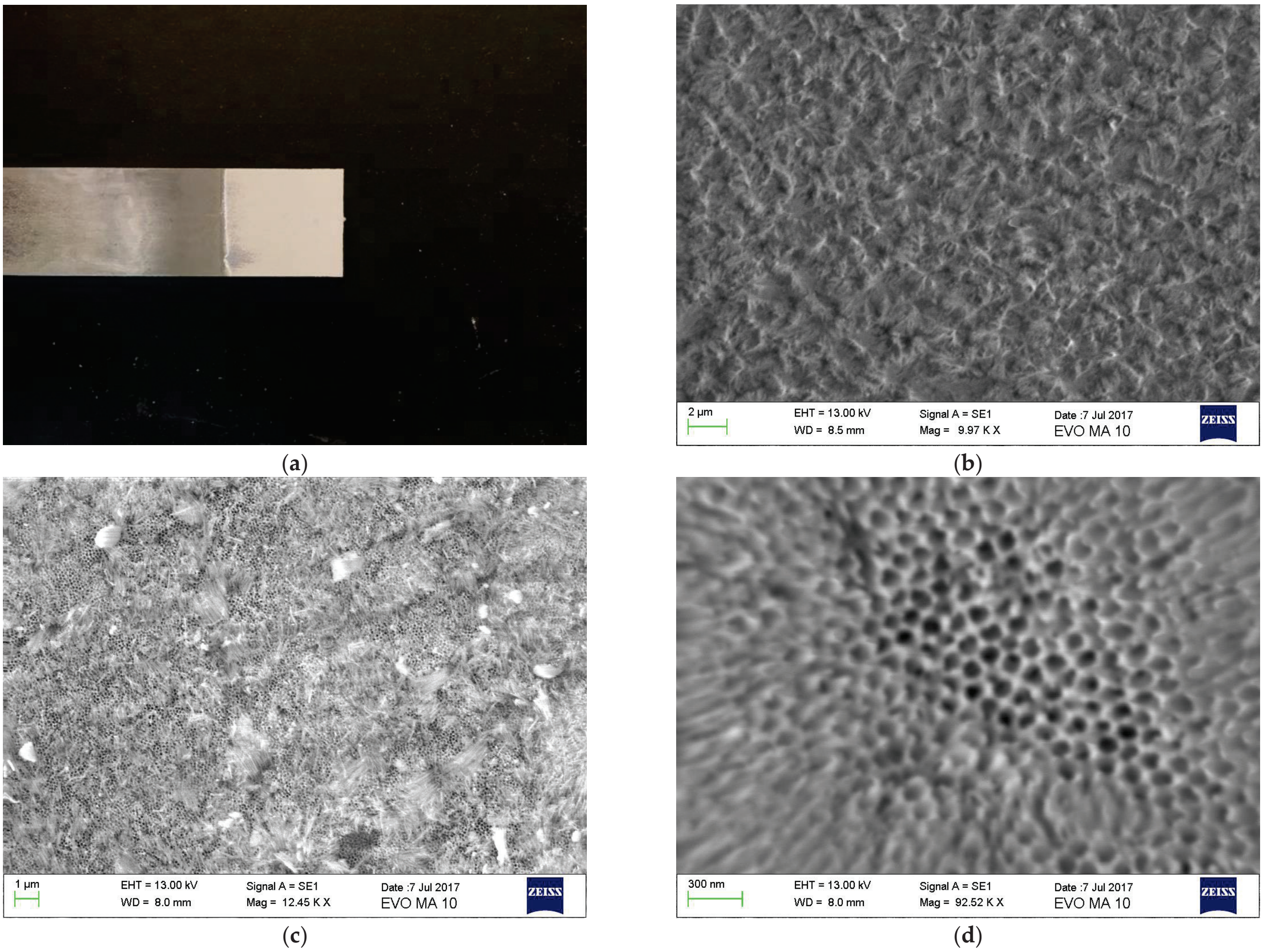

**Figure 6.** Micrographs of aluminum plate: (**a**) adherend after anodic treatment, (**b**) SEM after the second anodization step, (**c**) SEM after the third anodization step, without ultrasonication and (**d**) SEM after ultrasonication.

### 3.2. *Tension-Shear Testing*

In the present paragraph, results for the tension-shear tests of all types of joins manufactured, are presented.

Figure 7a shows load-displacement curves for joints with non-anodized and anodized aluminum adherends using Araldite and Super Sap adhesive. Average shear strengths values were found to be 9.92 MPa and 15.4 MPa respectively for the Araldite and 10.94 MPa and 21.92 MPa respectively for the Super Sap adhesive, as presented in Figure 7b.

To better quantify the results, average shear strength values for all four types of joints manufactured and tested in tension-shear, are given in Table 3. These values show separately both the effect of anodization and the adhesive type on the shear lap joints' shear strength values. Thus, by anodizing the aluminum in the Araldite joints, an increase of 55.5% in shear strength was achieved, while for the Super Sap joints, an increase of 100.9% in shear strength was obtained for the anodized aluminum joints.

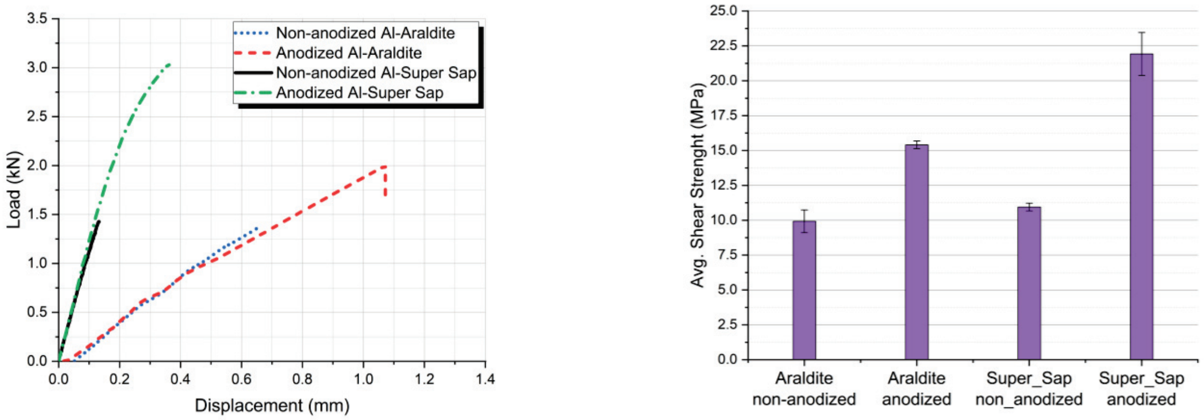

(**a**) (**b**)

**Figure 7.** Effect of aluminum adherends anodization on the aluminum single-lap joints bonded with Araldite and Super Sap adhesive tensile-shear behavior; (**a**) load-displacement curves, (**b**) bar diagram for the joints' average shear strength values.

**Table 3.** Comparison of the average shear strength values for the different types of adhesive aluminum single-lap joints manufactured and tested.

| Type of Joint (Anodization Effect) | Shear Strength (MPa) | Difference (%) | Type of Joint (Adhesive Effect) | Shear Strength (MPa) | Difference (%) |
|---|---|---|---|---|---|
| Araldite non-anodized | 9.9 | 55.5 | Araldite non-anodized | 9.9 | 10.1 |
| Araldite anodized | 15.4 | | Super Sap non-anodized | 10.9 | |
| Super Sap non-anodized | 10.9 | 100.9 | Araldite anodized | 15.4 | 42.2 |
| Super Sap anodized | 21.9 | | Super Sap anodized | 21.9 | |

However, in Table 3 the results are also cross-examined to quantify the adhesives effect on the joint. According to the results shown, Super Sap joints' shear strength are higher than Araldite joints' respective values, especially in the case of the anodized specimens, where an increase on the order of 42.2% was observed.

From the results presented in Table 3 it follows that:

1. For both types of adhesives applied, aluminum anodization resulted in shear strength enhancement.
2. The use of the eco-friendly adhesive resulted in a superior shear behavior of the joints as compared with the joints where Araldite adhesive was used.
3. The maximum tensile-shear strength was achieved when using both anodized aluminum adherends and the eco-friendly epoxy adhesive.

The above-mentioned findings can be explained through the parameters affecting the shear strength. Despite its simplicity, tension shear testing is characterized by several drawbacks. To mention, upon loading, a differential shear effect is observed, according to which a non-uniform stress and strain distribution in the adhesive-adherend interfacial area is developed, potentially affecting the results, and leading to incorrect values concerning the adhesive strength. More precisely, as the joint is under tensile loading, adherend tensile stress attains a maximum value at the overlap edge which is closer to the side of the applied load, decreasing subsequently, tending to zero at the other overlap edge. The same variation is observed for the adhesive-adherend interfacial strain leading to the development of complicated non-uniform interfacial stress and strain fields. These non-uniform stress and strain fields over the bond area result in the development of shear stress concentrations at the overlap edges, disturbing the reported shear stress experimental value, which is lower than the true ultimate strength of the adhesive. In addition, even if all measures have been taken for the development of a strong adhesive-adherend adhesion, environmental conditions, such as atmospheric moisture, strongly degrade the adhesion bond and shorten the adhesive joint life [48].

Adhesive-adherend adhesion is strongly affected by adherends' surface roughness since roughness changes the surface energy of the materials in contact. The term roughness refers to the deviation of a surface from its mean plane, and it is characterized by statistical parameters such as the variance of height, slope, and curvature. However, these parameters strongly depend on the roughness measuring instrument resolution, as well as on the measuring direction. As a result, according to its definition, surface roughness is a random non-stationary and multiscale process. Adherends surface topography greatly affects the load-carrying capability of adhesive joints.

In their study of the relationship between adherend surface roughness and adhesive bond strength, Ghumatkar et al. [49] discovered that there is an ideal surface roughness for a maximum bonding strength and that the roughness range depends on the adherend material, while joint strength changes are associated Also, they came to the conclusion that there are other factors contributing to the increase in strength, hence a simple connection with surface roughness is insufficient to predict joint performance.

Cho et al. [50] studied the impact of surface roughness on adhesive strength of the heat resistant adhesive RTV88 by experiments and parameter analysis. To more clearly describe how surface roughness affects adhesive strength, the terms effective area, peel failure area, and cohesive failure area were established. In general, when surface roughness increases, the effective area, cohesive failure area, and shear strength all increase. Although the effective area grows as surface roughness increases, the shear strength decreases because, as surface roughness reaches a critical value, the cohesive failure area reduces.

Moreover, Pereira et al. [51] have reported for their aluminum alloy adhesive lap joints that the decrease in surface roughness was found to increase the shear strength of SLJs.

These seemingly contradictory results found in the literature lead to the conclusion that, with increasing surface roughness, an initial increase in shear strength is obtained up to a specific surface roughness value where shear strength attains its maximum value, while for values beyond this critical roughness value, a decrease in shear strength is obtained. The critical surface roughness value depends on the adherends-adhesive materials combination as well as on the surface pretreatment type.

Based on the above-mentioned findings, our results show that the degree of adherends surface roughness achieved by electrochemical anodization is close to the so-called critical roughness value, leading to a high value of the anodized SLJs shear strength as compared to the non-anodized joints. In addition, since the overall shear behavior of the joints depends not only on the adhesive type applied alone but on the adherend-adhesive material combination and the surface roughness as well, the application of the eco-friendly adhesive better fulfills the requirements for a high-value shear strength according to the results found. As a result, shear strength values for the non-anodized joints are close for both adhesives, while in the case of anodized joints, Super Sup adhesive shows higher shear strength values as compared with respective Araldite adhesive joints.

### *3.3. Three-Point Bending*

The flexural behavior of all types of aluminum SLJs is evaluated by three-point bending tests under quasi-static conditions.

All results were plotted in terms of applied load versus center deflection of the specimens (Figure 8a). All specimens had the same geometry and were tested under the same crosshead speed, thus making it possible to superimpose the load/displacement plots for each group of samples. This allowed a more accurate comparison of the resulting curves.

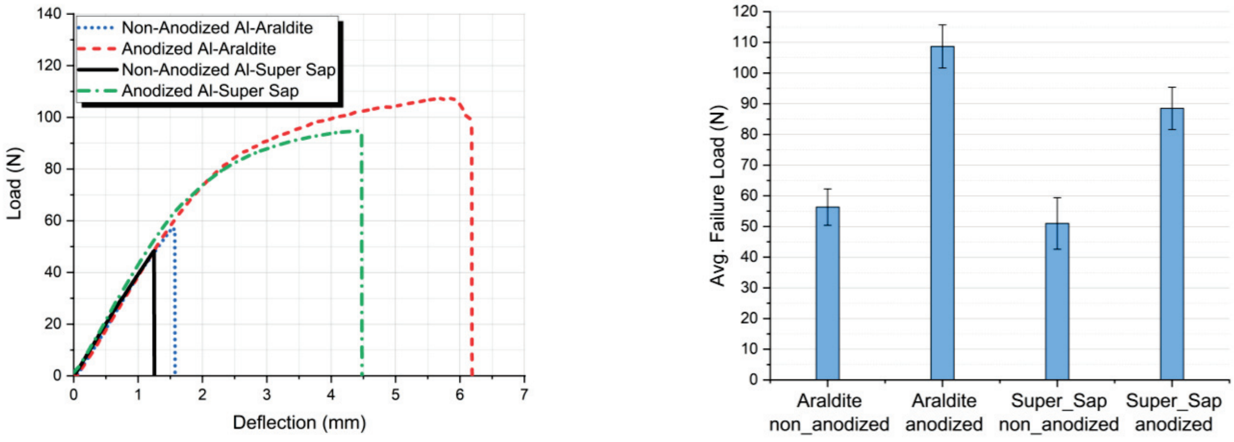

(**a**) (**b**)

**Figure 8.** Effect of aluminum adherends anodization on the aluminum single-lap joints bonded with Araldite and Super Sap adhesive three-point bending behavior; (**a**) load-deflection curve, (**b**) bar diagram for the joints' average flexural failure load.

The effect of anodization on the bending performance of the different types of joints can be deduced from the typical load-deflection curves shown in Figure 8a for non-anodized and anodized aluminum SLJs bonded with both Araldite and Super Sap adhesive.

From these curves it can be observed that non-anodized Al-Araldite SLJs show a linear elastic behavior which is independent on the adhesive type applied. In contrast, anodized aluminum joints show a ductile behavior with a higher ultimate load values and higher failure deflection as compared to the non-anodized aluminum joints. Thus, anodization always results to a better flexural behavior of the joints.

The observed behavior can be explained in combination with the adhesion mechanism described already in the previous paragraph where the anodized joints exhibited a stronger bond between adhesive and adherend. Thus, in the case of anodized joints, as the joint is under flexural load, the adhesion bond, due to its strength, resists to bending while the aluminum adherends are deformed leading to deformation values within their plasticity range, increasing thus the obtained overall joint failure load. The adherends plastic deformation observed during the joint flexural loading can be observed in Figure 5b.

Also, the effect of adhesive type used on the bending performance of the different types of joints can be deduced from the typical load-deflection curves shown in Figure 8a. From these curves it follows that joints bonded with Araldite adhesive show a superior bending performance for both anodized and non-anodized aluminum adherends. Finally, the slope in the linear region of the force-deflection response was measured and its value was found independent to both adhesive type and adherend surface treatment. This is because the slope in the linear region of the force-deflection response mainly depends on the adherend stiffness.

At this point, it is worth mentioning that there is a significant effect of anodization on the flexural failure load of the joints bonded with both adhesives. More precisely, in the case of joints bonded with Araldite adhesive, anodization of aluminum adherends resulted in an increase of 92.9% in the flexural failure load while the respective increase for the joints bonded with Super Sap adhesive was 73.5%. Comparing the effect of the adhesive type applied under the same aluminum surface treatment conditions, joints bonded with Araldite adhesive show a small increase in failure load values as compared to the joints bonded with Super Sap adhesive. Detailed numerical results and comparisons between the different types of joints with respect to the average failure load are given in Table 4.

**Table 4.** Comparison of average failure load values for the different types of Aluminum single-lap joints.

| Type of Joint (Anodization Effect) | Failure Load (N) | Difference (%) | Type of Joint (Adhesive Effect) | Failure Load (N) | Difference (%) |
|---|---|---|---|---|---|
| Araldite non-anodized | 56.3 | 92.9 | Araldite non-anodized | 56.32 | −9.4 |
| Araldite anodized | 108.6 | | Super Sap non-anodized | 51.00 | |
| Super Sap non-anodized | 51.0 | 73.5 | Araldite anodized | 108.6 | −18.5 |
| Super Sap anodized | 88.5 | | Super Sap anodized | 88.5 | |

Next, by comparing the failure deflections of the different types of joints, it can be concluded that adherends' anodization greatly affects their values. More precisely, in the case of joints bonded with Araldite, anodized joints show an increase of 283% in failure deflection values while a respective increase of 206% has been observed in joints bonded with Super Sap adhesive. On the other hand, the type of adhesive used plays an inferior role on the failure deflection values of the joints tested. Experimental results for failure deflection showed high standard deviations between the values of the numerous specimens tested and this is attributed to the fact that failure deflection is sensitive to a great number of manufacturing and experimental parameters such as void existence within the adherend-adhesive interface/interphase area, surface uniformity of nanotubes developed in the contact area, pressure applied uniformity during joint manufacturing, etc. Detailed results for the average failure deflection values are shown in both Figure 9 and Table 5.

Finally, since the slope in the linear region of the force-deflection response is a measure of the joint stiffness when under bending conditions, slope values for all types of joints were measured and analyzed. It was found that slope values are independent on adherends anodization and type of adhesive applied, having an almost constant value of 40 N/mm in all types of joints. This behavior shows that joint stiffness mainly depends solely on the adherends material type, and it is not affected by the adhesive applied, nor by the adherends surface treatment. Detailed numerical results are shown in both Figure 10 and Table 6.

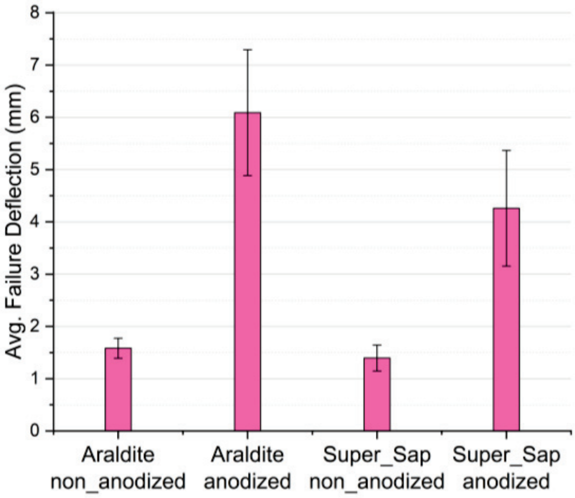

**Figure 9.** Bar diagram for the average flexural failure deflection values of all four types of joints manufactured and tested.

**Table 5.** Comparison of three-point bending average failure deflection values for the different types of aluminum single-lap joints.

| Type of Joint (Anodization Effect) | Failure Deflection (mm) | Difference (%) | Type of Joint (Adhesive Effect) | Failure Deflection (mm) | Difference (%) |
|---|---|---|---|---|---|
| Araldite non-anodized | 1.59 | 283.0 | Araldite non-anodized | 1.59 | −12.6 |
| Araldite anodized | 6.09 | | Super Sap non-anodized | 1.39 | |
| Super Sap non-anodized | 1.39 | 206.5 | Araldite anodized | 6.09 | −30.0 |
| Super Sap anodized | 4.26 | | Super Sap anodized | 4.26 | |

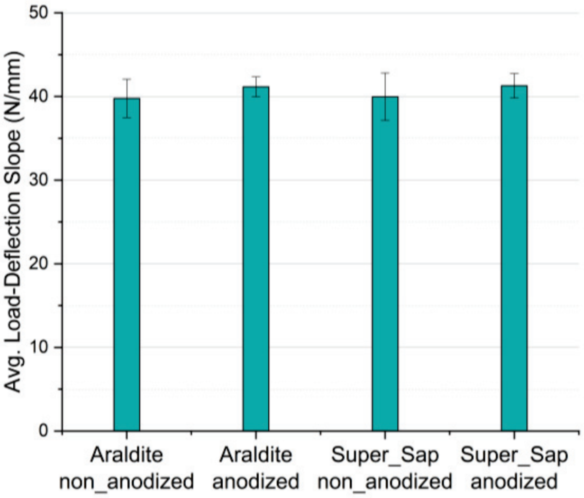

**Figure 10.** Bar diagram for the average load-deflection curves initial slope values of all the four types of joints manufactured and tested.

**Table 6.** Comparison of the three-point bending average load-deflection curves initial slope values for the different types of aluminum single-lap joints.

| Type of Joint (Anodization Effect) | Load-Deflection Slope (N/mm) | Difference (%) | Type of Joint (Adhesive Effect) | Load-Deflection Slope (N/mm) | Difference (%) |
|---|---|---|---|---|---|
| Araldite non-anodized | 39.8 | 3.5 | Araldite non-anodized | 39.8 | 0.5 |
| Araldite anodized | 41.2 | | Super Sap non-anodized | 40 | |
| Super Sap non-anodized | 40 | 3.3 | Araldite anodized | 41.2 | 0.2 |
| Super Sap anodized | 41.3 | | Super Sap anodized | 41.3 | |

## 4. Conclusions

In the present work, in an effort of replacing Araldite adhesive with an eco-friendly one, aluminum SLJs were manufactured and tested under tensile-shear testing and three-point bending. The effect of two parameters combinations such as the adhesive type applied and the aluminum adherends surface treatment by means of electrochemical anodization were studied. The main conclusions are as follows:

- For both types of adhesives applied, aluminum anodization resulted in shear strength enhancement,

- The use of the eco-friendly adhesive resulted in a superior shear behavior of the joints as compared with the joints where Araldite adhesive was used.
- A maximum tensile-shear strength enhancement of 42.2% was achieved when using anodized aluminum adherends bonded with the eco-friendly epoxy.
- In joints bonded with Araldite adhesive, anodization of aluminum adherends resulted to a considerable increase of 92.9% in the flexural failure load as compared with the non-anodized ones, while the respective increase for the joints bonded with Super Sap adhesive was 73.5%.
- The findings clearly showed that using anodized aluminum adherends bonded with the eco-friendly Super Sap adhesive we can achieve better mechanical performance of the aluminum single-lap joints as compared with the harmful for the environment aluminum single-lap joints bonded with Araldite epoxy adhesive, thus decreasing the environmental footprint.

**Author Contributions:** Conceptualization, G.C.P.; methodology, G.C.P. and L.C.K.; validation, G.C.P., L.C.K. and N.K.; formal analysis, L.C.K. and D.V.P.; investigation, N.K. and D.V.P.; resources, G.C.P.; data curation, D.V.P. and N.K.; writing—original draft preparation, G.C.P.; writing—review and editing, L.C.K.; visualization, G.C.P. and L.C.K.; supervision, G.C.P.; project administration, G.C.P.; funding acquisition, G.C.P. All authors have read and agreed to the published version of the manuscript.

**Funding:** This research received no external funding.

**Institutional Review Board Statement:** Not applicable.

**Informed Consent Statement:** Not applicable.

**Data Availability Statement:** The data presented in this study are available in manuscript.

**Conflicts of Interest:** The authors declare no conflict of interest.

## References

1. Papanicolaou, G.C.; Karagiannis, D.; Kousiatza, C.; Kontaxis, L.C.; Portan, D.V. Flexural behavior of single-lap joints of similar and dissimilar adherends. *J. Adhes. Sci. Technol.* **2022**, *37*, 624–648. [CrossRef]
2. Grant, L.D.R.; Adams, R.D.; da Silva, L.F.M. Experimental and numerical analysis of single-lap joints for the automotive industry. *Int. J. Adhes. Adhes.* **2009**, *29*, 405–413. [CrossRef]
3. PlasticsEurope Epoxy Resins Committee (ERC). *Epoxy Resins and Curing Agents: Toxicology, Health, Safety and Environmental Aspects*; Plastics Europe Epoxy Resins Committee: Brussels, Belgium, 2017.
4. Khoon Poh, A.; Choy Sin, L.; Sit Foon, C.; Cheng Hock, C. Polyurethane wood adhesive from palm oil-based polyester polyol. *J. Adhes. Sci. Technol.* **2014**, *28*, 1020–1033. [CrossRef]
5. Baroncini, E.A.; Kumar Yadav, S.; Palmese, G.R.; Stanzione, J.F., III. Recent advances in bio-based epoxy resins and bio-based epoxy curing agents. *J. Appl. Polym. Sci.* **2016**, *133*. [CrossRef]
6. Ma, S.; Li, T.; Liu, X.; Zhu, J. Research progress on bio-based thermosetting resins. *Polym. Int.* **2016**, *65*, 164–173. [CrossRef]
7. Celikbag, Y.; Nuruddin, M.; Biswas, M.; Asafu-Adjaye, O.; Via, B.K. Bio-oil-based phenol–formaldehyde resin: Comparison of weight- and molar-based substitution of phenol with bio-oil. *J. Adhes. Sci. Technol.* **2020**, *34*, 2743–2754. [CrossRef]
8. Bertomeu, D.; García-Sanoguera, D.; Fenollar, O.; Boronat, T.; Balart, R. Use of eco-friendly epoxy resins from renewable resources as potential substitutes of petrochemical epoxy resins for ambient cured composites with flax reinforcements. *Polym. Compos.* **2012**, *33*, 683–692. [CrossRef]
9. Kumar, S.; Samal, S.K.; Mohanty, S.; Nayak, S.K. Recent Development of Biobased Epoxy Resins: A Review. *Polym.-Plast. Technol. Eng.* **2017**, *57*, 133–155. [CrossRef]
10. Yang, X.; Guo, L.; Xu, X.; Shang, S.; Liu, H. A fully bio-based epoxy vitrimer: Self-healing, triple-shape memory and reprocessing triggered by dynamic covalent bond exchange. *Mater. Des.* **2020**, *186*, 108248. [CrossRef]
11. Valasek, P.; Muller, M. Recycling of waste rubber powder and micro-particles as filler of thermosets–abrasive wear. *Eng. Rural Develop.* **2014**, *13*, 396–400.
12. Nair, S.S.; Dartiailh, C.; Levin, D.B.; Yan, N. Highly Toughened and Transparent Biobased Epoxy Composites Reinforced with Cellulose Nanofibrils. *Polymers* **2019**, *11*, 612. [CrossRef]
13. Pizzi, A. Recent developments in eco-efficient bio-based adhesives for wood bonding: Opportunities and issues. *J. Adhes. Sci. Technol.* **2012**, *20*, 829–846. [CrossRef]
14. Cohen, E.; Binshtok, O.; Dotan, A.; Dodiuk, H. Prospective materials for biodegradable and/or biobased pressure-sensitive adhesives: A review. *J. Adhes. Sci. Technol.* **2013**, *27*, 1998–2013. [CrossRef]

15. Imam, S.H.; Bilbao-Sainz, C.; Chiou, B.S.; Glenn, G.M.; Orts, W.J. Biobased adhesives, gums, emulsions, and binders: Current trends and future prospects. *J. Adhes. Sci. Technol.* **2013**, *27*, 1972–1997. [CrossRef]
16. Heinrich, L.A. Future opportunities for bio-based adhesives–advantages beyond renewability. *Green Chem.* **2019**, *21*, 1866–1888. [CrossRef]
17. Magalhães, S.; Alves, L.; Medronho, B.; Fonseca, A.C.; Romano, A.; Coelho, J.F.J.; Norgren, M.; Se, M.N. Brief Overview on Bio-Based Adhesives and Sealants. *Polymers* **2019**, *11*, 1685. [CrossRef] [PubMed]
18. Xu, C.; Xu, Y.; Chen, M.; Zhang, Y.; Li, J.; Gao, Q.; Shi, S.Q. Soy protein adhesive with bio-based epoxidized daidzein for high strength and mildew resistance. *Chem. Eng. J.* **2020**, *390*, 124622. [CrossRef]
19. Adams, R.D.; Comyn, J.; Wake, W.C. *Structural Adhesive Joints in Engineering*, 2nd ed.; Springer: Dordrecht, The Netherlands, 1997; ISBN 978-0-412-70920-3.
20. Wake, W.C. *Adhesion and Adhesives: Science and Technology*; Kinloch, A.J., Ed.; British Polymer Journal; Chapman and Hall: London, UK, 1987; Volume 20, p. xii + 441. ISBN 0-412-27440-X.
21. Adams, R.D. *Adhesive Bonding: Science, Technology and Applications*, 1st ed.; Adams, R., Ed.; Woodhead Publishing: Cambridge, UK, 2005; ISBN 978-1-85573-741-9.
22. Volkersen, O. Rivet strength distribution in tensile-stressed rivet joints with constant cross-section. *Luftfahrforschung* **1938**, *15*, 41–47.
23. Goland, M.; Reissner, E. The Stresses in Cemented Joints. *J. Appl. Mech.* **1944**, *11*, A17–A27. [CrossRef]
24. Hart-Smith, L.J. *Adhesive-Bonded Double-Lap Joints*; NASA CR-112235; NASA: Washington, DC, USA, January 1973.
25. Pinto, A.M.G.; Magalhães, A.G.; Campilho, R.D.S.G.; de Moura, M.F.S.F.; Baptista, A.P.M. Single-Lap Joints of Similar and Dissimilar Adherends Bonded with an Acrylic Adhesive. *J. Adhes.* **2009**, *85*, 351–376. [CrossRef]
26. Wu, X.-F.; Jenson, R.A. Interfacial stresses of bonded single-lap joints under mechanical and thermomechani-cal loads. *Int. J. Solid Mater.* **2019**, *1*, 79–115.
27. Sayman, O. Elasto-plastic stress analysis in an adhesively bonded single-lap joint. *Compos. Part B Eng.* **2012**, *43*, 204–209. [CrossRef]
28. Tsai, M.Y.; Morton, J. The effect of a spew fillet on adhesive stress distributions in laminated composite single-lap joints. *Compos. Struct.* **1995**, *32*, 123–131. [CrossRef]
29. Hooda, A.; Goyat, M.S.; Pandey, J.K.; Kumar, A.; Gupta, R. A review on fundamentals, constraints and fabrication techniques of superhydrophobic coatings. *Prog. Org. Coat.* **2020**, *142*, 105557. [CrossRef]
30. Guo, L.; Liu, J.; Xia, H.; Li, X.; Zhang, X.; Yang, H. Effects of surface treatment and adhesive thickness on the shear strength of precision bonded joints. *Polym. Test.* **2021**, *94*, 107063. [CrossRef]
31. Salamat, A.; Islam, T. Fabrication of an anodized porous alumina relative humidity sensor with improved sensitivity. *Instrum. Sci. Technol.* **2020**, *48*, 128–145. [CrossRef]
32. Batista-Grau, P.; Sánchez-Tovar, R.; Fernández-Domene, R.M.; García-Antón, J. Formation of ZnO nanowires by anodization under hydrodynamic conditions for photoelectrochemical water splitting. *Surf. Coat. Technol.* **2020**, *381*, 125197. [CrossRef]
33. Wang, X.; Sun, M.; Murugananthan, M.; Zhang, Y.; Zhang, L. Electrochemically self-doped $WO_3/TiO_2$ nanotubes for photocatalytic degradation of volatile organic compounds. *Appl. Catal. B Environ.* **2020**, *260*, 118205. [CrossRef]
34. Papanicolaou, G.C.; Portan, D.V.; Petropoulos, G.N.; Kontaxis, L.C. Effect of $TiO_2$ nanotubes developed on pure titanium substrates on the mechanical performance of titanium-titanium single-lap adhesive joints. *Cienc. Tecnol. Mater.* **2016**, *28*, 130–137. [CrossRef]
35. Papanicolaou, G.C.; Kontaxis, L.C.; Portan, D.V.; Petropoulos, G.N.; Valeriou, E.; Alexandropoulos, D. Mechanical Performance Enhancement of Aluminum Single-Lap Adhesive Joints Due to Organized Alumina Nanotubes Layer Formation on the Aluminum Adherends. *Appl. Nano* **2021**, *2*, 206–221. [CrossRef]
36. Özel, A.; Kadioglu, F.; Sen, S.; Sadeler, R. Finite element analysis of adhesive joints in four-point bending load. *J. Adhes.* **2003**, *79*, 683–697. [CrossRef]
37. Özel, A.; Aydin, M.D.; Temiz, Ş. The effects of overlap length and adherend thickness on the strength of adhesively bonded joints subjected to bending moment. *J. Adhes. Sci. Technol.* **2004**, *18*, 313–325. [CrossRef]
38. 1050A Aluminium Properties Technical Information. Available online: https://www.metals4u.co.uk/blog/1050a-aluminium (accessed on 25 February 2023).
39. Super Sap INR System. Available online: https://www.pecepoxy.co.uk/data-sheets/TDS_INR_v2.pdf (accessed on 25 February 2023).
40. Araldite LY 1564*/Aradur 2954*-Mouldlife. Available online: https://www.yumpu.com/en/document/read/15623592/araldite-ly-1564-aradur-2954-mouldlife (accessed on 25 February 2023).
41. Zaraska, L.; Sulka, G.D.; Szeremeta, J.; Jaskuła, M. Porous anodic alumina formed by anodization of aluminum alloy (AA1050) and high purity aluminum. *Electrochim. Acta* **2010**, *55*, 4377–4386. [CrossRef]
42. Kozhukhova, A.E.; du Preez, S.P.; Bessarabov, D.G. Preparation of anodized aluminium oxide at high temperatures using low purity aluminium (Al6082). *Surf. Coat. Technol.* **2019**, *378*, 124970. [CrossRef]
43. Fredericks, P. The Complete Guide to Anodizing Aluminum Parts-Aerospace Metals. Available online: https://aerospacemetalsllc.com/the-complete-guide-to-anodizing-aluminum-parts/ (accessed on 25 February 2023).

44. Sulka, G.D.; Stroobants, S.; Moshchalkov, V.; Borghs, G.; Celis, J.-P. Synthesis of Well-Ordered Nanopores by Anodizing Aluminum Foils in Sulfuric Acid. *J. Electrochem. Soc.* **2002**, *149*, D97. [CrossRef]
45. Lim, J.H.; Wiley, J.B. Controlling pore geometries and interpore distances of anodic aluminum oxide templates via three-step anodization. *J. Nanosci. Nanotechnol.* **2015**, *15*, 633–641. [CrossRef]
46. Ozcan, M.; Tunca, B.; Biltas, İ.; Tuken, T. The effect of different pre-surface finishing method on the aluminium anodization of the 6xxx series alloy. *ACTA Metall. Slovaca* **2021**, *27*, 185–189. [CrossRef]
47. Araoyinbo, A.O.; Noor, A.F.M.; Sreekantan, S.; Aziz, A. Voltage effect on electrochemical anodization of aluminum at ambient temperature. *Int. J. Mech. Mater. Eng.* **2010**, *5*, 53–58.
48. Mubashar, A.; Ashcroft, I.A.; Critchlow, G.W.; Crocombe, A.D. Moisture absorption–desorption effects in adhesive joints. *Int. J. Adhes. Adhes.* **2009**, *29*, 751–760. [CrossRef]
49. Ghumatkar, A.; Budhe, S.; Sekhar, R.; Banea, M.D.; De Barros, S. Influence of Adherend Surface Roughness on the Adhesive Bond Strength. *Lat. Am. J. Solids Struct.* **2016**, *13*, 2356–2370. [CrossRef]
50. Cho, T.M.; Choo, Y.S.; Lee, M.J.; Oh, H.C.; Lee, B.C.; Park, T.H.; Shin, Y.S. Effect of Surface Roughness on the Adhesive Strength of the Heat-Resistant Adhesive RTV88. *J. Adhes. Sci. Technol.* **2012**, *23*, 1875–1882. [CrossRef]
51. Pereira, A.M.; Ferreira, J.M.; Antunes, F.V.; Bártolo, P.J. Analysis of manufacturing parameters on the shear strength of aluminium adhesive single-lap joints. *J. Mater. Process. Technol.* **2010**, *210*, 610–617. [CrossRef]

MDPI AG
Grosspeteranlage 5
4052 Basel
Switzerland
Tel.: +41 61 683 77 34

*Materials* Editorial Office
E-mail: materials@mdpi.com
www.mdpi.com/journal/materials

MDPI

Academic Open
Access Publishing

mdpi.com

ISBN 978-3-7258-5134-8